UNIVERSITY OF COPENHAGEN
FACULTY OF SCIENCE

Galaxies in the Early Universe
characterized in absorption and emission

Dissertation submitted for the degree of

Philosophiæ Doctor

to the PhD School of The Faculty of Science, University of Copenhagen

on August 28 2015, by

Jens-Kristian Krogager

Supervisors: *Johan P. U. Fynbo* and *Cédric Ledoux*

Galaxies in the Early Universe

characterized in absorption and emission

初期宇宙における銀河の観察

Abstract

Understanding how galaxies evolved from the early Universe through cosmic time is a fundamental part of modern astrophysics. In order to study this evolution it is important to sample the galaxies at various times in a consistent way through time. In regular luminosity selected samples, our analyses are biased towards the brightest galaxies at all times (as these are easier to observe and identify). A complementary method relies on the absorption imprint from neutral gas in galaxies, the so-called damped Lyα absorbers (DLAs) seen towards distant bright objects. This thesis seeks to understand how the absorption selected galaxies relate to the emission selected galaxies by identifying the faint glow from the absorbing galaxies at redshift $z \approx 2$.

In Chapters 2 and 3, the emission properties of DLAs are studied in detail using state-of-the-art instrumentation. The specific DLA studied in Chapter 3 is found to be a young, star-forming galaxy with evidence for strong outflows of gas. This suggests that the more evolved and metal-rich DLAs overlap with the faint end of the luminosity selected galaxies in terms of mass, metallicity, star formation rate, and age. DLAs are generally observed to have low dust content, however, indications of significant reddening caused by foreground absorbers have been observed. Since most quasar samples, from which the samples of DLAs are composed, are selected through optical criteria in large all-sky surveys, e.g., Sloan Digital Sky Survey (SDSS), there might exist a bias against dusty foreground absorbers due to the reddening causing the background quasars to appear star-like in their optical colours. In Chapters 4 and 5, these hypothesized dusty absorbers are sought for through a combination of optical and near-infrared colour criteria. While a large number of previously unknown quasars are identified, only a handful of absorbers are identified in the two surveys (a total of 217 targets were observed, 137 are previously unknown). One of these targets, quasar J2225+0527, is followed up in detail with spectroscopy from the X-shooter intrument at the Very Large Telescope. The analysis of J2225+0527 is presented in Chapter 6. The dust reddening along the line of sight is found to be dominated by dust in the metal-rich foreground DLA. Moreover, the absorbing gas has a high content of dense, cold and molecular gas with a projected area smaller than the background emitting region of the broad emission lines.

In the last Chapter, a study of the more evolved, massive galaxies is presented. These galaxies are observed to be a factor of $2-6$ times smaller than local galaxies of similar masses. A new spectroscopically selected sample is presented and the increased precision of the redshifts allows a more detailed measurement of the scatter in the mass–size relation. The size evolution of massive, quiescent galaxies is modelled by a "dilution" scenario, in which progressively larger galaxies at later times are added to the population of denser galaxies, causing an increase of the mean size of the population. This model describes the evolution of both sizes and number densities very well, however, the scatter in the model increases with time, contrary to the data. It is thus concluded that a combination of "dilution" and individual growth, e.g., through mergers, is needed.

Preface

In the beginning of the 20th century, it was realized that the Universe was not confined to our own galaxy – the Milky Way – but is instead made up of billions of individual galaxies like our own, the so-called 'island universes'. This shift in our cosmological understanding started a wave of exploratory endeavours looking beyond the edges of the Milky Way. As we looked farther away, we made ever more puzzling discoveries: violent galactic collisions, powerful explosions of stars, and super massive black holes feeding on surrounding gas. We are now starting to see the first galaxies as they looked shortly after the Big Bang; Irregular, clumpy, and full of young stars, gas and dust, these young galaxies are far from the breathtaking spiral- and immense elliptical galaxies we know from the local Universe. An immediate question springs to mind: How did these first clumps of stars turn into the myriad of beautifully arranged galaxies that surround us? A question so complex, that an answer is not to be found in a single lifetime, let alone in a mere Ph.D. thesis. Instead of embarking on a quest so seemingly impossible, as if to play a full orchestra singlehandedly, this thesis seeks to shed light on some of the building blocks that make up part of the answer.

This thesis consists of a collection of my first-author articles written during the last five years. The first chapters (2 through 6) are devoted to the study of gas in young galaxies, a matter best analysed by the use of absorption studies – a technique through which material in front of bright objects can be studied in great detail. In the first chapter, we will investigate how to see the unseen, that is, locating the emission from the material causing absorption towards distant, bright sources – in this case quasars. This will in turn lead us to a search for missing quasars obscured so heavily by the foreground material that these quasars escape detection through the common classification methods. In the last chapter of the first part, we will characterize one such example of a strongly obscuring galaxy.

The last chapter of the thesis (Chapter 7) focuses on the older and more evolved galaxies in the early Universe. These are observed to be more compact than their local analogs, and we will investigate how this evolution in size might have occurred. Rather than assuming an actual growth of each individual galaxy, we studied how the formation of larger galaxies at later times may dilute the compact population and mimic a size evolution.

With this short teaser in mind, we can start digging into the details of galaxy evolution...

Acknowledgements

First of all I want to thank my PhD supervisor, Johan, for the great supervision through the last five years and for granting me the chance to pursue my childhood dreams. I am deeply grateful for the freedom that I have had during my time as a PhD student thanks to Johan. Especially my two year studentship at ESO, Chile has been an unforgettable experience. I thank all of the staff and students at ESO for all the amazing times we have shared. The list of names is too long to mention, but I owe a great debt of gratitude to Joey and Gerrit for accepting me in their home when I arrived to Chile, to Cédric for his dedication and supervision during my studentship, to Claudio (Melo) for gently pushing me to stay in science, to Claudio (Saavedra) and Pablo for moral support and for introducing me to Chilean culture, to Dany, Charles, Simona, Karla, and Sebastian, las amo a mis huevonas enfermas, and last but definitely not least to Liz and Mirjam for always making me smile no matter what! You have all been my second family through my two years in Chile.

I also want to thank all of my exuberant colleagues at DARK. I cannot imagine a better place to be doing research. Thank you Michelle, Julie, Corinne, Brian and Damon for your amazing support both work related and personal. Thank you Sune and Andrew for accepting me in your group; it was a pleasure working with you. Also, I thank Martin (Sparre) for assisting me through the PhD and for sharing your knowledge and great spirit, I am sure we will have many more beers in the future!

And of course I thank my family without whom I would never have made it through. To my parents and all my siblings, Ida, Johanne, Svenning, Anna, and Kathrine, thanks for accepting all my crazy work these past years. And I am deeply grateful for the support of my best friend, Pernille. I am thank all my friends and my amazing choir for all the great times that helped me get my mind off work.

— I owe it all to you, thank you! Gracias! Tak!

Contents

1

Introduction

The first part of the thesis is devoted to the study of neutral hydrogen absorption systems observed towards background quasars. These come in various types depending on the strength of the Lyman α (Lyα) absorption line. In the first five chapters (Chapters 2 through 6), the focus will be on the strongest type of absorbers called damped Lyα absorbers. Below follows a general introduction to damped Lyα absorbers. The last chapter (Chapter 7) of this thesis is devoted to a study of the size evolution of massive, quiescent galaxies. A short summary of the background and the definition of *quiescence* will be presented later in Section 1.4. Throughout the thesis, I will assume a flat ΛCDM cosmology with $H_0 = 67.9\,\mathrm{kms}^{-1}\mathrm{Mpc}^{-1}$, $\Omega_\Lambda = 0.69$ and $\Omega_\mathrm{M} = 0.31$ (Planck Collaboration et al. 2014).

1.1 What are Quasars?

Quasi-stellar objects (QSOs) – or quasars – were first detected as radio sources appearing star-like in their optical counterparts (Schmidt 1963; Matthews & Sandage 1963; Hazard 1964). These intrinsically very luminous objects are now linked to the accretion process of gas onto a massive black hole in the centres of galaxies. Quasars are characterised by a very strong energy output at almost every wavelength from X-rays to radio, and at optical wavelengths the quasars show very characteristic, broad emission lines (Type I). Owing to their high luminosity over a large range of wavelengths, quasars can be selected in many ways, typically through radio or X-ray surveys, or in large optical all-sky surveys such as the Sloan Digital Sky Survey (York et al. 2000) or the 2dF QSO redshift survey (Croom et al. 2004). The quasar selection in optical surveys is primarily based on the fact that quasars appear more blue than stars (the so-called ultraviolet excess, UVX; e.g., Sandage 1965; Schmidt & Green 1983; Marshall et al. 1984). However, such optical criteria are only efficient out to redshift $z \approx 2.2$ where the Lyα forest starts to enter the optical blue filters. Moreover, the optical criteria are more susceptible to the effects of dust as they probe the rest-frame UV of the quasar where the reddening from dust is strongest. For these reasons, a selection method at larger wavelengths was introduced. The technical progress in near-infrared instrumentation lead to the development of the KX method, which utilizes the excess of quasars relative to stars in the K-band (Warren, Hewett, & Foltz 2000). The main principle of the KX method is demonstrated in Figure 1.1.

Recently, more advanced selection techniques are being used to select large samples of quasars based on optical photometry, e.g., neural networks and the so-called extreme deconvolution (see Ross et al. 2012, and references therein). Many of these methods obtain not only the classification, but also an estimate of the photometric redshift, z_phot. With the onset of large, high-cadence sky surveys,

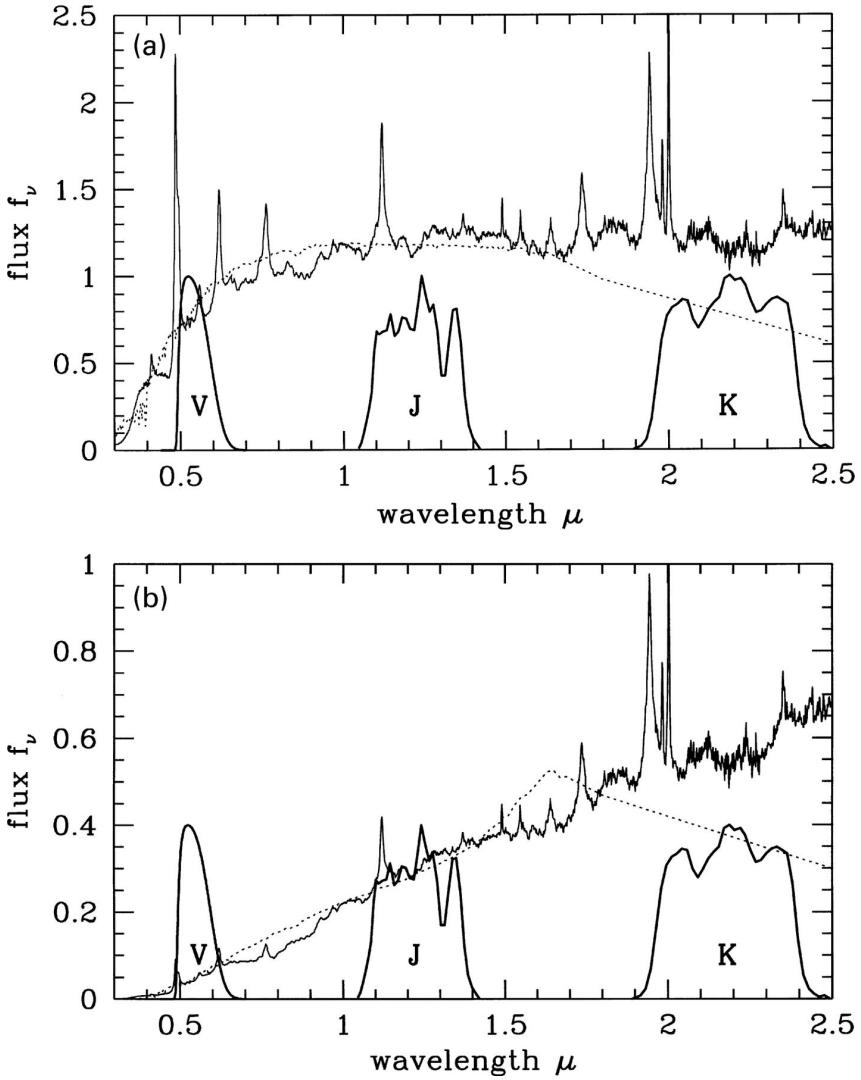

Figure 1.1: Comparison of the spectral energy distribution of quasars and stars, illustrating the principle of the KX method. In each panel, the quasar template is shown by the solid line, and a stellar template of similar $V - J$ colour is shown by the dotted line. The V, J and K transmission curves are over-plotted. The upper plot shows the spectra of an unreddened $z = 3$ quasar and an early K star. The lower plot shows the same quasar template reddened by $E(B–V) = 0.3$ in an intervening system at $z = 2.5$. The spectrum of an early M star is shown for comparison. The K-band excess is clearly visible in both panels, demonstrating the power of the KX method in identifying both reddened and unreddened quasars. This figure is adapted from Warren, Hewett, & Foltz (2000).

one can also use the fact that quasars exhibit temporal variations in brightness to select candidates based on their light curves (Schmidt et al. 2010; Graham et al. 2014). Selecting quasars on the basis of their variability will allow for an efficient selection, which is not biased by dust in the quasar nor in intervening systems. Furthermore, the extreme astrometric precision ($\sim$ 300 μas yr^{-1} in proper motion) of the *Gaia* mission (de Bruijne 2012) allows an unbiased selection of quasars due to the fact that quasars have zero proper motion. For more details about this selection method, see Heintz, Fynbo, & Høg (2015).

The quasars used throughout the thesis are optically selected quasars from the Sloan Digital Sky Survey (SDSS). In Chapters 4 and 5, we investigate a possible bias in the optically selected quasar samples by employing colour criteria in the optical and near-infrared – these criteria are similar to the KX method described above.

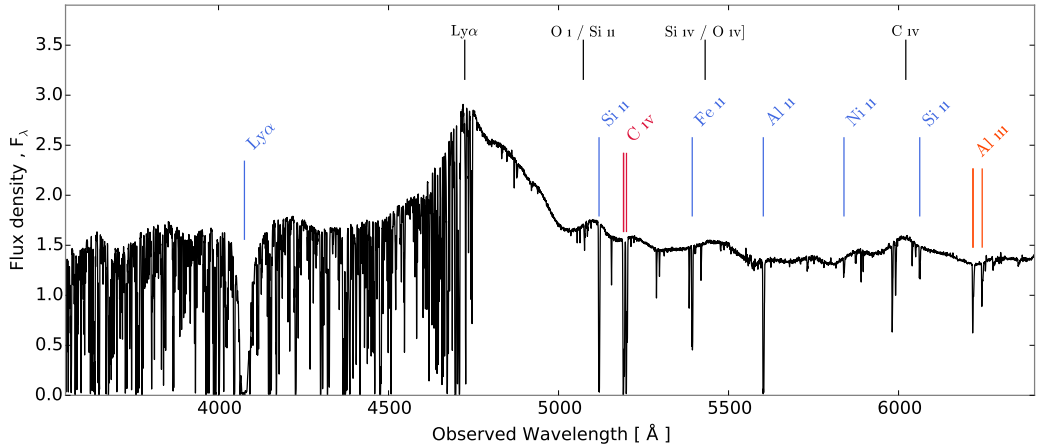

Figure 1.2: Spectrum of a quasar at $z = 2.89$ with an intervening DLA at $z = 2.35$. The strong, damped absorption line from Lyα is clearly seen in the Lyα forest. The most prominent broad emission lines from the quasar are marked in black, and the strongest low-ionization metal lines from the DLA are marked in blue. The higher ionization lines from the DLA are marked in orange and red.

1.2 What are damped Lyα absorbers?

For decades, damped Lyman-α absorbers (DLAs) have been used to study the cosmic reservoir of neutral gas from redshift $z \approx 1.6$ out to a redshift of $z \approx 5$ (Noterdaeme et al. 2012a; Rafelski et al. 2014). Rather than a physical cut, the lower limit on redshift is defined for ground-based surveys that are restricted by the atmospheric cut-off at 3200 Å. DLAs are observable at lower redshifts only from space. As mentioned above, damped Lyman-α absorbers are the strongest absorption features in the family of neutral hydrogen absorbers. In Figure 1.2, a typical quasar spectrum with an intervening DLA is shown. The strong absorption is clearly visible in the dense collection of weaker Lyα absorption lines, the so-called Lyα forest.

DLAs are defined as having column densities in excess of $N_{\rm HI} > 2\times10^{20}$ cm^{-2}. Although appearing rather arbitrary, this definition ensures a high neutrality of the gas in DLAs, i.e., the gas is almost entirely self-shielding contrary to other Lyα absorbers (Lyα forest and Lyman-limit systems). The high neutral gas fraction in DLAs means that ionization corrections are negligible when determining metal line abundances. For this reason it is valid to assume that the singly ionized metal lines[1] trace the total metal abundance, that is: $N({\rm Fe}) = N\,({\rm Fe\,II})$ and so on. Therefore, DLAs serve as some of the most precise probes of chemical enrichment at high redshift.

The first large sample of DLAs was published by Wolfe et al. (1986), who were looking for high-redshift gas-rich disc galaxies by searching for their Lyα absorption in quasar spectra. Since then, many surveys have been carried out (Lanzetta et al. 1991; Lanzetta, Wolfe, & Turnshek 1995; Wolfe et al. 1995; Storrie-Lombardi & Wolfe 2000; Ellison et al. 2001; Péroux et al. 2003), and especially the spectroscopic database of the Sloan Digital Sky Survey (SDSS) has increased the sample sizes significantly (Prochaska et al. 2003b; Noterdaeme et al. 2009b, 2012a). One of the main advantages of the absorption selection technique is that the galaxies are not selected based on their luminosity, but rather on their absorption cross-section. That way a more representative sample of the luminosity function is achieved (Wolfe et al. 1986).

[1]Throughout the thesis, the ionization state of a given element is marked by small roman numerals, e.g., the neutral state is referred to by I, the first ionized state is marked by II, and so forth.

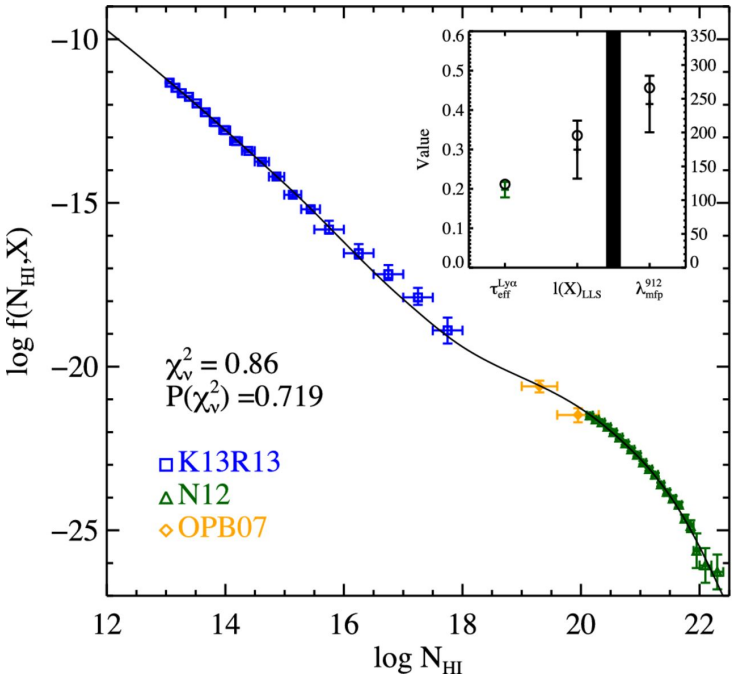

Figure 1.3: Column density distribution function of quasar absorbers normalized by the absorption redshift path. The data shown are a collection from Kim et al. (2013, K13), Rudie et al. (2013, R13), Noterdaeme et al. (2012a, N12), and O'Meara et al. (2007, OBP07). The figure is taken from Prochaska et al. (2014, their fig. 7).

Figure 1.3 shows the distribution function of neutral hydrogen absorbers as function of the column density of H I, $f(N_{\rm HI}, X)$, from Prochaska et al. (2014). The blue points mark Lyα forest absorbers, the yellow points show the so-called super Lyman-limit systems (also sometimes referred to as sub-DLAs), and the green points mark the DLAs. The normalizing quantity, X, represents the absorption path along a given line-of-sight out to redshift, z, and is defined as:

$$X(z) = \int_0^z \frac{H_0}{H(z')}(1+z')^2\, dz' \ ,$$

where H_0 is the Hubble constant, and $H(z)$ denotes the Hubble parameter which for a flat ΛCDM universe is $H(z) = H_0\ \sqrt{(1+z)^3\Omega_{\rm M} + \Omega_\Lambda}$. By integrating over $f(N_{\rm HI}, X)$, one can obtain the mass density of neutral gas:

$$\Omega_g(X)dX = \frac{H_0\ \mu\ m_H}{c\ \rho_c} \int_{N_{\rm min}}^{N_{\rm max}} N_{\rm HI} f(N_{\rm HI}, X)\ dN_{\rm HI}\ dX \ ,$$

where μ is the mean molecular weight ($\mu = 1.3$); m_H is the mass of a hydrogen atom, and ρ_c is the current critical density. If one sets the lower integration boundary to the limiting column density for DLAs ($N_{\rm min} = 2\times10^{20}\ cm^{-2}$) and integrates over all larger $N_{\rm HI}$ ($N_{\rm max} = \infty$), one obtains a measure of the contribution from DLAs to the total gas mass density. Due to the shape of the distribution function, damped Lyα absorbers dominate the neutral gas content in the Universe for all redshifts lower than $z \approx 5$ (Noterdaeme, Petitjean, Ledoux, & Srianand 2009b). And as such, DLAs are important tools in our understanding of galaxy formation and evolution since they probe the neutral gas that eventually may condense and form stars.

1.2.1 Metal Absorption in DLAs

Along with the strong Lyα absorption line seen in the quasar spectrum we always observe corresponding absorption lines from metal transitions, the dominant lines being from low-ionization lines. Higher ionization states are also typically observed, e.g., C IV, Al III, and O VI, indicating that a DLA sightline traces multiple interfaces of gas clouds. The low-ionization metal lines typically show very complex line structures with many components, especially at high metallicities (Prochaska & Wolfe 1997). There are several ways to recover the column densities of the metal absorption lines (e.g., Savage & Sembach 1991, and references therein); However, in this thesis I have chosen to fit the line profiles as this allows a better handling of blended and contaminated lines. For this purpose, the most appropriate method is to fit strong, though not saturated, absorption lines with a Voigt profile (saturated lines are defined later in Sect. 1.3). The Voigt profile is obtained by convolution of the Gaussian and the Lorentzian distribution functions; However, for practical purposes, an analytical approximation is used. An absorption line is defined by the column density of the given species, N, the broadening parameter, b, and a set of atomic parameters for the specific transition (here marked by subscript i): the resonant wavelength, λ_i; the oscillator strength, f_i; and the damping constant, Γ_i. When fitting the absorption lines, one seeks to recover N and b, assuming that the atomic parameters are well-determined. The details of the fitting method are presented in Appendix A.1.

Probing the nature of DLAs from metal absorption lines

By measuring the abundances of metals present in DLAs, e.g., S, Si, Fe, Zn, it is possible to map out the chemical enrichment in the densest regions throughout most of cosmic time[2] (Kulkarni & Fall 2002; Prochaska et al. 2003a; Rao et al. 2005; Rafelski et al. 2014). Figure 1.4 shows the latest compilation of metallicities, [M/H][3], as a function of redshift from Rafelski et al. (2014). The study presented by Rafelski et al. shows that DLAs on average are metal poor at all times relative to Solar and that the average metallicity (blue points) shows a gradual increase. If the relation is extrapolated to $z = 0$, a local value of $Z_0/Z_\odot \approx 0.2$ is found. However, the overall population of disc galaxies locally have metallicities around $Z/Z_\odot \sim 1$. This apparent metal deficiency led to the conclusion that DLAs could not be the progenitors of today's star-forming disc galaxies (e.g., Pettini 1999).

One of the hypotheses back when the first DLA samples were being assembled was that galaxies formed from a single collapse of a massive gas cloud, which would lead to the formation of a gaseous, thin disc (e.g., Eggen, Lynden-Bell, & Sandage 1962). The Lyα absorption seen towards quasars was thought to trace these gas discs of galaxies in the making. This was further studied through the kinematical information recovered from the velocity structure of the metal lines. Prochaska & Wolfe (1997) (and also Ledoux et al. 1998) use the velocity width, ΔV_{90}, of the low-ionization lines to investigate the underlying population of galaxies responsible for the absorption. These authors define ΔV_{90} as the velocity encompassing 90 percent of the apparent optical depth of the line, $\tau' = -\ln(I_{\rm obs})$.

[2] In the assumed cosmology, a redshift of $z = 5$ corresponds to a look-back time of 12.62 Gyr, i.e., around 90 per cent of the age of the Universe.

[3] Throughout the thesis I will use the notation [M/H] to denote the abundance ratio of an arbitrary indicator, usually a volatile element such as Zn or S, relative to the Solar abundance ratio.

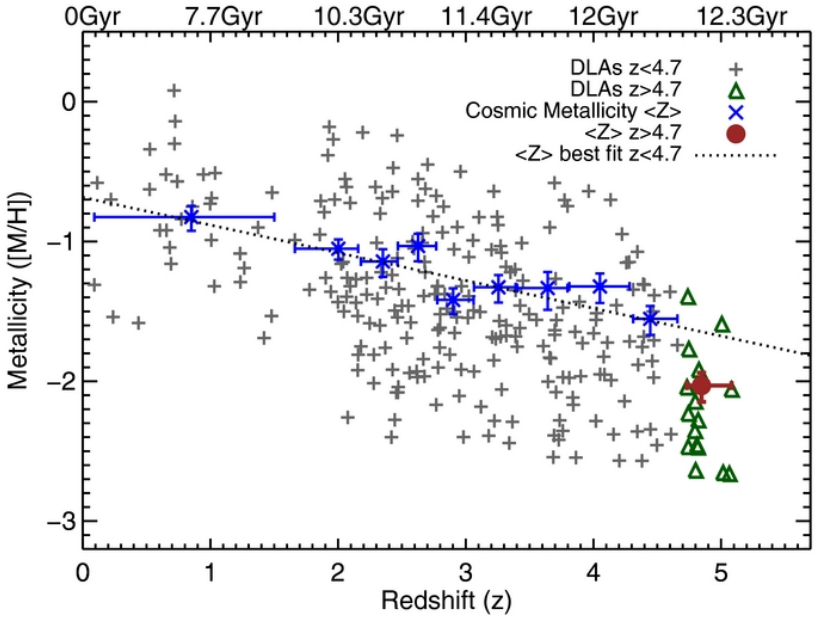

Figure 1.4: Cosmic metallicity evolution of DLAs as function of redshift. From Rafelski et al. (2014, their fig. 3).

From the distribution of τ' for a given line, one can calculate the line centroid, λ_0, along with the 5$^{\text{th}}$ and 95$^{\text{th}}$ percentiles, λ_5 and λ_{95}, respectively. The velocity width is then obtained as follows:

$$\Delta V_{90} = c\,\frac{\lambda_{95} - \lambda_5}{\lambda_0}\,.$$

By modelling absorption lines through various geometries and quantifying these modelled spectra in terms of ΔV_{90} and the component structure, Prochaska et al. conclude that the observed absorption line profiles are consistent with those expected from large rotating discs of gas (Prochaska & Wolfe 1997, 1998). However, within the ΛCDM paradigm of cosmology, galaxies are predicted to form via hierarchical merging of substructures; hence high-redshift DLAs should originate in these galactic clumps rather than being signatures of large disc galaxies (e.g., Tyson 1988; Gardner et al. 1997; Haehnelt, Steinmetz, & Rauch 1998).

How do we connect our knowledge about the gas phase absorption to the galaxies we observe in direct emission? Chapters 2 and 3 are devoted to the study of this puzzling link between absorption and emission properties of the galaxies causing DLAs.

1.2.2 Dust and Molecules in DLAs

Dust is a ubiquitous substance throughout the Universe and its presence is linked to many phases of the evolution of stars, galaxies and quasars. Nevertheless, most astronomers have a peculiar love-hate relationship with cosmic dust. On the one hand, dust properties are important and indeed very interesting to study as the dust grains serve as primary catalysts for the formation of molecular hydrogen in the interstellar medium (e.g., Hollenbach & Salpeter 1971). Moreover, the dust grains in the early stellar phases clump together to produce planetesimals and subsequently facilitate the formation of life (e.g., Lissauer 1993). On the other hand, dust scatters the light from distant objects hampering their detection and analysis.

The observable effect of dust

The main observable effect of dust grains is the scattering of incident light rays. This results in two effects: it makes the source appear fainter and redder, due to the wavelength dependent scattering. This is most commonly quantified in terms of a 'reddening curve' (or extinction law/curve), which ascribes a functional form to the wavelength dependent attenuation $A(\lambda)$ relative to the attenuation in the optical V-band, $A(V)$. This is also sometimes given in terms of the 'colour excess', $E(B-V) = A(B)-A(V)$, i.e., the difference between the observed colour $(B-V)$ and the intrinsic colour $(B-V)_0$. The colour excess and attenuation are linked through the parameter $R_V \equiv A(V)/E(B-V)$, which simply put is a measure of the slope of the reddening curve. Various functional forms exists; however, the main distinction can be made between Milky Way-type and Small Magellanic Cloud (SMC) type depending on the presence or absence, respectively, of the so-called 2175 Å bump. The exact origin of this feature is not known, but it is usually ascribed to carbonaceous dust grains (e.g., Draine 2003, and recently Misma & Li, 2015). A general functional form used to describe reddening curves is the Fitzpatrick & Massa (1990) formulation[4], which provides an analytical form with 7 parameters:

$$k(\lambda - V) \equiv \frac{E(\lambda - V)}{E(B-V)} = \begin{cases} c_1 + c_2 x + c_3 D(x, x_0, \gamma), & x \leq c_5 \\ c_1 + c_2 x + c_3 D(x, x_0, \gamma) + c_4 (x - c_5)^2, & x > c_5 \end{cases} \tag{1.1}$$

where $x = \lambda^{-1}$ is the reciprocal wavelength and $D(x, x_0, \gamma)$ is the broad Drude component to represent the 2175 Å bump:

$$D(x, x_0, \gamma) = \frac{x^2}{(x^2 - x_0^2)^2 + x^2\gamma^2} \, , \tag{1.2}$$

for which the peak location and width are given by x_0 and γ, respectively. In the following Chapters, I will use the extinction curve in terms of $A(V)$ rather than $E(B-V)$:

$$\xi(\lambda) = \frac{A(\lambda)}{A(V)} = \frac{1}{R_V} k(\lambda - V) + 1 \, . \tag{1.3}$$

In Chapter 4, we used the extinction curves parametrized by Pei (1992); whereas in Chapters 5 and 6, we used the best-fitting parameters from Gordon et al. (2003a), who obtain parameters for Small Magellanic Cloud (SMC), Large Magellanic Cloud (LMC), and Milky Way (MW) types.

Dust in DLAs

If DLAs are, as hypothesized, associated to the gas in star-forming galaxies then one would expect the DLAs to harbour dust grains, as dust is expected both in the formation process of stars and during the final stages of stellar evolution. Therefore, several studies have searched for dust in DLAs (e.g., Fall, Pei, & McMahon 1989; Pei, Fall, & Bechtold 1991). The way to look for dust in a DLA is usually to look at the reddening effect of the dust on the background quasar. This can either be done in a statistical approach, where one compares samples of quasars with and without DLAs, or in an individual object.

[4]Here I give the expanded formalism including the c_5 parameter introduced by Fitzpatrick & Massa (2007)

The statistical approaches can be divided into three groups:

1. The first approach is based on spectroscopic data where the reddening may be recovered by fitting the slope of the quasar spectrum in the rest-frame UV (Pei, Fall, & Bechtold 1991; Murphy & Liske 2004; Kaplan et al. 2010).

2. The second approach is purely photometric in nature and relies on the measurement of colours of the quasar (e.g., Maiolino et al. 2001; Vladilo, Prochaska, & Wolfe 2008; Maddox et al. 2008; Khare et al. 2012).

In both the first and second approaches, the reddening is estimated by comparing the metric (either UV slope or colour) for the sample of quasars with and without DLAs. This way the reddening can be estimated with no assumption regarding the extinction curve.

3. The third approach uses stacking to infer an average spectrum of quasars with and without DLAs. The ratio of these two stacked spectra will reveal the average wavelength dependent attenuation (Frank & Péroux 2010a; Khare et al. 2012). This approach is therefore sensitive to the type of extinction curve.

While these approaches work well on large statistical samples, they fall short when trying to estimate the amount of dust in any single DLA. Instead, the presence of dust in a DLA can be inferred purely by looking for the dust emission from the DLA galaxy and by analyzing the abundance ratio of metals (Khare et al. 2004; Vladilo & Péroux 2005; Vladilo, Prochaska, & Wolfe 2008, e.g.,). Elements such as iron, chrome, &c. (the so-called refractory elements) have a high affinity for dust. As the refractory elements condensate and form dust, the gas-phase abundance of these elements will decrease compared to non-refractory (volatile) elements, e.g., Zn or S. The commonly used ratio [Fe/Zn] thus indicates how much iron has been depleted from the gas-phase – assuming an intrinsic abundance pattern of the DLA. The exact intrinsic abundances for DLAs has been studied in great detail, however, no consensus has yet been reached (for a recent discussion, see Berg et al. 2015, and also Rafelski et al. 2012). The depletion can be translated to a measure of the attenuation through the theoretical relation between attenuation and the column density of iron in the dust phase (e.g., Vladilo et al. 2006; De Cia et al. 2013). This method as well as its caveats are described in more detail in Chapter 6.

Last but not least, one can use quasar templates (quasar spectra stacked to generate a mean spectrum) to fit the observed spectrum with an assumed dust model. This is the approach which is used in Chapters 4, 5, and 6 to infer $A(V)$ towards quasar sightlines. The model is presented in detail in Appendix A.2.

In general, the effect of dust in existing DLA samples is not large, and some studies completely dismiss any significant dust reddening from DLAs (Murphy & Liske 2004; Frank & Péroux 2010b). Nonetheless, the DLAs with higher metallicities are found to have higher depletion ratios ([Fe/Zn]) and thus probably higher dust content (Ledoux, Petitjean, & Srianand 2003). In later studies, it was shown that if the analysis is limited to the metal-rich DLAs, a significantly higher amount of dust is inferred (Kaplan et al. 2010; Khare et al. 2012). The subsequent detection of individual DLAs with high $A(V)$ (Fynbo et al. 2011; Noterdaeme et al. 2012b; Wang et al. 2012) led us to the search for dust reddened quasars. The hypothesis is that metal-rich and dusty DLAs might be missed in the optically selected quasar samples due to the reddening effects of dust in the foreground absorber (Fall, Pei, & McMahon

1989; Pei, Fall, & Bechtold 1991; Pei & Fall 1995; Pontzen & Pettini 2009). The current samples of DLAs would therefore be biased against systems with large dust column densities, high metallicities, and typically also high $N_{\rm HI}$ (see also Boissé et al. 1998). Following this hypothesis, we initiated a spectroscopic survey for red quasars, based on optical and near-infrared photometric criteria. The first pilot study is presented in Chapter 4. Building on the experience of the pilot study, the spectroscopic survey was expanded and revised. In Chapter 5, the revised criteria and results are presented.

Molecular hydrogen absorption in DLAs

Assuming that the gas in DLAs are related to *in-situ* star formation, the presence of H_2 would be expected in DLA sight lines. However, detections of H_2 are very scarce. The first detection of H_2 was reported by Levshakov & Varshalovich (1985) and Foltz, Chaffee, & Black (1988), and since then very few systems with molecular hydrogen have been detected (see Balashev et al. 2015, and references therein).

From the few detections at hand, a low molecular fraction, $f_{\rm H_2} \lesssim 0.01$, is usually inferred (Ledoux, Petitjean, & Srianand 2003; Noterdaeme et al. 2008; Srianand et al. 2008b; Noterdaeme et al. 2010; Jorgenson et al. 2014; Noterdaeme, Petitjean, & Srianand 2015). This is about a factor of 10 less than for sightlines through the interstellar medium (ISM) of the Milky Way. The low molecular fraction in DLAs is commonly ascribed to the low metallicities in the average population. As mentioned above, dust grains are important catalysts for the formation of H_2 and the amount of dust is related to the amount of metals in the gas phase. Therefore, the low metallicities in DLAs result in low efficiencies for H_2 formation. Also, the Milky Way sightlines probe the interstellar material in a different way than the DLA sightlines do. A DLA sightline will typically intersect multiple phases of the ISM of a galaxy, whereas the Milky Way sightlines usually only probe a single cloud (Noterdaeme, Petitjean, & Srianand 2015). The hydrogen column density for DLAs will therefore trace the entire multiphase medium, and not just the local medium around the molecular phase.

Furthermore, as we will see in Chapters 4, 5, and 6, the dust-rich DLAs, which are more likely to have strong H_2 absorption, might be underrepresented in current samples due to the dust obscuration bias against dusty sightlines mentioned above.

1.3 X-Shooter Data

A substantial part of this thesis is based on spectra obtained with the X-shooter spectrograph mounted on the Very Large Telescope operated by ESO at Paranal, Chile. The instrument splits the incoming light into three separate spectrographs (called arms: UVB, VIS, and NIR) thereby covering the full range of wavelengths from the atmospheric cut-off to the K-band simultaneously. The three arms operate at medium resolution ranging from $\mathcal{R} \sim 3000 - 10,000$ in UVB, $\mathcal{R} \sim 5000 - 18,000$ in VIS, and $\mathcal{R} \sim 4000 - 11,000$ in NIR depending on the used slit-width and seeing. Further details about the data are presented in the respective chapters.

For the spectral analysis in this thesis (Chapters 3 and 6), the spectra were obtained with a resolution of $\mathcal{R} = 11,000$ in the visual arm (VIS). The spectral resolution results in a broadening of spectral features, especially for features that are intrinsically narrower than the resolution. The broadening can lead to an effect called *hidden saturation*, where intrinsically narrow and saturated lines appear unsaturated due to the spectral broadening of the instrument. The effect of hidden saturation is shown

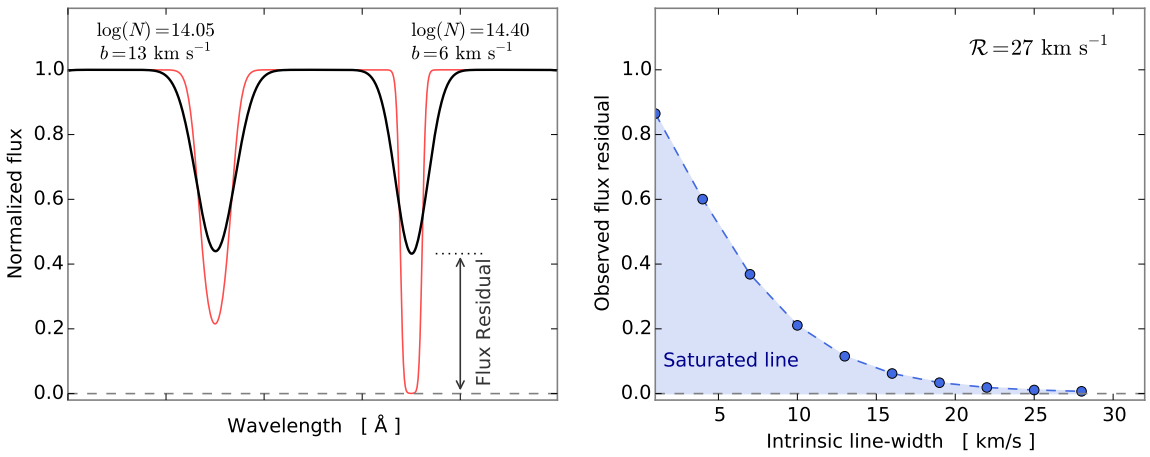

Figure 1.5: Simulated line profiles (*left*) and flux residual of a saturated line as function of its intrinsic line-width, b (*right*). The left panel shows two absorption lines with almost identical flux residuals. The thin, red line shows the intrinsic line profile, and the thick, black line shows the same line profile convolved with the instrumental resolution of $\mathcal{R} = 27$ km s^{-1} as it would be observed. For each line, the line-width, b, and column density, $\log(N)$, are given above the line. Although appearing similar in the observed line profile, the right absorption line is clearly saturated. This effect is due to the so-called hidden saturation caused by the instrumental line spread function, here assumed to be Gaussian. In the right panel, the flux residual of a saturated absorption line is shown as function of its intrinsic line-width. If the flux residual at peak absorption is below the curve, i.e., in the shaded region, the line will be saturated. Intrinsic line-widths for DLAs are typically larger than $b \gtrsim 4$ km s^{-1}; hence, a line with flux residual larger than ~ 0.6 will be unaffected by hidden saturation independent of the line-width. Note that for very small b-values, this function is not well-behaved as numerical artefacts start to dominate the evaluation of the line-centre.

schematically in Figure 1.5. Hidden saturation can have severe implications for the determination of the column densities of strong metal lines, since saturated lines are not sensitive to the column density. Therefore, strong lines should be avoided when inferring column densities from spectral absorption lines. The definition of a 'strong' line depends on the instrumental resolution as well as the unknown intrinsic line width. For X-shooter working at $\mathcal{R} = 11,000$ (27 km s^{-1}), an absorption line with flux residual at peak absorption of less than 0.6 is potentially affected by hidden saturation depending on the intrinsic line-width, b, see right panel of Figure 1.5.

By limiting the analysis to lines that have flux residuals at peak absorption of less than 0.6, we can be fairly sure that the results will not be biased, unless the lines are extreme narrow intrinsically. Such narrow lines, however, are not observed in the low-ionization metal lines, but are more often seen in molecular H_2 lines. In Chapter 6, we include a few transitions (Fe II and S II) which are slightly stronger than the limit derived above. However, since we also include a weaker iron transition, which is definitely not saturated, we can be sure that the fit will not be biased by any possible hidden saturation. The fit for the sulphur line might be slightly underestimated, since we cannot correct for the effect without other weaker transitions available in the spectral range.

1.4 Evolved Galaxies

Thanks to the development in near-infrared (NIR) instrumentation both from ground and space we have been able to study the $z = 2$ Universe in high detail. One of the most striking discoveries at high redshift is the existence of a population of old and evolved galaxies (Franx et al. 2003), the so-called distant red galaxies (DRGs). Using high quality NIR imaging from the *Hubble Space Telescope (HST)*, several works have shown that these massive ($M_\star > 10^{11}$ $M_\odot$) galaxies are much more compact than local galaxies with similar masses. The origin and subsequent evolution of these compact, evolved galaxies are still being investigated heavily. One of the most favoured evolutionary scenarios explains the formation of the compact galaxies through early gas-rich interactions at high redshift, which ignite a central starburst. The burst of star formation leads to a high central concentration of stars enshrouded in dust. In the centre of the resulting galaxy, a powerful quasar starts to clear out gas and dust from the central parts of the galaxy. The quasar quenches the star formation and a compact, quiescent galaxy is left behind. This compact galaxy hereafter grows via encounters with minor companions: a mechanism called minor, dry merging. "Dry" here refers to the fact that the merging does not involve any significant gas to trigger new star formation. The scenario is summarized in Fig. 1.6. Nevertheless, the proposed evolutionary scenario depicted above is highly debated. The exact mechanisms responsible for the size growth and for turning off star formation are still unknown.

Other mechanisms than merging have been proposed to explain the size growth, e.g., star formation at later times and quasar feedback; however, the most favoured mechanism has been minor merging. A cascade of merging events has been shown (Oser et al. 2012) to effectively increase the half-light radius without changing the central density much (in agreement with observations). Other studies, however, show that dry merging does not sufficiently describe the size evolution at all times (e.g., Newman et al. 2012).

At the same time, Newman et al. (2012) show that galaxies which formed at later times are larger on average. This is generally understood as a consequence of less gas-rich interactions at lower redshifts leading to less compact remnants. This indicates that individual galaxies themselves do not need to evolve strongly in size. Instead, the quenching of larger galaxies at later times may increase the average size of the evolved population as a whole. In Chapter 7, we will study the effect of this "dilution" through a spectroscopically selected sample at redshift $z \approx 2$.

1.4.1 Star-forming or Passively Evolving?

In order to study the quiescent galaxy population, one needs a way of separating the quiescent galaxies (QGs) from star-forming galaxies (SFGs). This is rather trivial at low redshift where the massive, red, elliptical galaxies are easily distinguished from blue, disc-dominated, star-forming galaxies. At redshift $z \sim 2$, the distinction between the two classes becomes less clear as the galaxies are only barely resolved. Moreover, a large fraction of the star-forming galaxies is enshrouded in dust, making the star-forming galaxies appear red. For this reason, a simple one-colour criterion is not sufficient, and either an additional colour or magnitude must be included. The UVJ selection is one such classification method out of many. The classification is based on photometry in rest-frame $U - V$ and $V - J$ colours (Labbé et al. 2005; Williams et al. 2009), and the method is therefore model-dependent and relies on the assumed spectral shape in order to calculate the fluxes at the rest-frame wavelengths (e.g., Brammer, van Dokkum, & Coppi 2008; Taylor et al. 2009). The UVJ method is illustrated in Figure 1.7.

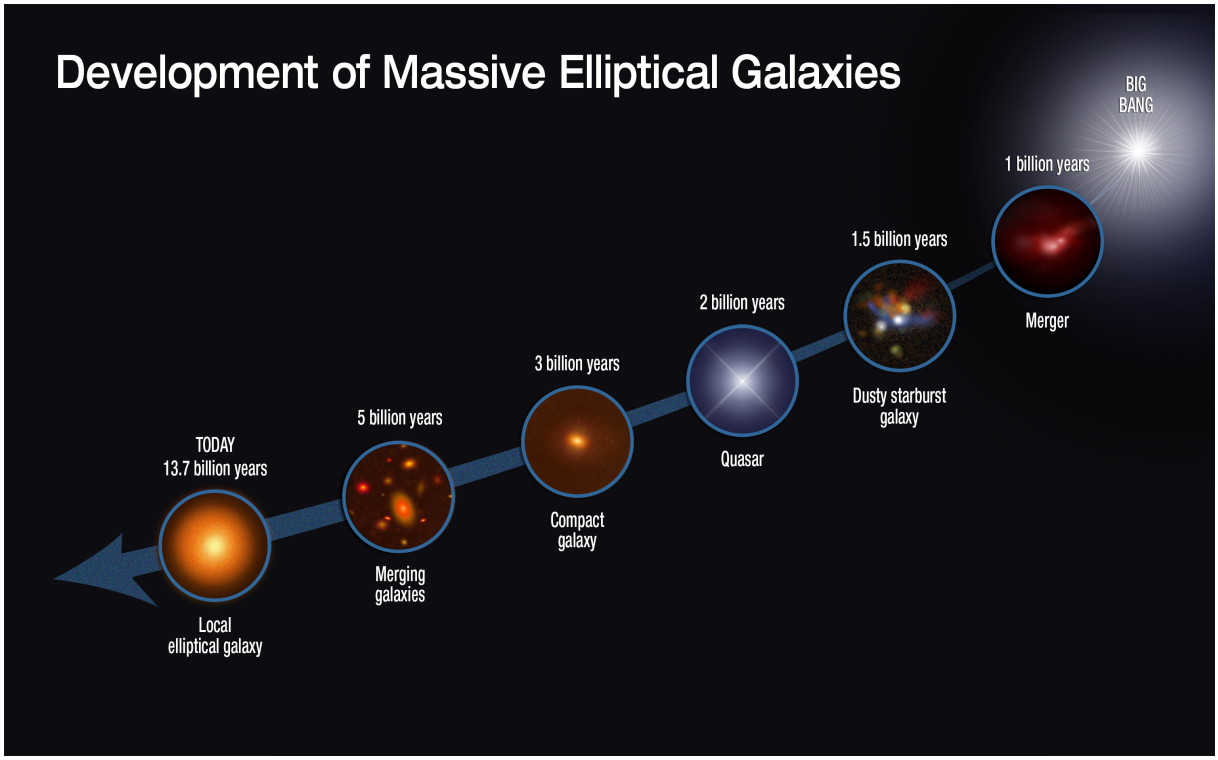

Figure 1.6: An illustration of the proposed evolutionary phases for large elliptical galaxies observed locally. The merging of gas-rich galaxies in the early Universe ignites a starburst, creating a remnant shrouded in dust. An active quasar phase quenches further star formation, resulting in a compact galaxy, which subsequently grows through merging with small, gas-poor satellite galaxies.
(Credit: Sune Toft and the NASA/ESA *Hubble Space Telescope* press office. Release number 14-028, January 2014.)

Another similar approach is the so-called BzK method, which relies on the observed $B-z$ and $z-K$ colours: $BzK \equiv (z-K)_{\rm AB} - (B-z)_{\rm AB}$ (Daddi et al. 2004). Since the BzK method uses observed colours rather than rest-frame colours, it is not as such prone to errors introduced by the interpolation of rest-frame colours. However, the distinction between SFGs and QGs is more clearly defined over a large redshift span for the UVJ method. For comparison, the BzK diagram is shown in Figure 1.8. While the separation between low- and high-redshift galaxies is easily identified in the BzK diagram, the distinction between star-forming and quiescent galaxies is less obvious. In the UVJ diagram, this separation into star-forming and quiescent galaxies is clearly identified for redshifts less than $z < 2$ (Williams et al. 2010). Due to the enhanced sensitivity to star-formation rate in the UVJ diagram, we have chosen to use the UVJ method in Chapter 7. The photometric classification is bolstered by the recovered star formation rates from the full photometric and spectral modelling, see Section 7.4 in Chapter 7. Furthermore, the sources that have significant (i.e., more than 3 σ) detections at 24 μm are all classified as star-forming using the UVJ method. Correspondingly, all the galaxies classified as quiescent from UVJ method are either detected at less than 3 σ or not detected at all. For reference, the 24 μm fluxes and the UVJ classifications for the spectroscopic sample in Chapter 7 are given in Table 1.1.

Table 1.1: MIPS 24 μm fluxes for the spectroscopic sample of Chapter 7.

ID	$F_{24\,\mu\mathrm{m}}$ (μJy)	Classification[a]
118543	321.80 ± 8.59	SFG
121761	84.48 ± 8.63	SFG
122398	$< 21.91\ (3\sigma)$	QG
123235	79.20 ± 8.84	SFG
124666	...	QG
126824	65.21 ± 8.77	SFG
127466	$< 24.65\ (3\sigma)$	QG
127603	43.61 ± 8.30	SFG
128061	...	QG
128093	149.55 ± 7.79	SFG
129022	...	QG
134068	489.63 ± 8.47	SFG
135878	...	QG
140122	$< 18.80\ (3\sigma)$	QG

[a] based on UVJ method.

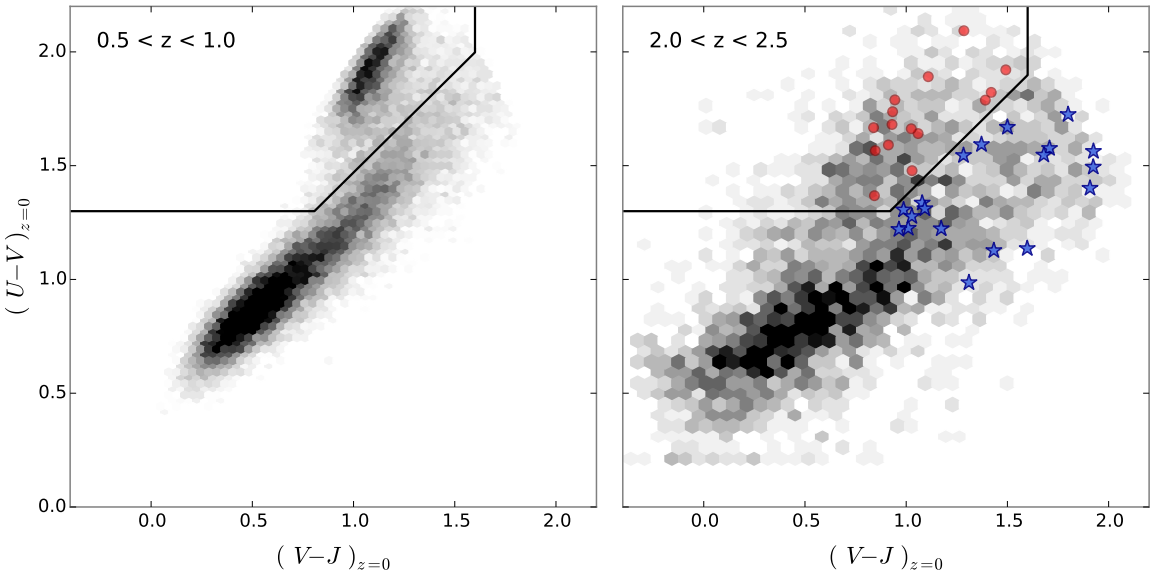

Figure 1.7: UVJ rest-frame colour-colour diagram. The left panel shows data for intermediate redshifts $0.5 < z < 1.0$ and the right panel shows data for high redshifts $2.0 < z < 2.5$. The 2D-histograms show photometric data from Muzzin et al. (2013). In each panel, the division between star-forming and quiescent from Williams et al. (2009) is shown by the black lines; quiescent galaxies reside in the upper left corner. In the right panel, the quiescent (red circles) and star-forming (blue stars) sub-samples from Chapter 7 are shown.

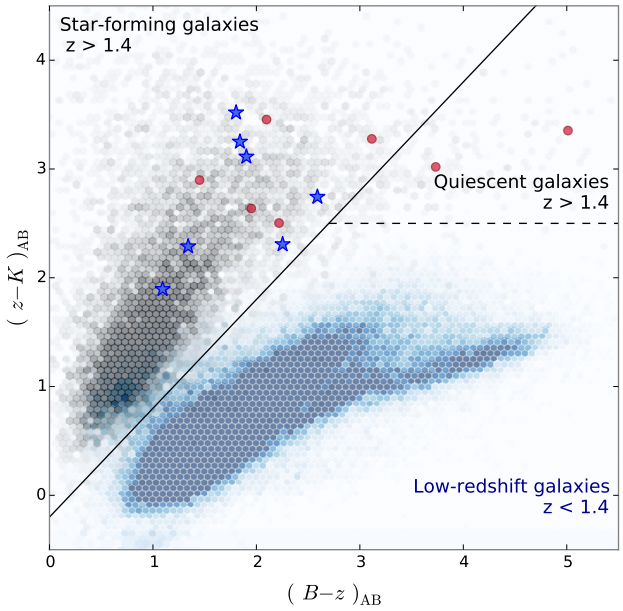

Figure 1.8: $B - z$ vs $z - K$ colour-colour diagram. Galaxies at low ($z < 1$) and high ($1.9 < z < 2.5$) redshifts are shown by the blue and black 2D-histograms, respectively. The photometric data are compiled from Muzzin et al. (2013). The BzK division between high and low redshift galaxies is shown by the black lines. Low-redshift galaxies reside in the lower right part of the diagram; high-redshift, quiescent galaxies reside in the upper right corner between the solid and dashed lines; and high-redshift, star-forming galaxies reside in the upper left corner. The quiescent (red circles) and star-forming (blue stars) sub-samples using the UVJ method from Chapter 7 are shown. The two sub-samples are not distinguishable using the BzK method.

2

Metal-rich damped Lyman-alpha absorbers as probes of low-luminosity galaxies

This chapter contains the following article:

"On the sizes of $z \gtrsim 2$ Damped Lyα Absorbing Galaxies" *

Published as a Letter in *Monthly Notices of the Royal Astronomical Society: Letters, vol. 424, pp. L1-L5, 2012.*

Authors:

J.-K. Krogager, J. P. U. Fynbo, P. Møller, C. Ledoux, P. Noterdaeme,
L. Christensen, B. Milvang-Jensen, & M. Sparre

Recently, the number of detected galaxy counterparts of $z \gtrsim 2$ damped Lyman α absorbers in QSO spectra has increased substantially so we today have a sample of 10 detections. Møller et al. in the year 2004 made the prediction, based on a hint of a luminosity–metallicity relation for DLAs, that H I size should increase with increasing metallicity. In this Letter we investigate the distribution of impact parameter and metallicity that would result from the correlation between galaxy size and metallicity. We compare our observations with simulated data sets given the relation of size and metallicity. The observed sample presented here supports the metallicity–size prediction: The present sample of DLA galaxies is consistent with the model distribution. Our data also show a strong relation between impact parameter and column density of H I. We furthermore compare the observations with several numerical simulations and demonstrate that the observations support a scenario where the relation between size and metallicity is driven by feedback mechanisms controlling the star-formation efficiency and outflow of enriched gas.

* Based on observations made with the Nordic Optical Telescope, operated on the island of La Palma jointly by Denmark, Finland, Iceland, Norway, and Sweden, in the Spanish Observatorio del Roque de los Muchachos of the Instituto de Astrofisica de Canarias. Based on observations collected at the European Organisation for Astronomical Research in the Southern Hemisphere, Chile under programs 084.A-0303(A) and 086.A-0074(A).

2.1 Introduction

The size of high-redshift galaxies, its correlation with other properties like mass or luminosity, and its evolution with redshift are fundamental quantities to measure (e.g., Rees & Ostriker 1977). Quasar absorption-line studies provide an interesting way to address these relations as the method is sensitive to galaxies over a large range of masses and sizes (e.g., Nagamine et al. 2007; Pontzen et al. 2008; Cen 2012) and because it is complementary to the information gathered from studying the stellar light of galaxies (e.g., Ferguson et al. 2004).

Damped Lyman-α absorbers (DLAs) are believed to be the absorption signature of neutral interstellar gas in galaxies (see Wolfe, Gawiser, & Prochaska 2005, for a review). When the first sample of DLAs was collected it was found that the total cross-section for DLA absorption was about five times higher than what would be expected from the density and sizes of local spiral galaxies (Wolfe et al. 1986, see also Møller & Warren 1998). Wolfe et al. (1986) and also Smith, Cohen, & Bradley (1986) put forward the view that DLAs could be forming disks with radii $\sim \sqrt{5}$ times larger than local spirals. In this view, galaxies were *larger* in the past, which would be at odds with the prevailing hierarchical model of galaxy formation. On the other hand, Tyson (1988) argued that DLAs could be caused by a population of many small (much smaller than local spirals), gas-rich dwarf galaxies (see also Haehnelt, Steinmetz, & Rauch 1998; Ledoux et al. 1998).

Detecting the absorbing galaxies in emission is the most obvious way to determine the sizes of DLAs from the distribution of impact parameters relative to the background QSOs. Another method is to measure the extent of 21 cm or X-ray absorption against extended background sources (Briggs et al. 1989; Dijkstra, Haiman, & Scharf 2005), but such extended background sources are currently rare. Also, information on sizes can be inferred from DLAs towards lensed QSOs (Smette et al. 1995; Ellison et al. 2004, 2007; Cooke et al. 2010), but such systems are also rare. Given the proximity of the bright QSO to the line of sight to the absorbing galaxy, the first approach adopted was to search for Lyα emission from the absorbing galaxy as the DLA itself here removes the light from the background QSO (Foltz, Chaffee, & Weymann 1986). Two observing strategies were adopted reflecting two different ideas about the nature of DLAs. Under the assumption that the H I extent of DLA galaxies is small their impact parameters relative to the QSO will also be small. Therefore a long-slit centred on the QSO should have a high probability of also covering the DLA (e.g., Hunstead, Pettini, & Fletcher 1990, and references therein). If, on the other hand, DLAs arise from large H I discs they may have large impact parameters relative to the QSO and narrow-band imaging will be a better approach as it eliminates the risk of missing the object on the slit (Smith, Cohen, & Bradley 1986; Møller & Warren 1993). Later, spectroscopy using integral field units has also been attempted (Christensen et al. 2007; Péroux et al. 2011; Bouché et al. 2012).

In the period 1986–2010 only two galaxy counterparts of bona-fide intervening DLAs at $z \gtrsim 2$ ($\log N_{\rm HI}/{\rm cm}^{-2} > 20.3$, $z_{\rm abs} \ll z_{\rm em}$, and $\Delta V > 6000$ km s^{-1}) were detected (Møller, Fynbo, & Fall 2004) despite many more systems being observed. This meagre detection rate has gradually been understood to reflect the fact that DLA galaxies, due to their cross-section selection, trace the faint end of the galaxy luminosity function (Fynbo et al. 2008). Møller et al. (2004) and Ledoux et al. (2006) found evidence that DLA galaxies obey a metallicity–luminosity relation similar to local galaxies and suggested that a survey specifically targeting high-metallicity DLAs should lead to a higher success-rate in searches for galaxy counterparts. Indeed, this strategy has more than doubled the number of detections

of $z \gtrsim 2$ DLA galaxy counterparts in the literature in the last two years (Fynbo et al. 2010, 2011).

The objective of this work is to test the correlation between metallicity and physical size of DLA galaxies predicted by Møller, Fynbo, & Fall (2004). Thanks to the recent increase in number of detections of emission from DLAs we can now analyze how the distribution of impact parameters and their corresponding metallicities match up with the expected distribution from the model of Fynbo et al. (2008), based on the assumption of the previously mentioned correlation.

2.2 Observations

Q 0338−0005 was observed on November 9, 2010 with the X-shooter spectrograph mounted on UT2 of European Southern Observatory's Very Large Telescope following the same strategy as that described in Fynbo et al. (2010) and Fynbo et al. (2011), i.e., securing 1 hour of integration at three position angles $0^{\rm o}$ and $\pm 60^{\rm o}$. For details on the reduction, we refer to the description in Fynbo et al. (2010) and Fynbo et al. (2011).

We detect the galaxy counterpart of the DLA in the trough of the damped Lyα line in all three spectra (PAs of $0^{\rm o}$, $\pm 60^{\rm o}$). The lower panel of Fig. 2.1 shows the stacked 2D spectrum around Lyα where the Lyα emission line can be seen in the bottom of the DLA trough. Using the triangulation described in Møller, Fynbo, & Fall (2004) and Fynbo et al. (2010) we infer an impact parameter of $0\farcs49 \pm 0\farcs12$. The metallicity is determined to be $[{\rm M/H}] = -1.25 \pm 0.10$ based on low-ionization absorption lines from Si II in a high resolution UVES spectrum of the QSO (Ledoux, private communication) and on the damped Lyα line from which we measure $\log N_{\rm HI}/{\rm cm}^{-2} = 21.05 \pm 0.05$.

The target PKS0458−02 was observed on November 24, 2009 with X-shooter. The slit was placed at a position angle of $-60\fdg4$ East of North with the purpose of measuring the precise impact parameter of the $z = 2.04$ DLA galaxy. In the X-shooter spectrum (shown in the top panel of Fig. 2.1) we measure an impact parameter of $0\farcs31 \pm 0\farcs04$. We have combined the data from Møller, Fynbo, & Fall (2004) with our new measurement of the impact parameter.

The galaxy counterpart of the $z = 2.58$ DLA towards Q 0918+1636, reported in Fynbo et al. (2011), has here been observed in a ground based imaging study using point spread function (PSF) subtraction to secure a more precise measure of the impact parameter. The field was observed with the Nordic Optical Telescope (NOT) using the ALFOSC instrument in service mode. The target was observed in the R-band over the nights March 27, 29 and April 9, 2011, giving a total of 16,380 sec exposure. The images were reduced and combined using standard methods for CCD imaging data.

The field around Q 0918+1636 is shown in the left panel of Fig. 2.2. The figure shows a 20×20 arcsec^2 region from the combined NOT image. In the right panel we show the field after PSF subtraction and smoothing with a 3×3 pixel box-car filter. Two sources, both with R-band magnitudes of approximately 25, are detected at impact parameters of $2\farcs0$ and $3\farcs5$. Closer to the position of the QSO there are residuals from the PSF subtraction. With dashed lines we show the positions of the three X-shooter slit positions used by Fynbo et al. (2011). As seen, the continuum source at $2\farcs0$ seen in Fig. 2.2 coincides both in position angle and impact parameter with the emission line source detected in the X-shooter spectrum and must hence be the continuum counterpart of the $z = 2.58$ DLA galaxy. The source at $3\farcs5$ falls outside of the X-shooter slits and it is on the basis of the data in hand not possible to establish if this source may be related to the $z = 2.41$ DLA also detected in the spectrum of Q0918+1636 (Fynbo et al. 2011).

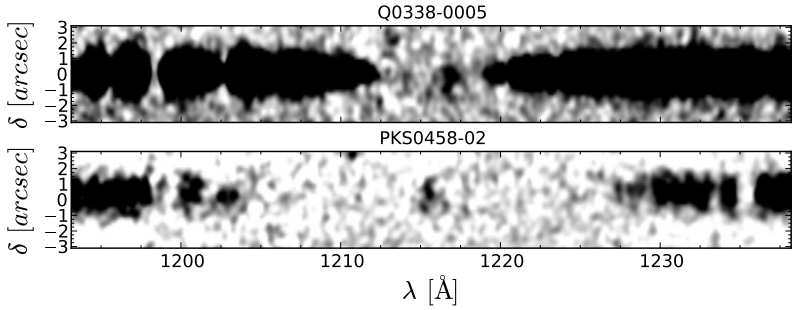

Figure 2.1: Two-dimensional spectra from X-shooter of PKS0458−02 (*top*) and Q0338−0005 (*bottom*) shifted to rest-frame wavelengths. In the centre of each spectrum the DLA troughs are seen with Lyα emission from the absorbing galaxies at spatial offsets of $0\farcs31\pm0\farcs04$ and $0\farcs49\pm0\farcs12$, respectively. The spectra have been smoothed for illustrative purposes.

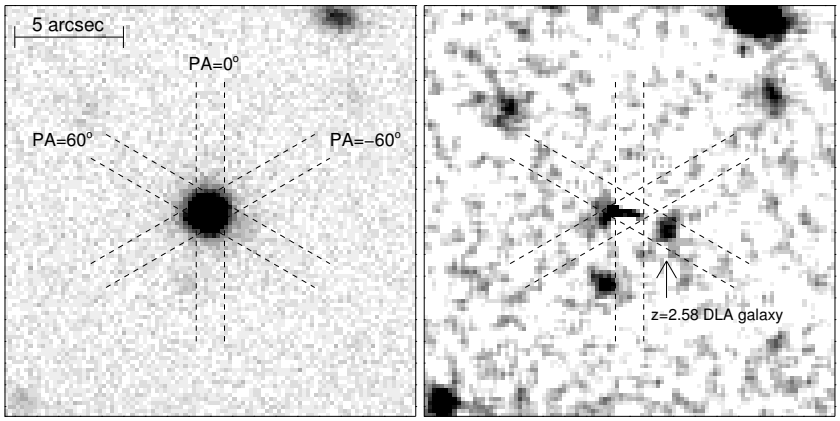

Figure 2.2: R-band image of the 20×20 arcsec^2 field of Q0918+1636. The left panel shows the image before PSF subtraction and the right panel after PSF subtraction and smoothing with a 3×3 pixel box-car filter. Also plotted are the three X-shooter slits used in the Fynbo et al. (2011) study. The galaxy counterpart of the $z = 2.58$ DLA detected in the X-shooter spectrum taken at PA $= +60°$ is indicated with an arrow. Also seen is another galaxy at a PA of about 163° and an impact parameter of $3\farcs5$.

2.2.1 Sample selection

In this Letter, we base our analysis on data combined from the literature along with our new data for three systems of DLA galaxies: Q0338−0035, Q0918+1636 and PKS0458−02. In addition to the systems in the literature, we include a confirmed candidate from an expanded sample based on the methods in Christensen et al. (2007) that has been confirmed by long-slit spectroscopy (Christensen et al., in preparation). We note, however, that no other candidates from that work has been confirmed. Bunker et al. in preparation also have a detection of Lyα emission from a DLA galaxy using long-slit spectroscopy (Weatherley et al. 2005, their table 1). The redshift, metallicity, and impact parameter of the systems used in our analysis are shown in Table 2.1. The $z_{\rm abs} \sim z_{\rm em}$ DLA towards PKS0528−250 has been shown to be unrelated to the nearby QSO and hence likely is similar to intervening DLAs (Møller & Warren 1993; Møller & Warren 1998).

Note: The metallicities and column densities of H I in Table 2.1 have been updated relative to the published version to use the measurements from Ledoux et al. (2006), since these are measured more homogeneously. The values have also been updated in Figures 2.3 and 2.4. The results of the analysis remains unaltered.

Table 2.1: $z \gtrsim 2$ DLAs with identified galaxy counterparts used in this study

QSO	$z_{\rm abs}$	$\log(N_{\rm HI}/{\rm cm}^{-2})$	[M/H]	b (arcsec)
Q2206−19$^{(1,12)}$	1.92	20.67 ± 0.05	-0.54 ± 0.05 [Zn]	0.99 ± 0.05
PKS0458−02$^{(1,5,12)}$	2.04	21.70 ± 0.10	-1.22 ± 0.10 [Zn]	0.31 ± 0.04
Q1135−0010$^{(7)}$	2.21	22.10 ± 0.05	-1.10 ± 0.08 [Zn]	0.10 ± 0.01
Q0338−0005$^{(5,8)}$	2.22	21.05 ± 0.05	-1.25 ± 0.10 [Si]	0.49 ± 0.12
Q2243−60$^{(4,12)}$	2.33	20.65 ± 0.05	-0.85 ± 0.05 [Zn]	2.80 ± 0.20
Q2222−0946$^{(2,12)}$	2.35	20.65 ± 0.05	-0.50 ± 0.03 [Zn]	0.8 ± 0.1
Q0918+1636$^{(3,5)}$	2.58	20.96 ± 0.05	-0.12 ± 0.05 [Zn]	2.0 ± 0.1
Q0139−0824$^{(6,9)}$	2.67	20.70 ± 0.15	-1.15 ± 0.15 [Si]	1.60 ± 0.05
PKS0528−250$^{(1,12)}$	2.81	21.35 ± 0.07	-0.91 ± 0.07 [Zn]	1.14 ± 0.05
Q0953+47$^{(10,11)}$	3.40	21.15 ± 0.15	-1.80 ± 0.30 [Si]	0.34 ± 0.10

References: (1) Møller, Fynbo, & Fall (2004); (2) Fynbo et al. (2010); (3) Fynbo et al. (2011); (4) Bouché et al. (2012); (5) this work; (6) Christensen et al. in prep.; (7) Noterdaeme et al. (2012b); (8) Ledoux, priv. comm.; (9) Wolfe et al. (2008); (10) A. Bunker (priv. communication); (11) Prochaska et al. (2003b); (12) Ledoux et al. (2006).

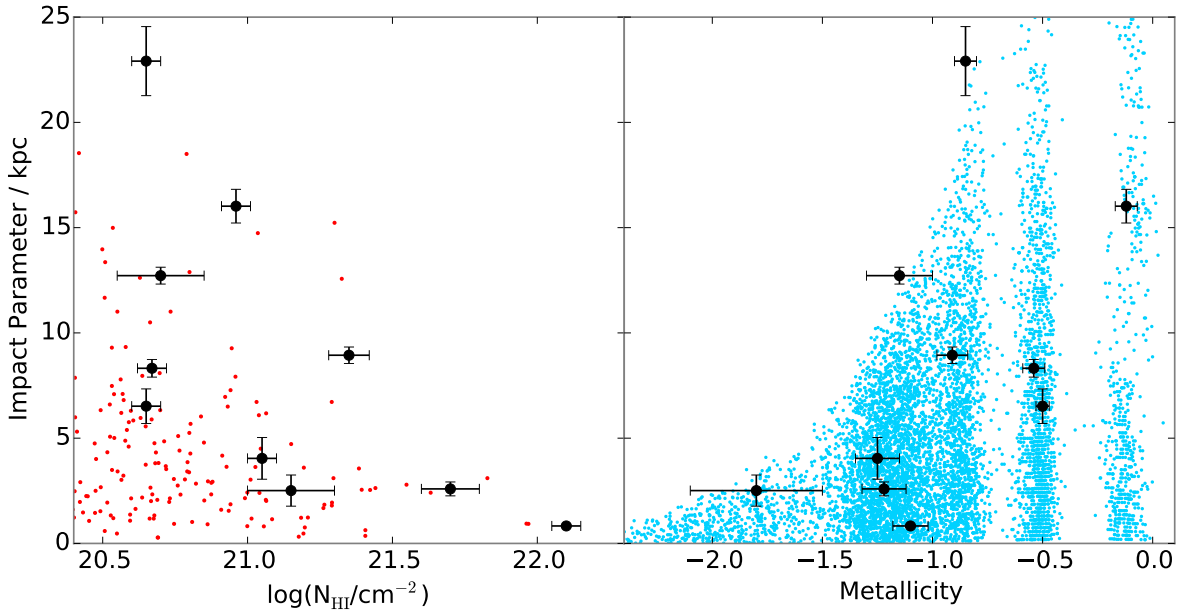

Figure 2.3: Impact parameters plotted against H I column density (*left*) and metallicity (*right*) for $z \gtrsim 2$ DLAs with securely identified galaxy counterparts (see table 2.1). The observed impact parameters have been converted to kpc at redshift $z = 3$ instead of arcsec for easier comparison. The blue points in the right panel show the simulated distribution of impact parameters as a function of metallicity for DLA galaxies at $z = 3$ from the model in Fynbo et al. (2008). The red points in the left panel show model points from Pontzen et al. (2008).

2.3 The metallicity–size correlation

The relation between metallicity and size modelled by Fynbo et al. (2008) is based on the assumption that DLAs seen in the spectra of background QSOs are caused by galaxies comparable to low luminosity Lyman break galaxies (LBGs). In this model, the galaxies are approximated by randomly inclined discs, each one assigned a size, metallicity, and metallicity gradient based on its luminosity. The different relations between the quantities listed above are all based on local, observationally motivated correlations for which indications of their validity at higher redshift have been seen. The more luminous galaxies have bigger discs, higher metallicities, and shallower metallicity gradients. The luminosity L is then drawn from the LBG luminosity function weighted by H I cross section. An impact parameter is also assigned again with the luminosity dependent cross section of H I as weighting factor. The random sight line is then given a metallicity from the before mentioned relations connecting [M/H] to L and the radial dependence of metallicity. For further details see Fynbo et al. (2008).

2.3.1 Testing the model

Though the sample we present here is currently the largest at hand, we still only have ten points. Therefore we need a simple statistical estimator to describe the data. We have chosen a two-parameter fit of the form: $\log(b) = \alpha + \beta\,[\mathrm{M/H}]$. Since the internal scatter in the data is larger than the individual measurement errors we fit a straight line to the measured data by least-squares minimization without weights.

We then use the model described above to generate simulated data sets to which we can compare the measured data. Because the measured data points are selected in different ways we cannot simply draw ten random points from the model. In order to make a valid comparison, we choose model points around the same metallicities as the measured points.

The simulated data points have metallicities taken randomly from a Gaussian distribution around each measured point using the measurement error as the width of the distribution. We then take the distribution of impact parameters from the model at the given metallicity and randomly pick an impact parameter. We do this for all ten points to simulate a complete data set 4000 times. Every set of points is then fitted by a straight line to give the intercept, slope, and scatter.

The 4000 simulated data sets are shown in the right-hand panel of Fig. 2.3 as blue points along with the measured data points in black. To make the plot less crowded only every fifth simulated data set has been shown. The left-hand panel of Fig. 2.3 shows impact parameter vs. neutral hydrogen column density for our data in big black points. The red small points in the panel are results from Pontzen et al. (2008).

In Fig. 2.4 we show the results of the fits to the data, both observed and simulated. The figure shows the 1σ (*solid*) and 2σ (*dashed*) contours of the distribution (*grey 2D histogram*) of fitted slope vs. intercept and slope vs. scatter. The red cross in each panel represents the best-fitting values to the data: $\alpha = 1.15 \pm 0.70\ \log(\mathrm{kpc})\,,\ \ \beta = 0.41 \pm 0.67\ \log(\mathrm{kpc})\,\mathrm{dex}^{-1}$ with a scatter around the fit of 0.26 dex. The mean values of the intercept and slope from the simulated data are $0.90 \pm 0.28\ \log(\mathrm{kpc})$ and $0.41 \pm 0.26\ \log(\mathrm{kpc})\,\mathrm{dex}^{-1}$, respectively, with a mean scatter of 0.27 dex.

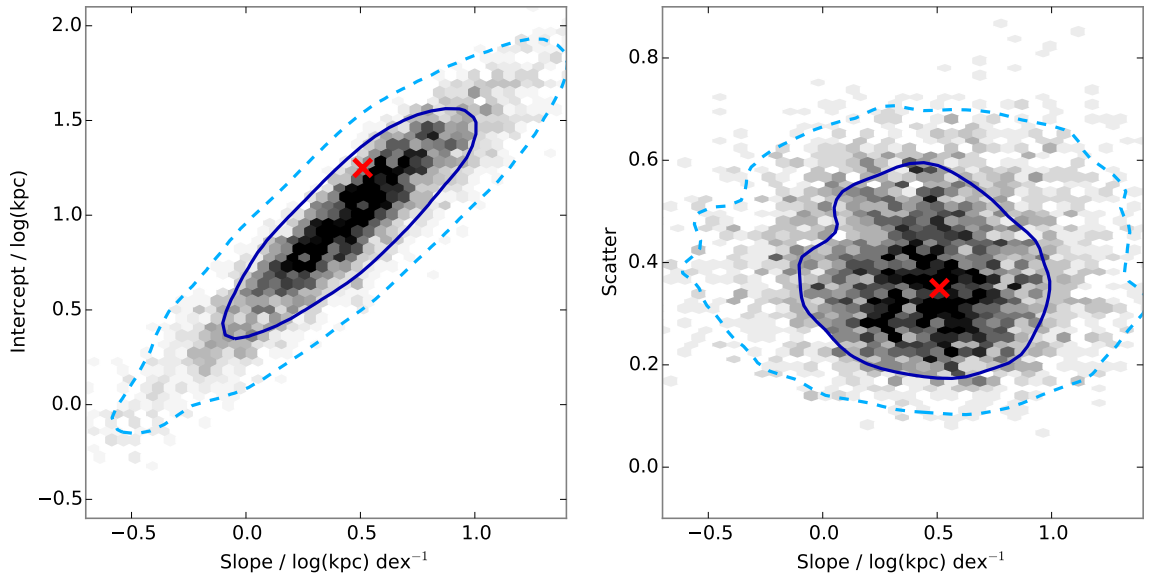

Figure 2.4: Distribution of slope vs. intercept (*top*) and slope vs. scatter (*bottom*) from the 4 000 simulated data sets (grey histogram). The solid and dashed blue lines represent the 1σ and 2σ confidence contours, respectively. The black cross shows the result from our fit to the data.

2.4 Discussion

The sample of spectroscopically confirmed $z \gtrsim 2$ DLA galaxies is now large enough to start determining statistical properties of DLA galaxies. Here we have presented a new detection, namely of the DLA galaxy counterpart of the relatively metal-poor DLA towards Q 0338−0005 and have detected the $z = 2.58$ DLA galaxy towards Q 0918+1636 in the continuum. Based on these and previous detections, we have analyzed the distribution of impact parameters vs. metallicity to study the underlying correlation between size and metallicity. The results presented in Fig. 2.4 show that our data are consistent with the model within the 1σ level for slope vs. intercept. Our data is well within the 1σ-contour in slope vs. scatter. The agreement is also seen in the distribution shown in the right panel of Fig. 2.3.

An important point to note is that four of the data points have specifically been chosen to have high metallicity (Fynbo et al. 2010, 2011). When comparing the observations with the model it is therefore important to remember that the observed sample is biased towards high-metallicity DLA galaxies which in our model are expected at the largest impact parameters. At the same time we may be losing points at the high-metallicity end because of dust bias (e.g., Pei, Fall, & Hauser 1999; Khare et al. 2011) and due to the fact that our method using three long-slits is less sensitive to DLAs with high impact parameters, see Fynbo et al. (2010) for a detailed description of the method. Nevertheless, the data on high-luminosity DLAs are consistent with the picture in which gas at large impact parameters of tens of kpc cause DLA absorption. These galaxies seem to follow relations between size, luminosity, and metallicity comparable to the relations we see for disc galaxies in the local universe.

From hydrodynamical simulations it has also been investigated in which kind of systems DLAs originate (e.g., Cen 2012; Pontzen et al. 2008; Razoumov et al. 2006; Gardner et al. 2001). In the simulation by Cen (2012) DLAs at $z = 3 - 4$ are dominated by low metallicity systems at large impact parameters, typically $b = 20 - 30$ kpc. In this simulation the contribution from gaseous discs to the DLA incidences is very small. Instead most DLAs arise in filamentary gas. The impact parameters at low metallicity from Cen (2012) are much larger than what we observe. The only metal poor DLA is found at an impact

parameter of 2.5 kpc, hence not supporting the model by Cen (2012). Razoumov et al. (2006) also find a large number of DLAs at large impact parameter from filamentary gas around large structures. But they find that the importance of these filamentary DLAs decreases as they increase the resolution.

Pontzen et al. (2008) are able to reproduce the properties of DLAs well with their simulation, which contains very detailed feedback mechanisms. From their simulation they see positive correlations between the DLA cross-section and the mass of the halo containing the DLA, and between the metallicity and the halo mass (see their Figures 4 and 18). From the correlation between $\sigma_{\rm DLA}$ and $M_{\rm vir}$, it is possible to infer a limit on the impact parameters of the corresponding DLAs by assuming a spherical gas disc with a radius given by: $R_{\rm DLA} \propto \sqrt{\sigma_{\rm DLA}}$. The largest possible cross-section found in the most massive haloes is $\sigma_{\rm max} \approx 10^3$ kpc^2. Hence, the impact parameters for DLAs around $z \approx 3$ in their simulation are expected to be $b \lesssim 30$ kpc. The correlation of [M/H] and halo mass suggests that the metal-poor systems are to be found in smaller haloes and therefore at smaller impact parameters. The opposite is true for metal-rich DLAs. This agrees well with the data presented here in Fig. 2.3.

We see a fairly strong anti-correlation between $\log(N_{\rm H\,I})$ and impact parameter (Spearman rank of -0.6; see left panel in Fig. 2.3). A similar trend is observed in studies by Møller & Warren (1998); Monier, Turnshek, & Rao (2009), and Péroux et al. (2011); however, we find a tighter and steeper correlation in our data. Gardner et al. (2001) also find a clear anti-correlation between impact parameter and $\log(N_{\rm H\,I})$ in their simulation of DLAs in different cosmologies, including ΛCDM. They too find a shallower relation for DLAs at $z = 3$. This is most probably a result of the very simplified algorithms to handle cooling and feedback in their simulation. Pontzen et al. (2008) find a clear relation between $\log(N_{\rm H\,I})$ and b (red points of Fig. 2.3) that coincides very well with our observed distribution as seen in the left-hand panel of Fig. 2.3. The good agreement between data and the simulation of Pontzen et al. (2008) indicates that the feedback mechanisms in their simulation, which control star formation and outflow of enriched gas, are responsible for the correlation between size and metallicity.

In conclusion, our analysis shows that our model well predicts the statistical properties of the observed sample without adjustment of any parameters, and as such provides strong support for the underlying size–metallicity relation. The nature of the metal poor population of DLA galaxies is, however, still unknown, as these DLA counterparts are much more difficult to observe.

Furthermore, this sample of spectroscopically confirmed DLA galaxies serves as constraints for future simulations that include modelling of DLAs.

Acknowledgments

The Dark Cosmology Centre is funded by the DNRF. JPUF acknowledges support form the ERC-StG grant EGGS-278202. We also thank Andrew Pontzen for constructive discussion and Andrew Bunker for sharing his data analysis with us.

3

Emission counterpart of a metal-rich DLA: Evidence for enriched galactic outflows

This chapter contains the following article:

"Comprehensive Study of a $z = 2.35$ DLA Galaxy: Mass, Metallicity, Age, Morphology and SFR from HST and VLT"

Published in *Monthly Notices of the Royal Astronomical Society, vol. 433, pp. 3091-3102, 2013.*

Authors:

J.-K. Krogager, J. P. U. Fynbo, C. Ledoux, L. Christensen, A. Gallazzi,
P. Laursen, P. Møller, P. Noterdaeme, C. Péroux, M. Pettini, & M. Vestergaard

We present a detailed study of the emission from a $z = 2.35$ galaxy that causes damped Lyman α absorption in the spectrum of the background quasar, SDSS J 2222−0946. We present the results of extensive analyses of the stellar continuum covering the rest-frame optical–UV regime based on broad-band *Hubble Space Telescope* imaging, and of spectroscopy from VLT/X-shooter of the strong emission lines: Lyα, [O II], [O III], [N II], Hα, and Hβ. We compare the metallicity from the absorption lines in the quasar spectrum with the oxygen abundance inferred from the strong-line methods (R_{23} and N2). The two emission-line methods yield consistent results: [O/H] = -0.30 ± 0.13. Based on the absorption lines in the quasar spectrum a metallicity of -0.49 ± 0.05 is inferred at an impact parameter of 6.3 kpc from the centre of the galaxy with a column density of hydrogen of $\log(N_{\rm HI}/{\rm cm}^{-2}) = 20.65 \pm 0.05$. The star formation rate of the galaxy from the UV continuum and the Hα line can be reconciled assuming an amount of reddening of $E(B-V) = 0.06 \pm 0.01$, giving an inferred SFR of 13 ± 1 M$_\odot$ yr^{-1} (Chabrier initial mass function). From the *HST* imaging, the galaxy associated with the absorption is found to be a compact (r_e=1.12 kpc) object with a disc-like, elongated (axis ratio 0.17) structure indicating that the galaxy is seen close to edge-on. Moreover, the absorbing gas is located almost perpendicularly above the disc of the galaxy suggesting that the gas causing the absorption is not co-rotating with the disc. We investigate the stellar and dynamical masses from SED-fitting and emission-line widths, respectively, and find consistent results of 2×10^9 M$_\odot$. We suggest that the galaxy is a young *proto*-disc with evidence for a galactic outflow of enriched gas. This galaxy hints at how star-forming galaxies may be linked to the elusive population of damped Lyα absorbers.

3.1 Introduction

Mapping the structure, properties and chemical enrichment of galaxies over cosmic history is a major goal of contemporary astrophysics. In the local Universe, important advances can be made by studying the age–metallicity relation of stars in the Solar neighbourhood (e.g., Holmberg, Nordström, & Andersen 2007; Caffau et al. 2011) or in local group dwarf galaxies (Frebel, Johnson, & Bromm 2007; Frebel et al. 2010). At redshifts higher than $z \approx 2$, a powerful method for studying chemical evolution is spectroscopy of Damped Lyα Absorbers (DLAs) detected either toward background QSOs (see Wolfe, Gawiser, & Prochaska 2005, and references therein) or against Gamma-ray Burst (GRB) afterglow light (Fynbo et al. 2006; Savaglio 2006; Prochaska et al. 2007). In those studies, abundances are determined from the gas phase as probed by the H I and metal absorption lines detected against the light of the background QSOs and GRB afterglows, respectively.

Mainly at lower redshifts, but recently also at $z \gtrsim 2$, H II region abundances are determined using the relative strengths of strong emission lines (e.g., Kewley & Ellison 2008; Shapley 2011, and references therein). Currently, there have only been very few cases where both methods have been applied to the same object. The first example is the case of the DLA toward SBS 1543+593 (Bowen et al. 2005) where the two methods yielded consistent results. Since then a handful of other cases have been studied (see the compilation in Péroux et al. 2012). As seen in fig. 8 of Péroux et al. (2012), the absorption-line measurements generally probe regions at larger galactocentric distances than the emission-line based measurements and on average indicate lower metallicities than the results based on emission-lines, possibly reflecting the early setup of metallicity gradients (O'Rourke, Shabala, & Alexander 2011). However, it is important to stress that different recipes to derive oxygen abundances using strong emission-line fluxes reveal very inconsistent results (Kewley & Ellison 2008). It is therefore of interest to expand the sample of sources where strong-line based abundances can be independently tested using other methods (see also Pettini 2006; Kudritzki et al. 2012). Also, the use of different elements, e.g., Fe, Zn or Si, to infer absorption metallicities may introduce systematic offsets when comparing galaxies within a heterogeneous sample.

Combining the two complementary methods of studying the metal enrichment in galaxies provides important hints to understanding how galaxies turn their gas into stars, as the absorption lines directly probe the cold gas, and the properties of the star forming region can be probed directly from the emission lines, and sometimes also from the continuum. However, linking the absorption characteristics of DLAs to the emission characteristics of the galaxies causing the absorption has been a great challenge at high redshift, due to the faint nature of DLA galaxies and due to their proximity to a very bright quasar. So far, only a few DLA systems with confirmed emission counterparts have been established at redshifts $z \gtrsim 2$ (Krogager et al. 2012).

Here we present an analysis of the DLA at $z = 2.35$ seen in the spectrum of the $z = 2.93$ quasar, J 2222−0946. The galaxy counterpart of the absorber was detected by Fynbo et al. (2010), and here we present new, deeper spectroscopic data allowing us to measure the metallicity directly from nebular [O II], [O III], and Balmer emission lines. Furthermore, we combine the spectroscopic data with imaging from Wide Field Camera 3 (WFC3) onboard the *Hubble Space Telescope* (*HST*). The high-resolution images from *HST* makes it possible to detect the continuum emission from the galaxy directly, allowing us to characterize the properties and structure of the absorbing galaxy. This enables us to start bridging the gap between the population of DLA galaxies and star-forming galaxies.

3.2 Observations and Data Reduction

3.2.1 X-shooter spectroscopy

QSO 2222−0946 was observed with the X-shooter spectrograph (Vernet et al. 2011) mounted on ESO's Very Large Telescope, Unit Telescope 2, for a total of 10 hours and 47 minutes during the nights of May 14, August 4, 29, and 30, 2011. The integrations were split into ten different exposures each made up of four sub-exposures dithered along the slit. The instrument is composed of three separate spectrographs (so-called arms): UVB covering 330 nm to 560 nm, VIS covering 550 nm to 1020 nm, and NIR covering 1020 nm to 2480 nm. For all observations slit-widths of $0\farcs8$, $0\farcs7$ and $0\farcs9$ were used for UVB, VIS and NIR, respectively, and we used the slow readout with 1×2 binning, i.e., 2 times binning in the spatial direction. The individual spectra have been processed using the official ESO pipeline (Modigliani et al. 2010) for nodded exposures (version 2.0.0). The spectra were individually flux-calibrated using the standard star observed at the beginning of the night for each integration. All spectra were taken during very good conditions with clear sky and good seeing. The error on the flux calibration is on the order of 5%, as determined from the robustness of the calibration when using different standard stars. We note that Fynbo et al. (2010) scale their spectrum of this target to the one available from the Sloan Digital Sky Survey. Given our very robust flux calibration we have chosen to trust the pipeline product. Also, comparison of spectra observed in very different epochs, as is the case here, is not straightforward given the random variability of quasars. We encountered issues with a too low flux level of the VIS spectra for unknown reasons. For this reason we scaled the VIS spectra to the overlapping regions of the well-determined UVB and NIR spectra. With a simple multiplicative factor we were able to match both UVB and NIR at the same time. The scaling does not affect any of the extracted emission lines as they are all in the NIR spectra, except for Lyα in the UVB.

The final 2D spectra were then spatially aligned and added by error-weighting, and we correct for slit-loss by calculating how much light gets dispersed outside the slit at the given seeing in each exposure before co-adding all the observations. We have not corrected for telluric absorption, since those regions are not crucial for our analysis. The effective seeing in the final flux and wavelength calibrated 2D spectrum is $0\farcs7$ (inferred from the width of the trace at 715 nm) and we measure the resolving power in the spectrum from telluric lines to be 11,000 and 7000 for the VIS and NIR arms, respectively. As there are no direct features in the UVB arm to indicate the resolving power we assume the resolving power in the UVB arm to be the expected 6200 from the specifications of the X-Shooter manual given a slit width of $0\farcs8$, as the average seeing in UVB was $0\farcs77$ (measured at 480 nm).

In Figure 3.1 the spectrum blueward of the quasar Lyα emission line is shown, demonstrating the quality of the combined spectrum; note the significant flux below the Lyman limit at $z = 2.87$.

3.2.2 *HST* / WFC3 imaging

The field was observed with the WFC3 on Nov 10, 2011 (with the UVIS detector in the $F606W$ filter) and on Sep 14 and 15, 2012 (with the IR detector in the $F105W$ and $F160W$ filters). The roll-angle of the telescope was set such that the galaxy counterpart of the DLA fell between the diffraction spikes of the point spread function (PSF). The two observations with the IR detector were taken using the WFC3-IR-DITHER-BOX-MIN pattern providing an optimal four-point sampling of the PSF. The UVIS observation was taken using the WFC3-UVIS-DITHER-BOX pattern.

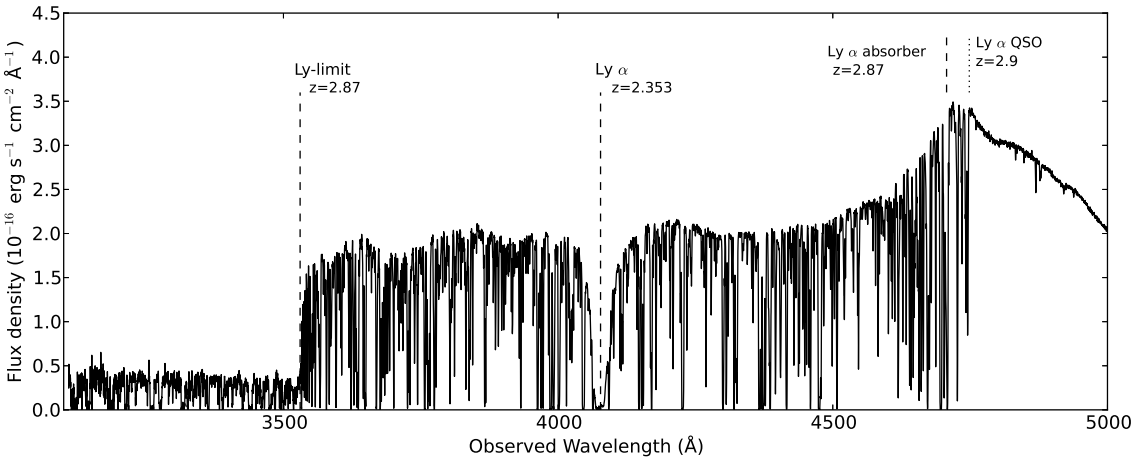

Figure 3.1: The final 1D spectrum from the UVB arm of the $z = 2.9$ J2222−0946. In the left-hand part of the spectrum, the Lyman limit from an absorber at redshift $z = 2.87$ is clearly seen and the damped Lyman α absorption line is identified in the middle of the figure by the vertical dashed line. The Lyman α emission line at the quasar redshift is seen in the right-hand part of the figure.

The field was observed using a 4-point sub-pixel dither pattern, which allowed us to regain more spatial information. We have used the software package MULTIDRIZZLE[1] to align and combine the images. By shifting and combining the images taken with sub-pixel offsets one achieves a better sampling of the PSF, which in the case of the NIR observations is quite crucial as the PSF is poorly sampled in the native $0\farcs13$ px^{-1} images. Furthermore, the drizzle-algorithm allows us to reduce the pixel size when combining the images providing sharper and better sampled images. For the combination in this work we have set the parameter `pixfrac` to 0.7 and used a final pixel scale of $0\farcs06$ px^{-1} for NIR and $0\farcs024$ px^{-1} for UVIS. For a detailed description of the parameters in the software we refer the user to the MULTIDRIZZLE[1] user manual.

3.3 Spectral PSF subtraction

In order to detect the faint emission lines from the foreground damped Lyman α absorbing galaxy we needed to subtract the quasar continuum. We did this by modelling the spectral trace and the spectral point spread function (SPSF) as a function of wavelength. The trace position and amplitude were fitted as a function of wavelength in a small (84 Å) region around each emission line from the galaxy, e.g., [O II], [O III], and [N II]. In the same region around the line, we estimated the SPSF by averaging the observed spatial profile along the spectral direction. The modelled 2D spectrum of the quasar was then subtracted from the observed spectrum, and a 1D spectrum for each line was extracted with the optimal extraction algorithm of Horne (1986). All extracted emission lines are shown in Figure 3.2.

[1] MULTIDRIZZLE is a product of the Space Telescope Science Institute, which is operated by AURA for NASA.

3.4 Extracting the Emission Lines

We were able to detect emission from Lyα, Hα, Hβ, the [O II] $\lambda\lambda\,3727, 3729$ doublet, the two [O III] lines at 4959 and 5007 Å, and [N II] $\lambda\,6583$. The line profiles for all the extracted lines were fitted with Gaussian profiles to measure the flux in the line. The parameters of the Gaussian were allowed to vary in all fits except for [O II] and [N II]. The linewidth and redshift of the two [O II] components were tied in the fit, because of a sky line that falls right between the two components. For the very faint [N II]-line, we re-binned the spectrum by a factor of two and fixed the redshift and linewidth to the values of the nearby Hα line. The errors on the fluxes were estimated by varying the line profile within the error of each fit parameter 1000 times. The uncertainty was then determined from the 1 σ width of the resulting distribution of fluxes. The fluxes and errors are listed in Table 3.1.

All the extracted lines with Gaussian line fits are shown in Figure 3.2 along with the best-fitting Gaussian profile. The grey shaded areas indicate telluric emission or absorption features. These regions were included in the fits to give the optimal estimate of uncertainties on the fit parameters. The Lyα line is shown in Figure 3.3. Due to the asymmetric shape and the complex nature of the resonant line, we determine the line flux simply by integrating the observed line profile as opposed to fitting the line.

3.5 Balmer Decrement

The ratio of the Hα and Hβ line fluxes provides us with information about the dust extinction in the system as we know what this ratio should be intrinsically, given the physical conditions of the emitting region. Assuming case B recombination with an electron temperature of $T_e = 10^4$ K and density of $n_e = 10^2$ cm^{-3}, which are standard assumptions in the literature for star forming regions, the line ratio has a value of 2.86. Requiring that our measured line ratio, after reddening, and the intrinsic ratio be the same, we estimate the reddening:

$$E(B-V) = \frac{2.5}{k(\mathrm{H}\beta) - k(\mathrm{H}\alpha)} \log\left(\frac{(\mathrm{H}\alpha/\mathrm{H}\beta)_{\mathrm{obs}}}{(\mathrm{H}\alpha/\mathrm{H}\beta)_0}\right) ,$$

where k denotes the reddening law evaluated at the given wavelength and $(\mathrm{H}\alpha/\mathrm{H}\beta)_0$ indicates the intrinsic line ratio. We use the extinction law from Calzetti et al. (2000) to quantify the extinction while adopting a R_V value of 4.05. From the measured ratio in our spectrum of $(\mathrm{H}\alpha\,/\,\mathrm{H}\beta)_{\mathrm{obs}} = 3.03 \pm 0.34$ we obtain the corresponding extinction of $E(B-V) = 0.05 \pm 0.10$. In this calculation we have not taken into account effects from differential slitloss, which arise from the wavelength dependence of the seeing and atmospheric dispersion. The slitloss is greater at lower wavelengths, i.e., for the Hβ line in the case of the Balmer line ratio. However, the effect in the K- and H-band, where we extract the Balmer lines, is minor ($\sim$ 2%) compared to the uncertainty introduced by the sky lines, especially at the position of the Hβ-line.

3.6 Metallicity

We have inferred the metallicity of the system using three independent methods; two measures of the emission-line metallicity using the strong-line ratios R_{23} and N2, respectively, and one measure of the absorption-line metallicity from Voigt-profile fitting. In the next sections, we present each determination in detail.

Table 3.1: Measured emission line fluxes

Transition	Wavelength$^{(a)}$	Flux$^{(b)}$	FWHM$^{(c)}$	z
Lyα	1215.67	14.3 ± 0.3	–	–
[O II]	3726.03, 3728.82	2.9 ± 0.3	121 ± 8	2.3536
Hβ	4861.33	1.9 ± 0.2	151 ± 15	2.3537
[O III]	4958.92	4.1 ± 0.3	129 ± 5	2.3537
[O III]	5006.84	11.6 ± 0.6	110 ± 2	2.3537
Hα	6562.80	5.7 ± 0.3	124 ± 4	2.3537
[N II]	6583.41	0.6 ± 0.2	–	–

$^{(a)}$ Transition rest-frame wavelength in Å.
$^{(b)}$ Flux in units of 10^{-17}erg s^{-1} cm^{-2}, before reddening correction.
$^{(c)}$ Linewidth at FWHM in units of km s^{-1} corrected for the instrumental resolution of 45 km s^{-1}.

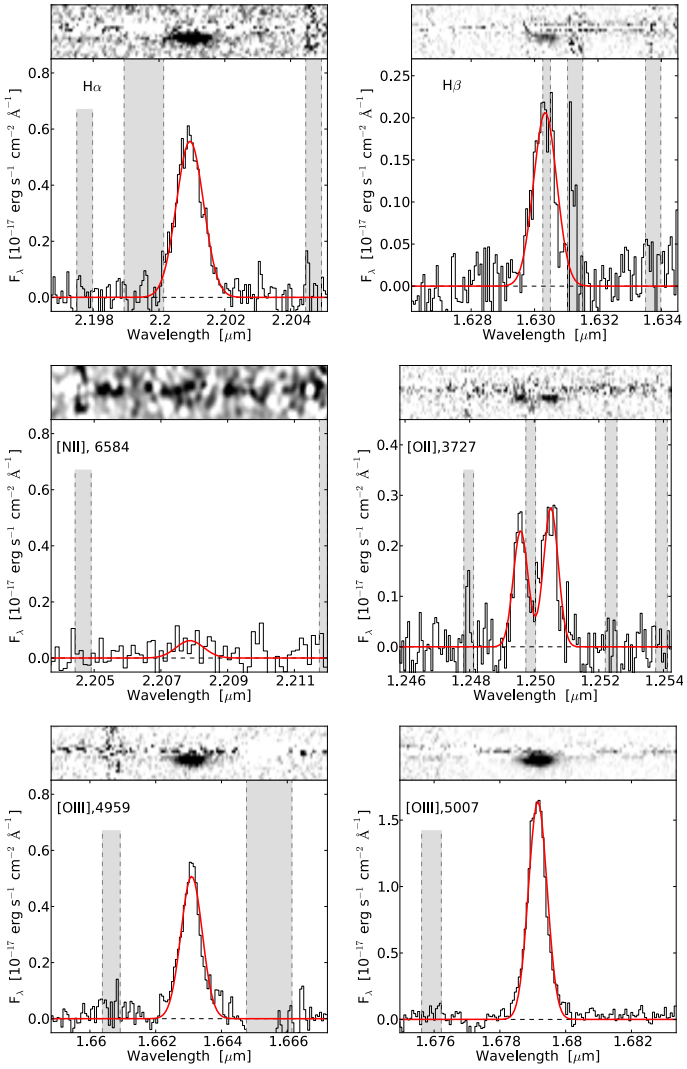

Figure 3.2: Emission lines extracted after the subtraction of the quasar continuum in the 2D spectrum. Each panel shows the 2D spectrum where the horizontal residuals from the quasar subtraction is seen (*top*) and the extracted 1D spectrum of the line (*bottom*). The red line in each panel indicates the best fitting Gaussian to the line profile. The grey filled areas indicate skylines or telluric absorption features.

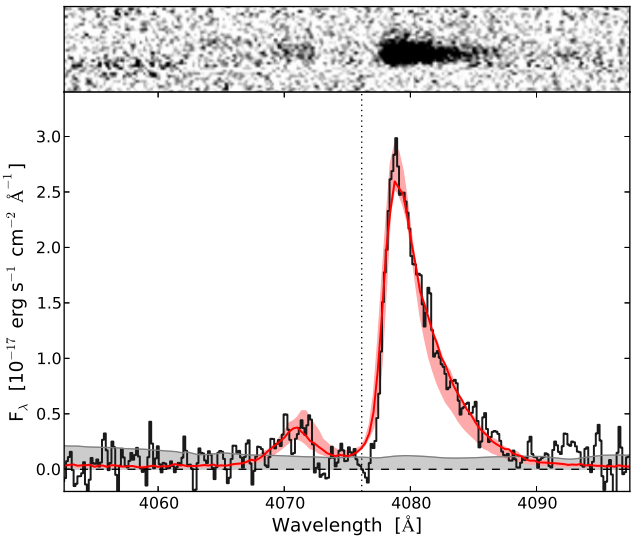

Figure 3.3: The Lyα emission line extracted from the DLA trough in the X-shooter spectrum. The top panel shows the observed 2D spectrum and the panel below shows the extracted 1D spectrum, and 1σ uncertainty (grey shaded area). The dotted vertical line shows the systemic line centre. The common asymmetric line shape of Lyα is seen in this case, where the blue-shifted part of the line is heavily absorbed. On top of the observed spectrum the best fitting model of the emission profile is shown (red line) along with the 68% confidence interval (red shaded area), see Section 3.9 for details.

3.6.1 R_{23} calibration

We determined the metallicity $12 + \log(\mathrm{O/H})$ by use of the strong-line diagnostic, R_{23} (Pagel et al. 1979), defined as:

$$R_{23} = \frac{[\mathrm{O\,II}]\,\lambda\lambda\,3727, 3729 + [\mathrm{O\,III}]\,\lambda\,4959 + [\mathrm{O\,III}]\,\lambda\,5007}{\mathrm{H}\beta}\,.$$

One complication of using this diagnostic is that the metallicity is double-valued for a given value of R_{23} (the so-called *upper* and *lower* branches). However, due to our relatively high value of R_{23} we are in the region of the diagram where the two branches are close to one another. The calibration by Kobulnicky & Kewley (2004) which we use depends on the ionization parameter, q, which can be determined by using the line ratio: $O_{32} = [\mathrm{O\,III}]\,\lambda5007$ / $[\mathrm{O\,II}]\,\lambda3727$, but requires prior knowledge of the metallicity. Given the two measured quantities, R_{23} and O_{32}, we can solve for both metallicity and q at the same time by iterating the two expressions given an initial guess of metallicity.

From our spectrum we measure $\log(R_{23}) = 1.00 \pm 0.05$ and $\log(O_{32}) = 0.55 \pm 0.05$. These line ratios are corrected for reddening as indicated by the Balmer decrement. However, in Sect. 3.10 we infer $E(B-V) = 0.06 \pm 0.01$, which is the value that we have adopted for the correction here. We perform the iterative calculation of metallicity 500 times while varying the two line-ratios (R_{23} and O_{32}) within their respective errors. The metallicity and uncertainty is then determined as the median and standard deviation of the resulting distribution. This in turn yields an inferred metallicity of $12+\log(\mathrm{O/H}) = 8.41 \pm 0.19$, see Fig. 3.4. We furthermore note that the result does not depend on the initial guess, and that the model uncertainty introduced by the error on the ionization parameter, q, is negligible. The uncertainty of 0.19 dex includes the contribution from the scatter in the R_{23} calibration which we conservatively set to 0.15 dex.

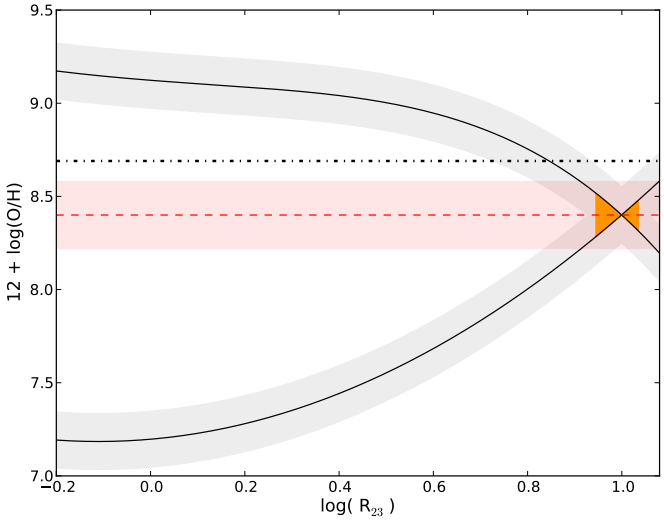

Figure 3.4: Plot of the R_{23} strong line ratio using the calibration by Kobulnicky & Kewley (2004) (two solid lines) with model uncertainty of 0.15 dex indicated by the light grey shaded area around the curves. The orange filled area between the two solid lines indicates the constraint from our measurement of R_{23}. The red, dashed line indicates the inferred metallicity of $12 + \log(\mathrm{O/H}) = 8.41$ and the red shaded area around it indicates the 1σ uncertainty of 0.19 dex. The black, dot-dashed line shows the Solar oxygen abundance of $12+\log(\mathrm{O/H})_\odot = 8.69$ (Asplund et al. 2009).

3.6.2 N2 calibration

Our detection of [N II] enables us to infer the metallicity independently from the N2 index ([N II] / Hα) as this line ratio has been found to correlate with metallicity (Pettini & Pagel 2004). The calibration from these authors give $12 + \log(\mathrm{O/H}) = 8.90 + 0.57 \cdot \log(\mathrm{N2})$ with a scatter of ± 0.18 dex. The small wavelength difference of Hα and [N II] means that we do not need to worry about reddening effects in the N2 ratio. The measured line fluxes yield a line ratio of $\mathrm{N2} = 0.11 \pm 0.03$, giving an inferred metallicity of $12 + \log(\mathrm{O/H}) = 8.36 \pm 0.19$.

Péroux et al. (2012) infer an upper limit of $12 + \log(\mathrm{O/H}) < 8.2$ from their non-detection of [N II]. Our measurement is slightly higher, but still consistent with theirs within the uncertainties.

Since the two measures of the emission metallicity, R_{23} and N2, are independent we can combine both measures to obtain a more precise estimate of $12 + \log(\mathrm{O/H}) = 8.39 \pm 0.13$. Adopting the Solar abundance presented by Asplund et al. (2009) this gives us $[\mathrm{O/H}] = -0.30 \pm 0.13$.

3.7 Absorption-line Abundances

In the following section, we present detailed measurements of the absorption-line abundances detected in the DLA system. Fynbo et al. (2010) present an analysis of the metal absorption-line system of this DLA using a three-component Voigt-profile fit. They derive fairly high metallicities from $[\mathrm{Zn/H}] = -0.46 \pm 0.07$, $[\mathrm{Si/H}] = -0.51 \pm 0.06$, and $[\mathrm{S/H}] = -0.6 \pm 0.1$, and see evidence for dust depletion from $[\mathrm{Mn/H}] = -1.23 \pm 0.06$, $[\mathrm{Ni/H}] = -0.85 \pm 0.06$, and $[\mathrm{Fe/H}] = -0.99 \pm 0.06$. Since our data have much better resolution (recall values in Section 3.2.1 compared to $\mathcal{R} = 4700, 6700, 4400$ in the Fynbo et al. study for the UVB, VIS and NIR arms, respectively) and much higher signal-to-noise ratio (SNR$\sim$100, compared to their SNR$\sim$50) we can alleviate the effect of hidden saturation, thereby further constraining the metal abundances.

In order to properly decompose the absorption profiles in different velocity components we have selected unsaturated, but well-defined low-ionization lines to infer the metallicity of the absorbing gas (see Fig. 3.5). Furthermore, we have access to a few high-ionization lines: C IV $\lambda\lambda\,1548, 1550$, O VI $\lambda\lambda\,1031, 1037$, and possibly S VI $\lambda 944$. We have ignored the Cr II $\lambda\,2066$ line because it is heavily blended with telluric absorption features. We found that a five-component fit provides a satisfactory description of the low-ionization lines. All the lines were fitted simultaneously using `FitLyman` in MIDAS (Fontana & Ballester 1995) while tying the broadening parameter, b, and the redshift for each velocity component for all lines. The results for the individual components of the fit are summarized in Table 3.2. We derive the total column densities from the fit by adding the column densities for all components of each species. These and the derived metallicities are listed in Table 3.3. For the Ti II $\lambda\lambda$ 1910 doublet we get an upper limit (3σ) of $[\mathrm{Ti/H}] \leq -0.1$, as the line is shallow and the continuum level in this part of the spectrum is uncertain. The abundance of Zn is probably overestimated due to blending with the weak Mg I $\lambda\,2026$ line. However, from the Mg I $\lambda\,2852$ line we are able to constrain the amount of contamination from Mg I to be $\sim$0.1 dex. The column density of neutral hydrogen is obtained from a fit to the Lyα line: $\log(N_{\mathrm{H\,I}}/\mathrm{cm}^{-2}) = 20.65 \pm 0.05$.

The inferred metallicities are in very good agreement with those determined by Fynbo et al. (2010). The uncertainty of our metallicities, which we estimate to be 0.05 dex from the variance in the data, is dominated by the uncertainty on the normalization of the quasar continuum.

For the high-ionization lines, we have let the redshifts and broadening parameters vary freely for each species. We used three components to fit C IV whereas we used two components for the more noisy O VI and S VI lines. The results from the fit are listed in the bottom part of Table 3.2. Our possible detection of S VI is quoted as an upper limit, and the first component of C IV is quoted as a lower limit since the line is saturated. The velocity of the main component of C IV is fully consistent with the systemic velocity from the emission lines within the uncertainty of 9 km s^{-1}. The oxygen and sulphur lines have slightly larger offsets relative to the emission redshift of +20 km s^{-1} and +55 km s^{-1}, respectively.

3.7.1 Molecular hydrogen

Our data exhibit a number of dips at the expected position of H_2 lines at $z_{\mathrm{abs}} = 2.354$, which suggest a detection of molecular hydrogen at the level of $\log(N_{\mathrm{H_2}}/\mathrm{cm}^{-2}) \sim 14$. However, asserting the presence of H_2 and deriving accurate column densities or limits requires much higher spectral resolution data than what we have available here (see, e.g., Ledoux, Petitjean, & Srianand 2003; Noterdaeme et al. 2008). This is needed in order to (*i*) deblend the possible H_2 lines from the Lyman-α forest, (*ii*) estimate the true continuum of the QSO from unabsorbed spectral regions, and (*iii*) resolve the velocity structure of the system. Fynbo et al. (2011) reported the detection of H_2 lines at a resolving power of $\mathcal{R} = 6400$ in the $z_{\mathrm{abs}} = 2.58$ DLA toward SDSS J 0918+1636, but the absence of strong damping wings makes the column density estimates uncertain ($\log N(\mathrm{H_2}) \sim 16 - 19$). The present tentative detection of H_2 lines toward SDSS J 2222−0946 and the corresponding column densities should therefore be verified via follow-up high resolution spectroscopy (i.e., $\mathcal{R} \gtrsim 50,000$).

Table 3.2: Ionic column densities for individual absorption components of low-ionization lines (top) and high-ionization lines (bottom). The errors quoted below only include the formal errors from `FitLyman`.

Component [a]	$\log(N/\mathrm{cm}^{-2})$	b km s^{-1}
Si II λ 1808		
$v = -32$ km s^{-1}	15.11 ± 0.01	9.1 ± 0.1
$v = 11$ km s^{-1}	14.97 ± 0.01	24.0 ± 0.2
$v = 73$ km s^{-1}	15.10 ± 0.01	10.1 ± 0.1
$v = 118$ km s^{-1}	14.73 ± 0.02	21.6 ± 0.3
$v = 174$ km s^{-1}	14.05 ± 0.07	23.7 ± 1.5
S II λ 1250		
$v = -32$ km s^{-1}	14.80 ± 0.01	9.1 ± 0.1
$v = 11$ km s^{-1}	14.56 ± 0.02	24.0 ± 0.2
$v = 73$ km s^{-1}	14.82 ± 0.01	10.1 ± 0.1
$v = 118$ km s^{-1}	14.35 ± 0.03	21.6 ± 0.3
$v = 174$ km s^{-1}	14.18 ± 0.04	23.7 ± 1.5
Mn II $\lambda\lambda\lambda$ 2576, 2594, 2606		
$v = -32$ km s^{-1}	12.41 ± 0.01	9.1 ± 0.1
$v = 11$ km s^{-1}	12.21 ± 0.01	24.0 ± 0.2
$v = 73$ km s^{-1}	12.33 ± 0.01	10.1 ± 0.1
$v = 118$ km s^{-1}	12.09 ± 0.01	21.6 ± 0.3
$v = 174$ km s^{-1}	11.43 ± 0.05	23.7 ± 1.5
Fe II $\lambda\lambda\lambda$ 2249, 2260, 2374		
$v = -32$ km s^{-1}	14.59 ± 0.01	9.1 ± 0.1
$v = 11$ km s^{-1}	14.39 ± 0.01	24.0 ± 0.2
$v = 73$ km s^{-1}	14.64 ± 0.01	10.1 ± 0.1
$v = 118$ km s^{-1}	14.38 ± 0.01	21.6 ± 0.3
$v = 174$ km s^{-1}	13.46 ± 0.02	23.7 ± 1.5
Ni II $\lambda\lambda\lambda$ 1709, 1741, 1751		
$v = -32$ km s^{-1}	13.49 ± 0.01	9.1 ± 0.1
$v = 11$ km s^{-1}	13.41 ± 0.02	24.0 ± 0.2
$v = 73$ km s^{-1}	13.45 ± 0.01	10.1 ± 0.1
$v = 118$ km s^{-1}	13.23 ± 0.02	21.6 ± 0.3
$v = 174$ km s^{-1}	12.31 ± 0.21	23.7 ± 1.5
Zn II λ 2026		
$v = -32$ km s^{-1}	12.14 ± 0.01	9.1 ± 0.1
$v = 11$ km s^{-1}	12.29 ± 0.01	24.0 ± 0.2
$v = 73$ km s^{-1}	12.31 ± 0.01	10.1 ± 0.1
$v = 118$ km s^{-1}	12.08 ± 0.02	21.6 ± 0.3
$v = 174$ km s^{-1}	11.16 ± 0.15	23.7 ± 1.5
C IV $\lambda\lambda$ 1548, 1550		
$v = 5$ km s^{-1}	>15.23 [b]	46.7 ± 0.3
$v = 134$ km s^{-1}	14.11 ± 0.02	28.0 ± 1.4
$v = 197$ km s^{-1}	14.34 ± 0.01	36.5 ± 0.8
O VI $\lambda\lambda$ 1031, 1037		
$v = 55$ km s^{-1}	15.24 ± 0.02	105 ± 6
$v = 242$ km s^{-1}	14.49 ± 0.08	54 ± 10
S VI λ 944		
$v = 20$ km s^{-1}	$\leq 14.1 \pm 0.1$ [c]	35 ± 9
$v = 210$ km s^{-1}	$\leq 13.6 \pm 0.2$ [c]	61 ± 33

[a] The velocity, v, indicated at each component shows the relative velocity with respect to the emission redshift $z = 2.3537$.
[b] Lower limit due to saturation.
[c] Upper limit due to possible blending.

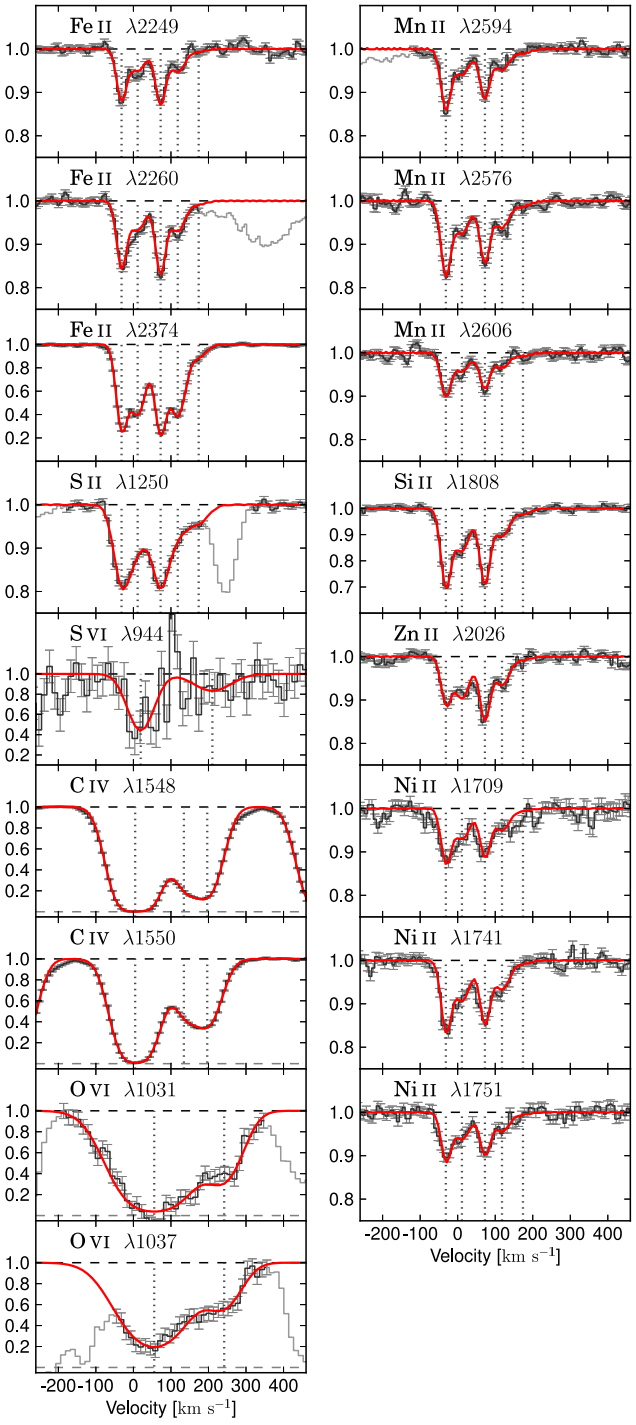

Figure 3.5: Results of Voigt-profile fitting to the metal absorption lines. The zero point of the velocity scale is fixed to the redshift from the emission lines, $z_{\mathrm{em}} = 2.3537$ with an uncertainty of 9 km s^{-1}. The figure shows the normalized spectra around each fitted line. The part of the spectrum plotted in light grey without error-bars in the panels of Mn II λ2594, S II λ1250, Fe II λ2260, and O VI $\lambda\lambda$1031,1037 shows absorption unrelated to the given line.

Table 3.3: Total column densities and metallicities.

Element	$\log(N_X/\mathrm{cm}^{-2})$	[X/H]	$\log(N_\odot/\mathrm{cm}^{-2})$
H	20.65 ± 0.05	–	12.00
Si	15.62 ± 0.01	-0.54 ± 0.05	7.51
S	15.31 ± 0.01	-0.49 ± 0.05	7.15
Mn	12.89 ± 0.01	-1.19 ± 0.05	5.43
Fe	15.13 ± 0.01	-1.02 ± 0.05	7.50
Ni	14.02 ± 0.01	-0.85 ± 0.05	6.22
Zn	12.83 ± 0.01	-0.38 ± 0.05	4.56

Note: Solar abundances are taken from Asplund et al. (2009).

3.8 Structural Fitting of the *HST* images

We started out by modelling the PSF in each image using the software TinyTim to create sub-sampled PSFs simulated for each of the individual frames at each position in the four-point dither pattern. We preferred this approach over using stellar sources as the TinyTim PSFs are more sensitive to the outer regions of the PSF, where the stellar sources are dominated by noise in the sky background.

After resampling the modelled PSFs to the native pixel size and convolving with the filter-specific charge diffusion kernel, these 'raw' PSF images were drizzled together in the same way as the actual data to replicate the effect of multidrizzle on the PSF shape. We were not able to simulate the PSFs for the infrared images properly because the images were mildly saturated. We therefore chose to use stellar PSFs generated by median combination of stars in the field. Since there are only a handful isolated stars in the field of view with signal-to-noise ratios similar to that of the quasar, we used a few stars with slightly lower SNR in order to reduce the background noise in the PSF.

We used the software Galfit (Peng et al. 2002) to subtract the quasar and to characterize the absorbing galaxy. Using the modelled PSF for the $F606W$ image, we first subtracted the quasar by simply modelling it as a point source while modelling a constant sky background. We then located the nearby galaxy in the residuals. Hereafter, we re-did the fit, this time simultaneously fitting the quasar, the background, and the galaxy using a Sérsic surface brightness profile:

$$\Sigma(r) = \Sigma_e \exp\left[-\kappa\left(\left(\frac{r}{r_e}\right)^{1/n} - 1\right)\right] ,$$

where Σ_e is the surface brightness at the effective radius, r_e, defined as the radius enclosing half the flux. The Sérsic index, n, determines the concentration of the profile, with high-n profiles having steeper inner slopes and larger extended wings. The opposite is the case for low n. The parameter κ is linked to n to ensure that half of the light is enclosed within the effective radius. The software Galfit uses a 2D Sérsic profile allowing for elliptical isophotes. The output from fitting the Sérsic profile is given in terms of the total flux from the integrated profile, the effective semi-major axis, a_e, the Sérsic index, n, the axis ratio of semimajor and -minor axes, b/a, and the angle of a_e with respect to the image-axes. We fitted the galaxy allowing all parameters to vary freely. This resulted in the following best-fitting parameters: $\mathrm{mag_{AB}} = 24.29 \pm 0.04$, $n = 0.95 \pm 0.15$, $a_e = 5.80 \pm 0.30$ px, $b/a = 0.17 \pm 0.02$, and $\mathrm{PA} = -26.45 \pm 1.34^{\circ}$ in the $F606W$ image.

Table 3.4: Results from GALFIT analysis

Filter	mag [AB]	a_e / kpc	n	b/a
$F606W$	24.29 ± 0.04	1.12 ± 0.06	0.95 ± 0.15	0.17 ± 0.02
$F105W$	24.51 ± 0.21	1.12^*	0.95^*	0.17^*
$F160W$	23.53 ± 0.13	1.12^*	0.95^*	0.17^*

* Parameters that were fixed in the corresponding fit.

Due to the broader PSF in the NIR images the quasar light is spatially overlapping with the galaxy. We therefore fixed the structural parameters in the Sérsic fit of the galaxy to those of the well-constrained $F606W$ fit. We note that simply locking all structural parameters of the Sérsic profile in the NIR images might not give the most accurate description of the galaxy, as parameters such as size and n depend on wavelength and thus yield different results when analysed in different wavelength band-passes (Kelvin et al. 2012). However, in order to obtain the most reliable fluxes and to get the fit to converge we had to keep the variables fixed. In order to estimate how robust our obtained fluxes are with respect to the parameters that were held fixed, we varied the Sérsic parameters within their errors (as given by the fit to $F606W$) and re-did the fit for each new set of profile parameters. The uncertainty on the flux was very minor (0.03 dex) compared to the large uncertainty caused by the PSF subtraction ($\sim$0.2 dex). All the obtained magnitudes are listed in Table 3.4.

In Fig. 3.6, we show the WFC3 images in the three filters and the residuals after subtracting the modelled quasar PSF. All images are rotated to have North up and East left. The galaxy causing the DLA seen in the quasar spectrum is located to the North-East of the quasar. The red circle in the $F105W$ and $F160W$ images indicates the position of the galaxy from the $F606W$ image. The identification is based on the fact that the position is consistent with the measured offset between the quasar trace and the emission lines in the X-shooter spectrum. The impact parameter of the galaxy with respect to the background quasar is $0\farcs74$ corresponding to a projected distance of 6.3 kpc at $z = 2.354$, and the angle between the major axis of the galaxy and the line connecting the quasar to the central region of the galaxy is $71 \pm 2^{\rm o}$.

3.9 Lyα emission modelling

We observe a typical, double-peaked Lyα emission line with a strong component redward of line centre and a less prominent blue component (Fig. 3.3). The large difference between the two peaks indicates that the Lyα photons escape through an expanding medium, and the purpose of this section is to investigate what constraints we can put on the outflow velocity, $V_{\rm out}$. Qualitatively we can see that the red wing extends to several hundreds of km s^{-1}. However, in order to get a more accurate description of the emission profile we have constructed a semi-realistic model of the system and run Lyα radiative transfer (RT) through it, to find the best-fitting spectrum. The RT is conducted using the code MOCALATA (Laursen, Razoumov, & Sommer-Larsen 2009; Laursen, Sommer-Larsen, & Andersen 2009), while the galaxy model is similar to the one described in (Laursen, Duval, & Östlin 2013). In short, the galaxy is modelled as a sphere of multiphase gas, with warm, neutral clouds floating in a hot, predominantly ionized medium. A similar procedure was used in Noterdaeme et al. (2012b), although here we employ a more rigorous approach.

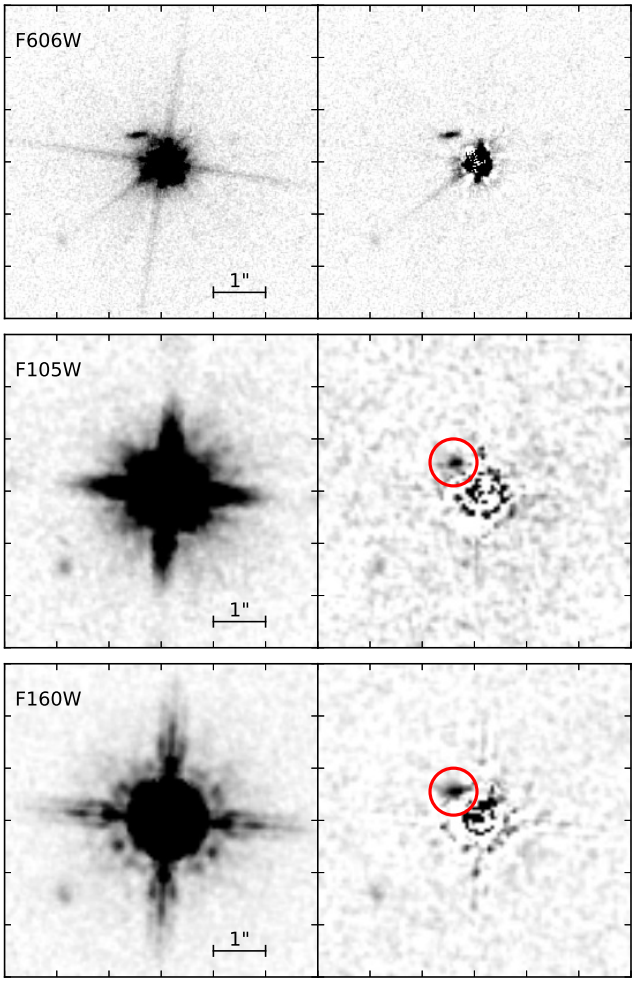

Figure 3.6: Data images (*left*) and PSF-subtracted residuals (*right*) from GALFIT in all three filters. All images are aligned North up and East left. The galaxy causing the absorption is clearly visible in the $F606W$ image even before PSF subtraction. The same position is shown by the red circle in the IR images.

A high number of parameters dictate the outcome of such a simulation. Luckily, our observations offer excellent constraints on many of these: The effective radius, $r_e = 1.12$ kpc, used to model the size of the emitting region, the metallicity $Z \simeq 0.31 Z_\odot$ [we assume that the amount of metals that condense to dust is similar to the local Universe (Zafar & Watson 2013)], and an average of 130 km s^{-1} from the measured emission-line widths are used as a proxy for the intrinsic Lyα linewidth. From the widths of the low-ionization absorption lines, we use a velocity dispersion of the clouds of 115 km s^{-1}. Finally, we infer an intrinsic equivalent width of 150 Å, in accordance with the $F606W$ magnitude. For details on the rest of the parameters, e.g., cloud size distribution, temperatures, densities of the two phases, &c., see Laursen, Duval, & Östlin (2013).

We set $r_{\rm gal} = 10$ kpc, but note that the exact size of the system is not important, rather the total column density $\langle N_{\rm HI} \rangle$ from the centre and out, averaged over all directions, determines the shape of the spectrum. This leaves us with two unknown parameters, $\langle N_{\rm HI} \rangle$ and $V_{\rm out}$, where $\langle N_{\rm HI} \rangle$ is dominated by the number of clouds ($N_{\rm cl}$). We first run a rough fit to the spectrum, providing us with information about the initial conditions for the system: $N_{\rm cl} = 10^5$ and $V_{\rm out} = 150$ km s^{-1}, and consequently run a grid of 11×11 models with $N_{\rm cl} \in [10^{4.5}, 10^{5.5}]$ and $V_{\rm out} \in [100, 200]$ km s^{-1}.

Instead of doing a regular χ^2 minimization of the pixel-wise difference between model and spectrum, we compare the observed and the simulated spectra using the following four observables: The peak separation in Å; the width of the red peak in Å; the ratio of the integrated flux in the two peaks; and the ratio of the peak heights. The best fit is defined as the model which minimizes all of the four above mentioned criteria simultaneously, given the constraints on metallicity, emission line velocity dispersion, Ly-alpha flux, and structure of the emitting region. From the best fit, we find an outflow velocity of $V_{\rm out} = 160^{+20}_{-40}$ km s^{-1}. Here, the confidence intervals are given by the range of models, for which *all* four estimators lie within the 68% confidence interval of those observed in our spectrum. In the best-fitting model, the average column density and number of clouds intercepted by a sightline toward the quasar at a distance of 6.3 kpc are $\log(N_{\rm HI}/{\rm cm}^{-2}) = 20.23^{+0.27}_{-1.15}$ and $n_c = 2\pm1$, respectively. This is somewhat lower although not inconsistent with the measured value of 20.65 ± 0.05 and the fact that five absorption profiles were used in Section 3.7.

The escape fraction of Lyα photons ($f_{\rm esc} \sim 90\%$) is higher than what is found when comparing the total Lyα-to-Hα ratio, and we find that a SFR of only 6.0 M$_\odot$ yr^{-1} is needed to match the observed spectrum. However, the galaxy was modelled as a spherically symmetric system, and the galaxy appears disc-like from the GALFIT analysis in Section. 3.8. For such a disc-like system, the escape fraction will be significantly lower when observed edge-on, which indeed seems to be the case here.

3.10 Star Formation Rate

The $F606W$ flux of the galaxy as measured from the *HST* data corresponds to a rest-frame wavelength of 1775 Å at the redshift of the galaxy. Based on the AB magnitude obtained from our GALFIT analysis (see Table 3.4) we get a luminosity after correcting for Galactic extinction. We use the emission redshift, $z_{\rm em} = 2.3537$, to compute the luminosity distance.
This gives a luminosity of $L_\nu = F_\nu \, 4\pi \, d_L^2 \, (1+z)^{-1} = 9.63 \times 10^{28}$ erg s^{-1} Hz^{-1}. We use the extinction correction factor for the $F606W$ band, $\Delta{\rm mag} = -0.11$ mag, from the NASA/IPAC Extragalactic Database[2] (NED). This luminosity corresponds to a star formation rate of ${\rm SFR_{UV}} = 13.5 \pm 0.5$ M$_\odot$ yr^{-1} using the relation from Kennicutt (1998).

For the Hα emission line, we take the observed line flux (see Table 3.1) and convert it to a luminosity of $L_{\rm H\alpha} = 2.40 \pm 0.10 \times 10^{42}$ erg s^{-1}. From the luminosity we calculate a star formation rate of ${\rm SFR_{H\alpha}} = 18.9 \pm 0.8$ M$_\odot$ yr^{-1}, again using Kennicutt (1998).

The discrepancy between the two inferred star formation rates indicates some degree of dust extinction. To quantify the amount of extinction we assume that the two measures should yield the same value, when corrected for dust reddening. The correction factor to the SFR can be expressed as:

$$ {\rm SFR_{int}} = {\rm SFR_{obs}} \times 10^{0.4 \cdot E(B-V) k(\lambda)} \, . $$

Requiring that the two SFRs from UV and Hα be equal we arrive at the following expression:

$$ E(B-V) = \frac{2.5}{k({\rm UV}) - k({\rm H\alpha})} \times \log\left(\frac{{\rm SFR_{H\alpha}}}{{\rm SFR_{UV}}}\right) \, , $$

where $k({\rm UV})$ and $k({\rm H\alpha})$ denote the Calzetti et al. (2000) extinction curve evaluated at the UV rest-

[2] `http://ned.ipac.caltech.edu/`

frame wavelength, 1755 Å, and at the rest-frame wavelength of Hα, respectively. From this relation, we derive a colour excess of $E(B-V) = 0.06 \pm 0.01$ consistent with the previously mentioned measure from the Balmer decrement (Section 3.5). The extinction-corrected star formation rate is SFR $= 22.8 \pm 1.2$ M$_\odot$ yr^{-1} with an assumed Salpeter initial mass function (IMF). If we convert this to the Chabrier IMF we get SFR$_{\rm ch} = 12.7 \pm 0.7$ M$_\odot$ yr^{-1}. This measurement agrees very well with the results of Fynbo et al. (2010) and Péroux et al. (2012) who find SFR > 10 M$_\odot$ yr^{-1} and SFR $= 17.1 \pm 6.0$ M$_\odot$ yr^{-1}, respectively.

We note that the two proxies for star formation do not trace star formation on the same physical time-scales, and therefore do not necessarily have to yield the same measured quantity. The Hα-line primarily traces the ongoing star formation responsible for ionizing the H II regions, whereas the UV continuum traces previous star formation as well, linked to the O and B stars already in place. However, the young, UV-bright stars may also contribute to photoionization of the gas, and the quantification of the difference depends on assumptions about IMF, star formation history, and the distribution of dust. The detailed, exact modelling of all these factors is beyond the scope of our simple extinction estimate, we have therefore chosen to neglect this effect in the above analysis.

The star formation rate can also be determined directly from the absorption lines associated with the DLA if the C II* absorption line is available (the method is described in Wolfe, Prochaska, & Gawiser 2003). Unfortunately the line is blended, so we cannot put any firm constraint on the star formation using this method.

3.11 Broad-Band SED Fitting

We fit the three broad-band photometric points from the *HST* imaging mentioned in Section 3.8 to obtain estimates of stellar mass, age, and star formation rate. But first, we apply a correction for Galactic extinction available from the NED online database[2]. To simplify the fit we subtract the emission-line fluxes from the broad-band fluxes and fit the continuum only, instead of fitting both continuum and emission lines simultaneously. The only filter which is influenced by strong emission lines is the $F160W$ band, which contains flux from Hβ and the two [O III] lines. In order to subtract the emission lines, we assume a flat continuum spectrum, since we only detect the emission lines, and subtract the integrated line fluxes from the total flux in the observed band, weighted by the filter curve. We find that the emission lines contribute 33% of the total flux, and we infer a corrected $F160W$ magnitude of $m_{160} = 23.94 \pm 0.19$.

Our fitting code uses the stellar population templates from Bruzual & Charlot (2003) convolved with a large Monte Carlo library of star formation histories (exponential plus random bursts) assuming a Chabrier (2003) IMF. Dust is added following the two-component model of Charlot & Fall (2000), with the parameters being the total optical depth, $\tau_{\rm v}$, and the fraction of dust contributed by the ISM, μ.[3] We restrict the range of metallicities of the models to be consistent with our measurement from the emission lines $\log(Z/Z_\odot) = -0.3 \pm 0.1$. We then adopt a Bayesian approach by comparing the observed photometry to the one predicted by all the models in the library, and we construct the probability density functions (PDFs) of stellar mass, mean light-weighted stellar age, and star formation rate. Taking the mean and 16$^{\rm th}$ and 84$^{\rm th}$ percentiles of the PDF, we obtain a stellar mass of M$_\star = 2.1\,^{+1.4}_{-0.9} \times 10^9$ M$_\odot$, an age of the galaxy of $t = 98^{+113}_{-48}$ Myr, and a star formation rate of SFR $= 8.4\,^{+4.3}_{-1.4}$ M$_\odot$ yr^{-1}. We also obtain an

[3]For details on the prior distribution of the SFH and dust parameters see Salim et al. (2005)

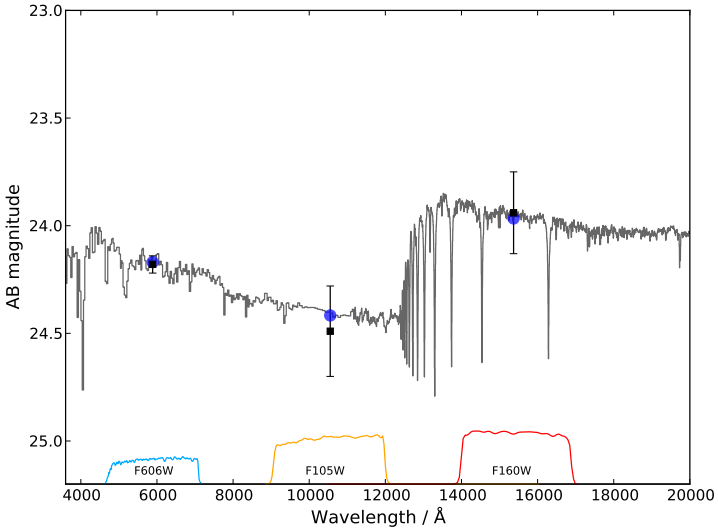

Figure 3.7: Best fitting template (in grey) to our three broad-band photometric points (black squares). The error-bars in y-direction indicate the 1σ uncertainty on the fluxes. In the bottom of the figure the transmission curves for each filter are shown, and the blue, round points indicate the model magnitudes calculated in each filter passband. The median age and mass of the fit is $t = 98$ Myr and $M_\star = 2.1 \cdot 10^9$ $M_\odot$, respectively.

estimate of the dust extinction from the fit by comparing the intrinsic template with the best fitting reddened template. From this we infer $A(V) = 0.08^{+0.29}_{-0.07}$, which corresponds to $E(B-V) = 0.02^{+0.07}_{-0.02}$. The SFR from the SED fit agrees well with the one inferred in Section 3.10 within 1σ, and also the median value of the dust is consistent with what we find in Sections 3.5 and 3.10. The photometry and best-fitting template are shown in Figure 3.7.

3.12 Discussion

3.12.1 Abundances

We have presented a measurement of the gas-phase metallicity in the H II regions of the emission counterpart of the DLA toward the quasar Q 2222−0946. The metallicity we infer using the R_{23} and N2 diagnostics expressed in Solar units is $[\mathrm{O/H}] = -0.30 \pm 0.13$. From the absorbing gas located 6.3 kpc away, we find a metallicity in the neutral ISM from sulphur of $[\mathrm{S/H}] = -0.49 \pm 0.05$, thus slightly lower than the metallicity inferred from the central emitting region. Sulphur is not depleted onto dust, and thereby traces the overall metallicity very well. We find a consistent metallicity from $[\mathrm{Si/H}] = -0.54 \pm 0.05$ and $[\mathrm{Zn/H}] = -0.38 \pm 0.05$ (note that [Zn/H] is probably overestimated by 0.1 dex). Neither Zn nor Si are significantly depleted onto dust and hence provide a good measurement of the gas-phase metallicity (Meyer & Roth 1990; Pettini et al. 1997). The observed metallicities of DLAs at these redshifts range from $[\mathrm{M/H}] \approx -2.5$ to $[\mathrm{M/H}] \approx -0.2$ with an average metallicity weighted by N_{HI} of -1.1 ± 0.1 (Rafelski et al. 2012). The DLA in our study is thus among the most metal-rich DLAs at this redshift.

From the elements Mn, Fe, and Ni, we clearly see that dust depletion is in fact at play. The metallicities are $[\mathrm{Fe/H}] = -1.0$, $[\mathrm{Ni/H}] = -0.9$, and $[\mathrm{Mn/H}] = -1.2$, indicating that the refractory elements are, to some degree, removed from the gas-phase, which is to be expected in a high-metallicity system as this particular one (Ledoux, Petitjean, & Srianand 2003). Also, we report a tentative detection of H_2.

Bowen et al. (2005) find similar results regarding gas phase metallicities for a low-redshift galaxy, where a quasar intersects the galaxy 3 kpc from a star-forming region. The authors find consistent metallicities based on the emission region and the absorbing, neutral gas, respectively. For a compilation of systems with emission and absorption based metallicities, see Péroux et al. (2012).

The presence of highly enriched material 6 kpc above (almost perpendicular to) the galactic plane of this galaxy with nearly the same metallicity as the star-forming regions within the galaxy indicates that metal-rich material has been expelled from the galaxy into the halo. We see independent evidence for outflowing gas from the Lyα emission line with a velocity of 160 km s^{-1}, see Section 3.9 for details. At this velocity we estimate that it would take of the order of 40 Myr for this enriched material to reach a distance of 6.3kpc from the galaxy plane. Given this relatively short time-scale it seems reasonable that the two metallicities are similar, since no large amount of enrichment has had time to occur after the expulsion of the outflowing gas, which is expected to mix with lower metallicity gas further out, lowering the observed metallicity in the absorbing gas. This scenario can be compared to the wind observed in the nearby galaxy M82, where neutral gas and molecules form a filamentary structure in the outflow extending to great distances from the disc (Veilleux, Rupke, & Swaters 2009; Melioli, de Gouveia Dal Pino, & Geraissate 2013).

A recent study by Bregman et al. (2013) shows evidence for a similar scenario, where near-Solar metallicity gas of a nearby, edge-on disc galaxy has been detected 5 kpc above the disc with a neutral hydrogen column density of 1.3×10^{20} cm^{-2}. However, as these authors study a local galaxy a direct comparison to high redshift might not be fully valid.

3.12.2 Dynamical Mass

We can use our information about the size of the galaxy and the kinematics, as probed by the emission lines (see FWHM measures in Table 3.1), to get an estimate of the dynamical mass of the system. We follow the method described in Rhoads et al. (2014) to estimate the dynamical mass given the measured size and velocity dispersion:

$$M_{\rm dyn} \approx \frac{4\,\sigma^2\,a_e}{G\sin^2(i)}\,,$$

where i denotes the inclination of the system with $i = 90^{\rm o}$ being edge-on. In order to estimate the velocity dispersion of the system we use the FWHM of the emission lines as a probe of the integrated gas-kinematics of the system. We then take a weighted mean of all the measured linewidths, and correct the FWHM for the instrumental resolution (45 km s^{-1}). This gives a measure the velocity dispersion of $\sigma = 49.1 \pm 7.7$ km s^{-1}, and we get the size from the GALFIT analysis in physical units: $a_e = 1.12 \pm 0.06$ kpc (see Table 3.4).

From the GALFIT analysis, we infer an axis ratio of the galaxy of $b/a = 0.17$. The system may be described as reasonably disc-like, given the elongated shape, and the fact that we see a value of Sérsic n very close to 1. Using the results of Haynes & Giovanelli (1984) that disc galaxies on average have axis ratios around $0.1 - 0.2$, we conclude that the galaxy in our study is very close to edge-on, even when assuming the lowest intrinsic value of 0.1. We thus adopt a value of $i = 90^{\rm o}$ and use the fitted half-light semi-major axis for our estimate of the dynamical mass of the system: $M_{\rm dyn} \approx 2.5 \times 10^9\,{\rm M}_\odot$. This estimate should only be considered a rough approximation (valid within a factor of ~ 2) as we have assumed the system to be in virial equilibrium, which it may not be.

3.12.3 Stellar Mass

From our SED fit to the broad-band imaging data, we obtain a stellar mass of $M_\star = 2.1 \times 10^9$ $M_\odot$. We can use this measurement to test the recently proposed evolving mass-metallicity relation for DLA systems (Ledoux et al. 2006, see also Møller, Fynbo, & Fall (2004); Møller et al. (2013); Neeleman et al. (2013)). Using the relation in Møller et al. (2013), which relates emission metallicity and redshift to stellar mass, with our direct measurement of the emission metallicity, we find a stellar mass of $M_\star = 6\,^{+9}_{-4} \times 10^9$ $M_\odot$. Though the scatter in their relation is substantial (~ 0.38 dex), the agreement between the relation and our best fit stellar mass from the SED fit is striking.

Moreover, the mass is in very good agreement with the median stellar mass of Lyman break galaxies (LBGs) at redshift $z = 1 - 3$ (Erb et al. 2006). Hathi et al. (2013) find $M_{\star,\mathrm{LBG}} = 2 \times 10^9$ $M_\odot$, and further characterize the general LBG population in terms of median age (∼125 Myr), median SFR ($\sim 15\,M_\odot\ \mathrm{yr}^{-1}$), and median dust extinction ($E(B-V) \approx 0.15$). All, but the median dust extinction, agree well with our inferred quantities. The dust extinction value is, however, still consistent with our value within the errors (see figure 6 of Hathi et al. 2013). The consistency between the galaxy in our study and the general LBG population shows that there is indeed some overlap between galaxies causing DLAs and star-forming galaxies selected with the Lyman break technique at redshifts $z = 2-3$ (Fynbo et al. 2003; Rauch et al. 2008). Nevertheless, it is important to remember that the DLA in question was specifically chosen to have high metallicity, and is of unusually high metallicity; it is an order of magnitude higher than the median metallicity of DLAs at $z = 2 - 3$, $[\mathrm{M/H}] \simeq -1.5$ or 1/30 of Solar (Noterdaeme et al. 2008; Rafelski et al. 2012). The proposed mass–metallicity relation for DLA galaxies (Ledoux et al. 2006), then supports the original suggestion by Fynbo, Møller, & Warren (1999) that most DLA galaxy counterparts are too faint to be identified via their stellar or nebular emission.

We are further able to infer the expected metallicity from the stellar mass and SFR using the fundamental metallicity relation from the work of Mannucci et al. (2010). Given the expression from these authors we find an oxygen abundance in the range from $[\mathrm{O/H}] = -0.3$ to $[\mathrm{O/H}] = -0.5$ depending on the fitting function assumed. Since the SFR of our target is slightly outside the range over which the relation is derived there will be uncertainty related to the extrapolation. The metallicity is, however, still in perfect agreement with our measurements. This indicates that the DLA in our study follows the same relation as other galaxies studied at both lower and higher redshifts, strengthening the link between this DLA galaxy and the general population of star-forming galaxies.

The Tully-Fisher Relation

We now turn to look at how this galaxy is located on the stellar-mass Tully-Fisher relation ($M_\star$-TFR) to test our assumption that the system is disc-like and relaxed. The Tully-Fisher relation, originally stated in terms of luminosity and velocity (Tully & Fisher 1977), can also be presented in terms of stellar mass (which correlates with luminosity) and velocity. The $M_\star$-TFR was studied in detail by Kassin et al. (2007) who gave their best fit to the data as:

$$\log(S_{0.5}) = 1.89 \pm 0.03 + 0.34 \pm 0.05 \times \log\left(\frac{M_\star}{10^{10}\ M_\odot}\right)\ ,$$

where $S_{0.5}$ is defined by the authors as $S_K^2 \equiv K\,V_{\mathrm{rot}}^2 + \sigma_g^2$, with $K = 0.5$. Using the measured velocity dispersion as a proxy for $S_{0.5}$ (see a discussion of this in Rhoads et al. 2014) we find that the inferred

stellar mass is $M_\star = 2.6^{+1.9}_{-1.2} \times 10^9 M_\odot$. This is in very good agreement with our previously mentioned mass estimates, including our rough estimate of the dynamical mass.

The stellar (and dynamical) mass inferred from the emission-line widths is subject to uncertainties caused by the fact that we do not know the detailed structure of the velocity field. The emission lines are most certainly influenced by turbulence in the gas, which we cannot quantify. This would overestimate our linewidths and thereby our TF-based stellar mass and dynamical mass estimates. Also, we required that the system be in virial equilibrium; however, we observe gas at large galactocentric radii, almost perpendicular to the disc, with similar metallicity as the line emitting region, indicating outflowing gas from the central parts. This has an impact on our calculation of the dynamical mass, and our ability to use the linewidths as a tracer of the ordered rotation of the system. Moreover, a non-negligible gas mass is expected in a young ($\sim$ 100 Myr), star-forming galaxy. This mass would not be accounted for in the stellar mass estimate from the SED fit, but would contribute to the dynamical mass, thus increasing the observed velocity dispersion. We estimate the gas mass from the star formation density (see Kennicutt 1998) using the half-light radius and the axis ratio of the galaxy. We infer a gas mass of $\mathrm{M_{gas}} = 1^{+3}_{-0.5} \times 10^9\ \mathrm{M_\odot}$. This estimate is a very rough approximation given the large scatter (~ 0.3 dex) in the relation, and is therefore not to be trusted as a true value of the amount of gas. It does, however, indicate that a gas mass of roughly half the stellar mass is present. We note that the inferred dynamical mass is consistent with our best-fitting stellar mass within $1\,\sigma$, and a significant gas mass is therefore not required in order to reconcile the two mass estimates, and within the (large) uncertainties, all three mass estimates agree well. The compact nature of the galaxy also means that the kinematics of the emission lines only probe the innermost region, and are therefore mostly sensitive to the *stellar* mass concentrated in the central region, and not the gas in the outer parts.

Studies of the TFR at higher redshifts find that the relation is offset to lower stellar masses for a given velocity. We see a similar though not statistically significant trend in our data. Cresci et al. (2009) find that LBGs at $z \approx 2$ are offset by 0.4 dex compared to the local TFR, and they find that the relation has *low* scatter. Gnerucci et al. (2011) find similar results in their sample of $z \approx 3$ galaxies with an offset up to 1 dex; however, the scatter in their data is very large. This may indicate that the TFR has not yet been established at these redshifts, and that the galaxies are influenced heavily by random motions.

3.13 Summary and Conclusion

We have presented our analysis of a high-redshift galaxy selected from its neutral hydrogen absorption seen in the spectrum of a background quasar. We have presented the extracted emission lines from the galaxy counterpart of the absorption, and combined these with our detailed absorption-line study to probe the metallicities seen in the two phases. We find that the two metallicities are similar, but the absorbing gas has a slightly lower metallicity than the emitting gas. We use *HST* imaging to constrain the stellar population; our data are consistent with the picture in which the galaxy causing the Lyα absorption is a young, small ($\sim$ 1 kpc), disc-like system, with a not fully ordered (proto-) disc structure. Moreover, we see evidence for a so-called *galactic fountain*, where enriched gas gets blown out from the star-forming regions, forms the neutral hydrogen absorption that we see $\sim$ 6 kpc above the galactic plane, and in the end may settle back onto the disc.

This galaxy demonstrates exactly how star-forming galaxies at high redshift may overlap with the population of the most metal-rich DLAs. However, the very faint nature of damped Lyman-α absorbing galaxies renders the majority of these almost impossible to detect. The few exceptions, such as the case reported here, thus offer a rare glimpse into this elusive galaxy population.

Acknowledgements

We thank the anonymous referee for the a nice and constructive report. The Dark Cosmology Centre is funded by the DNRF. JPUF and PL acknowledge support form the ERC-StG grant EGGS-278202. JK acknowledges support from an ESO Studenthip. CP has benefited from support of the Agence Nationale de la Recherche with reference ANR-08-BLAN-0316-01. This research has made use of the NASA/IPAC Extragalactic Database (NED) which is operated by the Jet Propulsion Laboratory, California Institute of Technology, under contract with the National Aeronautics and Space Administration. The RT simulations were conducted on the facilities provided by the Danish Center for Scientific Computing. A.G. acknowledges support from the EU FP7/2007-2013 under grant agreement n. 267251 AstroFIt. Based on observations collected at the European Organisation for Astronomical Research in the Southern Hemisphere, Chile, under program 087.A-0085(A). Based on observations made with the NASA/ESA Hubble Space Telescope, obtained at the Space Telescope Science Institute, which is operated by the Association of Universities for Research in Astronomy, Inc., under NASA contract NAS 5-26555. These observations are associated with program 12553.

4

Identifying Red Quasars

This chapter contains the following article:

"Optical/Near-Infrared Selection of Red Quasi-Stellar Objects: Evidence for Steep Extinction Curves toward Galactic Centers?"

Published in *The Astrophysical Journal Supplement Series, vol. 204, id. 6, 2013.*

Authors:

J. P. U. Fynbo, J.-K. Krogager, B. Venemans, P. Noterdaeme, M. Vestergaard, P. Møller, C. Ledoux, & S. Geier

We present the results of a search for red QSOs using a selection based on optical imaging from SDSS and near-infrared imaging from UKIDSS. Our main goal with the selection is to search for QSOs reddened by foreground dusty absorber galaxies. For a sample of 58 candidates (including 20 objects fulfilling our selection criteria that already have spectra in the SDSS) 46 (79%) are confirmed to be QSOs. The QSOs are predominantly dust-reddened except for a handful at redshifts $z \gtrsim 3.5$. However, the dust is most likely located in the QSO host galaxies (and for two the reddening is primarily caused by Galactic dust) rather than in intervening absorbers. More than half of the QSOs show evidence of associated absorption (BAL absorption). Four (7%) of the candidates turned out to be late-type stars, and another four (7%) are compact galaxies. We could not identify the remaining four objects. In terms of their optical spectra, these QSOs are similar to the QSOs selected in the FIRST-2MASS Red Quasar Survey except they are on average fainter, more distant, and only two are detected in the FIRST survey. As per the usual procedure, we estimate the amount of extinction using the SDSS QSO template reddened by SMC-like dust. It is possible to get a good match to the observed (restframe ultraviolet) spectra, but it is not possible to match the observed near-IR photometry from UKIDSS for nearly all the reddened QSOs. The most likely reasons are that the SDSS QSO template is too red at optical wavelengths due to contaminating host galaxy light and that the assumed SMC extinction curve is too shallow. Three of the compact galaxies display old stellar populations with ages of several Gyr and masses of about 10^{10} $M_\odot$ (based on spectral energy distribution modelling). The inferred stellar densities in these galaxies exceed 10^{10} $M_\odot$ kpc^{-2}, which is among the highest measured for early type galaxies. Our survey has demonstrated that selection of QSOs based on near-IR photometry is an efficient way to select QSOs, including reddened QSOs, with only small contamination from late-type stars and compact galaxies.

4.1 Introduction

QSO absorption line studies have led to major progress in our understanding of the intergalactic medium and of early galaxies (Rauch 1998; Wolfe, Gawiser, & Prochaska 2005). Using high-resolution spectroscopy of damped Lyman-α absorbers (DLAs) detected against the light of background QSOs the chemical enrichment in galaxies has been probed over most of cosmic history (e.g., Prochaska et al. 2003b). However, in order to interpret the available data it is important to understand to which extent the data are biased against dusty and, hence, likely more metal-rich sightlines. This issue has been discussed extensively in the literature for more than 30 years (e.g., Wright 1981; Pei, Fall, & Bechtold 1991; Pei, Fall, & Hauser 1999; Warren, Hewett, & Foltz 2000; Vladilo & Péroux 2005; Pontzen & Pettini 2009; Erkal, Gnedin, & Kravtsov 2012). One approach by which to gauge the importance of the dust bias is to establish the absorption statistics from a radio selected sample of QSOs. This approach has been followed both in the CORALS survey (Ellison et al. 2001, 2004) and the UCSD survey (Jorgenson et al. 2006). The largest of those studies is the UCSD survey, which includes the CORALS data. These authors conclude that while a dust bias is probably a minor effect, a four times larger sample is needed to absolutely confirm an absence of significant dust bias. The later study of Pontzen & Pettini (2009) confirm that dust-bias is likely to be a small effect, but they also find that the cosmic density of metals as measured from DLA surveys could be underestimated by as much as a factor of 2 due to dust bias. A factor of 2 is a sufficiently large deficit that it is interesting to pursue this issue further.

There is positive evidence that dust bias does systematically remove the most metal rich absorbers form the samples. The first direct evidence came with the study by Pei, Fall, & Bechtold (1991) that the spectra of QSOs with DLAs on average are redder than the spectra of QSOs without intervening DLAs. This work has been somewhat controversial as some studies confirmed the finding while other works rejected it (e.g., Murphy & Liske 2004; Frank & Péroux 2010a; Khare et al. 2012). The latest work of Khare et al. (2012) does seem to find robust evidence for statistically significant excess reddening of QSOs with foreground DLAs. Although it is difficult to unambiguously establish excess reddening in individual sightlines to QSOs, as the intrinsic slope cannot be determined a priori, there are also convincing detections of reddening towards individual systems with foreground DLAs, sub-DLAs or strong metal-line absorbers (Noterdaeme et al. 2009a, 2010; Kaplan et al. 2010; Fynbo et al. 2011; Noterdaeme et al. 2012b; Wang et al. 2012). Some of these QSOs have colors that place them on the edge of or outside of the SDSS QSO color selection. It is therefore reasonable to expect that there may be a significant population of metal-rich absorbers that are underrepresented in the current DLA samples.

Motivated by the detection of the reddened QSOs towards metal-rich absorbers mentioned above we decided to carry out a search for QSOs with red colours in order to establish if some fraction of red QSOs could be red due to dusty foreground absorbers. The search for red QSOs also has a long history (e.g., Webster et al. 1995; Benn et al. 1998; Warren, Hewett, & Foltz 2000; Gregg et al. 2002; Glikman et al. 2004, 2007; Hopkins et al. 2004; Maddox et al. 2008; Urrutia et al. 2009; Banerji et al. 2012; Glikman et al. 2012). The detection of red QSOs in most of these works relied on either radio or X-ray detections (see Warren et al. 2000 for an extensive discussion). However, recently large area surveys in the near-infrared has made it possible to select QSOs based on near-infrared photometry alone (Warren et al. 2000, 2007; Peth, Ross, & Schneider 2011) and this is the approach we have adopted in this work. In Section 4.2 we present our selection criteria. In Sections 4.3 and 4.4 we describe our observations and analysis of the candidate red QSOs selected in the regions of the sky covered both by UKIDSS and SDSS.

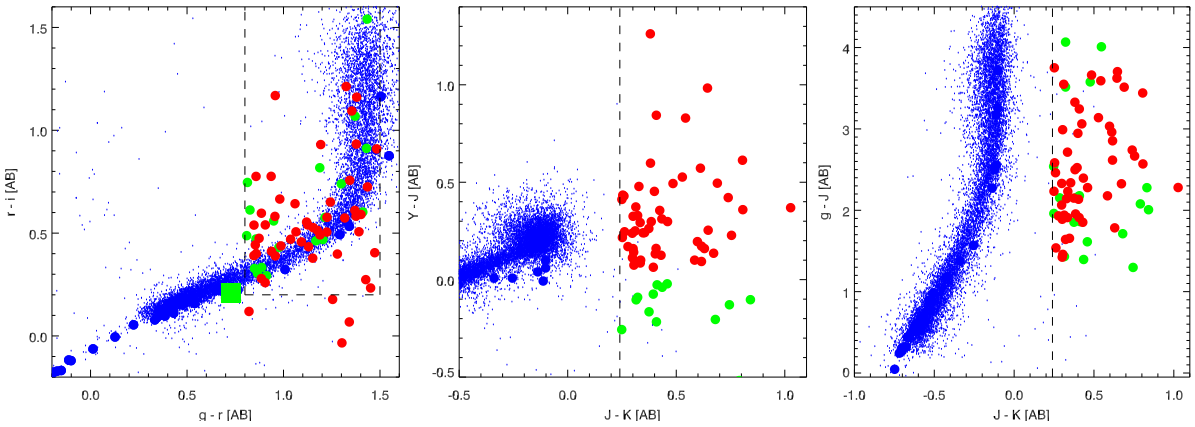

Figure 4.1: Color-color diagrams (in AB magnitudes) illustrating our selection of candidate reddened quasars. Candidates are shown with big red ($Y - J > 0$) and green ($Y - J < 0$) points. From left to right are shown: $r - i$ vs. $g - r$, $Y - J$ vs. $J - K$, and $g - J$ vs. $J - K$. The regions in color-color space in which we selected reddened quasars are outlined by dashed lines. The green square in the panel on the left represents the color of Q 0918+1636. Also shown are the colors of a random subsample of all point sources in our catalogues (small blue points) and a simulated stellar track (big blue points). With our optical–infrared color selection, we are able to robustly distinguish reddened quasars from the stellar locus.

4.2 Selection criteria

Rather than trying to build an unbiased sample our approach is to make a tailored search for red QSOs. Our goal is to make a selection of QSOs that are redder than the reddened QSO Q 0918+1636 studied by Fynbo et al. (2011) in the SDSS $g - r$ and $r - i$ colors. In our selection, we take advantage of a recent comprehensive study of the near-IR colors of QSOs found by matching SDSS and UKIDSS catalogs (Peth, Ross, & Schneider 2011). Based on this study, we select from regions on the sky covered both by SDSS and UKIDSS (mainly Stripe 82) point sources (classified as such both in UKIDSS and SDSS) with $J_{\rm AB} - K_{\rm AB} > 0.24$ (corresponding to $J_{\rm Vega} - K_{\rm Vega} > 1.2$) and $i - K_{\rm AB} > 0.1$ (corresponding to $i - K_{\rm Vega} > 2$). This leads to an efficient selection of QSOs and a sufficiently robust rejection of stars. In order to select reddened QSOs we next impose $0.8 < g - r < 1.5$ and $r - i > 0.2$. The limit $g - r < 1.5$ comes from the fact that we wish to avoid objects that are too red and hence too faint in the optical to allow the detection of the Lyman-α forest and in particular DLAs. We demand $J_{\rm AB} < 19$ in order to have sufficient signal to allow for spectroscopy in the optical (i.e. again to establish the presence of DLA and metal lines). We initially added a color cut of $Y - J > 0$ based on previous experience that sources with $Y - J < 0$ had problems with the photometry in UKIDSS. However, we subsequently dropped this criterion as some QSOs do have $Y - J < 0$, in particular at redshifts between 2 and 3.

We found that 54 sources in the overlapping region of UKIDSS and SDSS in Stripe 82 fulfill these selection criteria (see Fig. 4.1).

By combining the star/galaxy classifiers based on the images in both the SDSS and the UKIDSS Large Area Survey we are able to very efficiently remove compact galaxies from our sample of candidates. We tested the efficiency of galaxy removal from our sample with a set of 72,464 objects with both Sloan spectra and UKIDSS photometry. Out of the 39,814 objects we selected as point sources, only 69 (0.2%) are galaxies based on the SDSS spectrum. Therefore, our sample should contain less than one galaxy. Moreover, only 29 out of more than 30,000 objects spectroscopically classified as stars in the overlapping region with the UKIDSS equatorial block (which is almost 10 times larger than Stripe

82) data fulfill our selection criteria. Finally, we looked at the spectroscopically confirmed SDSS QSOs with UKIDSS photometry selected in an area of about 1500 deg^2 and only 36 (out of 21,174) satisfied our criteria. Of these, the majority are either BAL QSOs or red QSOs at $z < 1$. Interestingly, one of these QSOs is a red $z = 3.62$ QSOs with an intervening DLA – the exact systems we are looking for (SDSS J125306.73+130604.9). Given that Stripe 82 has an area of only 250 deg^2 we expect that our 54 candidates will have a different mix of BAL QSOs and dust-reddened QSOs. Independent of their nature, this survey will reveal the nature of a group of QSOs that are missed in most QSO surveys thus far.

4.3 Observations and Data reduction

In order to confirm or reject the candidate red QSOs we have carried out three runs of spectroscopic follow-up of the candidates. In order to use observing nights optimally we selected 7 additional targets at right ascensions around 8 hr with both SDSS and UKIDSS coverage. We also observed a single source with $J_{\rm AB} > 19$ and 4 sources that do not fulfill the $r_{\rm AB} - i_{\rm AB} > 0.2$ color criterion.

In August 2011 and January 2012 we observed 8 candidates at the Nordic Optical Telescope (NOT) on La Palma equipped with the Andalucia Faint Object Spectrograph and Camera (ALFOSC). At the NOT we used grism 4, which covers the wavelength range from about 3800 Å to 9000 Å at a resolution of about 350. Redward of about 7000 Å the spectra are strongly affected by fringing so the effective useful wavelength range for faint sources only extends to about 7000 Å. In November 2011 we observed another 40 candidates using the New Technology Telescope (NTT) at La Silla (ESO) equipped with the ESO Faint Object Spectrograph and Camera 2 (EFOSC2). At the NTT we used grism 6, which covers the wavelength range 3800–7980 Å at a resolution of about 450. This grism suffers from significant 2nd order contamination redward of 6200 Å. Unfortunately, we only realized this after the observing run, so no order sorter filter was used during the observations. The spectra were taken aligning the slit at the parallactic angle. After the release of SDSS DR8 we found that 20 of our candidates have been observed by SDSS and of these 10 were also observed by us. In total we have spectra, either from our run or from the SDSS, of 58 objects. Of these, 11 are not in our main sample (i.e., outside Stripe 82, have $r_{\rm AB} - i_{\rm AB} < 0.2$ or $J_{\rm AB} > 19$). We were unable to secure a spectrum for 10 of our main targets from Stripe 82 during the mentioned two observing runs.

The full list of observed targets is provided in Table 4.1. Observing conditions during the three runs appeared to be photometric, but with strongly variable seeing. In particular, on the first two nights of the NTT run the seeing was poor (1.″5–2.″5), whereas the seeing during the last night of the NTT run and during both NOT runs was below 1". During the two nights with poor seeing we used slits with widths 1.″5 and 2.″0, but we still had significant slit loss. Based on the photometric measurements from SDSS we estimate that the slitloss was predominant between 30% and 50%. However, the slit loss was for some sources significant: the spectral flux was suppressed by more than a factor of two.

Table 4.1: The sample.

Target	R.A. (J 2000)	Decl. (J 2000)	r_{SDSS} (mag)	Telescope	Exptime (sec)
CQ2143+0022	21 43 17.43	+00 22 11.0	19.63	SDSS	
CQ2144+0045	21 44 26.03	+00 45 17.0	17.36	NOT	1200
CQ2217+0033	22 17 14.27	+00 33 46.5	20.16	NTT	1200
CQ2227+0022	22 27 45.19	+00 22 16.8	20.21	NTT, SDSS	1200
CQ2241+0115	22 41 19.65	+01 15 16.3	20.61	NTT	1800
CQ2241−0012	22 41 15.86	−00 12 39.8	21.12	NTT, SDSS(DR9)	2400
CQ2254−0001[a]	22 54 19.23	−00 01 55.1	19.57	NTT, SDSS(DR9)	900
CQ2306+0108	23 06 39.65	+01 08 55.2	19.36	NTT, SDSS	900
CQ2316+0023	23 16 59.35	+00 23 19.4	20.26	NTT	1200
CQ2324−0105	23 24 31.32	−00 53 42.6	21.18	NTT	1200
CQ2342+0043	23 42 20.14	+00 43 43.5	20.49	NTT	1200
CQ2344−0001	23 44 58.71	−00 01 38.7	19.92	NTT	1200
CQ2347−0109	23 47 07.41	−01 09 03.5	19.34	SDSS	
CQ2355+0007	23 55 21.48	+00 07 19.2	20.19	NTT	1200
CQ2355−0041	23 55 26.78	−00 41 54.2	19.36	NOT, SDSS	2000
CQ0009−0020	00 09 33.18	−00 20 22.3	19.42	NTT	900
CQ0022+0020	00 22 55.07	+00 20 55.1	20.57	NTT	2000
CQ0027−0019[a]	00 27 58.75	−00 19 23.7	19.20	NOT, SDSS	800
CQ0043+0000	00 43 27.46	+00 00 02.0	19.82	SDSS	
CQ0046−0011	00 46 31.21	−00 11 46.1	20.58	NTT, SDSS(DR9)	1200
CQ0105+0000	01 05 03.39	+00 00 34.1	20.12	NTT	1000
CQ0107+0016	01 07 07.86	+00 16 06.1	20.15	NTT	1000
CQ0127+0114	01 27 02.52	+01 14 12.6	17.83	NOT	600
CQ0129−0059	01 29 25.80	−00 59 00.1	19.33	NTT	900
CQ0130+0013	01 30 11.42	+00 13 14.5	19.29	SDSS	
CQ0202+0010	02 02 48.74	+00 10 46.5	20.91	SDSS	
CQ0211+0030	02 11 53.71	+00 30 45.9	20.23	NTT	1800
CQ0212−0023	02 12 26.85	−00 23 14.2	21.25	NTT	2400
CQ0220−0107	02 20 07.65	−01 07 31.0	18.54	NTT, SDSS(DR9)	900
CQ0222−0019[a]	02 22 23.13	−00 19 38.7	19.18	NTT, SDSS(DR9)	1000
CQ0229−0029	02 29 07.71	−00 29 09.5	20.27	SDSS	
CQ0239+0115	02 39 24.90	+01 15 15.6	20.56	NTT	2400
CQ0242−0000	02 42 30.65	−00 00 29.6	19.50	NTT	900
CQ0247−0052	02 47 17.29	−00 52 05.8	20.27	NTT	1500
CQ0255+0048	02 55 18.58	+00 48 47.6	19.02	SDSS	
CQ0303+0105	03 03 40.01	+01 05 57.3	19.73	NTT, SDSS	1200
CQ0310+0055	03 10 36.84	+00 55 21.7	19.73	SDSS	
CQ0311+0103	03 11 42.35	+01 03 55.2	20.12	NTT, SDSS	1200
CQ0312+0032	03 12 14.24	+00 32 35.2	19.42	NTT	900
CQ0312+0035	03 12 13.37	+00 35 54.6	19.81	NTT	1200
CQ0321−0105	03 21 18.21	−01 05 39.9	18.38	SDSS	
CQ0326+0106	03 26 03.80	+01 06 03.9	20.30	NTT, SDSS	1500
CQ0327+0006	03 27 55.04	+00 06 15.9	19.94	NTT	1200
CQ0329−0057	03 29 19.89	−00 57 15.5	19.98	NTT, SDSS	1200
CQ0332−0013	03 32 48.39	−00 13 15.3	19.71	NTT	1200
CQ0336+0112	03 36 59.45	+01 12 39.2	20.91	NTT	2400
CQ0338+0004	03 38 06.76	+00 04 33.9	20.02	SDSS	
CQ0339+0022[b]	03 39 27.11	+00 22 41.8	20.39	NTT	1200
CQ0350−0031	03 50 53.29	−00 31 14.7	19.83	NOT, SDSS	2000
CQ0354−0012	03 54 18.16	−00 12 56.7	19.14	NTT	4000
CQ0354−0030	03 54 46.04	−00 30 29.5	20.36	NOT	1800
CQ0822+0004[c]	08 22 49.97	+00 04 32.2	19.92	NTT	900
CQ0822+0435[c]	08 22 02.32	+04 35 26.0	19.50	NOT	1800
CQ0826+0728[c]	08 26 24.71	+07 28 20.8	20.09	NOT	1800
CQ0831+0930[c]	08 31 42.36	+09 30 29.8	19.56	NTT	900
CQ0831−0022[c]	08 31 26.43	−00 22 26.7	19.57	NTT	900
CQ0832+0121[c]	08 32 29.34	+01 21 05.4	19.80	NTT	1200
CQ0832+0606[c]	08 32 29.02	+06 06 00.6	19.73	NTT	1200

Notes: [(a)] $r_{AB} - i_{AB} < 0.2$; [(b)] $J_{AB} > 19$; [(c)] Not in Stripe 82.

The spectra were processed using standard techniques for bias and flat-field corrections and for wavelength calibration. Cosmic rays were removed using the software developed by van Dokkum (2001a). One-dimensional spectra were extracted using the optimal extraction technique described by Horne (1986) as implemented in IRAF.[1] The spectra were first flux calibrated using observations of the spectrophotometric standard star Feige110, observed on the same nights as the science spectra. However, because the standard star observed for the NTT run is very blue (it is a white dwarf) it had strong second order contamination. Our targets, on the other hand, are red by selection and hence have week 2nd order contamination. This flux calibration made the flux-calibrated spectra appear too blue at $\lambda > 6200$ Å compared to the existing SDSS photometric measurements for the objects. We hence decided to use a red spectrophotometric standard observed on the 3rd of June 2011 (LTT7379). Flux-calibrating the NTT spectra using this standard star resulted in better agreement with the existing SDSS photometry, but our NTT spectra still appear slightly too blue redward of 6200 Å. Blueward of 6200 Å the responses inferred using the two different standard stars were in agreement to better than 10 percent.

The spectra were corrected for Galactic extinction using the extinction maps from Schlegel, Finkbeiner, & Davis (1998). Most of the sources have low Galactic extinction, but eight have $E(B-V) > 0.1$ and of these two have $E(B-V) \approx 0.4$.

On February 9 and 10 2012 we observed the field of Q 0918+1636 in the near-IR using the NOT equipped with the near-IR camera NOTCam in the Y, J, H and Ks bands. The purpose of this observations was to infer if this object, which basically is the motivation for our QSO search, has near-IR colours consistent with our selection criteria. For photometric calibration we observed the field of RU149 for which J, H and K photometry is available in Hunt et al. (1998) and Y-band photometry is available in the UKIDSS survey (Hewett et al. 2006).

4.4 Results

4.4.1 Photometry

For Q 0918+1636 we derive the following magnitudes on the AB system: $Y(AB) = 19.46 \pm 0.07$, $J(AB) = 19.32 \pm 0.07$, $H(AB) = 19.29 \pm 0.07$ and $K(AB) = 18.68 \pm 0.10$. In terms of its near-IR colours it falls well-within the near-IR color criteria of our sample.

4.4.2 Spectroscopy

In Fig. 4.2 we show the 1-dimensional spectrum of one of the 58 candidates observed either by us or SDSS. The full figure set is shown in Appendix 4.A. In these diagrams we plot both spectra and the photometry from SDSS (g, r, i, z) and UKIDSS (Y, J, H, and K_s). With the exception of four the nature of the sources can be established robustly. In Table 4.2 we provide our classification of the candidates in the cases where it could be established. We also provide the SDSS QSO selection flags as defined in Table 1 of Richards et al. (2002). We find four of the candidates to be late-type stars, four are compact galaxies, 46 are most likely QSOs, and for four candidates we were not able to establish the nature of the object.

[1] IRAF is distributed by the National Optical Astronomy Observatory, which is operated by the Association of Universities for Research in Astronomy (AURA) under cooperative agreement with the National Science Foundation.

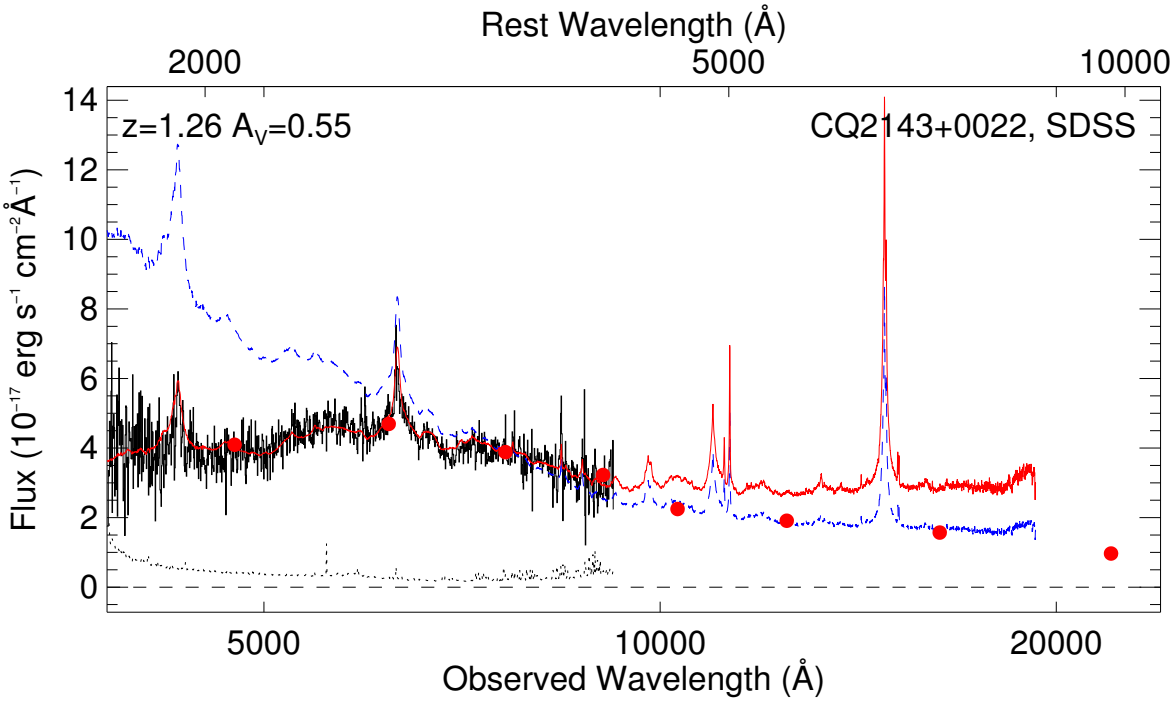

Figure 4.2: Shown are 1-dimensional spectra for one of the 58 candidate QSOs observed in our survey or by the SDSS. For each candidate the observed spectrum is plotted (solid) and the error spectrum (dotted line) is shown. In the upper left corner the estimated redshift and restframe V-band extinction is provided. With a blue dashed line we show the composite QSO spectrum from Vanden Berk et al. (2001) and Telfer et al. (2002) redshifted to the estimated redshift and with a solid red line the redshifted composite spectrum reddened by the indicated amount of extinction. Overplotted with filled circles is the SDSS and UKIDSS photometric points. The NOT and NTT spectra have been scaled to match the r-band photometric point from SDSS. Unless otherwise noted we have assumed an SMC-like extinction curve. Note that the spectra have not been corrected for telluric absorption. The SDSS spectra have been binned down by a factor of 4 for clarity.

For each QSO, we determine redshifts by visually matching the spectrum with the template spectrum of Vanden Berk et al. (2001) and Telfer et al. (2002) including reddening using the SMC, LMC or MW extinction curves as prescribed in Pei (1992). We here follow the approach of Urrutia et al. (2009). We assume that the dust is located at the redshift of the QSO as we find no evidence for absorber galaxies that could be responsible for the reddening. The inferred amounts of extinction should only be considered indicative for a number of reasons. As mentioned, the flux-calibration of our NTT spectra is affected by 2nd order contamination, which as discussed will tend to make the NTT spectra appear too blue. For 10 targets we have either NTT or NOT spectra and an SDSS spectrum. For those cases the inferred amounts of extinction are typically slightly higher in the SDSS spectra. In Table 4.2 we provide the redshifts and the amount of extinction A_V derived in this way.

For the majority of the candidate spectra, the QSO template reddened by an SMC-like extinction curve provide a good match to the data in the observed optical range. However, the reddened QSO template provides a poor match to the near-IR photometry from UKIDSS in most cases. We will return to this point in Sect. 4.5.1.

In Appendix 4.B we provide our notes on each spectrum.

4.4.3 The confirmed QSOs

The 46 confirmed QSOs are distributed broadly in redshift from $z = 0.438$ to $z = 4.01$. There is a curious lack of QSOs between $z = 2.6$ and $z = 3.4$, which is unfortunate as this is the redshift range we are primarily interested in for the detection of dusty intervening DLAs. The QSOs at $z > 3.5$ appear relatively normal, i.e., similar to the QSO template, and they have entered our selection due to their strong Lyman-α forest blanketing. Two confirmed QSOs are relatively normal QSOs that are primarily reddened by substantial Galactic extinction.

At $z < 3.5$ the majority of the remaining confirmed QSOs deviate from the QSO template, in addition to their redder spectra, either by showing BAL features or a combination of broad and narrow emission lines (e.g., CQ2342+0043 where C III is broad and C IV is narrow). This fact suggests that the source of the reddening is likely to be at the QSO redshift rather than in intervening galaxies. There is also no evidence for either strong metal-line absorbers nor intervening galaxies close to the line-of-sight in the imaging data.

In Fig. 4.4, we show how the derived $A_{\rm V}$ distribute with redshift for the confirmed QSOs in our sample. As mentioned, these $A_{\rm V}$ measurements are mainly indicative, but other surveys have determined $A_{\rm V}$ in a similar manner (e.g., Urrutia et al. 2009) and hence the values are still interesting for comparison. With red and blue symbols we show the upper and lower limits on $A_{\rm V}$, respectively, calculated using our color cuts in $g - r$ and by using the QSO template reddened by the SMC extinction curve. Many of the points fall below the blue curve, presumably due to an extra reddening caused by the fact that the emission lines are absorbed, but also due to the problem with flux calibration of our NTT spectra mentioned above.

4.4.4 Stars

Based on Hewett et al. (2006, their Table 9) M-dwarfs are expected to have $J - K < 1.2$ corresponding to $(J - K)_{\rm AB} < 0.24$. In the compilation of Hewett et al. (2006) there is one exception, namely an M8.5 dwarf with $J - K = 1.25$. In the lower right panel of Fig. 4.3 the four stars in our survey all lie very close to the cut-off in $J - K$. The colors and spectra of the two stars that are M-dwarfs indicate that they are relatively early type M-dwarfs (from M0 to M6) for which $J - K < 1.0$. They have presumably entered our sample either due to photometric errors or due to infrared excess emission, i.e., from circumstellar disks.

4.4.5 Galaxies

Three of the four galaxies we have identified are old and very compact stellar systems (CQ0105+0000, CQ0822+0004, and CQ0832+0121). The fourth object identified as a galaxy, CQ0009−0020, displays strong forbidden Oxygen and Neon emission lines. It also seems to have a relatively old underlying stellar continuum with a clear 4000 Å break. The galaxy fraction among our candidates is somewhat higher than expected, but is still sufficiently low that galaxy contamination is not a major obstacle for QSO searches based on this method.

Table 4.2: The Result of the Spectroscopic Follow-up.

Target	SDSS_flag	Type	Redshift	$A(V)$
CQ2143+0022	QSO_CAP	QSO	1.26	0.55
CQ2144+0045	None	M-dwarf		
CQ2217+0033	None	M-dwarf		
CQ2227+0022	None	QSO	2.23, 2.24	0.4, 0.8
CQ2241+0115	QSO_HIZ	unknown		
CQ2241−0012	QSO_HIZ	QSO		
CQ2254−0001	QSO_HIZ	QSO	3.69, 3.71	0.0
CQ2306+0108	STAR_CARBON, QSO_HIZ	QSO	3.65, 3.64	0.15, 0.0
CQ2316+0023	None	QSO	2.1?	
CQ2324−0105	None	QSO	2.25?	
CQ2342+0043	QSO_REJECT	QSO	1.65, 1.65	0.8, 1.1
CQ2344−0001	None	QSO	1.04	0.5
CQ2347−0109	QSO_SKIRT	QSO	1.08	0.80
CQ2355−0041	QSO_HIZ	QSO	1.01, 1.01	1.0, 1.6
CQ2355+0007	None	unknown		
CQ0009−0020	None	Galaxy	0.387	
CQ0022+0020	None	QSO	0.80?	1.9
CQ0027−0019	QSO_CAP, QSO_HIZ	QSO	3.52, 3.52	0.0, 0.0
CQ0043+0000	QSO_FIRST_CAP	STAR?		
CQ0046−0011	None	QSO	2.44, 2.467	0.3
CQ0105+0000	None	Galaxy	0.278	
CQ0107+0016	None	QSO	2.47	0.6
CQ0127+0114	QSO_FIRST_CAP	QSO	1.16, 1.14	1.1, 1.1
CQ0129−0059	QSO_FIRST_CAP, QSO_HIZ	QSO	0.71	1.5
CQ0130+0013	QSO_REJECT	QSO	1.05	0.8
CQ0202+0010	QSO_REJECT, QSO_HIZ	QSO	1.61	0.9
CQ0211+0030	ROSAT_D, ROSAT_E	QSO	3.45	0.30
CQ0212−0023	QSO_REJECT	QSO	1.87?	1.2
CQ0220−0107	None	QSO	3.43, 3.467	0.0
CQ0222−0019	QSO_HIZ	QSO	3.95, 3.947	0.0
CQ0229−0029	QSO_FAINT, QSO_HIZ	QSO	2.14, 1.97	1.40
CQ0239+0115	QSO_REJECT	QSO?	0.867	1.70
CQ0242−0000	STAR_CARBON, QSO_HIZ	QSO	2.48	0.30
CQ0247−0052	None	QSO	0.825	1.5
CQ0255+0048	QSO_HIZ	QSO	4.01	0.0
CQ0303+0105	QSO_HIZ	QSO	3.45	0.0
CQ0310+0055	QSO_FAINT, QSO_HIZ	QSO	3.78	0.0
CQ0311+0103	QSO_FAINT, QSO_HIZ	QSO	unknown, 3.27	0.30?
CQ0312+0032	None	QSO	1.25	0.8
CQ0312+0035	None	QSO	1.28	0.8
CQ0321−0105	QSO_HIZ	QSO	2.40	0.7
CQ0326+0106	SERENDIP_DISTANT	QSO	0.85, 0.85	1.0, 1.3
CQ0327+0006	None	QSO	3.50	0.15
CQ0329−0057	SERENDIP_MANUAL	QSO	1.31, 1.31	1.1, 1.4
CQ0332−0013	None	QSO	0.438	1.0
CQ0336+0112	None	M-dwarf		
CQ0338+0004	QSO_CAP	QSO	1.45	0.6
CQ0339+0022	None	QSO	1.41	0.5
CQ0350−0031	QSO_CAP	QSO	2.00, 2.00	0.4, 0.4
CQ0354−0012	None	QSO	2.45	0.0
CQ0354−0030	None	QSO	1.00	0.3
CQ0822+0004	QSO_HIZ	Galaxy	0.378	
CQ0822+0435	None	M-dwarf		
CQ0826+0728	None	QSO	1.77	0.6
CQ0831+0930	None	QSO	1.96	0.75
CQ0831−0022	None	QSO	2.53	0.23
CQ0832+0121	None	Galaxy	0.166	
CQ0832+0606	None	QSO	2.57	0.4

Note: We here provide the QSO selection flag from SDSS (if any), our classification (QSO, star, or galaxy), the inferred redshift (when two values are given it is our measurement and the one based on the SDSS spectrum, respectively), and the extinction.

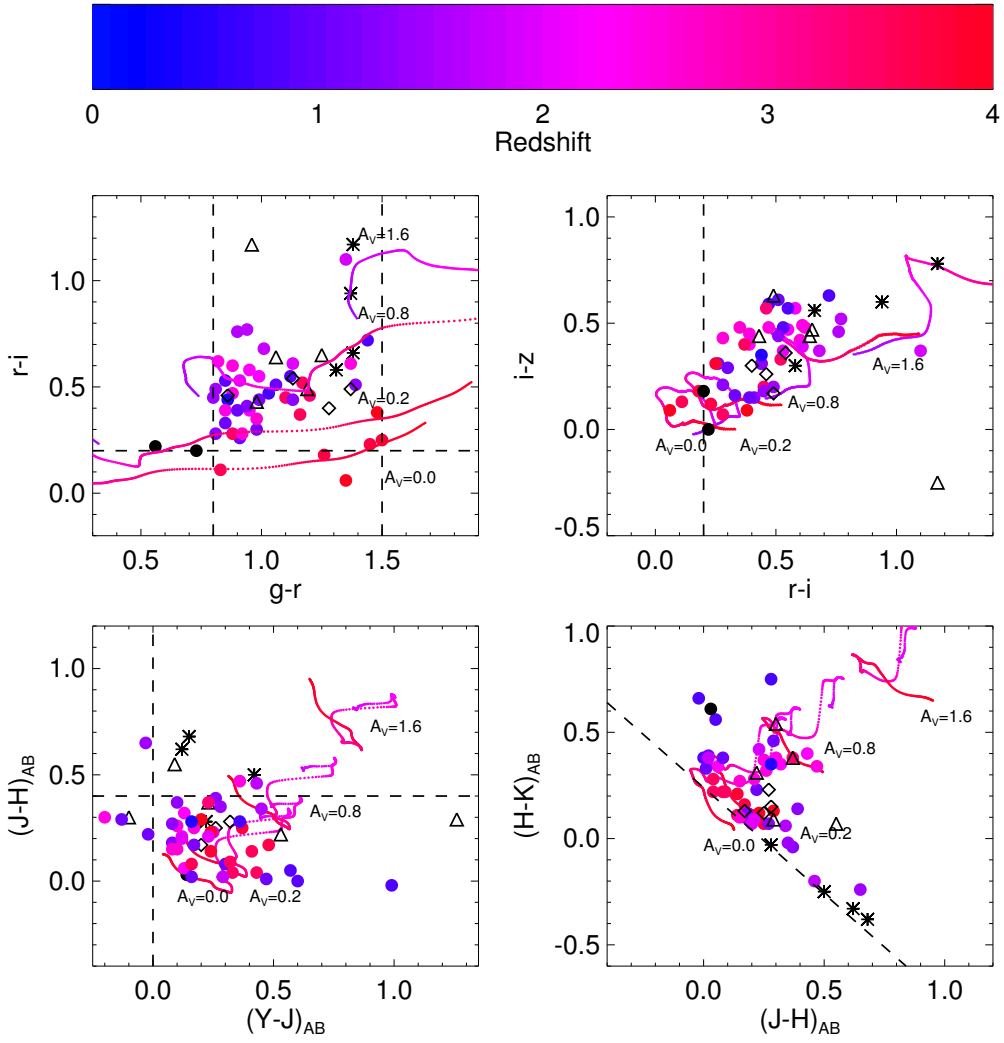

Figure 4.3: Color-color diagrams based on the SDSS and UKIDSS photometry. Filled black circles: Q 0918+1636 and Q 1135−0010. In the lower two panels we only include Q 0918+1636 as we do not have near-IR photometry for Q 1135−0010. Filled colored points: QSOs with measured redshifts. Asterisk: M-dwarfs. Rhombus: Galaxies. Triangles: objects of unknown nature or unknown redshift. The dashed lines mark the boundaries of our selection criteria. The four colored tracks marked by small colored points outline the expected colors of the QSO template in the redshift range from 1.5 to 4.0 and reddened by $A_V = 0, 0.2, 0.8$ and 1.6 mag assuming that the dust is at the QSO redshift.

4.5 Discussion and Conclusions

4.5.1 Implications for QSO searches

Seventy-nine percent of our candidate dust-reddened QSOs are confirmed QSOs. The contamination from stars and compact galaxies are each about ∼7% and the remaining 7% remains unclassified. The confirmed QSOs have a very broad redshift range from 0.4 to 4.0. Most of the QSOs appear significantly dust-reddened with an amount of extinction broadly consistent with our color-selection criterion on $g - r$. In most cases the spectral shape of the QSOs in the observed optical range can be well-matched by the template QSO spectrum reddened by an SMC-like extinction curve assuming that the dust is at the QSO redshift. However, that same model fails for most of the reddened QSOs in the near-IR. We consider the two most likely reasons for this failure in the following. First, there is a problem with the

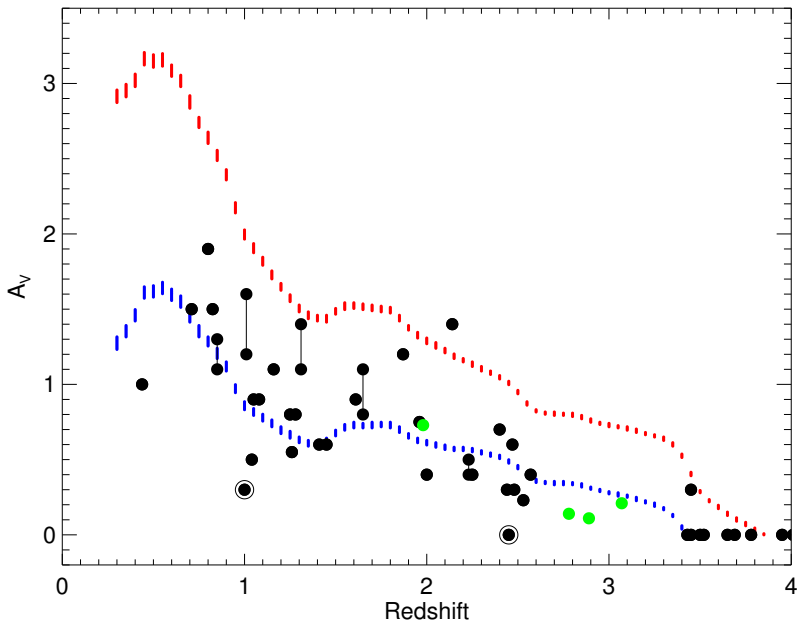

Figure 4.4: A_V vs. redshift for our confirmed QSOs. The red and blue points correspond to our color cuts in $g-r$ assuming the template QSO spectrum reddened by an SMC-like extinction curve. The greens points correspond to Q0918+1636, Q1135−0010, Q1604+2203 and Q1237+0647 that are all reddened by foreground absorbers (Noterdaeme et al. 2009a, 2010; Fynbo et al. 2011; Noterdaeme et al. 2012b). Note that for these QSOs the amount of absorption is derived assuming that the dust is at the redshift of the intervening absorbers, but the data points are plotted at the redshifts of the QSOs. Many of the data points fall below the blue curve, most likely due to the fact that the strong emission lines are absorbed away, but possibly also due to the fact that our flux calibration suffers from 2nd order contamination. Also, the flux calibration of our NTT spectra results in too blue spectra due to 2nd order contamination and this will also bias our measurements towards too low values of A_V. For the objects observed both by us and by SDSS we show the A_V deduced from both spectra connected by a vertical line. The two encircled points represents the two sources with strong Galactic absorption.

QSO template which, as also discussed by Vanden Berk et al. (2001), most likely contains significant contamination from host galaxy light redward of 5000 Å. Second, it is plausible that the SMC extinction curve is too shallow. There is growing evidence that the extinction curve towards the Galactic center is significantly steeper in the optical and near-IR than the standard MW extinction curve parametrisation (e.g., Sumi 2004; Nishiyama et al. 2008, 2009; Gosling, Bandyopadhyay, & Blundell 2009). Given that we obviously also probe regions towards galactic centers it is plausible that these environments have dust with similar extinction properties, i.e., very steep extinction curves, as towards the Galactic center. Steep extinction curves have also been identified against GRB afterglow light (Zafar et al. 2012).

To investigate the role of the QSO template we follow Wang et al. (2012) and build a template by merging the Vanden Berk et al. (2001) template at $\lambda_{\rm rest} < 3000$ Å with the Glikman, Helfand, & White (2006) near-IR template at $\lambda_{\rm rest} > 3000$ Å. In Fig. 4.5 we compare this template with the Vanden Berk et al. (2001) template and with the QSO templates from Richards et al. (2006). As can be seen, the templates agree well in the restframe UV, but at $\lambda_{\rm rest} > 4000$ Å the Vanden Berk et al. (2001) template clearly has excess light presumably due to host contamination. In Fig. 4.6 we re-plot the spectrum of CQ0127+0114 (here the SDSS spectrum) and attempt to match its spectral energy distribution using the merged QSO template described above. As can be seen here, we can match the optical and near-IR sections separately with different amounts of extinction, but not the full spectral range.

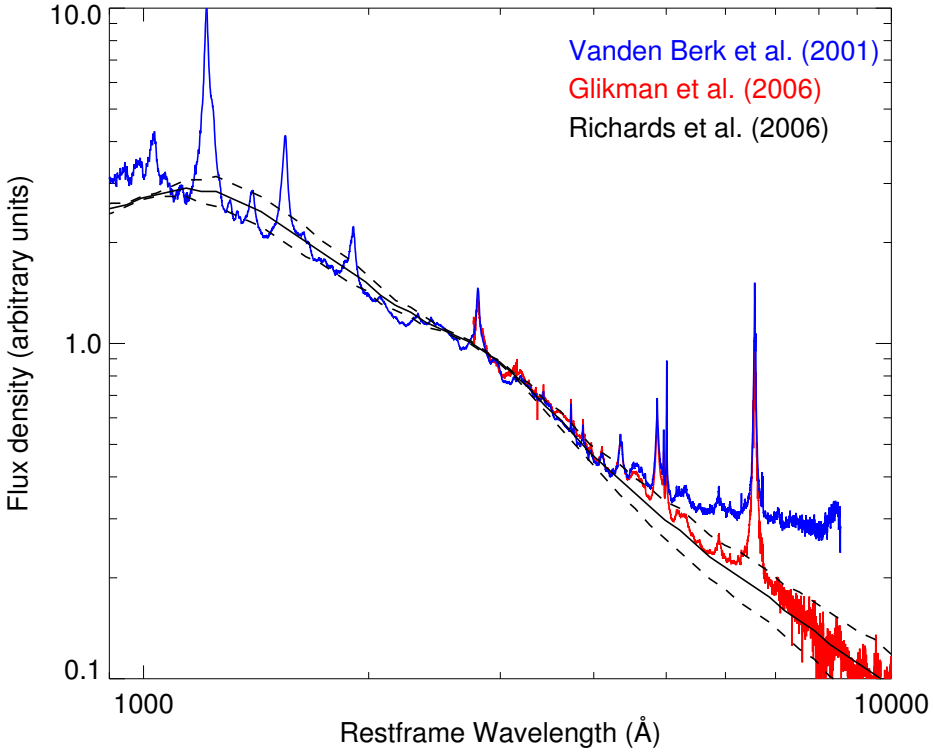

Figure 4.5: Here we compare the QSO templates of Vanden Berk et al. (2001), Glikman, Helfand, & White (2006) and Richards et al. (2006). For the Richards et al. (2006) templates, we also provide the $\pm 1\sigma$ curves relative to the average template. As seen, the Vanden Berk et al. (2001) template has excess emission in the restframe optical range presumably due to host galaxy contamination.

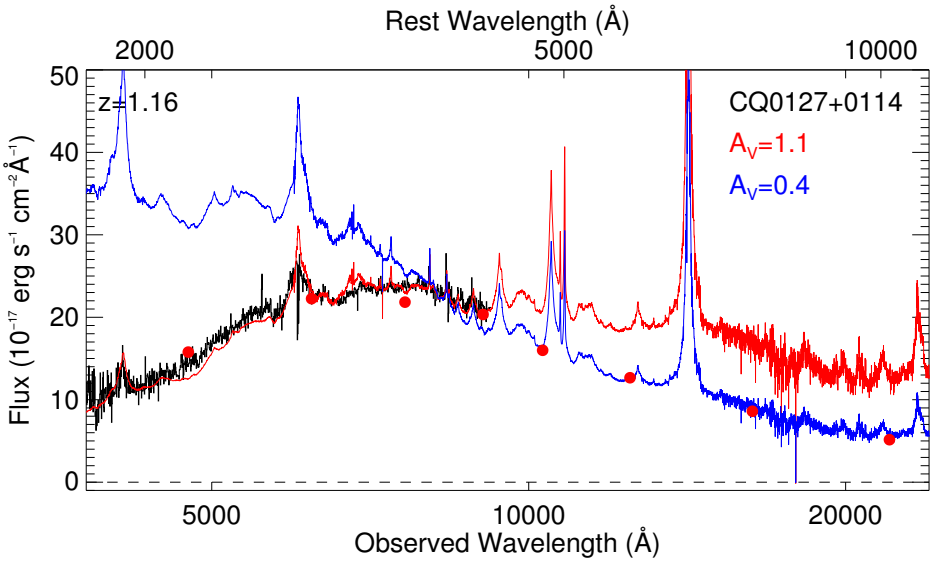

Figure 4.6: Here we use the merged QSO template described in the text to explore if the shape of the spectral energy distributions can be matched using this template (without host galaxy contamination) and the SMC extinction curve in the specific example of CQ0127+0114. The red solid curve is our best match to the optical data whereas the solid blue curve is our best fit to the near-IR data. As seen, it is possible to match the optical and near-IR regions separately, with different amounts of extinction, but it is not possible to match the full spectral range. An extinction curve with a steep UV rise is needed to explain the full spectral energy distribution.

We plan to investigate the second point, i.e., the question of whether an extinction curve similar to that observed towards the Galactic center can be inferred from our spectra, further in a future work.

More than half of the confirmed QSOs show signs of associated absorption (BAL, low-BALs, P-Cygni profiles) or unusual emission line profiles, i.e., broad C III emission and narrow C IV emission (e.g., CQ2342+0043, CQ0826+0728).

It is interesting to compare our confirmed QSOs with the QSOs identified in the FIRST-2MASS Red Quasar Survey of Urrutia et al. (2009). Their survey is targeting point sources detected by both FIRST and 2MASS, whereas only two of our targets are FIRST sources and the majority of our targets are too faint to be detected by 2MASS. For these reasons, the QSOs in our sample extend out to higher redshifts than the QSOs in the FIRST-2MASS survey. The FIRST-2MASS QSO color distribution is relatively wider. As an example, $g-r$ ranges from 0 to 2.5 for the FIRST-2MASS QSOs, compared to our (selected) range of colors, $0.8 < g-r < 1.5$. Our study confirms their finding that QSOs with BAL-features are very common among dust-reddened QSOs and extend the result to QSOs at higher redshifts. A study of point sources selected only by $J-K > 1.2$ and a K-band limit of about 19 would be very interesting as it would give a broad census of the AGN population at $0.5 < z < 3.5$. The many AGN with $J-K < 1.2$ are predominantly at low redshift (where the host galaxy contributes to the near-IR photometry) or at $z \approx 4$, where the Mg II emission enters the J-band. Here it is also interesting that Banerji et al. (2012) have done a study of $J-K > 2.5$ point sources from UKIDSS and these are all heavily reddened QSOs.

The incompleteness of classic color/morphology selection techniques of QSO samples was also addressed by the purely magnitude limited VVDS QSO sample (Gavignaud et al. 2006; Bongiorno et al. 2007) where it was shown that faint QSO samples may miss up to 35% of the population due partly to the color selection and partly to the requirement that the candidates must be point-sources. We have shown here that at least part of this missed population can be understood as dust-reddened QSOs.

About half of our confirmed QSOs were not flagged as QSOs based on the SDSS photometry and our survey therefore provides some insight into the completeness of the SDSS QSO catalog. In total, there are 10,925 spectroscopically confirmed quasars in Stripe82 in DR8, the latest data release. However, only for a subset of these is UKIDSS photometry available. Of the spectroscopically confirmed quasars in Stripe82 with UKIDSS photometry 2246 have $J_{\rm AB} < 19.0$. Of these only 927 are point sources in both UKIDSS and SDSS. Only 14 of the 927 fulfill our additional color criteria. We have in this survey detected 45 QSOs with $J_{\rm AB} < 19.0$ in Stripe 82 and, of these, only 4 were already spectroscopically confirmed by SDSS. Hence, it is clear that SDSS is incomplete for red QSOs, but these constitute a tiny fraction of all QSOs with $J_{\rm AB} < 19.0$.

Finally, we note that a very similar study to ours, i.e., a QSO search based on SDSS and UKIDSS photometry, has recently been submitted for publication (Wu et al. 2013). Their study has a slightly different aim, namely, a targeted search for QSOs at $z = 2.2 - 3.5$.

4.5.2 Implications for QSO host galaxies

Our survey has found that there exists a subsample of dust-reddened QSOs that is missed by classic QSO selection methods. This result is consistent with those of Gavignaud et al. (2006) and Urrutia et al. (2009). We have further found that the reddening is in general caused by the QSO host galaxy rather than intervening absorbers, and that the reddened galaxies only make up a comparatively small fraction of the underlying QSO host galaxy population. The implication is that either QSO host galaxies in general contain very little dust, or the QSO itself is able to create a dust-free sightline along the emission cone.

From Figure 4.4, it is seen that there is an apparent drop in the number of reddened hosts at redshifts larger than $z = 2.6$ (note that the green points in Figure 4.4 do not belong to the sample). At redshifts larger than $z = 3.5$ our color selection is not well-tuned to finding reddened QSOs, but in the range $z = 2.6-3.5$ our selection is tuned for A_V in the range $0.2-0.8$ and we find only a single reddened host at $z = 3.45$. At redshifts around $1-2$ our sample contains 16–17 reddened hosts per unit redshift so the sudden drop at $z = 2.6$ to 1.1 per unit redshift appears to be significant. This could possibly indicate that QSO host galaxies at $z > 2.6$ contain less dust than those below $z = 2.6$. A similar result has been reported for high redshift galaxies selected by their Lyα emission line (Nilsson et al. 2009) where it was found that there is a significant evolution in the dust properties of Lyα emitters from $z = 3$ to $z = 2$. In particular it has been found that there is a very sharp transition in the ULIRG fraction of Lyα emitters at a redshift of z≈ 2.5 (Nilsson & Møller 2009). The drop we see in the dust properties of QSO hosts at $z = 2.6$ appears to be equally sudden and it is possible that the two observations are related to a common evolutionary event. However, we obviously need a larger sample to confirm this tentative result.

4.5.3 Implications for the study of compact Galaxies

Three of the galaxies we have detected are old stellar systems (see Section 4.4.5). The spectrum of CQ0822+0004 has Balmer absorption lines and hence most likely has an age of about a Gyr, whereas the other two have older stellar populations. We use the LePhare software (Arnouts et al. 1999; Ilbert et al. 2006) to fit to the SDSS + UKIDSS photometry fixing the redshift to the measured values. Based thereon we infer stellar ages of several Gyr (the exact value depending on the assumed metallicity) and stellar masses of the order 10^{10} $M_\odot$. Interestingly, they are all point sources - even in the K-band, where the seeing is about $0\farcs6$ in the UKIDSS images. This implies that the galaxies must have stellar densities in excess of 10^{10} $M_\odot$ kpc^{-2}, which is similar to the compact 'distant red galaxies' found at redshifts around 2 (e.g., van Dokkum et al. 2008a) and among the highest measured at any redshift (Franx et al. 2008). However, the stellar masses of the compact galaxies found at high redshifts are significantly larger than for the three galaxies found here. Taylor et al. (2010) find that massive, compact galaxies are much rarer in the local Universe than at $z \approx 2$.

4.5.4 Dusty DLAs

We did not find any obvious cases of QSOs being reddened by foreground dusty absorbers and this confirms that such absorbers are rare. We are currently working on refining our selection criteria with the goal of selecting fewer strongly reddened $z < 2$ QSOs and fewer $z > 3.5$ unreddened QSOs.

Acknowledgements

We thank our anonymous referee for a constructive and helpful report and T. Zafar, K. Denny, J. Hjorth, B. Milvang-Jensen, A. de Ugarte Postigo and Richard McMahon for helpful discussions. JPUF acknowledges support from the ERC-StG grant EGGS-278202. The Dark cosmology centre is funded by the DNRF. Funding for the SDSS and SDSS-II has been provided by the Alfred P. Sloan Foundation, the Participating Institutions, the National Science Foundation, the U.S. Department of Energy, the National Aeronautics and Space Administration, the Japanese Monbukagakusho, the Max Planck Society, and the Higher Education Funding Council for England. The SDSS Web Site is http://www.sdss.org/. The SDSS is managed by the Astrophysical Research Consortium for the Participating Institutions. The Participating Institutions are the American Museum of Natural History, Astrophysical Institute Potsdam, University of Basel, University of Cambridge, Case Western Reserve University, University of Chicago, Drexel University, Fermilab, the Institute for Advanced Study, the Japan Participation Group, Johns Hopkins University, the Joint Institute for Nuclear Astrophysics, the Kavli Institute for Particle Astrophysics and Cosmology, the Korean Scientist Group, the Chinese Academy of Sciences (LAMOST), Los Alamos National Laboratory, the Max-Planck-Institute for Astronomy (MPIA), the Max-Planck-Institute for Astrophysics (MPA), New Mexico State University, Ohio State University, University of Pittsburgh, University of Portsmouth, Princeton University, the United States Naval Observatory, and the University of Washington. We acknowledge the use of UKIDSS data. The United Kingdom Infrared Telescope is operated by the Joint Astronomy Centre on behalf of the Science and Technology Facilities Council of the U.K.

4.A All Spectra

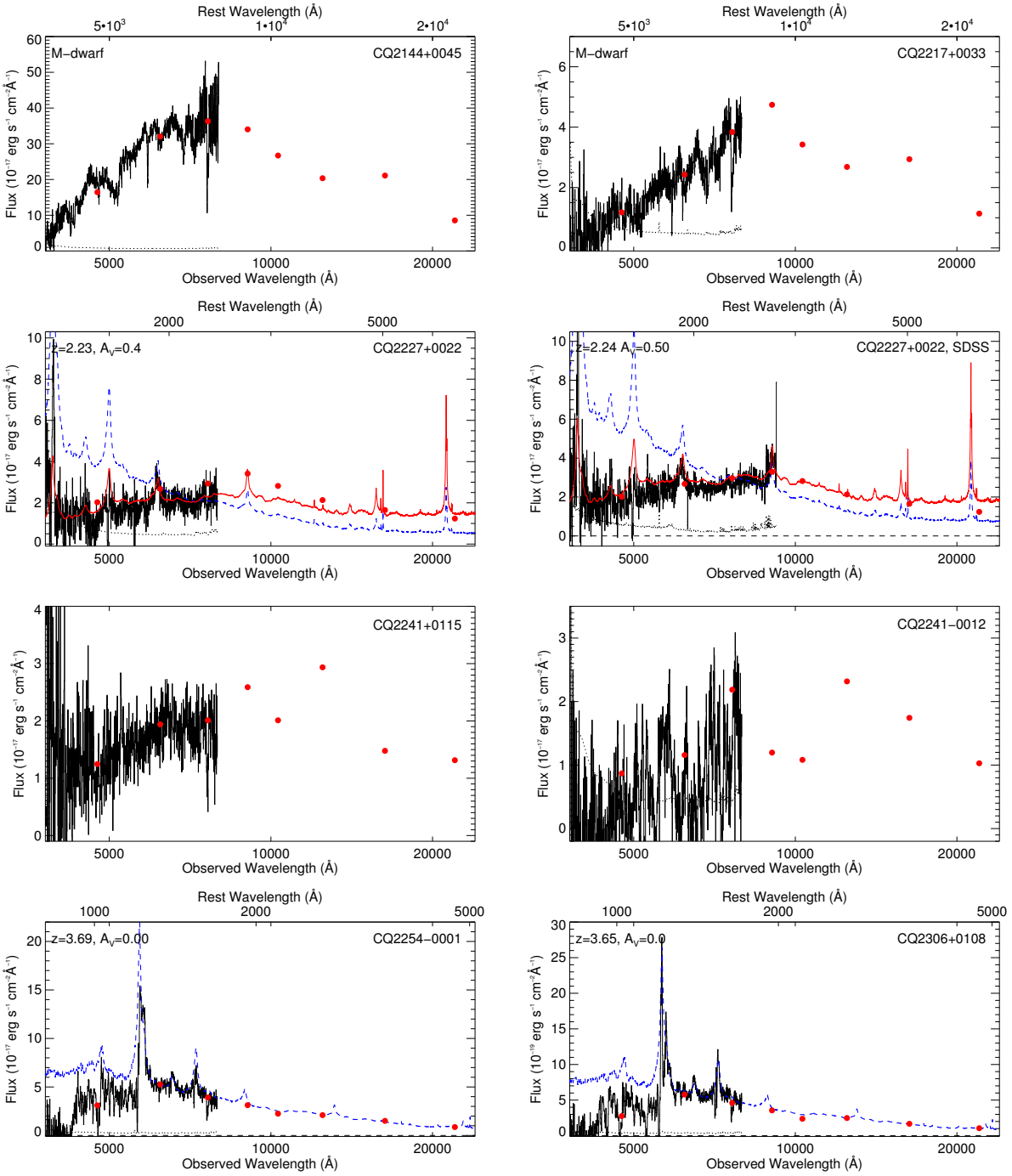

Figure 4.7: One-dimensional spectra for the candidate QSOs observed in our survey or by the SDSS. For each candidate the observed spectrum is plotted (solid) and the error spectrum (dotted line) is shown. With a blue dashed line we show the composite QSO spectrum from Vanden Berk et al. (2001) and Telfer et al. (2002) redshifted to the estimated redshift and with a solid red line the redshifted composite spectrum reddened by the indicated amount of extinction. Overplotted with filled circles is the SDSS and UKIDSS photometric points. The NOT and NTT spectra have been scaled to match the r-band photometric point from SDSS. Unless otherwise noted we have assumed an SMC-like extinction curve. Note that the spectra have not been corrected for telluric absorption. The SDSS spectra have been binned down by a factor of 4 for clarity.

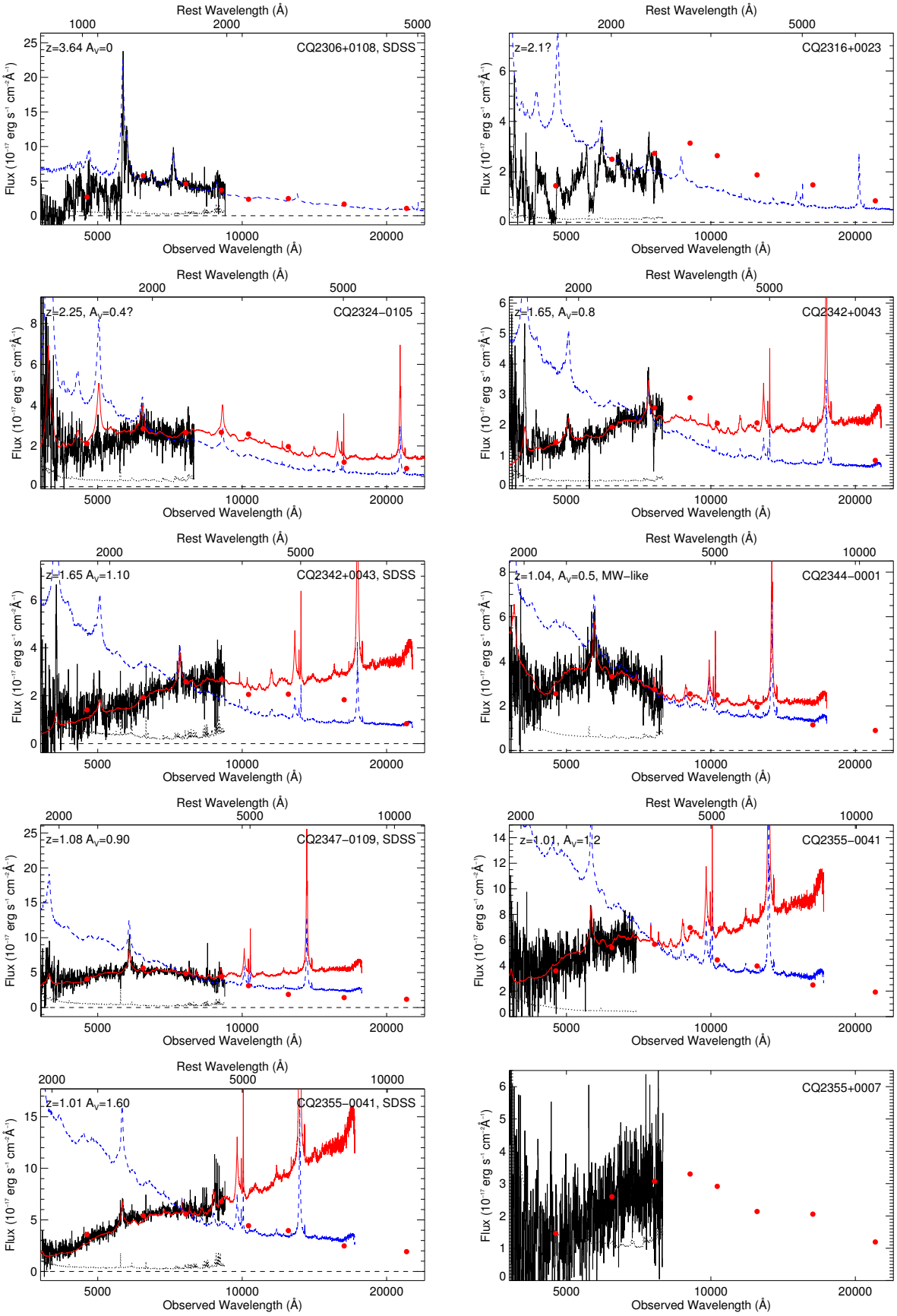

Figure 4.7 (Cont.): One-dimensional spectra for the candidate red QSOs in our survey.

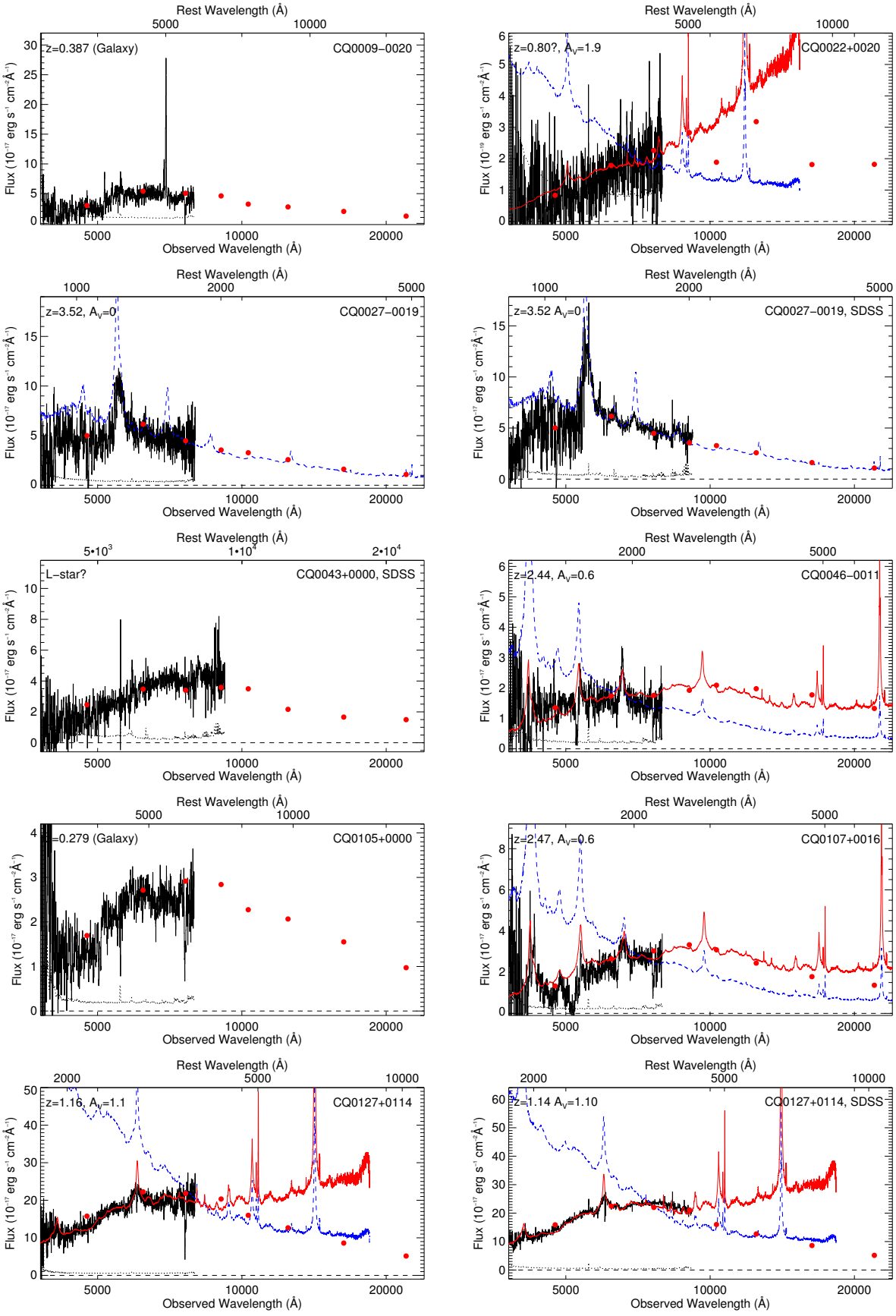

Figure 4.7 (Cont.): One-dimensional spectra for the candidate red QSOs in our survey.

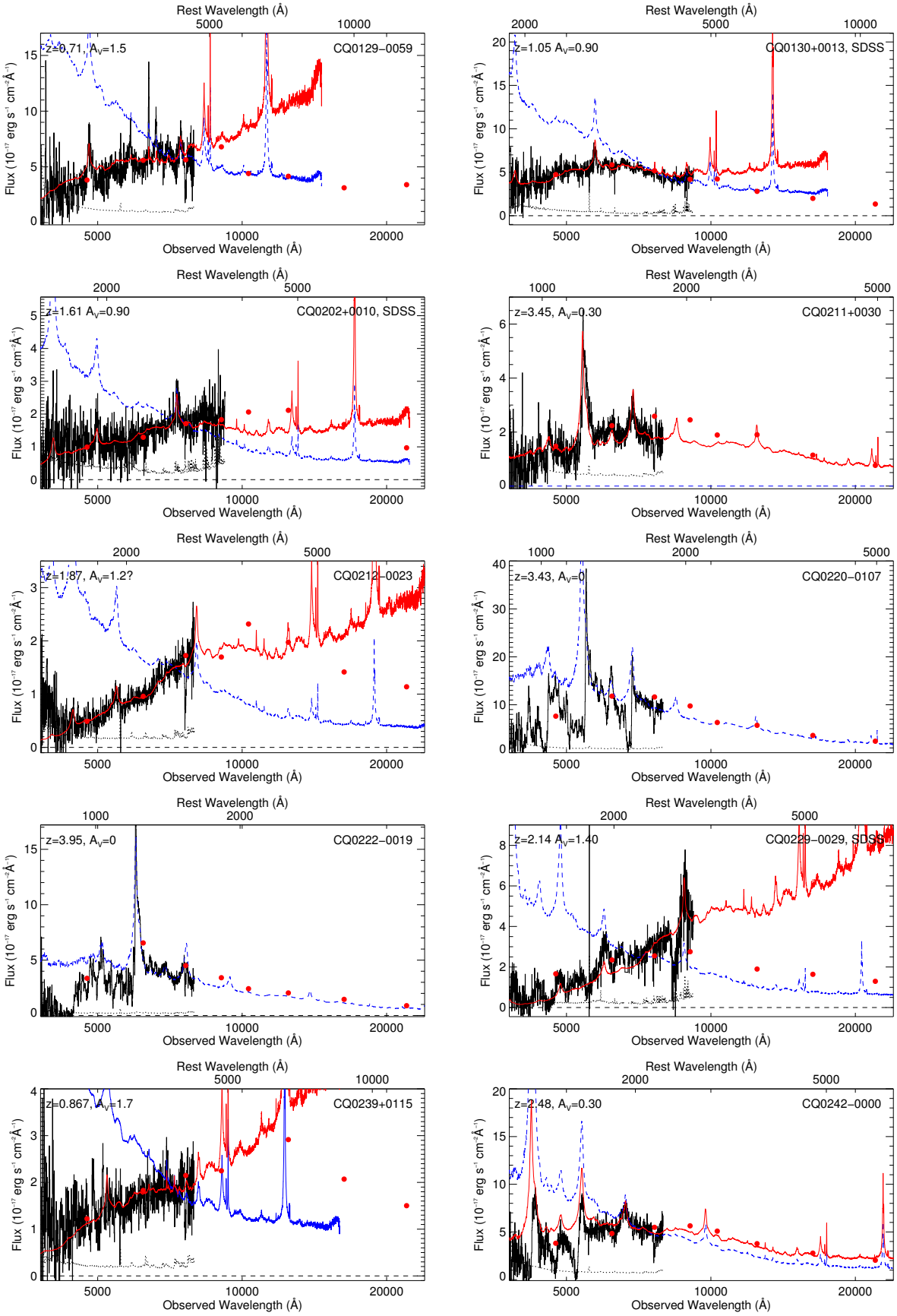

Figure 4.7 (Cont.): One-dimensional spectra for the candidate red QSOs in our survey.

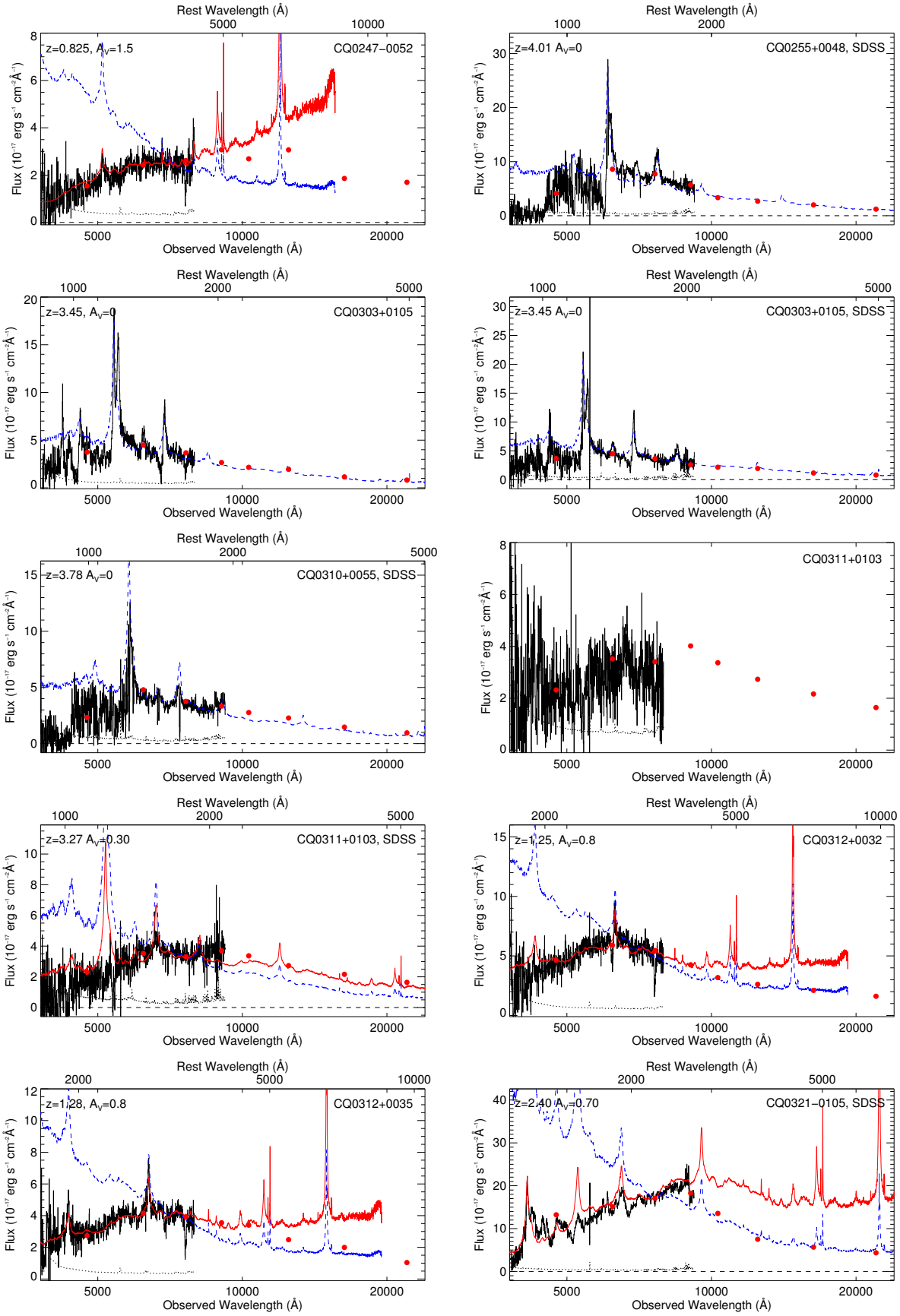

Figure 4.7 (Cont.): One-dimensional spectra for the candidate red QSOs in our survey.

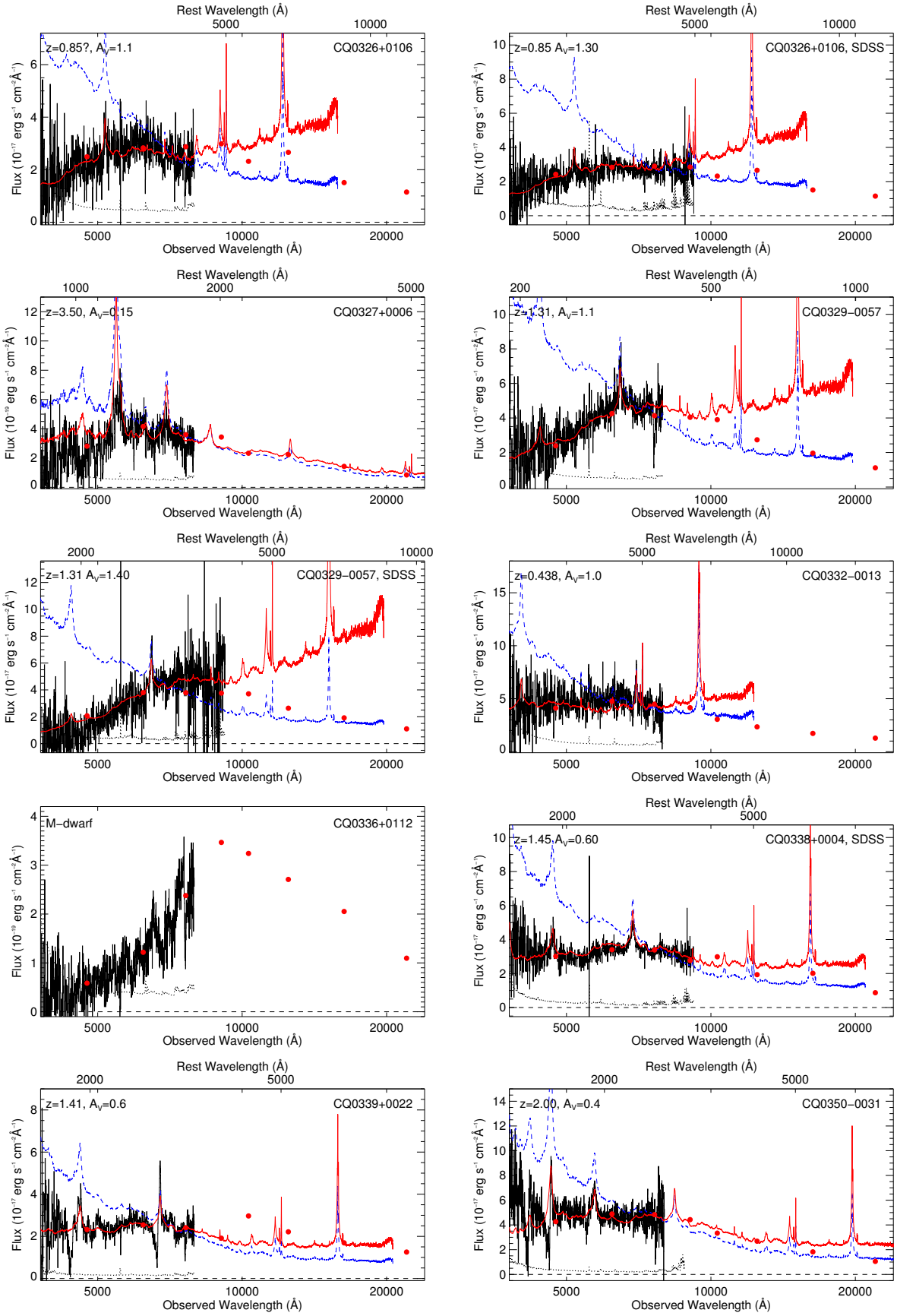

Figure 4.7 (Cont.): One-dimensional spectra for the candidate red QSOs in our survey.

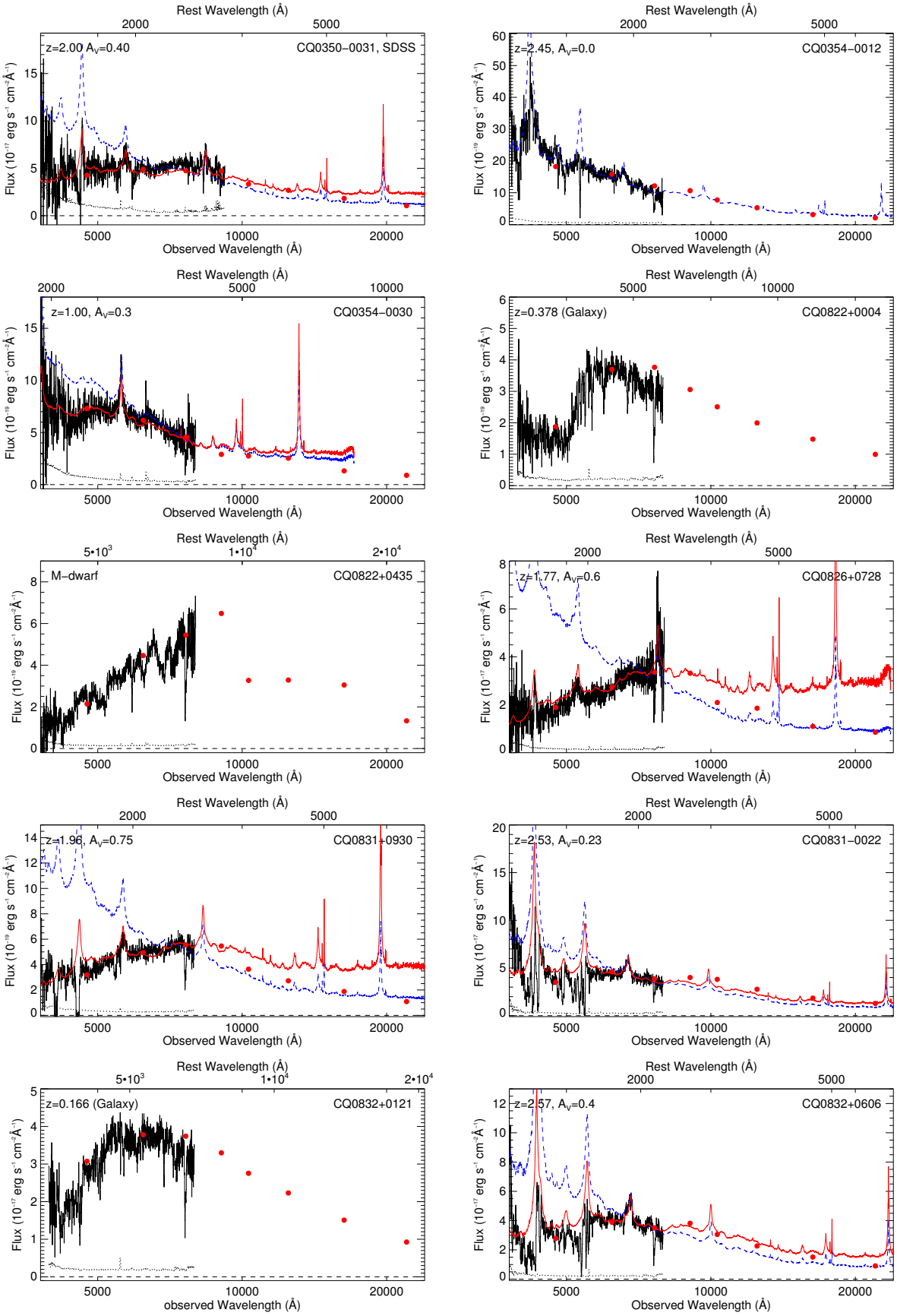

Figure 4.7 (Cont.): One-dimensional spectra for the candidate red QSOs in our survey.

4.B Notes on individual objects

CQ2143+0022 ($z = 1.26$)

This object is only observed by SDSS where a redshift of $z = 1.26$ is derived (presumably based on two emission lines interpreted as Mg II and C III). The object is a dust-reddened QSO with an estimated amount of extinction corresponding to $A_V = 0.55$. The SMC-extinction reddened QSO template provides a good match to the SDSS spectrum and photometry, but it does not match the UKIDSS photometry. This is a problem that is common to most of our spectra of reddened QSOs. In SDSS the source is flagged QSO_CAP.

CQ2144+0045 ($z = 0$)

This is an M-dwarf. Based on the SDSS photometry the source is not flagged as a QSO.

CQ2217+0033 ($z = 0$)

This is an M-dwarf. Based on the SDSS photometry the source is not flagged as a QSO.

CQ2227+0022 ($z = 2.23$)

This is a reddened $z = 2.23$ QSO observed both by us and by SDSS (SDSS infer a redshift of $z = 2.24$). The redshift is based on the detection of (narrow) Lyα and (broad) C III in emission and C IV in absorption. It has an estimated extinction of $A_V = 0.4$ (our spectrum) and 0.5 (SDSS spectrum). In this case the reddened QSO template provides a reasonably good match to the near-IR photometry out to around 5000 Å in the rest frame. Based on SDSS photometry this source is not flagged as a QSO.

CQ2241+0115 (redshift unknown)

The nature of this object could not be established. It has a narrow emission line at 5258 Å, a tentative narrow line at 6970 Å and a broad emission feature around 6400 Å, but we have not been able to establish the nature of these features. The near-IR photometry shows evidence for an emission line in the H band and possibly also in the Y band. Based on the SDSS photometry this source is flagged as QSO_HIZ.

CQ2241–0012 (redshift unknown)

This spectrum is very complex with a mix of broad and narrow absorption lines over the full spectral range covered by the instrument. The colors of the object are peculiar, in particular $r - i = 1.17$ and $Y - J = 1.26$ are extreme values (see Fig. 4.3. It is most likely an extreme BAL QSO at $z > 2.5$ (e.g., Hall et al. 2002). Based on the SDSS photometry this source is flagged as QSO_HIZ. The object is also included in SDSS DR9 (released after our paper was submitted) where a redshift of 0.699 is derived. This redshift appears to be wrong.

CQ2254–0001 ($z = 3.69$)

This is a relatively normal QSO at redshift of $z = 3.69$ with no evidence for excess reddening. Based on SDSS photometry it is flagged as QSO_HIZ. It entered our selection due to its relatively high redshift. The spectrum shows relatively weak Lyα, probably due to associated absorption also seen in Lyβ,

Lyman-limit absorption and in the C IV line. The N V line is very strong. The object is also included in SDSS DR9 (released after our paper was submitted) where a redshift of 3.707 is derived.

CQ2306+0108 ($z = 3.65$)

This is a QSO at a relatively high redshift of $z = 3.65$ with no evidence for extinction. The spectrum shows somewhat narrower emission lines compared to the template spectrum. In particular, Lyα and N V are clearly separated. The source is also observed spectroscopically by SDSS, where a redshift of $z = 3.64$ is derived. The spectrum displays a strong Lyα absorber at around 5300 Å that could be damped. There is also Lyman-limit absorption at $z_{abs} = z_{em}$. Based on the SDSS photometry this object is flagged as STAR_CARBON and QSO_HIZ.

CQ2316+0023 ($z \approx 2.1$?)

This is a BAL QSO, but we have not been able to establish the precise redshift. Given the positions of the main absorption troughs around 5600 Å and 4600 Å we estimate that it is likely close to $z = 2.1$ if these are from Si IV, C IV and Al III. There is a bright emission spike around 3900 Å, which could be the onset of the Lyα / N V emission. Based on the SDSS photometry this object is not flagged as a QSO.

CQ2324–0105 ($z = 2.25$?)

The nature of this object has not been securely established. It has a strong absorption feature at 5108 Å and a broad emission line at the very blue end of the wavelength range. There is also a broad emission bump around 6200 Å. A possible solution is a reddened QSO at $z = 2.25$ (i.e. very similar to CQ2227+0022), where the absorption feature is $z_{abs} > z_{em}$ absorption from C IV and the broad emission features are from Lyα and C III. Based on the SDSS photometry this object is not flagged as a QSO.

CQ2342+0043 ($z = 1.65$)

This is a reddened QSO at $z = 1.65$ with an estimated extinction of $A_{\rm V} = 0.8$. The spectrum displays broad emission lines from Mg II and C III, but a significantly narrower C IV line. The source is also observed spectroscopically by SDSS. From their spectrum we infer a larger amount of extinction ($A_{\rm V} = 1.1$), which also leads to a better match with the Y band photometry. However, we match the JHK photometry very badly. In SDSS the object is flagged as QSO_REJECT.

CQ2344–0001 ($z = 1.04$)

This is a reddened ($A_{\rm V} = 0.5$) QSO at $z = 1.04$. The redshift is based on the detection of Mg II emission and of the Fe II emission bump redward of Mg II. In this case we had to invoke the MW extinction curve to match the shape of the spectrum so most likely the dust in this system contains the carriers of the 2175 Å extinction feature. In SDSS the object is not flagged as a QSO.

CQ2347–0109 ($z = 1.08$)

This is a reddened ($A_{\rm V} = 0.9$) QSO at $z = 1.08$ observed by SDSS. The redshift is presumably based on the detection of emission lines from Mg II and C III. In SDSS the object is flagged as QSO_SKIRT.

CQ2355–0041 ($z = 1.01$)

This spectrum displays a single emission line, which we interpret as Mg II at $z = 1.01$. Given that we can get a good match of the shape of the optical spectrum with a reddened QSO template ($A_V = 1.2$) at this redshift we consider the nature of the object fairly secure. The object is also covered by SDSS where a redshift of $z = 1.00$ is determined. From the SDSS spectrum we infer a larger amount of extinction ($A_V = 1.6$). There is a very poor match of the near-IR photometry. In SDSS the object is flagged as QSO_HIZ.

CQ2355+0007 (unknown redshift)

This is a faint target and we are not able to establish its nature based on our spectrum. The spectrum is much fainter than expected based on the SDSS photometry (by a factor of 6) so either the object is variable or there was a problem with the observation. In SDSS the object is not flagged as a QSO.

CQ0009–0020 ($z = 0.387$)

This is a star-forming galaxy or possibly a narrow-line AGN. The spectrum displays strong O II, O III and Ne III emission and a 4000-Å break in the continuum. There are no Balmer lines in emission, but note that the Hβ line falls in the atmospheric A-band. There is also a hint of Ne V emission at 4750 Å. The object is not flagged as a QSO in SDSS.

CQ0022+0020 ($z = 0.80$?))

This is a faint target. The object has a single narrow emission line at 6700 Å and a hint of a broad line at 7900 Å. This is most likely a dust reddened QSO at $z = 0.80$, where identified narrow line is O II and the broad line is Hγ. The object is also observed by SDSS-III where the same features are detected with higher significance (Noterdaeme, private communication). The object is not flagged as a QSO in SDSS.

CQ0027–0019 ($z = 3.55$)

This spectrum displays a single broad emission line, which we interpret as Lyα at $z = 3.55$ as there seems to be Lyα forest absorption blueward of it including a strong (possibly damped) Lyα absorber at 4780 Å ($z = 2.93$). However, C IV emission is very weak or absent. The object appears similar to CQ0327+0006 at $z = 3.50$. There is no sign of reddening and the object likely entered our sample due to its high redshift. The object is also observed spectroscopically by SDSS where a redshift of $z = 3.52$ is derived. The object is flagged as QSO_CAP and QSO_HIZ in SDSS.

CQ0043–0000 ($z = 0$?)

This object is observed by SDSS. The object is flagged by SDSS as an L5.5 star, but we believe this classification to be wrong as the near-IR colors are bluer than for late-type stars. The object has possible emission lines at 5900 Å and 8090 Å but we have not been able to establish the nature of these features.

CQ0046–0011 ($z = 2.44$)

This is a reddened QSO at $z = 2.44$. The redshift is based on the detection of C III emission and absorption at the positions of C IV and Lyα at this redshift. The shape of the optical spectrum is reasonably

well fitted with the template QSO spectrum reddened by an SMC-like extinction curve with $A_V = 0.6$. The object is not flagged as a QSO in SDSS. The object is also included in SDSS DR9 (released after our paper was submitted) where a redshift of 2.467 is derived.

CQ0105+0000 ($z = 0.279$)

This object is a compact galaxy with an old stellar population at $z = 0.279$. Both in the SDSS and UKIDSS imaging the object is consistent with being a point source. Hence, this is a galaxy that bears some resemblance to the compact quiescent galaxies seen at redshifts around 2 (e.g., van Dokkum et al. 2008a). The object is not flagged as a QSO in SDSS.

CQ0107+0016 ($z = 2.47$)

This is a reddened QSO at $z = 2.47$. The spectrum displays C III in emission, C IV is nearly absorbed away and Lyα is weak. Narrow emission from N V is also detected. The shape of the spectrum is fairly well fitted with the template QSO spectrum reddened by an SMC-like extinction curve with $A_V = 0.6$ except redward of Hβ in the restframe where the reddened template spectrum is too red. The object is not flagged as a QSO in SDSS.

CQ0127+0114 ($z = 1.16$)

This is a bright reddened QSO at $z = 1.16$. The redshift is based on the detection of a broad Mg II emission line. This source has also been observed by the SDSS where a slightly lower redshift ($z = 1.14$) is derived. This source is also detected in the FIRST survey (Becker, White, & Helfand 1995a). The QSO is reddened by an amount corresponding to $A_V = 1.1$ as determined from both our and the SDSS spectrum. The near-IR photometry for this source is very blue - even bluer than the unreddened QSO template. In SDSS the source is flagged as QSO_FIRST_CAP.

CQ0129–0059 ($z = 0.71$)

This is a strongly reddened ($A_V = 1.5$) QSO at $z = 0.71$. The spectrum displays broad emission from Balmer-lines (Hγ and Hδ), Ne III and Mg II and narrower O II emission. This source is also detected in the FIRST survey (Becker, White, & Helfand 1995a). In SDSS the source is flagged as QSO_FIRST_CAP. The near-IR photometry for this source is very blue and the reddened QSO template fails completely in matching this.

CQ0130+0013 ($z = 1.05$)

This is a reddened QSO ($A_V = 0.9$) at $z = 1.05$ observed by the SDSS. The redshift is presumably based on the detection of Mg II emission. Also for this source the reddened QSO template does not match the near-IR photometry. In SDSS the object is flagged as QSO_REJECT.

CQ0202+0010 ($z = 1.61$)

This is a reddened QSO ($A_V = 0.9$) at $z = 1.61$ observed by the SDSS. The redshift is presumably based on the detection of Mg II, C III and C IV emission. In SDSS the object is flagged as QSO_REJECT, QSO_HIZ.

CQ0211+0030 ($z = 3.45$)

This is a reddened ($A_V = 0.30$) QSO at a relatively high redshift of $z = 3.45$. The redshift is based on the detection of C IV and Lyα emission. The source is also detected by the ROSAT survey (Truemper 1982). This object is really what we are searching for in terms of redshift, but there is no indication of a DLA at $z > 2$ in the spectrum. The spectrum shows associated absorption. The only flags for the object in the SDSS catalog are ROSAT_D and ROSAT_E.

CQ0212–0023 ($z = 1.87$?)

The nature of this source is not secure. There is an indication of broad emission lines around 4400 and 5400 Å, which we interpret as C III and C IV at $z = 1.87$. If correct the inferred extinction based on the QSO template reddened by an SMC-like extinction curve is $A_V = 1.2$. Again, this model is far too red to match the near-IR photometry. In SDSS the object is flagged as QSO_REJECT.

CQ0220–0107 ($z = 3.43$)

This is a BAL QSO at $z = 3.43$. The redshift is based on the identification of emission and BAL features from C IV, Si IV, Lyα and O VI/Lyβ. There is no evidence for reddening. In SDSS the object is not flagged as a QSO. The object is also included in SDSS DR9 (released after our paper was submitted) where a redshift of 3.461 is derived.

CQ0222–0019 ($z = 3.95$)

This is the 2nd most distant source in our survey. It is also flagged as a high-z QSO by SDSS (QSO_HIZ). There is no evidence for reddening and the source has hence entered our selection due to its high redshift. The spectrum displays relatively strong associated absorption seen both in C IV, Lyα and at the Lyman-limit. The object is also included in SDSS DR9 (released after our paper was submitted) where a redshift of 3.947 is derived.

CQ0229–0029 ($z = 2.14$)

This is a BAL QSO observed by the SDSS. In SDSS the object is listed to have redshift of $z = 1.97$. However, the redshift we infer based on identification of the C IV, C III and Mg II emission lines is $z = 2.14$. The inferred amount of extinction is $A_V = 1.40$ (based on the QSO template reddened by SMC-like extinction), but this model fails completely in matching the near-IR photometry. Based on the SDSS photometry the object is flagged as QSO_FAINT, QSO_HIZ.

CQ0239+0115 ($z = 0.867$)

The nature of this object could not been established based on our spectrum. The object has narrow emission lines at 5122 Å and 5231 Å and a P-Cygni-like feature around 4890 Å. There is also tentative evidence for an emission line at 6960 Å. The photometry shows a red continuum with a break in the J band to a blue continuum from J to K. Based on the SDSS photometry the object is flagged as QSO_REJECT. After submission of our paper DR9 was released. The object is included here and based on this spectrum a redshift of $z = 0.867$ is reported (presumably based on narrow O II and O III emission as well as broad Hβ and Hδ). The emission lines in the blue end of the spectrum are also detected in

the DR9 spectrum. Their nature remains unclear. Based on the shape of the spectrum we infer strong extinction corresponding to $A_V = 1.7$, but the assumption that the underlying spectrum is similar to the QSO template spectrum may be questionable in this case.

CQ0242−0000 ($z = 2.48$)

This is a reddened BAL-like QSO at $z = 2.48$ ($A_V = 0.3$). The redshift is based on the identification of emission and BAL features from C IV, Si IV and Lyα. Broad C III emission is also detected. Based on the SDSS photometry the source is flagged as STAR_CARBON, QSO_HIZ.

CQ0247−0052 ($z = 0.825$)

This is a strongly reddened QSO at $z = 0.825$ with an estimated amount of extinction of $A_V = 1.5$. The spectrum displays emission from Mg II, O II, and indications of Ne III and Balmer lines. The reddened QSO model is again too red to match the near-IR photometry. Based on the SDSS photometry the object is not flagged as a QSO.

CQ0255+0048 ($z = 4.01$)

This object, observed by the SDSS, is the most distant QSO in our sample at a redshift of $z = 4.01$. The object shows no sign of reddening. It has a strong $z_{abs} = z_{em}$ absorber detected both in Lyα and at the Lyman limit. Based on the SDSS photometry the object is flagged as QSO_HIZ.

CQ0303+0105 ($z = 3.45$)

This is a $z = 3.45$ QSO with relatively weak BAL-features and no evidence for reddening. C IV has a P-Cygni profile, Lyα is weak and narrow, but N V appears very strong. The narrow feature at 4224 Å is an energetic cosmic ray hit that has not been completely removed by the rejection algorithm. The object is also observed spectroscopically by SDSS leading to a consistent redshift measurement. The object is flagged as QSO_HIZ based on the SDSS photometry.

CQ0310+0055 ($z = 3.78$)

This is a high redshift ($z = 3.78$) QSO observed by the SDSS. There is no evidence for reddening. The object has strong associated absorption detected both in C IV, Si IV and at the Lyman-limit. Based on the SDSS photometry the source is flagged as QSO_FAINT, QSO_HIZ.

CQ0311+0103 (unknown redshift?)

The nature of this object is not established based on our spectrum. The signal-to-noise ratio is low, but there seems to be a double absorption line at 5400 Å and possible a broad emission line at 6600 Å. The object is also observed by SDSS where a redshift of 3.27 is determined. At this redshift the broad feature at 6600 Å would be C IV emission. The photometry is consistent with a reddened QSO ($A_V = 0.3$) at this redshift. However, we still consider this redshift measurement insecure as there does not seem to be an onset for Lyα forest absorption (and Lyα emission or absorption at $z = 3.27$ is absent). The doublet at 5400 Å is consistent with Ca II at $z = 0.36$. Based on the SDSS photometry the object is flagged as QSO_FAINT, QSO_HIZ.

CQ0312+0032 ($z = 1.25$)

This is a reddened QSO at $z = 1.25$. The redshift is based on the detection of Mg II emission (with a P-Cygni profile). The shape of the optical spectrum is well matched with the template spectrum reddened by an $A_V = 0.8$ extinction curve except C III seems to be weak/absent. Based on the SDSS photometry the object is not flagged as a QSO.

CQ0312+0035 ($z = 1.28$)

This object looks very similar to CQ0312+0032, except here Mg II is not absorbed and C III is well detected. The redshift is slightly larger ($z = 1.28$). Based on the SDSS photometry the object is not flagged as a QSO. Note that CQ0312+0032 and CQ0312+0035 are only a few arcmin from each other on the sky. The redshifts of the two sources seems to be significantly different that this must be a coincidence.

CQ0321–0035 ($z = 2.40$)

This is a very bright BAL QSO at $z = 2.40$ observed by the SDSS. The inferred amount of extinction corresponds to $A_V = 0.70$. based on the SDSS photometry the source is flagged as QSO_HIZ. Again, the reddened QSO template spectrum fails complete to match the UKIDSS photometry.

CQ0326+0106 ($z = 0.85$?)

The nature of this objet is not well established from our spectrum. There is an emission line at around 5200 Å and the shape of the optical spectrum can be well matched assuming that the line is Mg II at $z = 0.85$ and assuming SMC-like extinction with $A_V = 1.1$. The object is also observed by SDSS where a redshift of $z = 0.85$ is determined. Based on the SDSS spectrum we infer an extinction of $A_V = 1.30$. In SDSS the only flag for the object is SERENDIP_DISTANT.

CQ0327+0006 ($z = 3.50$?)

The spectrum shows a broad emission line around 5500 Å, which most likely is Lyα at $z = 3.50$. There is evidence for mild reddening ($A_V = 0.15$). The object is not flagged as a QSO based on the SDSS photometry.

CQ0329–0057 ($z = 1.31$)

This object appears very similar to CQ0312+0032 and CQ0312+0035. It is a reddened QSO at $z = 1.31$ with an inferred extinction of $A_V = 1.1$. The redshift is based on the detection of the Mg II emission line. The object is also observed by SDSS. Based on the SDSS spectrum we infer a somewhat larger amount of extinction ($A_V = 1.4$). The object is not flagged as a QSO based on the SDSS photometry.

CQ0332–0013 ($z = 0.438$)

This is the lowest redshift QSO in our sample. This object is a reddened ($A_V = 1.0$) QSO at $z = 0.438$. The spectrum displays narrow O II and O III emission and broad lines from Hβ and Ne III. The object is not flagged as a QSO based on the SDSS photometry.

CQ0336+0112 ($z = 0$)

This is an M-dwarf. Based on the SDSS photometry the source is not flagged as a QSO.

CQ0338+0004 ($z = 1.45$)

This is a reddened QSO at $z = 1.45$ observed by the SDSS. The redshift is presumably based on the detection of Mg II and C III emission lines. Based on the SDSS spectrum we infer an amount of extinction corresponding to $A_V = 0.6$. In the SDSS catalog the source is flagged QSO_CAP.

CQ0339+0022 ($z = 1.41$)

This is a reddened QSO at $z = 1.41$. The shape of the optical spectrum is well matched with the template spectrum reddened by SMC-like extinction with $A_V = 0.6$. The spectrum displays emission lines from Mg II and C III. Mg II has a P-Cygni profile and there is broad Al III absorption blueward of the C III emission line, characteristic of lo-BAL QSOs. The object is not flagged as a QSO based on the SDSS photometry.

CQ0350−0031 ($z = 2.00$)

This is a reddened QSO at $z = 2.00$. A spectrum has also been secured by the SDSS team. Based on both our and the SDSS spectrum we infer an amount of extinction corresponding to $A_V = 0.4$. The spectrum displays emission lines from C III, C IV, and Si IV. In the SDSS catalog the source is flagged QSO_CAP.

CQ0354−0012 ($z = 2.45$)

This is a reddened QSO at $z = 2.45$, but in this case the dust is Galactic ($E(B-V) = 0.37$) and there is no evidence for excess extinction in the host galaxy or intervening along the line-of-sight. Yet, the spectrum is still an unusual QSO spectrum in the sense that both C IV and Lyα are strongly absorbed. The object is not flagged as a QSO based on the SDSS photometry.

CQ0354−0030 ($z = 1.00$)

This is a reddened QSO at $z = 1.00$. The redshift is based on the detection of the Mg II emission line. The objects is significantly reddened by Galactic extinction ($E(B-V) = 0.45$), but it also has intrinsic excess reddening corresponding to $A_V = 0.3$. The object is not flagged as a QSO based on the SDSS photometry.

CQ0822+0004 ($z = 0.378$)

This spectrum shows strong Balmer absorption at $z = 0.378$, but no emission lines. This is most likely a compact post-starburst galaxy (so-called E+A galaxy). The object is flagged as QSO_HIZ based on the SDSS photometry.

CQ0822+0435 ($z = 0$)

This is an M-dwarf. Based on the SDSS photometry the source is not flagged as a QSO.

CQ0826+0728 ($z = 1.77$)

This is a reddened QSO at $z = 1.77$. The spectrum displays broad emission lines from Mg II and C III and narrower emission from C IV. The shape of the spectrum is well matched with the template spectrum reddened by an SMC-like extinction curve with $A_{\rm V} = 0.6$. The object is not flagged as a QSO based on the SDSS photometry.

CQ0831+0930 ($z = 1.96$)

This is a reddened QSO at $z = 1.96$. The inferred amount of extinction corresponds to $A_{\rm V} = 0.75$. The spectrum displays broad emission from C III, whereas C IV and Si IV are only detected in absorption. The object is not flagged as a QSO based on the SDSS photometry.

CQ0831–0022 ($z = 2.53$)

This is a mildly reddened QSO at $z = 2.53$. The inferred amount of extinction corresponds to $A_{\rm V} = 0.23$. The spectrum displays broad C III emission and complex absorption at the positions of C IV, Si IV, N V and Lyα. The object is not flagged as a QSO based on the SDSS photometry.

CQ0832+0121 ($z = 0.166$)

This object is a compact, old galaxy (similar to CQ0105+0000). The object is not flagged as a QSO based on the SDSS photometry.

CQ0832+0606 ($z = 2.57$)

This spectrum is a reddened QSO at $z = 2.57$ – similar to that of the nearby CQ0831–0022. The inferred amount of extinction corresponds to $A_{\rm V} = 0.4$. The spectrum displays broad C III emission and complex absorption at the positions of C IV, Si IV, N V and Lyα. The object is not flagged as a QSO based on the SDSS photometry.

5

Dust in intervening absorption systems toward red quasars

This chapter contains the following article:

"The High A_V Quasar Survey: Reddened Quasi-Stellar Objects selected from Optical/Near-infrared Photometry – II"

Published in *The Astrophysical Journal Supplement Series, vol. 217, id. 5, 26 pp, 2015.*

Authors:

J.-K. Krogager, S. Geier, J. P. U. Fynbo, B. P. Venemans, C. Ledoux, P. Møller, P. Noterdaeme, M. Vestergaard, T. Kangas, T. Pursimo, F. G. Saturni, & O. Smirnova

Quasi-stellar objects (QSOs) whose spectral energy distributions (SEDs) are reddened by dust either in their host galaxies or in intervening absorber galaxies are to a large degree missed by optical colour selection criteria like the one used by the Sloan Digital Sky Survey (SDSS). To overcome this bias against red QSOs, we employ a combined optical and near-infrared colour selection. In this paper, we present a spectroscopic follow-up campaign of a sample of red candidate QSOs which were selected from the SDSS and the UKIRT Infrared Deep Sky Survey (UKIDSS). The spectroscopic data and SDSS/UKIDSS photometry are supplemented by mid-infrared photometry from the Wide-field Infrared Survey Explorer. In our sample of 159 candidates, 154 (97%) are confirmed to be QSOs. We use a statistical algorithm to identify sightlines with plausible intervening absorption systems and identify nine such cases assuming dust in the absorber similar to Large Magellanic Cloud sightlines. We find absorption systems toward 30 QSOs, 2 of which are consistent with the best-fit absorber redshift from the statistical modelling. Furthermore, we observe a broad range in SED properties of the QSOs as probed by the rest-frame 2 μm flux. We find QSOs with a strong excess as well as QSOs with a large deficit at rest-frame 2 μm relative to a QSO template. Potential solutions to these discrepancies are discussed. Overall, our study demonstrates the high efficiency of the optical/near-infrared selection of red QSOs.

5.1 Introduction

Quasi-stellar objects (QSOs) are enigmatic objects in the Universe and due to their very high intrinsic luminosities they can be seen out to very large cosmological distances. Although great breakthroughs have developed since the first detection of quasi-stellar radio sources (Matthews & Sandage 1963, since then the term *QSO* or *quasar* has gained prevalence), many questions regarding their physical nature remain unsolved. In order to draw robust conclusions concerning the population of QSOs as a whole, it is important to have a representative sample; however, most studies in the past have relied on colour selections of QSOs from large optical surveys, e.g., the Sloan Digital Sky Survey (SDSS, York et al. 2000) and the 2dF QSO redshift survey (Croom et al. 2004). Although any selection on colour inherently biases the selected sample, the power of colour selection lies in the ability to quickly build a large sample without investing large amounts of time on spectroscopic classification.

QSOs are thought to be transitional phenomena originating in the environments of super-massive black holes in the cores of galaxies. The QSO activity is triggered by mechanisms that cause material to be accreted onto the central back holes, e.g., mergers or hydrodynamical instabilities within the galaxies. Such major events are also believed to induce strong star formation activity leading to the formation of large amounts of dust. Some part of the population is thus expected to be found in dust-rich environments leading to red optical colours. The search for red QSOs has a long history (e.g., Benn et al. 1998; Warren, Hewett, & Foltz 2000; Gregg et al. 2002; Richards et al. 2003; Hopkins et al. 2004; Polletta et al. 2006; Glikman et al. 2007, 2012, 2013; Lacy et al. 2007; Maddox et al. 2008; Urrutia et al. 2009; Banerji et al. 2012; Maddox et al. 2012). The detection of red QSOs in most of these works relied on either radio or X-ray detections (see Warren, Hewett, & Foltz 2000, for an extensive discussion). Recently, large area surveys in the near-infrared have made it possible to select QSOs based on near-infrared photometry (Warren et al. 2007; Peth, Ross, & Schneider 2011; Maddox et al. 2012) and this is the approach we have adopted in this work.

The red colours of QSOs may be caused by dust in intervening absorption systems as well. If the intervening absorber is very dust-rich, then it may cause reddening and dimming of the background QSO to the point where optical selection will fail to identify the source as a QSO. A bias may therefore exist against very dusty and hence very metal-rich absorption systems, leading to the underestimation of the cosmic chemical abundance in absorption systems (Pontzen & Pettini 2009; Khare et al. 2012). In Fynbo et al. (2013a, hereafter Paper I), we investigated the population of red QSOs missing in the SDSS DR7 sample, motivated by the discoveries of intervening absorbers causing reddening of the background QSOs to the point where these QSOs were close to dropping out of the colour criteria invoked by SDSS-I/II (Noterdaeme et al. 2009b, 2010; Kaplan et al. 2010; Fynbo et al. 2011; Noterdaeme et al. 2012b; Wang et al. 2012). Selecting candidate QSOs on basis of their near-infrared colours showed that QSOs were indeed missing in the SDSS DR7 sample of QSOs, see Paper I. Any bias in QSO samples affects both the study of the QSOs themselves, absorption features in the QSOs (e.g., broad absorption line (BAL) QSOs, see Saturni et al. 2015), and the samples of intervening absorption systems (Richards et al. 2003; Maddox et al. 2012).

In this work, we present revised criteria compared to those utilized in Paper I to target more reddened QSOs. The colour criteria allow us to select a pure (though not complete) sample of reddened QSO candidates. Here we present and discuss our spectroscopic follow-up campaign.

5.2 Photometric Data and Selection

5.2.1 Photometric data

The selection of candidate red QSOs is based purely on optical and near-infrared photometry. The photometry was selected from the overlap region between the SDSS data release 7 (u, g, r, i, and z bands) and the UKIRT Infrared Deep Sky Survey (Y, J, H, and K_s).

In our analysis, we also include data from the Wide-field Infrared Survey Explorer (WISE) providing photometry in four bands in the mid-infrared at 3.4, 4.6, 12, and 22 μm. In case of non-detections, we quote the flux in the given band as a $2\,\sigma$ upper limit.

5.2.2 Selection Criteria

Our aim is to look for this population of red QSOs, which is missed in the optical QSO samples, by using a set of colour selection criteria that were refined with respect to those of Paper I. By studying the distribution of colours (see Fig. 5.1) of the various identified targets in our pilot study, we find that we can significantly reduce the small fraction of contaminating galaxies and stars using these refined colour criteria (all on the AB magnitude system):

$$J - K_s > 0\,;\, H - K_s > 0\,;\, J - H < 0.4\,;\, 0.5 < g - r < 1.0\,;\, 0.1 < r - i < 0.7.$$

Moreover, the revised criteria also improve the selection of QSOs with redshifts in the range $2.5 < z < 3.5$, which were missing in the sample presented in Paper I. In total, we have selected 901 point sources common to the SDSS and UKIDSS survey fields fulfilling these refined selection criteria down to a flux limit of $J_{\rm AB} < 19$. Of these, $\sim 45\%$ had already been observed by SDSS (DR8) and found to be QSOs (either dust reddened, BALs, or at $z \gtrsim 3$). From the remaining 492 targets without spectroscopy from SDSS, we selected our sample for spectroscopic follow-up.

In Fig. 5.1, we compare the selection criteria from Paper I with the refined criteria described above. We only show the criteria for $g - r$, $r - i$, and $J - K$ as these are the colours that both sets of criteria have in common. As can be seen in Fig. 5.1, the two selections overlap in these two colour spaces. In total, 15 out of 58 objects from Paper I also fulfill all of the revised selection criteria. The targets from Paper I that were not spectroscopically classified as QSOs (i.e., stars and galaxies) are shown in Fig. 5.1 as large blue squares. Since these concentrate in a specific part of the colour-colour diagram shown in Fig. 5.1, we can effectively remove them by excluding these regions of colour space. For comparison, we indicate the colours of stars as black points. While the colours of stars coincide with the quasar colours in the optical, when we include the infrared colours the two populations separate more easily.

5.3 Spectroscopic Observations and Data Reduction

During a range of observing runs in 2012, 2013, and 2014, 159 candidate red QSOs were observed with the Nordic Optical Telescope (NOT) on La Palma, using the Andalucia Faint Object Spectrograph and Camera (ALFOSC). As in Paper I, we used grism #4, which covers the wavelength range from about 3200 Å to 9100 Å at a resolution of about 300 with a slit width of 1.3 arcsec. Redwards of about 7500 Å the spectra are strongly affected by fringing, which was alleviated by dithering along the slit. In order to prevent 2$^{\rm nd}$ order contamination from wavelengths shorter than 3500 Å, a blocking filter

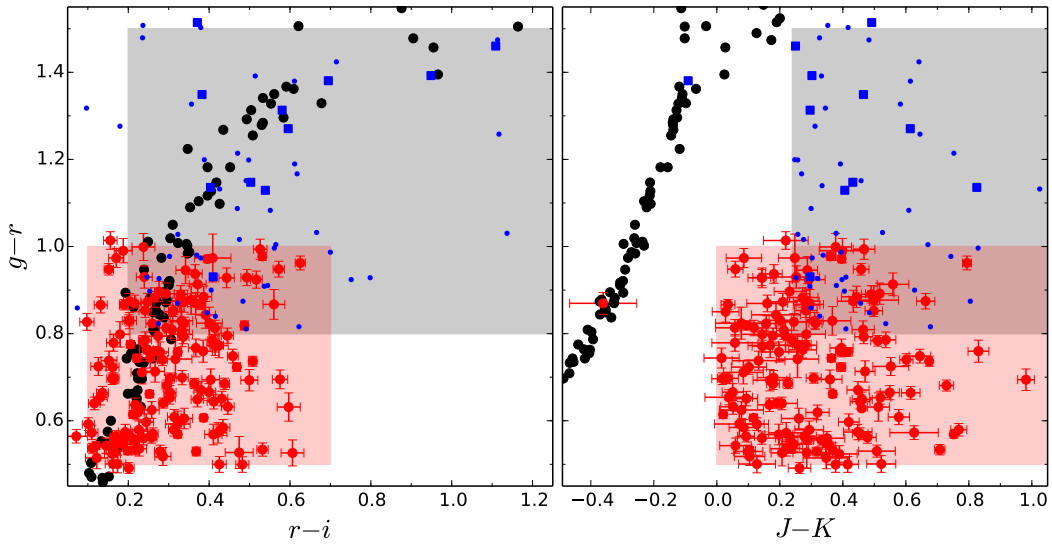

Figure 5.1: Comparison of the colour criteria used in this work (red region) to those from Paper I (gray region). The left and right panels show $g-r$ vs. $r-i$ and $g-r$ vs. $J-K$, respectively. The big, red points with error-bars represent the sample that was observed in this work. Typical stellar colours are shown in black points. The blue points represent the sample from Paper I; QSOs are shown as small, blue points while contaminants are shown as big, blue squares. These contaminants (galaxies and stars) are primarily concentrated in the upper part of the colour-colour diagrams. This distribution is part of the motivation for the revised criteria resulting in a higher efficiency of QSO selection.

was used for the observations with grism #4. We used filter no. #94 which blocks out wavelengths shorter than 3560 Å. Given the red nature of the targets (by selection) and the reduced intensity of the second order spectrum the contamination from the remaining flux which is not blocked by the filter (from $3560 - 4500$ Å) will be low. The overlap from the second order starts at 7120 Å, which is furthermore the spectral range affected by strong fringing. Moreover, we have the overall spectral shape from the broad-band photometry to make sure that we are not affected by significant second order contamination. Hence we consider second order contamination to be negligible. The spectra were taken aligning the slit at the parallactic angle. In some cases of bad seeing, we observed with a 1.8 arcsec slit. Four sources (HAQ0047+0826, HAQ0151+1453, HAQ1115+0333, and HAQ2300+0914) were also observed with grism #6 which covers the wavelength range from about 3200 Å to 5500 Å at a resolution of about 500 with the 1.0 arcsec slit. Two targets (HAQ1115+0333 and HAQ2225+0527) were observed with grism #7 to look for intervening absorption. Grism #7 covers wavelengths from about 3850 Å to 6850 Å at a resolution of about 650 with the 1.0 arcsec slit. We binned the CCD pixels by a factor of 2 along the wavelength axis.

After the release of SDSS-DR9 in August 2012 we noted that 11 of the candidates, which we followed up, had been observed by SDSS. With the new release of DR10, the number of candidates with spectra from SDSS is now 25. For targets that were observed by the Baryon Oscillation Spectroscopic Survey (BOSS), we present the spectra from the NOT along with BOSS spectra. However, we preferentially use the BOSS spectra in our analysis if available, since they have larger wavelength coverage, higher signal to noise and better resolution ($R \sim 2000$) (Dawson et al. 2013). In Table 5.1, we give a full list of all the observed targets.

The spectra were reduced using a combination of IRAF[1] and MIDAS[2] tasks for low-resolution spectroscopy. Cosmic rays were rejected using the software written by van Dokkum (2001b). In case of photometric observing conditions, the spectrophotometric standard star observed on the same night as the science spectra was used for the flux calibration. Otherwise we used a standard response curve to calibrate the spectra. The spectra and photometry were corrected for Galactic extinction using the extinction maps from Schlegel, Finkbeiner, & Davis (1998). In order to improve the absolute flux-calibration, we scaled the spectra to the r-band photometry from SDSS.

5.4 Results

In Fig. 5.2, we show the 1-dimensional spectra of one of the targets in our sample along with the photometry from SDSS and UKIDSS. We are able to securely identify 154 out of 159 targets as QSOs. The full set of figures for all targets is shown in Appendix B. We have a tentative identification of the source HAQ2247+0146 which is probably a highly absorbed BAL QSO at redshift $z \approx 2.1$. Of the remaining four objects one is unidentified, one is most probably a BL Lacertae object (Stein, Odell, & Strittmatter 1976), and two objects are identified as a stars. We thus have a purity (or efficiency) of $P \sim 97\%$, defined as the ratio of QSOs to total objects in the sample. One of the stars in our sample (an M dwarf) was observed by mistake[3] and is the result of a wrong object in the field being put on the slit. The real candidate for HAQ2254+0638 has therefore not been observed. The other star (a G dwarf) has entered our selection due to an error in the K_s-band photometry for this candidate. In the right panel of Fig. 5.1, the single outlying red point (overlapping with the stellar sources) corresponds to this G dwarf and reflects the erroneous photometry in the K_s-band. The star is located at high galactic latitude toward the Galactic center with high foreground extinction ($A(V) = 0.52$) due to the so-called North Galactic Spur. In Table 5.2, we present the identification of all objects, their radio flux from FIRST, and an estimate of the extinction assuming Small Magellanic Cloud (SMC) type dust at the redshift of the QSO unless specified otherwise. Only three QSOs in our sample were flagged as QSO candidates by SDSS. These are marked with the SDSS flag 'QSO_HIZ' or 'QSO_CAP' in Table 5.2. This low number of QSO identifications in SDSS is caused by the overlap of the sources with the stellar locus in colour-colour space. Hence SDSS flags these sources as stars and not QSOs. By expanding the colour-space with the near-infrared photometry we are able to break the degeneracy and separate stars from QSOs. More of our targets were identified by the BOSS survey, since BOSS relies on many other QSO selection algorithms than just colour criteria (Ross et al. 2012, and references therein). In the notes of Table 5.2, we give the redshift inferred by BOSS for the cases with BOSS spectra, along with remarks on available spectra observed with other grisms, e.g., grism #6 or #7. We note that the targets marked as BAL QSO do not follow a stringent classification of BAL QSOs; however, this is to indicate that the QSO has intrinsic absorption. For a more detailed analysis and classification, see Saturni et al. (2015, in review).

[1] IRAF is distributed by the National Optical Astronomy Observatory, which is operated by the Association of Universities for Research in Astronomy (AURA) under cooperative agreement with the National Science Foundation.

[2] ESO MIDAS is a copyright protected software product of the European Southern Observatory. The software is available under the GNU General Public License.

[3] The correct target ID for this star in SDSS is: J225430.23+063833.8

Table 5.1: Full sample observed with the NOT

Target	α (J 2000)	δ (J 2000)	$r_{\rm SDSS}$ (AB mag)	Telescope	Exptime (sec)
HAQ 0000+0557	00 00 33.979	+05 57 53.77	19.75	NOT, BOSS	3×780
HAQ 0001+0233	00 01 21.685	+02 33 04.87	17.86	NOT	2×600
HAQ 0008+0835	00 08 15.020	+08 35 25.68	18.24	NOT	2×450
HAQ 0008+0846	00 08 25.327	+08 46 26.20	18.81	NOT	2×600
HAQ 0011+0122	00 11 04.665	+01 22 56.02	18.28	NOT	900
HAQ 0012+0651	00 12 55.339	+06 51 22.76	18.70	NOT	2×600
HAQ 0012+0657	00 12 43.499	+06 57 36.74	18.98	NOT	2×600
HAQ 0012+0944	00 12 01.587	+09 44 02.21	18.13	NOT	2×500
HAQ 0014+0444	00 14 05.324	+04 44 09.35	17.75	NOT	2×600
HAQ 0014+0939	00 14 13.425	+09 39 06.47	18.77	NOT, BOSS	2×600
HAQ 0015+0736	00 15 35.496	+07 36 37.54	19.09	NOT, BOSS	3×600
HAQ 0015+0811	00 15 31.492	+08 11 36.96	19.00	NOT	2×600
HAQ 0015+1129	00 15 22.046	+11 29 59.89	17.89	NOT	2×600
HAQ 0015+1340	00 15 58.255	+13 40 05.37	19.61	NOT	3×600
HAQ 0018+1133	00 18 25.423	+11 33 01.62	19.03	NOT	2×600
HAQ 0020+0259	00 20 20.401	+02 59 13.88	19.03	NOT	2×600
HAQ 0022+0147	00 22 24.417	+01 47 31.23	17.52	NOT	3×250
HAQ 0024+1037	00 24 06.099	+10 37 58.03	17.06	NOT	3×250
HAQ 0025+0220	00 25 10.345	+02 20 06.35	18.93	NOT	2×600
HAQ 0026+0640	00 26 12.462	+06 40 36.80	18.83	NOT	2×600
HAQ 0031+1328	00 31 16.660	+13 28 48.44	17.60	NOT	2×600, 300
HAQ 0033+0915	00 33 57.209	+09 15 53.66	19.23	NOT, BOSS	3×600
HAQ 0034+0950	00 34 28.096	+09 50 20.64	18.33	NOT	900
HAQ 0038+1426	00 38 06.431	+14 26 02.78	18.79	NOT	2×600
HAQ 0042+1220	00 42 15.000	+12 20 08.00	19.24	NOT	3×600
HAQ 0043+0549	00 43 16.644	+05 49 42.33	18.77	NOT	2×600
HAQ 0043+1136	00 43 28.876	+11 36 26.49	19.26	NOT	3×540
HAQ 0044+0817	00 44 30.382	+08 17 13.79	18.84	NOT, BOSS	3×400
HAQ 0044+1250	00 44 45.699	+12 50 19.86	19.17	NOT	2×900
HAQ 0045+1217	00 45 43.339	+12 17 11.83	17.43	NOT	3×400
HAQ 0046+0839	00 46 33.895	+08 39 13.78	19.71	NOT, BOSS	3×720
HAQ 0047+0826	00 47 37.196	+08 26 38.47	17.29	NOT	4×200
HAQ 0051+1542	00 51 54.685	+15 42 05.90	18.83	NOT	2×600
HAQ 0053+0216	00 53 36.998	+02 16 36.60	18.58	NOT	2×600
HAQ 0056+1132	00 56 45.104	+11 32 38.72	19.11	NOT	3×600
HAQ 0057+1155	00 57 31.960	+11 55 12.13	18.61	NOT	2×600
HAQ 0059+1238	00 59 48.164	+12 38 36.79	18.75	NOT	2×600
HAQ 0102+0249	01 02 16.770	+02 49 52.52	18.68	NOT	600
HAQ 0110+0303	01 10 13.499	+03 03 56.17	18.91	NOT	2×600
HAQ 0118+0323	01 18 13.583	+03 23 34.30	18.62	NOT	2×600
HAQ 0118+0700	01 18 57.315	+07 00 29.15	19.16	NOT, BOSS	2×600
HAQ 0119+0817	01 19 09.186	+08 17 53.87	19.08	NOT	2×900
HAQ 0120+0351	01 20 30.091	+03 51 46.88	18.95	NOT	3×480
HAQ 0121+0455	01 21 45.522	+04 55 04.50	18.16	NOT	2×900

Table 5.1 — *Continued*

Target	α (J 2000)	δ (J 2000)	$r_{\rm SDSS}$ (AB mag)	Telescope	Exptime (sec)
HAQ 0122+0325	01 22 09.876	+03 25 43.64	17.87	NOT	600
HAQ 0130+1439	01 30 16.520	+14 39 53.71	19.93	NOT	4×600
HAQ 0138+0124	01 38 02.071	+01 24 24.47	18.26	NOT, BOSS	2×600
HAQ 0138+0636	01 38 19.887	+06 36 36.05	18.92	NOT	2×600
HAQ 0143+1509	01 43 17.885	+15 09 15.41	19.35	NOT	2×1000
HAQ 0151+0618	01 51 36.733	+06 18 31.67	19.16	NOT	3×600
HAQ 0151+1453	01 51 57.714	+14 53 08.34	19.53	NOT	3×360
HAQ 0155+0438	01 55 03.728	+04 38 30.42	18.38	NOT	900
HAQ 0201+0223	02 01 14.291	+02 23 33.29	19.07	NOT	1080
HAQ 0204+0327	02 04 58.663	+03 27 03.22	18.55	NOT	2×600
HAQ 0206+0624	02 06 14.665	+06 24 54.44	19.01	NOT	2×600
HAQ 0208+0521	02 08 15.802	+05 21 06.01	19.10	NOT	2×900
HAQ 0211+1214	02 11 23.395	+12 14 01.20	18.32	NOT	2×600
HAQ 0226+0729	02 26 50.310	+07 29 52.78	19.06	NOT	2×900
HAQ 0236+0619	02 36 46.962	+06 19 03.15	19.03	NOT	2×600
HAQ 0243+0355	02 43 29.118	+03 55 59.50	17.84	NOT	3×240
HAQ 0318+0424	03 18 16.302	+04 24 06.35	19.50	NOT	5×400
HAQ 0318+0434	03 18 33.519	+04 34 43.48	19.20	NOT	1500
HAQ 0319+0623	03 19 01.776	+06 23 39.04	18.92	NOT	4×450
HAQ 0329+0553	03 29 15.624	+05 53 39.57	18.92	NOT	2×600
HAQ 0329+0609	03 29 09.017	+06 09 14.30	19.14	NOT	4×500
HAQ 0337+0539	03 37 38.075	+05 39 10.95	18.18	NOT	2×600
HAQ 0339+0420	03 39 30.630	+04 20 31.11	18.75	NOT	4×360
HAQ 0340+0408	03 40 14.148	+04 08 31.94	19.36	NOT	4×600
HAQ 0345−0009	03 45 50.472	−00 09 07.56	18.53	NOT	4×375
HAQ 0347+0115	03 47 48.060	+01 15 44.52	19.06	NOT	2×600
HAQ 0355−0025	03 55 52.570	−00 25 04.22	18.70	NOT	4×400
HAQ 0355−0053	03 55 46.908	−00 53 39.83	19.46	NOT	2×780
HAQ 1106+0300	11 06 12.667	+03 00 49.10	17.62	NOT	3×300
HAQ 1114+1330	11 14 15.151	+13 30 59.64	17.59	NOT	3×400
HAQ 1115+0333	11 15 49.737	+03 33 51.35	18.89	NOT	3×600
HAQ 1148−0117	11 48 22.193	−01 17 29.20	18.02	NOT	2×500, 3×400
HAQ 1207+1341	12 07 59.229	+13 41 15.28	18.40	NOT	3×500
HAQ 1233+1304	12 33 55.605	+13 04 09.21	17.71	NOT	3×250
HAQ 1247+3403	12 47 02.054	+34 03 58.17	18.36	NOT, BOSS	2×500
HAQ 1248+2951	12 48 48.423	+29 51 06.73	18.19	NOT	2×400
HAQ 1315+0440	13 15 21.006	+04 40 00.56	18.70	NOT	3×500
HAQ 1319+3214	13 19 02.712	+32 14 51.29	19.50	NOT	4×600
HAQ 1327+3206	13 27 57.361	+32 06 50.63	18.55	NOT	2×600
HAQ 1332+0052	13 32 54.515	+00 52 50.63	18.35	NOT, BOSS	2×600
HAQ 1339+3331	13 39 41.381	+33 31 12.64	18.57	NOT	1200
HAQ 1355+3407	13 55 57.499	+34 07 39.03	18.77	NOT	2×800
HAQ 1358+2401	13 58 59.897	+24 01 07.00	18.86	NOT	2×900
HAQ 1400+0219	14 00 47.108	+02 19 34.80	19.81	NOT	4×600
HAQ 1409+0940	14 09 52.589	+09 40 23.73	19.65	NOT, BOSS	3×600

Table 5.1 — *Continued*

Target	α (J 2000)	δ (J 2000)	$r_{\rm SDSS}$ (AB mag)	Telescope	Exptime (sec)
HAQ 1411−0104	14 11 59.671	−01 04 42.60	19.28	NOT	3×600
HAQ 1434+0448	14 34 15.006	+04 48 46.83	19.77	NOT	4×750
HAQ 1444+0752	14 44 43.539	+07 52 24.28	19.45	NOT, BOSS	3×600, 5×750
HAQ 1451+3239	14 51 56.221	+32 39 51.69	19.09	NOT	2×600
HAQ 1506+0438	15 06 29.847	+04 38 44.27	19.97	NOT	4×600
HAQ 1509+1214	15 09 53.554	+12 14 44.98	18.54	NOT, BOSS	2×600
HAQ 1517+0817	15 17 55.714	+08 17 27.66	19.15	NOT	2×600
HAQ 1524−0053	15 24 44.652	−00 53 09.70	19.50	NOT	3×600
HAQ 1527+0250	15 27 10.942	+02 50 19.20	17.06	NOT	5×200
HAQ 1534+0013	15 34 52.677	+00 13 17.71	18.82	NOT	2×600
HAQ 1535+0157	15 35 53.854	+01 57 11.36	18.86	NOT	2×600
HAQ 1545−0130	15 45 49.013	−01 30 09.26	19.34	NOT	3×600
HAQ 1546+0005	15 46 58.586	+00 05 38.33	19.01	NOT, BOSS	2×750
HAQ 1600+2911	16 00 33.974	+29 11 16.46	19.82	NOT	4×900
HAQ 1603+2512	16 03 28.589	+25 12 14.33	20.18	NOT	2×1350
HAQ 1606+2902	16 06 01.112	+29 02 18.85	19.58	NOT	4×600
HAQ 1606+2903	16 06 28.064	+29 03 33.80	17.53	NOT, BOSS	3×480
HAQ 1607+2611	16 07 21.764	+26 11 07.06	19.67	NOT	4×600
HAQ 1611+2453	16 11 41.495	+24 53 22.21	19.69	NOT	3×600
HAQ 1620+2955	16 20 40.932	+29 55 06.56	19.21	NOT, BOSS	1200
HAQ 1626+2517	16 26 21.102	+25 17 14.00	19.33	NOT, BOSS	2×1000
HAQ 1633+2851	16 33 50.413	+28 51 56.77	19.45	NOT	2×900
HAQ 1634+2811	16 34 39.605	+28 11 38.28	19.25	NOT	2×900
HAQ 1639+3157	16 39 57.963	+31 57 26.71	19.60	NOT, BOSS	3×600
HAQ 1643+2944	16 43 32.810	+29 44 23.42	19.48	NOT	3×600
HAQ 1645+3056	16 45 53.184	+30 56 07.27	19.14	NOT, BOSS	3×600
HAQ 1645+3130	16 45 47.802	+31 30 03.28	19.50	NOT, BOSS	3×600
HAQ 1655+3051	16 55 23.891	+30 51 37.71	19.38	NOT	3×600
HAQ 2159+0212	21 59 36.617	+02 12 33.51	18.73	NOT	600, 2×600
HAQ 2203−0052	22 03 08.631	−00 52 34.54	19.05	NOT	2×900
HAQ 2217+0359	22 17 40.515	+03 59 33.78	19.43	NOT	2×900
HAQ 2221+0145	22 21 43.557	+01 45 37.37	19.05	NOT, BOSS	2×600
HAQ 2222+0604	22 22 06.684	+06 04 15.71	19.38	NOT	2×900
HAQ 2225+0527	22 25 14.695	+05 27 09.10	18.11	NOT	2×600, 2×450
HAQ 2229+0324	22 29 15.168	+03 24 52.71	19.90	NOT, BOSS	3×600
HAQ 2231+0509	22 31 15.996	+05 09 48.62	19.10	NOT	2×900
HAQ 2241+0818	22 41 51.844	+08 18 59.09	19.06	NOT	2×900
HAQ 2244+0335	22 44 53.750	+03 35 23.29	18.66	NOT, BOSS	2×600
HAQ 2245+0457	22 45 28.459	+04 57 20.38	18.32	NOT	2×600, 2×600
HAQ 2246+0710	22 46 03.823	+07 10 50.92	18.02	NOT	2×600
HAQ 2247+0146	22 47 20.277	+01 46 04.95	19.18	NOT	5×600
HAQ 2252+0434	22 52 45.969	+04 34 36.75	16.03	NOT	4×90
HAQ 2253+1141	22 53 30.058	+11 41 18.31	19.20	NOT	2×600
HAQ 2254+0638	22 54 32.268	+06 38 26.01	18.41	NOT	600
HAQ 2300+0914	23 00 56.010	+09 14 03.85	18.86	NOT	2×600

Table 5.1 — *Continued*

Target	α (J 2000)	δ (J 2000)	$r_{\rm SDSS}$ (AB mag)	Telescope	Exptime (sec)
HAQ 2301+0832	23 01 22.475	+08 32 01.43	17.26	NOT	2×600
HAQ 2303+0238	23 03 17.785	+02 38 09.60	18.75	NOT	2×600
HAQ 2303+0630	23 03 12.032	+06 30 14.21	18.67	NOT	2×600
HAQ 2305+0117	23 05 48.832	+01 17 41.63	19.55	NOT	3×650
HAQ 2310+1117	23 10 46.942	+11 17 21.55	20.06	NOT	4×600
HAQ 2311+1444	23 11 38.547	+14 44 36.72	19.18	NOT, SDSS	3×600
HAQ 2313+0955	23 13 34.552	+09 55 00.03	18.91	NOT	2×600
HAQ 2318+0255	23 18 12.807	+02 55 38.98	18.31	NOT	2×600
HAQ 2326+0642	23 26 48.823	+06 42 35.96	18.79	NOT	2×600
HAQ 2326+1423	23 26 40.965	+14 23 03.37	19.02	NOT	2×450
HAQ 2330+1009	23 30 59.933	+10 09 49.42	19.19	NOT	3×500
HAQ 2333+0113	23 33 35.516	+01 13 29.32	19.85	NOT, BOSS	4×900
HAQ 2333+0619	23 33 11.434	+06 19 31.18	19.31	NOT	2×900
HAQ 2335+1407	23 35 12.070	+14 07 31.56	19.71	NOT	4×600
HAQ 2337+1343	23 37 18.332	+13 43 06.02	19.00	NOT	2×600
HAQ 2339+1232	23 39 38.008	+12 32 01.49	18.40	NOT	2×600
HAQ 2340+0121	23 40 54.272	+01 21 41.34	18.81	NOT	2×600
HAQ 2343+0615	23 43 44.229	+06 15 00.60	19.39	NOT	3×600
HAQ 2348+0716	23 48 44.464	+07 16 58.34	18.49	NOT	900
HAQ 2351+1429	23 51 06.509	+14 29 39.41	20.12	NOT	4×750
HAQ 2352+0105	23 52 38.088	+01 05 52.35	17.33	NOT, BOSS	4×225
HAQ 2358+0339	23 58 33.476	+03 39 55.79	17.91	NOT	2×300
HAQ 2358+0359	23 58 16.016	+03 59 44.69	19.95	NOT	4×600
HAQ 2358+0520	23 58 46.404	+05 20 52.00	19.47	NOT	3×600
HAQ 2358+1436	23 58 19.661	+14 36 42.03	19.45	NOT	3×600

5.4.1 Confirmed QSOs

As in Paper I, the redshifts have been determined by the emission lines visible in the spectra. In Fig. 5.3, we show the redshift distribution of the HAQ sample. The redshift distribution shows a peak around $z_{\rm QSO} \sim 1$, and is more even for redshifts $z_{\rm QSO} > 2$, however, it is not completely uniform. For comparison, we show the distributions of QSO redshifts from the SDSS-I/II (DR7) and SDSS-III/BOSS (DR10). The distribution of the SDSS-I/II sample peaks around $z_{\rm QSO} \sim 1.5$ and quickly drops off for higher redshifts where the QSO colours begin to resemble stellar colours. The more complex selection algorithms utilized for the SDSS-III/BOSS were designed to increase the number of QSOs with $z_{\rm QSO} > 2.15$. This explains the strong peak in the SDSS-III/BOSS redshift distribution.

We estimate the extinction of each QSO by fitting a QSO template to the photometry and spectrum combined. Spectral regions that are influenced by strong emission and absorption lines are masked out in the fit. As in Paper I, we use a combined template from Vanden Berk et al. (2001) and Glikman, Helfand, & White (2006). We disregard photometric points on the blue side of the Lyα emission line, upper limits, and data points influenced by strong absorption (especially in case of BALs). Furthermore, we always exclude the r band from the fit since this band has been used to scale the spectra to match the photometry. In order to test whether we primarily observe signs of dust in the QSO itself or dust

along the line of sight, we fit two sets of models: one model assuming that the dust is located in the QSO host galaxy (the null hypothesis) and another model allowing both dust in the QSO and in an intervening absorption system (the general model). Furthermore, we run each set of models for two different reddening laws, Small Magellanic Cloud (SMC) and Large Magellanic Cloud (LMC) as parametrized by Gordon et al. (2003a) with a modification for wavelengths greater than 4400 Å (see Fitzpatrick & Massa 2005). The model we fit can be summarized as follows:

$$F_{\rm obs} = C \cdot F_0 \cdot \exp\left(-\frac{1}{2.5\log(e)}\left[A({\rm V})\cdot k_{\rm QSO} + A({\rm V})_{\rm abs}\cdot k_{\rm abs}\right]\right),$$

where F_0 denotes the rest-frame QSO template before reddening is applied, $F_{\rm obs}$ refers to the reddened template, and $A(V)$ is the amount of extinction applied in the QSO's rest-frame given the reddening law, $k_{\rm QSO}$. We assume that the dust in the QSO is SMC type (e.g., Hopkins et al. 2004). Likewise, $A(V)_{\rm abs}$ denotes the amount of extinction applied in the putative absorber's rest-frame at $z_{\rm abs}$ given the reddening law for the absorber, $k_{\rm abs}$ (SMC or LMC). C is an arbitrary scale factor, since we do not know the intrinsic flux of the QSO before reddening is applied. The null hypothesis can then be constructed by restricting the extinction and redshift for the absorber in the general model: $A(V)_{\rm abs} = z_{\rm abs} = 0$. This nested nature of the models allows us to use a likelihood ratio test to compare the two models.

For a given reddened template, $F_{\rm obs}$, we calculate synthetic fluxes for the template in each photometric band, weighted by the appropriate filter transmission curve. Next, we interpolate the template onto the wavelength grid of the observed spectrum, thereby creating a "model spectrum" which can be directly compared to the observed spectrum. For the fitting, we re-bin the spectra by a factor of two to decrease the influence of noise. We calculate the residuals using both the spectroscopic and photometric data available for each given object. The fit is then performed using χ^2 minimization utilizing a Levenburg–Marquardt algorithm as implemented in the Python package `lmfit`.[4] For the null hypothesis, we keep the absorber parameters fixed ($A(V)_{\rm abs} = z_{\rm abs} = 0$) and only fit the remaining two parameters: the extinction at the QSO redshift, $A(V)$, and the scale factor, C. The parameter $A(V)$ is restricted to values larger than $A(V) > -0.2$. The inclusion of negative values of $A(V)$ takes into account any possible variation in the intrinsic slope of the QSO spectra. A negative value of $A(V)$ occurs if the QSO slope is intrinsically steeper than the template and no or little dust is present in the QSO. The limit of $A(V) > -0.2$ is motivated by the spread in $g-r$ colour distribution of QSOs from Richards et al. (2001, see their fig. 8). The assumption that steeper QSO UV slopes can be approximated by including negative $A(V)$ values relies on the fact that, to first order, the SMC extinction law itself is a power law (valid to within an error of $\lesssim 5\%$).

For the general model, we allow $z_{\rm abs}$ and $A(V)_{\rm abs}$ to vary as well, however, the extinction at the absorber redshift is restricted to $A(V)_{\rm abs} > 0$, since a negative extinction in the absorber is non-physical. Moreover, the absorber redshift is restricted to be $0 < z_{\rm abs} < z_{\rm QSO}$. We stress that when referring to the null hypothesis, we quote the amount of extinction in the QSO rest-frame as just $A(V)$; however, in order to avoid confusion when referring to the general model, we quote the amount of extinction in the QSO rest-frame and absorber rest-frame as $A(V)_{\rm QSO}$ and $A(V)_{\rm abs}$, respectively.

[4]Written by Matthew Newville. Full documentation available at: `http://cars9.uchicago.edu/software/python/lmfit/`

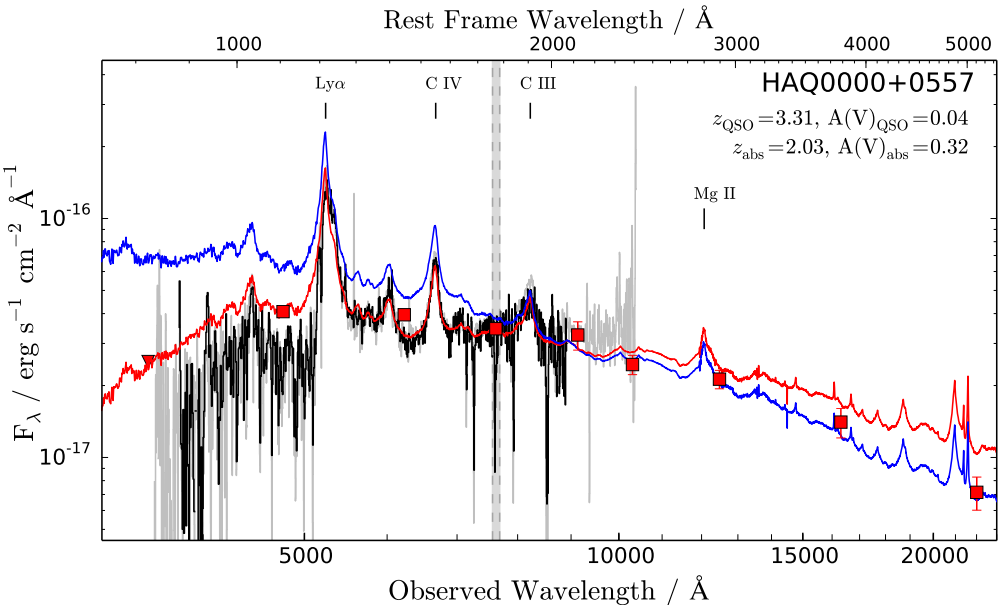

Figure 5.2: The observed spectrum is plotted as a solid black line. For targets observed with both grism 4 and 6, we show both the grism 4 and grism 6 spectra. In case of available SDSS data the spectrum from SDSS is shown in gray. In the upper right corner, the estimated emission redshift and rest-frame V-band extinction are provided. The unreddened composite QSO spectrum is shown in blue, redshifted to the spectroscopic redshift, and in red we show the redshifted composite spectrum reddened by the indicated amount of extinction. Overplotted with filled squares are the SDSS and UKIDSS photometric data points. The NOT spectra have been scaled to match the r-band photometric data point from SDSS. Unless otherwise noted we have assumed an SMC-like extinction curve. Note that the spectra have not been corrected for telluric absorption (marked with a gray band at $\sim$ 7600 Å). (The full set of figures is shown in Appendix B.)

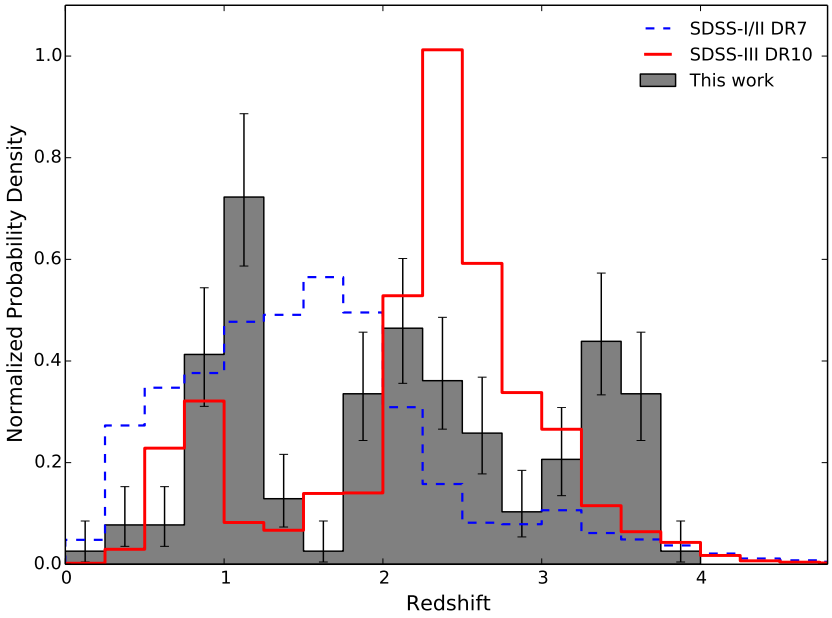

Figure 5.3: Probability density distribution of QSO redshifts for the HAQ sample (gray filled histogram) compared to the distributions of SDSS-I/II data release 7 (blue dashed histogram) and SDSS-III/BOSS data release 10 (red line histogram). The errorbars on the gray histogram indicate the 1σ Poisson errors for each bin. The errors for the SDSS data are negligible due to the much larger sample sizes ($\sim$ 1000 times larger).

Model Comparison

In order to evaluate whether the general model with dust in an intervening system provides a significantly better fit, we use a likelihood ratio test. This test quantifies how likely the observed improvement is, given the added free parameters. The logarithmic likelihood ratio is defined as $L = -2\ln(\Lambda_0/\Lambda_\mathrm{G})$, where Λ_0 and Λ_G are the likelihoods for the null hypothesis and the general model, respectively. This can be simplified in our case since we assume that our uncertainties are Gaussian. In this case, $\chi^2 = -2\ln(\Lambda)$ is a direct measure of the logarithmic likelihood. We thus obtain $L = \chi^2_0 - \chi^2_\mathrm{G}$, where χ^2_0 and χ^2_G are the χ^2 of the best fit for the null model and the general model, respectively. The ratio, L, will be distributed approximately as a χ^2 distribution with the number of degrees of freedom, ν, given by the change in degrees of freedom between the two models, which is equal to the change in the number of parameters ($\Delta\nu$ = 2). For each set of models for a given data set, we can then calculate the chance probability of encountering the calculated change in χ^2 given the addition of two extra free parameters. This is the so-called p value. In order to reject the null hypothesis, i.e., preferring a model with dust in the intervening system, we use a 5σ level significance, and hence the p value must be less than $p < 5.7 \cdot 10^{-7}$. For a χ^2 distribution with $\nu = 2$ this corresponds to a threshold of $L > 28.75$. The change in χ^2 must therefore be larger than 28.75 in order to reject the null hypothesis. We use such a strict criterion since the reddening estimates are very degenerate when introducing a second reddening system. Moreover, we require that the fit with intervening absorption (the general model) provide a *good* fit, since a model which to begin with provides a bad fit easily can improve significantly in terms of χ^2 when adding two free parameters but still provide a bad fit.

For a model to provide a good fit to the data, the distribution of normalized residuals[5] should be normally distributed, i.e., follow a Gaussian distribution of $\mu = 0$ and $\sigma^2 = 1$. We subsequently use a Kolmogorov–Smirnov (KS) test to check the departure of the normalized residuals from normality. The one-sample KS test measures the difference between the cumulative distribution of the test sample and that of a normal distribution. One can then assign a probability (P_KS) of encountering at least this difference given the hypothesis that the test sample is drawn from a normal distribution. Hence, a high value of P_KS means that the test sample is consistent with being drawn from a normal distribution. For our purpose, we require that the distribution of normalized residuals have $P_\mathrm{KS} > 0.1$, i.e., at the 10% confidence level, we have no probabilistic evidence against the hypothesis that the residuals are normally distributed. Finally, we disregard fits where one or more parameters have reached the limit of the allowed range, thus not giving a fully converged fit.

For the model fits assuming SMC-type dust in the absorber, we find no evidence for improved fits when including intervening dusty absorbers. However, when assuming that the dust in the absorber is LMC-type we find 9 QSOs for which the model with intervening dust is preferred. The best-fit parameters for these 9 QSOs are given in Table 5.3. In all other cases where the null hypothesis is preferred, we list the extinction, $A(V)$, at the QSO redshift assuming SMC-type dust in Table 5.2. In Appendix 5.A, we present a table with all of the details for the cases with significant evidence for dust in an intervening system. The table shows the best-fit parameters to both the null model and the general model along with the resulting χ^2 for each model. Furthermore, we give the P_KS value from the KS test to the normalized residuals for each model. Finally, we give the overall p value, i.e., the chance probability of the observed improvement (in terms of χ^2) given the extra free parameters.

[5]Also sometimes referred to as standardized residuals: $(\mu - x)/\sigma$, where μ, x, and σ denote, respectively, model, data, and uncertainty.

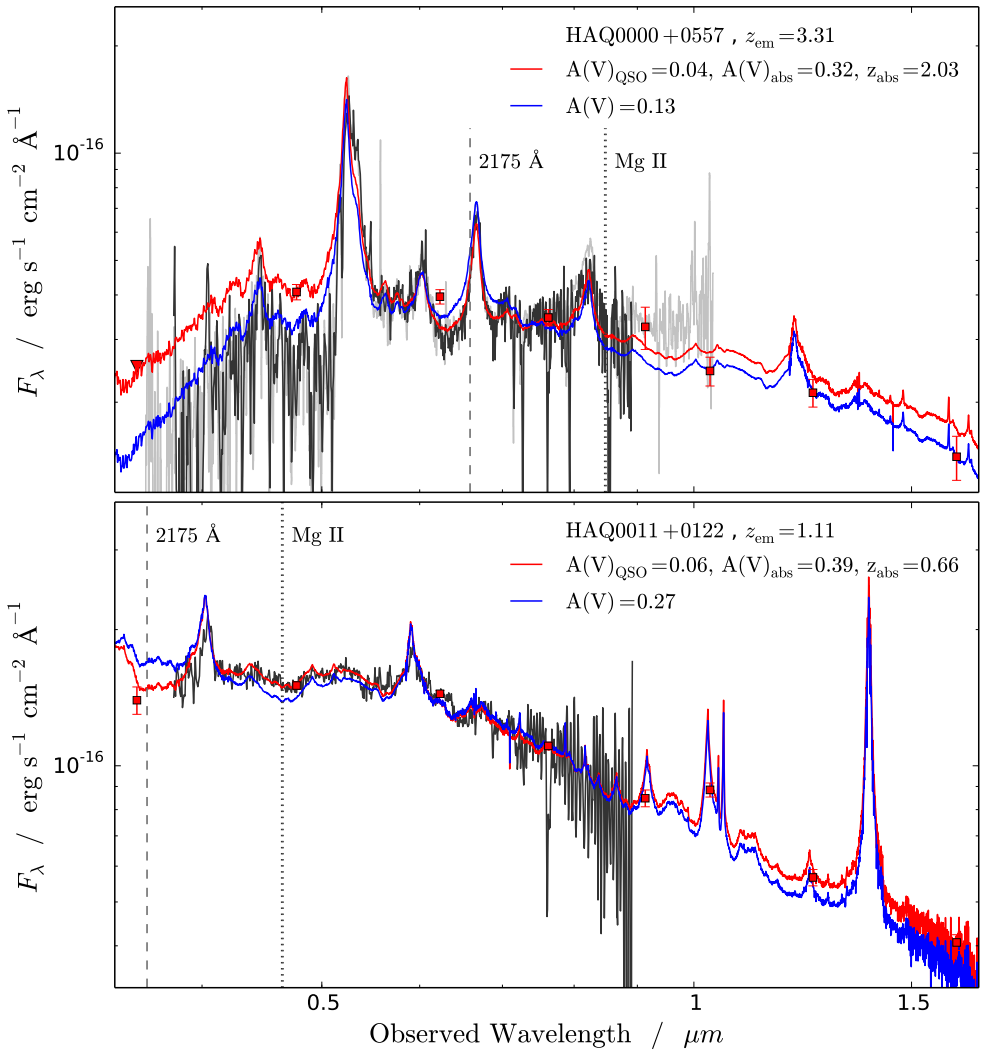

Figure 5.4: Spectra and photometry for two of the QSOs with evidence for dust in an intervening absorption system. Each panel shows the NOT spectrum in black and the SDSS and UKIDSS photometry as red squares. The blue and red templates show the best-fit null model and general model, respectively (see text for definition). In the top panel, the underlying gray spectrum is the SDSS spectrum which has been smoothed with a three pixel Gaussian kernel for presentation purposes. The dashed and dotted vertical lines indicate the locations of the 2175 Å bump and Mg II at the best-fit redshift for the absorber.

The uncertainties on the fit parameters for the general model have been obtained by using a Markov chain Monte Carlo method in order to provide a robust evaluation of the confidence intervals. Details on the Monte Carlo simulations are given in Appendix 5.A. Two of these nine cases are shown in Fig. 5.4 to demonstrate the improvement of the fit when including intervening dust. The remaining cases are shown in Appendix 5.C.

Table 5.2: Results of the spectroscopic follow-up

Target	Type	z_{QSO}	$A(V)$	$F_{1.4\,\mathrm{GHz}}$ (mJy)	Notes
HAQ 0000+0557	QSO	3.31	$0.32^{(a)}$	$<$0.34	(BOSS: z=3.31)
HAQ 0001+0233	BAL QSO	1.89	0.06	< 0.40	
HAQ 0008+0835	QSO	1.19	0.00	< 0.31	
HAQ 0008+0846	QSO	1.23	0.04	< 0.36	
HAQ 0011+0122	QSO	1.11	$0.39^{(a)}$	5.03$\pm$0.14	
HAQ 0012+0651	QSO	1.12	0.36	< 0.39	
HAQ 0012+0657	BAL QSO	2.43	0.00	< 0.39	
HAQ 0012+0944	BAL QSO	2.03	0.00	< 0.39	
HAQ 0014+0444	QSO	1.05	0.48	< 0.36	
HAQ 0014+0939	BAL QSO	3.19	0.00	< 0.39	(BOSS: z=3.23)
HAQ 0015+0736	QSO	3.63	-0.05	< 0.39	(BOSS: z=3.67)
HAQ 0015+0811	BAL QSO	2.43	0.16	< 0.35	
HAQ 0015+1129	QSO	0.87	0.78	1.64$\pm$0.16	
HAQ 0015+1340	QSO	3.11	0.14	1.64$\pm$0.16	
HAQ 0018+1133	QSO	1.90	0.18	< 0.46	
HAQ 0020+0259	BAL QSO	2.47	0.15	< 0.40	
HAQ 0022+0147	QSO	1.15	0.27	< 0.33	
HAQ 0024+1037	QSO	1.22	0.27	0.77$\pm$0.15	
HAQ 0025+0220	QSO	2.04	0.39	< 0.37	
HAQ 0026+0640	QSO	1.20	0.22	< 0.36	
HAQ 0031+1328	QSO	1.02	$0.35^{(a)}$	< 0.36	
HAQ 0033+0915	QSO	3.28	0.00	< 0.38	(BOSS: z=3.31)
HAQ 0034+0950	QSO	0.28	0.51	< 0.36	
HAQ 0038+1426	BAL QSO	2.55	0.00	< 0.49	
HAQ 0042+1220	BAL QSO	2.56	0.00	< 0.42	
HAQ 0043+0549	QSO	1.22	0.47	< 0.33	
HAQ 0043+1136	QSO	3.32	0.00	< 0.41	
HAQ 0044+0817	QSO	3.35	0.00	< 0.26	(BOSS: z=3.31)
HAQ 0044+1250	BAL QSO	2.35	0.25	< 0.26	
HAQ 0045+1217	BL Lac	$\cdots$	$\cdots$	83.81$\pm$0.15	
HAQ 0046+0839	BAL QSO	2.85	0.28	< 0.35	(BOSS: z=2.84)
HAQ 0047+0826	BAL QSO	1.95	0.18	< 0.35	Grism 6
HAQ 0051+1542	BAL QSO	1.90	$0.39^{(a)}$	< 0.35	
HAQ 0053+0216	QSO	0.99	0.71	< 0.36	
HAQ 0056+1132	QSO	3.57	0.00	< 0.48	
HAQ 0057+1155	QSO	0.60	1.20	< 0.47	
HAQ 0059+1238	QSO	3.50	0.00	< 0.43	
HAQ 0102+0249	QSO	3.49	0.01	< 0.37	
HAQ 0110+0303	QSO	3.50	0.00	< 0.41	
HAQ 0118+0323	BAL QSO	2.16	0.09	< 0.33	
HAQ 0118+0700	QSO	3.50	0.00	< 0.34	(BOSS: z=3.50)
HAQ 0119+0817	BAL QSO	1.95	0.22	< 1.14	
HAQ 0120+0351	QSO	3.09	0.00	< 0.34	
HAQ 0121+0455	QSO	0.84	0.77	< 0.34	

Table 5.2 — *Continued*

Target	Type	$z_{\rm QSO}$	$A(V)$	$F_{1.4\,\rm GHz}$ (mJy)	Notes
HAQ 0122+0325	BAL QSO	2.10	0.04	< 0.64	
HAQ 0130+1439	QSO	1.84	0.40	< 0.64	
HAQ 0138+0124	BAL QSO	2.53	0.00	< 0.45	(BOSS: z=2.61)
HAQ 0138+0636	BAL QSO	1.80	0.09	< 0.40	
HAQ 0143+1509	QSO	3.76	0.00	< 0.40	
HAQ 0151+0618	QSO	0.95	0.72	20.23±0.16	
HAQ 0151+1453	QSO	1.18	0.05	20.23±0.16	Grism 6
HAQ 0155+0438	QSO	1.13	0.46	167.63±0.29	
HAQ 0201+0223	QSO	2.24	0.19	165.22±0.10	
HAQ 0204+0327	QSO	0.83	0.66	7.53±0.13	
HAQ 0206+0624	QSO	1.20	0.83	1.57±0.13	
HAQ 0208+0521	QSO	1.07	0.40	< 0.37	Grism 6
HAQ 0211+1214	QSO	2.11	0.05	< 0.37	
HAQ 0226+0729	QSO	2.21	0.25	< 0.52	
HAQ 0236+0619	BAL QSO	2.43	0.12	< 0.46	
HAQ 0243+0355	QSO	3.30	0.00	< 0.33	
HAQ 0318+0424	BAL QSO	3.06	0.14	< 0.42	
HAQ 0318+0434	BAL QSO	2.38	0.00	< 0.54	
HAQ 0319+0623	QSO	2.10	0.13	< 0.51	
HAQ 0329+0553	QSO	1.11	0.15	23.72±0.24	
HAQ 0329+0609	QSO	1.44	0.00	23.72±0.24	
HAQ 0337+0539	QSO	3.28	0.03	7.73±0.15	
HAQ 0339+0420	QSO	1.80	$0.44^{(a)}$	1.28±0.14	
HAQ 0340+0408	QSO	1.62	0.13	< 0.41	
HAQ 0345−0009	BAL QSO	1.77	0.18	< 0.41	
HAQ 0347+0115	QSO	0.99	0.40	< 0.40	
HAQ 0355−0025	QSO	1.07	0.00	< 0.40	
HAQ 0355−0053	QSO	2.15	0.00	< 0.40	
HAQ 1106+0300	QSO	0.73	1.29	< 0.41	
HAQ 1114+1330	BAL QSO	1.10	0.00	< 0.43	
HAQ 1115+0333	QSO	3.10	0.15	< 0.45	Grism 6, 7
HAQ 1148−0117	BAL QSO	2.70	0.12	< 0.45	
HAQ 1207+1341	BAL QSO	2.37	0.12	< 0.41	
HAQ 1233+1304	BAL QSO	2.34	0.02	< 0.44	
HAQ 1247+3403	QSO	1.18	0.48	< 0.43	(BOSS: z=1.17)
HAQ 1248+2951	QSO	3.55	$0.20^{(a)}$	< 0.41	
HAQ 1315+0440	BAL QSO	2.17	0.13	< 0.43	
HAQ 1319+3214	QSO	3.50	0.00	< 0.42	
HAQ 1327+3206	QSO	2.48	0.01	< 1.64	
HAQ 1332+0052	QSO	3.52	0.05	< 0.41	(BOSS: z=3.51)
HAQ 1339+3331	QSO	3.40	0.00	< 0.41	
HAQ 1355+3407	QSO	3.16	0.00	< 0.44	
HAQ 1358+2401	QSO	3.40	0.03	< 0.41	
HAQ 1400+0219	QSO	0.86	0.85	< 0.46	
HAQ 1409+0940	QSO	0.92	0.93	< 0.44	(BOSS: z=0.93)

Table 5.2 — *Continued*

Target	Type	$z_{\rm QSO}$	$A(V)$	$F_{1.4\,\rm GHz}$ (mJy)	Notes
HAQ 1411−0104	QSO	3.50	0.00	<0.44	
HAQ 1434+0448	QSO	1.20	0.57	<0.45	
HAQ 1444+0752	BAL QSO	2.42	0.05	6.17±0.14	(BOSS: z=2.45)
HAQ 1451+3239	QSO	3.55	0.00	<0.41	
HAQ 1506+0438	QSO	1.04	0.61	<0.44	
HAQ 1509+1214	BAL QSO	2.80	0.45[a]	<0.45	(BOSS: z=2.89)
HAQ 1517+0817	QSO	0.66	0.57	<0.40	
HAQ 1524−0053	G-dwarf	0.00	0.52	<0.40	MW type extinction
HAQ 1527+0250	BAL QSO	2.13	0.20	<0.81	
HAQ 1534+0013	QSO	3.44	0.00	<0.42	
HAQ 1535+0157	QSO	3.12	0.17	<0.44	
HAQ 1545−0130	QSO	3.49	0.00	<0.44	
HAQ 1546+0005	QSO	3.61	0.00	<0.77	(BOSS: z=3.61)
HAQ 1600+2911	QSO	2.00	0.41	<0.43	
HAQ 1603+2512	BAL QSO	1.92	0.55	<0.41	
HAQ 1606+2902	BAL QSO	1.82	0.25	<0.44	
HAQ 1606+2903	QSO_CAP	0.43	0.72	<0.45	(BOSS: z=0.43)
HAQ 1607+2611	Unknown	···	···	<0.43	
HAQ 1611+2453	QSO	0.78	0.78	<0.45	
HAQ 1620+2955	QSO	3.36	0.11	<0.43	(BOSS: z=3.36)
HAQ 1626+2517	QSO	1.25	0.30	6.72±0.14	(BOSS: z=1.26)
HAQ 1633+2851	QSO	1.14	0.52	<0.43	
HAQ 1634+2811	QSO	2.60	0.10	<0.39	
HAQ 1639+3157	QSO	0.81	0.79	<0.41	(BOSS: z=0.81)
HAQ 1643+2944	QSO	1.08	0.44	<0.45	
HAQ 1645+3056	BAL QSO	2.50	0.10	<0.41	(BOSS: z=2.53)
HAQ 1645+3130	QSO	0.93	0.69	<0.40	(BOSS: z=0.93)
HAQ 1655+3051	QSO	1.27	0.53	<0.43	
HAQ 2159+0212	QSO	1.26	0.10	<0.37	
HAQ 2203−0052	QSO	1.24	0.74[a]	<0.37	
HAQ 2217+0359	QSO	0.98	0.52	<0.37	
HAQ 2221+0145	QSO	3.43	−0.05	<0.37	(BOSS: z=3.43)
HAQ 2222+0604	BAL QSO	2.45	0.25	<0.46	
HAQ 2225+0527	QSO	2.32	0.29	882.52±0.11	Grism 6, 7
HAQ 2229+0324	QSO	2.64	0.28	<0.40	(BOSS: z=2.66)
HAQ 2231+0509	BAL QSO	1.76	0.35	<0.40	
HAQ 2241+0818	QSO	2.43	0.04	<0.33	
HAQ 2244+0335	QSO	3.37	0.00	<0.37	(BOSS: z=3.36)
HAQ 2245+0457	BAL QSO	2.10	0.12	<0.36	
HAQ 2246+0710	QSO	1.20	0.12	<0.37	
HAQ 2247+0146	BAL QSO	∼2.1	∼0.20	<0.39	Tentative identification
HAQ 2252+0434	QSO	0.35	0.84	5.42±0.08	
HAQ 2253+1141	BAL QSO	2.40	0.17	<0.30	
HAQ 2254+0638[b]	M-dwarf	0.00	0.00	<0.39	Wrong target on slit
HAQ 2300+0914	QSO	1.99	0.29	64.79±0.13	Grism 6

Table 5.2 — *Continued*

Target	Type	$z_{\rm QSO}$	$A(V)$	$F_{1.4\,\rm GHz}$ (mJy)	Notes
HAQ 2301+0832	BAL QSO	1.10	0.03	< 0.31	
HAQ 2303+0238	BAL QSO	2.22	0.11	< 0.37	Grism 6
HAQ 2303+0630	QSO	0.99	0.36	< 0.38	
HAQ 2305+0117	QSO	2.67	0.13	< 0.40	
HAQ 2310+1117	QSO	0.83	0.92	< 0.65	
HAQ 2311+1444	QSO_HIZ	3.31	0.00	< 0.65	(SDSS legacy: z=3.31)
HAQ 2313+0955	QSO	1.06	0.55	< 0.65	
HAQ 2318+0255	QSO	3.50	0.00	< 0.37	
HAQ 2326+0642	QSO	1.25	0.37	< 0.39	
HAQ 2326+1423	BAL QSO	2.54	0.17	< 0.39	
HAQ 2330+1009	BAL QSO	3.11	0.19	18.39 ± 0.17	
HAQ 2333+0113	BAL QSO	3.25	0.05	< 0.44	(BOSS: z=3.28)
HAQ 2333+0619	BAL QSO	2.72	0.13	< 0.53	
HAQ 2335+1407	QSO	0.97	0.54	< 0.53	
HAQ 2337+1343	QSO	3.57	0.00	< 0.53	
HAQ 2339+1232	QSO	1.24	0.19	< 0.44	
HAQ 2340+0121	BAL QSO	2.15	0.15	< 0.44	
HAQ 2343+0615	QSO	2.16	$0.29^{(a)}$	< 0.32	
HAQ 2348+0716	QSO	0.88	0.22	< 0.36	
HAQ 2351+1429	BAL QSO	2.96	0.23	< 0.40	
HAQ 2352+0105	QSO_HIZ	2.14	0.06	< 0.40	(BOSS: z=2.99)
HAQ 2358+0339	BAL QSO	2.09	0.06	< 0.36	
HAQ 2358+0359	BAL QSO	2.89	0.20	< 0.35	
HAQ 2358+0520	QSO	3.47	0.00	< 0.37	
HAQ 2358+1436	QSO	1.05	0.65	< 0.26	

Notes: In cases where SDSS legacy had flagged the object as QSO for follow-up this is indicated by 'QSO_HIZ' or 'QSO_CAP' as object 'Type'. In the 'Notes' column, we list the targets with spectra available in BOSS or SDSS legacy along with their inferred redshift. Other remarks such as complementary observations with different grisms are also listed here.

The classification of broad absorption line (BAL) QSOs does not follow a stringent methodology. For a detailed study and classification of BAL QSOs in our sample, we refer to Saturni et al. (2014), submitted.

$^{(a)}$ Marks systems with intervening dust. We here give the estimated $A(V)_{\rm abs}$ at the absorber redshift assuming the LMC extinction curve.

$^{(b)}$ The spectrum for this target does not correspond to the photometry in SDSS, since a wrong target was accidentally put on the slit. The real SDSS identifier for this spectrum is J225430.23+063833.8.

Robustness and precision of the likelihood ratio test

When determining whether a given QSO spectrum was better fitted by the general model than the null model, we assigned a probability of observing the given increase in likelihood assuming that the null model is true. We rejected the null model when this probability was below $5\,\sigma$. Hence, we might have rejected the null model in cases where this was indeed the true model, and vice versa. In order to quantify how robust our method is, we therefore generate a set of model QSOs with varying amounts of both intrinsic and intervening dust. We then quantify how many absorption systems are recovered using the likelihood ratio test at different signal-to-noise ratios (SNR), and how well the input parameters are estimated by the fit. Each QSO model is described by four parameters: the QSO redshift ($z_{\rm QSO}$), the extinction at the QSO redshift ($A(V)_{\rm QSO}$), the absorber redshift ($z_{\rm abs}$), and the extinction at the absorber redshift ($A(V)_{\rm abs}$). We assume that the dust in the QSO is of SMC type in all cases and generate two sets of models with the dust in the absorber being, respectively, of SMC or LMC type. For each model, we then generate synthetic data sets mimicking the SDSS and UKIDSS photometric bands and the spectral coverage of the NOT observations. We generate 500 models of synthetic data sets for each of the absorber extinction curves (LMC or SMC) and for both high and low signal-to-noise ratios: in total 2000 models. High and low signal-to-noise ratios here refer to $\mathrm{SNR}_{\rm spec} = 15$, $\mathrm{SNR}_{\rm phot} = 20$ and $\mathrm{SNR}_{\rm spec} = 5$, $\mathrm{SNR}_{\rm phot} = 10$, respectively, where $\mathrm{SNR}_{\rm spec}$ refers to the average SNR per pixel in the synthetic spectral data and $\mathrm{SNR}_{\rm phot}$ refers to the SNR of each synthetic photometric band. For the spectral noise model, we further add a noise component mimicking the fringing in the red part of the CCD of the ALFOSC spectrograph. Specifically this is $\sim 20\,\%$ (peak-to-peak fringe level) for wavelengths greater than 8000 Å.

We use the same fitting method as described in Sect. 5.4.1 to fit both the null model and the general model. Hereafter, we apply the same criteria for rejecting the null model as were used in the analysis of our data. That way we quantify how well we were able to identify intervening systems and with what precision the parameters are recovered. For models with LMC extinction in the absorber, we recover 39.8 % of the intervening systems down to $A(V)_{\rm abs} > 0.2$ with high signal-to-noise ratio. While we at low SNR only recover 15.0 % and only with $A(V)_{\rm abs} > 0.4$. For models with SMC type extinction, we recover 18.2 % of the absorbers down to $A(V)_{\rm abs} \gtrsim 0.5$ in the high SNR data and 0.0 % in the low SNR data. The precision on the best-fit parameters for the recovered intervening systems are given in Table 5.4 for each of the extinction curves (LMC or SMC) and for both high and low SNR. Here we show the 16th, 50th, and 84th percentiles of the residuals for the three fit parameters. In Appendix 5.B, we present the details of the recovered intervening systems along with details about the initial parameter distributions and noise models.

In order to estimate the robustness of the likelihood ratio test, we also perform a sanity check of the null hypothesis. For this we generate 2×500 spectra with dust only at the QSO redshift at high and low SNR and fit these with both the null model and the general model. In *all* cases, we reject the general model; in other words, the preferred model is the model with dust only in the QSO itself. The agreement between input and best-fit parameter allows us to quantify the precision in the $A(V)$ estimates using this method of fitting templates to the data. We observe no bias in the estimated parameters and find a statistical uncertainty of ±0.01 on the $A(V)$ estimates for high SNR, while we get ±0.02 at low SNR. These are only statistical uncertainties; the actual error on a single measurement in *real* data may be larger due to the template not being a perfect description for every QSO.

Table 5.3: Dust in Intervening Absorbers

Target	$z_{\rm QSO}$	$z_{\rm abs}$	$A(\rm V)_{\rm abs}$	$A(\rm V)_{\rm QSO}$
HAQ0000+0557	3.31	$2.03\ ^{+0.03}_{-0.03}$	$0.32\ ^{+0.03}_{-0.03}$	$0.04\ ^{+0.01}_{-0.01}$
HAQ0011+0122	1.11	$0.66\ ^{+0.02}_{-0.02}$	$0.39\ ^{+0.04}_{-0.05}$	$0.06\ ^{+0.02}_{-0.02}$
HAQ0031+1328	1.02	$0.79\ ^{+0.01}_{-0.01}$	$0.35\ ^{+0.02}_{-0.02}$	$0.08\ ^{+0.01}_{-0.01}$
HAQ0051+1542	1.90	$1.24\ ^{+0.03}_{-0.03}$	$0.39\ ^{+0.04}_{-0.03}$	$-0.15\ ^{+0.02}_{-0.03}$
HAQ0339+0420	1.80	$1.10\ ^{+0.06}_{-0.07}$	$0.44\ ^{+0.07}_{-0.06}$	$0.01\ ^{+0.03}_{-0.04}$
HAQ1248+2951	3.55	$2.36\ ^{+0.10}_{-0.09}$	$0.20\ ^{+0.02}_{-0.02}$	$-0.03\ ^{+0.01}_{-0.01}$
HAQ1509+1214	2.80	$1.71\ ^{+0.06}_{-0.04}$	$0.45\ ^{+0.13}_{-0.12}$	$-0.15\ ^{+0.05}_{-0.06}$
HAQ2203−0052	1.24	$0.65\ ^{+0.04}_{-0.03}$	$0.73\ ^{+0.07}_{-0.07}$	$-0.11\ ^{+0.02}_{-0.03}$
HAQ2343+0615	2.16	$1.48\ ^{+0.03}_{-0.03}$	$0.29\ ^{+0.04}_{-0.04}$	$-0.05\ ^{+0.03}_{-0.03}$

Notes: The estimates of $A(V)_{\rm abs}$ are calculated assuming the LMC extinction curve by Gordon et al. (2003).

Table 5.4: Precision of recovered parameters from the likelihood ratio test

	High SNR			Low SNR		
	$\Delta A(V)_{\rm QSO}$	$\Delta A(V)_{\rm abs}$	$\Delta z_{\rm abs}$	$\Delta A(V)_{\rm QSO}$	$\Delta A(V)_{\rm abs}$	$\Delta z_{\rm abs}$
LMC	$0.00^{+0.04}_{-0.04}$	$0.01^{+0.08}_{-0.09}$	$0.00^{+0.05}_{-0.03}$	$-0.02^{+0.07}_{-0.07}$	$0.03^{+0.14}_{-0.10}$	$0.00^{+0.06}_{-0.05}$
SMC	$-0.08^{+0.12}_{-0.16}$	$0.09^{+0.24}_{-0.15}$	$0.04^{+0.17}_{-0.18}$	...	...	...

Notes: For each input extinction law, we show the residuals (input – output) of the various model parameters.

Intervening Absorption Systems

Our next step is to go through all of the spectra manually to look for intervening absorption systems such as DLAs or Mg II systems that would provide a host for dust at lower redshift. Due to the limited SNR and low resolution, we are not able to detect weak absorption systems. Also, the limited wavelength coverage means that we might miss absorption systems if the Lyα or Mg II lines fall outside the spectral range for the given absorption system. We identify 27 QSOs with clearly visible absorption systems and three tentative detections (due to low signal-to-noise ratio). The systems are mainly identified by the characteristic Mg II $\lambda\lambda$ 2796, 2803 doublet, one target is identified by the Ca II $\lambda\lambda$ 3934, 3969, and eight systems are identified by Lyα, C IV, or both. The identifications are secured by detections of other absorption lines (such as Fe II lines) at the same redshift. All absorption systems are listed in Table 5.5. Out of the nine QSOs that have preferred solutions with intervening dust in the model comparison, two have Mg II systems at redshifts close to the best-fit absorption redshift, one target has inconsistent redshifts between the absorption system and the best-fit, and one target (HAQ2343+0615) has slight indications of an Mg II absorption system at the best-fit absorber redshift $z_{\rm abs} = 1.49$. However, the quality of the data does not allow a firm detection. In the rest of the cases where the absorber dust model was preferred, we either do not have good enough SNR to securely detect any intervening systems (HAQ2203-0052 and HAQ2343+0615), the Mg II doublet is not covered by the spectral range (HAQ1248+2951 and HAQ1509+1214 where Mg II falls on top of the telluric absorption), or the algo-

rithm picks up spectra that differ significantly from the template. Such cases could be caused by differences in the QSO continuum or variations in the intensity of weak and blended iron emission lines (Pitman, Clayton, & Gordon 2000). Nevertheless, many of these quasars selected by our analysis may still be reddened by foreground absorbers; we are just not able to confirm the existence of the absorbing galaxy with this modelling approach.

The target, HAQ0000+0557, shows a very strong Mg II ($EW_{rest}\,(2796) = 4.5$Å) absorber at $z_{\rm Mg\,II} = 2.048$. This QSO is one of the QSOs for which the general model with dust in an intervening absorber was preferred, see Sect. 5.4.1. The preferred redshift for the absorber from the fitting was $z_{\rm abs} = 2.03 \pm 0.03$, in agreement with the Mg II system. This strongly suggests that the dust reddening (with $A(V)_{\rm abs} = 0.32$) is caused by this Mg II system. Although the spectrum is well fit by the intervening dust model, the IR photometry is matched better by the model with only QSO dust; see the top panel of Fig. 5.4. Further analysis of the extinction curve is needed in order to fit all of the data. However, for this we would need a longer spectroscopic wavelength range observed simultaneously to rule out offsets in the photometry due to intrinsic QSO variability.

The spectrum of HAQ0339+0420 has a Mg II absorption system at a redshift of $z_{\rm Mg\,II} = 1.21$ coinciding with the preferred redshift for an intervening system from the fit at $z_{\rm abs} = 1.10$ with $A(V)_{\rm abs} = 0.44$. Although the best-fit redshift is lower than the redshift for the Mg II absorber, the two are consistent when considering the $3\,\sigma$ confidence interval for the absorber redshift $0.92 < z_{\rm abs} < 1.24$.

The spectrum of HAQ1248+2951 shows a Mg II system at $z_{\rm Mg\,II} = 1.56$, however, the best-fit absorption redshift from the statistical modelling is $z_{\rm abs} = 2.36 \pm 0.10$. At this absorbing redshift, the Mg II absorption lines would fall outside the spectral coverage of our setup. Hence, the system at $z_{\rm Mg\,II} = 1.56$ may simply be an intervening system, which hosts no dust. However, with the current data it is not possible to constrain the dust properties further, since we do not have coverage of the full spectral range. Moreover, the addition of a second absorber in the fit will increase the degeneracy of the fit parameters, which is not possible to break with the data at hand.

The QSO, HAQ1115+0333, was observed with grisms #6 and #7 to provide higher-resolution spectroscopy of the absorber which was identified in the spectrum taken with grism #4. The QSO shows a strong Mg II absorber at $z = 1.18$ and a weaker (Lyα, C IV) system at $z = 2.57$. However, the spectrum of this system is consistent with the dust being at the QSO redshift $z_{\rm QSO} = 3.10$. The rest of the identified absorption systems in Table 5.5 are all either consistent with no dust or with the dust residing in the QSO system only. However, one target (HAQ 2225+0527) is the exception to the rule. This system has a Damped Lyα absorption system at redshift $z_{\rm DLA} = 2.131$. The extinction toward the QSO is quite high ($A(V) = 0.29$), and is consistent with the dust extinction being caused by SMC-type dust in the DLA when taking into account the added constraint on $z_{\rm abs}$. The reason why this system was not identified in our statistical analysis is due to the fact that SMC-type dust is extremely difficult to identify with this approach, since the featureless extinction curve does not provide any redshift-dependent features. Hence, the degeneracy between the various fit parameters is very large. In Sect. 5.4.1, we discussed the limitations of the statistical approach and we found that for SMC-type dust only absorption systems with $A(V)_{\rm abs} \gtrsim 0.5$ are recovered. Given the value of $A(V)$ =0.29 for HAQ2225+0527 we therefore do not expect to detect the intervening reddening with this particular modelling approach.

Table 5.5: Intervening absorption systems

Target	$z_{\rm QSO}$	$z^{(a)}_{\rm spec}$	$z^{(b)}_{\rm abs}$	$A(V)^{(b)}_{\rm abs}$	$A(V)_{\rm QSO}$	Notes
HAQ0000+0557	3.31	2.05	2.03±0.03	0.32±0.03	0.04±0.01	Strong Mg II absorber
HAQ0008+0835	1.19	0.85	···	···	0.00	Mg II absorber
HAQ0008+0846	1.23	1.07	···	···	0.04	Mg II absorber
HAQ0015+0736	3.63	2.47	···	···	−0.05	Strong Mg II absorber with associated Lyα
HAQ0015+1129	0.87	0.81	···	···	0.78	Mg II absorber
HAQ0024+1037	1.22	0.29	···	···	0.27	Ca II absorber
HAQ0044+0817	3.35	2.90	···	···	0.00	Damped Lyα absorber
HAQ0053+0216	0.99	0.90:	···	···	0.71	Mg II absorber, low SNR
HAQ0059+1238	3.50	3.21	···	···	0.00	Lyα and C IV absorber
HAQ0143+1509	3.76	1.24	···	···	0.00	Mg II absorber
HAQ0211+1214	2.11	1.02	···	···	0.05	Mg II absorber
HAQ0337+0539	3.28	1.20	···	···	0.03	Mg II absorber
HAQ0339+0420	1.80	1.21	1.10±0.07	0.44±0.07	0.01±0.03	Mg II absorber
HAQ0340+0408	1.62	1.03:	···	···	0.13	Mg II absorber, low SNR
HAQ0355−0053	2.15	1.24	···	···	0.00	Mg II absorber
HAQ1115+0333	3.10	1.18	···	···	0.15	Mg II absorber
HAQ1115+0333	3.10	2.57	···	···	0.15	Weak Lyα and C IV absorber
HAQ1248+2951	3.55	1.56	2.36±0.10	0.20±0.02	−0.03±0.01	Mg II absorber
HAQ1327+3206	2.48	0.63	···	···	0.01	Mg II absorber
HAQ1355+3407	3.16	1.08	···	···	0.00	Mg II absorber
HAQ1534+0013	3.44	2.86	···	···	0.00	Damped Lyα absorber
HAQ1633+2851	1.14	0.71:	···	···	0.52	Mg II absorber, low SNR
HAQ2159+0212	1.26	1.04	···	···	0.10	Mg II absorber
HAQ2222+0604	2.45	1.29	···	···	0.25	Mg II absorber
HAQ2225+0527	2.32	2.13	···	···	0.29	Damped Lyα absorber
HAQ2231+0509	1.76	1.21	···	···	0.35	Mg II absorber
HAQ2241+0818	2.43	2.32	···	···	0.04	Damped Lyα absorber
HAQ2244+0335	3.37	2.89	···	···	0.00	Damped Lyα absorber
HAQ2303+0238	2.22	1.47	···	···	0.11	Mg II absorber
HAQ2305+0117	2.67	1.49	···	···	0.13	Mg II absorber
HAQ2305+0117	2.67	2.67	···	···	0.13	Damped Lyα absorber at QSO redshift
HAQ2311+1444	3.31	1.67	···	···	0.00	Mg II absorber

$^{(a)}$ $z_{\rm spec}$ here denotes the spectroscopic redshift of the absorption system. Redshifts followed by a colon (:) denote tentative detections due to low SNR.
$^{(b)}$ Redshift and extinction values are only given in cases where the absorber model was preferred in the likelihood ratio test described in Sect. 5.4.1. The values reported here assume LMC-type dust in the absorber.

Spectral Energy Distributions

We investigate the average behaviour of the QSOs in our sample by stacking their rest-frame, dust-corrected energy distributions. We correct for dust assuming the best-fit reddening obtained as described above. Hereafter, we linearly interpolated all the rest-frame SEDs onto a common wavelength grid. We then normalize each SED at rest-frame wavelength 5100 Å. The average SED is computed using the median as well as the 50 and 90 % confidence intervals. The confidence intervals only take into account the variance in the sample because this, along with the interpolation, is the dominant source of uncertainty. For reference, the typical uncertainty on the photometric measurements is of the order of 5 %. In Fig. 5.5, we show the median SED and its confidence intervals. We show the continuum model from Richards et al. (2006) for comparison. In the top panel of the figure, we show the number of individual SEDs that contribute to a given wavelength bin.

In the blue part of the SED, for $\lambda < 1500\,\text{Å}$, we observe the largest discrepancy between our data and the template. This is, however, expected due to the low number of sources contributing to the stack in this range and due to the fact that we have not corrected for BAL QSOs in our sample, which significantly redden the overall SED blue-wards of C IV. Apart from this discrepancy at short wavelengths, the sample is very homogenous for wavelengths less than rest-frame 1 μm. At longer wavelengths, the sample exhibits a higher degree of variance. We therefore study the properties of the deviant SEDs at rest-frame 2 μm, since at this wavelength the number of objects contributing to the stack is still high ($> 80\,\%$). Above 3μm the large variance is dominated by the fact that only a small number of objects contribute to the stack. We classify outliers as SEDs whose flux in the rest-frame 2 μm data point differs by more than 5 σ from the template at the given wavelength.

In total, we find 27 QSOs that differ more than 5 σ from the template at rest-frame 2 μm, 11 of which have an apparent excess compared to the template, and 16 have a deficit compared to the template. We included one additional target (HAQ1639+3157) that was not selected by this criterion because the large error on the WISE band 1 in this case falsely enhanced the uncertainty in the interpolated flux at rest-frame 2 μm. The QSOs with rest-frame infrared excess are shown in Fig. 5.6 and 5.7. We construct a simple model in which the excess emission is caused by re-emission from hot dust. We approximate the emission by a black-body emission with a single temperature, T_{dust}. By adding this component to the reddened template (here from Richards et al. 2006) and fitting the reddened template plus dust emission to the H and K bands along with the four WISE bands, we are able to get a very good agreement in most cases with dust-temperatures in the range of 800 K$< T_{\text{dust}} <$1600 K. The best-fit dust emission model is shown in Figs. 5.6 and 5.7 together with the best-fit template without extra dust emission.

The QSOs with rest-frame infrared deficit are summarized in Fig. 5.8. These QSOs (except three: HAQ0011+0122, HAQ1233+1304, and HAQ1527+0250; see Sect. 5.5.2) all have rest-frame infrared SEDs consistent with no or very little reddening; however, from our fits to the rest-frame UV and optical data, we infer a significant amount of reddening. This seems to indicate a problem with the assumed extinction law. In order to test this, we re-fit the overall SED while changing the slope of the extinction law. We do this in terms of the parameter, $R_V \equiv A(V)/E(B-V)$, where $E(B-V) = A(B) - A(V)$. A large value of R_V thus gives rise to a flat extinction curve, whereas small values indicate steeper extinction curves; for comparison, the SMC extinction curve from Gordon et al. (2003a) has $R_V = 2.74$. Only for two QSOs (HAQ1106+0300, HAQ0206+0624) did the fit converge, in these cases yielding $R_V = 0.8 \pm 0.2$ and $R_V = 0.6 \pm 0.2$. The other fits failed to converge or failed to reproduce the IR fluxes, however, this does not rule out the fact that the extinction law may differ from the assumed SMC law. Instead, this reflects that simply varying R_V is not enough to get the shape of the extinction curve to match the data. A detailed analysis of these extinction curves for a subset of our sample is currently underway (Zafar et al. 2015, submitted). All the individual SEDs are shown in Appendix B.

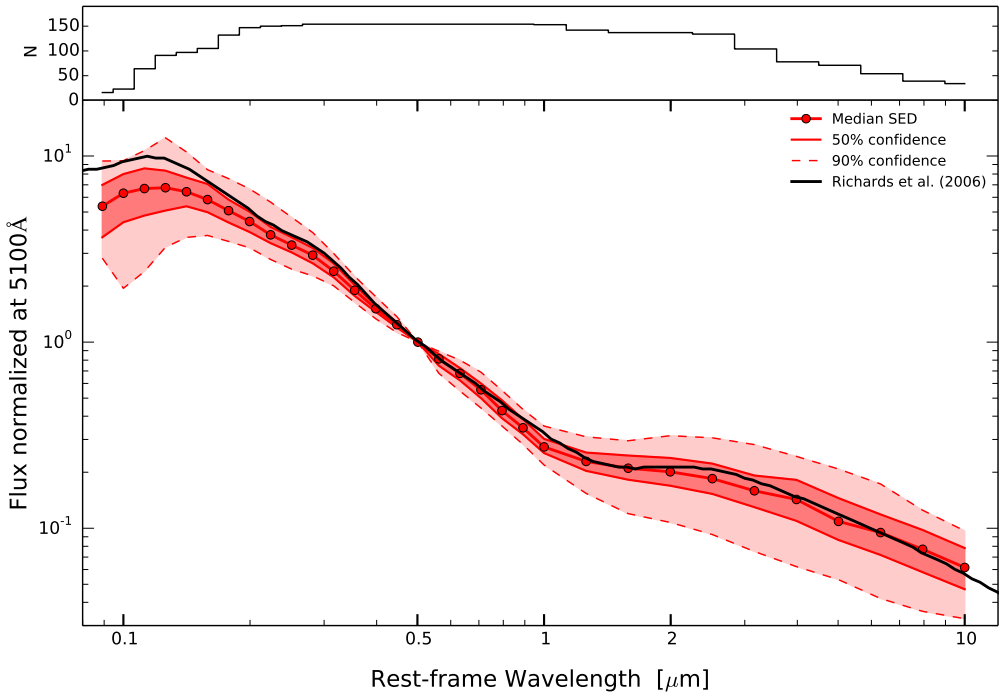

Figure 5.5: Median rest-frame stacked spectral energy distribution (SED) for all QSOs in our sample (red points). The individual SEDs have been scaled at 5100 Å before stacking. The dark and light red shaded areas show the 50 and 90% confidence intervals, respectively. The overplotted black line shows the continuum template of Richards et al. (2006). The top panel shows the number of individual SEDs that contribute to a given wavelength bin.

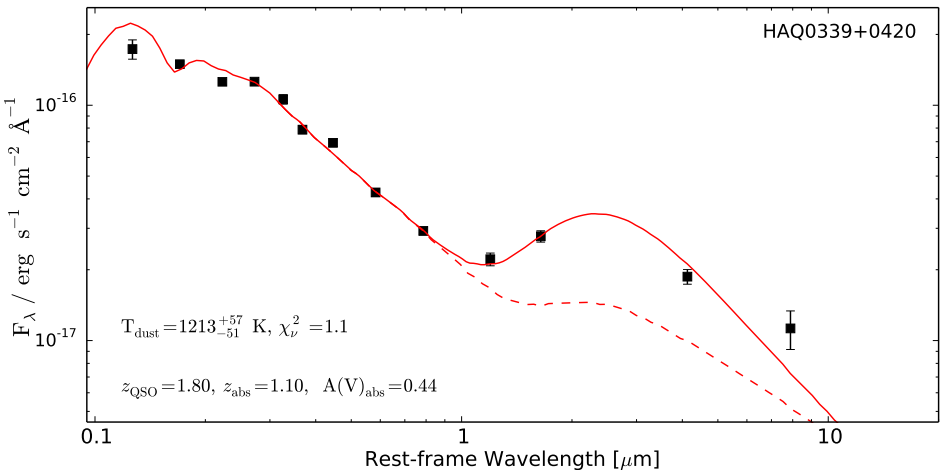

Figure 5.6: A QSO with rest-frame infrared excess at 2 μm (black points). The dashed line shows the best-fit template from fits to the spectra and SDSS and UKIDSS photometry as described in Sect. 5.4.1. The solid line shows the same template with an extra dust component fitted to the H, K and WISE bands. In the bottom left corner, we give the best-fit dust temperature, $T_{\rm dust}$ and the reduced χ^2 from the dust component fit. This particular QSO was identified as a system with intervening absorption (see Section 5.4.1), and we therefore indicate the QSO redshift, the inferred absorption redshift, and the best-fit extinction at the absorption redshift. We emphasize that the reddening law in the absorber's rest-frame is assumed to be of LMC type.

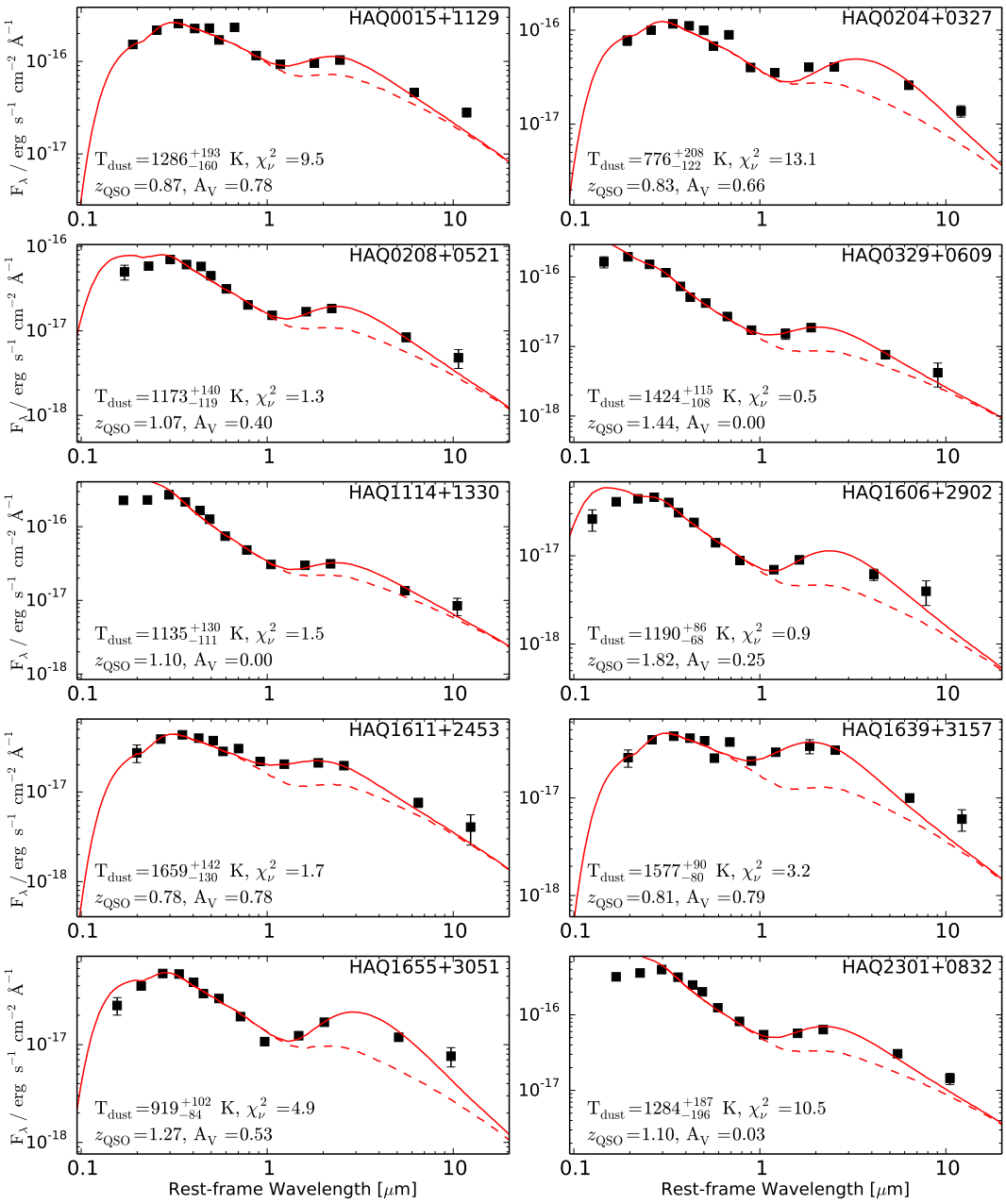

Figure 5.7: Individual QSOs with rest-frame infrared excess at 2 μm (black points). The dashed line shows the best-fit template from fits to the spectra and SDSS and UKIDSS photometry as described in Sect. 5.4.1. The solid line shows the same template with an extra dust component fitted to the H, K, and WISE bands. In each panel, we give the best-fit dust temperature, $T_{\rm dust}$, the QSO redshift, the inferred extinction at the QSO redshift, and the reduced χ^2 from the dust component fit.

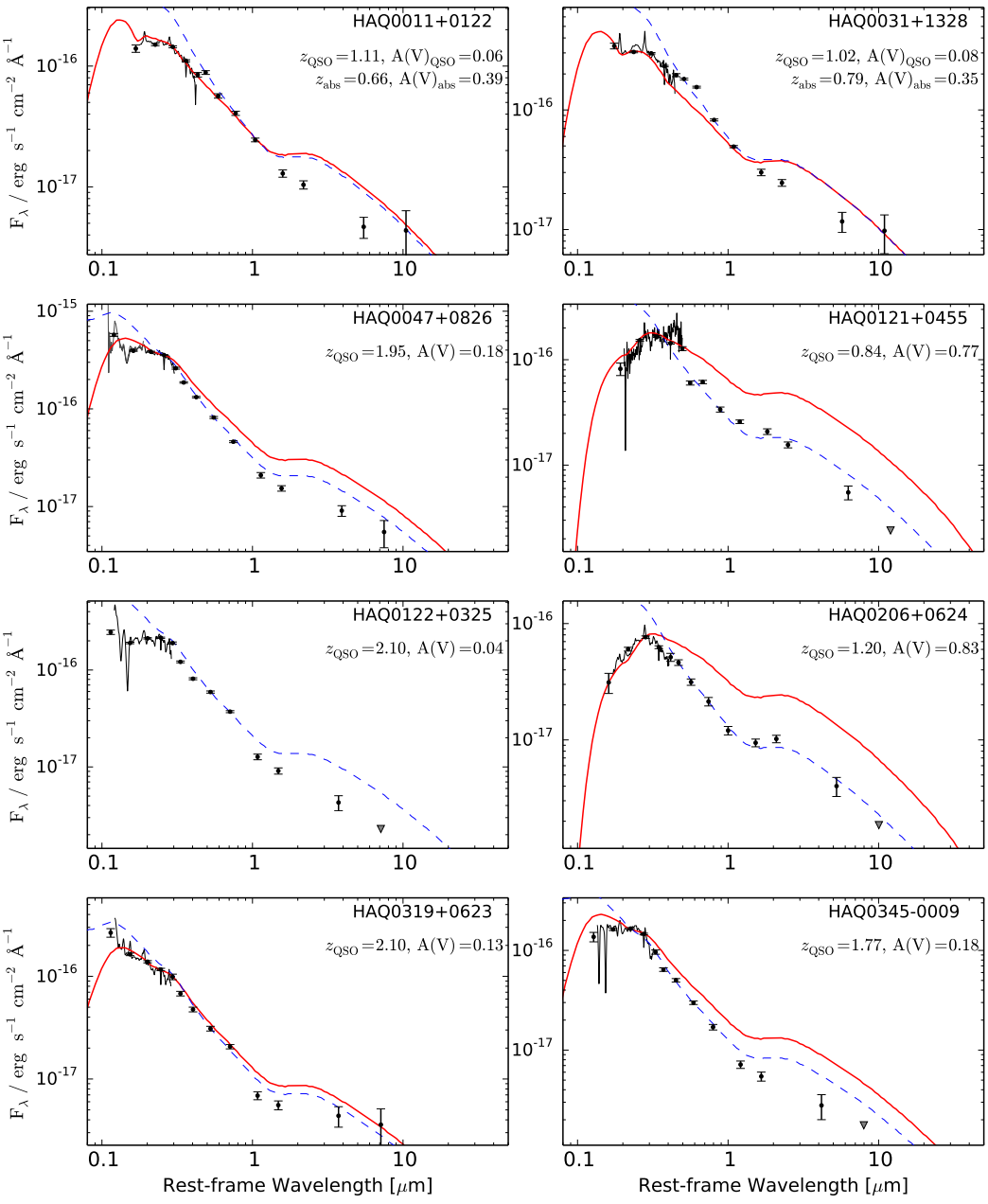

Figure 5.8: Individual QSOs with rest-frame infrared deficit at 2 μm (black points). In each panel, the dashed, blue line shows the unreddened template from Richards et al. (2006). The red, solid line shows the same template reddened by the amount given in each panel. In two cases the reddening is very low (consistent with zero), therefore only the dashed line is shown.
(Continued on next page.)

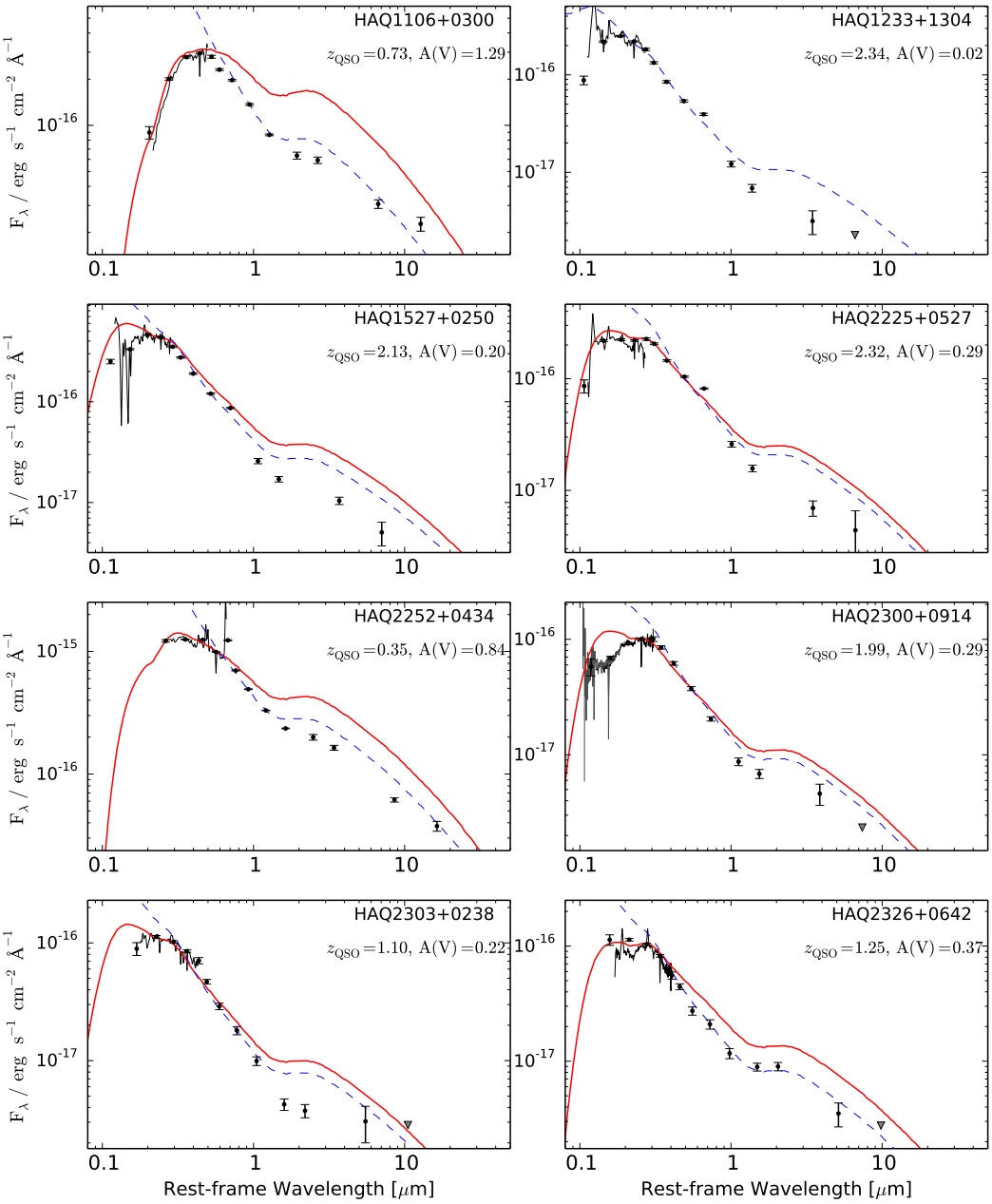

Figure 5.8: *Continued.*

Radio Properties

We have matched our catalog to the VLA FIRST Survey (Becker, White, & Helfand 1995b) to check for radio detections in our sample. Although our selection has not been based on radio detections, we have compiled data from the VLA/FIRST survey to compare the radio properties in our sample with other studies, e.g., Glikman et al. (2012, 2013). The survey provides measurements at 1.4 GHz ($\lambda = 20$ cm) with a typical rms level of 0.15 mJy. A search through the survey's publicly available database[6] reveals that 18 (out of 159) sources have radio detections at 1.4 GHz within a search radius of 10 arcsec. Thirteen targets in our sample lie outside the FIRST survey area. The radio fluxes (or 3 σ upper limits for non-detections) are given in Table 5.2. We characterize the radio properties in terms of *radio loudness*. The term radio loudness has been defined in various ways, e.g., using the rest-frame radio luminosity or the ratio of radio-to-optical flux. We have chosen to use the ratio of radio-to-optical flux since this is independent of redshift and cosmological assumptions. We use the definition of the radio-to-optical ratio, R_m from Ivezić et al. (2002) to quantify the radio-loudness of QSOs.
The authors define R_m as the ratio of the radio flux to the optical flux:

$$R_m = \log\left(\frac{F_{\rm radio}}{F_{\rm optical}}\right) = 0.4\,(m-t)\ ,$$

where m refers to the AB magnitude in any of the SDSS bands and t is the *"radio AB magnitude"* at 1.4 GHz: $t = -2.5\,\log\left(\frac{F_{\rm int}}{3631{\rm Jy}}\right)$. Following this definition, a radio-loud source will have $R_m > 1$. For our analysis we use the i band of SDSS in order to compare with the work of Ivezić et al. (2002); switching to the g or r band does not change the inferred radio-loud fraction. In Fig. 5.9, we show the dust-corrected radio-to-optical ratio, R_{i_0}, for the detected sources in our sample using the $A(V)$ inferred from the combined fit to spectroscopy and photometry to de-redden the i-band magnitude. We also show the non-detected sources as conservative 5 σ upper limits. As seen in Fig. 5.9, all non-detections except for four are consistent with being radio-quiet. Hence, we are able to put very firm constraints on the fraction of radio-loud QSOs. If we assume that *all* non-detections are radio-quiet (consistent at the 3σ level), then we find a radio-loud fraction ranging from 9–12%, including the uncertainty of the dust-correction.

Ivezić et al. (2002) and Baloković et al. (2012) find a radio-loud fraction of $8 \pm 1\%$ and $10 \pm 1\%$, respectively, for QSOs with $i < 18.5$. For the same i-band magnitude limit, we find a radio-loud fraction of 12–14%. This is slightly higher but consistent with the previous results. A higher fraction of radio-loud QSOs would be expected when targeting red QSOs as the radio flux has been shown to correlate with optical $(g-r)$ colour (White et al. 2007). We further note that due to the colour selection of our sample, the estimate of radio-loud fraction is not representative of the overall QSO population.

[6] `http://sundog.stsci.edu/index.html`

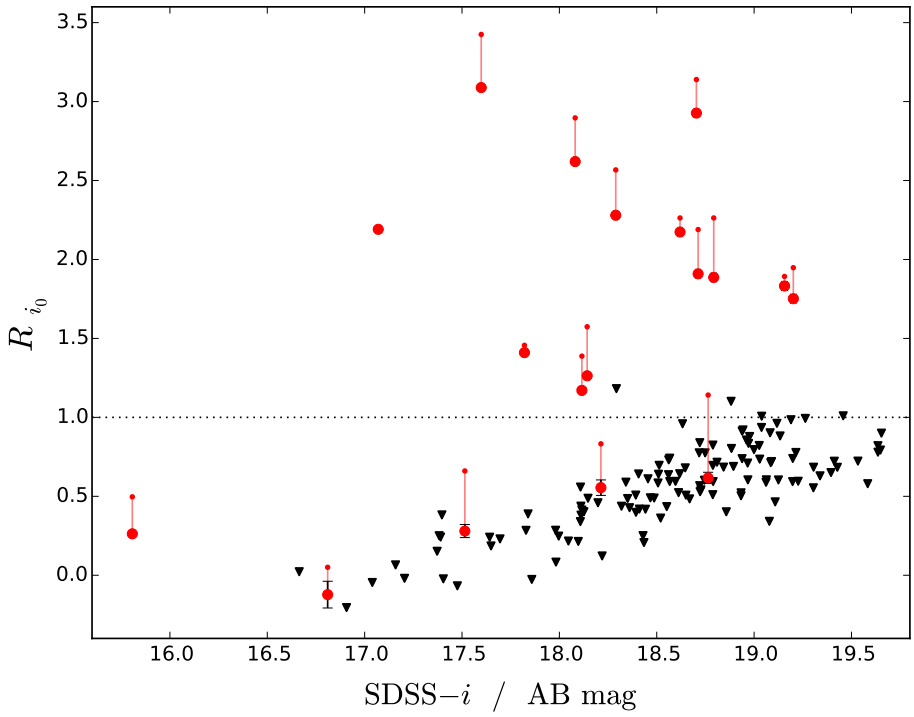

Figure 5.9: Dust corrected radio-to-optical index, R_{i_0}, as function of observed i band magnitude are shown as red circles with error bars. The small red dots connected by thin lines to each data point mark the values of R_i before correcting for dust. The dotted horizontal line marks the proposed boundary between radio loud ($R > 1$) and radio quiet ($R < 1$). Non-detections from our sample are shown as 5 σ upper limits (black triangles).

5.4.2 Contaminants

Two objects in our sample are identified as stars (marked in Table 5.2): one M-dwarf and one G-dwarf. Their spectra are plotted together with stellar templates from SDSS[7] in Appendix 5.D. The G-dwarf template has been reddened ($A(V) = 0.6$) to match the observed spectrum by assuming MW type dust from Gordon et al. (2003a).

We find two objects (HAQ1607+2611 and HAQ2247+0146) that are not securely identified. The object HAQ1607+2611 is probably a QSO with very weak emission lines, whereas HAQ2247+0146 is most likely a special subclass of BAL QSOs (so-called FeLoBALs) with very strong and broad absorption on the blue side of Mg II. However, the spectra do not provide enough clues to firmly secure the identification and redshift.

5.5 Discussion

Our primary goal was to search for intervening absorption systems hosting metals and dust, which would go undetected in optically selected samples of QSOs (e.g., SDSS-I/II). We found 30 such absorption systems, however, with varying amounts of dust. Moreover, we found interesting dust features most likely caused by dust within the QSO system. In the following, we take a closer look at the intervening systems in our sample and at the dust properties in the environment of the QSOs.

[7] `http://www.sdss.org/dr5/algorithms/spectemplates`

5.5.1 Dust in Intervening Absorbers

In order to check whether any of the QSOs showed signs of intervening absorption, we analysed all the spectra with an automated likelihood algorithm. In Sect. 5.4.1, we found nine cases where the code returned a preferred intervening dusty system. These are listed in Table 5.3. For all nine systems, we found that the extinction was caused by dust in the absorber only; the extinction at the QSO redshift was consistent with no reddening. All the other systems in our sample were fully consistent with either no reddening or dust at the QSO redshift, but note that our method is mainly sensitive to intervening absorbers with extinction curves displaying the 2175 Å extinction feature (see below).

Most statistical studies of absorption systems (Mg II or DLAs) find that the average reddening, though small, is consistent with SMC-type extinction (York et al. 2006; Vladilo, Prochaska, & Wolfe 2008; Khare et al. 2012). However, indications of the 2175 Å bump, typical in Milky Way and LMC sightlines, are observed in some cases both statistically using stacking (Malhotra 1997) and in individual absorbers (Junkkarinen et al. 2004; Wang et al. 2004; Ellison et al. 2006; Srianand et al. 2008a; Elíasdóttir et al. 2009; Noterdaeme et al. 2009a; Jiang et al. 2010; Zhou et al. 2010; Wang et al. 2012; Zafar et al. 2012). Interestingly, we found *no* systems with preferred SMC extinction in an intervening system from our algorithm although the overall population seems to indicate SMC-type dust. This is, however, to be expected when taking into account the limitations of the method we utilized. In Sect. 5.4.1, we found that absorbers needed to cause very high extinction ($A(V) \gtrsim 0.5$) with the SMC law in order to be detected, even at high SNR. This is due to the high degeneracy between dust at the absorber redshift and intrinsic dust in the QSO because the SMC extinction curve is mostly featureless. Our simulations showed that we were much more sensitive to LMC-type extinction due to the very characteristic 2175 Å bump which provided a rather unique imprint in the spectra. This allowed for a much more secure determination of the redshift of the absorber if this feature was available in the spectrum. Still, we are limited to absorbers with extinction higher than $A(V) > 0.2$ at high SNR (an average SNR per spectral pixel of 15).

Since these estimates were purely based on statistical modelling, the results could be improved if an absorption system at a corresponding redshift could be identified. This would then serve as an anchor for $z_{\rm abs}$, which allows us to measure the extinction curve in the absorber with greater precision. For the nine cases reported here, two of them had a detection of a Mg II absorption system close to the best-fit redshift and one sightline showed a tentative detection. This indicates that the dust model was indeed detecting physical features and not just artefacts in the spectra. Furthermore, one DLA was found to be a plausible host of SMC-type dust causing reddening of the background QSO when restricting the dust absorber redshift. This system, which will be discussed in more detail in a future work, is the kind of system we originally looked for with this survey.

Our results suggest that previous studies of dust extinction caused by intervening absorbers might have been biased against LMC-type dust. This is plausibly caused by two effects. On one hand, for absorbers causing low amounts of extinction (as is usually the case for intervening absorbers found to date) the 2175 Å feature characteristic of the LMC and MW extinction curves may be very weak. This will generally lead an observer to classify the extinction as SMC-type, as the 2175 Å bump disappears in the noise (see discussion in Khare et al. 2012). On the other hand, for dust-rich absorbers causing high amounts of extinction, where a distinction between various extinction curves is more easily done, the reddening of the background QSO may cause the QSO to drop out of the optical colour selection utilized

in previous samples. It has indeed been shown that such highly reddened QSOs are underrepresented in previous samples of QSOs from optical colour selection (Fynbo et al. 2013a; Glikman et al. 2012, 2013). However, with the advance in near- and far-infrared photometric surveys and various new QSO classification algorithms populations of highly reddened QSOs will be identified in larger numbers (Maddox et al. 2012; Graham et al. 2014).

5.5.2 Dust in the QSOs

For our entire sample, we find a median attenuation of $A(V)$ = 0.13, corresponding to a median $E(B-V)$ of 0.047, assuming the value of $R_V = 2.74$ from Gordon et al. (2003a). The individual dust-corrected SEDs show a very homogeneous behaviour at wavelengths $\lambda < 1\mu$m. However, at larger wavelengths we see some variance. We find that the QSOs with excess IR flux can be explained well by a simple single-temperature blackbody dust component. The dust temperatures inferred in these cases lie in the range from $800 \lesssim T_{\rm dust} \lesssim 1600$ K with typical uncertainties of $100 - 200$ K. This is in good agreement with dust temperatures found in active galactic nuclei (Sanders et al. 1989; Rodríguez-Ardila & Mazzalay 2006). In the cases of very bad fits (e.g., HAQ0204+0327), the discrepancy might be explained by adding a host galaxy component or a model with multiple dust temperatures. However, such modelling is beyond the scope of this discussion and is not possible due to the few data points currently available in this wavelength range.

As mentioned in Sect. 5.4, we find 16 cases where the flux at rest-frame 2 μm is significantly lower than what is predicted by the template. There may be more such QSOs, but we chose a conservative cut at 5σ to limit the influence of template variance. In these cases, the mismatch seems to hint at a problem with the assumed extinction law, since the unreddened template in all but two cases provide a good fit in the rest-frame infrared and optical, while a large amount of reddening is required to fit the rest-frame ultraviolet data. Although uncommon, similarly steep extinction curves have been observed in previous works (Welty & Fowler 1992; Larson, Whittet, & Hough 1996; Hall et al. 2002; Fynbo et al. 2013a, 2014; Jiang et al. 2013; Leighly et al. 2014, e.g.,). For the two targets where this is not the case (HAQ0011+0122 and HAQ1233+1304), the lack in flux may be explained by intrinsic differences in the QSO energy distribution relative to the template. A lack of dust emission compared to the template would explain the lower rest-frame IR fluxes in these cases. This was also noted by Richards et al. (2006). Internal variations in the dust emission (both deficit and excess) may be linked to physical properties in the obscuring material, such as temperature, geometry, and viewing effects (inclination).

In targets where we see indications of non-SMC-type dust, we need an extinction curve that is *steeper* or with different curvature than SMC in order to explain the strong UV reddening and little or no reddening in the infrared. In Sect. 5.4.1, we modelled this behaviour of the extinction law by varying the value of R_V. This analysis only converged to meaningful values (non-negative values for $A(V)$ and R_V) for two QSO, which resulted in best-fit values of $R_V = 0.8 \pm 0.2$ and $R_V = 0.6 \pm 0.2$. This indeed hints at the need for a very steep extinction curve, but this should only be taken as a preliminary analysis. In Paper I, we reported similar indications of extinction curve mismatches. Furthermore, many of these targets exhibit extremely weak emission lines, indicating that the central region, which is emitting these lines, may be somewhat obscured. These QSOs are similar to the peculiar red QSOs discussed by Hall et al. (2002), Meusinger et al. (2012) and Jiang et al. (2013). The QSOs found by Hall et al. (2002) show similar characteristics, i.e., missing strong emission lines and a continuum mismatch at wavelengths shorter than $\lambda < 3000$ Å. Many plausible explanations for such a continuum shape are

discussed by these authors, however, they conclude that a steeper extinction curve (steeper than SMC or with different shape, e.g., a break) is the most likely explanation given the apparent lack of BAL features. Similar conclusions are reached by Meusinger et al. (2012).

In contrast to the QSOs in the studies of Meusinger et al. (2012) and Hall et al. (2002) four of the peculiar QSOs in this work show BAL features, two of which (HAQ0122+0325 and HAQ1233+1304) show very little apparent reddening, consistent with $A(V) = 0$. The remaining BAL QSOs (HAQ0047+0826, HAQ0345-0009, and HAQ1527+0250), which show signs of non-SMC-type dust, have very weak emission lines and their SEDs at $\lambda > 3000$ Å are well represented by the unreddened QSO template. Further work on larger samples over a larger wavelength range is needed to shed light on the nature of these peculiar targets and to investigate the actual shape of the extinction curve needed to explain the SEDs of these QSOs. Similar steep extinction curves have been observed toward the Milky Way centre (Nishiyama et al. 2008, 2009; Sumi 2004). It is thus not clear whether the detections toward these reddened QSOs are caused by the central engine in the QSOs or simply by the fact that we observe the central parts of the host galaxy. Leighly et al. (2014) argue that by modelling the dust around the QSO with a spherical geometry and dust grain properties similar to those of the LMC or the Milky Way, they can reproduce the steep extinction curve in the rest-frame UV observed in Mrk 231. In this case, the dust in the central region is provided by a central star-burst. The scattering and absorption properties of the dust in a spherical distribution then gives rise to multiple scatterings, which causes the UV photons to suffer from higher extinction than the redder wavelengths. In contrast to the results of Leighly et al., Jiang et al. (2013) use a different grain size distribution to reproduce a similarly steep extinction curve toward a high-redshift QSO. In the work of Jiang et al. (2013), the steep extinction curve is caused by a lack of larger grains, i.e., their grain size distribution is truncated at a maximum size of 70 nm. The authors invoke dust destruction in the QSO environment as a plausible mechanism, or differences in dust production and growth in QSO outflows (as argued by Elvis, Marengo, & Karovska 2002). This lack of large grains causes extinction in the UV to be relatively higher than in the optical and near-infrared. The question about the origin of the steep extinction curve is thus still open for debate. Furthermore, as is noted by Leighly et al., it is curious why this anomalous type of extinction is only observed toward a few reddened QSOs and not seen in the overall population of reddened QSOs.

5.6 Conclusions

In this paper, we present a clean selection method that only relies on optical and near-infrared photometry down to a flux limit of $J_{\rm AB} < 19$, i.e., we do not require detections from radio or X-ray surveys. The method is a modification of the criteria applied in Paper I rejecting the small contamination of cool stars and evolved galaxies found in Paper I. The refined method allows us to effectively select reddened QSOs regardless of their X-ray and radio properties over a large area of the sky. In our sample of 159 objects, only 2 turn out not to be QSOs and 2 remain unidentified. Our primary goal with this selection was not to compile a complete sample of red QSOs, but instead we designed the criteria to provide a high purity to investigate any hidden population of absorption systems toward heavily reddened QSOs. We used a statistical algorithm to identify whether the SEDs were better represented by dust in the QSO or in an intervening system. This way we identified nine QSOs where dust in an intervening system was preferred. All of these were identified as having LMC-type dust showing signs of the 2175 Å feature. Two (tentatively three) of these systems have Mg II absorption at a corresponding redshift to the best-fit

redshift indicating that the statistical modelling was capable of correctly identifying dust in absorption systems. Moreover, we discovered a DLA toward a highly reddened QSO. Although this system was not selected in our likelihood ratio test, the data are consistent with the dust reddening being caused by SMC-type dust in the DLA. This system will be studied in more detail in a forthcoming paper.

Complementary to our primary search for dusty intervening systems, our selection serendipitously discovered QSOs with a wide range of dust properties. More work on expanding the sample and quantifying the physical dust properties toward these obscured QSOs is currently underway. A complete list of all the candidate QSOs in our survey is given in Table 5.7 in Appendix 5.E.

Acknowledgements

The authors thank the anonymous referee whose constructive feedback improved the quality of this work. The authors thank the many students who dedicated their time to observing QSOs during the summer schools at the NOT in the years 2012, 2013, and 2014. JK acknowledges support from a studentship at the European Southern Observatory in Chile. JPUF acknowledges support from the ERC-StG grant EGGS-278202. The Dark Cosmology Centre is funded by the DNRF. BPV acknowledges funding through the ERC grant 'Cosmic Dawn'. Based on observations made with the NOT, operated on the island of La Palma jointly by Denmark, Finland, Iceland, Norway, and Sweden, in the Spanish Observatorio del Roque de los Muchachos of the Instituto de Astrofísica de Canarias. Funding for the SDSS and SDSS-II has been provided by the Alfred P. Sloan Foundation, the Participating Institutions, the National Science Foundation, the U.S. Department of Energy, the National Aeronautics and Space Administration, the Japanese Monbukagakusho, the Max Planck Society, and the Higher Education Funding Council for England. The SDSS Web Site is http://www.sdss.org/. The SDSS is managed by the Astrophysical Research Consortium for the Participating Institutions. The Participating Institutions are the American Museum of Natural History, Astrophysical Institute Potsdam, University of Basel, University of Cambridge, Case Western Reserve University, University of Chicago, Drexel University, Fermilab, the Institute for Advanced Study, the Japan Participation Group, Johns Hopkins University, the Joint Institute for Nuclear Astrophysics, the Kavli Institute for Particle Astrophysics and Cosmology, the Korean Scientist Group, the Chinese Academy of Sciences (LAMOST), Los Alamos National Laboratory, the Max-Planck-Institute for Astronomy (MPIA), the Max-Planck-Institute for Astrophysics (MPA), New Mexico State University, Ohio State University, University of Pittsburgh, University of Portsmouth, Princeton University, the United States Naval Observatory, and the University of Washington. We acknowledge the use of UKIDSS data. The United Kingdom Infrared Telescope is operated by the Joint Astronomy Centre on behalf of the Science and Technology Facilities Council of the U.K. This publication makes use of data products from WISE , which is a joint project of the University of California, Los Angeles, and the Jet Propulsion Laboratory/California Institute of Technology, funded by the National Aeronautics and Space Administration.

5.A Uncertainty Estimates

In order to estimate the confidence intervals of the best-fit parameters, we used a Markov chain Monte Carlo method. The simulations were performed using the `emcee` package for Python (Foreman-Mackey et al. 2013). We used flat priors on all parameters and ran 100 walkers for 700 iterations of which the first 100 were discarded as the "burn in" phase. In Table 5.6, we give the 68 and 99.7% confidence intervals of the parameter distributions.

Table 5.6: Dust Model Comparison

Null Model				
Target	$z_{\rm QSO}$	$A(V)$	χ^2_0	$P_{\rm KS,\,0}$
HAQ0000+0557	3.31	0.13 ± 0.01	380.1	0.002
HAQ0011+0122	1.11	0.27 ± 0.01	345.6	0.135
HAQ0031+1328	1.02	0.28 ± 0.01	692.0	0.001
HAQ0051+1542	1.90	0.13 ± 0.01	362.4	0.002
HAQ0339+0420	1.80	0.23 ± 0.01	167.1	0.797
HAQ1248+2951	3.55	0.01 ± 0.01	298.9	0.148
HAQ1509+1214	2.80	0.09 ± 0.01	182.6	0.016
HAQ2203−0052	1.24	0.13 ± 0.01	391.6	0.545
HAQ2343+0615	2.16	0.17 ± 0.01	193.2	0.203

General Model						
Target	$z_{\rm abs}$	$A(V)_{\rm abs}$	$A(V)_{\rm QSO}$	$\chi^2_{\rm G}$	$P_{\rm KS,\,G}$	p
HAQ0000+0557	$2.03^{+0.03}_{-0.03}(1\,\sigma)^{+0.08}_{-0.08}(3\,\sigma)$	$0.32^{+0.03}_{-0.03}(1\,\sigma)^{+0.11}_{-0.09}(3\,\sigma)$	$0.04^{+0.01}_{-0.01}(1\,\sigma)^{+0.04}_{-0.04}(3\,\sigma)$	257.2	0.914	2.1×10^{-27}
HAQ0011+0122	$0.66^{+0.02}_{-0.02}(1\,\sigma)^{+0.05}_{-0.05}(3\,\sigma)$	$0.39^{+0.04}_{-0.05}(1\,\sigma)^{+0.14}_{-0.13}(3\,\sigma)$	$0.06^{+0.02}_{-0.02}(1\,\sigma)^{+0.07}_{-0.07}(3\,\sigma)$	250.0	0.347	1.7×10^{-21}
HAQ0031+1328	$0.79^{+0.01}_{-0.01}(1\,\sigma)^{+0.03}_{-0.04}(3\,\sigma)$	$0.35^{+0.02}_{-0.02}(1\,\sigma)^{+0.07}_{-0.07}(3\,\sigma)$	$0.08^{+0.01}_{-0.01}(1\,\sigma)^{+0.04}_{-0.04}(3\,\sigma)$	472.4	0.803	2.1×10^{-48}
HAQ0051+1542	$1.24^{+0.03}_{-0.03}(1\,\sigma)^{+0.10}_{-0.08}(3\,\sigma)$	$0.39^{+0.04}_{-0.03}(1\,\sigma)^{+0.11}_{-0.09}(3\,\sigma)$	$-0.15^{+0.02}_{-0.03}(1\,\sigma)^{+0.07}_{-0.08}(3\,\sigma)$	211.8	0.750	2.0×10^{-33}
HAQ0339+0420	$1.10^{+0.06}_{-0.07}(1\,\sigma)^{+0.14}_{-0.18}(3\,\sigma)$	$0.44^{+0.07}_{-0.06}(1\,\sigma)^{+0.22}_{-0.17}(3\,\sigma)$	$0.01^{+0.03}_{-0.04}(1\,\sigma)^{+0.09}_{-0.13}(3\,\sigma)$	112.9	0.625	1.7×10^{-12}
HAQ1248+2951	$2.36^{+0.10}_{-0.09}(1\,\sigma)^{+0.26}_{-0.21}(3\,\sigma)$	$0.20^{+0.02}_{-0.02}(1\,\sigma)^{+0.10}_{-0.06}(3\,\sigma)$	$-0.03^{+0.01}_{-0.01}(1\,\sigma)^{+0.02}_{-0.04}(3\,\sigma)$	184.8	0.806	1.7×10^{-25}
HAQ1509+1214	$1.71^{+0.06}_{-0.04}(1\,\sigma)^{+0.27}_{-0.11}(3\,\sigma)$	$0.45^{+0.13}_{-0.12}(1\,\sigma)^{+0.36}_{-0.28}(3\,\sigma)$	$-0.15^{+0.05}_{-0.06}(1\,\sigma)^{+0.12}_{-0.16}(3\,\sigma)$	127.0	0.381	8.4×10^{-13}
HAQ2203−0052	$0.65^{+0.04}_{-0.03}(1\,\sigma)^{+0.09}_{-0.08}(3\,\sigma)$	$0.73^{+0.07}_{-0.07}(1\,\sigma)^{+0.20}_{-0.22}(3\,\sigma)$	$-0.11^{+0.02}_{-0.03}(1\,\sigma)^{+0.08}_{-0.08}(3\,\sigma)$	297.0	0.257	2.9×10^{-21}
HAQ2343+0615	$1.48^{+0.03}_{-0.03}(1\,\sigma)^{+0.08}_{-0.11}(3\,\sigma)$	$0.29^{+0.04}_{-0.04}(1\,\sigma)^{+0.13}_{-0.12}(3\,\sigma)$	$-0.05^{+0.03}_{-0.03}(1\,\sigma)^{+0.09}_{-0.10}(3\,\sigma)$	144.2	0.404	2.3×10^{-11}

Notes: Model parameters for the null model (top) and the general model (bottom) for the QSOs where the null model was rejected. $P_{\rm KS}$ refers to the p value from the KS test of the normalized residuals, and p refers to the chance probability of the observed improvement in χ^2 given the two extra free parameters in the general model.

5.B Robustness of the Likelihood Ratio Test

In order to test the robustness of the likelihood method, we generate a set of mock QSO data sets and analyse them with our algorithm the same way as we analysed our data. Below, we summarize the details of how the data sets were generated. The initial parameters were drawn randomly, following a uniform distribution, within the following limits. For the QSO redshift we use: $1 < z_{\rm QSO} < 3.5$; for the extinction at the QSO redshift we constrain the $A(V)$ to be $A(V)_{\rm QSO} > -0.1$. The selection of candidates in terms of $g-r$ colour implies that the extinction in the QSO's rest-frame will be redshift dependent. Assuming the SMC extinction law in the QSO's rest-frame, this means that less reddening is needed at higher redshifts in order to match the $g-r$ colour criterion ($0.5 < g-r < 1$). We mimic this selection effect by invoking the following limit on the modelled extinction at the QSO redshift: $A(V)_{\rm QSO} < 1.5 - 0.37 \times z_{\rm QSO}$. For the extinction at the absorber redshift we use $0 < A(V)_{\rm abs} < 1.0$; and for the absorber redshift we use $0.1 < z_{\rm abs} < 0.9 \times z_{\rm QSO}$. Here the upper limit is invoked to keep the absorption redshift well-defined in the fits. This also ensures that the absorption system will be physically separated from the QSO environment.

These four randomly drawn parameters are used to generate a QSO model assuming the combined QSO template by Vanden Berk et al. (2001); Glikman, Helfand, & White (2006). We use the SMC extinction curve for the reddening at the QSO redshift and we generate two sets of models: one assuming SMC-type dust in the absorber and one assuming LMC-type dust. The QSO model is then smoothed to match the resolution of the ALFOSC instrument at the NOT and hereafter interpolated onto a wavelength grid similar to the spectral data from the aforementioned instrument. Then we generate synthetic photometric data by calculating the flux in each of the SDSS ($ugriz$) and UKIDSS ($YJHK_s$) bands by weighting the model with the appropriate filter curve. We denote the synthetic spectral and photometric data as a *synthetic data set*.

We then add noise to the synthetic data set following a Gaussian noise model. We generate two sets for each assumed absorber extinction curve: one with high SNR and one with low SNR. High and low signal-to-noise ratios here refer to $\mathrm{SNR}_{\rm spec} = 15,\ \mathrm{SNR}_{\rm phot} = 20$ and $\mathrm{SNR}_{\rm spec} = 5$, $\mathrm{SNR}_{\rm phot} = 10$, respectively, where $\mathrm{SNR}_{\rm spec}$ refers to the average SNR per pixel in the synthetic spectral data and $\mathrm{SNR}_{\rm phot}$ refers to the SNR of each synthetic photometric band. For the spectral noise model, we further add a noise component mimicking the fringing in the red part of the CCD of the ALFOSC spectrograph. Specifically, this is $\sim 20\,\%$ (peak-to-peak fringe level) for wavelengths greater than $8000\,$Å.

In the following figures, we show the results of the analysis of our synthetic data sets. In Figure 5.10, we show the analysis of the models with dust added only at the QSO redshift. We plot the difference between input parameter and the recovered best-fit parameter as function of input extinction and input QSO redshift. We observe no bias and the $1\,\sigma$ scatter in the recovered $A(V)$ is ± 0.010 and ± 0.019 for high and low SNR, respectively. In Figures 5.11 and 5.12, we show the best-fit parameters (output) as functions of the model parameters (input). We also show the fraction of correctly identified systems using the likelihood ratio test. We only show the results for SMC at high SNR since no absorbers are recovered at low SNR.

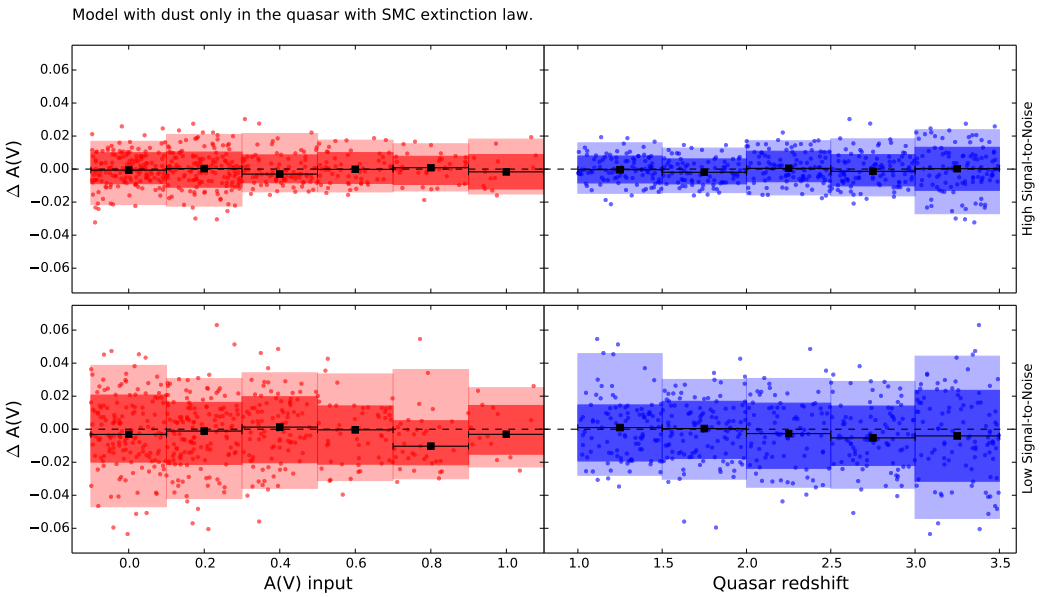

Figure 5.10: Residuals of the recovered $A(V)$ in the null model tests where we only add reddening at the QSO redshift. The top and bottom rows show the results of modelling at high and low SNR, respectively. In each row, the left panel shows the residuals of the best-fit $A(V)$ as function of the input $A(V)$. The right panel shows the same residuals as function of QSO redshift. We observe no bias (i.e., no systematic offset in the residuals) and no significant dependence on input parameters.

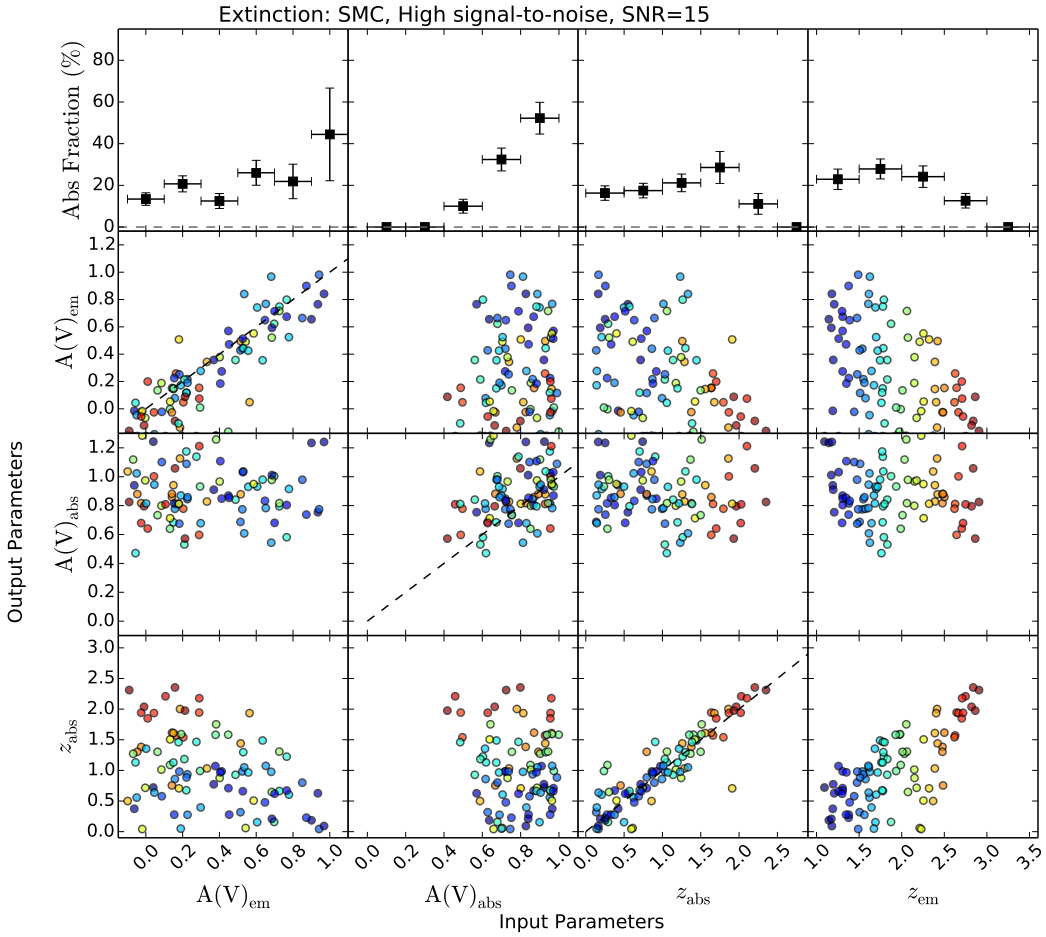

Figure 5.11: The top row shows the recovered fraction of correctly identified absorbers using the likelihood ratio test and in the three subsequent rows, we show the best-fit output parameters as function of the input parameters. The data shown are for model runs with high SNR and assuming the SMC extinction curve. We only show the results for the correctly identified absorbers. The points are colour-coded by redshift of the QSO (blue corresponds to $z = 1$, and red indicates $z = 3.5$.

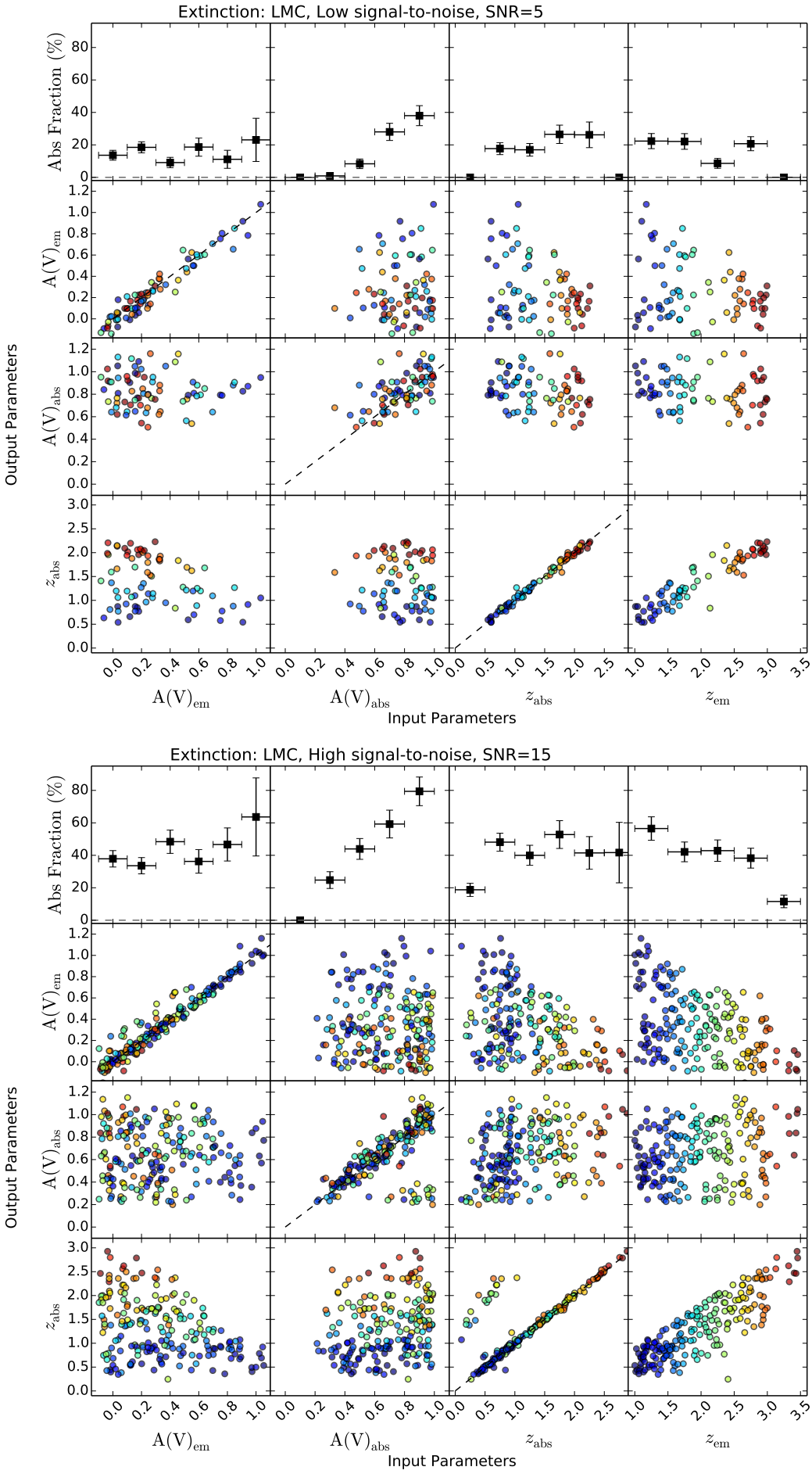

Figure 5.12: Same as Fig. 5.11 but assuming the LMC extinction curve for high (top) and low (bottom) SNR.

5.C QSOs with intervening absorbers from statistical modelling

The remaining targets where an intervening dusty systems was identified with our statistical algorithm (see Section 5.4.1) are shown in Figure 5.13. We show both the simple model (in blue) with dust only in the quasar itself and the general model (in red) with dust in both the quasar and the absorber.

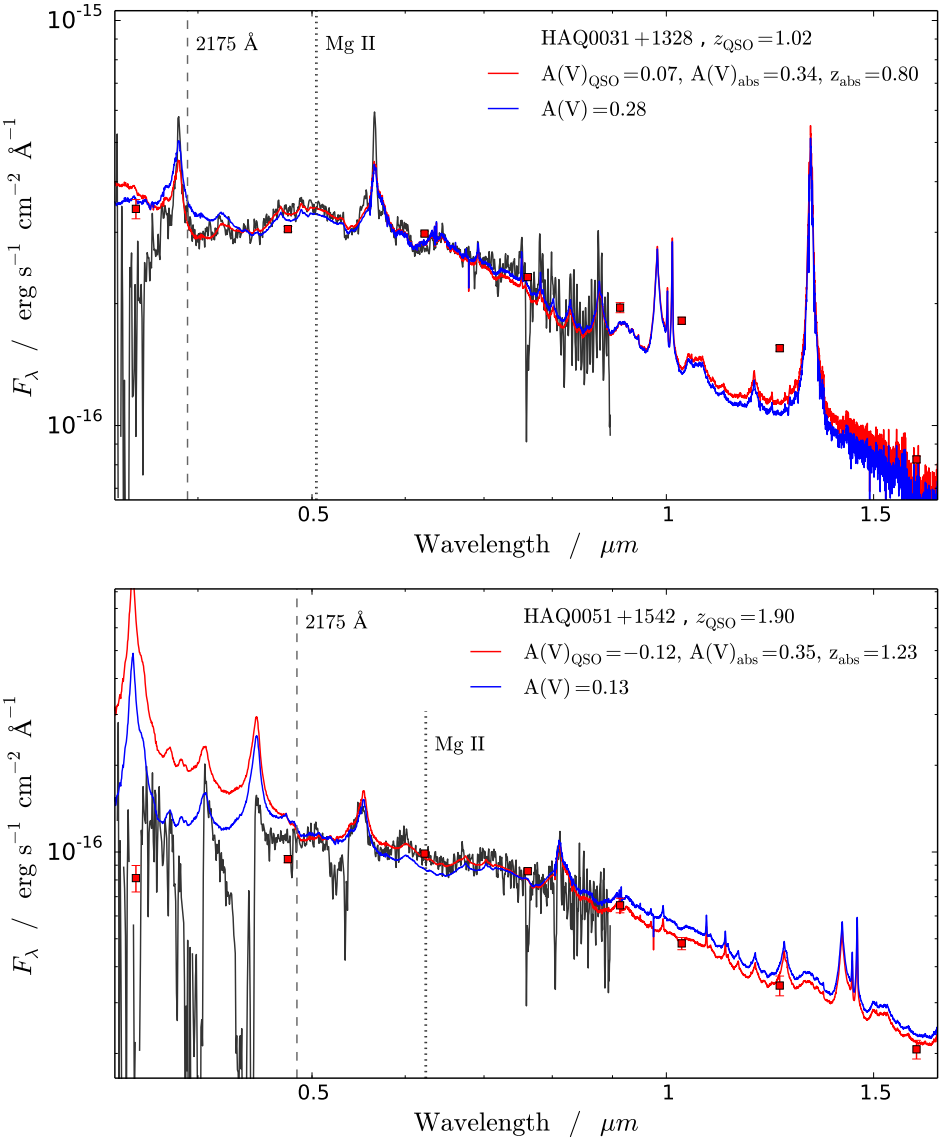

Figure 5.13: Spectra and photometry for the QSOs with preferred dust in an intervening absorption system. The figure shows the spectral data in black and the SDSS and UKIDSS photometry as red squares. In cases where both SDSS and NOT spectra are available, we show the SDSS spectrum as black and the NOT spectrum in gray since the SDSS spectrum was used in the analysis. The SDSS spectrum, if available, has been smoothed with a 3-pixel Gaussian kernel for presentation purposes. The blue and red templates show the best-fit null model and general model, respectively. The dashed and dotted vertical lines indicate the locations of the 2175 Å bump and Mg II at the best-fit redshift for the absorber. *(Continued on next page.)*

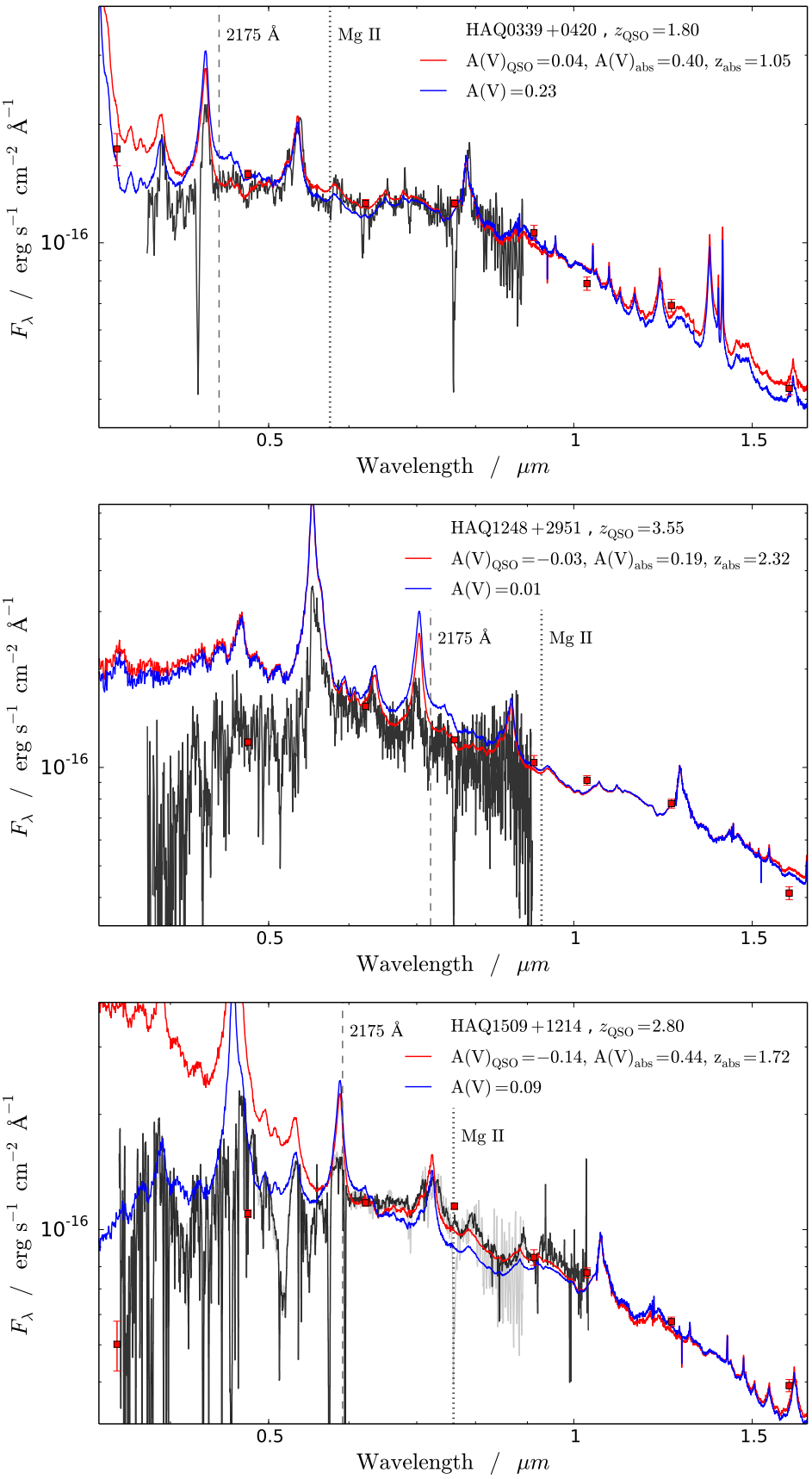

Figure 5.13: *Continued.*

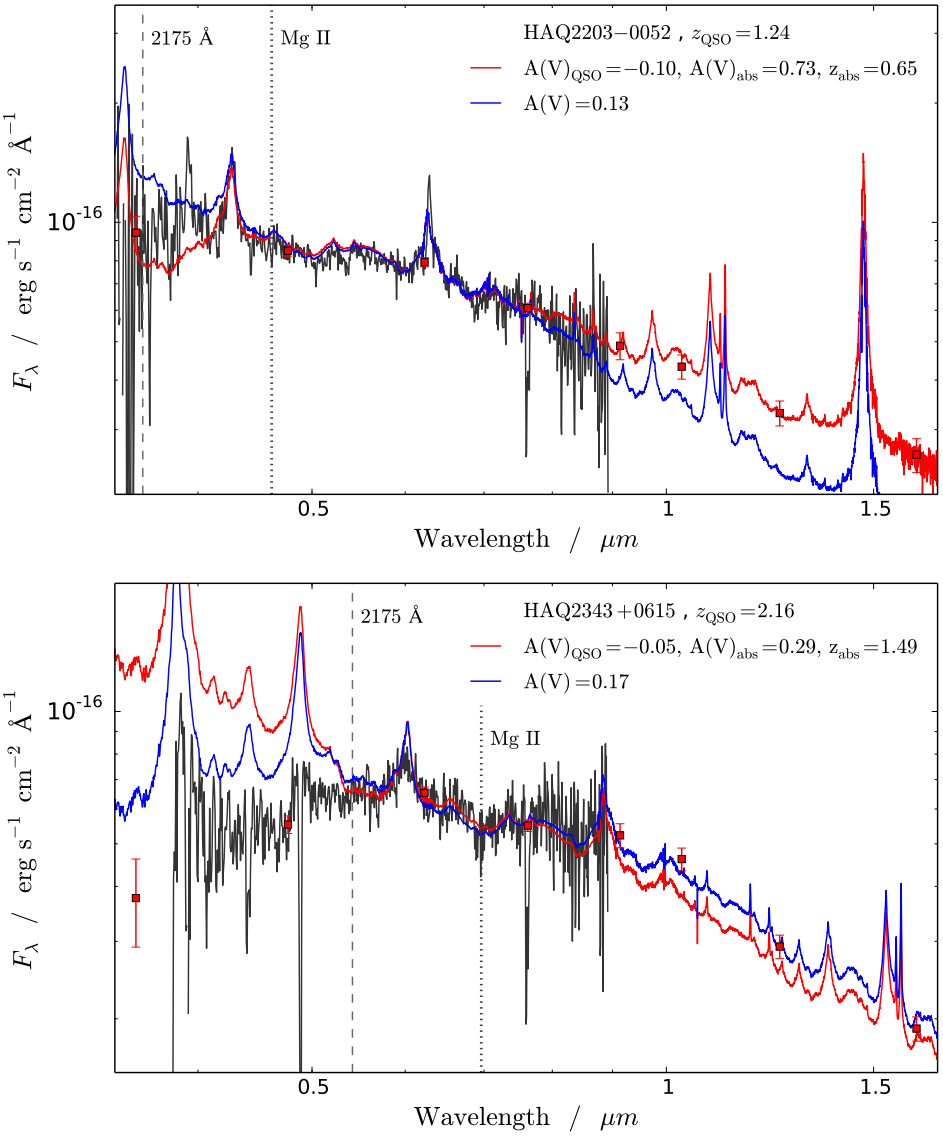

Figure 5.13: *Continued.*

5.D Spectra not classified as QSOs

The three targets that were not classified as QSOs are shown in Figures 16, 17, and 18. The first two targets (Figures 5.14 and 5.15) are stellar spectra that entered the sample by mistake. The first target (HAQ1524-0053) is a Galactic G dwarf, which was selected due to an error in the K_s band photometry. The second target (HAQ2254+0638) was observed by mistake, as the wrong target in the field was centred on the slit. The last target (HAQ1607+2611, shown in Figure 5.16) remains unidentified.

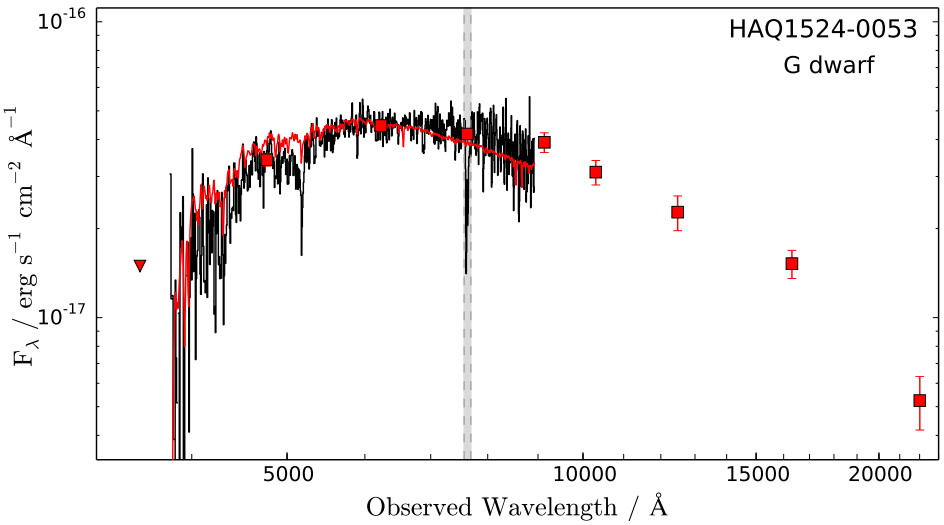

Figure 5.14: The observed spectrum is plotted as a solid black line. The red line shows a stellar template reddened by $A(V) = 0.52$ mag (assuming Milky Way type extinction) to match the observed spectrum. The reddening is the measured extinction from the Schlegel, Finkbeiner, & Davis (1998) dust map. Overplotted with filled squares are the SDSS and UKIDSS photometric data points. The NOT spectrum has been scaled to match the r-band photometric data point from SDSS. Note that the spectrum has not been corrected for telluric absorption (marked with a gray band at ~ 7600 Å).

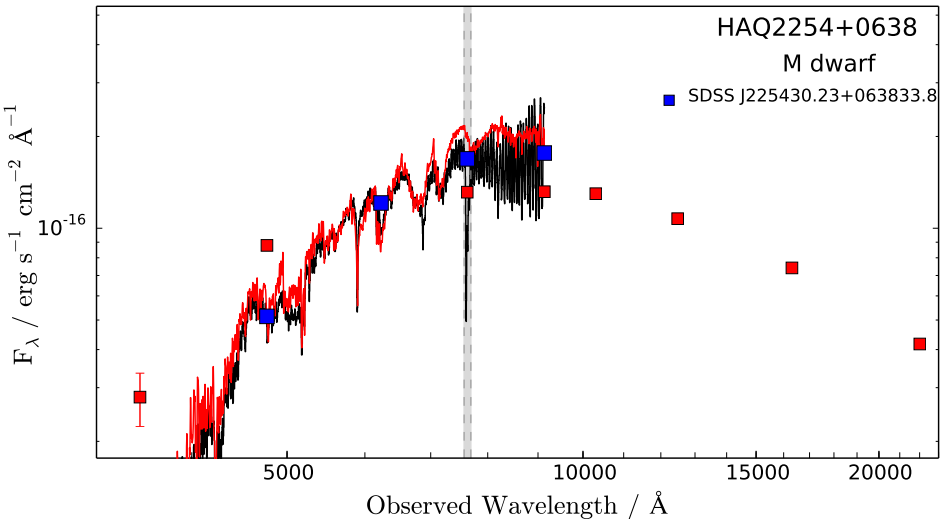

Figure 5.15: The observed spectrum is plotted as a solid black line. The red line shows a stellar template to match the observed spectrum. During the observations of HAQ2254+0638 a nearby star was accidentally placed on the slit instead of the QSO candidate. In red squares, we show the SDSS and UKIDSS photometric data points for the HAQ candidate and in blue squares we show the SDSS photometry of the actual star. The SDSS identifier of the star is given in the upper right corner. The mix up explains the apparent mismatch between the photometry of the candidate (in red squares) and the spectrum. The NOT spectrum and the blue photometric points have been scaled to match the r-band photometric data point (red square) from SDSS, since both are almost 2 orders of magnitude brighter than the candidate photometry. Note that the spectrum has not been corrected for telluric absorption (marked with a gray band at $\sim$ 7600 Å).

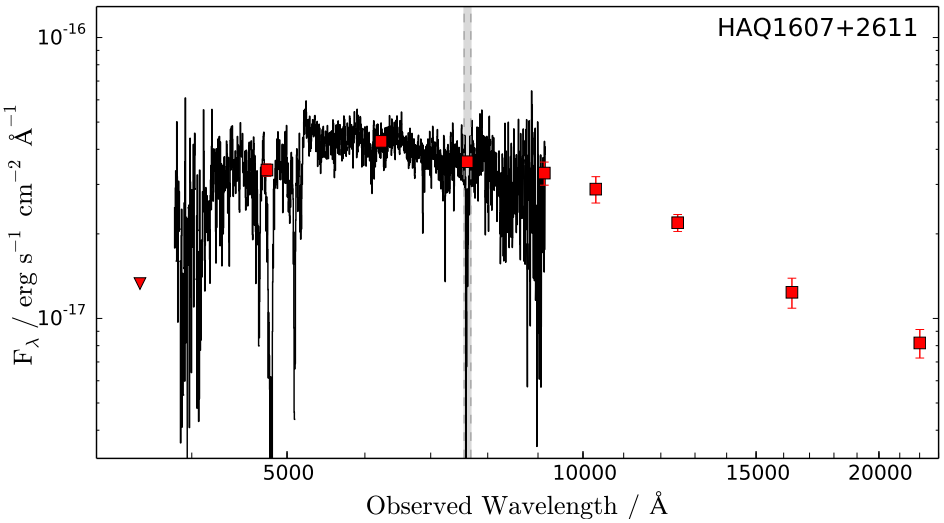

Figure 5.16: Unidentified target. The observed spectrum is plotted as a solid black line. Overplotted with filled squares are the SDSS and UKIDSS photometric data points. In this case, we have not been able to securely classify the target. The NOT spectrum has been scaled to match the r-band data from SDSS. Note that the spectrum has not been corrected for telluric absorption (marked with a gray band at $\sim$ 7600 Å).

5.E Candidates

All the remaining candidates from our sample that were not followed-up with spectroscopy are listed below in Table 5.7.

Table 5.7: Remaining Candidate QSOs.

Target	α (J 2000)	δ (J 2000)	r_{SDSS} (AB mag)
HAQ0000+1250	00 00 08.483	+12 50 33.48	18.84
HAQ0001+0411	00 01 43.455	+04 11 55.69	19.44
HAQ0001+0431	00 01 42.854	+04 31 38.89	19.44
HAQ0003+0221	00 03 43.674	+02 21 29.39	19.17
HAQ0012+1535	00 12 15.986	+15 35 51.08	19.71
HAQ0014+1403	00 14 39.454	+14 03 07.74	19.93
HAQ0015+1213	00 15 10.919	+12 13 53.30	19.85
HAQ0019+0657	00 19 57.289	+06 57 45.71	19.42
HAQ0021+0633	00 21 02.642	+06 33 25.69	19.50
HAQ0022+1049	00 22 44.368	+10 49 02.85	20.09

Notes: The table is published in its entirety in the electronic edition of the journal. A portion is shown here for guidance regarding its form and content. The full table is also available on the survey homepage: `http://dark-cosmology.dk/~krogager/redQSOs/targets.html`.

6

The tip of the dusty iceberg

This chapter contains the following article:

"A Quasar reddened by a sub-parsec sized, metal-rich and dusty damped Lyman-α absorbing cloud at $z = 2.13$"

Submitted to *Monthly Notices of the Royal Astronomical Society on Aug 3rd, 2015.*
Positive referee report received on Aug 13th, 2015.

Authors:
J.-K. Krogager, J. P. U. Fynbo, P. Noterdaeme, T. Zafar, P. Møller,
C. Ledoux, T. Krühler, & A. Stockton

We present a detailed analysis of a red quasar at $z = 2.322$ with an intervening damped Lyman-α absorber (DLA) at $z = 2.13$. Using high quality data from the X-shooter spectrograph at ESO Very Large Telescope we find that the absorber has a metallicity consistent with Solar. Moreover, we observe strong C I and H_2 absorption indicating a cold and dense absorbing medium. Partial coverage effects are observed in the C I lines, from which we infer a covering fraction of 27 ± 6 % and a physical diameter of the cloud of 0.1 pc. From the covering fraction and size, we can estimate the size of the background quasar's broad line region. We search for the emission counterpart of the DLA in optical and near-infrared imaging from the Nordic Optical Telescope and the Keck Observatory. We observe no emission in the optical data. However, we see tentative evidence for a counterpart in the H and K' band images. The DLA shows a high level of depletion (as probed by $[\mathrm{Fe/Zn}] = -1.22$). This indicates that significant amounts of dust must be present in the DLA. By fitting the spectrum with various dust reddened quasar templates we find a best-fitting amount of dust in the DLA of $\mathrm{A(V)_{DLA}} = 0.28 \pm 0.01|_{\mathrm{stat}} \pm 0.07|_{\mathrm{sys}}$ with no dust in the quasar needed to explain the reddening. The dust-to-gas ratio of the DLA is similar to that of the local interstellar medium. We conclude that dust in the DLA is causing the colours of this intrinsically very luminous background quasar to appear much redder than average quasars, thereby not fulfilling the criteria for quasar identification in the Sloan Digital Sky Survey. Such chemically enriched and dusty absorbers are thus underrepresented in current samples of DLAs.

6.1 Introduction

Damped Lyman-α absorbers (DLAs) are a class of neutral hydrogen absorbers seen in the spectra towards bright background sources (typically quasars and gamma ray bursts). Due to their high degree of self-shielding, these absorbers allow a precise characterization of the chemical evolution in the gas phase of galaxies over a large cosmic timespan (for a review, see Wolfe, Gawiser, & Prochaska 2005). DLAs thereby play a significant role in understanding the interstellar medium (ISM) and star formation at high redshift.

However, in order to interpret the available data it is important to understand to which extent our quasar samples are biased against dusty and hence likely more metal-rich sightlines (Pei, Fall, & Hauser 1999). This issue has been discussed extensively in the literature for more than 20 years (e.g., Pei, Fall, & Bechtold 1991; Murphy & Liske 2004; Vladilo & Péroux 2005; Pontzen & Pettini 2009; Kaplan et al. 2010; Khare et al. 2012). Over the past few years a handful of systems have been discovered in which the DLAs host significant amounts of dust (Fynbo et al. 2011; Noterdaeme et al. 2012b; Wang et al. 2012). This poses a problem to the way we sample the population of absorbing galaxies. As DLAs are detected towards bright background sources, the presence of dust in the absorbing medium will cause the background source to appear fainter and redder. Up until now, large area quasar samples have mainly been compiled from optical photometry (e.g., the Sloan Digital Sky Survey, SDSS; York et al. 2000). Hence optical colour criteria were the basis for selection algorithms of quasars. Recently the search for quasars has been refined and an increasing number of selection techniques are used to probe the quasar population to gather a more complete census of the quasars, and thereby also the absorbers along their sightlines (e.g., Ross et al. 2012; Schmidt et al. 2010; Graham et al. 2014; Heintz, Fynbo, & Høg 2015). The importance of the dust bias can be studied by compiling a radio selected sample of quasars, since the radio emission is not affected by dust. This approach has been followed both in the CORALS survey (Ellison et al. 2001, 2004) and the UCSD survey (Jorgenson et al. 2006), which includes the CORALS survey. The authors of these surveys conclude that a dust bias is probably a minor effect, however, a larger sample is necessary to robustly confirm an absence of a significant dust bias. The later study of Pontzen & Pettini (2009) confirm that a dust bias is most likely a small effect. Nevertheless, they find that the cosmic density of metals measured in DLA surveys could be underestimated by up to a factor of 2 due to a dust bias.

The effects from dust obscuration in a foreground absorber were identified clearly toward the quasar Q 0918+1636 presented in the work by Fynbo et al. (2011). The reddening of the background quasar, caused by dust in the foreground DLA, changed the colours of the quasar to the point where the quasar was close to dropping out of the SDSS quasar sample. In other words, had the dust extinction in the DLA been a little higher than the modest $A(V) = 0.2$ mag, the background quasar would not have been identified as a quasar in SDSS. Following this discovery, we set out to look for quasars that would be missing in the SDSS quasar catalogs due to such reddening effects. The resulting surveys from our targeted search have identified almost 150 quasars that were not classified as such in SDSS-II (Fynbo et al. 2013a; Krogager et al. 2015, see Chapters 4 and 5). Although the vast majority of the quasars in these surveys were reddened by dust in the hosts rather than in foreground DLAs, we did encounter one very strong candidate: a DLA at redshift $z = 2.13$ toward the quasar J 2225+0527. Interestingly, this target, although not classified as such in SDSS, is a well-known radio source discovered by Gower, Scott, & Wills (1967) and identified as 4C 05.84. The QSO was later spectroscopically observed and a redshift

of $z = 2.323$ was measured (Barthel, Tytler, & Thomson 1990). Barthel et al. also identified the $z_{\rm abs} = 2.132$ DLA. However, this did not come to our attention before starting the follow-up observations. The previous low-resolution data were also not adequate for the detailed absorption line analysis in this work.

In this work, this specific target was observed in greater detail at the European Southern Observatory's Very Large Telescope to characterize the absorber and the extinction plausibly caused by it. We have combined the deep spectrum with new optical imaging from the Nordic Optical Telescope together with archival near-infrared imaging from the Keck observatory to search for the emission counterpart of the DLA. Such DLA galaxies have been exceedingly difficult to observe and the current sample of detections at redshift $z \approx 2$ consists of only 10 galaxies (Krogager et al. 2012, see Chapter 2). It has been argued that the more evolved and metal-rich DLAs might also be associated with more massive systems and hence would be more readily detected in emission (Møller, Fynbo, & Fall 2004; Fynbo et al. 2008; Neeleman et al. 2013). In that case, metal-rich and dusty DLAs should be caused by the most evolved and massive systems, which subsequently are more likely to be missed in optically selected quasar samples.

6.2 Observations and data reduction

6.2.1 Spectroscopy

We observed the target as a candidate quasar from the High $A(V)$ QSO (HAQ) survey (Krogager et al. 2015) on the night of August 27, 2014 at the Nordic Optical Telescope. The initial observations were carried out using the Andalucia Faint Object Spectrograph and Camera (ALFOSC) with a low resolution setup. The DLA was identified during the observing run and was followed up with higher resolution spectra covering the absorber the following nights.

After the identification in the HAQ survey we observed the target with the X-shooter spectrograph (Vernet et al. 2011) at the VLT during October 30, 2014 and November 23, 24, 25, 2014 under director's discretionary time program ID 293.A-5033. The X-shooter covers the wavelength range from 3000 Å to 2.5 μm simultaneously by splitting the light into three separate spectrographs, the so-called arms: UVB ($3000 - 5500$ Å), VIS ($5500 - 10,000$ Å), and NIR ($10,000 - 25,000$ Å). All observations were carried out with the same slit widths (see Table 6.1) to allow us to search for emission from the DLA galaxy counterpart at small projected distances from the quasar. However, since the atmospheric dispersion correction did not function properly we were forced to observe at parallactic slit angle to limit slitloss. For this reason only two different slit angles were obtained, one for the Oct 30 observations (PA $\sim -4^\circ$ east of north) and three almost identical slit angles for the November observations (PA $\sim 39^\circ$ east of north). The data were reduced using the official X-shooter pipeline `esorex` version 2.3 for stare mode, whereafter the four individual 2-dimensional spectra were combined and the final 1-dimensional spectrum was extracted (this was separately done for each arm: UVB, VIS, NIR). This spectrum was then corrected for Galactic extinction ($E(B-V) = 0.132$) using the maps of Schlafly & Finkbeiner (2011). The effective resolving power was measured in the final spectrum to be $\mathcal{R} = 11,000$ for VIS and $\mathcal{R} = 7000$ for NIR. As there are no telluric lines appropriate for determining the resolution in the UVB, we obtained the resolving power by interpolating between the tabulated values of resolving power for given slit widths. Given the seeing of $\sim 0\farcs7$ in V-band we inferred a resolving power of $\mathcal{R} \approx 6000$ in the UVB.

Table 6.1: Observations of the quasar J 222514.97+052709.1

Date	Instrument	Setup	Exp. Time (sec)
2006 Sep 1	Keck/NIRC2 AO	H, K' imaging	2700
2007 Aug 21	Keck/NIRC2 AO	J imaging	1620
2014 Oct 30	VLT/X-shooter	$1\farcs3$, $1\farcs2$, $1\farcs2$ [a]	3000
2014 Nov 23	VLT/X-shooter	$1\farcs3$, $1\farcs2$, $1\farcs2$ [a]	3000
2014 Nov 24	VLT/X-shooter	$1\farcs3$, $1\farcs2$, $1\farcs2$ [a]	3000
2014 Nov 25	VLT/X-shooter	$1\farcs3$, $1\farcs2$, $1\farcs2$ [a]	3000
2014 Nov, Dec	NOT/ALFOSC	r'-band imaging	13, 860

[a] The slit widths of the three arms of X-shooter given as UVB, VIS, and NIR.

6.2.2 Imaging

In order to look for extended emission from the galaxy counterpart of the DLA, we observed the region around the quasar with the ALFOSC instrument at the NOT in imaging mode. We used the r' filter centred at 618 nm. The observations were carried out in a five-point dither pattern with sub-integrations of 330 s over many nights during November and December under program P49-422. The images were bias subtracted and flat field corrected using standard IRAF routines. In order to subtract fringes and large scale variations in the background we subsequently created a master background image. In each frame, we masked out any sources above 4 σ of the sky noise estimated by the robust median absolute deviation. The masked frames were normalized by the median of each frame and combined. The resulting background image was then scaled to and subtracted from each frame. For each frame, we measured the seeing and only the 50 per cent best frames (21 out of 42) in terms of seeing were aligned and median combined to create the final image. This resulted in a much sharper and more symmetric point spread function (PSF) compared to the image of all frames combined. The seeing in the optimally combined image was $0\farcs74$ compared to the $0\farcs85$ of the combined image from all frames.

Furthermore, we have included imaging data in the J, H, and K'-bands from the Keck II telescope observed with the NIRC2 instrument fed by the Keck Laser-Guide-Star Adaptive-Optics system to enhance the image resolution. The observations in H and K' bands had total exposure times of 2700 s each, performed in sub-integrations of 300 s. The J band image was obtained with sub-integrations of 180 s for a total exposure time of 1620 s. The NIRC2 images were reduced using an IRAF scripted pipeline that does an iterative removal of the sky background, flat fielding, registration og the individual images, and drizzling onto the final grid with a pixel size of 40 mas pixel^{-1}. The full width at half maximum (FWHM) of the point spread function in the H and K' images are $0\farcs089$ and $0\farcs092$, respectively. The shallower J-band image was obtained with slightly worse AO correction resulting in a less symmetric point spread function with a FWHM of $0\farcs093$. Moreover, the wings of the PSF were more dominant for the J-band image than in the H and K'-band images.

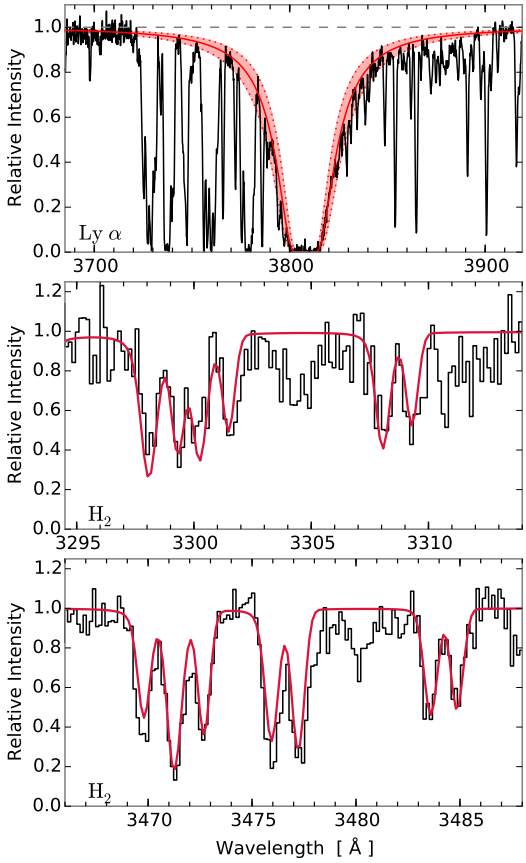

Figure 6.1: In the top panel, the Lyα transition is shown. The best-fitting Voigt profile is shown in solid red with 3σ range indicated by the red shaded area. In the middle and lower panels, a zoom-in around some of the available H_2 lines is shown. The red line marks the best-fitting model to the ro-vibrational lines.

6.3 Absorption Line Analysis

We detected molecular hydrogen in absorption from rovibrational transitions in the rest-frame far-UV. We fitted the Lyman and Werner bands of H_2 assuming two components for the $J = 0, 1, 2, 3$ levels. The relative velocities and broadening parameters were kept fixed for all J-levels. For the first component we inferred $z_1 = 2.13123$ ($v_{\rm rel} = -120$ km s^{-1}) and $b = 1.3$ km s^{-1}, and for the second component we inferred $z_2 = 2.13240$ ($v_{\rm rel} = -9$ km s^{-1}) and $b = 8.1$ km s^{-1}. Due to the poor resolution of the UVB arm, the very narrow molecular lines were not resolved and hence the fit was very degenerate. We therefore do not state all the column densities of each individual transition. However, the total column density remained rather unaffected of the degeneracies as it was dominated by only one component in the damped regime. From the fit we obtained a total column density of molecular hydrogen of $\log N(H_2)/{\rm cm}^{-2} = 19.4 \pm 0.1$. We observed tentative evidence of partial coverage (this effect is described in more detail in Section 6.3.1) from the H_2 lines at the Lyβ and O VI lines, but higher resolution spectroscopy is needed to confirm. In order to measure the column density of neutral hydrogen, we fitted the Lyα transition, for which we obtained $\log N({\rm H\,I})/{\rm cm}^{-2} = 20.69 \pm 0.05$. The molecular fraction $f_{H_2} = 2N(H_2)/(2N(H_2) + N({\rm H\,I})) = 0.09$ is thus among the highest observed in high-redshift quasar-DLAs (e.g. Noterdaeme et al. 2008; Srianand et al. 2008b; Noterdaeme et al. 2010; Jorgenson et al. 2014). The fitted profiles to neutral and molecular hydrogen are shown in Fig. 6.1.

We detected metal absorption lines from various ionization states, ranging from neutral species (C I, Cl I) to highly ionized transitions (C IV, Si IV). The full list of absorption lines detected and their equivalent widths are given in Table 6.4 of the Appendix. In order to obtain the column densities for the low ionization lines, we fitted the weak unsaturated lines using Voigt profiles. We used the iron and manganese lines (Fe II$\lambda 2374$ and Mn II$\lambda 2576$) with high signal-to-noise ratios to obtain a solution for the number of velocity components, their relative velocities, and their broadening parameters. The best-fitting solution to these lines gave 10 components ranging from $v = -183$ to $+214$ km s^{-1} relative to the strongest absorption component, $z_{\rm sys} = 2.13249$. The relative velocities and broadening parameters of the individual components are given in Table 6.2 for reference. We assumed the broadening to be purely turbulent. This velocity structure was then kept fixed and all lines were fitted simultaneously to infer their column densities. We included the uncertainty on the continuum normalization in the fitting. The best-fitting column densities are reported in Table 6.2. The neutral magnesium transition Mg I $\lambda 2852$ was included in order to constrain the contribution from Mg in the line-blend of Zn, Cr, and Mg at 2026 Å. Since the signal-to-noise for the Mg I line was high, we fitted a separate set of 7 components to this line. Because of the different velocity structure of the magnesium line we do not include the individual components in Table 6.2. We further note that the contribution from Co II to the line-blend is negligible due to the weak strength of this transition and the non-detection of other Co transitions, see Table 6.4. For lines with lower signal-to-noise ratios, we were not able to constrain all 10 components. These unconstrained components are marked with '...' in Table 6.2. The total abundances from the fit and the calculated metallicities are given in Table 6.3. We observe a relatively low [S/Zn] ratio of -0.31, this is lower than the average DLA, however, not uncommon given the large uncertainty regarding this element (e.g., Rafelski et al. 2012; Berg et al. 2015). Furthermore, the abundance of sulphur may be underestimated due to hidden saturation given the lower resolution in the UVB arm. For a resolution of $\mathcal{R} = 6000$ we find that absorption lines with a flux residual at peak absorption of less than roughly 0.75. One of the S II lines is thus right at the border, but this line is blended with Lyα forest. The other sulphur line is stronger and should therefore be viewed as a lower limit. The hidden saturation might cause the column density to be underestimated by as much as 0.4 dex.

From the low ionization metal lines, we were able to recover information about the kinematics of the DLA through the measure ΔV_{90}. We followed the definition by Prochaska & Wolfe (1997), who define ΔV_{90} in terms of the wavelengths encompassing the central 90 per cent of the apparent optical depth. In order to avoid saturation effects biasing the apparent optical depth we chose the Si II $\lambda 1808$ absorption line instead of the stronger Fe II $\lambda 2374$ transition. Following the definition by Prochaska & Wolfe, we first converted the normalized spectral line to apparent optical depth: $\tau = -\ln(F)$, where F denotes the continuum normalized flux. From the distribution of τ, we then calculated the line centre, λ_0 along with the 5$^{\rm th}$ and 95$^{\rm th}$ percentiles, λ_5 and λ_{95}, respectively (see Fig. 6.3). To minimize the contribution from noise in the continuum, we only calculated the percentiles within a set of boundaries obtained from visual inspection of the absorption line profiles. The boundaries used for this analysis were -250 and $+290$ km s^{-1}. We then obtained the velocity spread as:

$$\Delta V_{90} = c\,(\lambda_{95} - \lambda_5)/\lambda_0 = 331 \pm 30 \text{ km s}^{-1}\,.$$

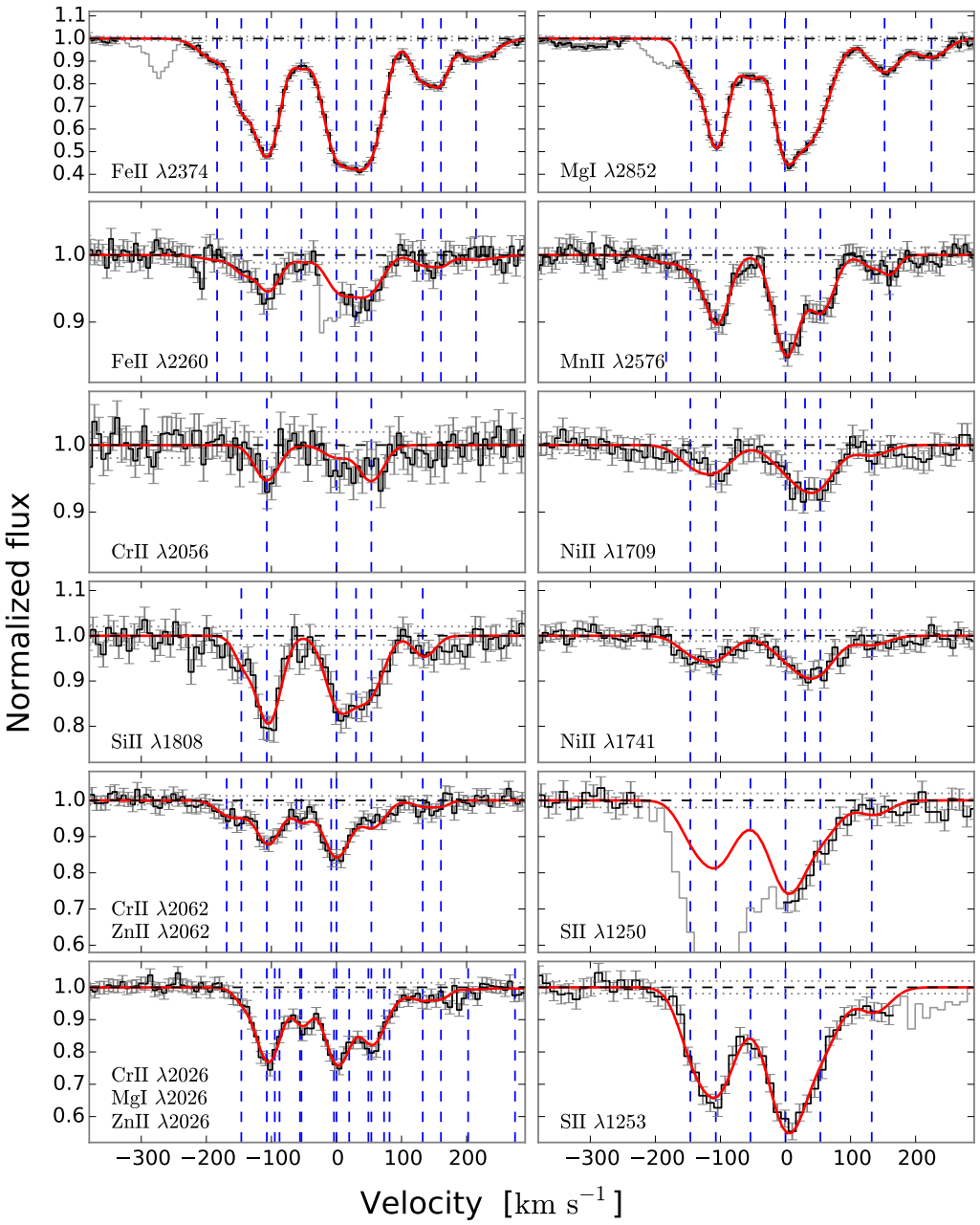

Figure 6.2: Voigt profile fits to low ionization lines. The data are shown in black with error-bars. Grey areas were excluded in the fits due to blends with other lines. The red line shows the best-fitting model, and the blue dashed lines show the fitted components. Velocities are relative to $z_{\rm sys} = 2.13249$.

We note that the result does not depend on the extent of the boundaries; only the uncertainty increases for more inclusive boundaries. The uncertainty on ΔV_{90} was determined by varying the spectral profile within the errors 10,000 times. For each realization, we measured ΔV_{90}. The 1 σ uncertainty was then inferred from the distribution of velocities as the 16$^{\rm th}$ and 84$^{\rm th}$ percentiles. Furthermore, we obtained consistent results for the Fe II line. However, the possible hidden saturation affecting absorption lines with a flux residual at peak absorption of less than 0.6 yields the Fe II less reliable (given the resolution of 27.3 km s^{-1}).

Table 6.2: Column densities for individual components of the Voigt profile fit to eight elements. All entries below are given as $\log(N/\mathrm{cm}^{-2})$.

v_{rel} [a] km s^{-1}	b km s^{-1}	Si II	S II	Cr II	Mn II	Fe II	Ni II	Zn II
-183	32	...	...	...	11.49 ± 0.26	13.50 ± 0.03	...	...
-146	11	14.30 ± 0.17	14.45 ± 0.07	...	11.38 ± 0.25	13.69 ± 0.02	12.93 ± 0.15	11.70 ± 0.15
-107	20	15.00 ± 0.04	14.81 ± 0.04	12.65 ± 0.09	12.31 ± 0.03	14.21 ± 0.01	13.22 ± 0.08	12.64 ± 0.02
-54	10	...	14.00 ± 0.19	...	...	13.30 ± 0.03	...	12.06 ± 0.07
0	22	14.90 ± 0.06	15.02 ± 0.02	12.21 ± 0.27	12.50 ± 0.02	14.20 ± 0.01	13.10 ± 0.16	12.68 ± 0.02
30	19	14.51 ± 0.20	...	...	...	13.93 ± 0.02	13.03 ± 0.29	...
54	21	14.71 ± 0.11	14.52 ± 0.05	12.67 ± 0.10	12.23 ± 0.04	14.12 ± 0.01	13.33 ± 0.11	12.43 ± 0.03
133	17	14.30 ± 0.18	14.14 ± 0.10	...	11.50 ± 0.20	13.62 ± 0.02	12.81 ± 0.17	11.74 ± 0.16
161	5	...	...	...	11.49 ± 0.18	13.39 ± 0.03	...	11.48 ± 0.24
214	35	...	...	...	...	13.52 ± 0.03	...	...

[a] Relative to the systemic redshift $z_{\mathrm{sys}} = 2.13249$.

Table 6.3: Metal abundances from the $z = 2.13249$ DLA.

Element (X)	$\log(N_X/\mathrm{cm}^{-2})$	[X/H][a]
Si II, λ1808	15.49 ± 0.04	-0.71 ± 0.07
S II, $\lambda\lambda$1250, 1253	15.41 ± 0.02	-0.40 ± 0.06
Cr II, $\lambda\lambda\lambda$2026, 2056, 2062	13.04 ± 0.08	-1.29 ± 0.09
Mn II, λ2576	12.91 ± 0.02	-1.21 ± 0.06
Fe II, $\lambda\lambda$2374, 2260	14.87 ± 0.01	-1.32 ± 0.05
Ni II, $\lambda\lambda$1709, 1741	13.90 ± 0.07	-1.01 ± 0.10
Zn II, $\lambda\lambda$2026, 2062	13.16 ± 0.02	-0.09 ± 0.05
C I, $\lambda\lambda$1560, 1656	13.86 ± 0.04	...
C I*	13.80 ± 0.04	...
C I**	12.98 ± 0.11	...
Cl I, λ1347	13.34 ± 0.03	...
Mg I, $\lambda\lambda$2026, 2852	12.93 ± 0.02	...
H_2	19.4 ± 0.1	...

[a] With respect to solar abundances from Asplund et al. (2009).

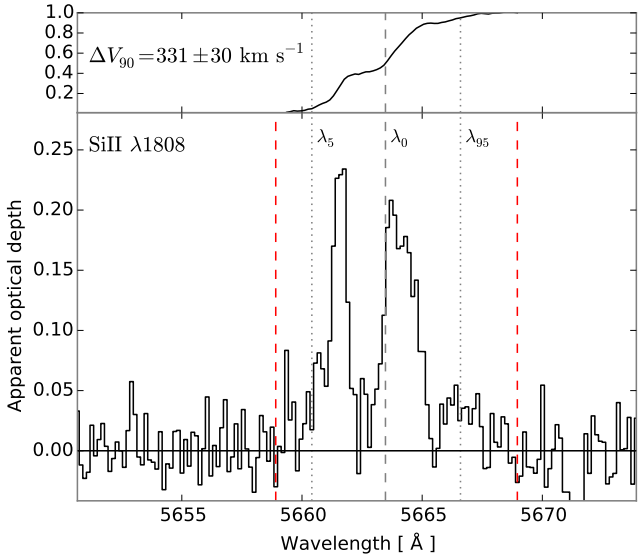

Figure 6.3: Apparent optical depth of the Si II λ1808 line used to calculate ΔV_{90}. In the top panel, we show the cumulative distribution of apparent optical depth. The grey dashed line marks the absorption line centre, and the grey dotted lines mark the 5th and 95th percentiles of this distribution. The red dashed lines mark the boundaries of the absorption line within which the apparent optical depth distribution is calculated. The boundaries used are -250 and 290 km s^{-1} with respect to the systemic redshift, $z_{\mathrm{sys}} = 2.13249$.

6.3.1 Atomic Carbon

Strong absorption from atomic carbon (C I) and its fine-structure levels $^3P_1$ and $^3P_2$ (here denoted as C I* and C I**, respectively) was clearly detected in the rest-frame UV. We fitted these transitions with a two component Voigt profile for each of the three levels ($v_1 = -110$ km s^{-1} and $v_2 = -4$ km s^{-1}, relative to $z_{\rm sys} = 2.13249$). Due to the limited resolution of the spectra we fixed the relative velocities and doppler broadening parameters of the various transitions and fitted them all simultaneously. We were not able to get both the transitions at 1560 Å and 1656 Å to fit simultaneously. The depth of the absorption lines was over-estimated for the 1656 Å line while under-estimated for the 1560 Å line. This may be explained due to so-called partial coverage. The effect arises when only a fraction of the emitted flux from the background source passes through the absorbing medium, i.e., the absorbing medium has a covering fraction less than unity (see Balashev et al. 2011). The partial coverage leads to an observable effect where saturated absorption lines do not reach zero flux since a fraction of background emission is able to reach the observer unabsorbed. This excess flux is here referred to as the line flux residual, LFR. We follow Balashev et al (2011) in their definition of LFR. We call the total emitted flux $F_{\rm tot}(\lambda)$, and the flux that is affected by absorption $F_{\rm cloud}(\lambda)$. The observed flux is thus given by

$$F_{\rm obs}(\lambda) = F_{\rm tot}(\lambda) - F_{\rm cloud}(\lambda) \times [1 - e^{-\tau(\lambda)}] \, , \tag{6.1}$$

where $\tau(\lambda)$ is the optical depth of the absorption line. The LFR is the normalized flux which is not covered by the cloud:

$$\text{LFR} = (F_{\rm tot} - F_{\rm cloud})/F_{\rm tot} \, . \tag{6.2}$$

The phenomenon may also arise if the background source is gravitationally lensed and not all deflected paths pass through the absorbing medium; however, as will be argued later on, we disregard this effect in our analysis.

We assume a structure for the quasar as follows: the accretion disc around the black hole is responsible for the continuum emission and is assumed to be a point source; the broad emission lines are emitted from a more extended structure of gas called the broad line region (BLR). In this geometry, an absorption line on top of a continuum region will be unaffected as the cloud covers all of the continuum source. However, an absorption line on top of a broad emission line will absorb the full continuum source but only part of the BLR flux due to the partial coverage of the BLR. Absorption lines on top of broad emission lines will therefore exhibit a line flux residual depending on the covering fraction of the BLR. An idealised schematic view of the assumed geometry is shown in Fig 6.4. The figure shows the case of an absorption line on top of a broad emission line and one in a continuum region only. For clarity, we show saturated lines in the figure, as this allows the LFR to be visualized more easily.

In case of gravitational lensing, the LFR for absorption lines in continuum regions and on top of broad emission lines will be identical, since the light from both the central continuum source and the BLR is deflected and reach the observer unabsorbed. Only in special cases, where the extended BLR is lensed differently from the continuum source, will the LFR be different. We therefore assume that the mismatch observed in the two C I lines is caused by partial coverage due to the absorbing cloud being small in projection compared to the BLR.

Since the C I lines were not saturated, we could not easily measure the LFR as is indicated in Fig 6.4. Instead we had to infer the LFR by fitting the absorption lines with various values for the LFR. We de-

fined a grid of discrete value of LFR and for each grid point, we fitted the two absorption line complexes. The likelihood for each grid point was saved and used to fit a polynomial for the likelihood as function of LFR. We then obtained the best-fitting LFR by identifying the maximum likelihood from the polynomial fit, and the uncertainty was given by the curvature of the likelihood function, see top panel in Fig. 6.5. The lower panel in Fig. 6.5 shows the best-fitting C I absorption profile for the two transitions at 1560 and 1656 Å in red. The blue line in the figure shows the fit without taking into account partial coverage. The best fit resulted in a line flux residual of 16 ± 3 %. Fitting the absorption lines for this value of the LFR, we recovered the column densities for C I, C I*, and C I** as given in Table 6.3.

The 1560 Å transition is located in a part of the spectrum where the total incident flux is coming from the continuum source in the quasar ($F_{\rm cloud}(1560) = F_{\rm cont}$). The other transition (1656 Å) is located on top of the broad C IV emission line from the quasar; the incident flux is therefore a combination of the continuum flux and the flux from the more extended broad line region which is only partially covered ($F_{\rm cloud}(1656) = F_{\rm cont} + f_{\rm cov} \cdot F_{\rm BLR}$). The $F_{\rm cov}$ here denotes the fraction of the BLR covered by the cloud. For the assumed quasar geometry, we can then relate $f_{\rm cov}$ to the estimated LFR:

$$\begin{aligned} \text{LFR} \cdot F_{\rm tot} &= F_{\rm tot} - F_{\rm cloud} \\ &= (F_{\rm cont} + F_{\rm BLR}) - (F_{\rm cont} + f_{\rm cov} \cdot F_{\rm BLR}) \ , \end{aligned} \tag{6.3}$$

which yields

$$\text{LFR} = (1 - f_{\rm cov}) \cdot \frac{F_{\rm BLR}}{F_{\rm tot}} \ . \tag{6.4}$$

In order to recover $f_{\rm cov}$, we thus need to measure the two quantities $F_{\rm tot}$ and $f_{\rm cont}$ (since $F_{\rm BLR} = F_{\rm tot} - F_{\rm cont}$) in the spectrum at the wavelength of the C I $\lambda 1656$ absorption line. The total flux is easy to measure with good precision; however, the continuum flux is more cumbersome as the intrinsic quasar continuum is notoriously difficult to assess. We infer $F_{\rm cont}$ by interpolating a spline locally in the regions around the C IV emission line (for details see Fig. 6.11 of the Appendix). Due to the high level of uncertainty in the continuum evaluation, we assign an error of 10 per cent on the continuum flux. This way we obtain $F_{\rm cont} = 22.9 \pm 2.3$ and $F_{\rm tot} = 29.3 \pm 1.5$, both in units of 10^{-16} erg s^{-1} cm^{-2} Å^{-1}. Given the best-fitting value of the LFR of 16 ± 3 %, the flux measurements result in a covering fraction of the BLR of $f_{\rm cov} = 27 \pm 6$ %.

6.4 Dust Extinction

In Krogager et al. (2015), we assigned the reddening to the quasar itself due to the limited data available. However, in this work we have accurate abundance ratios from the DLA and a much extended wavelength coverage from the X-shooter spectrum. The observed [Fe/Zn] ratio indicates a significant amount of dust in the DLA. First we constrain the dust extinction, $A(V)$, along the line of sight by fitting a quasar template to the observed spectrum. We then compare the best-fitting $A(V)$ to an estimate from the observed depletion ratio of refractory to volatile elements. In the following, we will describe both methods in detail.

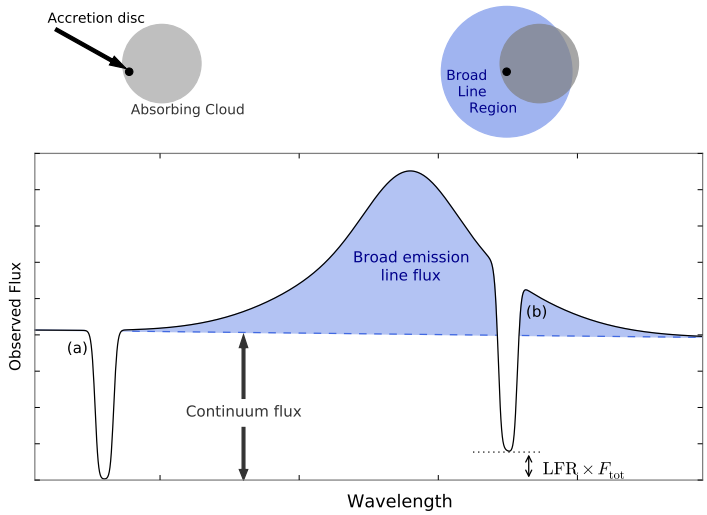

Figure 6.4: Schematic view of partially absorbing cloud. The top left panel shows the projected view of the background quasar's accretions disc (black dot) and the foreground absorbing cloud (grey circle). The top right panel shows the same configuration but with the quasar's broad line region shown as the blue circle. Absorption from different transitions in the foreground cloud are seen in the observed spectrum in the lower panel. Here the line marked (a) corresponds to the top left scenario at a wavelength where there is no contribution from broad emission line flux. The line marked (b) shows the top right scenario at a wavelength where broad emission line flux is contributing to the total observed flux. Due to the partial coverage of the broad line region indicated in the top right panel, a residual line flux (LFR) is observed in the saturated line, i.e., the line does not reach zero.

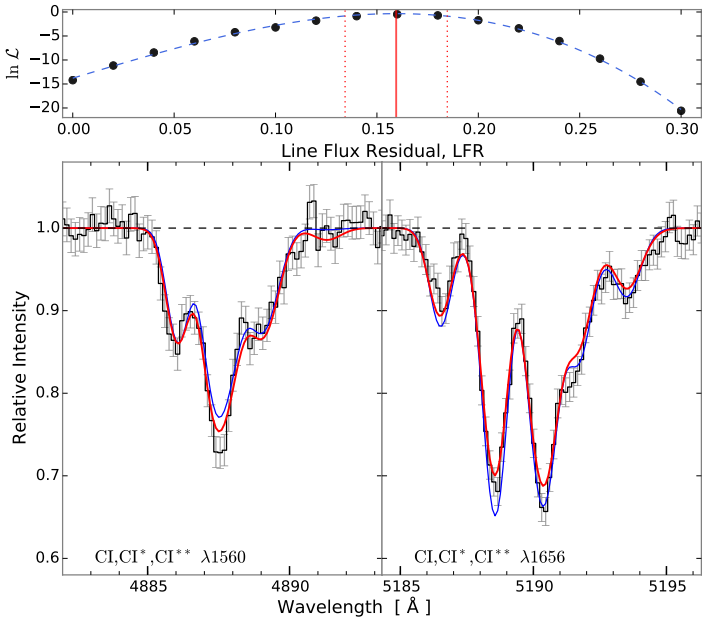

Figure 6.5: Voigt profile fit to neutral carbon (C I) and its fine structure transitions (C I* and C I**). The thick red line and thin blue line show the best-fitting model with and without partial coverage, respectively. The model without partial coverage poorly estimates the depth of the lines. The top panel shows the likelihood, $\mathcal{L}$ (normalized to the maximum likelihood) as function of the line flux residual, LFR, for each evaluation in black points. The blue dashed line shows a polynomial fit to the likelihood function. The maximum likelihood estimate (LFR $= 0.16 \pm 0.03$) is shown by the red vertical line with 1 σ confidence interval shown by the dotted lines.

6.4.1 Template Fitting

By fitting a quasar template to the spectroscopic data, we were able to model the dust extinction along the line-of-sight independently from the depletion analysis. We parametrized our model following the method in Krogager et al. (2015); However, we expanded the model to contain a variable intrinsic power-law slope, β, to be able to propagate the correlation between the reddening and the unknown intrinsic slope. In this work, we used the quasar template of Selsing et al. (2015, in preparation) and fitted for both the intrinsic quasar dust, $\mathrm{A(V)_{QSO}}$, and for dust in the DLA, $\mathrm{A(V)_{DLA}}$. We applied SMC, LMC and LMC2 type extinction curves by Gordon et al. (2003b) in the fitting routine, and for the quasar dust we furthermore applied a new extinction curve derived explicitly for quasars (see Zafar et al. 2015, submitted). We fitted the entire spectrum red-wards of Lyα excluding the regions influenced by the broad emission lines and telluric absorption. Furthermore, we used photometric data from WISE band 1 at 3.5 μm. The WISE bands at longer wavelength were not used since the quasar template does not cover these wavelengths. We did not include optical nor NIR photometric data points since all the available photometry was covered by the spectrum. During the initial fit, we noted an apparent mismatch between the template and the data in the spectral range around the C III] emission line of the quasar. We first suspected this to be caused by the 2175 Å bump feature characteristic of the LMC and LMC2 types of extinction curves. However, neither LMC nor LMC2 extinction curves resulted in better fits. Instead we discovered that the mismatch could be explained by variations in the broad emission from Fe II and Fe III, which form a pseudo-continuum in this wavelength range. We used the template of Vestergaard & Wilkes (2001) to model the iron emission. The contributions of Fe II and Fe III were separated into two individual templates, and subsequently smoothed to match the observed width of the broad emission lines of the quasar ($\sim$ 1500 km s^{-1}). By including the variable iron templates, we obtained a much improved fit, see Fig. 6.6. The best-fitting solution was obtained for the following parameters: $\mathrm{A(V)_{QSO}} = 0.005^{+0.008}_{-0.004}$, $\mathrm{A(V)_{DLA}} = 0.280^{+0.005}_{-0.009}$, and $\beta = 0.128 \pm 0.007$ assuming SMC type dust in the DLA. The results were insensitive to the extinction law in the quasar due to the negligible amount of dust at the redshift of the quasar. The best fit was obtained for an excess of Fe II and a deficit of Fe III relative to the average quasar template. The errors stated here only represent the statistical errors from the fit. We note that a fit to the data without the parameter $A(V)_{\mathrm{DLA}}$, i.e., with only dust in the quasar, gives an equally good fit. However, from the high level of depletion ([Fe/Zn] $= -1.22$) we have a strong prior indicating dust in the DLA. Moreover, the presence of strong H_2 indicates dust in the absorbing medium.

The extinction derived from the fit is strongly correlated with the intrinsic slope of the quasar power-law; this introduces a large systematic uncertainty, since we do not a priori know the intrinsic quasar slope. Previous studies have shown the intrinsic slope of quasars to be normally distributed with a width of ~ 0.2 (Vanden Berk et al. 2001, but see also Krawczyk et al. 2015 and Selsing et al. 2015) . By propagating this intrinsic uncertainty on the slope in our fitting, we can estimate the systematic effect on $A(V)_{\mathrm{DLA}}$. A steeper intrinsic slope (smaller β) yields a larger extinction. The change in extinction varies approximately as a linear trend with the slope as $\Delta\mathrm{A(V)_{DLA}} = -0.07 \cdot (\Delta\beta/0.02)$, where $\Delta\mathrm{A(V)_{DLA}}$ and $\Delta\beta$ denote the change in best-fitting extinction and slope, respectively. We can include this as a systematic uncertainty in our result: $\mathrm{A(V)_{DLA}} = 0.28 \pm 0.01|_{\mathrm{stat}} \pm 0.07|_{\mathrm{sys}}$. We note, that in cases of very shallow slopes the extinction becomes very small and these models prefer dust in the quasar. However, such solutions are inconsistent with the broad-band data from WISE at 3.5 μm and the measure of extinction from the depletion ratio of metals lines in the DLA, see above. Furthermore,

the very high luminosity of the quasar (among the top 0.1 per cent brightest quasars at this redshift, $\lambda L_K = 7.9 \times 10^{46}$ erg s^{-1}) renders such models highly unlikely as bright quasars typically have steeper slopes (Davis, Woo, & Blaes 2007), which would increase our best-fitting value for $A(V)_{\rm DLA}$.

6.4.2 Depletion of Iron relative to Zinc

Following Vladilo et al. (2006) and De Cia et al. (2013), we calculated the column density of iron in the dust phase, $\log(\hat{N}_{\rm Fe})$. This quantity is expected theoretically to correlate with $A(V)$, and we used the empirical relation from Vladilo et al. (2006) to calculate $A(V)_{\rm DLA}$ assuming that the intrinsic abundance ratio of (Fe/Zn) is Solar. Although zinc is usually assumed to be depleted very little onto dust grains, and as such a good estimator of the volatile elements, this is not the case for high metallicity systems. For around Solar metallicity and above, even zinc may show signs of weak depletion (Vladilo et al. 2006). In order to correct for this differential depletion of both iron and zinc, we assumed that the depletion of iron and zinc follow that of the interstellar medium in the Milky Way, see De Cia et al. (2013). Given the high metallicity inferred from zinc ([Zn/H] $= -0.09$), both the Solar intrinsic abundance ratio and the Galactic depletion pattern are valid assumptions. We measured a high depletion of [Fe/Zn] $= -1.22 \pm 0.06$, from which we inferred an amount of dust extinction of A(V) $= 0.39^{+0.13}_{-0.10}$ mag. We note that neglecting differential depletion of zinc relative to iron for such high metallicities would underestimate $A(V)$ by 0.11 mag. This value is consistent with, although slightly higher than, the value of $A(V)$ inferred from template fitting in the previous section. The intrinsic ratio of [Zn/Fe] has been studied extensively (for a recent study, see Berg et al. 2015), and a large spread is generally observed. Berg et al. (2015) show that the intrinsic [Zn/Fe] ratio is most probably *lower* than Solar. This would lead to a higher $A(V)$ in this case. Even with a higher than Solar intrinsic ratio of [Zn/Fe] ($+0.2$ dex), the high level of depletion observed in this DLA requires a significant amount of dust in order to reconcile the observed zinc-to-iron ratio with the intrinsic ratio.

6.5 The DLA Galaxy Counterpart

In order to identify the galaxy associated with the DLA we have searched for stellar continuum emission in broad-band imaging as well as nebular emission lines in the X-shooter spectrum. However, the bright background quasar impedes detection of the faint glow from the DLA galaxy, and it is therefore necessary to subtract as much of the quasar's light as possible. The methods utilized for this subtraction is described below for each dataset.

6.5.1 Optical Imaging

For the broad-band images, we had to replicate the point spread function (PSF) in order to subtract the point-like quasar emission. In the NOT r'-band image, we modelled the PSF by combining bright, though not saturated, stars in the field. The light from the quasar was then subtracted using this empirical PSF. This way we could probe the regions closer to the quasar. However, the central part (within $0\farcs9$) was still not accessible due to strong residuals from the PSF subtraction. The PSF subtracted r'-band image is shown in Fig. 6.7. In the residual image, we observed no emission consistent with that of a DLA galaxy. However, when smoothing the image with a Gaussian filter we detect a fuzzy blob of emission around 4 arcsec South-West of the quasar. This extended emission is consistent with the

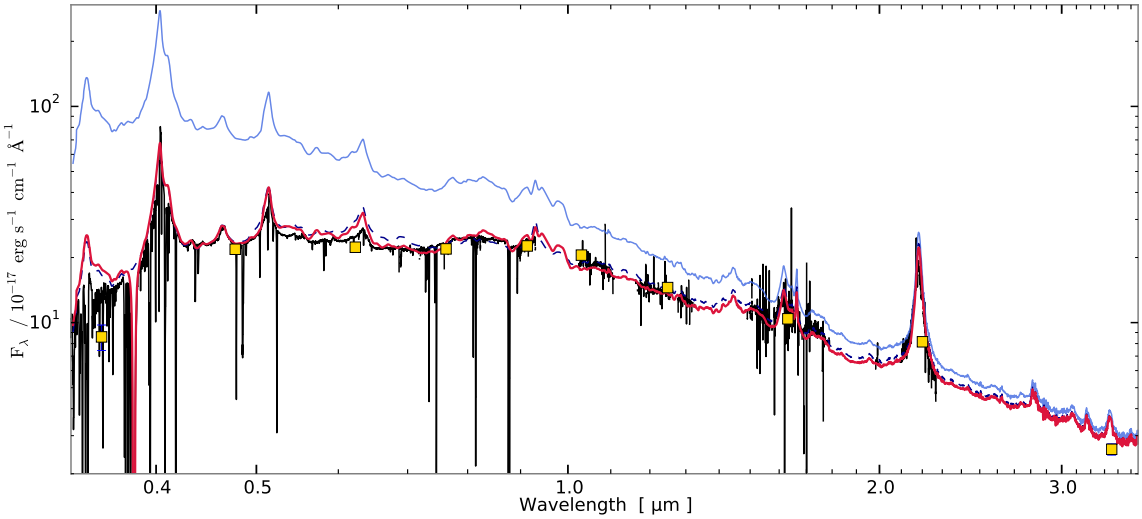

Figure 6.6: The X-shooter spectrum of quasar J 2225+0527 shown in black together with the photometry from SDSS, UKIDSS, and WISE band 1 (shown in yellow squares, the errorbars are too small to be seen). The spectrum in the top panel has been smoothed for presentation purposes. The telluric absorption regions in the near-IR (at ∼1.0, 1.1, 1.5 and 1.9 μm) have been masked out. The blue solid curve shows the unreddened quasar template, and the red solid curve shows the same template assuming the best-fitting dust model with iron emission and Lyα absorption included, see Sect 6.4. For reference, the blue dashed line shows the best-fitting dust model without including the iron emission template. The largest offset between the red and the dashed line is observed around the C III] emission line at ~ 0.6 μm.

Lyα nebula observed by Heckman et al. (1991), and moreover is located at the same spatial position as the extended radio lobes reported by Barthel et al. (1988). We therefore ascribe this extended emission to the C III line of the Lyα nebula, rather than emission from the DLA galaxy. Hence, the DLA galaxy remains undetected down to a limit of $m_{\rm AB} > 24.79$ mag (3 σ limit). Since we were not able to probe the region closest to the quasar we used apertures placed around the quasar at a distance of 1.″9 from the quasar to estimate the flux limit. This corresponds to a physical separation of 16 kpc at the redshift of the DLA. The observed r'-band probes flux at $\sim$ 1900 Å in the rest-frame of the DLA galaxy. This part of the UV continuum is sensitive to recent star formation, and the flux limit thus allows us to constrain the star-formation rate using Kennicutt (1998). First we applied a correction for Galactic extinction of $A_{r'} = 0.347$ from the maps of Schlafly & Finkbeiner (2011), and converted the corrected flux to a luminosity given the luminosity distance for $z = 2.13$. Finally, we converted the luminosity to star-formation rate (using Chabrier initial mass function) correcting for dust in the DLA assuming an extinction of 1.5 mag at rest-frame 1900 Å. This way we obtained a 3σ limit on star formation rate of SFR < 21 M$_\odot$ yr^{-1}, under the assumption that the impact parameter is more than 16 kpc. For smaller impact parameters, the star formation rate may be even higher.

6.5.2 Near-infrared Imaging

Due to the lack of suitable PSF stars in the small field of view of the Keck AO images we used the quasar itself to make an azimuthally averaged radial PSF profile. We then generated a spherically symmetric PSF from the average radial profile for each image and subtracted the model PSF from the images. In the H and K' images, we observed a small excess flux at roughly 0.″5 south of the quasar's centroid, see Fig. 6.8. The emission was observed at the same location in the two images, which is not expected for

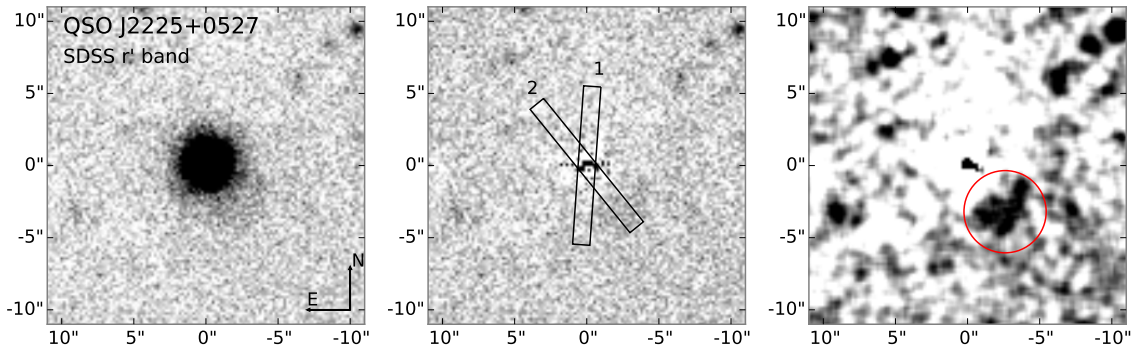

Figure 6.7: *r'*-band image from the Nordic Optical Telescope of the quasar J 2225+0527. The three panels show (left to right) the combined image, the residuals after subtraction of the point spread function, and the residual image smoothed by a (5×5 pixel^2) Gaussian filter with $\sigma_{\rm filter} = 2$ pixels. In the middle panel, the two slit positions used for the X-shooter observations are shown as rectangles. In the right panel, an extended excess of emission is visible about 4 arcsec southwest of the quasar (marked by a red circle).

a random excess due to a spurious peak in the residuals. We thus regarded this as a tentative detection of the DLA galaxy counterpart. We extracted the flux from the small excess by fitting a 2-dimensional Gaussian model to the excess emission. By using the measured flux of the quasar in UKIDSS photometry as reference, we obtained the following magnitudes for the tentative DLA counterpart: $H = 23.6$ and $K' = 23.8$ mag, both on the AB system. The PSF in the J band image was less symmetric than in the other two AO images. This made the PSF modelling more difficult to perform; As a result, we did not obtain a good subtraction of the PSF and no excess emission was observed in the J-band at the same position.

6.5.3 X-shooter Spectroscopy

In order to detect weak nebular emission lines from the DLA galaxy in the spectrum, we subtracted the quasar trace from the 2-dimensional spectrum following the method in Krogager et al. (2013). We did not detect any emission from the nebular lines Hα, Hβ or [O III] at the redshift of the DLA in our X-shooter spectrum. We obtained flux limits for [O III] $\lambda5007$ and Hα of $F_{\rm O\,III} < 5.3\times10^{-17}$ erg s^{-1} cm^{-2} (3σ) and $F_{\rm H\alpha} < 16.5\times10^{-17}$ erg s^{-1} cm^{-2}, respectively. The spatial extent of the aperture used for the flux limit estimation was determined from the width of the spectral trace (FWHM = 5 pixels at the location of Hα). We used an aperture size of twice the FWHM (1.5 arcsec) centred on the position of the quasar. In the spectral direction, we used the velocity width of the absorption lines (330 km s^{-1}) centred around the absorption systemic redshift $z_{\rm sys} = 2.132489$. This provides a conservative upper limit which takes into account the fact that we do not know the exact emission redshift, however, the emission redshift is probably within the velocity spread observed in the different absorption components. Also, we assumed that the emission is at very small impact parameter, which seems plausible given the hints from the Keck imaging described above. Unfortunately the Hα line is located in a region of Telluric absorption lines. The flux limit is therefore not very constraining; However, it still allows us to put a limit on the star formation rate by using the relation from Kennicutt (1998). This yields an upper limit on the star formation rate of SFR$_{\rm H\alpha} < 29$ M$_\odot$, assuming Chabrier IMF and correcting for dust.

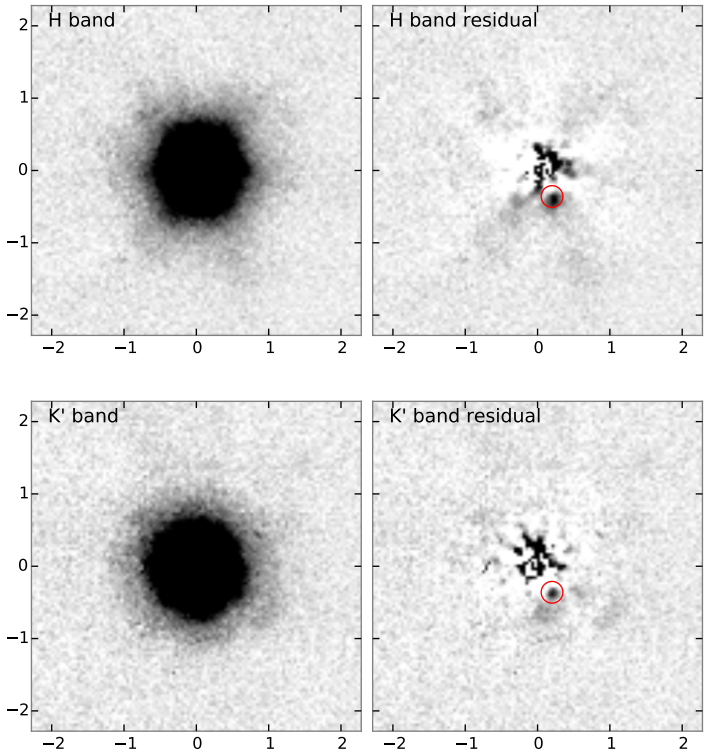

Figure 6.8: Keck AO images of the quasar J 2225+0527 in H and K' bands. The left and right panels in each row show, respectively, the image before and after subtraction of a model PSF (see text). Each images are oriented North to the top and East to the left. The red circle in each residual image marks the location of the tentative detection of the emission counterpart of the DLA at redshift $z = 2.13$. The radial structure observed in the H-band residuals is an artefact of the circular averaging of the PSF. The J-band image did not result in a successful PSF subtraction and is therefore not shown.

6.6 Discussion

The quasar observed in this work, although identified in previous radio catalogs, was missing in the SDSS quasar database due to significant amounts of dust causing the optical colours of the quasar to appear stellar-like in the SDSS colour spaces. However, since the quasar is a radio-loud quasar it would be expected to appear in the SDSS database. The reason why this quasar does not appear in SDSS is that the cross matching of SDSS and the FIRST radio catalog was performed in 2008, whereas Q2225+0527 was not observed until 2009. It is thus an unfortunate coincidence of various factors that resulted in the misclassification of Q2225+0527 in the SDSS database.

The foreground DLA at $z = 2.13$ was first reported by Barthel, Tytler, & Thomson (1990) and later by Junkkarinen, Hewitt, & Burbidge (1991) and Ryabinkov, Kaminker, & Varshalovich (2003); However, the dust reddening towards the quasar has so far not been studied in detail. Based on the detection of C I and H_2 together with high depletion from [Zn/Fe], we had strong evidence for dust in the DLA. This was further bolstered by our spectral fitting. Models with dust in the DLA were preferred to those with dust only in the quasar at more than 5 sigma. We found the DLA to be of Solar metallicity with $[\mathrm{Zn/H}] = -0.09 \pm 0.05$ and we inferred a dust-to-gas ratio of $\mathrm{A(V)}/N(\mathrm{H\,I}) = 5.5 \times 10^{-22}$ mag cm^2 consistent with that of the local ISM ($4 - 6 \times 10^{-22}$ mag cm^2; Liszt 2014). This value of dust-to-gas ratio is much higher than the average DLA ($\mathrm{A(V)}/N(\mathrm{HI}) = 2-4\times10^{-23}$ mag cm^2; Vladilo et al. 2008).

This shows that dusty DLAs indeed do exist and that they are, to some degree, missed in optically selected quasar samples. The quasar studied here is intrinsically very bright and red (among the top 0.1 per cent most luminous and top 1 per cent most red quasars at these redshifts, see left panel of Fig. 6.9). A bias against dusty DLAs, and absorption systems in general, is therefore not only limited to the faint end of the quasar luminosity function. The bright quasars are also affected due to the reddening caused by dust allowing the quasars to escape detection by optical colour criteria. To illustrate the effect of the reddening along the line of sight, we show the $u - g$ vs. $g - r$ colour-colour diagram in the right panel of Fig. 6.9. The colour criteria used by SDSS are not easily translated to this two-dimensional colour space, since the selection is performed in a higher dimensional colour space. However, the distribution of points are highly concentrated in the blue part of the diagram. The individual points at redder colours are added to the SDSS sample by various other criteria such as radio selection (for comparison, see Richards et al. 2001, 2002). When correcting the observed colours of Q2225+0527 for the dust reddening introduced by the DLA, we find that the intrinsic colours of the quasar is consistent with the bulk of the optically selected quasars of SDSS.

Owing to its very bright radio emission, the quasar presented here was identified in radio surveys. However, only about 10 per cent of quasars are radio loud (Baloković et al. 2012). Hence, more dusty absorbers might be missing toward red, radio quiet quasars. The DLA presented here is similar to the recent sample of neutral carbon absorbers by Ledoux et al. (2015, in press) both in terms of C I abundance and dust extinction. These authors also argue that the most dusty absorption systems are missing in current samples selected using optical criteria. Any bias in the current DLA samples will affect the metal-rich end of the DLA distribution, since these are on average more dusty. A dust bias is therefore not a significantly affecting the average metal-poor DLAs. This is consistent with what has been found in radio surveys of DLAs (Ellison et al. 2001; Jorgenson et al. 2006), i.e., dust biasing does not have a strong effect on the bulk of the DLA population.

6.6.1 Partial Coverage and Size of the BLR

In Sect. 6.3.1, we derived the line flux residual from the C I absorption lines. If we interpret the LFR as a geometric effect caused by partial coverage of the background emitting source (in this case the broad line region of C IV) then the LFR can be converted to a covering fraction. Other explanations for the LFR would be gravitational lensing of the quasar or a double quasar, see the discussion in Balashev et al. (2011). As argued in Sect. 6.3.1 we favour the geometric effect since the other scenarios require a somewhat unlikely conspiracy of alignments. However, with the current data, we cannot exclude the other scenarios and we caution the reader that the following exercise is merely suggestive.

Given the covering fraction of 27 ± 6 per cent of the BLR, inferred in Sect. 6.3.1, we can calculate the size of the BLR assuming a simple spherical geometry of both the absorbing cloud and the BLR, as depicted in the schematic view of Fig. 6.4. A prerequisite for this calculation is the physical size of the absorbing cloud, which we can estimate from the fine structure levels of C I. These fine structure levels are excited by the background radiation field and by collisions with other species predominantly hydrogen (both atomic and molecular). The population of the various levels will therefore depend on the density and temperature of the gas. In the following, we assume that neutral carbon arises from the cold self-shielding cloud where molecular hydrogen is the primary collisional partner. We then use the numerical code POPRATIO (Silva & Viegas 2001) to calculate the population of various fine-structure levels for a grid of temperatures ($50-500$ K) and densities ($1-1000$ cm^{-3}). Assuming that the column

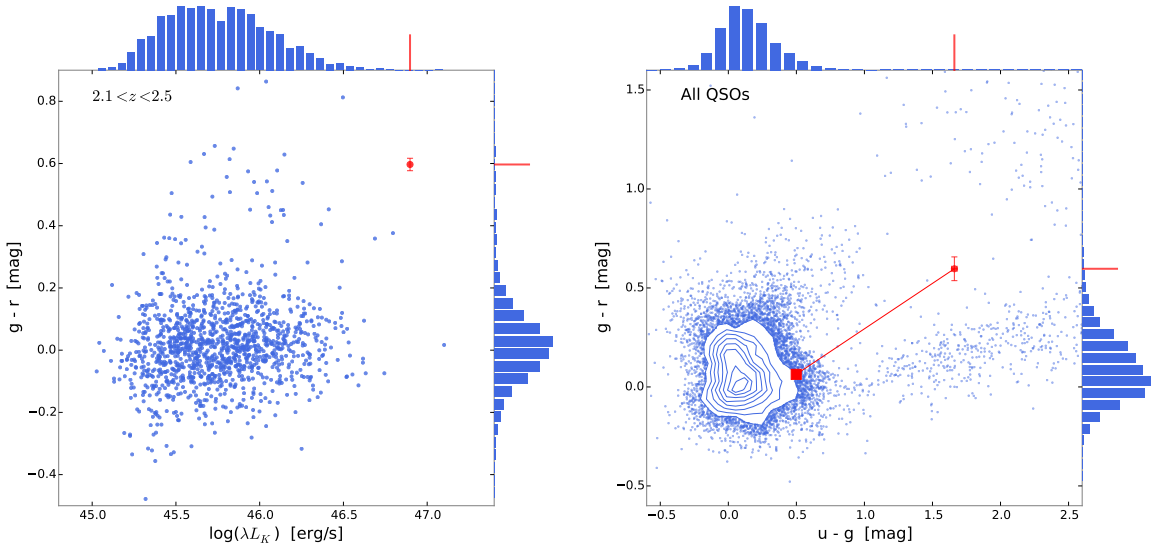

Figure 6.9: Distribution of $g-r$ colour and K-band luminosity for quasars with redshifts from $2.1 < z < 2.5$ (*left*). Distribution of $u-g$ and $g-r$ colours from all quasars with spectroscopic redshifts (*right*). Both sets of quasars are selected from the sample of Peth, Ross, & Schneider (2011). The quasar presented in this work is shown by a red circle. In the right panel, we show the unreddened colours of the quasar Q2225+0527 assuming an amount of dust of $A(V) = 0.28$ at the redshift of the DLA (large red square connected by a line to the observed point). All magnitudes have been corrected for Galactic extinction. It is evident that the unreddened colours of the quasar are consistent with the overall population of SDSS quasars.

densities derived in Sect. 6.3.1 trace the physical densities, i.e., $N(\mathrm{C\,I})/N(\mathrm{C\,I^*}) = n(\mathrm{C\,I})/n(\mathrm{C\,I^*})$, we can then calculate the allowed range in temperature and density ($n_{\mathrm{H_2}}$). The temperature and density are highly degenerate and the temperature remains unconstrained, though typical values for the cold, neutral phase lie in the range of $50-200$ K. However, we obtain a range of allowed densities from 90 to 400 cm^{-3} with a most probable density around 100 cm^{-3} for $T = 100$ K.

With the physical density of H_2 at hand, we can infer a physical length scale of the small absorbing cloud from the ratio of column density to volumetric density: $l_{\mathrm{cloud}} = N/n \approx 0.1$ pc. We assume that the cloud is spherically symmetric with radius $r_{\mathrm{cloud}} = l_{\mathrm{cloud}}/2$. In projection as shown in the top right panel of Fig. 6.4, the system will therefore appear like two overlapping disks with an offset between the two centres, Δl. Since we do not know this projected separation we calculate a grid of various separations and radii of the BLR. For each grid point, we can then evaluate the covering fraction of the BLR by the small cloud of radius $r_{\mathrm{cloud}} = 0.05$ pc. Since the quasar and absorbing cloud are independent the projected separation between the centres of the two disks will be randomly distributed. For the spherically symmetric geometry that we assume, the probability of a given Δl will depend linearly on the separation $p(\Delta l) \propto \Delta l$, i.e., there is zero probability of a perfect alignment. We furthermore require $\Delta l \leq r_{\mathrm{cloud}}$ since the continuum source (the accretion disk) in the centre of the BLR must be covered by the absorbing cloud. These two requirements serve as our prior on the separation: $p(\Delta l) = 2\Delta l/r_{\mathrm{cloud}}^2$ for $\Delta l \leq r_{\mathrm{cloud}}$ and $p(\Delta l) = 0$ for $\Delta l > r_{\mathrm{cloud}}$. Given the measurement of the covering fraction we can convert the 2-dimensional grid of covering fraction as a function of R_{BLR} and Δl to a likelihood function. By multiplying the likelihood function with the prior on Δl and marginalizing over all separations, we obtain the most probable radius of the C IV broad line region, $R_{\mathrm{BLR}} = 0.1$ pc. However, given the large uncertainties on the density and temperature, the size of the cloud (and thereby the size of the BLR) is not constrained to better than a factor of $\sim$2, i.e., $R_{\mathrm{BLR}} \approx 0.05 - 0.2$ pc.

From the observed correlation between the physical size of the broad line region and luminosity, we can furthermore calculate the radius of the BLR. We use the relation for C IV from Kaspi et al. (2007), who quantify the relation in terms of the luminosity at 1350 Å. In the X-shooter spectrum, we measure $\lambda L_\lambda(1350) = 3.48 \times 10^{46}$ erg s^{-1}, which corresponds to $R_{\rm BLR} = 0.17$ pc with an uncertainty of 54 % dominated by the scatter in their calibration. This is slightly larger than our estimated size from the covering fraction, however, consistent within the 1σ scatter of the radius-luminosity relation. The good agreement between the two size estimates provides evidence for the partial coverage due to the small projected size of the cloud compared to the BLR, despite the very simple geometry.

6.6.2 Stellar Mass of the DLA Galaxy

The velocity structure of the absorbing gas contains 10 individual components spread over a total range of 397 km s^{-1}. Such a wide span of velocities is in fact quite common for absorbers with a similar high metallicity (Ledoux et al. 2006), and it is believed to be related to the deep potential well of the massive dark matter haloes that host high metallicity galaxies (Møller et al. 2013; Arabsalmani et al. 2015). In Sect. 6.3, we quantified the velocity width of the system using $\Delta\, V_{90}$ for which we obtain a value of 331 km s^{-1}. The resolution of X-shooter at the observed wavelength of the line is 27.2 km s^{-1}, and we use the method described by Arabsalmani et al. (2015) to correct the $\Delta\, V_{90}$ measured and obtain the intrinsic value $\Delta\, V_{90} = 329$ km s^{-1}.

The $\Delta\, V_{90}$ has been shown to correlate with metallicity, a correlation which depends on the redshift (Ledoux et al. 2006). The evolution of the zero-point of the relation is shown in Fig. 6.10 (black points and full red line from Møller et al. (2013)). The 1σ of the intrinsic scatter of the relation is marked by the dashed red lines, and the DLA (blue star) is seen to lie well within this scatter. Christensen et al. (2014) confirmed the expectation that the relation in reality is a mass-metallictiy relation, and using the prescription from Christensen et al. (2014), and [M/H] = -0.1, we obtain a stellar mass of $\log(\mathrm{M}_\star/\mathrm{M}_\odot) = 10.78 \pm 0.55$ which is among the few most massive DLA galaxies known at any redshift. We note that because we do not know the impact parameter for this galaxy we use the average value 0.44 for $C_{\rm [M/H]}$. In case the true impact parameter is very small, $C_{\rm [M/H]}$ would be somewhat smaller and likewise then the stellar mass (as discussed below).

Comparing to the three known DLA galaxies at similar redshifts (Christensen et al. 2014, Tables 2 and 3), those have masses computed from the same formula in the range $\log(\mathrm{M}_\star/\mathrm{M}_\odot) = 9.9 - 11.0$, and rest-frame optical AB magnitudes of 23.6, 24.4, and 25.2. In case we assume that the DLA galaxy in our case is perfectly aligned with the quasar (i.e., impact parameter of zero) then we can use equation (3) from Christensen et al. and obtain the lowest possible stellar mass of $\log(\mathrm{M}_\star/\mathrm{M}_\odot) = 10.00$. This is still a very high stellar mass for a DLA galaxy, but the galaxy would remain hidden under the glare of the quasar.

We searched for the emission counterpart of the DLA both in the X-shooter spectrum and in imaging. From the spectrum we only obtained upper limits on the [O III] and Hα line fluxes, and the r'-band image only provided a flux limit for impact parameters larger than 16 kpc. Interestingly, we observed tentative signs of the emission counterpart in the near-infrared AO images in the H and K' bands. Although this is highly uncertain given the relatively simple PSF subtraction, it is however reassuring that the excess emission is observed at the same spatial location in the two images. We can thus speculate that the DLA is associated with the excess emission observed in the near-infrared images at an

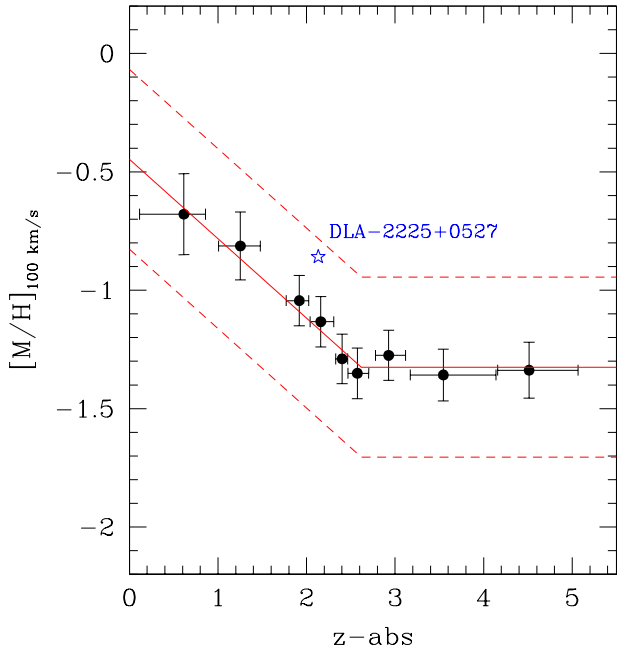

Figure 6.10: Comparison to the redshift evolution of the global metallicity-ΔV_{90} relation of DLAs. Black dots and full red line marks the binned data and simple linear fit, red dashed lines mark the 1 σ internal scatter of the relation (from Møller et al. 2013). DLA-2225+0527 is seen to lie well within the general distribution of intervening DLAs.

impact parameter of roughly 4 kpc. The inferred H-band magnitude of the emission counterpart would then be 23.6 mag which is in good agreement with the observed fluxes in the sample of Christensen et al. (2014). In previous studies of emission counterparts of DLAs, we inferred star formation rates of 13 and 27 $M_\odot$ yr^{-1} (Krogager et al. 2013; Fynbo et al. 2013b) for DLAs with slightly lower metallicities of [Zn/H] ≈ -0.5. The upper limit on the star formation rate of SFR < 29 $M_\odot$ yr^{-1} derived in Sect. 6.5 is therefore consistent with previous detections.

6.7 Summary and Conclusion

In this work, we presented imaging and spectroscopic observations of the quasar J 2225+0527 and found that the DLA at $z = 2.13$ has high metallicity (consistent with Solar), high level of depletion (inferred from [Fe/Zn]), and strong molecular hydrogen absorption. Moreover, we detected neutral carbon absorption lines showing signs of partial coverage due to the projected size of the absorbing cloud being small compared to the background source. By deriving the covering fraction and a rough size estimate of the absorbing cloud, we were able to infer the size of the broad line region of C IV in the quasar to be 0.10 ± 0.03 pc. This is consistent with the estimate from the radius-luminosity relation from Kaspi et al. (2007) to within the $1\,\sigma$ scatter of 54 per cent of their relation.

From the depletion ratio, we estimated the amount of dust in the DLA to be $\mathrm{A(V)} = 0.39^{+0.13}_{-0.10}$ mag. Spectral modelling of the quasar resulted in a best-fitting A(V) of $\mathrm{A(V)_{DLA}} = 0.28$ mag with no dust in the quasar itself. We therefore concluded that the reddening of the quasar is caused by dust located in the DLA, and that this reddening caused the quasar to be misclassified as a star in SDSS.

We observed tentative evidence for an emission counterpart to the DLA in the near-infrared H and K' band images at an impact parameter of roughly $0\farcs5$ or 4 kpc. The flux of the tentative DLA galaxy in the H-band was estimated to be roughly 23.6 AB mag. This corresponds to a stellar mass of roughly $10^9 - 10^{10}$ $M_\odot$ consistent with the estimate from the mass-metallicity relation of Christensen et al. (2014).

The quasar studied in this work, although identified previously in radio surveys, was misidentified as a star in SDSS due several factors. Had this been a more typical quasar in terms radio-loudness, the quasar would have been missed by the optical criteria utilized by SDSS and furthermore missed by radio surveys. Therefore, enriched and dusty galaxies detected in absorption towards quasars are underrepresented in the current optically selected samples. This has important implications for the mapping of chemical enrichment, as it introduces a bias against the most enriched systems at high redshift. The impact of this bias, i.e., the frequency of dusty DLAs, is still to be determined quantitatively, however, radio surveys have shown that the bias is not affecting the bulk of the DLA distribution significantly.

Acknowledgments

We thank Marianne Vestergaard for insightful discussion and for sharing her iron emission template with us. We thank the ESO Director General for allocating our observing program under the director's discretionary time. The Dark Cosmology Centre is funded by the DNRF. The research leading to these results has received funding from the European Research Council under the European Union's Seventh Framework Program (FP7/2007-2013)/ERC Grant agreement no. EGGS-278202. Based on observations made with the Nordic Optical Telescope, operated by the Nordic Optical Telescope Scientific Association at the Observatorio del Roque de los Muchachos, La Palma, Spain, of the Instituto de Astrofisica de Canarias. Based on Very Large Telescope observations carried out at the European Organisation for Astronomical Research in the Southern Hemisphere, Chile under DDT program 293.A-5033. Some of the data presented herein were obtained at the W.M. Keck Observatory, which is operated as a scientific partnership among the California Institute of Technology, the University of California and the National Aeronautics and Space Administration. The Observatory was made possible by the generous financial support of the W.M. Keck Foundation.

6.A Absorption Lines

The full list of identified absorption lines belonging to the DLA is given in Table 6.4. We further quote the equivalent widths for each line.

Table 6.4: List of absorption lines from the $z = 2.13249$ DLA.

Transition	EW[a]
Fe II, λ1144	0.623±0.009
S II, λ1250[b]	<0.392±0.007
S II, λ1253	0.339±0.005
S II, λ1259 + Si II + Fe II, λ1260	2.294±0.006
O I, λ1302 + Si II, λ1304	3.157±0.004
C II, λ1334 + C II*, λ1335	2.243±0.006
Ni II, λ1370	0.105±0.005
Ni II, λ1454	0.045±0.004
Al II, λ1670	1.967±0.004
Ni II, λ1709	0.074±0.005
Ni II, λ1741	0.119±0.004
Si II, λ1526	1.662±0.006
Fe II, λ1608	0.754±0.004
Si II, λ1808	0.184±0.008
Co II, λ1941	<0.018 (3 σ)
Co II, λ2012[b]	<0.04±0.02
Mg I + Zn II, λ2026	0.276±0.006
Cr II, λ2056	0.055±0.007
Cr II + Zn II, λ2062	0.137±0.006
Fe II, λ2249	0.042±0.005
Fe II, λ2260	0.086±0.005
Fe II, λ2344	1.899±0.005
Fe II, λ2374	0.946±0.004
Fe II, λ2382	2.682±0.003
Mn II, λ2576	0.160±0.004
Fe II, λ2586	1.741±0.004
Mn II, λ2594	0.144±0.004
Fe II, λ2600[b]	2.973±0.003
Mn II, λ2606[b]	0.278±0.003
Mg II, λ2796	4.759±0.005
Mg II, λ2803	4.350±0.005
Mg I, λ2852	0.909±0.005
Cl I, λ1347	0.060±0.005
C I + C I* + C I**, λ1328	0.231±0.004
C I + C I* + C I**, λ1560	0.216±0.004
C I + C I* + C I**, λ1656	0.390±0.003
N I, λ1199 + N I,λ1200	2.228±0.010
N I, λ1134.4	1.451±0.009
C IV, λ1550, 1548	2.924±0.007
Al III, λ1854	0.559±0.009
Al III, λ1862	0.392±0.009
Si IV, λ1393	1.041±0.006
Si IV, λ1402	0.645±0.006

[a] Rest-frame equivalent width in units of Å.
[b] Contaminated line.

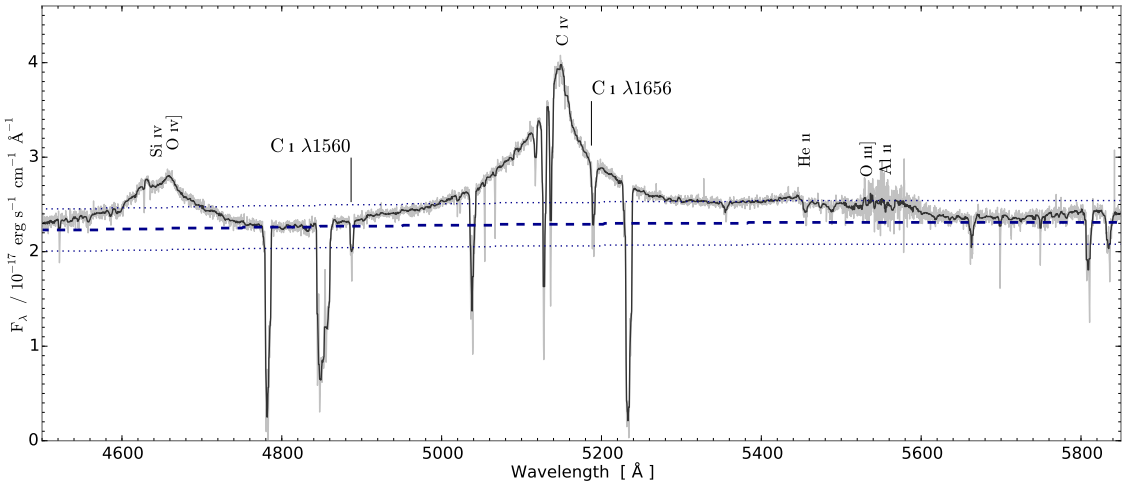

Figure 6.11: Spectrum of QSO J 2225+0527 around the C IV emission line. The spectrum has been smoothed by a 21 pixel median filter for clarity (the dark grey line). The lighter grey underlying line indicates the spectrum before smoothing. The two absorption line complexes from C I are marked. The estimated quasar continuum is shown by the dashed line. The conservative uncertainty of 10 per cent is shown by the dotted lines. The vertical labels indicate the strongest emission lines from the quasar.

6.B Continuum Determination

The continuum flux of the quasar around the C IV line is obtained by interpolation of relatively emission-line free regions. This is however very uncertain, as many broad and weak lines can blend together, which may create a so-called *pseudo continuum*. For this reason we assume a conservative uncertainty of 10 per cent for the placement of the continuum. The estimated continuum is shown in Fig. 6.11.

7

The size evolution of massive, evolved galaxies from redshift 2 to 0

This chapter contains the following article:

"A spectroscopic sample of massive, quiescent $z \sim 2$ galaxies: Implications for the evolution of the mass–size relation"

Published in *The Astrophysical Journal, vol. 797, id. 17, 2014.*

Authors:

J.-K. Krogager, A. W. Zirm, S. Toft, A. Man, & G. Brammer

We present deep, near-infrared *Hubble Space Telescope*/Wide Field Camera 3 grism spectroscopy and imaging for a sample of 14 galaxies at $z \approx 2$ selected from a mass-complete photometric catalog in the COSMOS field. By combining the grism observations with photometry in 30 bands, we derive accurate constraints on their redshifts, stellar masses, ages, dust extinction and formation redshifts. We show that the slope and scatter of the $z \sim 2$ mass–size relation of quiescent galaxies is consistent with the local relation, and confirm previous findings that the sizes for a given mass are smaller by a factor of two to three. Finally, we show that the observed evolution of the mass–size relation of quiescent galaxies between $z = 2$ and 0 can be explained by quenching of increasingly larger star-forming galaxies at a rate dictated by the increase in the number density of quiescent galaxies with decreasing redshift. However, we find that the scatter in the mass–size relation should increase in the quenching-driven scenario in contrast to what is seen in the data. This suggests that merging is not needed to explain the evolution of the median mass–size relation of massive galaxies, but may still be required to tighten its scatter, and explain the size growth of individual $z = 2$ quiescent galaxies.

7.1 Introduction

Over the past decade, studies of the $z \sim 2$ Universe have been revolutionized by the availability of deep near-infrared (NIR) imaging surveys. One of the primary early results was the discovery of a population of optically-faint, massive galaxies which are missed in optical (rest-frame UV) surveys (Franx et al. 2003; Daddi et al. 2004; Wuyts et al. 2007). Large photometric surveys have since shown that at $z = 2$, roughly half of the most massive ($\log \mathrm{M}/\mathrm{M}_{\odot} > 11$) galaxies are dusty and star-forming, and half are old, quiescent systems (e.g. Franx et al. 2008; Toft et al. 2009; Williams et al. 2010; Brammer et al. 2011), a result that has been confirmed through low resolution spectroscopy of a small sample of the brightest examples (Kriek et al. 2008, 2009a,b).

Using high-resolution NIR imaging, it was shown that most of the quiescent galaxies at $z > 2$ have effective radii, r_e, a factor of $2 - 6$ smaller than local elliptical galaxies with the same stellar masses (e.g., Daddi et al. 2005; Trujillo et al. 2006; Zirm et al. 2007; Toft et al. 2007; Buitrago et al. 2008; van Dokkum et al. 2008b; Szomoru et al. 2010; Cassata et al. 2011; Bruce et al. 2012; Newman et al. 2012). Their inferred stellar mass densities (within r_e) therefore greatly exceed those of local galaxies at the same stellar mass. However, recent studies show that if one compares the stellar densities within the inner 1 kpc the discrepancy is much less pronounced (Bezanson et al. 2009; Patel et al. 2013). The discovery that the inner regions of these massive galaxies correspond well with their local counterparts supports the so-called *inside-out* scenario, in which galaxies form at high redshift as compact galaxies presumably from a gas rich merger funnelling the gas to the center and igniting a massive, compact star burst (e.g., Hopkins et al. 2006; Wuyts et al. 2010). These resulting compact stellar cores subsequently grow by adding mass to their outer regions. How this size growth is accomplished is the big question; A cascade of merger events with smaller systems, known as minor merging, is a plausible explanation as simulations have shown that it is possible to obtain the needed mass increase in the outer regions while leaving the central core mostly intact (Oser et al. 2012). However, observations of the merger rate of massive galaxies between $z = 2$ and 0 do not find as many mergers as required to account for the observed size evolution (Man et al. 2012; Newman et al. 2012).

Some studies of high-redshift, quenched galaxies have suggested that their structure may differ from that of local elliptical galaxies when quantified using a Sérsic profile. Chevance et al. (2012) find that the high-z galaxies show lower Sérsic indices ($n \sim 2$ on average) than the local population of ellipticals ($n \sim 4$), see also Weinzirl et al. (2011). This is further supported by the detection of galaxies at redshift $z \sim 2.5$ with apparently disc-like morphologies (Stockton, Canalizo, & Maihara 2004; Stockton et al. 2008). This has motivated suggestions that the high-z population might be more disc-like and hence might contain a faint, extended stellar component which would be undetected in present observations due to cosmological surface-brightness dimming (van der Wel et al. 2011). Deeper and higher resolution imaging, along with image stacking, has confirmed that the massive, red galaxies indeed are compact, and has failed to detect any extended stellar haloes around these compact cores (van Dokkum et al. 2008b, 2010). Moreover, Szomoru, Franx, & van Dokkum (2012) find Sérsic indices for galaxies at high redshift ($z \sim 2$) consistent with the local values. They report a median value for the Sérsic indices at high redshift of $n = 3.7$.

Now, with the advent of the next generation of NIR spectrographs on 8-m class telescopes, we can study the stellar populations via continuum detections and absorption line indices (Toft et al. 2012; Onodera et al. 2012; van de Sande et al. 2013; Belli, Newman, & Ellis 2014; Belli et al. 2014, Zirm et al.

in prep); The quiescent galaxies can be further sub-divided into post-starbursts (those that show strong Balmer absorption lines) and more evolved systems with metal absorption lines. However, even with state-of-the-art instrumentation, target samples are limited to the rare and bright examples.

Grism spectroscopy from space with *Hubble Space Telescope* (*HST*) allows us to obtain redshifts for fainter, less massive examples of $z \sim 2$ galaxies. While these data have poor spectral resolution, they do not suffer from the strong atmospheric emission lines, poor transmission and bright background that limit ground-based observations. A near-infrared spectroscopy survey, 3D-HST, has recently been carried out using the Wide Field Camera 3 (WFC3) onboard the *HST*. The survey provides imaging in the F140W-band and grism observations in the G141 grism. In total the survey provides rest-frame optical spectra of ∼7000 galaxies in the redshift range from $z = 1 - 3.5$. Moreover, the pointings cover approximately three quarters of the deep NIR survey, CANDELS (Grogin et al. 2011; Koekemoer et al. 2011). The combination of imaging and spectroscopic data from 3D-HST and CANDELS allows for powerful analysis of the redshift $1 < z < 3.5$ Universe. For more details about the 3D-HST survey, see Brammer et al. (2012).

Until now, spectroscopic samples of quiescent, high-redshift galaxies with structural data have been sparse; van Dokkum et al. (2008b) presented a sample of nine galaxies at $z \sim 2$, Gobat et al. (2013) presented five quiescent galaxies from a proto-cluster at $z = 2$, Tanaka et al. (2013) presented spectroscopy of a $z = 2.16$ proto-cluster with four quiescent members, and recently Belli et al. (2014) presented a sample of 6 quiescent galaxies at $2 < z < 2.5$. At slightly lower redshifts Onodera et al. (2012) presented sample of 18 quiescent galaxies at $z \sim 1.6$ and Belli, Newman, & Ellis (2014) presented a large sample of 103 galaxies with redshifts $0.9 < z < 1.6$. Samples of $z \sim 2$ quiescent galaxies with measured velocity dispersions and dynamical masses are even smaller; so far only a handful of examples have been published (van Dokkum, Kriek, & Franx 2009; Onodera et al. 2010; van de Sande et al. 2011; Toft et al. 2012; Belli et al. 2014).

We have compiled a mass-complete sample ($\log(M/M_{\odot}) > 10.8$) of galaxies in the COSMOS region of the 3D-HST survey. By matching the photometric sample of galaxies to the spectra extracted from the 3D-HST data we can improve the redshift determinations compared to the photometric redshifts used so far. By inferring sizes, redshifts, and stellar population parameters including age, star-formation rate, and mass, we are able to populate the mass–size relation using a mass-complete, quiescent sample of galaxies at $z \sim 2$. This provides strong constraints on what drives the size evolution of the massive galaxies. We explore different physical explanations for the apparent size growth. Specifically, we create a simplistic model to investigate the effect of progenitor bias, i.e., addition of newly quenched, larger galaxies to the mass–size relation, a mechanism proposed by previous studies (Cassata et al. 2011; Trujillo, Carrasco, & Ferré-Mateu 2012; Poggianti et al. 2013) and recently investigated in detail out to redshift $z \sim 1$ by Carollo et al. (2013).

7.2 Data

The analysis is based on public grism spectroscopy data from the 3D-HST survey from which we have used 25 pointings in the COSMOS field. We have combined the spectroscopic data with photometric data in 30 bands covering 0.15–24 μm from the latest K_s-selected catalog by Muzzin et al. (2013).

The 25 pointings in COSMOS are covered by imaging in the F140W filter and by NIR spectroscopy using the G141 grism providing wavelength coverage from 1.1 μm to 1.6 μm with a spectral resolution of $R \sim 130$ (for a point source) with a sampling of 46.5 Å per pixel. Since these are slitless spectroscopic data the effective resolution depends on the size and morphology of the dispersed source. This results in an effective resolution of the order of $R \sim 50$ due to morphological broadening. Furthermore, we have used the structural parameters from van der Wel et al. (2012) obtained from the WFC3/F160W (H_{160}) images as part of the public CANDELS survey (Grogin et al. 2011; Koekemoer et al. 2011).

7.2.1 Data Reduction

Each pointing was observed in a four-point dither pattern with half-pixel offsets in order to increase the resolution of the final image. Both the undispersed, direct images and the dispersed grism images were observed with this pattern for a total exposure of around 800 sec and 4700 sec for undispersed and dispersed, respectively.

The data sets were reduced using the publicly available pipeline *threedhst* [1] (Brammer et al. 2012). The pipeline handles the combination and reduction of the dithered exposures, source identification using SExtractor, and extraction of the individual spectra. Since we are dealing with slitless spectroscopy some sources will have spatially overlapping spectra. This is handled in the pipeline and each extracted spectrum is provided with an estimate of the amount of contamination from nearby sources. For our analysis, we have subtracted the contaminating flux from the total extracted flux.

We have used the standard extraction parameters in the pipeline except for the final pixel scale used in the call to the IRAF-task `multidrizzle`, where we chose $0\farcs09$ px^{-1} instead of $0\farcs06$ px^{-1}. This was chosen to reduce the noise in the extracted spectra. For further details about the observations and data reduction see Brammer et al. (2012). We used a detection threshold of 4 σ to identify sources in the F140W images.

After the initial reduction we encountered some issues with the background not being flat. We were not able to correct this gradient sufficiently to recover a completely flat background, which meant that some spectra were disregarded due to background issues. However, when we increased the pixel size from $0\farcs06$ px^{-1} to $0\farcs09$ px^{-1} the noise decreased and the background subtraction was performed more successfully. In the process of selecting our sample we removed three sources due to background-subtraction issues. In these cases (IDs 133915, 133784, and 207144) there were discontinuities in the background, that we could not correct for. See appendix 7.A for details.

[1] `http://code.google.com/p/threedhst`

Table 7.1: Description of the full sample of galaxies.

Catalog ID	Grism ID	α (deg)	δ (deg)	z_{phot}	H_{160} (AB mag)	Type
118543	ibhm42.014	150.1039700	2.1864245	$2.09^{+0.12}_{-0.12}$	22.50 ± 0.10	SFG
119753		150.1430800	2.2003083	$1.99^{+0.17}_{-0.16}$	22.00 ± 0.09	QG
121761	ibhm42.243	150.1172600	2.2238793	$1.97^{+0.11}_{-0.10}$	21.96 ± 0.05	SFG
122398	ibhm30.211	150.1539200	2.2323158	$1.95^{+0.10}_{-0.09}$	21.84 ± 0.05	QG
123235	ibhm41.170	150.0981300	2.2428155	$2.01^{+0.21}_{-0.20}$	22.85 ± 0.13	SFG
123324		150.0905500	2.2441640	$2.26^{+0.11}_{-0.12}$	22.54 ± 0.12	SFG
123780		150.0768000	2.2492609	$2.26^{+0.20}_{-0.20}$	22.42 ± 0.18	SFG
123817		150.0765800	2.2496693	$2.13^{+0.13}_{-0.13}$	22.36 ± 0.11	SFG
124168		150.1064100	2.2515926	$2.04^{+0.08}_{-0.10}$	22.65 ± 0.13	SFG
124666	ibhm33.161	150.0656400	2.2609785	$1.98^{+0.10}_{-0.11}$	21.04 ± 0.04	QG
124686		150.0639300	2.2611351	$2.11^{+0.17}_{-0.13}$	21.95 ± 0.06	QG
126073		150.1429400	2.2785251	$2.21^{+0.11}_{-0.09}$	22.15 ± 0.07	QG
126301		150.0778700	2.2811451	$2.05^{+0.11}_{-0.11}$	22.10 ± 0.07	SFG
126824	ibhm40.143	150.1213500	2.2851899	$2.19^{+0.13}_{-0.13}$	22.06 ± 0.09	SFG
126952		150.0705900	2.2892091	$2.28^{+0.27}_{-0.29}$	23.21 ± 0.22	SFG
127466	ibhm51.200	150.1553000	2.2948477	$1.97^{+0.14}_{-0.12}$	22.01 ± 0.07	QG
127603	ibhm51.292	150.1593200	2.2968187	$1.96^{+0.19}_{-0.17}$	22.60 ± 0.11	SFG
127617		150.1196100	2.2958610	$2.07^{+0.07}_{-0.07}$	20.73 ± 0.02	SFG
128061	ibhm54.240	150.0739400	2.2979755	$2.09^{+0.02}_{-0.02}$	20.44 ± 0.02	QG
128093	ibhm54.256	150.0746200	2.3020012	$2.18^{+0.10}_{-0.09}$	21.87 ± 0.05	SFG
128977		150.1122100	2.3140118	$2.23^{+0.20}_{-0.21}$	23.23 ± 0.21	SFG
129022	ibhm52.157	150.0961200	2.3134823	$2.05^{+0.12}_{-0.11}$	21.47 ± 0.04	QG
132654		150.0918400	2.3567889	$1.97^{+0.22}_{-0.21}$	23.04 ± 0.14	QG
133784		150.1292900	2.3695824	$2.03^{+0.22}_{-0.24}$	22.84 ± 0.13	QG
133915		150.1335800	2.3703971	$1.86^{+0.12}_{-0.12}$	21.58 ± 0.05	SFG
134068	ibhm46.116	150.1635700	2.3724642	$2.02^{+0.10}_{-0.09}$	21.89 ± 0.06	SFG
134172		150.1102600	2.3741243	$2.26^{+0.21}_{-0.22}$	22.53 ± 0.12	QG
135214		150.1841100	2.3863766	$1.89^{+0.10}_{-0.10}$	22.23 ± 0.08	SFG
135878	ibhm53.253	150.1085100	2.3938241	$1.94^{+0.09}_{-0.08}$	21.33 ± 0.04	QG
139823		150.1546300	2.4443281	$1.87^{+0.08}_{-0.08}$	20.69 ± 0.02	QG
140122	ibhm35.195	150.0796800	2.4495835	$2.16^{+0.15}_{-0.17}$	21.88 ± 0.05	QG
204878		150.1114000	2.4530017	$2.07^{+0.14}_{-0.12}$	22.48 ± 0.10	SFG
207084		150.1361200	2.4815121	$2.05^{+0.14}_{-0.14}$	21.97 ± 0.07	SFG
207144		150.1395000	2.4818728	$1.91^{+0.13}_{-0.11}$	21.00 ± 0.04	QG

Notes: The galaxy type refers to the UVJ classification as either star-forming (SFG) or quiescent (QG), see Section 1.4.1 for details.

7.3 Sample Selection

We selected all sources in the survey area (25 pointings in the COSMOS field from the 3D-HST survey) from a mass complete sample by Muzzin et al. 2013 with stellar masses larger than $\log(\mathrm{M}_\star/\mathrm{M}_\odot) > 10.8$. Only sources with photometric redshifts in the range of $1.85 < z_{\mathrm{phot}} < 2.3$ were included in order to sort out low-redshift interlopers. The redshift cut ensured that the 4000 Å break will be visible in the spectra, as this is the only strong spectral feature available at this resolution and wavelength coverage. In total we have 34 galaxies above the mass limit with photometric data.

The photometric targets were then matched by coordinates to the catalog of extracted sources in the 3D-HST data. Next step was to sort out incomplete spectra. We required that at least 80per cent of the pixels be well-defined, i.e., non-zero and non-negative. In some cases where the objects were located close to the edge of the CCD some light was dispersed out over the edges, and hence the spectral range was reduced in those cases. By only allowing spectra with more than 80 per cent well-defined pixels, we ensured that our targets were fully covered in the wavelength range from 1.1–1.6 μm. For each spectrum, we calculated the median SNR per pixel. We discarded two targets (IDs 123780 and 124168) with a median SNR per pixel less than 1, i.e., more than half of the pixels were heavily noise dominated.

The sources with spectra were then scaled to the J-band flux, which is fully covered by $G141$. Sources whose J-band flux could not be calculated due to too many noisy pixels within the J-band wavelength coverage were discarded. We scaled the spectra to account for the loss of flux due to the limitations of the spectral extraction aperture. Finally, we checked how well the contamination (if any) had been subtracted. We discarded the most heavily contaminated spectra and the spectra where the contamination had been subtracted incorrectly leaving gaps and holes in the extracted spectra. This was done by visual inspection as not only the amount of contamination is important, but also the shape of the contaminating flux. In some cases the contaminating flux can enhance or even create a break in the spectrum, and this is difficult to quantify in a comparable way for all targets.

In the end we end up with a spectroscopic sample of 14 galaxies. The properties of the full sample consisting of 34 galaxies (of which 14 have spectral data available) are summarized in Table 7.1. In appendix 7.A, we give a list of the spectra that were discarded along with remarks on why they were removed from our sample.

7.3.1 Quiescent versus Star-Forming

Since we only wish to study the quiescent population, we need at method to distinguish between star-forming and quiescent galaxies. For this we use the so-called UVJ selection, based on the rest-frame $U - V$ and $V - J$ colours following Williams et al. (2009). The rest-frame colours for our sample are included in the catalog from Muzzin et al. (2013). The classification from the UVJ criteria is given for each sample member in Table 7.1: 'QG' for quiescent galaxies and 'SFG' for star-forming galaxies.

In Sect. 7.4, we analyse the spectral energy distributions (SEDs) and compare the UVJ-classification with the star formation rates inferred from the SEDs.

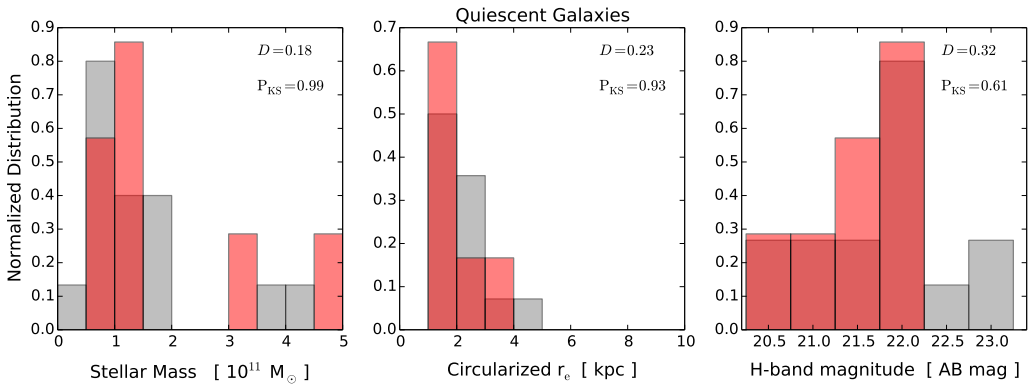

Figure 7.1: Normalized distributions of stellar mass, effective radii, and H-band AB magnitudes. In each panel, the underlying fray histogram shows the full photometric parent sample of quiescent galaxies, which was selected from the mass-complete catalog. The red histogram shows the spectroscopic sub-sample. In the corner of each panel, we show the KS statistic, D, and the p-value, $P_{\rm KS}$.

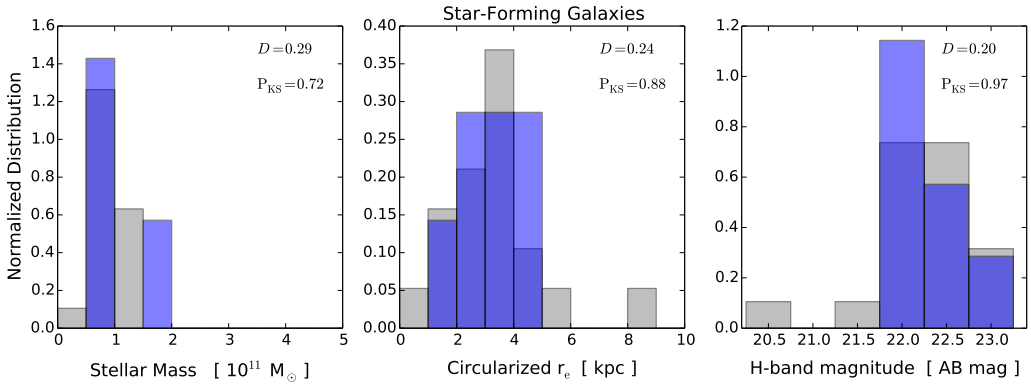

Figure 7.2: Same as Fig. 7.1 for the star-forming galaxies.

7.3.2 Spectral completeness

In the process of discarding galaxies from the photometric sample based on their available spectra we may have introduced biases in the final spectroscopic sample, e.g., the sizes and masses may be systematically underestimated due to low SNR and faint sources being discarded. In this section, we address the selection effects. We perform a Kolmogorov-Smirnov (KS) test on the distributions of masses, sizes and H-band magnitudes comparing the spectroscopic sub-sample to the full photometric sample, the details as to how we infer masses and sizes are described in Sect. 7.4 and 7.5. In Fig. 7.1, we show the distributions of stellar mass, circularized effective radii and H-band AB magnitudes for quiescent galaxies. In each panel, we give the calculated KS statistic along with the p value. For the star-forming galaxies, we perform the same analysis; this is shown in Fig. 7.2. All distributions are fully consistent with being drawn from the same distribution, and hence no significant bias is introduced in the spectroscopic selection. Nevertheless, we do note that the spectroscopic selection for the quiescent galaxies seems to exclude the faintest sources with $H > 22.25$. However, this does not translate into a bias in the inferred masses and sizes. On the other hand, the brightest star-forming galaxies seem to be discarded by the spectroscopic selection. This may be explained by the star-forming galaxies on average being more extended and thus having their flux distributed among more noisy pixels, thereby lowering the SNR in the spectrum.

7.4 Spectral fitting

All galaxies in our sample were fitted by the FAST code (Kriek et al. 2009b) using their photometry and photometric redshifts only. The code performs template fitting combining the photometric data with our grism spectra using exponentially declining star-formation histories (with $\log(\tau)$ from 7.0 to 9.9 in steps of 0.1), stellar population synthesis models by Bruzual & Charlot (2003) and a Chabrier (2003) initial mass function. All fits (both with and without spectra) were performed with variable metallicity among four discrete values: $Z = 0.004, 0.008, 0.02, 0.05$. We used templates with a grid of ages from $7.5 < \log(\text{age/yr}) < 9.7$ in steps of 0.1, and always less than the age of the Universe at the given redshift, and with a grid of dust attenuation of $0 < A_V < 2.5$ in steps of 0.1. The subsample of sources with spectra were then fitted again with the added spectral information along with the photometry. Before fitting the spectra, we binned them by a factor of 8. We did this to avoid being affected by differences in the resolution of the models and the actual spectra. Some of this difference was caused by morphological broadening which arises due to the fact that we are using slitless spectroscopy on extended objects. We chose to re-bin the spectra as this is much faster than having to match entire grid of templates in the fit to the resolution and sampling of the grism spectra, especially since the resolution is different for each source. The addition of spectral information improved the parameter estimation. However, the strong re-binning of the spectra made the improvement on the redshift very limited. We therefore used the spectral fits to improve the redshifts by comparing the best-fit template to the original spectrum before the re-binning. We cross-correlated the two to obtain a higher precision on the best-fit redshift. Before comparing the spectra and templates we match the resolution and sampling of the templates to those of the spectra. For spectra with low SNR we re-binned the spectra by a factor of 2 or 4 until we reached a SNR per pixel of at least 4. The uncertainty on the redshift is thus mainly determined by the spectral re-binning.

To estimate the improvement on the stellar mass with the higher precision on redshifts, we performed a last fit to the spectroscopic subsample while keeping the redshifts fixed to the spectrophotometric redshifts determined above. We note that this approach slightly underestimates the uncertainties on the masses, however, we were not able to propagate the redshift uncertainties directly using the FAST code. Instead, we performed two further fits, this time using the upper and lower $1\ \sigma$ limits on the spectro-photometric redshifts. The effect of varying the redshift this way did in most cases not lead to any significant change. In Fig. 7.3, we show the individual mass estimates from the best-fit and the effect on the mass determination by using the upper and lower boundaries on the redshift. For all sources the variations are within the $1\ \sigma$ limits from the fixed-redshift fits. We therefore neglect the effect from the redshift uncertainties on the stellar mass estimates. Figure 7.5 shows the individual spectra and SEDs along with their best fitting template for the spectroscopic sample. All the parameters from the SED fits are summarized in Table 7.2 where we also list the strength of the 4000 Å break for comparison with other studies. These are calculated using the original definition from Bruzual A. (1983).

In the previous section, we described the UVJ method we use to select quiescent galaxies. Now with the stellar population parameters we can investigate the relation between the classification from the UVJ criteria and the inferred star formation rates. When looking at the specific star formation rate ($\text{sSFR} \equiv \text{SFR}/\text{M}_\star$), we find a strong correlation between the classification of quiescent galaxies from the UVJ method and galaxies with $\text{sSFR} < -10.5\ \text{yr}^{-1}$. There are only two star-forming galaxies (from

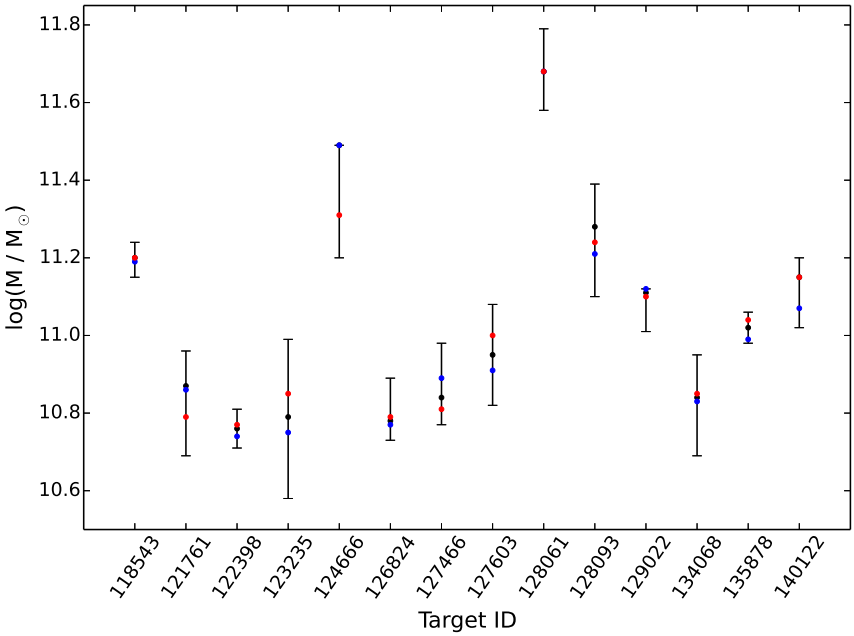

Figure 7.3: Effects of varying spectro-photometric redshift in the SED fits from FAST. The black points with errorbars show the best-fit stellar mass and 68% confidence intervals with the assumed redshift for each target. The effect on stellar mass when using the upper and lower boundaries on the redshifts is shown by the red and blue points, respectively.

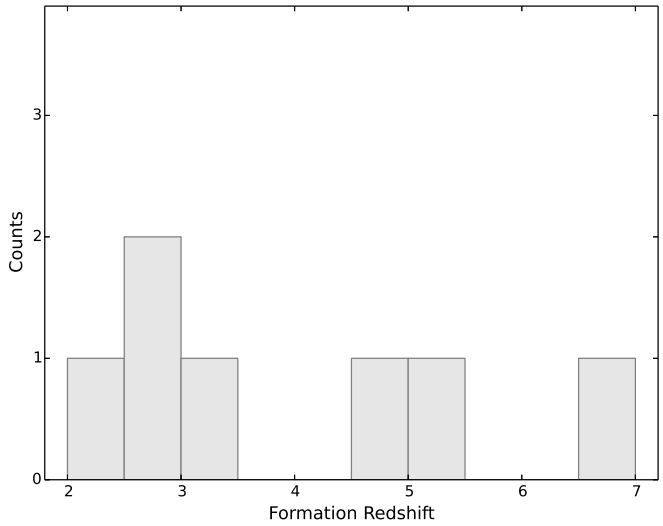

Figure 7.4: Distribution of formation redshifts for the quiescent galaxies. The gray distribution shows the full photometric and spectroscopic sample. The red distribution is the spectroscopic sub-sample only. Due to the much larger uncertainties on both redshift and stellar age for the photometric sample, these formation redshifts should only be considered indicative.

UVJ criteria) below this cut-off, and one quiescent galaxy above it. For the spectroscopic sample, only one star-forming galaxy lies below the sSFR limit of -10.5 yr^{-1}.

Lastly, we use the inferred ages and redshifts for the spectroscopic sample to compute formation redshifts. In Fig. 7.4, we show the distribution of formation redshifts for the full sample as well as for the spectroscopic sub-sample of quiescent galaxies.

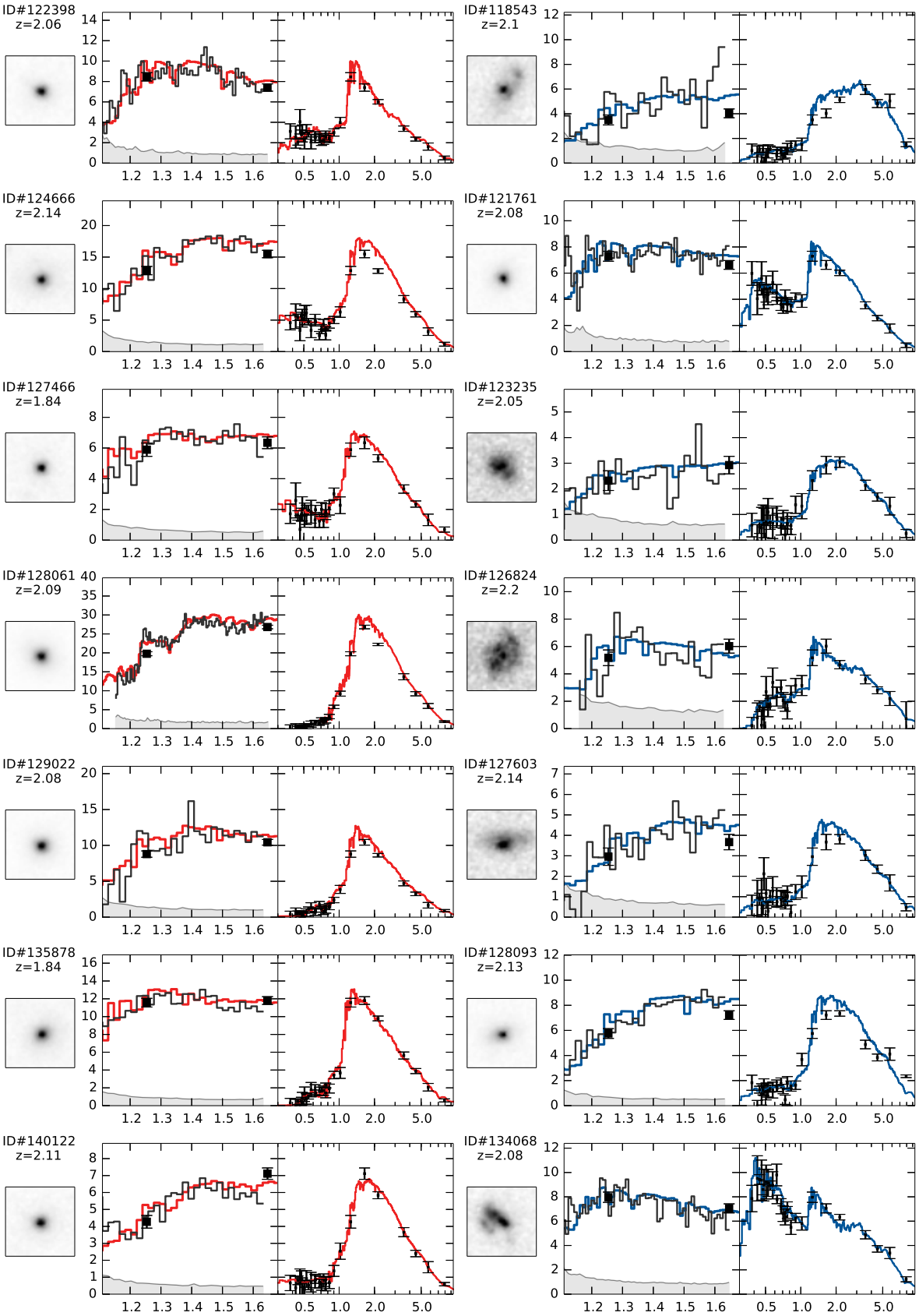

Figure 7.5: (*left*) 2.4×2.4 arcsec^2 H_{160}-band image, (*middle*) 1D extracted grism spectrum in black and error spectrum in grey, and (*right*) photometric SED. Both the middle and right panels show wavelength in units of μm vs. f_λ in units of 10^{-19} erg^{-1}s^{-1}cm^{-2}Å^{-1}. The colored line shows the best-fit model from FAST convolved and rebinned to match the resolution of the grism spectra. Quiescent (star-forming) galaxies are shown in the left (right) column in red (blue).

Table 7.2: Parameters from SED fitting.

ID	z	$\log(M_\star)$ $(M_\odot)$	log(Age) (yr)	$\log(Z/Z_\odot)$	A_v (mag)	log(SSFR) (yr^{-1})	$\log(\tau)$ (yr)	$D(4000)$
118543	2.10 ± 0.05	$11.20^{+0.04}_{-0.05}$	$8.80^{+0.20}_{-0.19}$	$0.050^{+0.000}_{-0.014}$	$1.80^{+0.20}_{-0.30}$	$-9.72^{+0.26}_{-0.19}$	$8.20^{+0.20}_{-0.19}$	3.05 ± 1.76
121761	2.08 ± 0.02	$10.87^{+0.09}_{-0.18}$	$8.80^{+0.30}_{-0.57}$	$0.004^{+0.015}_{-0.000}$	$1.30^{+0.27}_{-0.43}$	$-9.26^{+0.27}_{-0.39}$	$8.40^{+0.36}_{-0.75}$	1.09 ± 0.10
122398	2.06 ± 0.02	$10.76^{+0.05}_{-0.05}$	$8.80^{+0.19}_{-0.16}$	$0.050^{+0.000}_{-0.040}$	$0.20^{+0.36}_{-0.20}$	$-10.53^{+0.09}_{-0.10}$	$8.00^{+0.19}_{-0.16}$	1.30 ± 0.13
123235	2.05 ± 0.10	$10.79^{+0.20}_{-0.21}$	$9.10^{+0.40}_{-0.78}$	$0.004^{+0.036}_{-0.000}$	$1.60^{+0.40}_{-0.62}$	$-9.74^{+0.55}_{-1.02}$	$8.60^{+0.51}_{-1.18}$	1.59 ± 0.68
124666	2.14 ± 0.05	$11.49^{+0.00}_{-0.29}$	$9.40^{+0.00}_{-0.42}$	$0.004^{+0.046}_{-0.000}$	$0.50^{+0.21}_{-0.50}$	$-10.62^{+0.36}_{-0.38}$	$8.70^{+0.01}_{-0.52}$	1.30 ± 0.13
126824	2.20 ± 0.02	$10.78^{+0.11}_{-0.05}$	$8.10^{+0.19}_{-0.12}$	$0.050^{+0.000}_{-0.031}$	$1.50^{+0.32}_{-0.20}$	$-11.26^{+1.38}_{-1.09}$	$7.10^{+0.38}_{-0.10}$	1.67 ± 0.44
127466	1.84 ± 0.05	$10.84^{+0.14}_{-0.07}$	$9.30^{+0.20}_{-0.24}$	$0.008^{+0.019}_{-0.004}$	$0.50^{+0.28}_{-0.11}$	$-10.53^{+0.18}_{-0.18}$	$8.60^{+0.23}_{-0.24}$	1.34 ± 0.35
127603	2.14 ± 0.05	$10.95^{+0.13}_{-0.13}$	$9.10^{+0.30}_{-0.61}$	$0.020^{+0.030}_{-0.016}$	$0.90^{+0.96}_{-0.21}$	$-10.35^{+0.54}_{-0.50}$	$8.40^{+0.33}_{-0.81}$	1.19 ± 0.30
128061	2.09 ± 0.01	$11.68^{+0.11}_{-0.10}$	$9.40^{+0.10}_{-0.40}$	$0.008^{+0.015}_{-0.004}$	$0.10^{+0.42}_{-0.10}$	< -12.28	$8.20^{+0.30}_{-1.20}$	1.73 ± 0.10
128093	2.13 ± 0.05	$11.28^{+0.11}_{-0.18}$	$9.00^{+0.40}_{-0.07}$	$0.020^{+0.030}_{-0.016}$	$1.20^{+0.15}_{-0.75}$	$-10.26^{+0.00}_{-0.46}$	$8.30^{+0.40}_{-0.15}$	1.28 ± 0.13
129022	2.08 ± 0.05	$11.11^{+0.01}_{-0.10}$	$9.00^{+0.12}_{-0.09}$	$0.020^{+0.012}_{-0.004}$	$0.40^{+0.09}_{-0.40}$	< -12.10	$8.00^{+0.12}_{-1.00}$	1.86 ± 0.36
134068	2.08 ± 0.02	$10.84^{+0.11}_{-0.15}$	$8.90^{+0.23}_{-0.46}$	$0.050^{+0.000}_{-0.016}$	$1.30^{+0.22}_{-0.17}$	$-8.74^{+0.30}_{-0.21}$	$9.90^{+0.00}_{-1.45}$	1.11 ± 0.10
135878	1.84 ± 0.10	$11.02^{+0.04}_{-0.04}$	$8.90^{+0.06}_{-0.14}$	$0.020^{+0.009}_{-0.007}$	$0.70^{+0.30}_{-0.12}$	< -12.01	$7.80^{+0.17}_{-0.80}$	1.04 ± 0.15
140122	2.11 ± 0.10	$11.15^{+0.05}_{-0.13}$	$9.50^{+0.00}_{-0.38}$	$0.004^{+0.039}_{-0.000}$	$0.50^{+0.21}_{-0.50}$	$-11.17^{+0.27}_{-0.60}$	$8.70^{+0.02}_{-0.36}$	1.40 ± 0.19
119753	$1.99^{+0.17}_{-0.16}$	$11.24^{+0.17}_{-0.34}$	$9.45^{+0.15}_{-0.62}$	$0.008^{+0.042}_{-0.004}$	$1.00^{+1.27}_{-1.00}$	$-10.44^{+1.16}_{-0.78}$	$8.80^{+1.10}_{-0.68}$	
123324	$2.26^{+0.11}_{-0.12}$	$10.62^{+0.31}_{-0.45}$	$8.80^{+0.80}_{-1.18}$	$0.050^{+0.000}_{-0.046}$	$1.80^{+0.70}_{-0.53}$	$-9.12^{+0.88}_{-0.54}$	$8.50^{+1.40}_{-1.50}$	
123780	$2.26^{+0.20}_{-0.20}$	$10.80^{+0.32}_{-0.59}$	$9.00^{+0.60}_{-1.29}$	$0.004^{+0.046}_{-0.000}$	$1.60^{+0.90}_{-1.46}$	< -7.86	$8.80^{+1.10}_{-1.80}$	
123817	$2.13^{+0.13}_{-0.13}$	$10.98^{+0.12}_{-0.33}$	$9.50^{+0.10}_{-0.60}$	$0.004^{+0.046}_{-0.000}$	$1.00^{+0.64}_{-0.59}$	$-9.64^{+0.78}_{-0.43}$	$9.30^{+0.60}_{-0.89}$	
124168	$2.04^{+0.08}_{-0.10}$	$11.16^{+0.30}_{-0.32}$	$9.55^{+0.05}_{-0.96}$	$0.050^{+0.000}_{-0.041}$	$2.20^{+0.30}_{-0.78}$	$-9.52^{+0.60}_{-0.64}$	$9.60^{+0.30}_{-1.41}$	
124686	$2.11^{+0.17}_{-0.13}$	$10.96^{+0.23}_{-0.27}$	$9.20^{+0.40}_{-0.71}$	$0.004^{+0.041}_{-0.000}$	$0.50^{+1.52}_{-0.50}$	< -9.91	$8.30^{+0.70}_{-1.30}$	
126073	$2.21^{+0.11}_{-0.09}$	$10.67^{+0.35}_{-0.07}$	$9.10^{+0.37}_{-0.42}$	$0.008^{+0.042}_{-0.004}$	$0.00^{+0.73}_{-0.00}$	< -11.32	$7.60^{+0.93}_{-0.60}$	
126301	$2.05^{+0.11}_{-0.11}$	$11.11^{+0.27}_{-0.17}$	$9.20^{+0.40}_{-0.37}$	$0.050^{+0.000}_{-0.045}$	$1.20^{+0.96}_{-0.42}$	$-10.09^{+0.71}_{-0.44}$	$8.60^{+1.12}_{-0.35}$	
126952	$2.28^{+0.27}_{-0.29}$	$10.70^{+0.51}_{-0.37}$	$8.35^{+1.25}_{-0.37}$	$0.004^{+0.046}_{-0.000}$	$2.50^{+0.00}_{-2.01}$	< -8.97	$7.30^{+2.60}_{-0.30}$	
127617	$2.07^{+0.07}_{-0.07}$	$11.14^{+0.22}_{-0.14}$	$8.40^{+0.62}_{-0.50}$	$0.008^{+0.030}_{-0.004}$	$1.80^{+0.27}_{-0.47}$	$-8.90^{+0.37}_{-3.36}$	$8.00^{+1.90}_{-1.00}$	
128977	$2.23^{+0.20}_{-0.21}$	$11.03^{+0.27}_{-0.59}$	$9.50^{+0.10}_{-1.72}$	$0.020^{+0.030}_{-0.016}$	$1.90^{+0.60}_{-1.31}$	$-9.57^{+1.03}_{-2.69}$	$9.40^{+0.50}_{-2.40}$	
132654	$1.97^{+0.22}_{-0.21}$	$10.81^{+0.21}_{-0.50}$	$9.55^{+0.05}_{-1.26}$	$0.004^{+0.046}_{-0.000}$	$1.50^{+1.00}_{-1.50}$	< -9.82	$8.90^{+1.00}_{-1.90}$	
133784	$2.03^{+0.22}_{-0.24}$	$10.86^{+0.25}_{-0.45}$	$9.25^{+0.35}_{-0.99}$	$0.004^{+0.046}_{-0.000}$	$1.20^{+1.30}_{-1.07}$	< -9.39	$8.40^{+0.86}_{-1.40}$	
133915	$1.86^{+0.12}_{-0.12}$	$10.87^{+0.18}_{-0.25}$	$9.10^{+0.50}_{-0.79}$	$0.008^{+0.034}_{-0.004}$	$1.00^{+0.73}_{-0.44}$	$-9.54^{+0.81}_{-0.34}$	$8.70^{+1.20}_{-0.97}$	
134172	$2.26^{+0.21}_{-0.22}$	$11.13^{+0.09}_{-0.42}$	$9.45^{+0.11}_{-0.63}$	$0.004^{+0.046}_{-0.000}$	$0.70^{+0.87}_{-0.70}$	< -10.62	$8.60^{+0.27}_{-1.60}$	
135214	$1.89^{+0.10}_{-0.10}$	$10.71^{+0.18}_{-0.17}$	$8.85^{+0.54}_{-0.47}$	$0.050^{+0.000}_{-0.030}$	$1.30^{+0.37}_{-0.46}$	$-9.22^{+0.38}_{-0.37}$	$8.50^{+1.40}_{-0.58}$	
139823	$1.87^{+0.08}_{-0.08}$	$11.19^{+0.29}_{-0.06}$	$9.20^{+0.26}_{-0.20}$	$0.008^{+0.017}_{-0.004}$	$0.20^{+0.49}_{-0.20}$	$-11.50^{+0.29}_{-0.94}$	$8.30^{+0.31}_{-0.29}$	
204878	$2.07^{+0.14}_{-0.12}$	$10.95^{+0.41}_{-0.24}$	$9.15^{+0.45}_{-0.93}$	$0.008^{+0.042}_{-0.004}$	$2.50^{+0.00}_{-1.53}$	< -9.36	$8.70^{+1.20}_{-1.70}$	
207084	$2.05^{+0.14}_{-0.14}$	$10.75^{+0.25}_{-0.27}$	$8.90^{+0.70}_{-1.04}$	$0.004^{+0.040}_{-0.000}$	$1.70^{+0.45}_{-0.92}$	$-8.95^{+0.60}_{-3.31}$	$8.90^{+1.00}_{-1.90}$	
207144	$1.91^{+0.13}_{-0.11}$	$11.62^{+0.07}_{-0.32}$	$9.50^{+0.09}_{-0.51}$	$0.020^{+0.030}_{-0.016}$	$0.10^{+1.37}_{-0.10}$	$-11.78^{+1.07}_{-0.16}$	$8.60^{+0.28}_{-0.55}$	

Notes: The upper part (above the line) shows the fits with spectral data available. The redshift is in this case the spectro-photometric redshift, see text. The lower part shows the photometric sample, where z here refers to the photometric redshift.

7.5 Structural Fitting

When possible we use the tabulated values from van der Wel et al. (2012). In cases of bad fits (flag values 1, 2 and 3 in their table), we redid the fits ourselves in order to improve the fit. For this purpose, we used the same point spread functions as were used by van der Wel et al. (private communication). See below for individual comments on the sources where a standard Sérsic fit was not adequate. All neighbouring objects were included in the modelling as either individual Sérsic components or point sources. In three cases (124666, 128093, and 207144), the fits did not converge immediately and we therefore kept the magnitude fixed to the value obtained from the CANDELS catalog. This way we were able to get the fit to converge.

For the target 127466, we were not able to get a good fit with a Sérsic component due to the source being very compact. The target is furthermore surrounded by a few companions and a very spatially extended low surface brightness component. This makes it hard to separate the various components and estimate the actual background, which caused the divergent behaviour of GALFIT. Instead we tried to estimate the size using a curve-of-growth approach. We use circular apertures to infer the effective radius since the source has very low ellipticity (minor-to-major axis ratio is 0.98). This results in a size estimate of $r_e = 0.22 \pm 0.01$ arcsec.

Finally, we note that the target 133915 resides in a very dense area with many compact neighbours, the size may therefore be slightly overestimated.

All the inferred sizes are included in Table 7.3 as circularized half-light radii (r_e) in kpc. Throughout the rest of the paper, circularized radii will be used. We use the minor-to-major axis ratio, q, from the GALFIT analysis to calculate the circularized radii: $r_{\rm e} = a_{\rm e}\sqrt{q}$. The details (models and residuals) of the analysis are shown in Appendix 7.B.

7.6 The Mass–Size Relation

We have used our sample of spectroscopically confirmed galaxies at redshift $z \approx 2$ to investigate the mass–size relation of quiescent galaxies at high redshift. We parameterize the relation following Newman et al. (2012) and others:

$$r_e = \gamma \left(\frac{\mathrm{M}_\star}{10^{11}\mathrm{M}_\odot} \right)^\beta = \gamma\, \mathrm{M}_{11}^\beta \,. \tag{7.1}$$

We fit the relation in log-log space using the errors on both the stellar masses and sizes, hence we wish to minimize the perpendicular distance from the line to each point and not simply the vertical distance. This can be expressed in terms of the likelihood estimator, assuming Gaussian uncertainties:

$$\ln(L) = -\sum \frac{\Delta_i^2}{2(\sigma_i^2 + V)} - \frac{1}{2}\sum (\sigma_i^2 + V)\,, \tag{7.2}$$

where

$$\Delta_i = (y_i - \beta x_i - b)/\sqrt{1+\beta^2} \;\text{ and }\; \sigma_i^2 = \sigma_{y_i}^2 + \beta^2 \sigma_{x_i}^2 \;\; .$$

Δ_i here denotes the orthogonal distance from the datapoint (x_i, y_i) to the line, and σ_i^2 denotes the projected variance for each datapoint taking into account the errors on stellar mass and size. In this notation x refers to $\log(M_\star/10^{11}M_\odot)$ and y refers to $\log(r_e/\mathrm{kpc})$. The V that enters in the likelihood

Table 7.3: Morphological Parameters from GALFIT.

ID	r_e (kpc)	Sérsic n	b/a	Ref.
118543	4.41 ± 0.39	2.57 ± 0.30	0.51 ± 0.03	2
121761	1.19 ± 0.04	4.66 ± 0.29	0.87 ± 0.02	2
122398	1.59 ± 0.05	6.30 ± 0.36	0.70 ± 0.02	2
123235	2.78 ± 0.11	0.72 ± 0.10	0.74 ± 0.02	2
124666[a]	10.00 ± 0.10	9.88 ± 0.08	0.69 ± 0.01	1
126824	4.39 ± 0.13	0.53 ± 0.07	0.74 ± 0.02	2
127466	1.84 ± 0.10	$\cdots$	0.98 ± 0.03	1, 2
127603	3.05 ± 0.15	1.37 ± 0.13	0.48 ± 0.02	2
128061	2.58 ± 0.05	4.69 ± 0.17	0.82 ± 0.01	2
128093[a]	3.04 ± 0.15	8.53 ± 0.98	0.53 ± 0.04	1
129022	1.34 ± 0.03	3.02 ± 0.14	0.87 ± 0.02	2
134068	2.85 ± 0.03	0.57 ± 0.02	0.58 ± 0.01	2
135878	3.42 ± 0.20	5.27 ± 0.23	0.78 ± 0.02	1
140122	1.67 ± 0.09	4.92 ± 0.50	0.79 ± 0.04	2
119753	2.57 ± 0.17	0.99 ± 0.18	0.36 ± 0.03	2
123324	2.16 ± 0.34	3.61 ± 0.63	0.39 ± 0.04	1
123780	1.73 ± 0.17	1.41 ± 0.35	0.55 ± 0.06	2
123817	3.10 ± 0.16	4.61 ± 0.19	0.85 ± 0.02	1
124168	3.33 ± 0.55	2.46 ± 0.58	0.68 ± 0.05	2
124686	1.51 ± 0.05	5.65 ± 0.21	0.74 ± 0.01	1
126073	1.58 ± 0.09	5.43 ± 0.36	0.86 ± 0.02	1
126301	5.67 ± 0.46	4.18 ± 0.20	0.81 ± 0.02	1
126952	3.35 ± 0.24	0.44 ± 0.14	0.43 ± 0.04	2
127617	0.46 ± 0.01	8.00 ± 0.63	0.67 ± 0.03	2
128977	3.36 ± 0.14	0.50 ± 0.08	0.28 ± 0.02	2
132654	2.49 ± 0.13	1.46 ± 0.15	0.42 ± 0.02	2
133784	2.12 ± 0.08	0.77 ± 0.09	0.51 ± 0.02	2
133915	8.75 ± 0.46	5.60 ± 0.14	0.70 ± 0.01	1
134172	2.54 ± 0.40	5.11 ± 1.07	0.84 ± 0.06	2
135214	2.76 ± 0.05	0.64 ± 0.04	0.39 ± 0.01	2
139823	1.37 ± 0.02	4.65 ± 0.15	0.44 ± 0.01	2
204878	3.33 ± 0.32	1.70 ± 0.26	0.46 ± 0.04	2
207084	1.25 ± 0.04	3.08 ± 0.19	0.53 ± 0.02	2
207144[a]	2.88 ± 0.06	2.25 ± 0.08	0.77 ± 0.02	1

[a] Sources where the magnitude was kept fixed, see text.

Notes: The top part of the table (above the horizontal line) shows the spectroscopic sample. Below the line is the rest of the photometric sample.

References: (1) This work; (2) van der Wel et al. (2012).

Table 7.4: Parameter estimates for mass–size relation of quiescent galaxies.

	β	$\log(\gamma/\mathrm{kpc})$	$\sigma_{\log r_e}$
Photometry	0.82 ± 0.22	$0.30^{+0.07}_{-0.08}$	$0.05^{+0.09}_{-0.04}$
Photometry and spectra	$0.53^{+0.29}_{-0.21}$	0.29 ± 0.07	$0.17^{+0.05}_{-0.04}$

refers to the intrinsic (Gaussian) variance perpendicular to the line, which also is a free parameter in the fit. We fit the relation to the data using a Bayesian approach to estimate the parameters and their confidence intervals. We use flat priors on all parameters: $-10 < \beta < 10$, $-2 < b < 2$, and $-10 < \ln(V) < 1$.

Firstly, we fit the quiescent galaxies using only the photometric data. Hereafter we include the spectroscopic data to investigate the improvement. All the fit values are summarized in Table 7.4. The scatter we infer from the fit is the scatter perpendicular to the line, however, the quantity we are interested in is the scatter in the sizes. We thus transform the scatter to the vertical scatter as follows: $\sigma^2_{\log r_e} = V(1 + \beta^2)$.

The addition of spectroscopic information significantly improves the estimate of the scatter since the large uncertainty on the photometric masses leads to an underestimation of the scatter. The mass-normalized size (γ) remains almost unaffected. In the rest of the paper, we will refer to the fit obtained using the spectroscopic data combined with the full photometric sample of quiescent galaxies. The slope is poorly constrained due to the low number of data points and the large uncertainty on the stellar masses, thus still consistent with what is found by Newman et al. (2012) at similar redshifts. Recently, van der Wel et al. (2014) studied the evolution of size, slope and scatter from redshift $z \sim 2$, however, they use the effective semi-major axis and not circularized radii as in previous studies. Therefore, their results on slope and scatter cannot be directly compared to the parameters obtained in this analysis.

In Fig. 7.6, we show the mass–size relation for the sample of quiescent galaxies with and without spectra as red squares and triangles, respectively. We compare our data to local early type galaxies with kinematical data from ATLAS^{3D} (Cappellari et al. 2011). In order to compare our high redshift sample to the that of the ATLAS^{3D}-team we fit the power-law relation given above to their data using the same mass-limit as for our data. From the best fit to the ATLAS^{3D} sample, we find the following slope of $\beta_0 = 0.68 \pm 0.06$, a mass-normalized size of $\log(\gamma_0/\mathrm{kpc}) = 0.59 \pm 0.03$, and a scatter of $\sigma_0 = 0.13 \pm 0.01$. For this analysis, we have used the tabulated values from Cappellari et al. (2013). Specifically, we note that we used the $\log(r_{1/2})$ to infer the sizes. The inferred slope for the local relation is significantly steeper than the value found by Shen et al. (2003) ($\beta_{z=0} = 0.56$). Guo et al. (2009) find a slightly higher value for the slope of $\beta_{z=0} = 0.70 \pm 0.05$ which is in very good agreement with the result from the ATLAS^{3D} data.

It is clearly visible that the quiescent galaxies from this work are smaller than local quiescent galaxies at the same mass. Moreover, the figure shows that the various samples of local galaxies infer slightly different normalizations and slopes of the relation. The slope derived from the ATLAS^{3D} data is in very good agreement with the slope derived by Guo et al. (2009). On the other hand, the relation derived by Newman et al. (2012) and Shen et al. (2003) is much shallower. These differences are most likely caused by the different fitting techniques as well as the different approaches used to separate quiescent and star-forming galaxies. The scatter inferred for the relation locally is found to be $\sigma_0 = 0.16$ by Newman et al. (2012) using SDSS data, this is in good agreement with, though slightly larger than, the

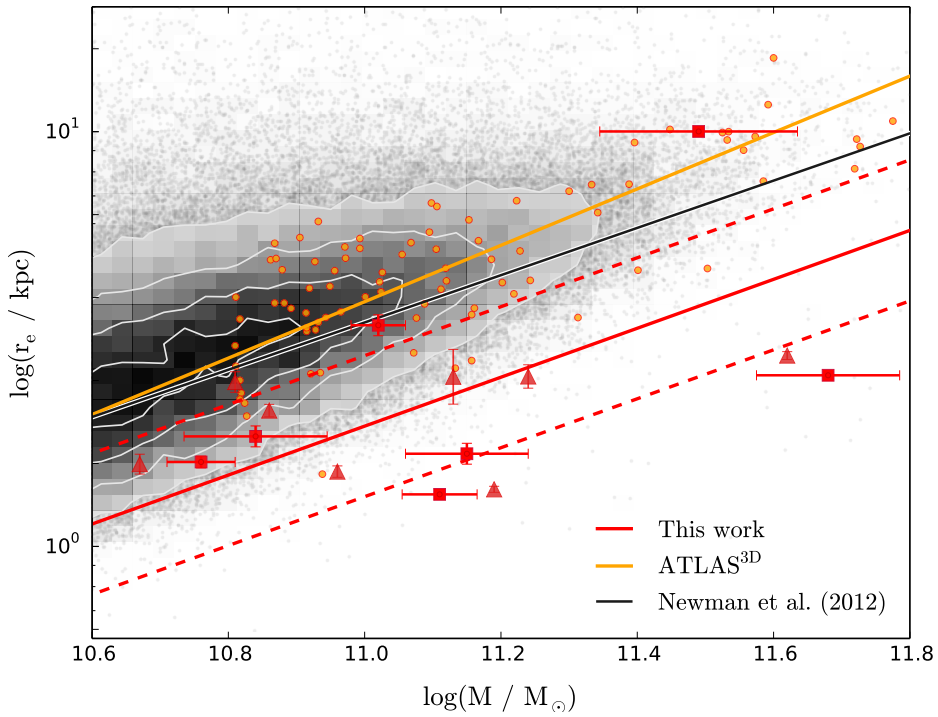

Figure 7.6: Mass–size relation using circularized effective radii for quiescent galaxies. The galaxies at high redshift (red points and red line) are smaller than the local relation inferred from ATLAS^{3D} data (orange points and solid line). For comparison, we show the local relation from Newman et al. (2012) as the black line. Local data from SDSS quiescent galaxies with Sérsic indices larger than $n > 2.5$ (following Shen et al. (2003)) are shown as the underlying distribution in gray. The red squares with error bars on both mass and size indicate the spectroscopic sample. The sample with only photometry available is shown as red triangles. Here we do not show the uncertainties on the mass estimates, but they are typically of the order $\sim 0.2-0.3$ dex, the uncertainties are listed in Table 7.2 of Appendix **??** for reference.

scatter inferred from the ATLAS^{3D} data. Given the value we infer at high redshift, $\sigma = 0.17^{+0.05}_{-0.04}$, this indicates that the scatter remains constant with redshift.

Although we cannot compare our values directly with the van der Wel et al. (2014) study, we can still compare to their evolutionary trends. They find no evidence for evolution in scatter and slope with time, consistent with the results presented here.

7.6.1 Size Evolution

We now take a closer look at the offset towards smaller sizes visible in Fig.7.6 between our sample at high redshift and the local sample. This offset has been studied in great detail (e.g., Daddi et al. 2005; Trujillo et al. 2006; Toft et al. 2007; Zirm et al. 2007; Buitrago et al. 2008; van Dokkum et al. 2008b; Damjanov et al. 2011; Bruce et al. 2012; Newman et al. 2012) and various explanations have been put forward to explain the required evolution in sizes, e.g., merging or feedback from quasars (Fan, Lapi, De Zotti, & Danese 2008). We here investigate a simple scenario in which the individual galaxies themselves do not need to increase significantly in size, but rather that the average of the population as a whole increases (e.g., Cassata et al. 2011; Trujillo, Carrasco, & Ferré-Mateu 2012; Carollo et al. 2013; Poggianti et al. 2013). We use our measurements of sizes and scatter at high redshift in combinations with those from Newman et al. (2012) to motivate the initial values for the size evolution.

Newman et al. (2012) study the size evolution of massive galaxies both star-forming and quiescent and find that the star-forming galaxies on average are a factor of 2 larger than the quiescent population at all times above redshift $z > 0.5$. This is consistent with the fact that the star-forming galaxies in our sample on average are a factor of 1.8 larger than the quiescent galaxies at a fixed mass (10^{11} $M_{\odot}$). The evolution of the mean size of quiescent galaxies might then simply be driven by the addition of larger, newly quenched galaxies at lower redshifts to the already quenched population. Carollo et al. (2013) recently showed that the evolution of the sizes of passively evolving galaxies at $z < 1$ is driven by this "dilution" of the compact population. In order to test this picture and evaluate the effect on the scatter in sizes, we have taken the measured sizes normalized to a stellar mass of 10^{11} $M_{\odot}$ from Newman et al. (2012) at redshift $2.0 < z < 2.5$ and generated an initial population of quiescent (QG) and star-forming (SFG) galaxies taking into account the observed number densities at that redshift for galaxies with comparable masses from Brammer et al. (2011). We have shifted the data from Newman et al. from a Salpeter IMF to the assumed Chabrier IMF in this work. The distribution of sizes for the populations are drawn from a log-normal distribution with an average size initially dictated by the observations for QGs while for SFGs we simply use the fact that star-forming galaxies on average are twice as big. The distribution of QGs is assumed to have a scatter of 0.17 dex initially, motivated by the findings in this work. The study by van der Wel et al. (2014) show that the scatter of star-forming galaxies remains constant with redshift and that the scatter is roughly 0.5 dex larger than that of quiescent galaxies. We therefore use a value of 0.22 for the scatter of SFGs in our model. We note that the chosen value for the initial scatter of SFGs does not change the conclusions of the model, it only enhances the increase in the modelled evolution of the scatter.

We then simply assume that the SFGs at the given redshift will be quenched after a fixed time, $t_{\rm quench}$, and add them to the already existing population of quiescent galaxies. For each time-step, we generate a new population of SFGs with a mean size that is twice as big as the mean size of the quiescent galaxies already in place, and after another $t_{\rm quench}$ these will be added to the quiescent population. The generated number of SFGs varies according to the observed number density of SFGs. We have assumed that the scatter of the SFG population is constant with time and that no galaxy-galaxy interactions occur, i.e., no new massive galaxies form by merging of lower-mass galaxies. Furthermore, we assume that galaxies maintain their sizes after they have been quenched and that no further star formation occurs once the galaxies have been quenched. We run this model three times for various quenching time-scales, $t_{\rm quench}$: 1.0, 1.2, and 1.5 Gyr. These time scales are consistent with the results of Bedregal et al. (2013).

The results of this simple model are shown in Fig. 7.7. The top panel shows the evolution in number density. The red and blue points are data from Brammer et al. (2011) for quiescent and star-forming galaxies, respectively. The black and grey points show the modelled evolution in the number density assuming different quenching times indicated in Gyr by the number at each of the tracks. The middle panel shows the evolution in average size of the sample of quiescent galaxies. Data from Newman et al. (2012) is shown in red circles, our sample is indicated by the blue square, and the local size measurements from Shen et al. (2003) and ATLAS^{3D} are shown by the red plus and triangle, respectively. Again, the black and grey points indicate the modelled evolution at different quenching times. The bottom panel shows the evolution of the scatter, σ, of the distribution of quiescent galaxies relative to the initial value at $z = 2.45$.

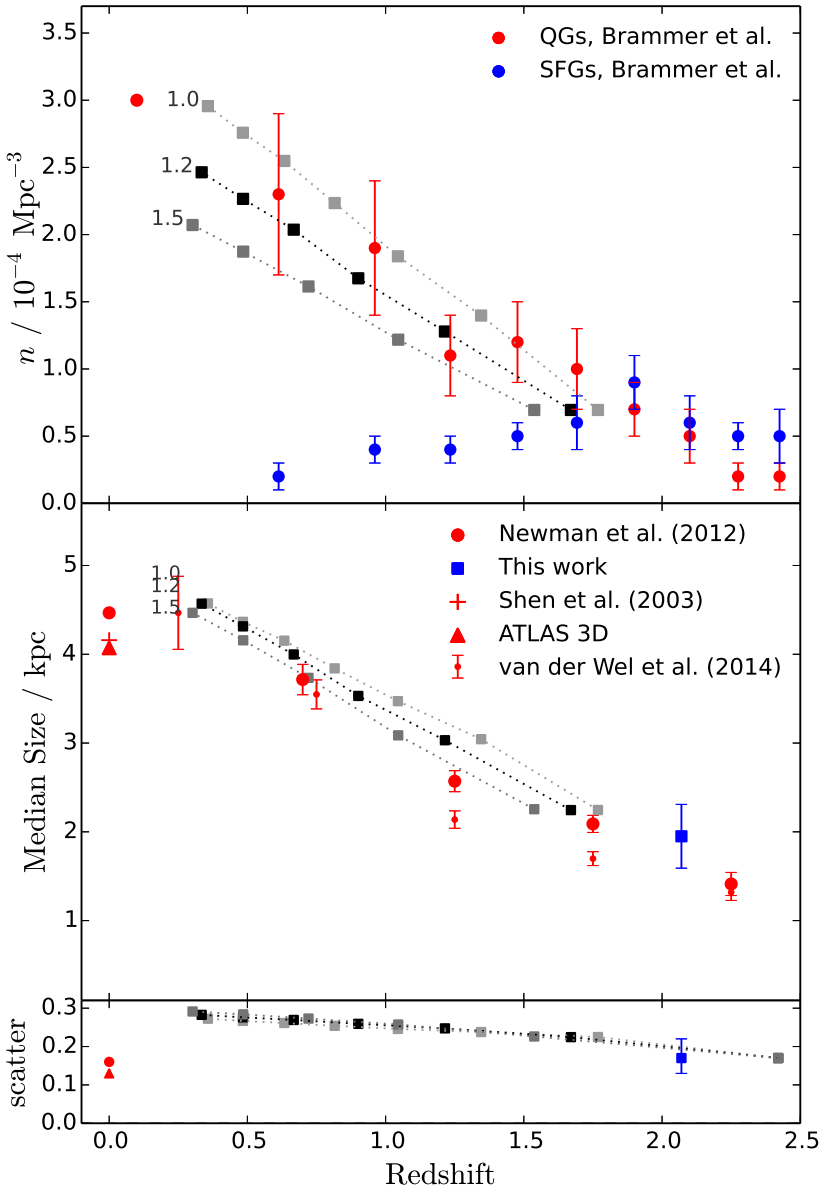

Figure 7.7: (*Top*) Number density evolution with redshift. The red and blue points show the observed number densities for quiescent and star-forming galaxies, respectively, with masses $\log(\mathrm{M}/\mathrm{M}_{\odot}) > 11$ from Brammer et al. (2011). The black and grey, connected points indicate our modelled evolution with varying quenching time indicated in Gyr by the small number at each line. (*Middle*) Average size of the quiescent galaxy population at fixed mass of $10^{11}\mathrm{M}_{\odot}$ as function of redshift. The black and grey points are the same as in the top plot. The various points show other literature data. (*Bottom*) Modelled scatter as a function of redshift relative to the initial scatter of 0.20 dex at redshift $z = 2.4$, the first redshift-bin from Brammer et al. (2011). The evolution in number density and size is very well matched by the model. However, the scatter of the population increases with time contrary to what is observed.

From these assumptions, we are able to reproduce the observed increase in number density and size of quiescent galaxies. However, the modelled scatter *increases* by ~ 0.15 dex on average towards lower redshifts in contrast with the constant scatter observed in this work and by van der Wel et al. (2014).

7.7 Discussion

The evolution of galaxies in the mass–size plane is undoubtedly influenced by merging, star-formation and its cessation. As we increase the samples of well-studied, spectroscopically confirmed galaxies over a range of redshifts we can forge new diagnostic tools to address the weight with which each of these processes influences the evolution of galaxies.

In Sect. 7.6, we investigated the relation between stellar mass and half-light radius by parametrizing the relationship with a power-law. From the best fit to our quiescent grism sample, we found the slope, $\beta = 0.53$, and the scatter, $\sigma_{\log r_e} = 0.17$ dex, consistent with their $z = 0$ values. From the ATLAS^{3D} data and from a large SDSS sample from the work of Shen et al. (2003), Guo et al. (2009) and Newman et al. (2012), a local slope and scatter of $\beta_0 = 0.56 - 0.70$ and $\sigma_0 = 0.13 - 0.16$ dex was inferred. One complication in comparing samples of galaxies at different redshifts, and from different samples, lies in the fact that the distinction between star-forming and quiescent galaxies becomes less clear at higher redshifts. Various studies use different criteria to define quiescence, e.g., a cut in morphology, sSFR or rest-frame colors, which makes comparison between different datasets non-trivial. Even at low redshift, the classification of early type galaxies is performed in different ways.

The importance of a clean separation and definition of star-forming and quiescent galaxies becomes clear when we look at the scatter as a tool to unravel the evolution in the mass–size relation, since the scatter is highly sensitive to outliers. Newman et al. (2012) find a scatter of $\sigma_{\log r_e} = 0.26$ dex for galaxies at redshifts $2.0 < z < 2.5$, much higher than what we find in our data. The large scatter observed in the Newman et al. sample may be due, at least partly, to the uncertainty in photometric redshifts and contamination from star-forming galaxies.

7.7.1 Mechanisms for size growth

In large photometric samples it has also been shown that the slope of the mass–size relation evolves very little from $z \sim 2$ to $z \sim 0.2 - 0.4$ despite there being strong redshift evolution of the galaxy distribution in the mass–size plane (primarily a shift to larger sizes, see Newman et al. 2012, McLure et al. (2013), and van der Wel et al. (2014)). While the unchanging slope may be theoretically plausible as the slope may reflect initial formation rather than subsequent evolution (Ciotti, Lanzoni, & Volonteri 2007), the lack of evolution in the scatter observed in this work and in the work of van der Wel et al. (2014) is puzzling. The scatter about the mean mass–size relation should evolve with redshift according to the underlying physical driver for the evolution in the mass–size plane, i.e., merging, quenching, or further star formation.

Merging will typically move galaxies to higher masses and larger radii, with the direction and amplitude of the change in the mass–size plane determined by the mass ratio, orbital parameters and gas content of the merger (Naab, Johansson, & Ostriker 2009). In gas-rich mergers, the remnant may become more compact due to the gas falling to the center, which leads to strong star formation activity (Shankar et al. 2013). Star formation at later times (e.g., merger induced) will increase the mass, alter the size depending on the location of the star formation, and will decrease the mean age of the sample of *quiescent* galaxies at subsequent redshifts.

Quenching of star-forming galaxies will conserve mass while the individual galaxy sizes may even slightly decrease (as low-surface brightness star-forming regions fade) but is operating on a separate

galaxy population that has intrinsically larger sizes than most of the quiescent galaxies already in place (Khochfar & Silk 2006). The addition of these quenched galaxies will then drive the evolution of the mean size of the whole population without changing the individual galaxies that have already been quenched. However, it is still not entirely clear what happens to star-forming galaxies after they stop forming stars in terms of morphology and size; star-forming galaxies show a variety of morphologies but the quiescent population is more dominated by spheroidal morphologies.

7.7.2 Evolution of the scatter in sizes

Each of the above processes, in addition to directing the mass–size evolution, will affect the observed scatter of the mass–size relation and its evolution in different ways. Merging has been shown by Nipoti et al. (2012) to increase the scatter in the mass–size relation. The authors show that size evolution within a dissipation-less ("dry") merger-only scenario leads to significantly higher scatter than is observed at $z = 0$ (Nipoti, Treu, Leauthaud, Bundy, Newman, & Auger 2012). Mergers are certainly on-going between $z = 2$ and $z = 0$ and Nipoti et al. conclude that there must be a finely tuned balance between the different processes in their merging model in order to reproduce the tight observed relation at $z = 0$. This type of fine tuning is not a general characteristic of the galaxy population(s) and is extremely unlikely to persist in real-world systems. However, the models by Nipoti et al. 2012 only consider dry mergers of spheroids, which given the diverse population of galaxies at high redshift is an unrealistic scenario. More recently, Shankar et al. (2013) study the size evolution of galaxies by running simulations taking into account the various galaxy-galaxy interactions. They find that the scatter in sizes remains constant at all times. However, they over predict the scatter by $\sim 40\,\%$.

In the case of "dilution" of the population via quenching, the scatter will increase due to the addition of a new population of larger, quiescent galaxies. By using our toy model (see Sect. 7.6.1) for the quenching case, we have shown that we are able to reproduce the observed increase in both number density and median size of quenched galaxies as functions of redshift out to $z \sim 2$, see Fig. 7.7. However, our model shows that the scatter should increase by up to ~ 0.15 dex in the redshift range, $0.4 < z < 2.5$. This is inconsistent with the observations presented here and by van der Wel et al. (2014), i.e., the observed scatter in sizes is consistent with being constant from redshift $z \approx 2$ to $z = 0$.

Carollo et al. (2013) have found similar results regarding the evolution of sizes and number density out to $z \sim 1$ assuming the dilution of the quiescent population by younger and larger galaxies. Other studies, however, have shown that quenched galaxies with younger ages are not significantly larger than older quenched galaxies (e.g., Whitaker et al. 2012), as would be predicted in a "dilution" scenario. The results of Whitaker et al. (2012) are based on post-starburst galaxies split into "young" and "old" galaxies separated by colour cuts resulting in median ages of the two samples of 1 Gyr and 2 Gyr, respectively, and do not as such span a very large dynamic range in ages. Moreover, determinations of stellar ages are highly uncertain and depend strongly on metallicity, dust attenuation, and star-formation histories. The separation of "old" and "young" galaxies is thus not straight-forward and introduces large uncertainties in sample selection.

So far, most studies have focused on the role of merging only, especially dry minor merging, as the driver of size evolution since this mechanism is very efficient in terms of increasing the size of a galaxy without adding too much mass to the system (McLure et al. 2013). However, Nipoti et al. (2009, 2012) find that dry merging in a ΛCDM cosmology is insufficient to explain the needed increase in size. As we show with our model for size evolution in Sect. 7.6.1, the addition of larger, quenched galaxies means

that each individual galaxy needs to undergo less size-evolution. The combination of different galaxy-galaxy interactions, both gas-rich and gas-poor, may then regulate the size-evolution of individual systems such that the scatter remains constant through time. Also, individual systems must evolve at high redshift as such compact galaxies locally are very rare (Trujillo et al. 2009, 2014; van der Wel et al. 2014) and merging of galaxies is an obvious mechanism for this evolution (Damjanov et al. 2009; Taylor et al. 2010; van de Sande et al. 2011; Toft et al. 2012). A cascade of mergers is also the most likely way for galaxies to undergo morphological changes from clumpy and in some cases disc-like at high redshift to spheroidal at low redshift (Naab & Trujillo 2006; Ciotti, Lanzoni, & Volonteri 2007; Wuyts et al. 2010). Belli et al. (2014a) study the evolution of galaxies at fixed velocity dispersion as the velocity dispersion has been shown to correlate with age, such that the older populations locally have higher velocity dispersions (Belli, Newman, & Ellis 2014). They target galaxies at redshifts $0.9 < z < 1.6$ with a preselected spheroidal morphology. Assuming that the velocity dispersion does not change during the lifetime of a galaxy the authors find that individual galaxies must evolve significantly, and that size evolution driven by the addition of larger galaxies at later times is inconsistent with the velocity dispersion data. The preselection on morphology in the study by Belli et al., however, may introduce a bias against larger sizes since galaxies with high ellipticity or disk-like appearance on the sky would not be included. Stockton et al. (2014) find very low axis ratios for a sample five galaxies at $z \sim 0.5$ (all five having $b/a < 0.5$). This may indicate a disk-like or prolate nature of a large fraction of quiescent galaxies.

At higher redshifts, $z > 2$, Belli et al. (2014) use similar methods to study the evolution of galaxies at fixed velocity dispersion (Belli, Newman, Ellis, & Konidaris 2014). Though their sample at high redshift is not complete, they conclude that a strong evolution of individual systems is needed in order to reconcile the high-redshift size-distribution with the locally observed distribution. Furthermore, the inferred size evolution happens at too high a rate compared to the expectations from dry, minor merging (Oser et al. 2012; Nipoti et al. 2012). Newman et al. (2012) find consistent results, that is, at lower redshifts $z \lesssim 1$ the rate of size evolution is consistent with dry, minor merging, while at higher redshifts the size increase happens too fast to be driven purely by minor merging.

The fast increase in sizes at high redshift might be explained by the addition of larger, recently quenched galaxies as the number of star-forming galaxies at this epoch in cosmic time is comparable or even dominating. Under the assumption that the galaxy population turns off star formation more or less simultaneously, quenching of a big population of star-forming galaxies (in comparison to the size of the passive population in place) will cause a large increase in the median size of the distribution of quiescent galaxies, see Sect. 7.6.1. This effect will be stronger at higher redshifts when the number density of star-forming galaxies is high. At later times, $z \lesssim 1.5$, the quiescent population starts to dominate and hence the "dilution" effect contributes less. This is consistent with the scenario from Newman et al. and Belli et al., in which the size evolution of galaxies at lower redshifts is dominated by minor merging.

In order to study the evolution of galaxies and disentangle the various processes, high resolution, cosmological simulations are needed, which take into account both gas-rich and gas-poor galaxy interactions on the entire population of star-forming and quenched galaxies. These may be able to reproduce the lack of evolution in the scatter.

7.8 Conclusion

We have presented for the first time for a *spectroscopic* sample that the slope and scatter of the mass–size relation at $z = 2$ are consistent with their local values. We use the fact that the scatter remains constant from $z = 2$ to $z = 0$ as a tool to study the evolutionary mechanism that drives the size-increase of this population. We find that while the addition of larger galaxies quenched at later times can explain the increase of the average size of the population the scatter increases in contrast with the results presented here. Other processes, such as the combined influence from dry and wet mergers, is therefore needed to keep the scatter constant and to make the number density of the most compact galaxies evolve in a way that is consistent with their rarity in the local Universe.

Acknowledgements

The Dark Cosmology Centre is funded by the DNRF. JK acknowledges support from an ESO studentship. ST and AZ acknowledge support from the Lundbeck foundation. This work is based on observations taken by the 3D-HST Treasury Program (GO 12177 and 12328) with the NASA/ESA HST, which is operated by the Association of Universities for Research in Astronomy, Inc., under NASA contract NAS5-26555. This work is based on observations taken by the CANDELS Multi-Cycle Treasury Program with the NASA/ESA *HST*, which is operated by the Association of Universities for Research in Astronomy, Inc., under NASA contract NAS5-26555.

7.A The individual spectra

The discarded spectra can be grouped into the following categories. These are shown in Figure 7.8.

1. Spectra with bad background subtraction
   133784, 133915, 207144. These have breaks in the blue side of the spectra which could not be corrected for.

2. Spectra that are heavily noise dominated where more than half the pixels have SNR< 1:
   123780, 124168.

3. Highly contaminated:
   132654, 126073.

4. Flux-calibration issues, i.e., mismatch between the photometric J and H band:
   119753, 134172.

5. Targets that fall outside our sample criteria after adding the spectral data to the fits: 124686, 126301, 135214, 204878, 127617. The target 127617 presents a strong and broad emission line in the spectrum, which indicates that this is not a passively evolving galaxy. We therefore remove it from our sample. The others in the category fall below the redshift definition when the spectra were fitted together with the photometry.

For the following targets, no spectra were extracted:
123324, 123817, 126952, 128977, 139823, and 207084.

7.B GALFIT results

In Figure 7.9, we show the images and the residuals from Galfit after subtracting the model.

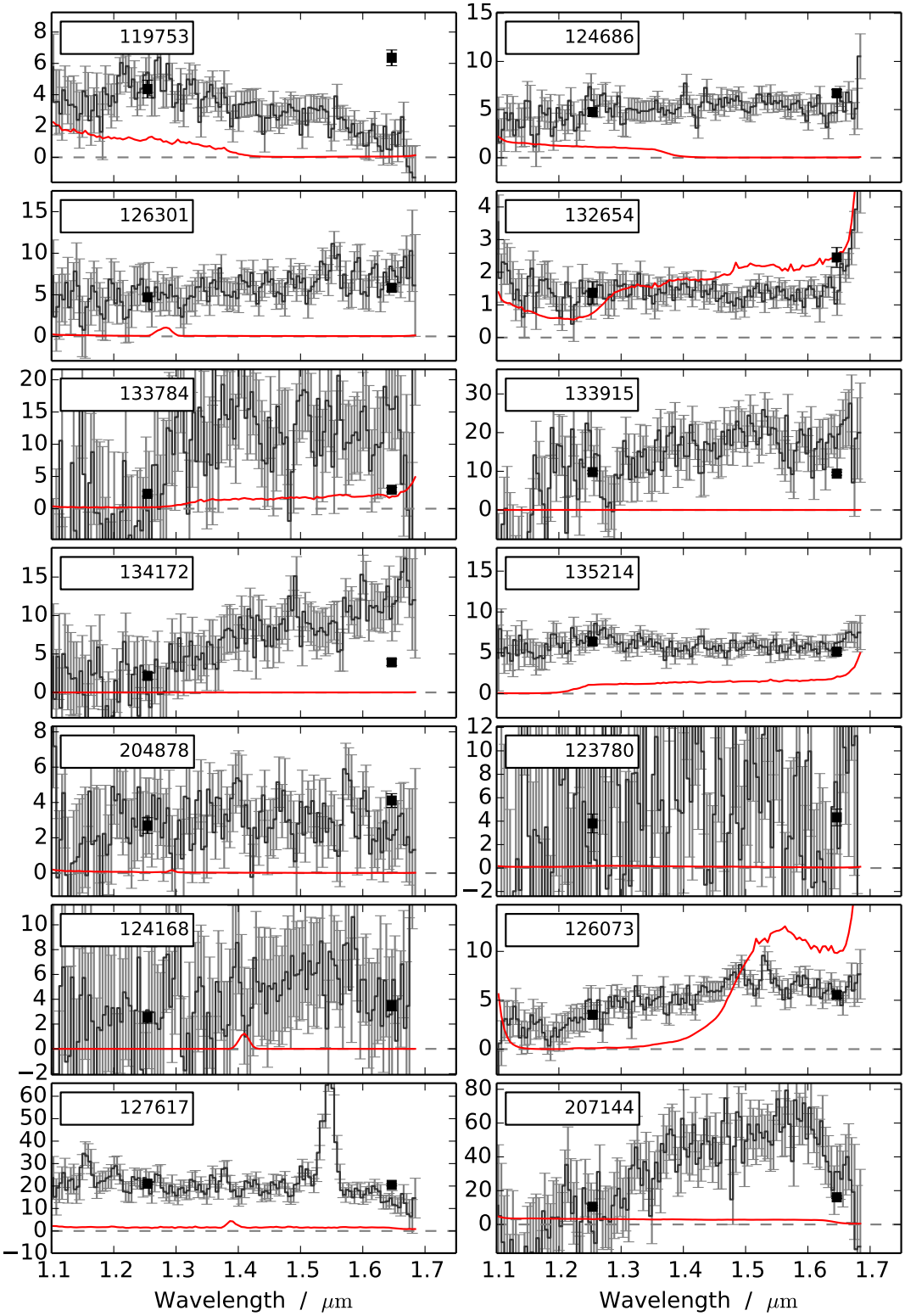

Figure 7.8: Discarded spectra from the sample; for individual notes see Appendix 7.A. The spectra are shown as black with grey error bars in units of 10^{-19} erg^{-1}s^{-1}cm^{-2}Å^{-1}. The red line shows the contamination estimate.

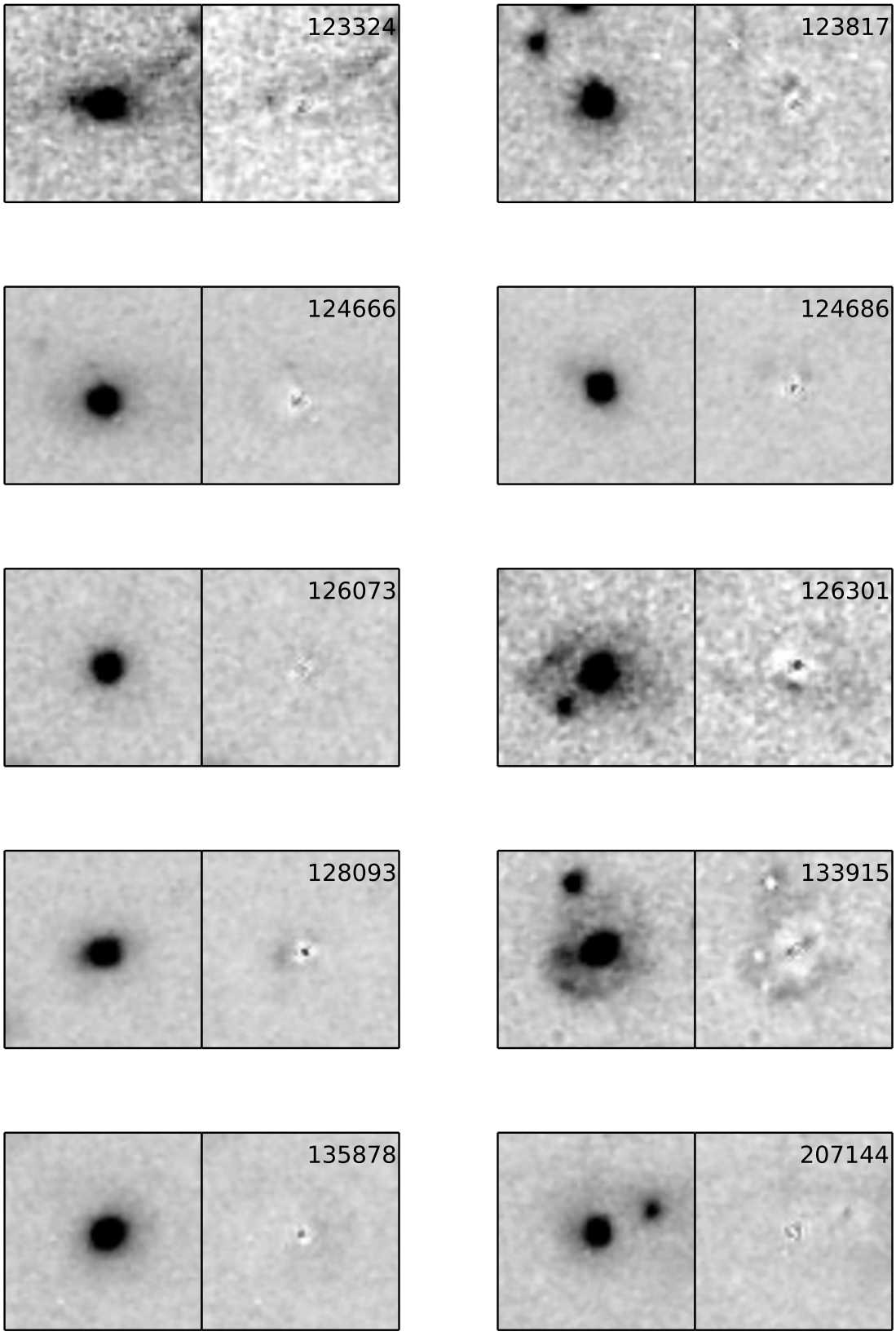

Figure 7.9: 3.6×3.6 arcsec^2 cutouts of the H_{160}-band images. The left and right subplots for each target show, respectively, the raw data and the residuals after subtracting the best-fit model. The best-fit parameters are summarized in Table 7.3. Nearby sources are fitted simultaneously assuming either a point source or an extended Sérsic model. Two targets (126301 and 133915) are strongly affected by their close (plausibly interacting) companions.

8

Conclusions and Outlook

In Chapter 2, we studied the elusive nature of galaxies causing damped Lyα absorbers. In order to enhance the chances of detecting the faint glow from the DLA galaxies, we targeted the metal-rich absorbers only as these had been hypothesized to have more luminous counterparts. Indeed, this approach led to 4 detections out of a sample of 9 DLAs. We found that the relation between metallicity and impact parameter was consistent with DLAs being drawn from the low-luminosity population of star-forming galaxies (Lyman-break galaxies, LBGs). In Chapter 3, one of these metal-rich absorbers was studied in high detail using state-of-the-art instrumentation both from ground and space. This revealed a small, actively star-forming galaxy associated with the absorption. By modelling the Lyα emission we found that outflows must be important to explain the line profile. We therefore concluded that the DLA was caused by enriched material blown out from the star-forming galaxy. Furthermore, we were able to measure the stellar mass of the galaxy: $M_\star = 2 \times 10^9$ M$_\odot$. This was the first direct measurement of the stellar mass of a high-redshift DLA galaxy.

Although the DLAs presented in Chapter 2 make up a heterogeneous and biased sub-sample of the general DLA population, the increase in sample size allowed us to start probing the underlying nature of DLAs in direct emission (see Christensen et al. 2014). So far, the thesis has only presented the detections of emission counterparts in the sample. The full analysis including the non-detections will be presented in a future paper. This will provide a more complete census of metal-rich DLAs, which can be more easily compared to other studies of the DLA population.

Recently, Fumagalli et al. (2014, 2015) presented a sample of 32 DLAs with which they study *in-situ* star formation in the far-UV by imaging below the Lyman-limit caused by unrelated absorbers at higher redshifts. The authors find that the overall star formation rate associated directly with DLAs is very low SFR < 2 M$_\odot$ yr^{-1}; however, these rates do not take into account the possible effects of dust and intergalactic absorption. These results are consistent with a scenario in which DLAs trace the neutral gas around low-luminosity star-forming galaxies. The increasing amount of evidence for an underlying mass–metallicity relation for DLAs (Møller et al. 2013; Neeleman et al. 2013; Christensen et al. 2014) further corroborates these claims: the average DLA will be associated with galaxies of low mass and low luminosity, whereas the more metal-rich DLAs will belong to increasingly larger haloes hosting more massive and luminous galaxies. This picture is furthermore supported by recent cross-correlation analyses and simulations of DLAs within the ΛCDM paradigm (e.g., Font-Ribera et al. 2012; Barnes & Haehnelt 2014; Bird et al. 2014, 2015). Although the picture is not fully painted, the overall frame is present and most of the main observables are matched well.

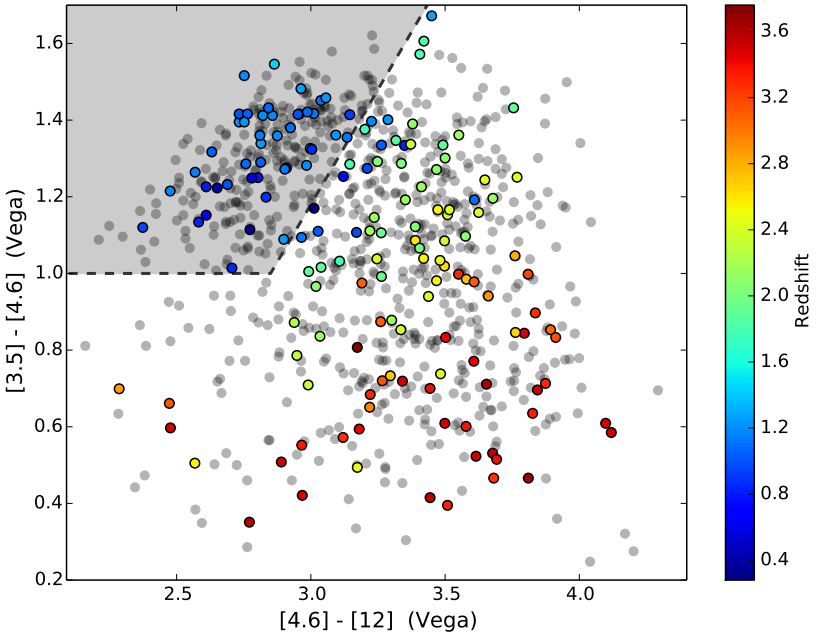

Figure 8.1: Colour-colour plot from WISE photometry. The full HAQ sample is shown as grey points and the spectroscopically confirmed quasars are shown by coloured points, where the colour indicates the quasar redshift. The grey shaded area in the upper left corner is the exclusion region for the eHAQ survey introduced to remove low-redshift interlopers.

One aspect of understanding the nature of DLAs, which remains unanswered, is the question of dust in DLAs and whether our samples are systematically missing the most chemically enriched systems. This led us to the red quasar surveys presented in Chapters 4 and 5. We found that most of the targeted quasars were not reddened by intervening absorbers; however, in Chapter 5, we did find a few quasars with foreground absorbers potentially harbouring dust. One of the quasars from the HAQ survey (QSO J 2225+0527) was studied in detail in Chapter 6. We here found that the dust was indeed located in the absorber and not in the quasar. Furthermore, the background quasar was not identified in the SDSS database due to the strong reddening from the foreground dust. This shows that dusty DLAs are missed by optical quasar selection criteria. The impact of this bias will be studied in future projects where we will compare the different selection functions of SDSS and our surveys to the resulting quasar+DLA population. We have initiated an extension of the HAQ survey (the eHAQ survey) to target quasars at higher redshifts and with larger amounts of reddening by selecting quasars from their mid-infrared properties. We use the near- and mid-infrared photometry from UKIDSS and WISE to separate stars and galaxies from quasars. The WISE photometry furthermore allows us to discard low-redshift quasars, see Figure 8.1. A similar approach was recently published on arXiv.org (Richards et al. 2015, arXiv:1507.07788, Jul 28$^{\rm th}$, *accepted for publication in ApJS*).

A key goal for the eHAQ survey is to identify *redder* quasars than the HAQ survey and at higher redshifts. This will allow us to constrain the incidence of dusty DLAs to a larger degree than what was possible in the HAQ survey. In order to look for more dusty absorbers we will need to extend the survey to more red quasars in terms of their $g-r$ colour. This was originally introduced to have sufficient flux in the blue part of the spectra to look for Lyα absorption. We have simulated the colours of quasars at $z \approx 3$ with foreground DLAs at $z_{\rm DLA} = 2.5$ causing various amounts of reddening, in order to have an idea of the expected behaviour in colour-colour space. These simulated colours are shown in Figure 8.2.

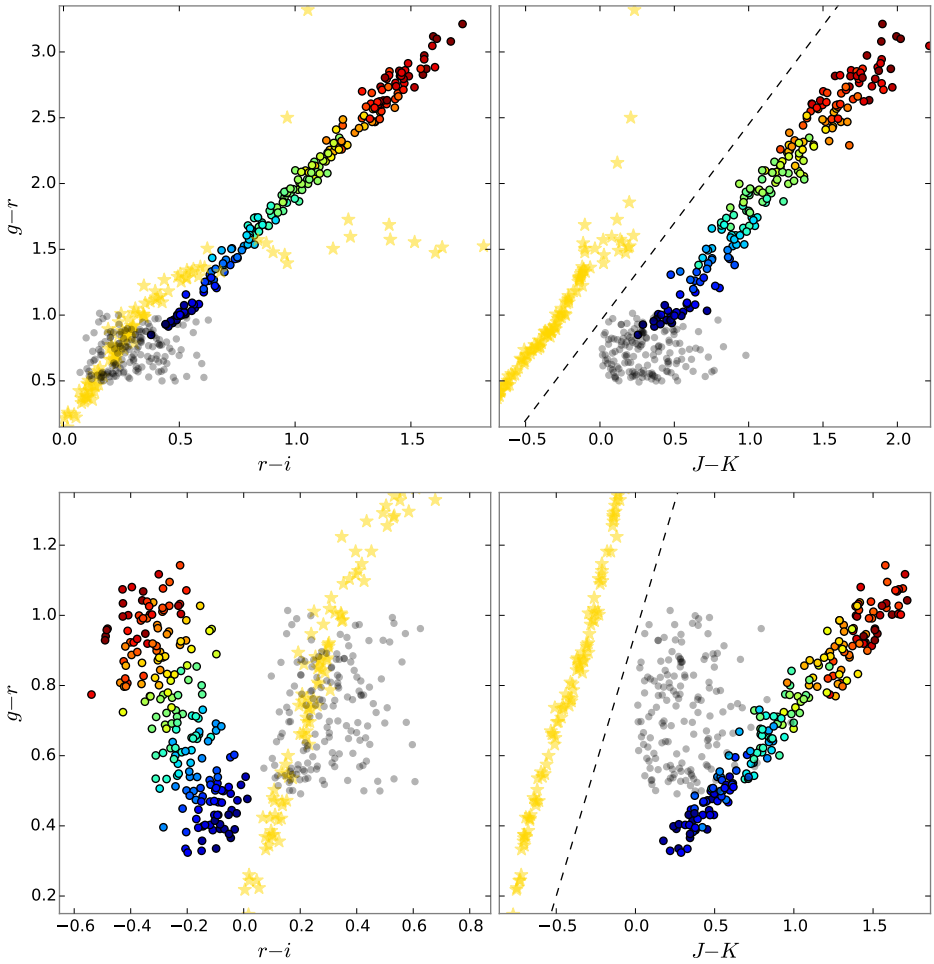

Figure 8.2: Colour-colour diagrams for simulated quasars with intervening DLAs. The coloured points indicate quasars at $z \approx 3$ where the colour corresponds to the amount of reddening $A(V)$ (blue for $A(V) = 0.5$ and red for $A(V) = 2.0$). The grey points show the quasars from the HAQ survey and the yellow stars indicates the stellar locus taken from Hewett et al. (2006). The top row shows colours assuming the SMC extinction curve in the DLA, and the bottom row assumes the LMC extinction curve in the DLA. The combination of optical ($g - r$) and near-infrared ($J - K$) colours clearly separates quasars from stars (indicated by the dashed line).

Moreover, we have simulated spectra for such reddened quasars with foreground DLAs. One such spectrum is shown in Figure 8.3. It is clear that the high amount of reddening suppresses the blue end of the spectrum significantly and the direct search for the Lyα absorption line is not feasible for noisy spectra (the spectrum in Figure 8.3 has an average signal-to-noise ratio of about 20). Instead, the rest-frame UV metal absorption lines serve as probes for the foreground absorption. A quasar with an intrinsic brightness of $r = 19$, shown in Figure 8.3, has an observed r-band magnitude of roughly 23 mag due to the dust reddening from the DLA. Such targets thus require long integration times and/or large telescopes. This will be the aim of the eHAQ survey, which was initiated earlier this year in March.

The issue of a dust bias in optically selected samples at lower redshifts ($z < 1.5$) will also be studied in the future MeerKAT Absorption Line Survey (MALS), which is a large radio survey of the southern hemisphere carried out with the MeerKAT in South Africa. This survey will target 1000 radio and mid-infrared selected quasars, which will have complementary optical spectra. As part of my PhD I have been involved in the optical follow-up for this survey. The goals of MALS will complement the higher redshift eHAQ sample perfectly.

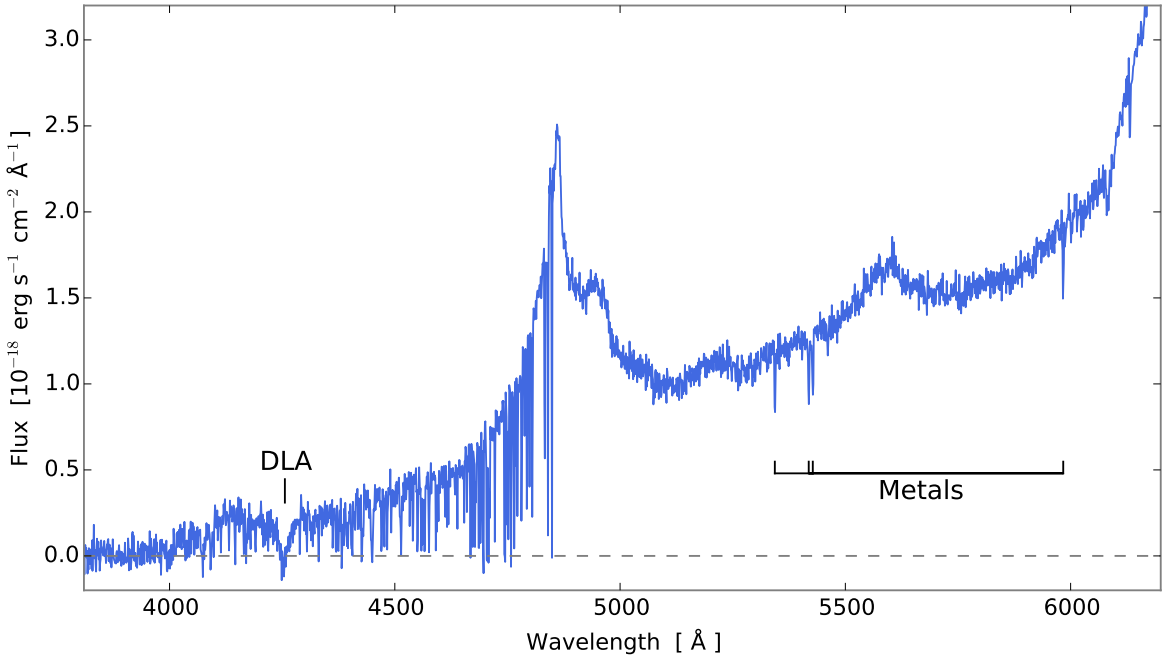

Figure 8.3: Simulated spectrum of a quasar at $z \approx 3$ with a DLA at $z = 2.5$. The simulation was performed for an intrinsic quasar brightness of $r = 19$ mag, $A(V)_{\rm DLA} = 1.0$ assuming the SMC law, a spectral resolution of $\mathcal{R} = 2000$, and average signal-to-noise of about 20. The strong Lyα line as well as associated metals lines are clearly visible.

In Chapters 4 and 5, we identified a large number of missing quasars and a fraction of these had extinction curves steeper than the SMC extinction curve. These were analysed in a separate article, where we have found that the extinction curves towards these quasars seem to be very similar (Zafar et al. 2015). This opens up new questions about the origin of such dust properties: How frequent is the steep extinction curve? Is the excess reddening caused by different grain properties related to the accreting black hole? Or is this due to different chemistry? The eHAQ survey will provide a larger sample of quasars which we intend to follow-up with the X-shooter spectrograph to study the quasar emission lines in detail.

Lastly, in Chapter 7, we presented a spectroscopic sample of quiescent galaxies at $z \sim 2$. With the improved redshift information, we could constrain the mass–size relation better, allowing us to study the intrinsic scatter in this relation. We used the scatter as an extra observable to constrain our 'dilution'-driven size-evolution model in which increasingly larger galaxies are formed at later times, subsequently quenched and added to the quiescent population. We concluded that although the evolution of the average size of the population was well-explained by our model, the resulting increase in scatter was inconsistent with the data. Therefore, an interplay of various processes (e.g., 'dilution', mergers and star formation) is most likely needed to explain the evolution at all times.

Resumé på Dansk

I starten af det 20. århundrede begyndte man at indse, at vort univers ikke blot udgøres af vor egen galakse – Mælkevejen – men i stedet indeholder millioner af galakser ligesom vor egen. Efterhånden som vi observerer mere og mere fjerne galakser, både i tid og rum, dukker et åbenlyst spørgsmål frem: "Hvordan udviklede de første galakser sig til de mageløse og smukt sammensatte galakser vi ser omringe os i dag?" Dette er udgangspunktet for denne afhandling.

Dæmpede Lyα Absorptionslinjesystemer og deres Emissionsmodstykker

I kapitlerne 2 og 3 analyseres de såkaldte "dæmpede Lyman-α absorptionslinjesystemer" (DLA'er), en bestemt type absorptionslinjesystem, med henblik på at identificere de galakser, der forårsager absorptionen i lyset fra bagvedliggende kvasarer. Ved at lave en model for de galakser, som danner DLA'er, og sammenholde denne med data, både nye og fra litteraturen, bliver følgende konklusion draget:

- Fordelingen af stødparametre og metallicitet for DLA'er er konsistent med forventningen fra den udviklede model, hvori DLA'er er associeret med lyssvage, men ellers almindelige, stjernedannende galakser (Lyman-break galakser).

En af disse DLA'er analyseres i større detalje med data fra "Very Large Telescope" (VLT) i Chile og "*Hubble Space Telescope*" (*HST*). I kapitel 3 præsenteres de nye data, og på baggrund af disse konkluderes det at DLA-galaksen er en ung (~ 100 Myr), stjernedannende galakse med kraftige udstrømninger af gas ($v_{\rm ud} \approx 160\,{\rm km\ s^{-1}}$). Med de nye data er det muligt for første gang at bestemme massen af stjernerne i en DLA-galakse: $M_\star = 2 \times 10^9\ M_\odot$.

Søgning efter Røde Kvasarer

På baggrund af observationer, der indikerer, at visse DLA'er indeholder betydelige mængder af støv, igangsættes et større opfølgende studium af dette støvs indvirkning på vores udvælgelsesmetoder af DLA'er. Støvet i DLA'er medfører nemlig, at den bagvedliggende kvasars lys bliver svagere. Ydermere ændrer støvet kvasarens spektrale karakteristika, da de korte bølgelængder undertrykkes mere end de lange. På den måde kan støv i DLA'er medvirke til, at kvasarer bagved DLA'er med store mængder støv (og dermed også metaller) ikke opdages med traditionelle metoder. I kapitel 4 præsenteres vore nye udvælgelseskriterier, baseret på optisk og nær-infrarød fotometri, samt resultaterne af de opfølgende observationer af 58 kandidater. Ud af disse er 46 (79%) bekræftet som værende kvasarer. Kun omkring halvdelen af disse 46 røde kvasarer er identificeret som sådan på baggrund af den traditionelle metode, som anvendes i "The Sloan Digital Sky Survey" (SDSS). Yderligere er kun fire observeret med spektroskopi i SDSS databasen. Mængden af støv, givet som $A(V)$, bestemmes udfra kvasarspektrene, og følgende slutninger drages:

- Støvet er primært forårsaget af kvasarens værtsgalakse, og støvet følger i de fleste tilfælde kendte rødfarvningslove udledt for den Lille Magellanske Sky.
- Der observeres ingen foranliggende absorptionslinjesystemer.
- For visse kvasarer kan rødfarvningen ikke beskrives vha. kendte love. I stedet må en rødfarvningslov med stejlere hældning anvendes.

I et forsøg på at mindske kontamination fra stjerner og galakser i udvælgelsen af kvasarer revideres kriterierne fra kapitel 4 efterfølgende. De reviderede kriterier og observationerne af 159 dermed udvalgte kandidater præsenteres i kapitel 5: "*The High A(V) Quasar Survey*". Ud af de 159 kandidater bekræftes 154 (97%) som værende kvasarer. I modsætning til undersøgelsen i kapitel 4 identificeres 30 absorptionslinjesystemer. Det undersøges derfor om rødfarvningen af kvasarerne skyldes støv i kvasaren selv eller i et foranliggende absorptionslinjesystem. Dette testes vha. en statistisk sammenligning af modeller med og uden hypotetiske absorptionslinjesystemer ved rødforskydning, $z_{\rm abs}$, som giver anledning til rødfarvning. I afhandlingen benyttes størrelsen $A(V)_{\rm abs}$ til at beskrive ekstinktionen i det visuelle V-bånd forårsaget af det foranliggende absorptionslinjesystem. Den anvendte model er beskrevet i detalje i Appendix A.2. Ud fra analysen konkluderes følgende:

- Ni spektre beskrives bedst med en model hvor støvet er i et foranliggende absorptionslinjesystem. To af disse bekræftes yderligere af en detektion af et egentligt absorptionslinjesystem ved samme rødforskydning som modellen forudsiger.
- Elleve kvasarer har et signifikant overskud af emission ved 2 μm i kvasarens referenceramme. Dette forklares ved et overskud af emission fra varmt ($T \sim 1500$ K) støv.
- Sektsen kvasarer har et signifikant underskud af emission ved 2 μm i kvasarens referenceramme. Ligesom i kapitel 4 tyder dette på at rødfarvningsloven i disse tilfælde har stejlere hældning end den antagne lov for den Lille Magellanske Sky.

Støv i Dæmpede Lyα Absorptionslinjesystemer

En af kvasarerne i HAQ undersøgelsen, HAQ 2225+0527, havde et foranliggende DLA, men den præliminære analyse viste, at rødfarvningen skyldes støv i kvasaren selv. I kapitel 6 præsenteres nye data fra X-shooter-instrumentet på VLT. Med de nye data er det muligt at foretage en detaljeret undersøgelse af både DLA og kvasar. De nye analyser viser, at det er støv i DLA'et, som giver anledning til rødfarvningen af kvasaren. Ekstinktionen estimeres ud fra spektral modellering: $A(V)_{\rm DLA} = 0.28 \pm 0.01|_{\rm stat} \pm 0.07|_{\rm sys}$ mag. Dette er konsistent med $A(V)$ bestemt ud fra jern-zink forholdet: $A(V)_{\rm DLA} = 0.39^{+0.13}_{-0.10}$ mag. Den bagvedliggende kvasar er pga. den kraftige rødfarvning ikke blevet identificeret som en kvasar in SDSS, og dette metal-rige DLA er derfor ikke repræsenteret i nuværende kataloger fra SDSS. Dette system giver således direkte evidens for, at metal-rige DLA'er underrepræsenteres i optisk udvalgte kataloger. Derudover observeres såkaldt "delvis dækning" i absorptionslinjerne fra neutralt kulstof og dettes finstrukturlinjer (C I, C I* og C I**). Dette forklares ved, at det absorberende medium har en lille projiceret udstrækning i forhold til den bagvedliggende emissionskilde (i dette tilfælde kvasarens bredlinje-emissionsregion, BLR). Størrelsen af både det absorberende medium og BLR bestemmes til ~ 0.1 parsec.

Størrelsesudviklingen af Kompakte, Tunge Galakser siden Rødforskydning 2

I det sidste kapitel (kap. 7) studeres de tungeste galakser i det tidlige univers. De første observationer af disse fjerne og røde galakser ("distant red galaxies") viste, at disse galakser typisk er 2–6 gange mindre en tilsvarende galakser i det lokale univers ved rødforskydning 0. Siden da har mange studier forklaret dette som konsekvensen af en række sammenstød med mindre galakser. I kapitel 7 præsenteres et spektroskopisk udvalg af galakser observeret med Rumteleskopet *HST*. Den øgede præcision i bestemmelserne af rødforskydning gør det muligt for første gang at undersøge spredningen i sammenhængen mellem stellar masse og fysisk størrelse. Det vises, at størrelsesudviklingen kan beskrives som en udvikling af hele ensemblets gennemsnitlige størrelse, i stedet for en egentlig udvikling af hver enkel galakse. Denne udvikling drives af dannelsen af større og større galakser ved lavere rødforskydninger. Spredningen i relationen kan derimod ikke beskrives korrekt, da denne ifølge modellen vokser med tiden i modsætning til data. Det sluttes derfor, at en kombination af forskellige scenarier må virke i fælleskab for at forklare udviklingen som funktion af kosmisk tid.

Resumen en Español

En el principio del siglo XX fue descubierto que nuestro universo no estaba limitado a nuestra propia galaxia – La Vía Láctea – sino que estaba compuesto por millones de galaxias individuales como la nuestra. Progresivamente cuando observamos galaxias aún más lejanas, tanto en el tiempo como en el espacio, aparece una pregunta fundamental: "¿Cómo evolucionaron las primeras galaxias a las magníficas y bellas estructuras que vemos en el universo local?" Éste es el punto de partida de esta tesis.

Sistemas Amortiguados Lyα y sus Contrapartes de Emisión

En los Capítulos 2 y 3 se analizan los "sistemas amortiguados Ly-α" (DLAs), que son una clase de sistemas de absorción, con la finalidad de identificar las galaxias que causan la absorción de la luz de los cuásares de fondo. Haciendo un modelo físico de las galaxias que causan los DLAs, y comparando éste con los datos, se concluye lo siguiente:

- La distribución de los parámetros de impacto y metalicidad de los DLAs es consistente con la expectativa del modelo, en el cual los DLAs están asociados con galaxias de baja luminosidad que forman activamente estrellas (llamadas Galaxias Lyman-break, LBGs).

Uno de estos DLAs se analiza en más detalle con datos del "Very Large Telescope" en Chile y del "*Hubble Space Telescope*". En el Capítulo 3 se presentan los nuevos datos, y a la luz de éstos se concluye que la galaxia asociada con el DLA es joven (~ 100 Myr) y tiene una formación de estrellas activa con efusión potente de gases (con una velocidad de 160 km s^{-1}). Por primera vez es possible determinar la masa de la galaxia asociada con un DLA altamente desplazado hacia el rojo gracias a los nuevos datos de alta calidad. Se mide una masa de $M_\star = 2 \times 10^9\ M_\odot$.

La búsqueda de los Cuásares Rojos

En base a observaciones que indican que algunos DLAs contienen polvo se comenzó un estudio de seguimiento para investigar cómo este polvo afecta a nuestros métodos de selección de DLAs. El polvo en ellos tiene el efecto de extinguir los cuásares de fondo. Además se cambian las características espectrales de los cuásares por el polvo, porque las longitudes de onda cortas se suprimen más que las longitudes de onda largas. De este modo el polvo en los DLAs podría cambiar las características de los cuásares al grado de que no se descubran los cuásares por métodos tradicionales. Este efecto es más grave para los DLAs que contienen mucho polvo (por lo tanto, también muchos metales). En el Capítulo 4 se presentan nuestros criterios de selección nuevos, que se basan en la fotometría óptica y del infrarrojo cercano, y los resultados de las observaciones espectrales de seguimiento. De los 58

candidatos que observamos se confirman 46 (79%) cuásares. Los demás son cuatro galaxias rojas, cuatro estrellas frías de tipo M y cuatro objetos que no se identifican con certeza. Sólo la mitad de los 46 cuásares confirmados han sido identificados como tales usando los métodos tradicionales, como los que usa el Sloan Digital Sky Survey (SDSS). Además, sólo cuatro están observados con la espectroscopía en la base de datos del SDSS. La cantidad de polvo, aquí llamado $A(V)$, se determina de los espectros, y se puede concluir lo siguiente:

- El polvo está principalmente asociado a la galaxia del cuásar, y el polvo está descrito por la relación de enrojecimiento de la Pequeña Nube de Magallanes (SMC).
- No se observa ningún sistema de lineas de absorción delante de los cuásares.
- El enrojecimiento de algunos cuásares no se describe bien por la relaión de la SMC. En este caso, se necesita una relación con pendiente más pronunciada.

Intentando eliminar la contaminación de estrellas y galaxias en la selección de cuásares, se revisan los criterios posteriormente. Los criterios revisados y las observaciones de los 159 candidatos se presentan en el Capítulo 5: "*The High A(V) Quasar Survey*". De los 159 candidatos se confirman 154 (97%). En contraste con el estudio en el Capítulo 4 se identifican 30 sistemas de líneas de absorción. Por lo tanto, se examina si el enrojecimiento está causado por el polvo en los cuásares o en los sistemas de absorción delante de ellos. Ésto se prueba mediante la comparación estadística de varios modelos con y sin polvo en un sistema de absorción hipotético. El corrimiento hacia el rojo del sistema de absorción se denota $z_{\rm abs}$, y el monto de extinción causado por el sistema de absorción se denota $A(V)_{\rm abs}$. El modelo se describe en el Apéndice A.2. Tras el análisis se concluye:

- Nueve de los espectros son consistentes con el modelo en el cual un sistema de absorción causa el enrojecimiento. Dos de estos se confirman posteriormente por una detección de un sistema de absorción con el mismo corrimiento hacia el rojo como la expectativa del modelo.
- Once cuásares tienen un exceso significativo en 2 μm en el marco de referencia del cuásar. Ésto se explica por un exceso de emisión de polvo caliente ($T \sim 1500$ K).
- Dieciséis cuásares tienen un déficit significativo en 2 μm en el marco de referencia del cuásar. Esto indica que la relación del enrojecimiento tiene una pendiente más pronunciada.

Polvo en los Sistemas Amortiguados Lyα

Uno de los cuásares en el estudio HAQ, el objeto HAQ 2225+0527, tuvo un DLA delante, pero el análisis principal mostró que el enrojecimiento fue causado por polvo en el cuásar. En el Capítulo 6 se presentan nuevos datos del instrumento X-shooter en el Very Large Telescope. Con estos datos se hace una investigación más detallada. El nuevo análisis muestra que en realidad es polvo en el DLA que causa el enrojecimiento del cuásar. La extinción se calcula con dos métodos independientes: Haciendo un análisis espectral se estima $A(V)_{\rm DLA} = 0.28 \pm 0.01|_{\rm stat} \pm 0.07|_{\rm sys}$ mag, y en base de la relación de hierro a zinc se determina $A(V)_{\rm DLA} = 0.39^{+0.13}_{-0.10}$ mag. Debido al enrojecimiento de la DLA, el cuásar detrás del DLA no está clasificado como tal en SDSS. Así, este sistema de absorción presta evidencia directa de que los DLAs que contienen muchos metales y polvo están subrepresentados en los catálogos actuales seleccionados ópticamente. Además se observa "cobertura parcial" en las líneas de absorción

de carbono neutral y sus niveles de estructura fina (C I, C I* y C I**). La cobertura parcial indica que el medio absorbente es más pequeño (en proyección) comparado con la fuente de emisión de fondo (en este caso, la región de emisión de líneas anchas). El tamaño del medio absorbente y la región de emisión de líneas anchas se determina que es 0.1 pársec.

La evolución del Tamaño de Galaxias Compactas y Masivas

En el último Capítulo (el Cap. 7) se presenta un estudio de las galaxias más masivas y muy corridas hacia el rojo ($z = 2$). Las primeras observaciones de estas galaxias rojas y lejanas (llamadas "distant red galaxies") han mostrado que las galaxias son 2–6 veces más pequeñas que las galaxias equivalentes en el universo local (es decir, cero corrimiento hacia el rojo). Desde entonces muchos estudios han explicado esta evolución con una secuencia de fusión galáctica con satélites. En el Capítulo 7 se presenta una investigación espectral de galaxias que tienen un corrimiento al rojo de aproximadamente 2 ($z \approx 2$) usando el telescopio espacial "Hubble". Con la mejor precisión en la medición del corrimiento al rojo es posible investigar la dispersión en la relación entre masa estelar y tamaño. Se muestra que la evolución de tamaño puede ser explicado como una evolución del promedio de la distribución de tamaño y no necesariamente un crecimiento de cada galaxia individualmente. Esta evolución está impulsada por la formación de galaxias progresivamente más grandes hacia bajo corrimiento al rojo. Sin embargo, la dispersión de la relación no se explica correctamente, ya que ésta, según el modelo, crece con el tiempo contrariamente a los datos. Por consiguiente, se concluye que se necesita una combinación de varios mecanismos juntos para explicar la evolución en todas épocas de la historia cósmica.

Appendices

A

Appendix to Chapter 1

A.1 Voigt Profile Fitting

In order to measure the column densities of metal lines in damped Lyman α absorbers, I fit the absorption lines with Voigt profiles. For that purpose, I wrote my own fitting routine in Python, `VoigtLineFit`. The following sections describe the main outline of the software.

A.1.1 Absorption Line Profile

The absorption line arising from a transition i of element X can be described by the line's optical depth, τ, which is determined by the column density of the element X along with a set of atomic parameters describing the line strength, f_i, the damping constant, Γ_i, and the resonance wavelength, λ_i, for the transition, i:

$$\tau_{i,X}(\lambda) = C_i \; N_X \; a_i \; H[a_i, x(\lambda)] \qquad \text{(eq. A.1)}$$

where C_i and a_i are given by:

$$C_i \equiv \frac{4\, e^2\, \sqrt{\pi^3}}{m_e\; c}\; \frac{f_i}{\Gamma_i} \qquad \text{and} \qquad a_i \equiv \frac{\lambda_i\, \Gamma_i}{4\pi b} \qquad \text{(eq. A.2)}$$

The line profile is determined by the *Voigt–Hjerting function*, $H(a_i, x)$:

$$H(a_i, x) \equiv \frac{a_i}{\pi} \int_{-\infty}^{+\infty} \frac{e^{-y^2}}{(x-y)^2 + a_i^2}\, \mathrm{d}y \qquad \text{(eq. A.3)}$$

where $x(\lambda) = (\lambda - \lambda_i)/\lambda_D$ is the rescaled wavelength and $y = v/b$ is the velocity of the absorbing atom in units of the broadening parameter, b. $\lambda_D = (b/c)\; \lambda_i$ is the Doppler wavelength.

Since the integral in the Voigt–Hjerting function is very laborious to evaluate for every iteration in the fit, an analytical approximation is used instead:

$$H(a_i, x) \approx h - \frac{a_i}{x^2\sqrt{\pi}} \left[h^2\, (4x^4 + 7x^2 + 4 + 1.5x^{-2}) - 1.5x^{-2} - 1\right] \qquad \text{(eq. A.4)}$$

where $h = e^{-x^2}$ (Tepper-García 2006, 2007, see). The implementation in Python is shown in A.1.3.

Given the optical depth for the given transition, the resulting flux is given by:

$$I(\lambda) = I_0(\lambda)\, e^{-\tau(\lambda)} \qquad \text{(eq. A.5)}$$

where I_0 is the incident flux, in the case of DLAs I_0 is the spectrum of the background quasar.

A.1.2 Fitting Spectra

The first input required for the fit is obviously the spectral data and information about the spectral resolution. After the data has been loaded, the absorption lines are defined. The code generates a small (defined in terms of velocity, typically ± 500 km s^{-1}) region of the spectral data around every single absorption line to be fitted. If spectral regions overlap, they are merged into one region. Next, the velocity components (z, b) are defined for each line. The code then normalizes each region, if the input data are not normalized, and unwanted parts of the spectra are interactively masked out. Before fitting, linked and fixed parameters are initialized as well as parameter boundaries. The code then fits all the, N, regions simultaneously.

For every fit iteration, the code calculates the intrinsic optical depth, τ (described above) for the lines defined in each region on the same wavelength grid as the data. The optical depths for all lines in a region are summed and converted to a total intrinsic line profile, I. The intrinsic line profile is subsequently convolved with the instrumental line spread function (LSF; assumed to be Gaussian with a width determined by the spectral resolution, $\mathcal{R}$). The χ^2 is calculated as the sum over all regions:

$$\chi^2 = \sum_{n=1}^{N} \sum_{m=1}^{M} \frac{(\mathcal{F}_{n,m} - \mathcal{M}_{n,m})^2}{(\sigma_{n,m})^2 + (\sigma_{\rm norm})^2}\,, \qquad \text{(eq. A.6)}$$

where $\mathcal{F}_{n,m}$ denotes the $m^{\rm th}$ spectral pixel of the data in the $n^{\rm th}$ region, similarly $\mathcal{M}(= I * {\rm LFS})$ denotes the model spectrum of the given region, and σ refers to the uncertainty of the spectral data. The uncertainty on the continuum normalization for the $n^{\rm th}$ region, $\sigma_{\rm norm}$, is included. The χ^2 minimization and parameter attributes (e.g., ties and boundaries) are handled by the Python package `lmfit`[1].

[1]Written by Matthew Newville. Full documentation available at: http://cars9.uchicago.edo/software/python/lmfit/

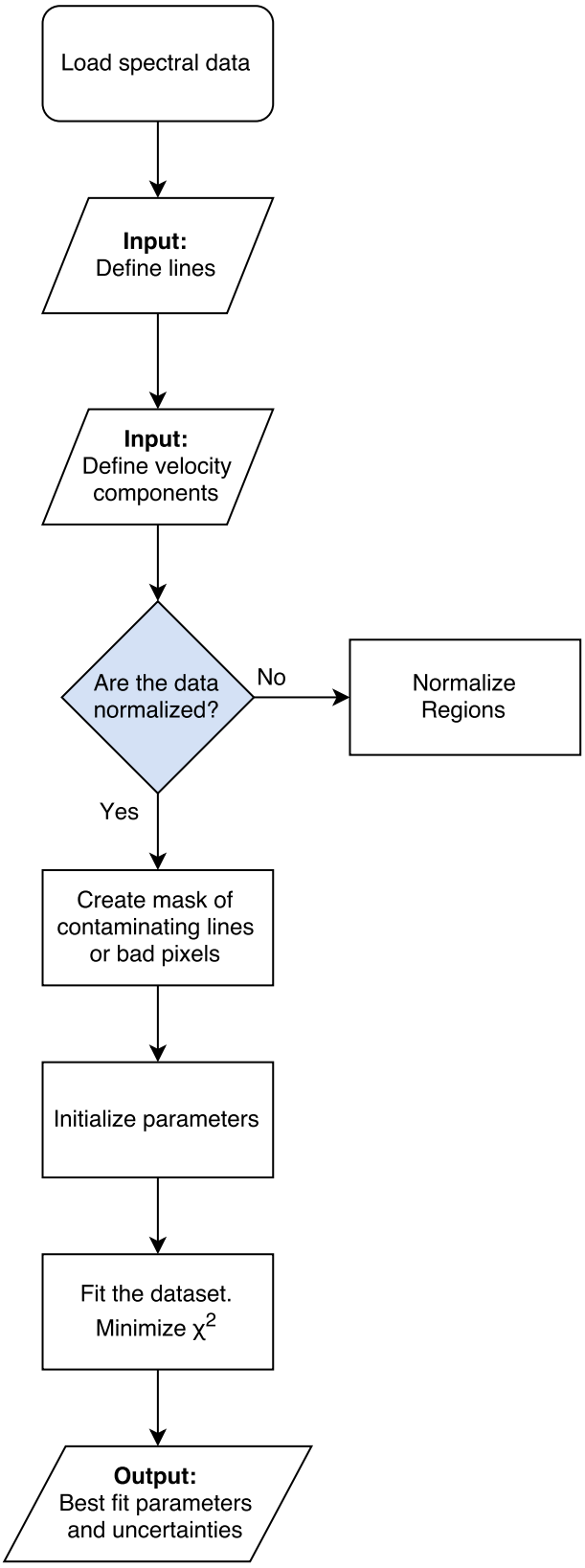

Figure A.1: Flowchart illustrating the overview of the fitting routine `VoigtLineFit`.

A.1.3 Python Implementation of the Voigt–Hjerting Function

```
from numpy import exp, sqrt, pi

def H(a, x):
    # Analytic approximation to the Voigt-Hjerting Function.
    # For details, see Tepper-García 2006, MNRAS, 369, 2025.
    P = x**2
    H0 = exp(-x**2)
    Q = 1.5/x**2
    return H0 - a/sqrt(pi)/P * (H0*H0*(4.*P*P + 7.*P + 4. + Q) - Q - 1)

def Voigt(l, l0, f, N, b, gam, z=0):
    # Calculate the Voigt profile optical depth
    # rest frame transition wavelength: 'l0'  Å
    # oscillator strength: 'f'
    # damping constant: 'gam'
    # redshift: 'z'
    # column density: N  cm^-2
    # velocity width: b  cm/s

    #==== PARAMETERS =====================

    c   = 2.99792e10     #cm/s
    m_e = 9.1095e-28     #g
    e   = 4.8032e-10     #cgs units

    #=====================================

    C_a  = sqrt(pi)*e**2*f*l0*1.e-8/m_e/c/b
    a    = l0*1.e-8*gam/(4.*pi*b)

    dl_D = b/c*l0
    l = l/(z+1.)
    x = (l - l0)/dl_D
    x += 0.0001          # add tiny offset:
                         # H(a,x=0) is not
                         # defined.
    tau  = C_a*N*H(a,x)

    return tau
```

A.2 Fitting Dust towards Quasar Sightlines

In Chapters 4, 5, and 6, I estimate the amount of dust along quasar sightlines using template fitting. Below I summarize the full model, which is an expanded formalism of the modelling performed in Chapter 5. The model is parametrized by the following set of parameters, $\vec{x}$:

$$\vec{x} = \{z_{\rm abs},\ A(V)_{\rm QSO},\ A(V)_{\rm abs},\ \Delta\beta,\ f_0,\ Fe_2,\ Fe_3\}\ ,$$

where $z_{\rm abs}$ is the redshift of the absorber; $A(V)_{\rm QSO}$ and $A(V)_{\rm abs}$ denote the V-band extinction in the rest-frame of the QSO and absorber, respectively; $\Delta\beta$ denotes the power-law slope relative to the intrinsic slope of the quasar template; f_0 is an arbitrary scaling as we do not know the intrinsic brightness of the quasar prior to reddening; Fe_2 and Fe_3 denote the strengths of the emission template for Fe II and Fe III, respectively.
For each set of parameters, the model template is calculated as:

$$\begin{aligned} T(\vec{x},\lambda) = f_0 \times & \left[T_{\rm QSO} \cdot \left(\frac{\lambda}{\lambda_0}\right)^{\Delta\beta} + Fe_2 \cdot T_{\rm FeII} + Fe_3 \cdot T_{\rm FeIII} \right] \\ & \times\ \exp\left[-\frac{1}{2.5\log_{10}(e)} \left(\xi_{\rm QSO}(\lambda)\cdot A(V)_{\rm QSO} + \xi_{\rm abs}(\lambda)\cdot A(V)_{\rm abs}\right) \right]\ , \end{aligned} \qquad \text{(eq. A.7)}$$

where $T_{\rm QSO}$ denotes the quasar template from Selsing, Fynbo, Christensen, & Krogager (2015, in preparation) shifted to the redshift of the quasar, $z_{\rm QSO}$, $T_{\rm FeII}$ and $T_{\rm FeIII}$ denote the iron emission template from Vestergaard & Wilkes (2001), see Sect. A.2.1, $\xi_{\rm QSO}$ and $\xi_{\rm abs}$ denote the wavelength dependent reddening curve in the rest-frame of the QSO and absorber, respectively. The reddening curve, $\xi_{\rm abs}$, is therefore implicitly a function of $z_{\rm abs}$.

The χ^2 (which is related to the likelihood, $\mathcal{L}$) is calculated assuming a Gaussian error distribution, neglecting the correlation between neighbouring pixels.

$$\chi^2 = -2\ln(\mathcal{L}) = \sum_i^N \frac{\left(D_i - T(\vec{x},\lambda_i)\right)^2}{\Sigma_i^2}\ . \qquad \text{(eq. A.8)}$$

The sum is over all N data points D_i. The model T is evaluated at the corresponding wavelengths as the data points[2]. Moreover, the errors are convolved with the template error function, $\sigma_T(\lambda)$, which incorporates the quasar-to-quasar variations. The template error function is given as a relative error ($\sigma_T = \frac{\delta T}{T}$, see Figure A.2). The effective uncertainty for each data point, Σ_i, is given by adding the intrinsic error (σ_i) and the template error in quadrature:

$$\Sigma_i^2 = \sigma_i^2 + \left(D_i \cdot \sigma_T(\lambda_i)\right)^2\ . \qquad \text{(eq. A.9)}$$

The χ^2 function is minimized with respect to the model parameters, $\vec{x}$, in order to find the best-fitting parameters. For the minimization, I use the Levenburg–Marquardt algorithm as implemented in the Python package `lmfit`[3]. Since a negative $A(V)$ is non-physical, the parameters $A(V)_{\rm QSO}$ and $A(V)_{\rm abs}$

[2]For photometric data, the template is weighted by the appropriate filter transmission curve to generate a synthetic photometric point. For spectra, the template is interpolated onto the same wavelength grid as the observed spectrum.
[3]Written by Matthew Newville. Full documentation available at: http://cars9.uchicago.edo/software/python/lmfit/

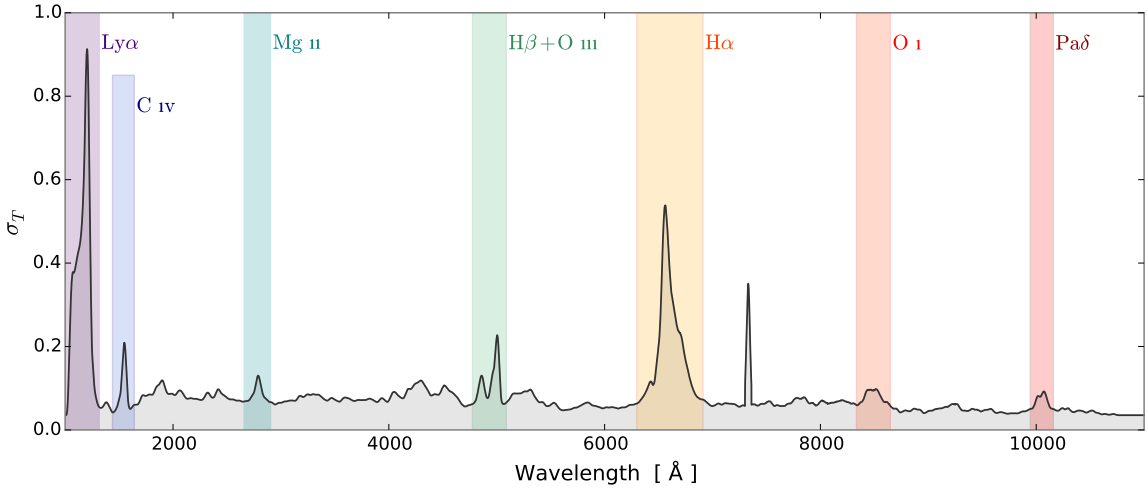

Figure A.2: Quasar template error function. The data are provided by Selsing et al. (2015, in preparation). The most prominent emission lines are labeled.

are only allowed to vary within the given bounds: $A(V) \geq 0$. Similarly, the absorption redshift is kept within $0 < z_{\rm abs} < z_{\rm QSO}$. In practice, though, the upper limit on $z_{\rm abs}$ is set to $0.95 \times z_{\rm QSO}$ in order to reject absorbers that are very close to the quasar in redshift space. The implementation of the parameter boundaries is handled by `lmfit`.

A.2.1 Iron emission template

The iron emission used together with the quasar template in the model described above is obtained from Vestergaard & Wilkes (2001). In order to allow the two components (Fe II and Fe III) to vary independently, the template has been split into two separate templates with varying strengths, Fe_2 and Fe_3. The two templates are shown in Figure A.3. Before introducing the iron template to the model, the template has to be smoothed to match the velocity width of the broad emission lines in the input quasar spectrum.
Following Vestergaard & Wilkes, I convolve the template with a Gaussian kernel of width, $\mathrm{FWHM}_{\rm conv}$, given by:

$$\mathrm{FWHM}_{\rm conv} = \sqrt{(\mathrm{FWHM}_{\rm QSO})^2 - (\mathrm{FWHM}_{\rm temp})^2},$$

where $\mathrm{FWHM}_{\rm QSO}$ denotes the full width at half maximum (FWHM) of broad emission lines in the input quasar, and $\mathrm{FWHM}_{\rm temp}$ refers to the width of the broad emission lines of the quasar used to compile the template (900 km s^{-1}). The template is rebinned logarithmically to have a constant pixel-size in velocity-space. This keeps the convolution kernel constant across the template. After the convolution, the template is interpolated back onto a linear wavelength grid matching the spectral sampling of the data.

A similar velocity broadening is not necessary for the quasar template, $T_{\rm QSO}$, since the broad emission lines are masked out during the fit. These emission lines are much too variable to provide a good fit with a single template (this is also reflected by the template error function in Figure A.2).

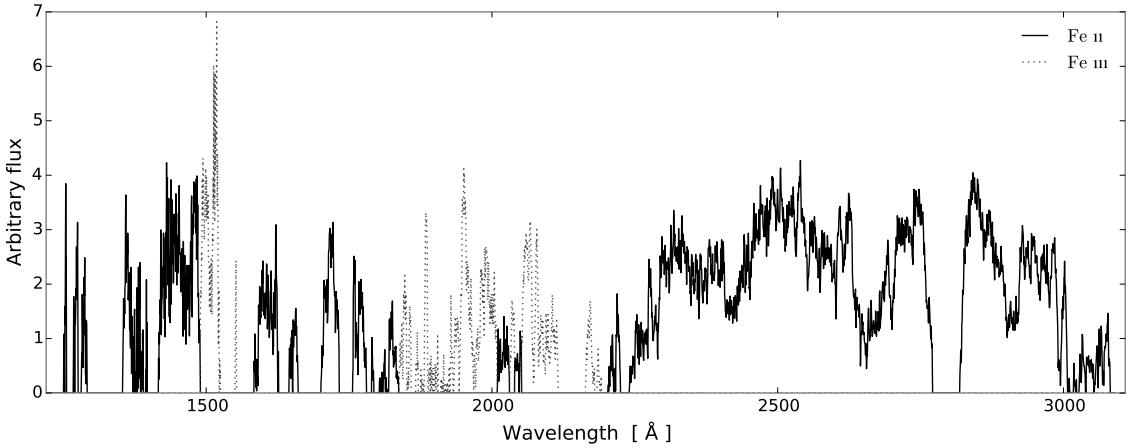

Figure A.3: Ultraviolet iron emission template from Vestergaard & Wilkes (2001).

A.2.2 Bayesian Parameter Estimation and Priors

The inclusion of boundaries in the regular χ^2 minimization leads to incorrect handling of the uncertainties for parameters close to the bounds. Therefore, the fitting code allows a higher degree of accuracy by using a Markov chain Monte Carlo (MCMC) method for the parameter estimation. Also, the MCMC method allows the inclusion of priors on the various parameters. I use the Python package `emcee` (Foreman-Mackey et al. 2013) to sample the posterior probability distribution, P:

$$P(\vec{x}\,|\,D_i) = \frac{\mathcal{L}(D_i|\,\vec{x}\,)\,p(\vec{x})}{p(D_i)}\,, \qquad \text{(eq. A.10)}$$

where $\mathcal{L}(D_i|\,\vec{x}\,)$ is the likelihood defined in eq. A.8, $p(\vec{x})$ refers to the prior probability of the parameters (also simply referred to as the *prior* on $\vec{x}$), and $p(D_i)$ is the probability of the data, D_i, which is constant and can be regarded as a normalization constant.

Setting the priors

When including a variable slope in the modelling I use a Gaussian prior for the slope: $p(\Delta\beta) = \mathcal{N}(0, 0.2)$. The intrinsic uncertainty on the power-law slope of 0.2 dex is motivated by previous studies (Vanden Berk et al. 2001; Krawczyk et al. 2015). For all other parameters, I use naïve priors, unless other data suggest differently. For instance, in Chapter 6, I could have included a very restrictive prior on $z_{\rm abs}$, since this quantity is known spectroscopically with very high confidence. I chose, however, to run the chain with this parameter fixed to the spectroscopic value to speed up the process. In the same Chapter, I could include a prior on $A(V)_{\rm abs}$ since this parameter is constrained independently from the abundance ratio analysis. In fact, doing so did not change the best-fitting parameters, since the prior is relatively weak compared to the wealth of data from the full range of the X-shooter spectrum. Moreover, I include the physically motivated boundaries on $A(V)_{\rm QSO} \geq 0$, $A(V)_{\rm abs} \geq 0$, and $0 < z_{\rm abs} < z_{\rm QSO}$.

Initiating the chain

The software `emcee` uses a set of so-called 'walkers' to investigate the parameter space. Each walker is basically its own chain, but the behaviour of one walker depends on the position of the other walkers. The walkers need to be initiated at some location in the $N_{\rm par}$ dimensional parameter space (here $N_{\rm par} = 7$). From that initial location, the walkers branch out and sample the posterior probability for n iterations. The first phase of the sampling is referred to as the 'burn in' phase where the walkers are exploring a large part of parameter space. As the chain progresses, the walkers converge towards the maximum likelihood. Hereafter, the walkers sample the posterior probability and the recovered samples are used to infer the posterior probability distribution for the parameters. The 'burn in' samples are rejected from the chain, since they are not representative of the posterior distribution.

In Chapter 6, I initiate the sampler with 100 walkers and run the chain for 800 iterations, 300 of which are removed as 'burn in', see Figure A.4. The walkers are initiated around the best-fitting solution from the simple χ^2 minimization. The results for the quasar J 2225+0527 analysed in Chapter 6 are shown in Figure A.5. The best-fitting parameters are quoted as the median of the marginalized posterior with 1 (3) sigma uncertainty given by the 16 and 84 (0.2 and 99.8) percentiles.

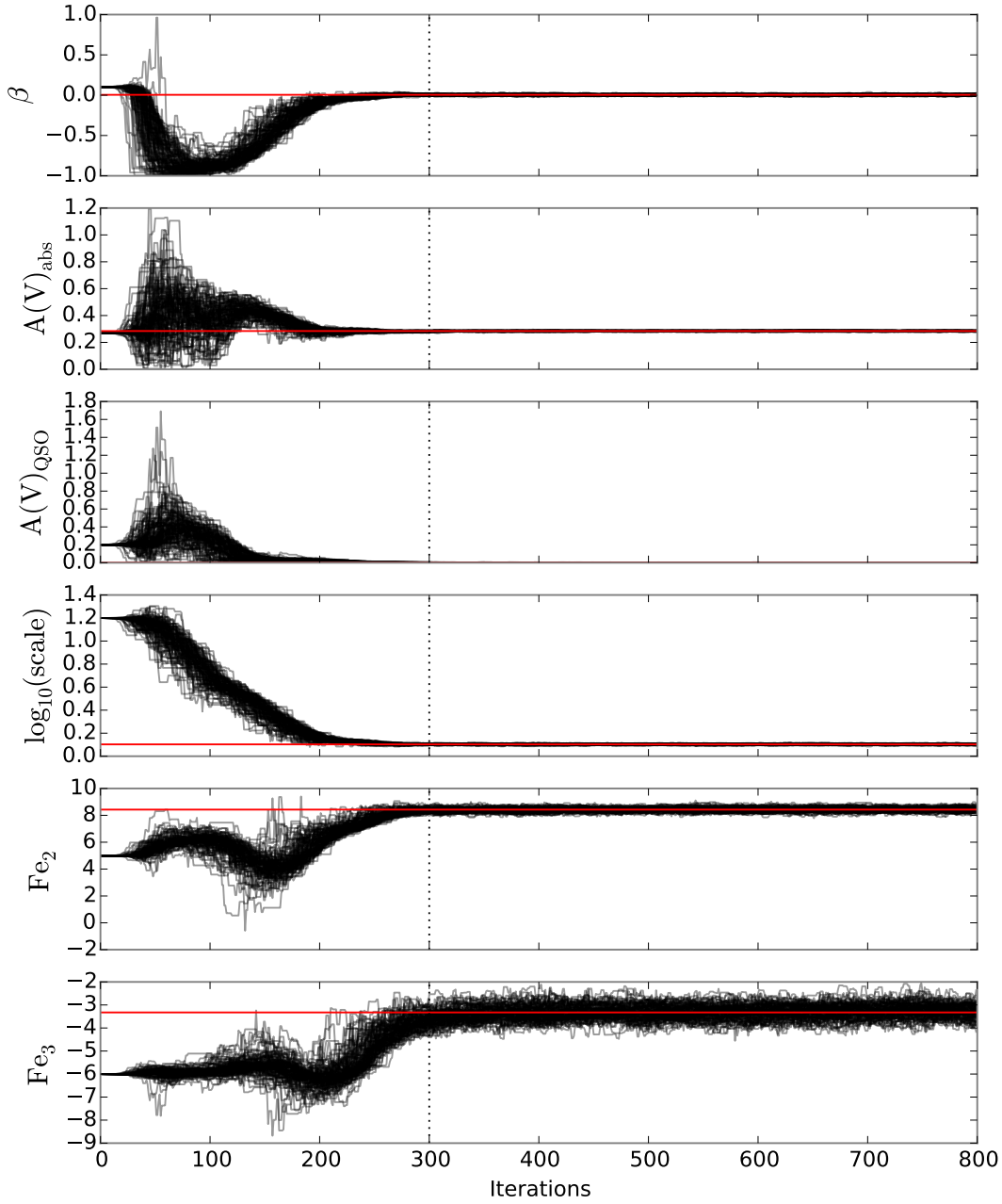

Figure A.4: The MCMC chain from `emcee` for each parameter. The best-fit parameters are indicated in each panel with red lines. The first 300 iterations (dotted vertical line) are discarded as 'burn in' phase.

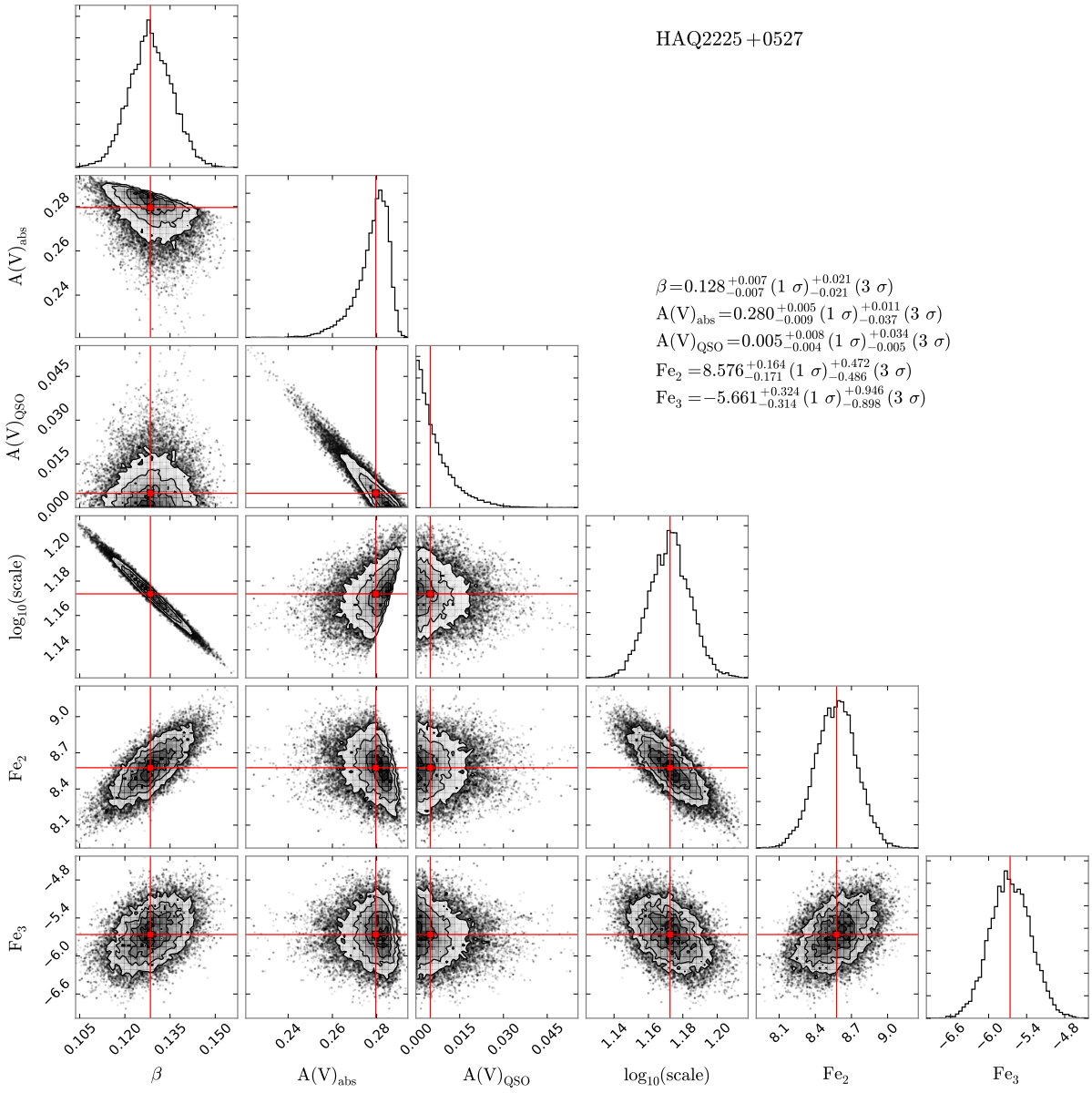

Figure A.5: Marginalized posterior probabilities and the correlations among various parameters. The best-fit parameters are stated in the upper right corner. These are indicated in the figure with red lines.

B

Appendix to Chapter 5

Below are given the full set of figures for the "*High A(V) Quasar Survey*" from Chapter 5. The figure set is also available in the online version of the published article and on the survey webpage, `http://www.dark-cosmology.dk/~krogager/redQSOs/data.html`. For each target, the observed spectrum and the full SED are shown in the left and right panels, respectively.

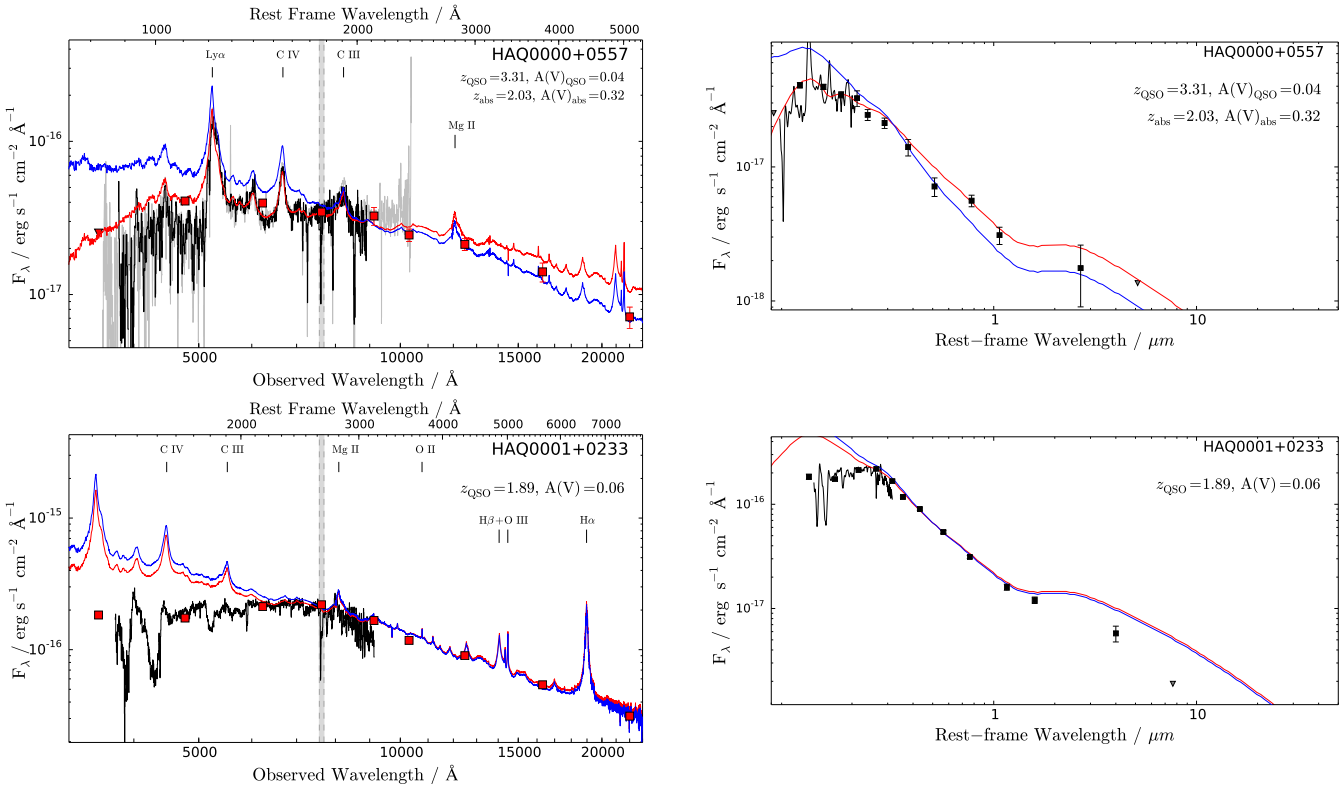

Figure B.1: (*left*) The observed spectrum is plotted as a solid black line. For targets observed with both grism 4 and 6, we show both the grism 4 and grism 6 spectra. In case of available SDSS data the spectrum from SDSS is shown in grey. In the upper right corner, the estimated emission redshift and rest-frame V-band extinction are provided. The unreddened composite QSO spectrum is shown in blue, redshifted to the spectroscopic redshift, and in red we show the redshifted composite spectrum reddened by the indicated amount of extinction. Filled squares show the SDSS and UKIDSS photometric data points. The NOT spectra have been scaled to match the r-band from SDSS. Unless otherwise noted we have assumed a SMC extinction curve. The spectra have not been corrected for telluric absorption (marked with a grey band at $\sim$ 7600 Å).
(*right*) Spectral energy distribution from photometry from SDSS, UKIDSS and WISE. The NOT spectra have been smoothed for visual purposes. We show the continuum template from Richards et al. (2006) reddened by the amount of reddening inferred from fitting the spectra (*red line*). In blue we show the unreddened template. Upper limits ($2\,\sigma$) are shown as grey triangles.

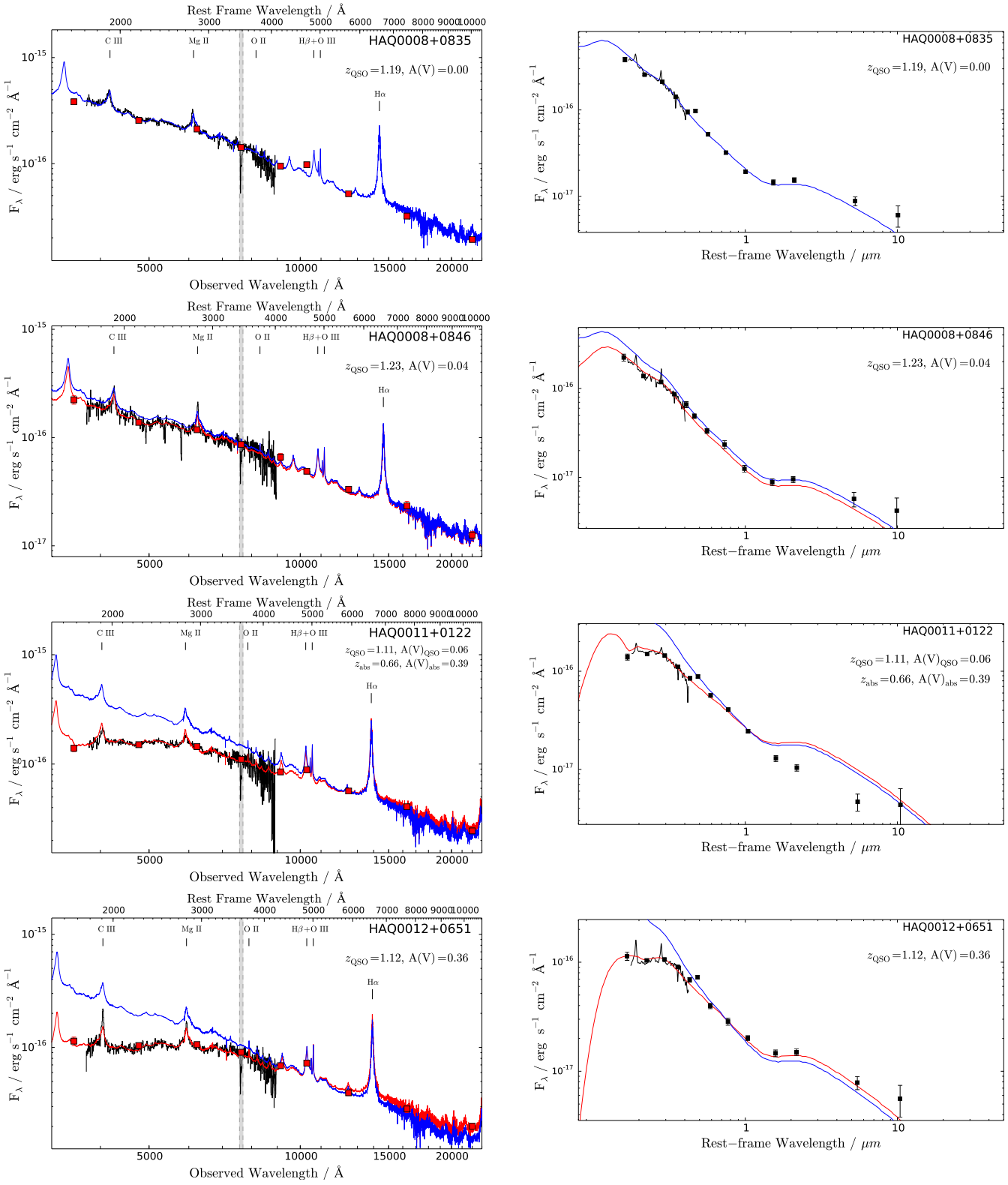

Figure 2.1 (Cont.): The observed spectrum (*left*) and the spectral energy distribution from photometry from SDSS, UKIDSS and WISE (*right*).

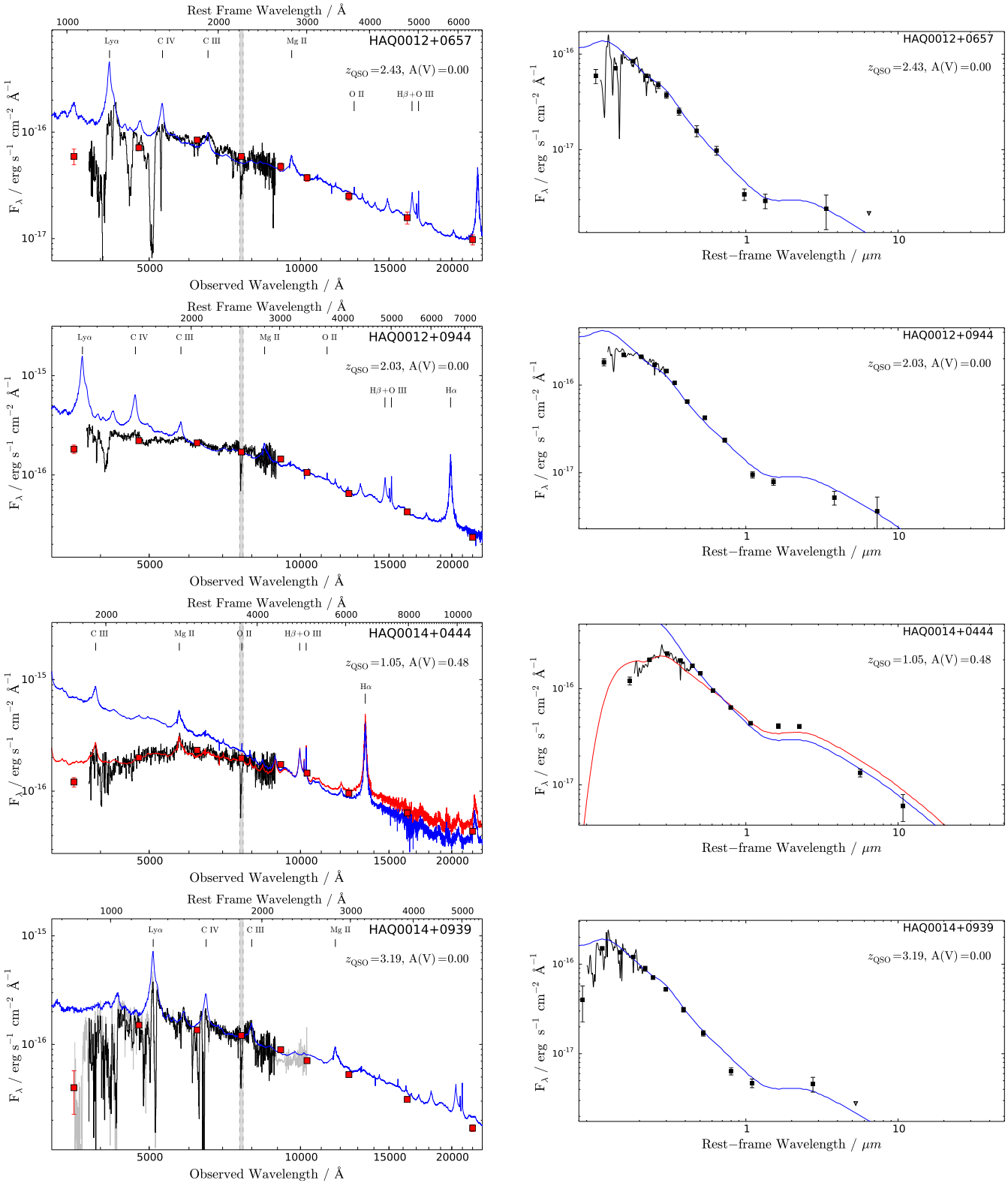

Figure 2.1 (Cont.): The observed spectrum (*left*) and the spectral energy distribution from photometry from SDSS, UKIDSS and WISE (*right*).

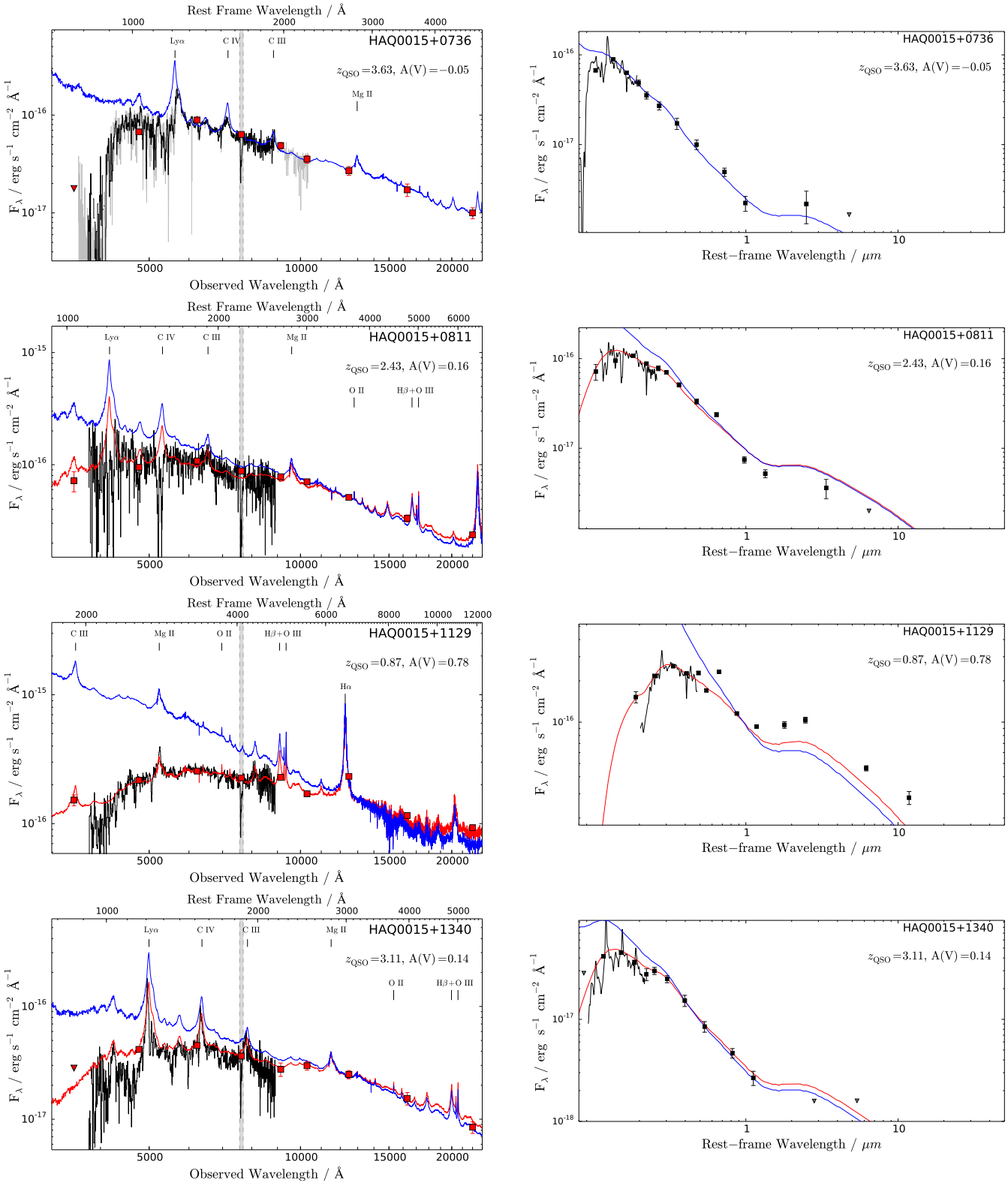

Figure 2.1 (Cont.): The observed spectrum (*left*) and the spectral energy distribution from photometry from SDSS, UKIDSS and WISE (*right*).

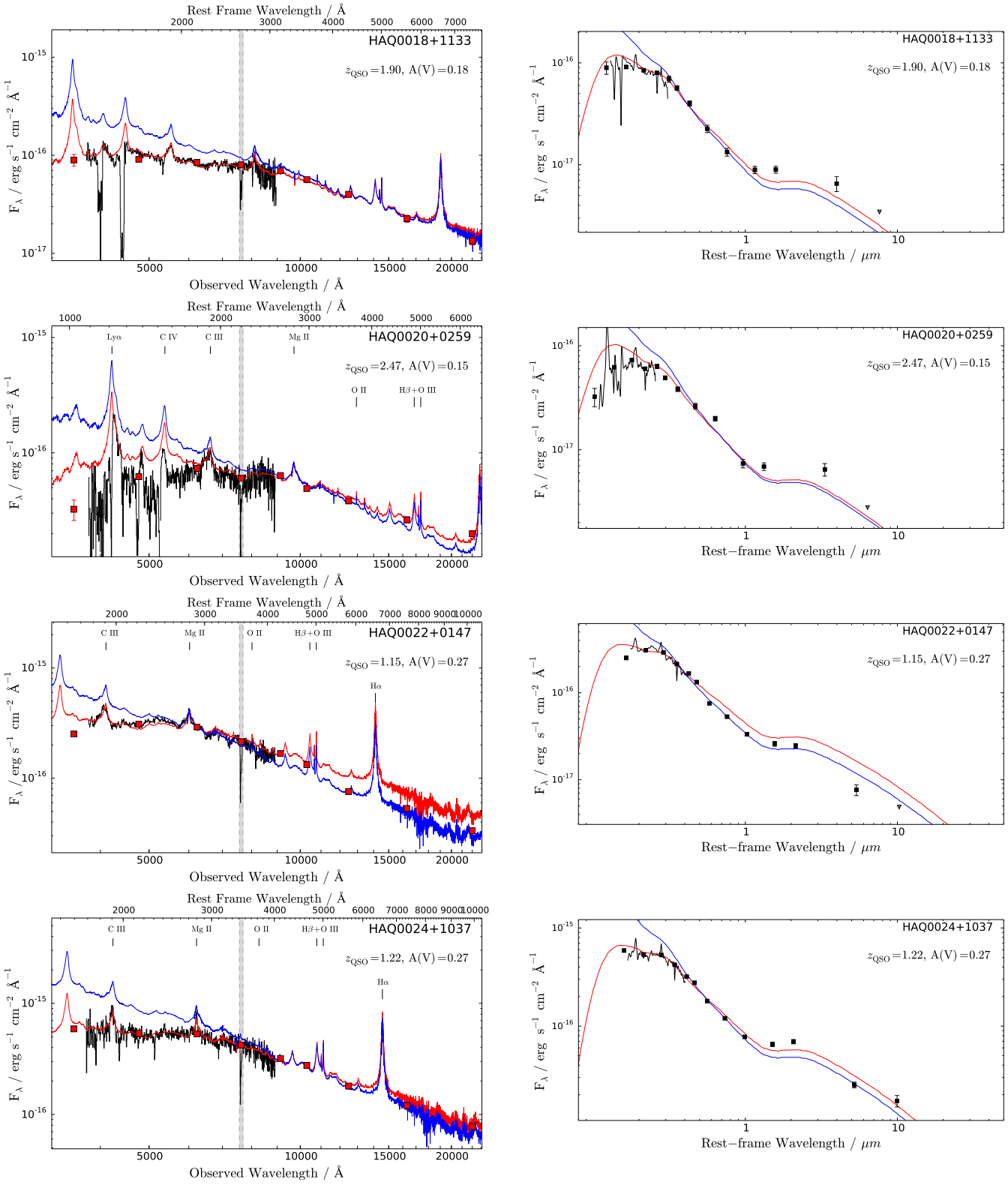

Figure 2.1 (Cont.): The observed spectrum (*left*) and the spectral energy distribution from photometry from SDSS, UKIDSS and WISE (*right*).

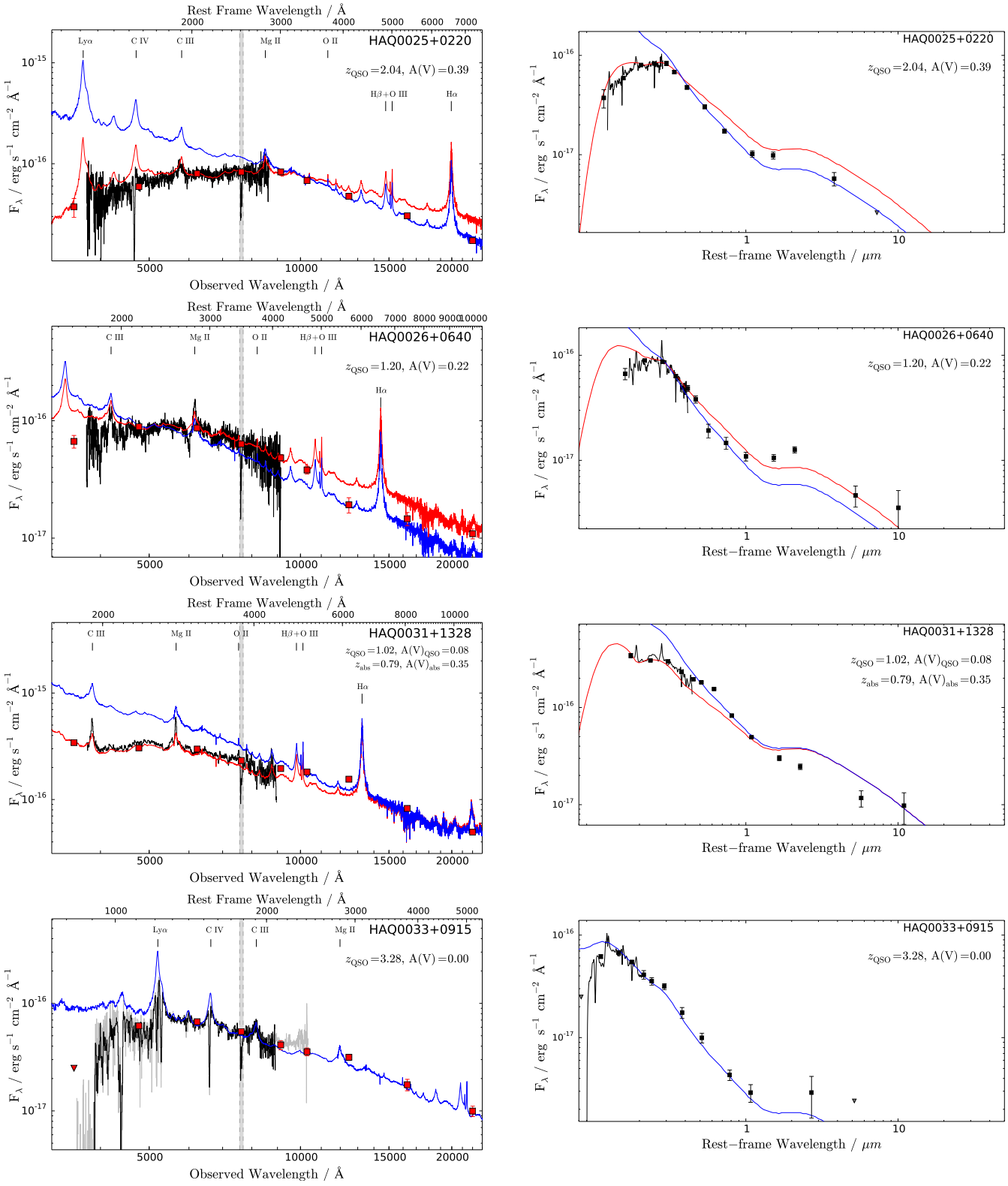

Figure 2.1 (Cont.): The observed spectrum (*left*) and the spectral energy distribution from photometry from SDSS, UKIDSS and WISE (*right*).

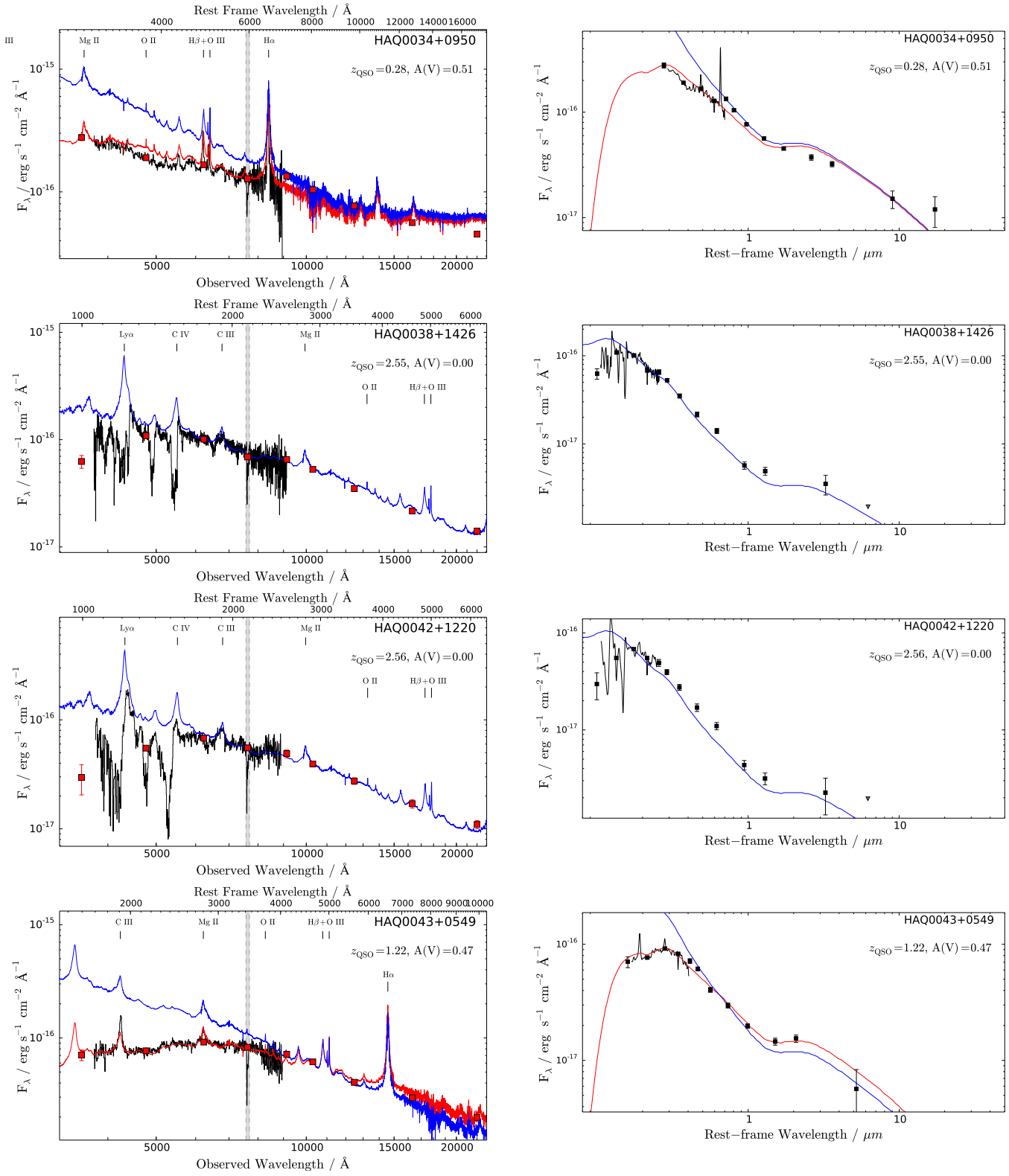

Figure 2.1 (Cont.): The observed spectrum (*left*) and the spectral energy distribution from photometry from SDSS, UKIDSS and WISE (*right*).

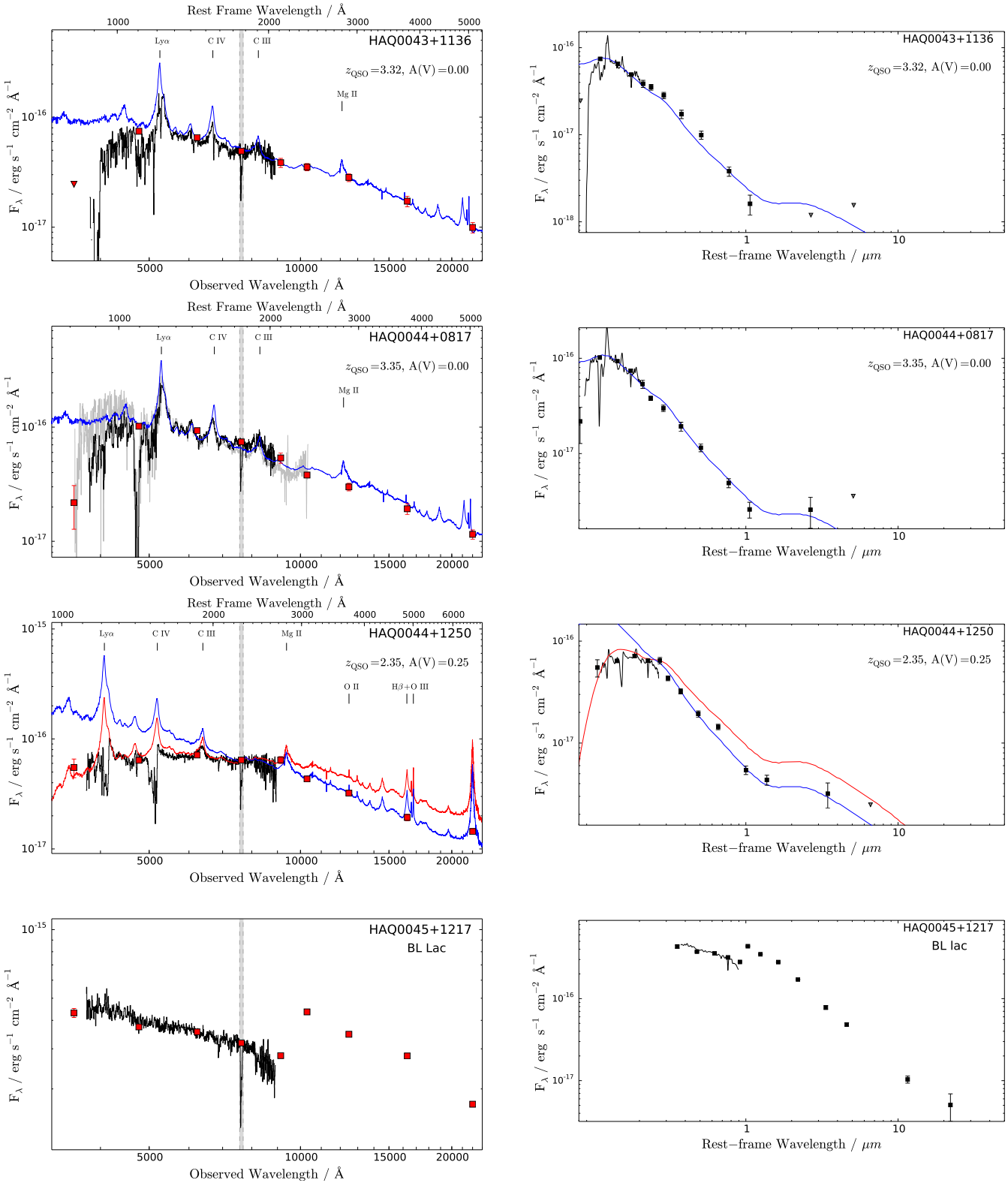

Figure 2.1 (Cont.): The observed spectrum (*left*) and the spectral energy distribution from photometry from SDSS, UKIDSS and WISE (*right*).

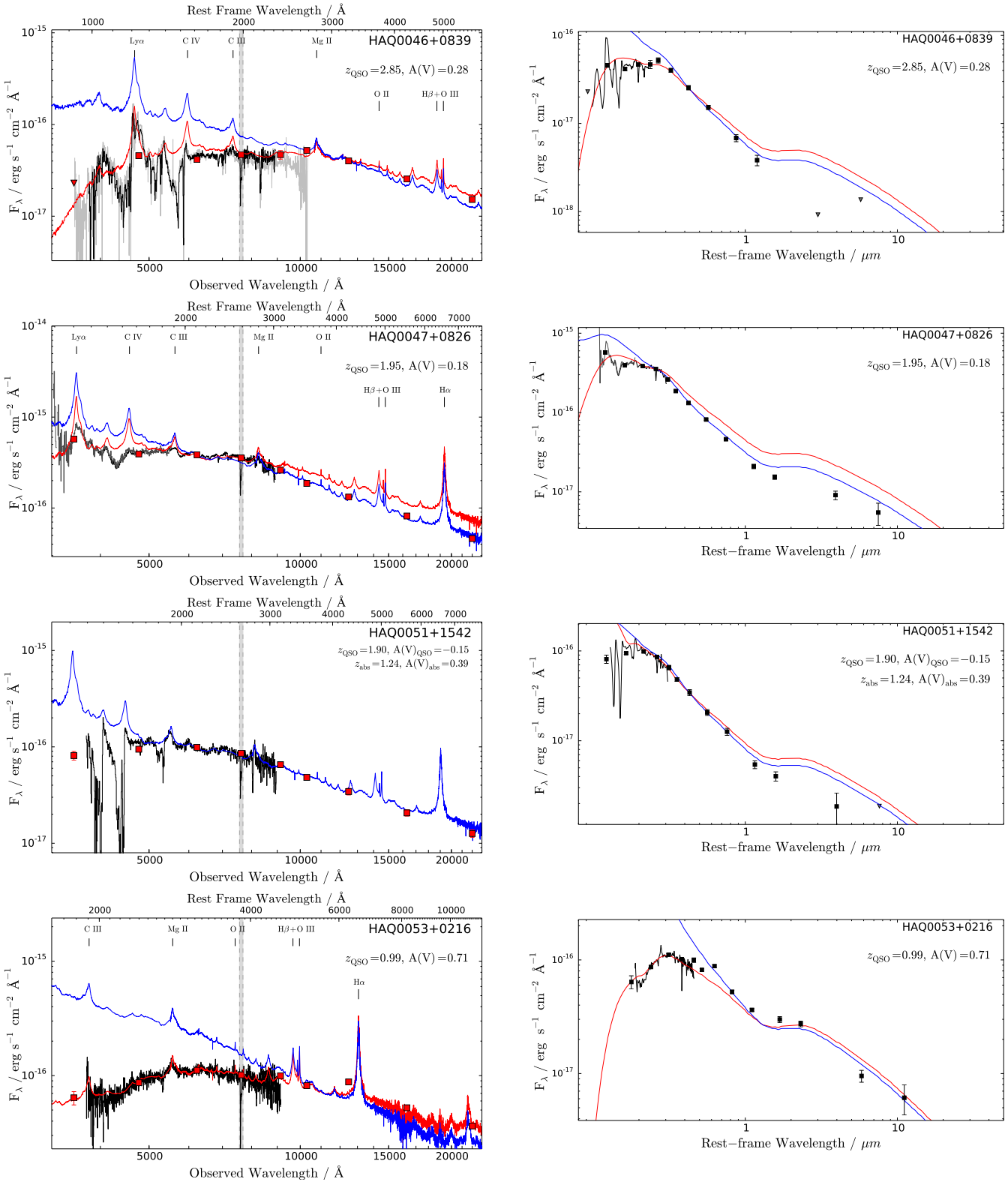

Figure 2.1 (Cont.): The observed spectrum (*left*) and the spectral energy distribution from photometry from SDSS, UKIDSS and WISE (*right*).

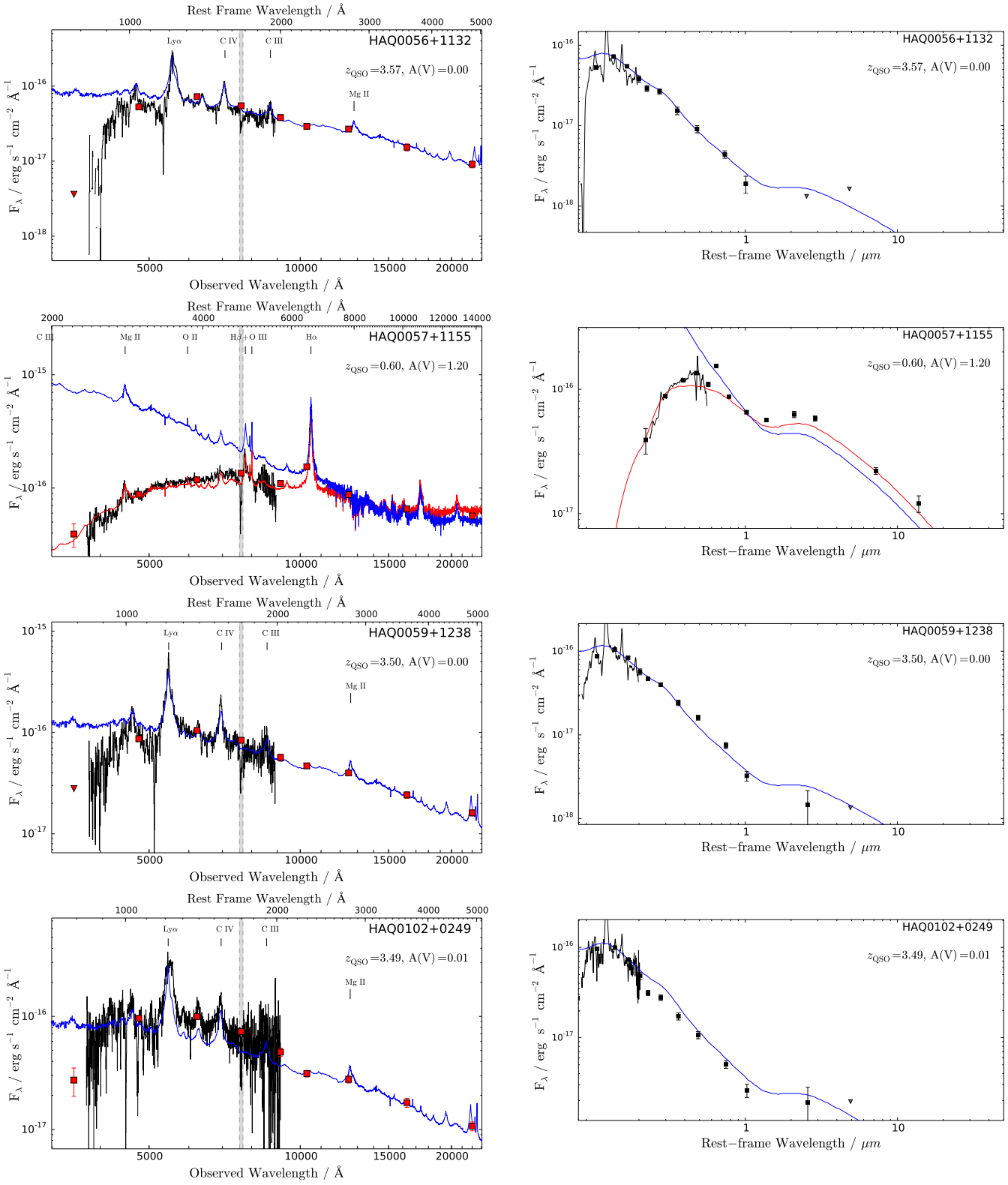

Figure 2.1 (Cont.): The observed spectrum (*left*) and the spectral energy distribution from photometry from SDSS, UKIDSS and WISE (*right*).

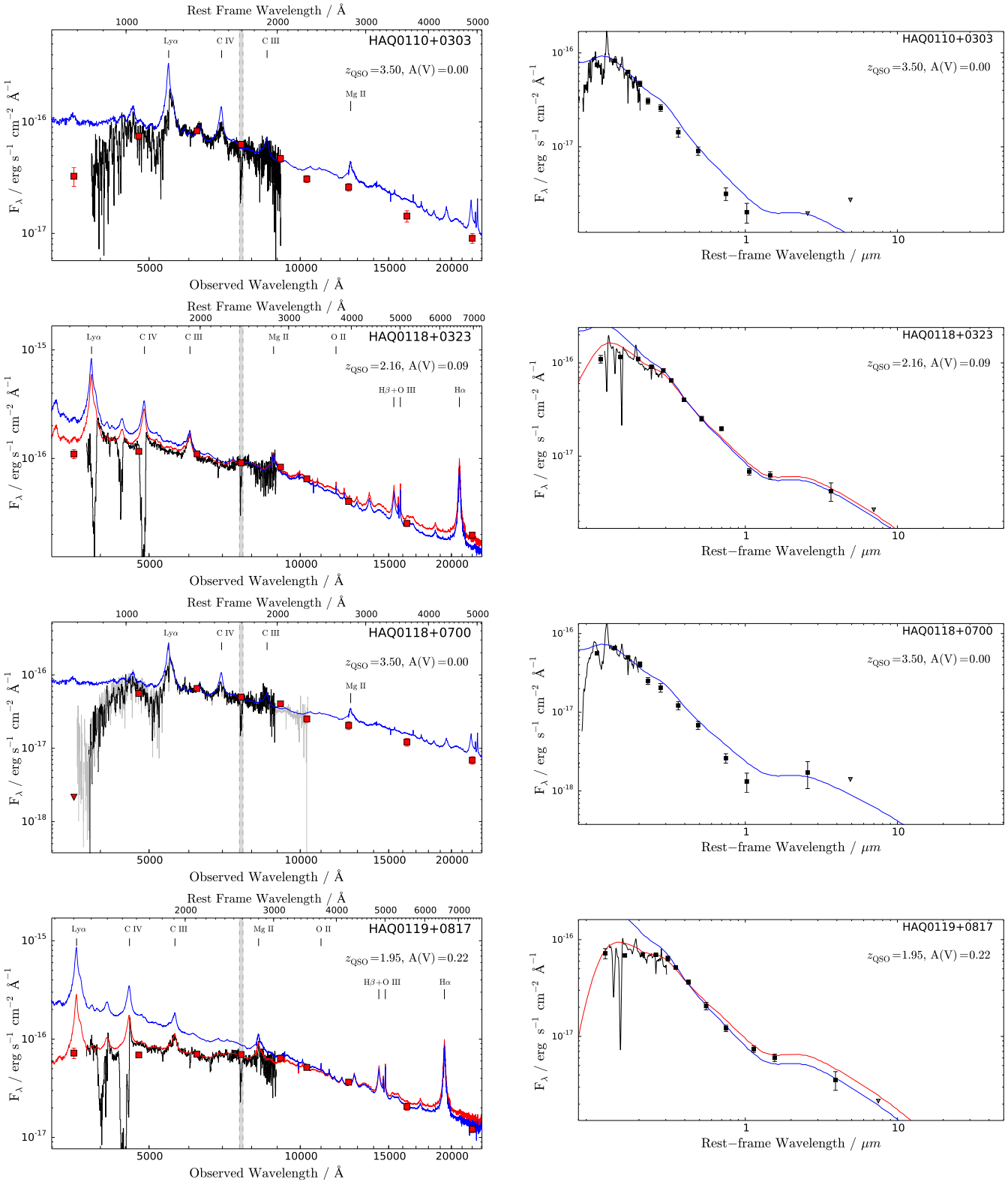

Figure 2.1 (Cont.): The observed spectrum (*left*) and the spectral energy distribution from photometry from SDSS, UKIDSS and WISE (*right*).

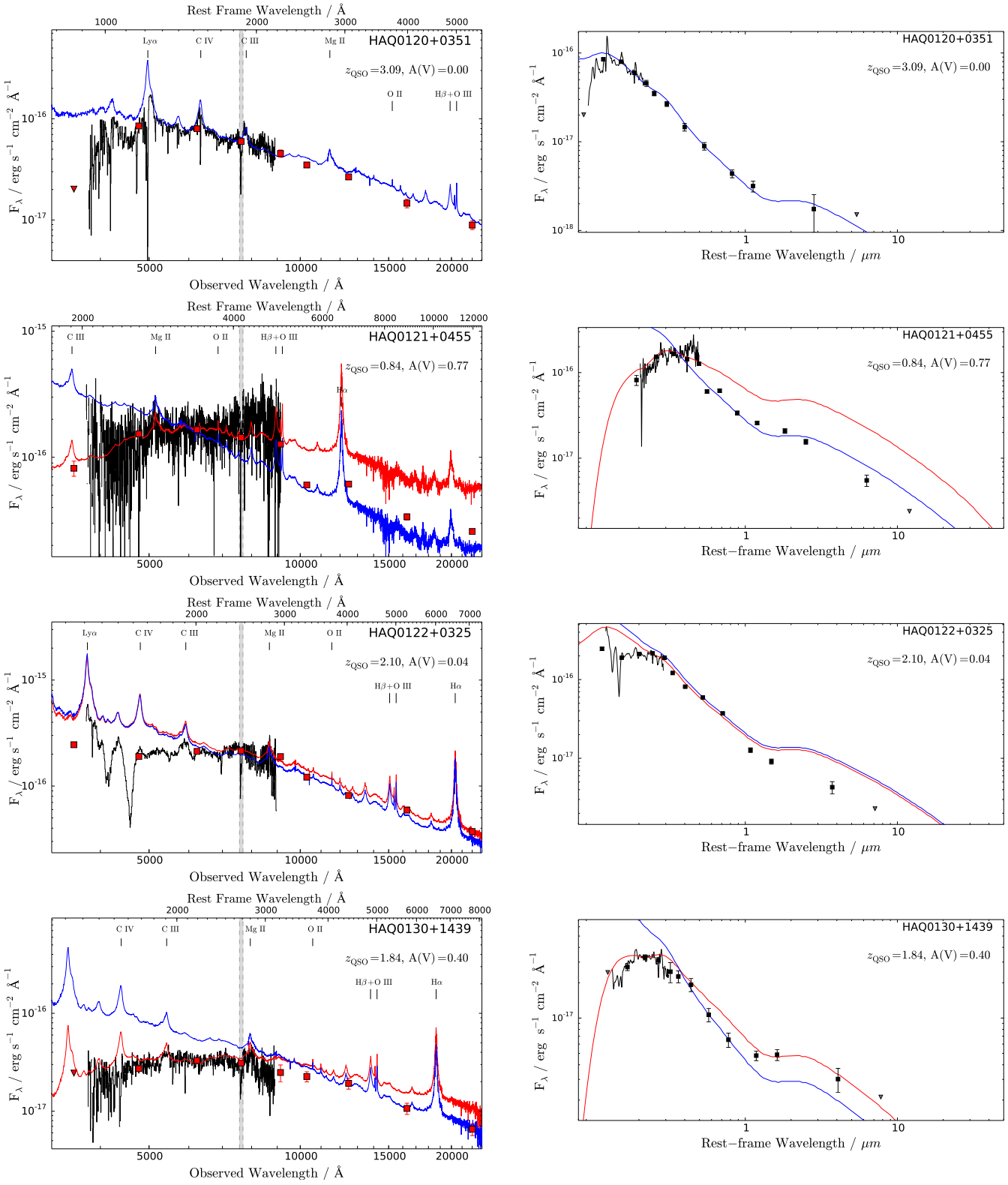

Figure 2.1 (Cont.): The observed spectrum (*left*) and the spectral energy distribution from photometry from SDSS, UKIDSS and WISE (*right*).

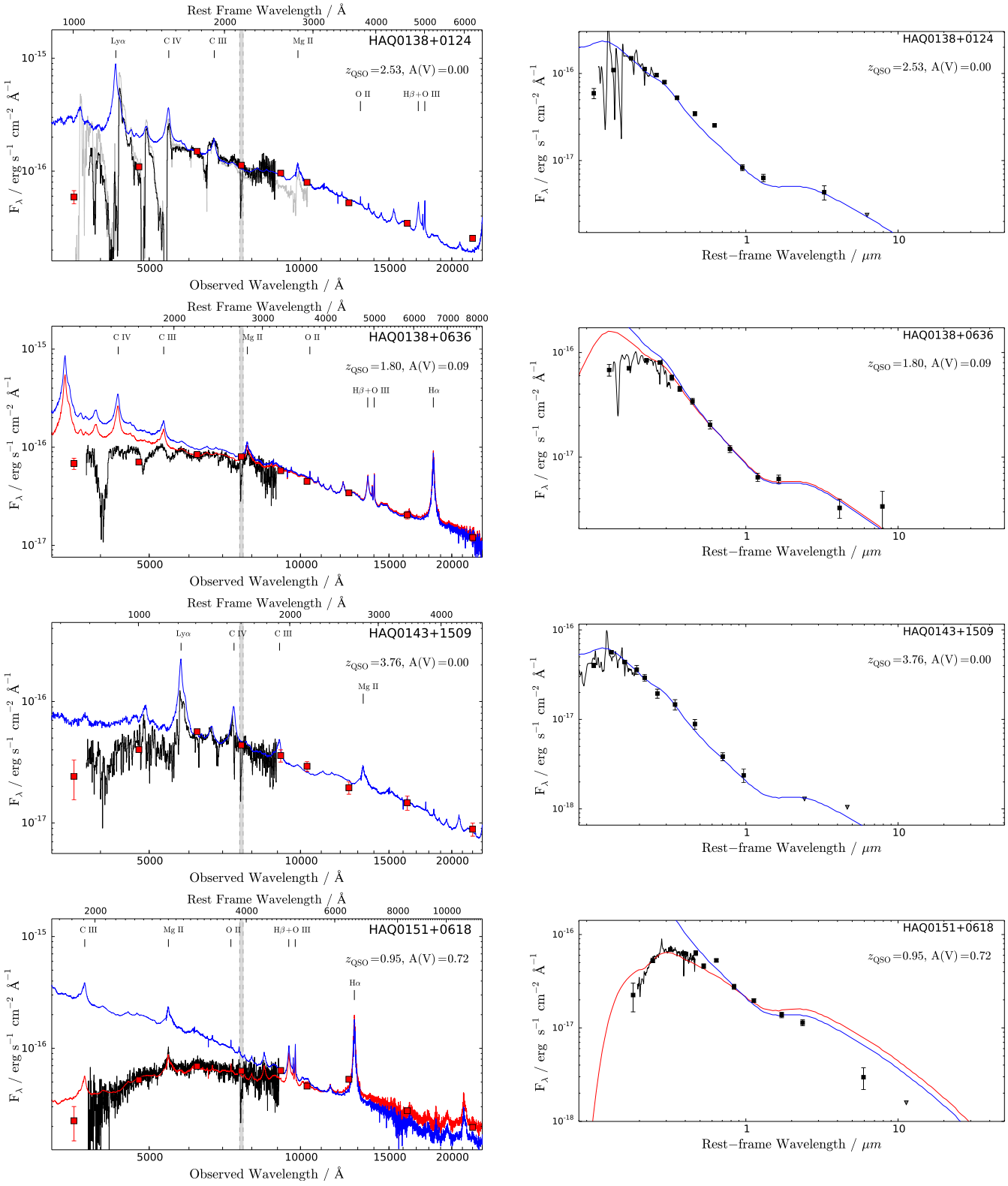

Figure 2.1 (Cont.): The observed spectrum (*left*) and the spectral energy distribution from photometry from SDSS, UKIDSS and WISE (*right*).

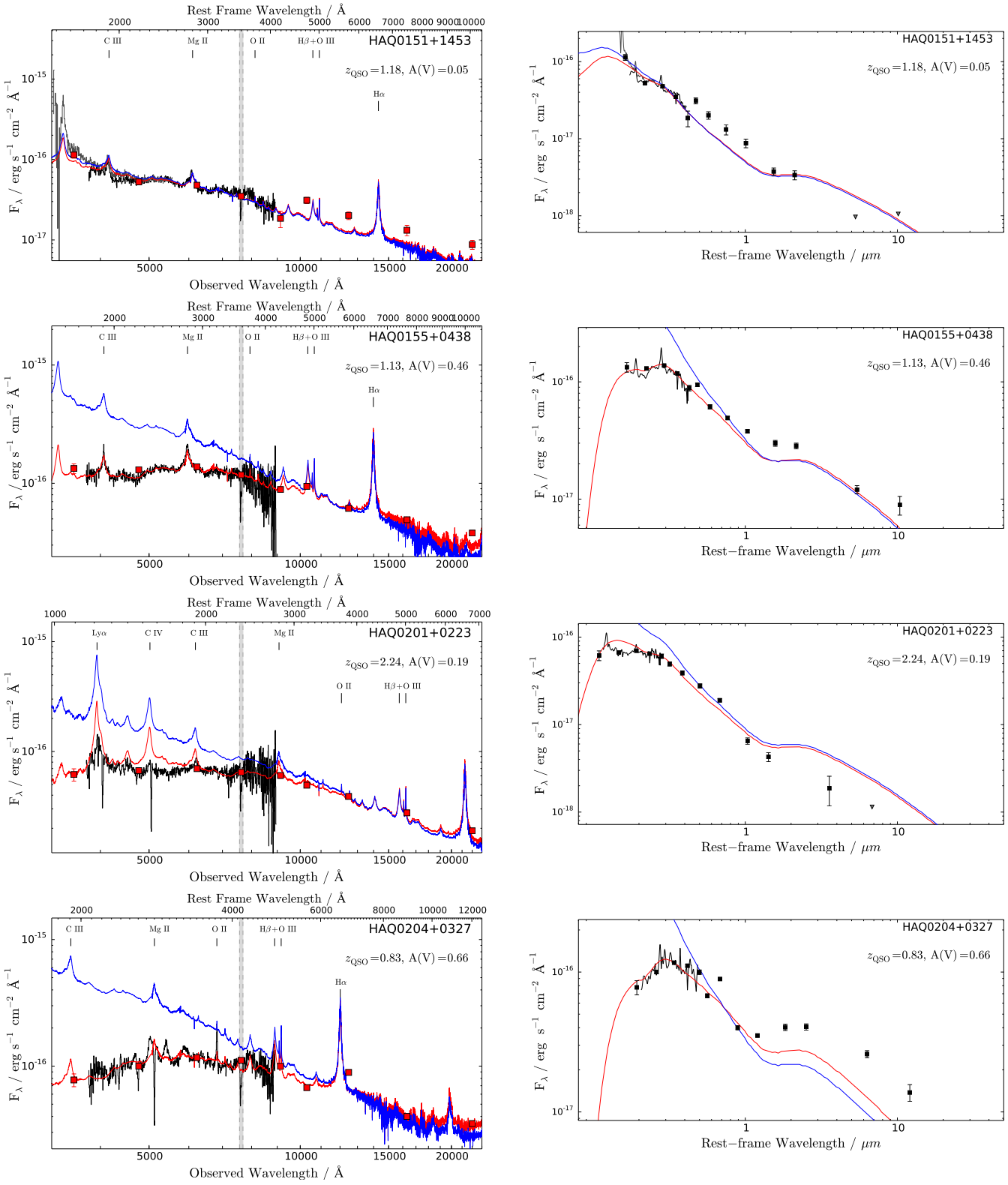

Figure 2.1 (Cont.): The observed spectrum (*left*) and the spectral energy distribution from photometry from SDSS, UKIDSS and WISE (*right*).

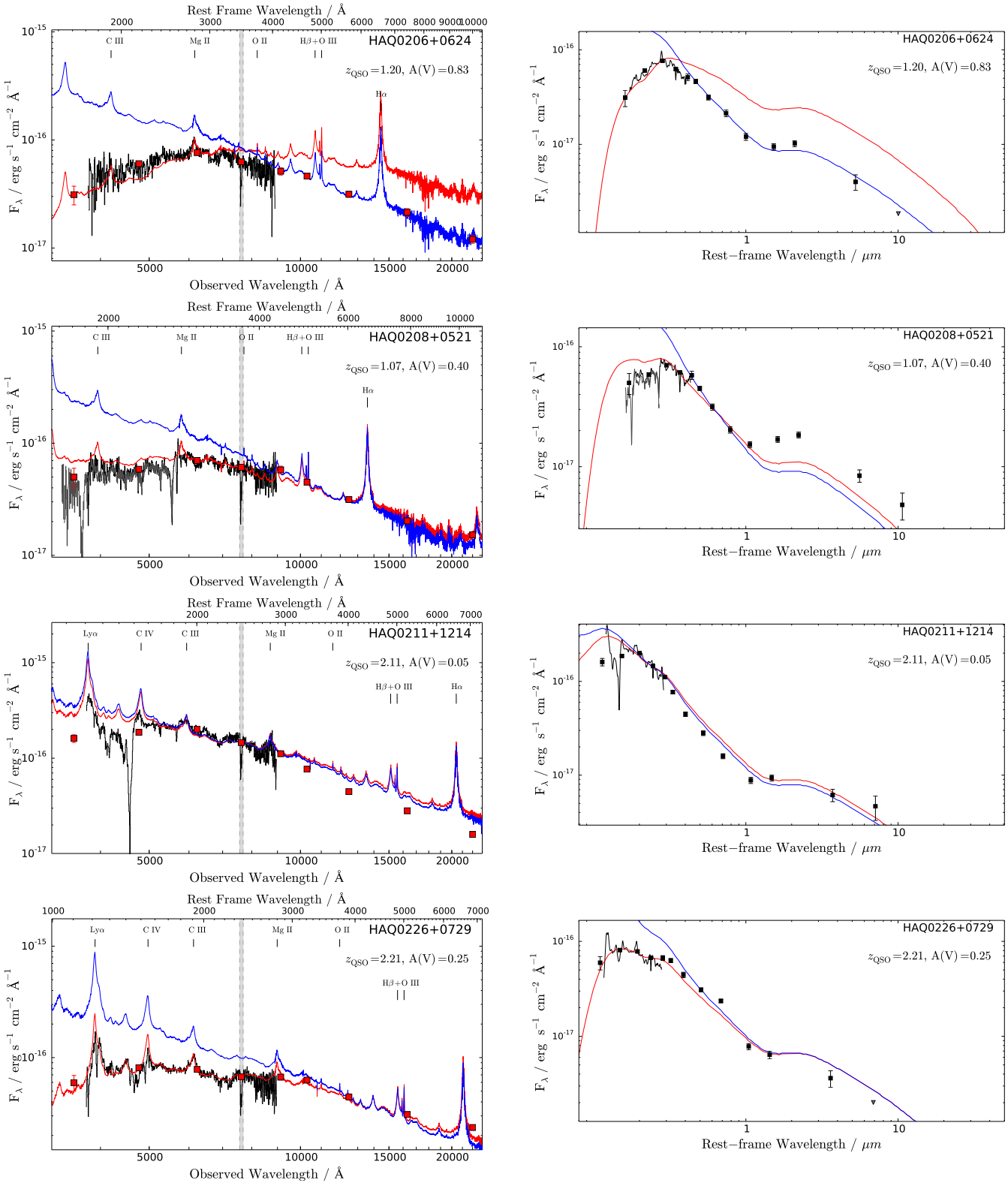

Figure 2.1 (Cont.): The observed spectrum (*left*) and the spectral energy distribution from photometry from SDSS, UKIDSS and WISE (*right*).

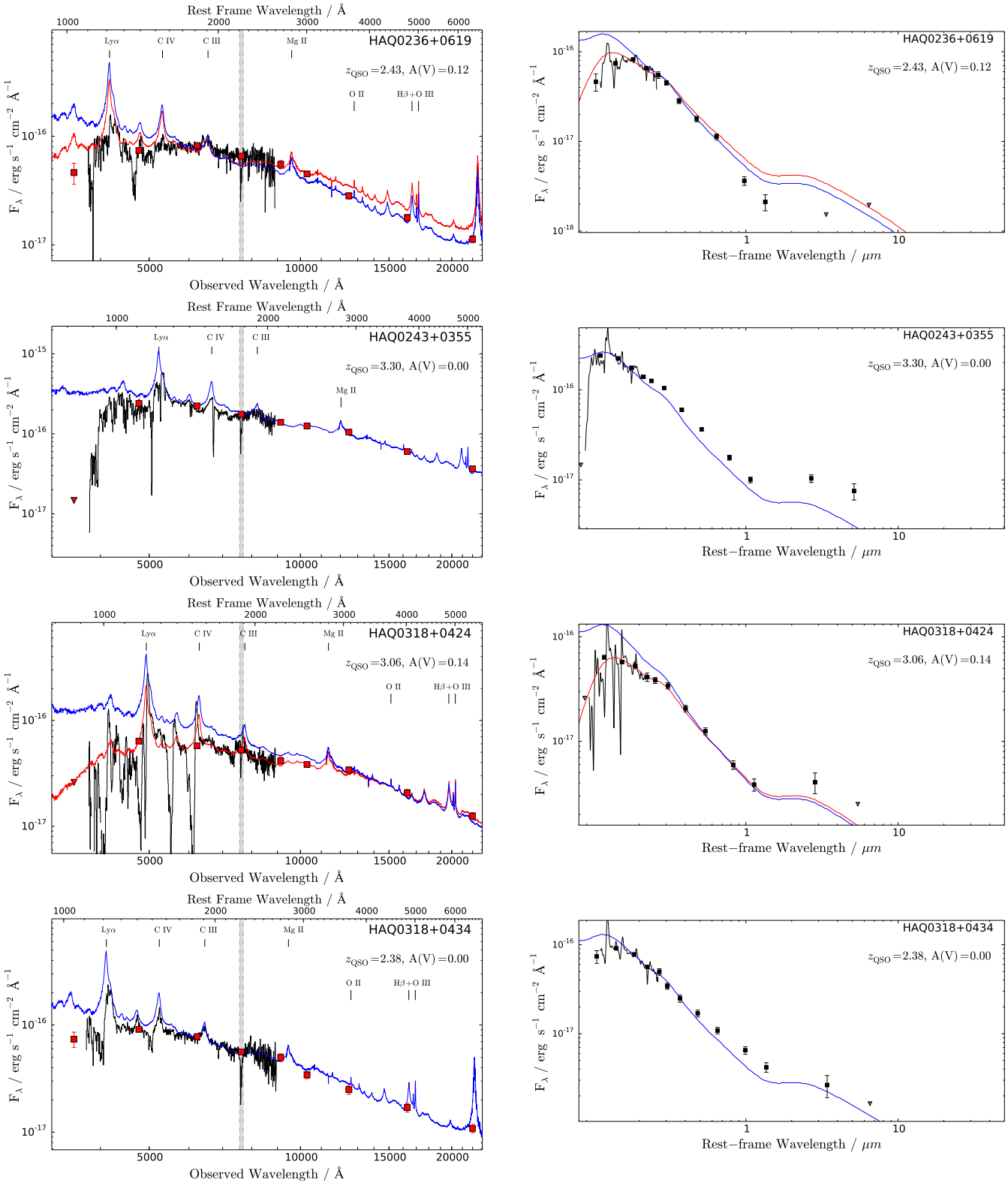

Figure 2.1 (Cont.): The observed spectrum (*left*) and the spectral energy distribution from photometry from SDSS, UKIDSS and WISE (*right*).

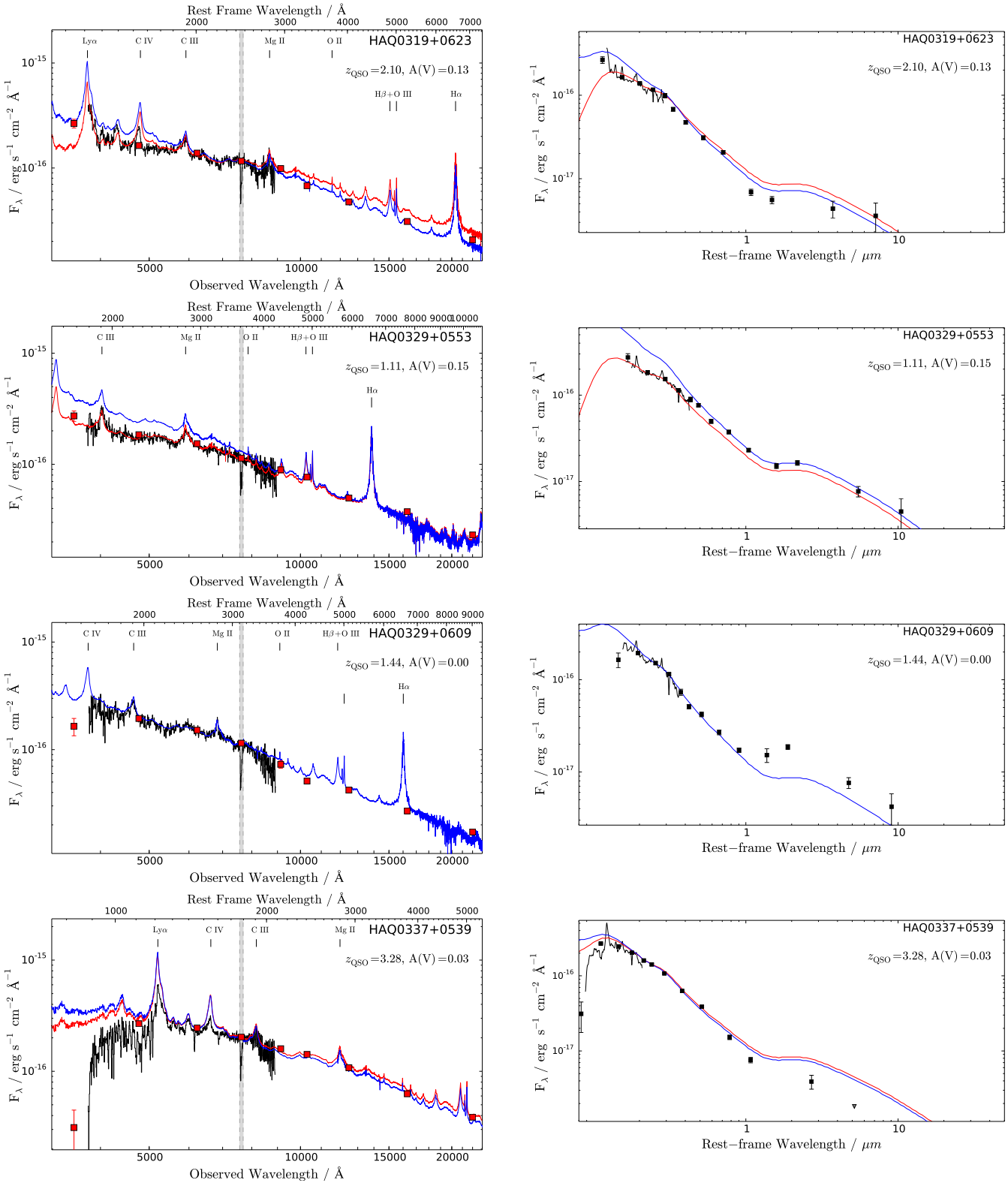

Figure 2.1 (Cont.): The observed spectrum (*left*) and the spectral energy distribution from photometry from SDSS, UKIDSS and WISE (*right*).

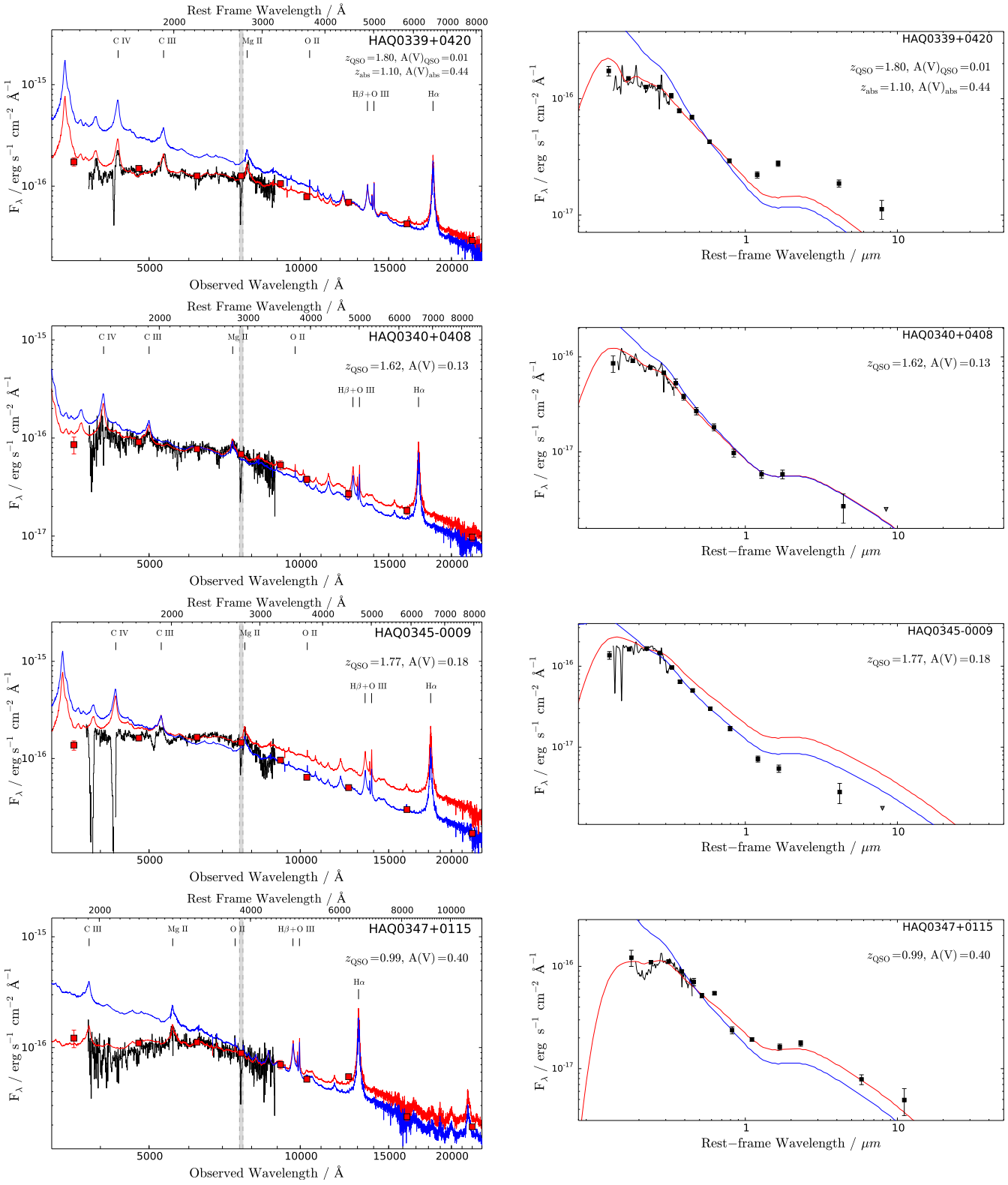

Figure 2.1 (Cont.): The observed spectrum (*left*) and the spectral energy distribution from photometry from SDSS, UKIDSS and WISE (*right*).

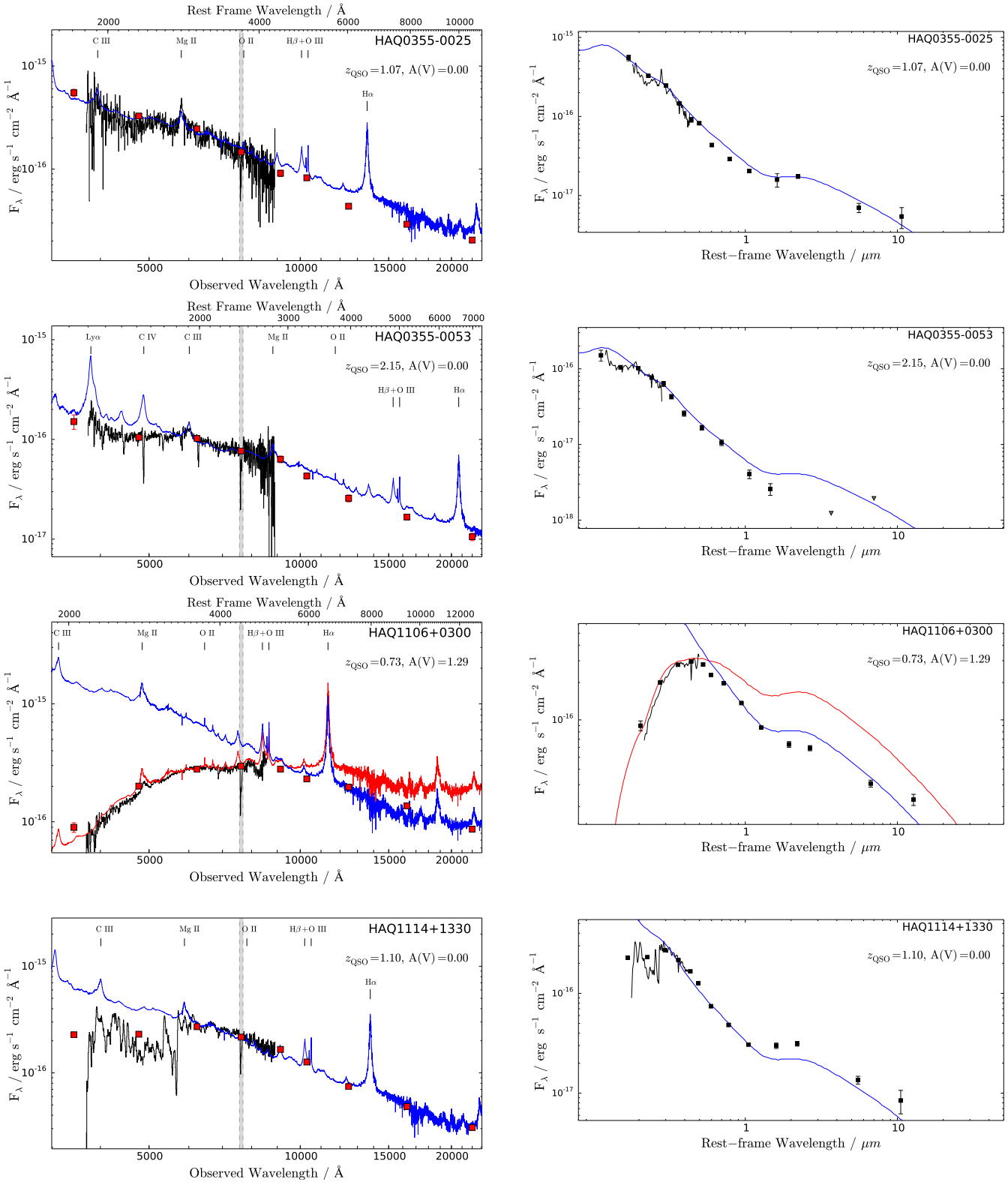

Figure 2.1 (Cont.): The observed spectrum (*left*) and the spectral energy distribution from photometry from SDSS, UKIDSS and WISE (*right*).

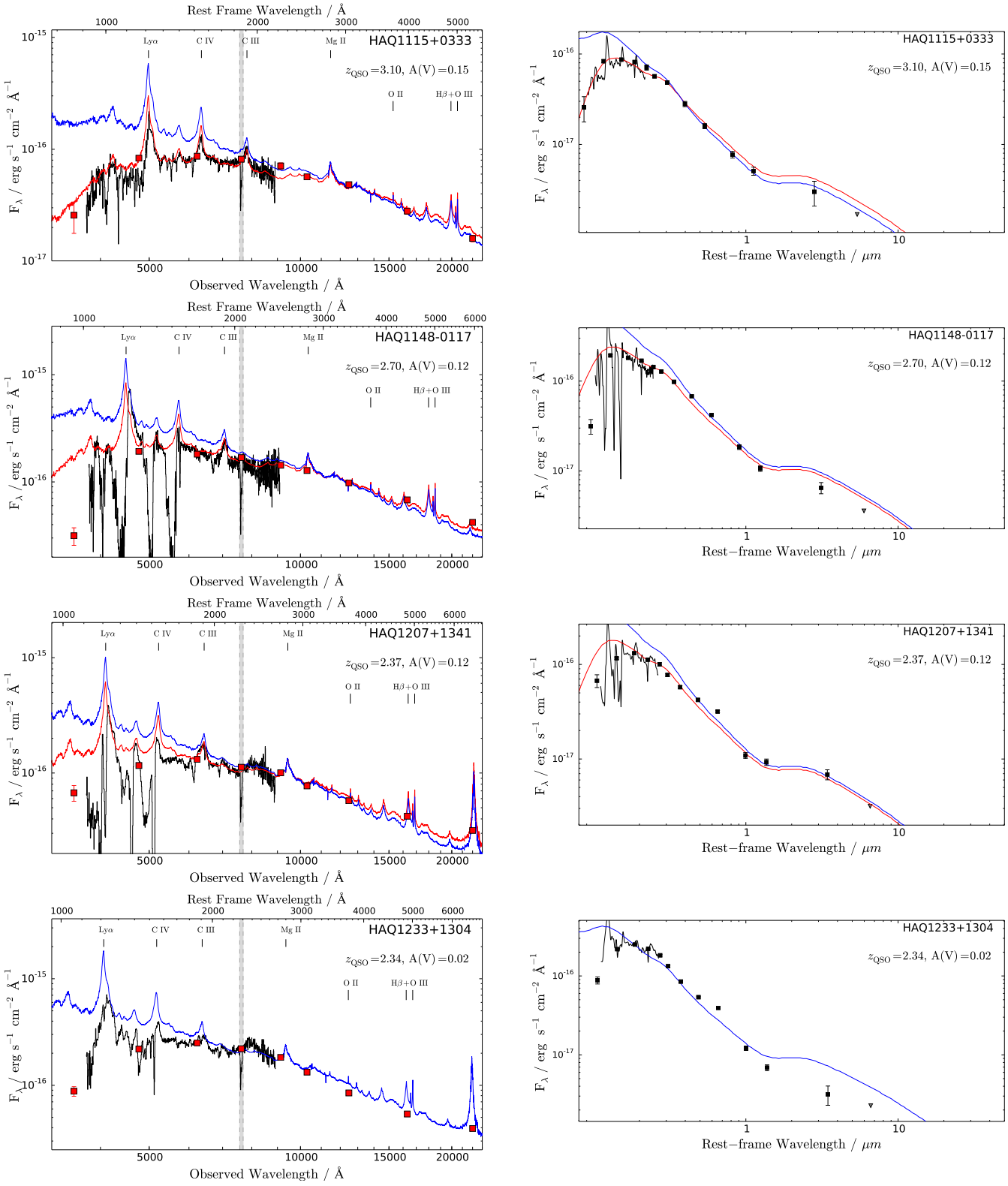

Figure 2.1 (Cont.): The observed spectrum (*left*) and the spectral energy distribution from photometry from SDSS, UKIDSS and WISE (*right*).

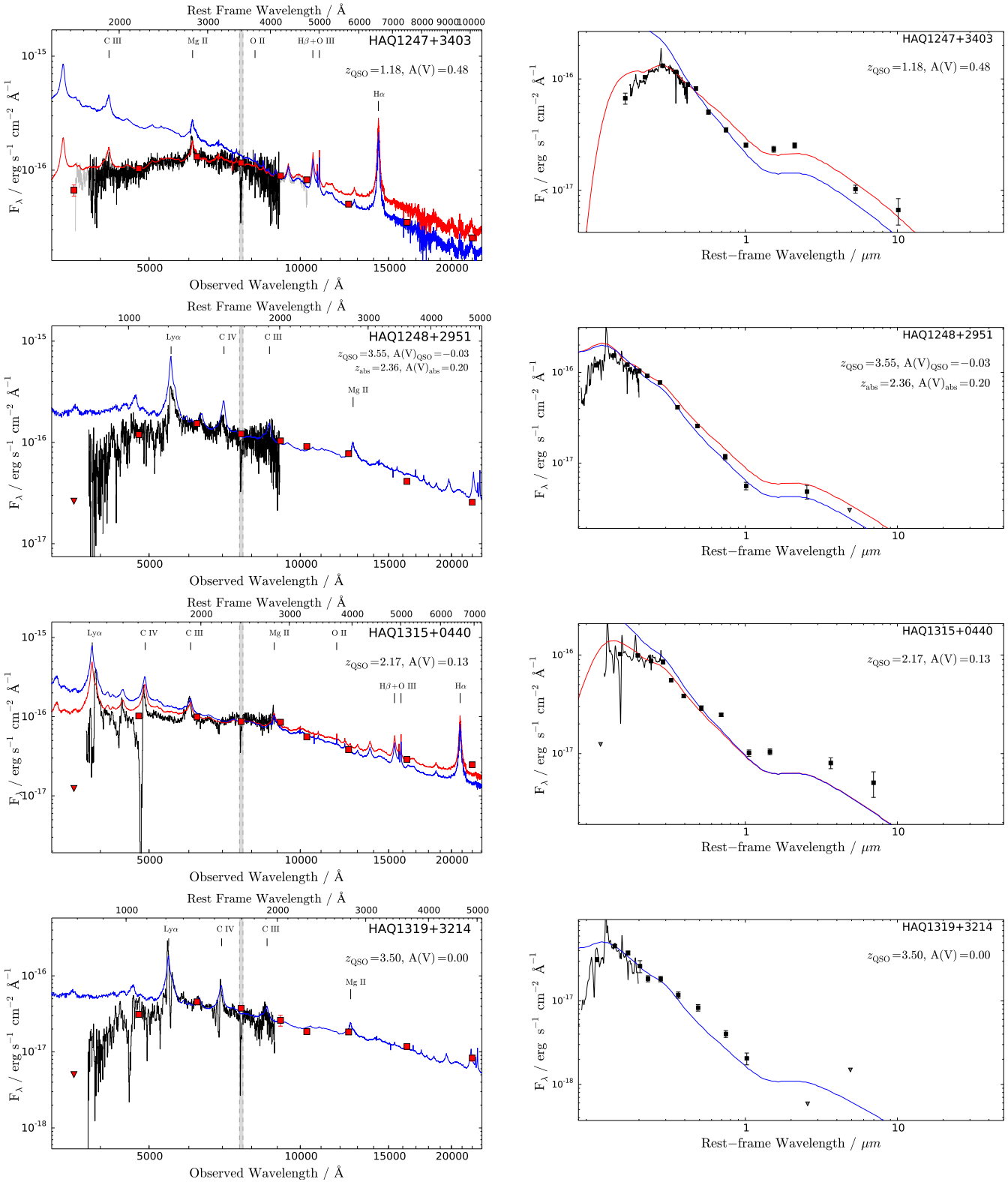

Figure 2.1 (Cont.): The observed spectrum (*left*) and the spectral energy distribution from photometry from SDSS, UKIDSS and WISE (*right*).

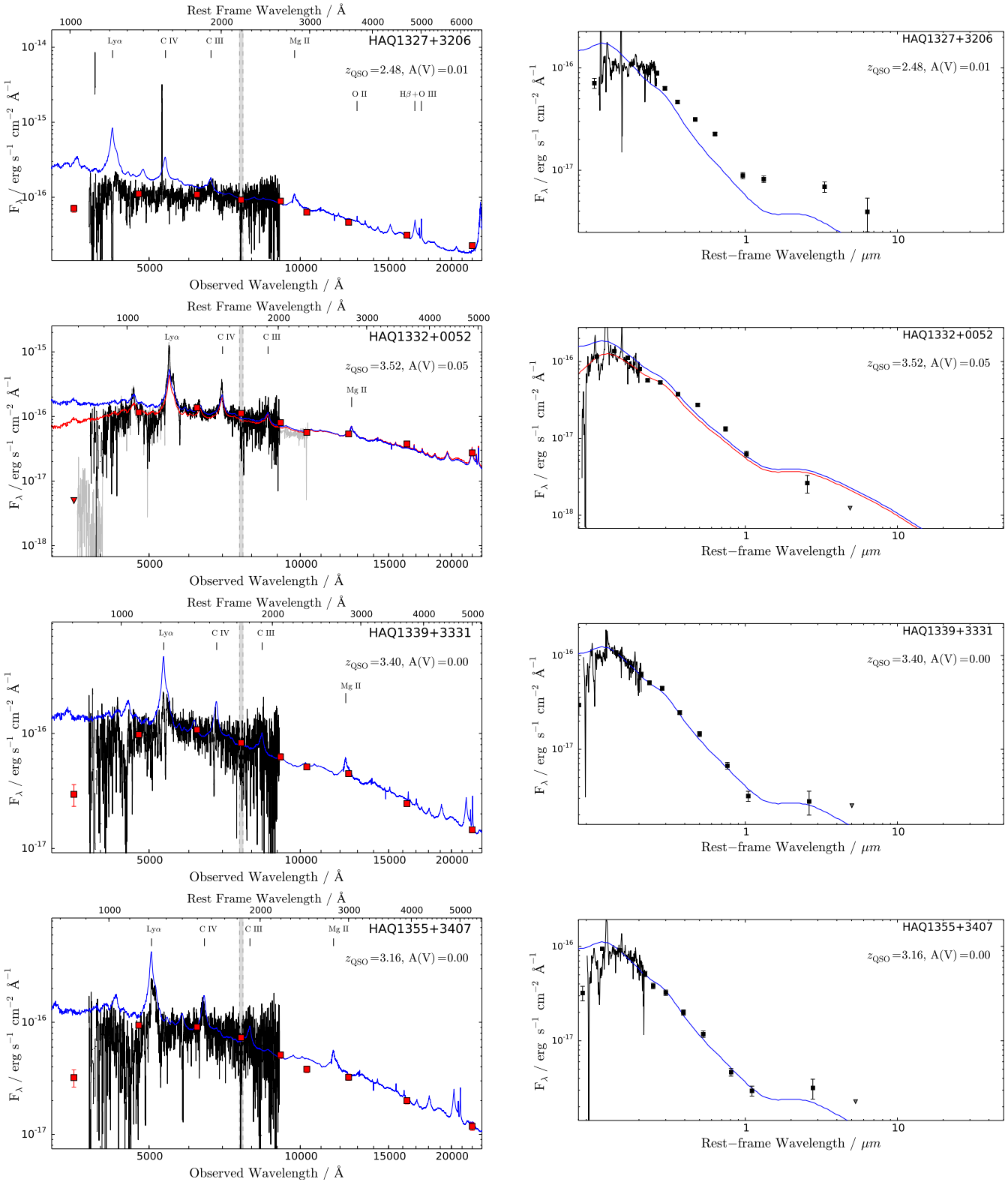

Figure 2.1 (Cont.): The observed spectrum (*left*) and the spectral energy distribution from photometry from SDSS, UKIDSS and WISE (*right*).

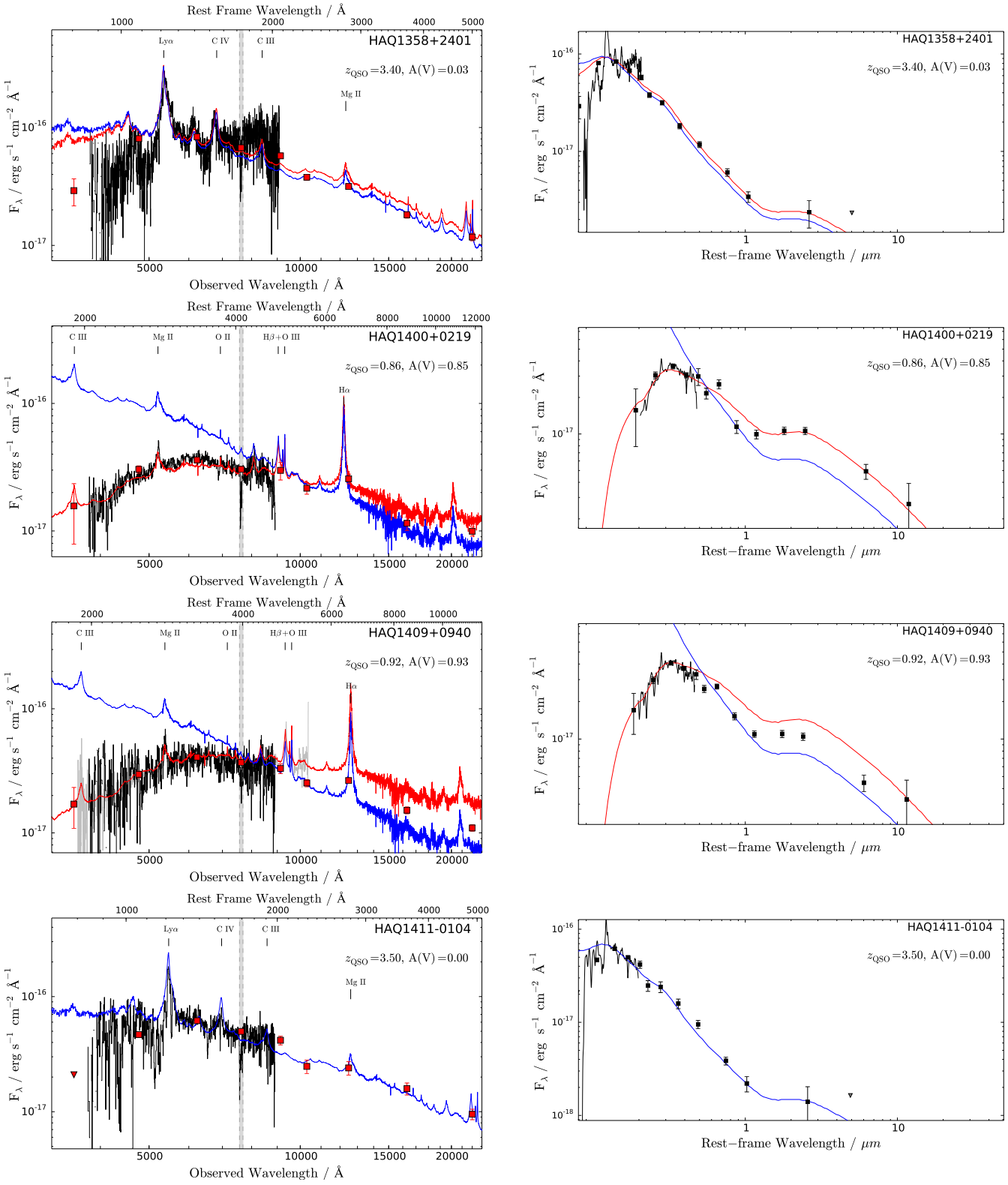

Figure 2.1 (Cont.): The observed spectrum (*left*) and the spectral energy distribution from photometry from SDSS, UKIDSS and WISE (*right*).

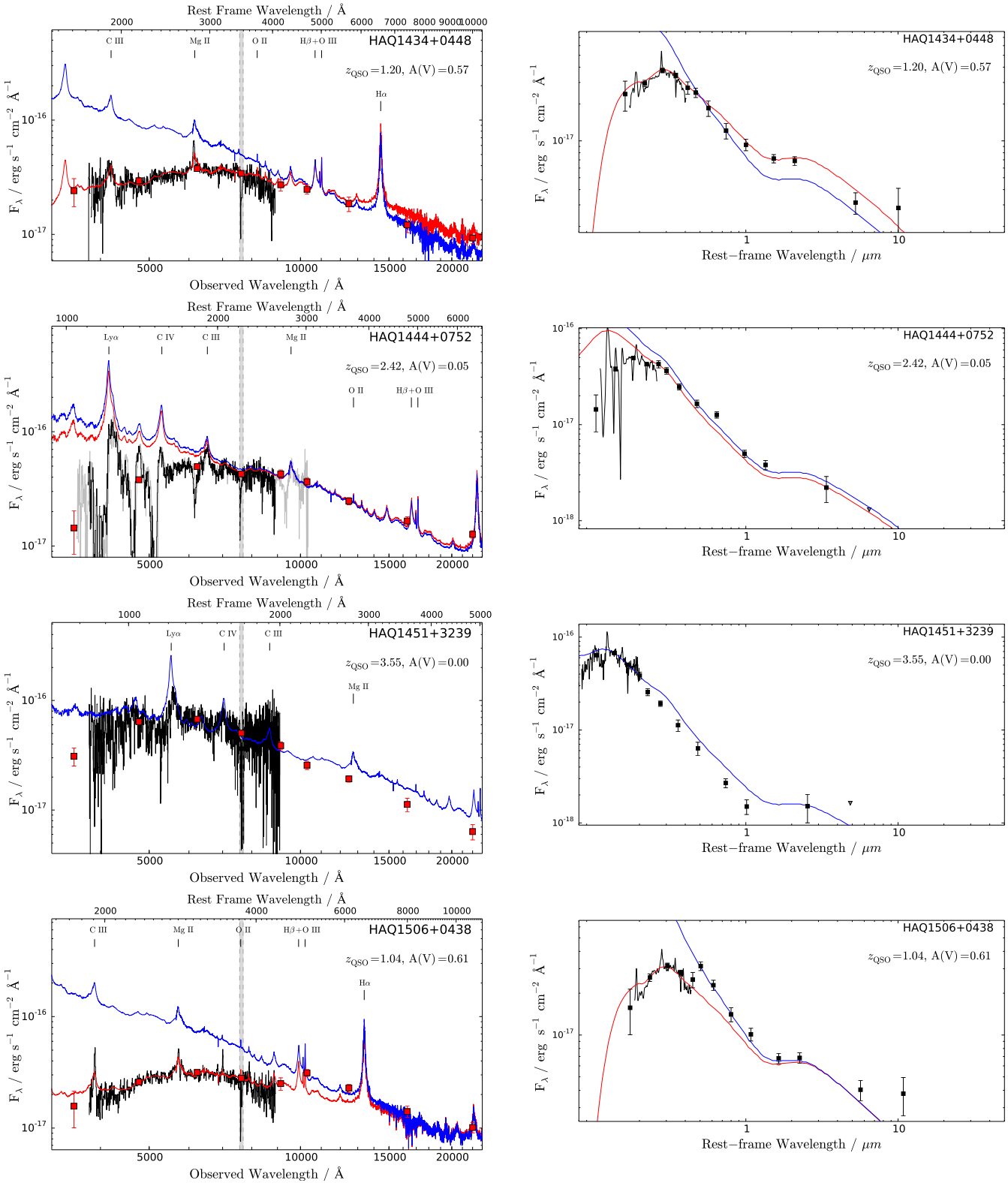

Figure 2.1 (Cont.): The observed spectrum (*left*) and the spectral energy distribution from photometry from SDSS, UKIDSS and WISE (*right*).

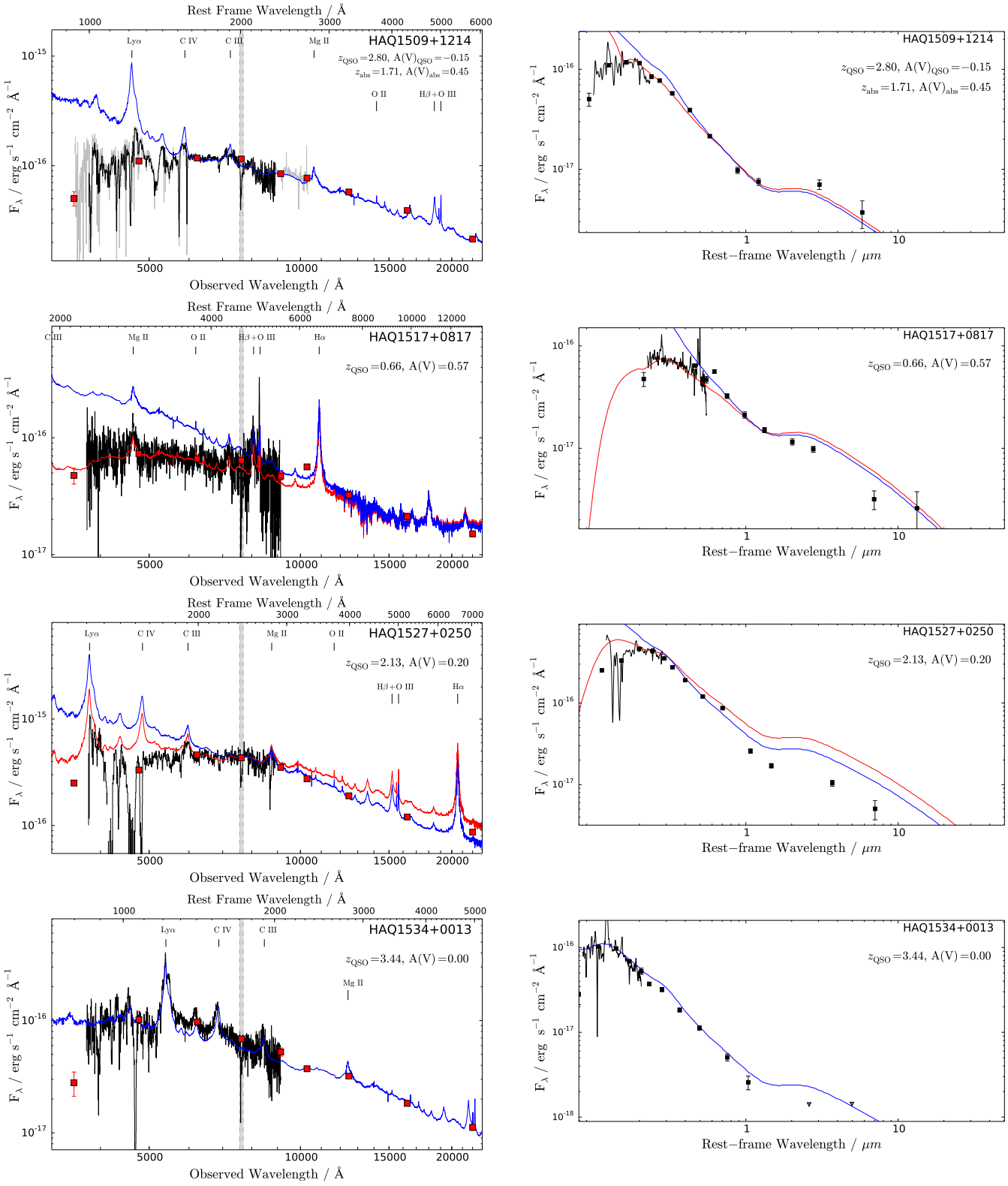

Figure 2.1 (Cont.): The observed spectrum (*left*) and the spectral energy distribution from photometry from SDSS, UKIDSS and WISE (*right*).

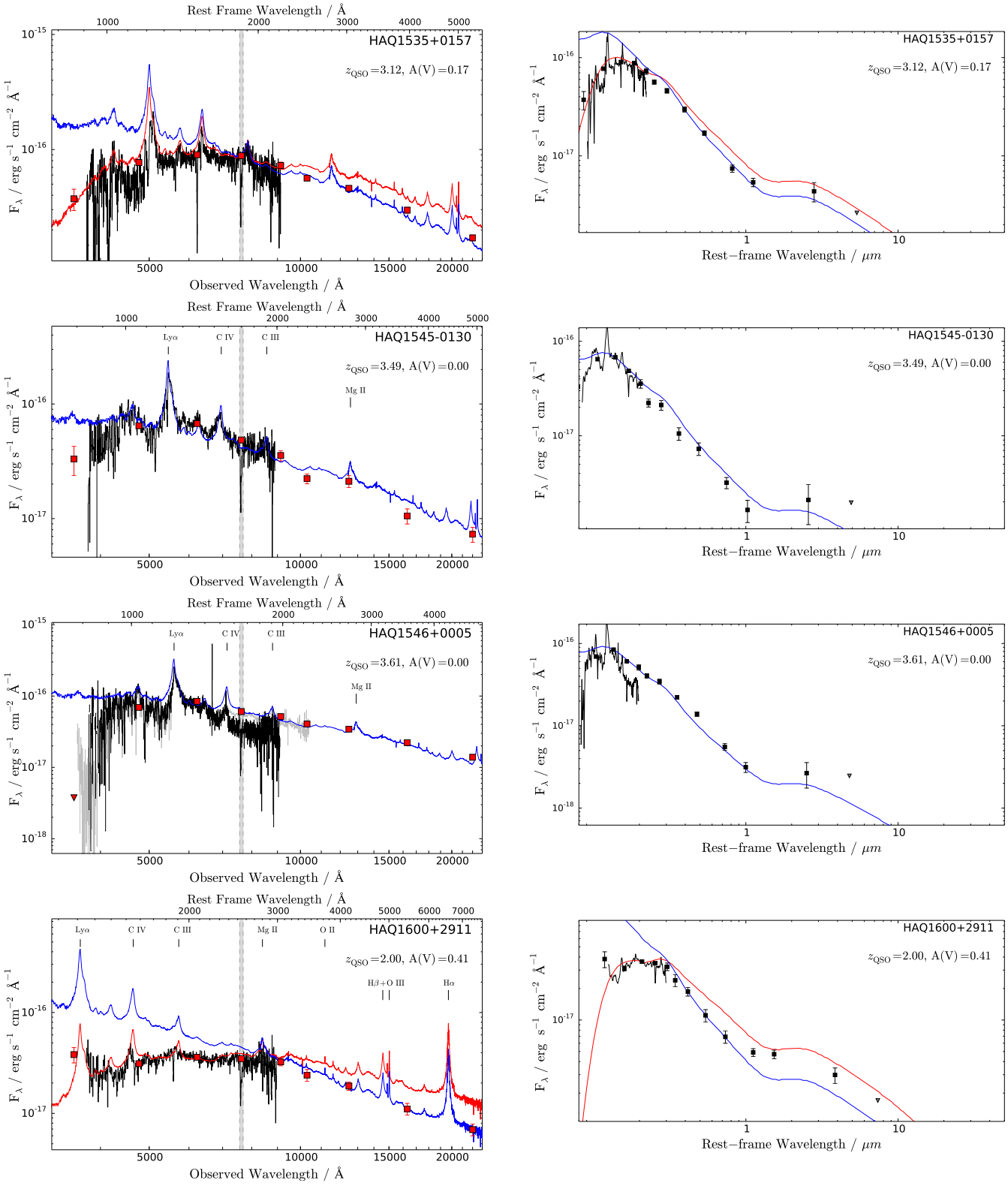

Figure 2.1 (Cont.): The observed spectrum (*left*) and the spectral energy distribution from photometry from SDSS, UKIDSS and WISE (*right*).

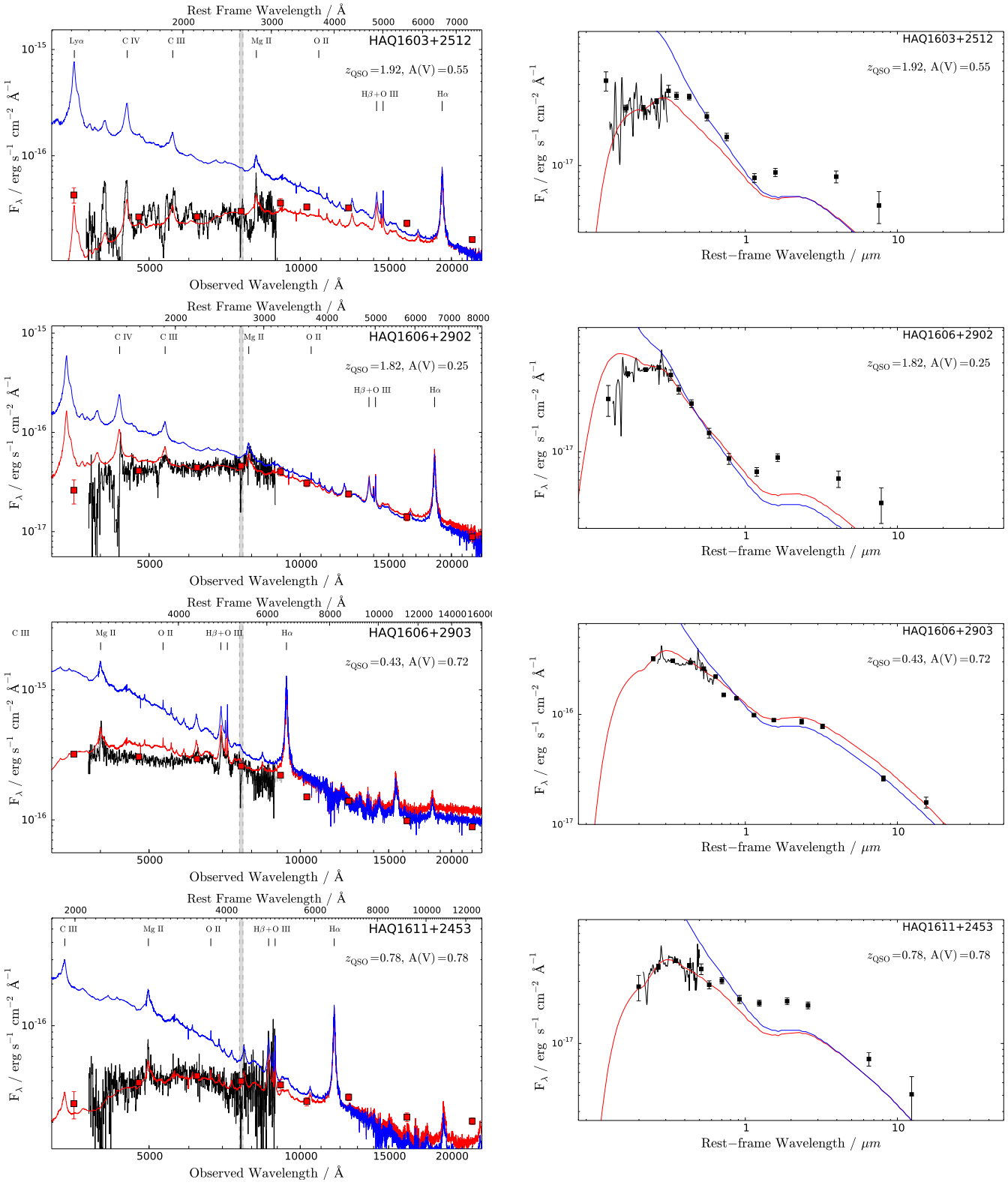

Figure 2.1 (Cont.): The observed spectrum (*left*) and the spectral energy distribution from photometry from SDSS, UKIDSS and WISE (*right*).

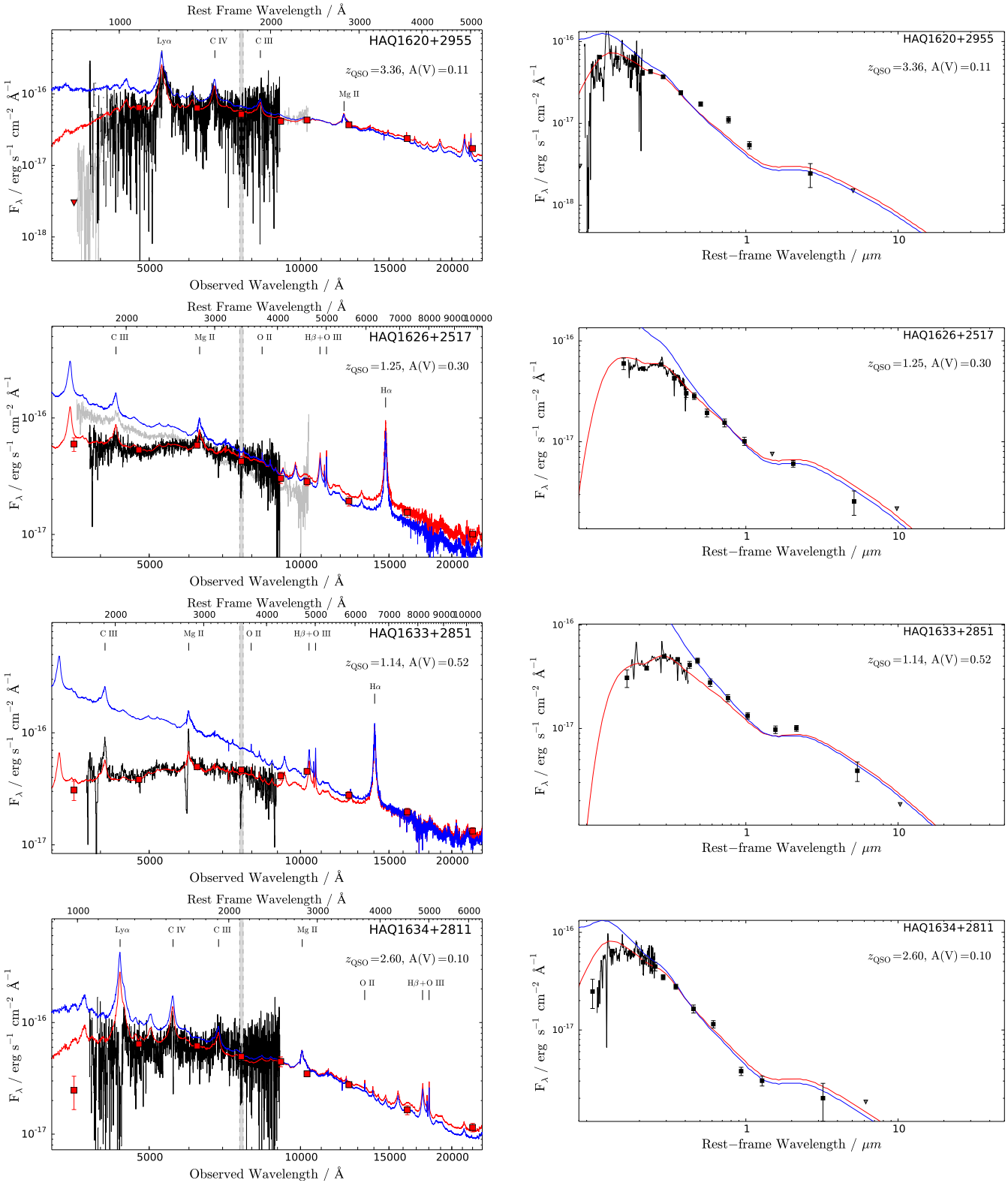

Figure 2.1 (Cont.): The observed spectrum (*left*) and the spectral energy distribution from photometry from SDSS, UKIDSS and WISE (*right*).

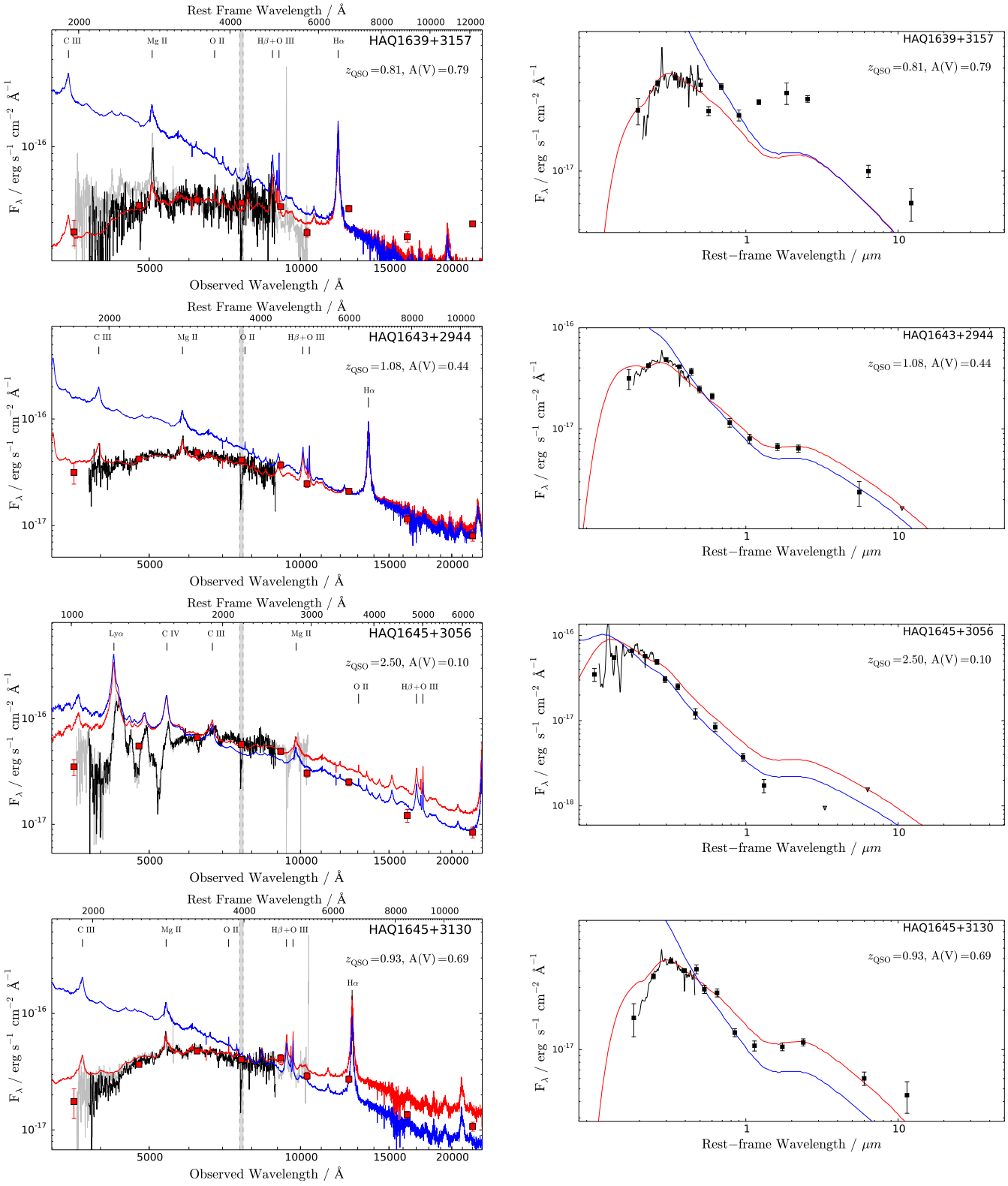

Figure 2.1 (Cont.): The observed spectrum (*left*) and the spectral energy distribution from photometry from SDSS, UKIDSS and WISE (*right*).

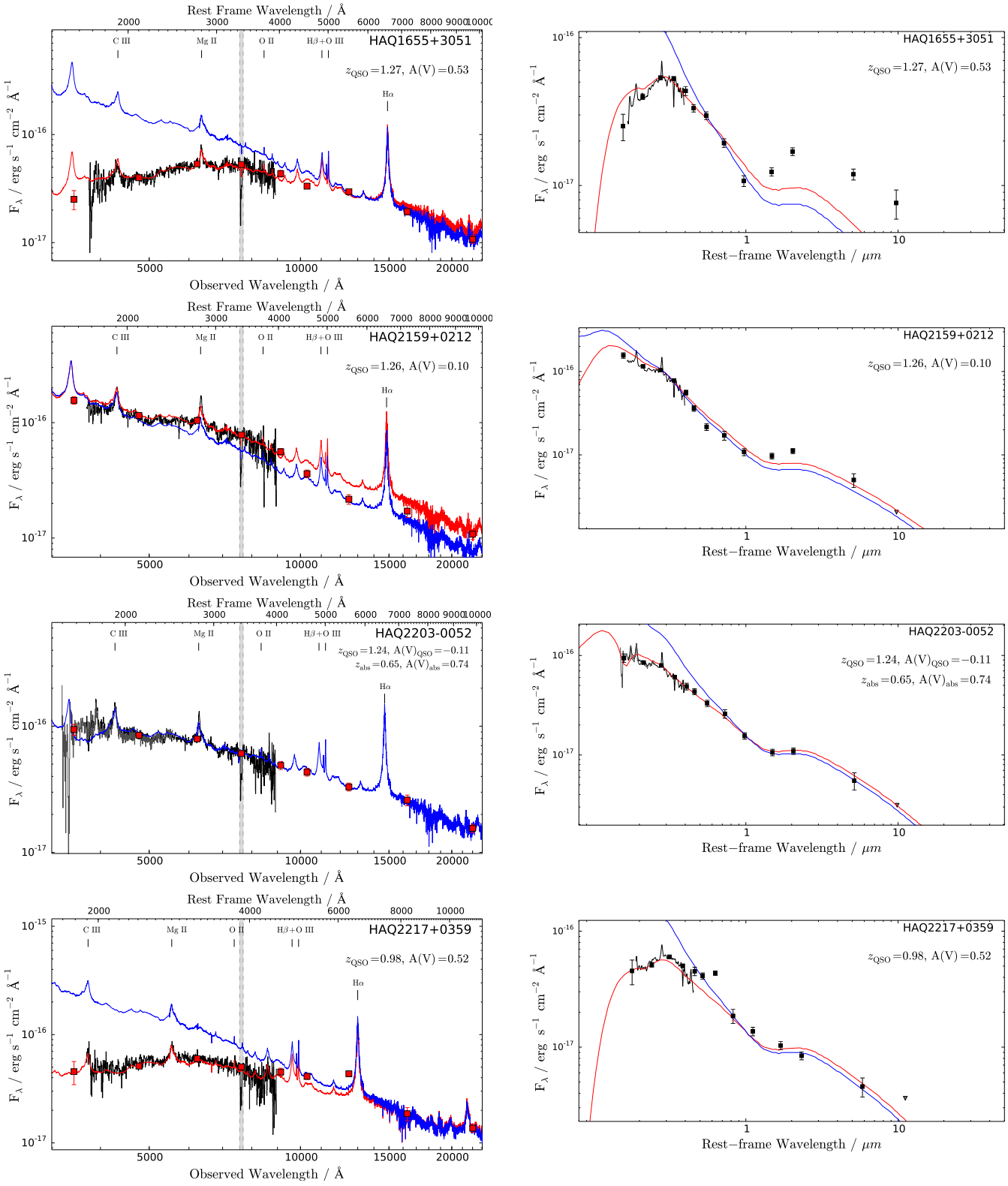

Figure 2.1 (Cont.): The observed spectrum (*left*) and the spectral energy distribution from photometry from SDSS, UKIDSS and WISE (*right*).

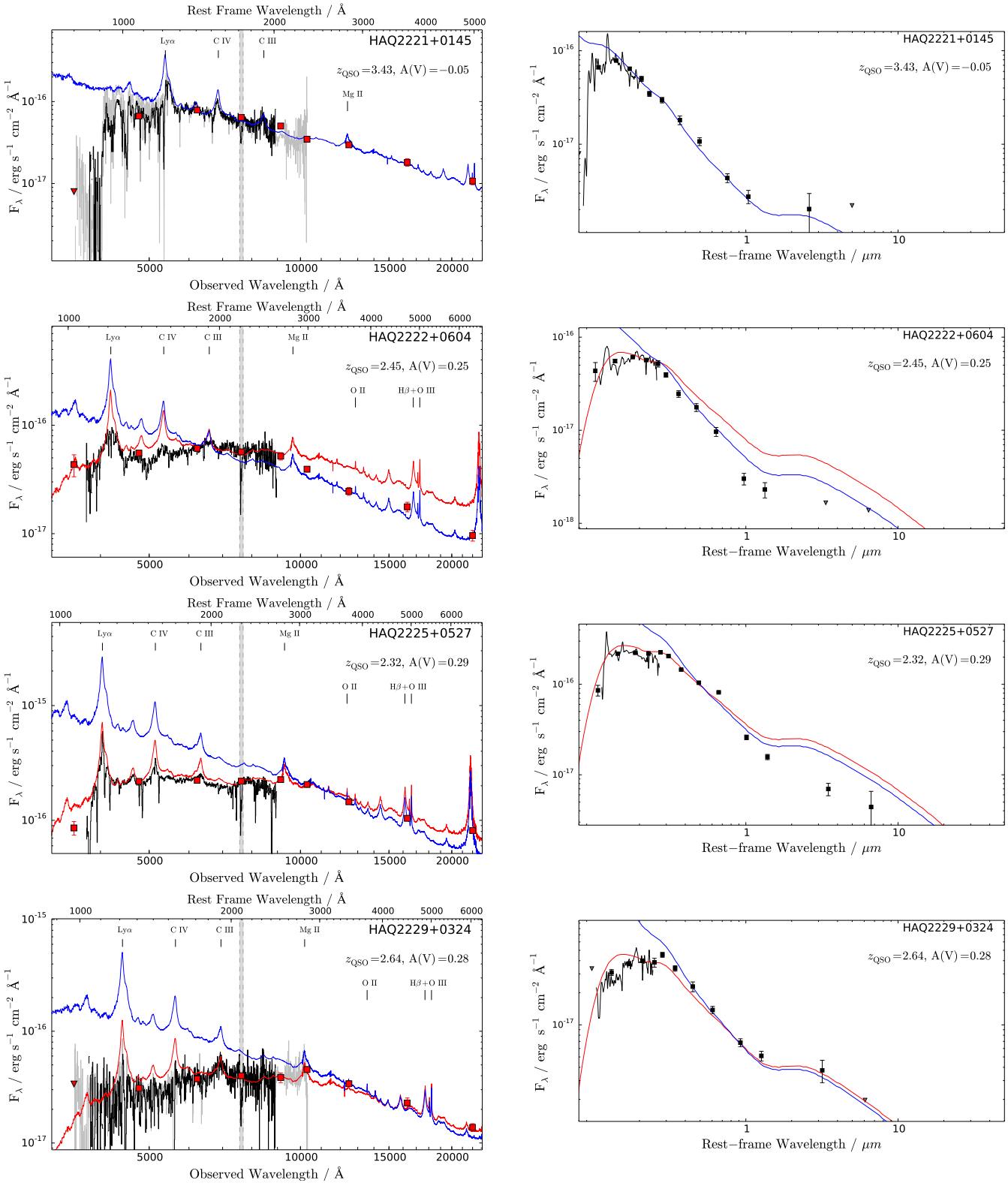

Figure 2.1 (Cont.): The observed spectrum (*left*) and the spectral energy distribution from photometry from SDSS, UKIDSS and WISE (*right*).

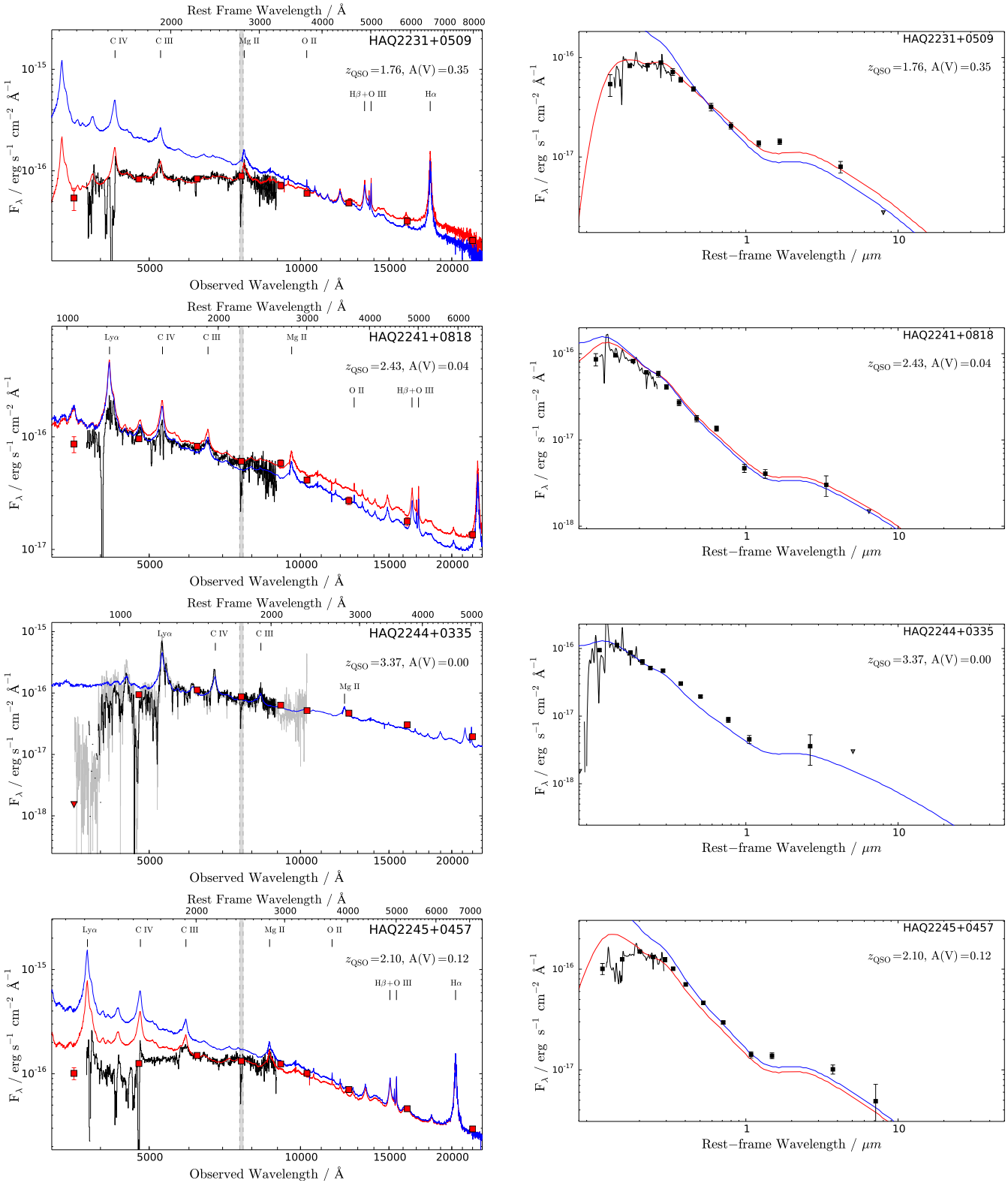

Figure 2.1 (Cont.): The observed spectrum (*left*) and the spectral energy distribution from photometry from SDSS, UKIDSS and WISE (*right*).

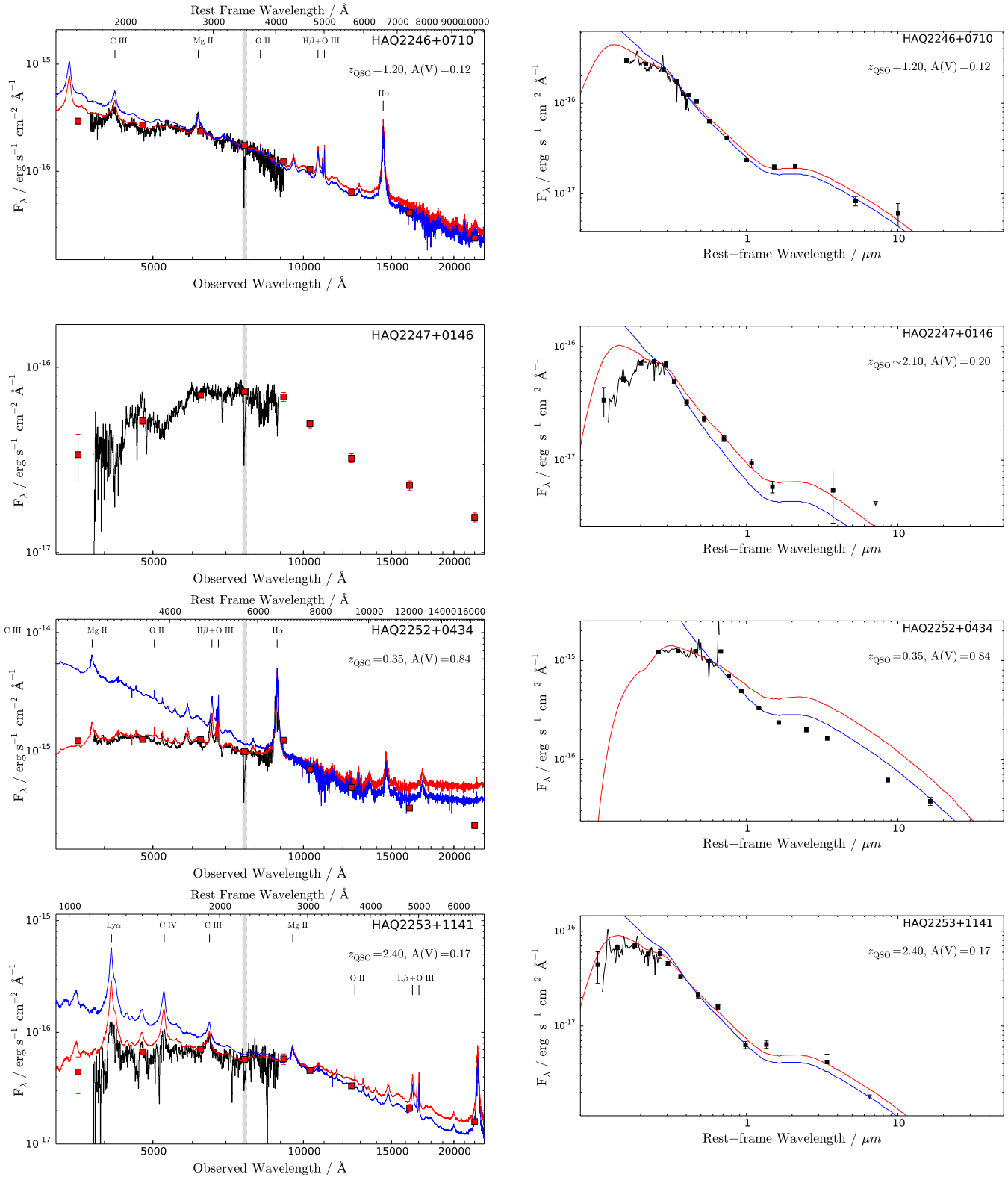

Figure 2.1 (Cont.): The observed spectrum (*left*) and the spectral energy distribution from photometry from SDSS, UKIDSS and WISE (*right*).

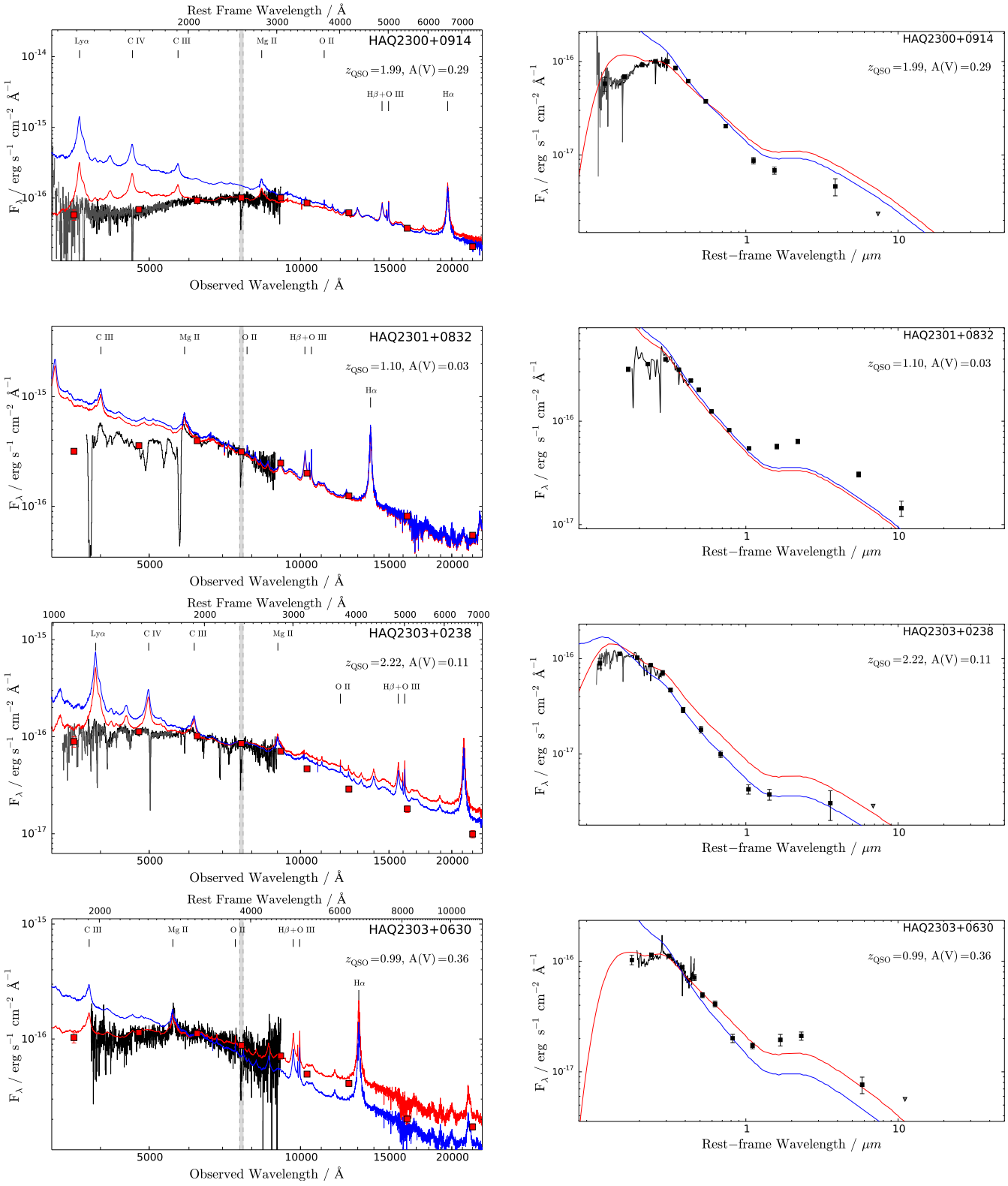

Figure 2.1 (Cont.): The observed spectrum (*left*) and the spectral energy distribution from photometry from SDSS, UKIDSS and WISE (*right*).

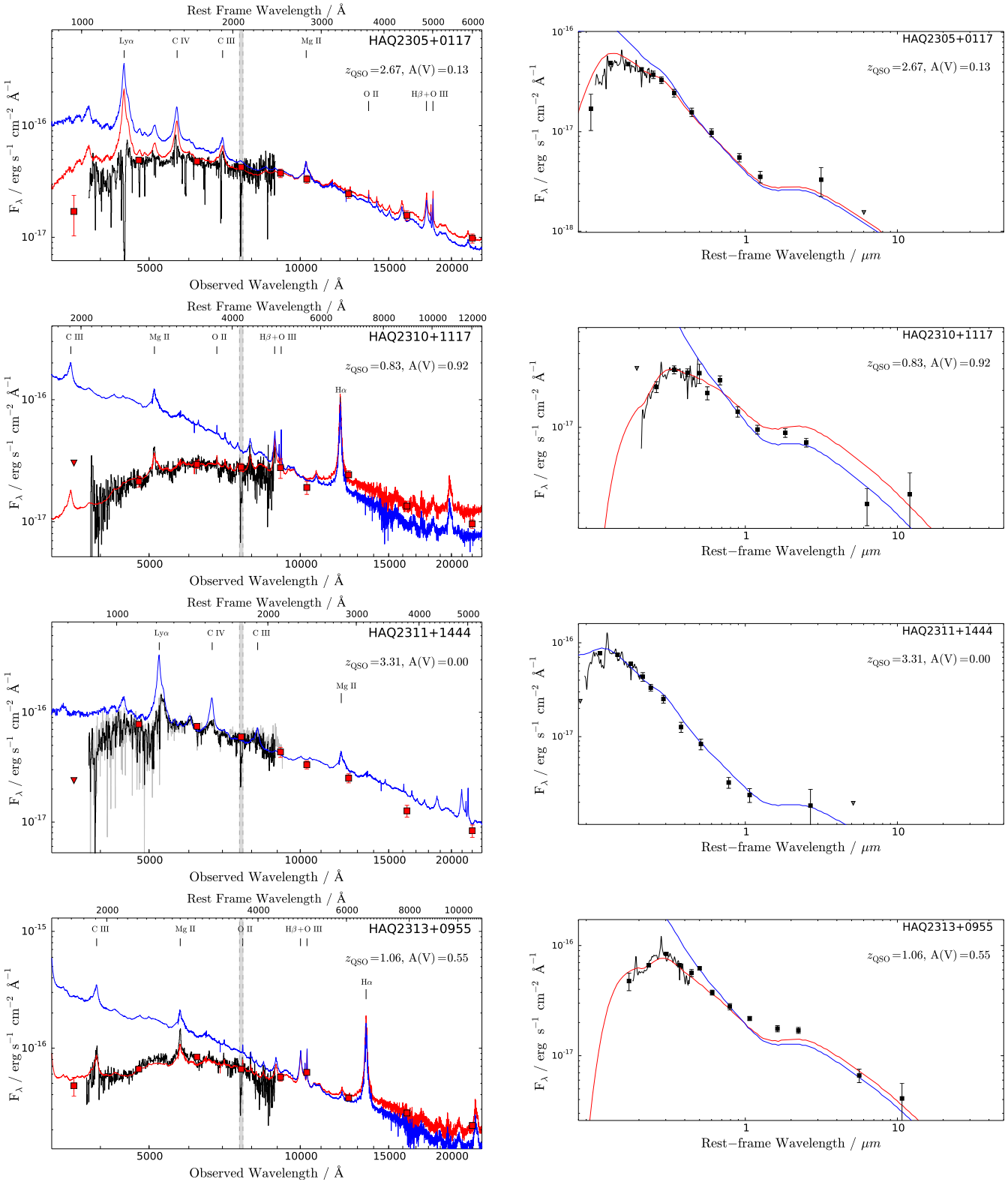

Figure 2.1 (Cont.): The observed spectrum (*left*) and the spectral energy distribution from photometry from SDSS, UKIDSS and WISE (*right*).

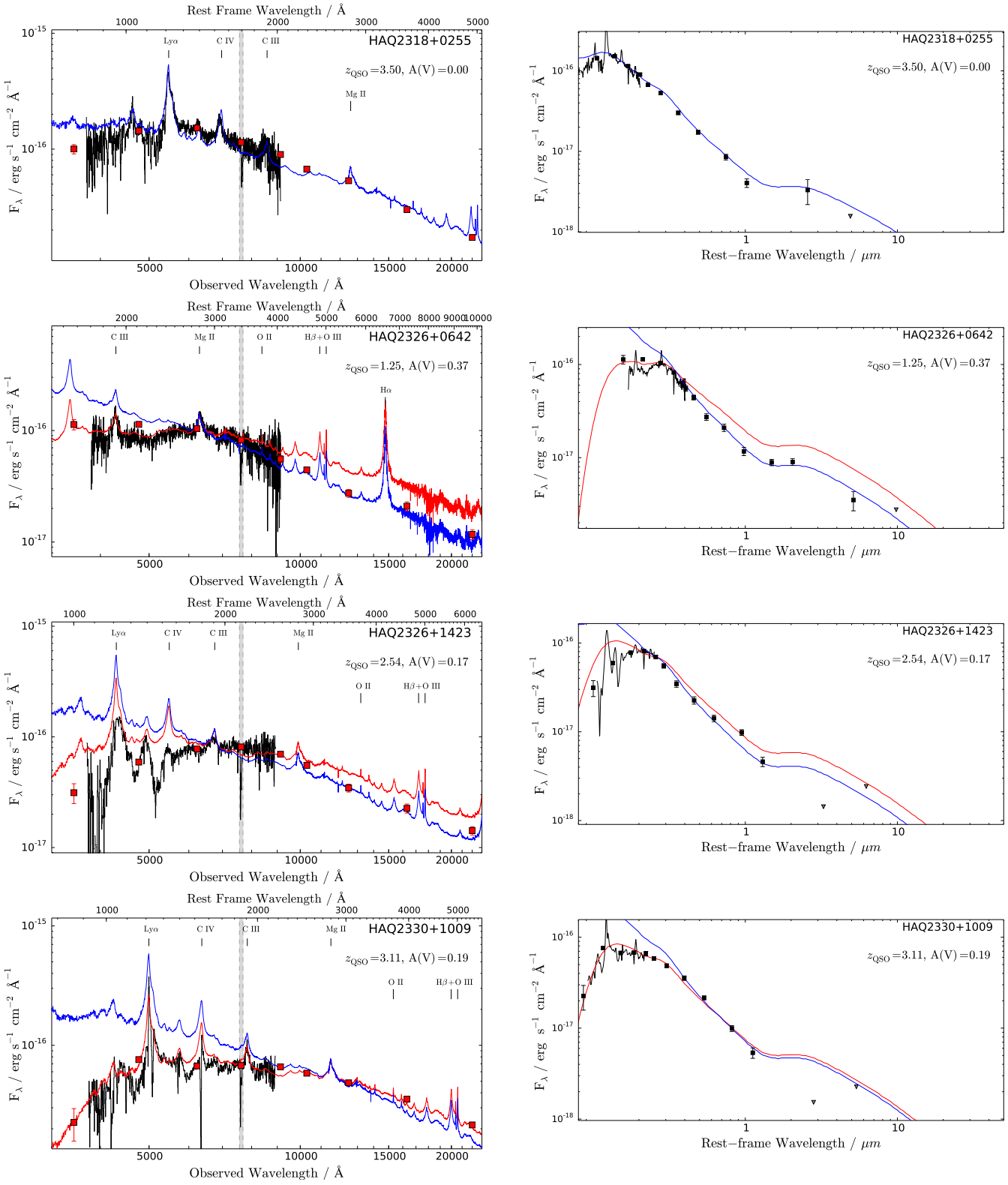

Figure 2.1 (Cont.): The observed spectrum (*left*) and the spectral energy distribution from photometry from SDSS, UKIDSS and WISE (*right*).

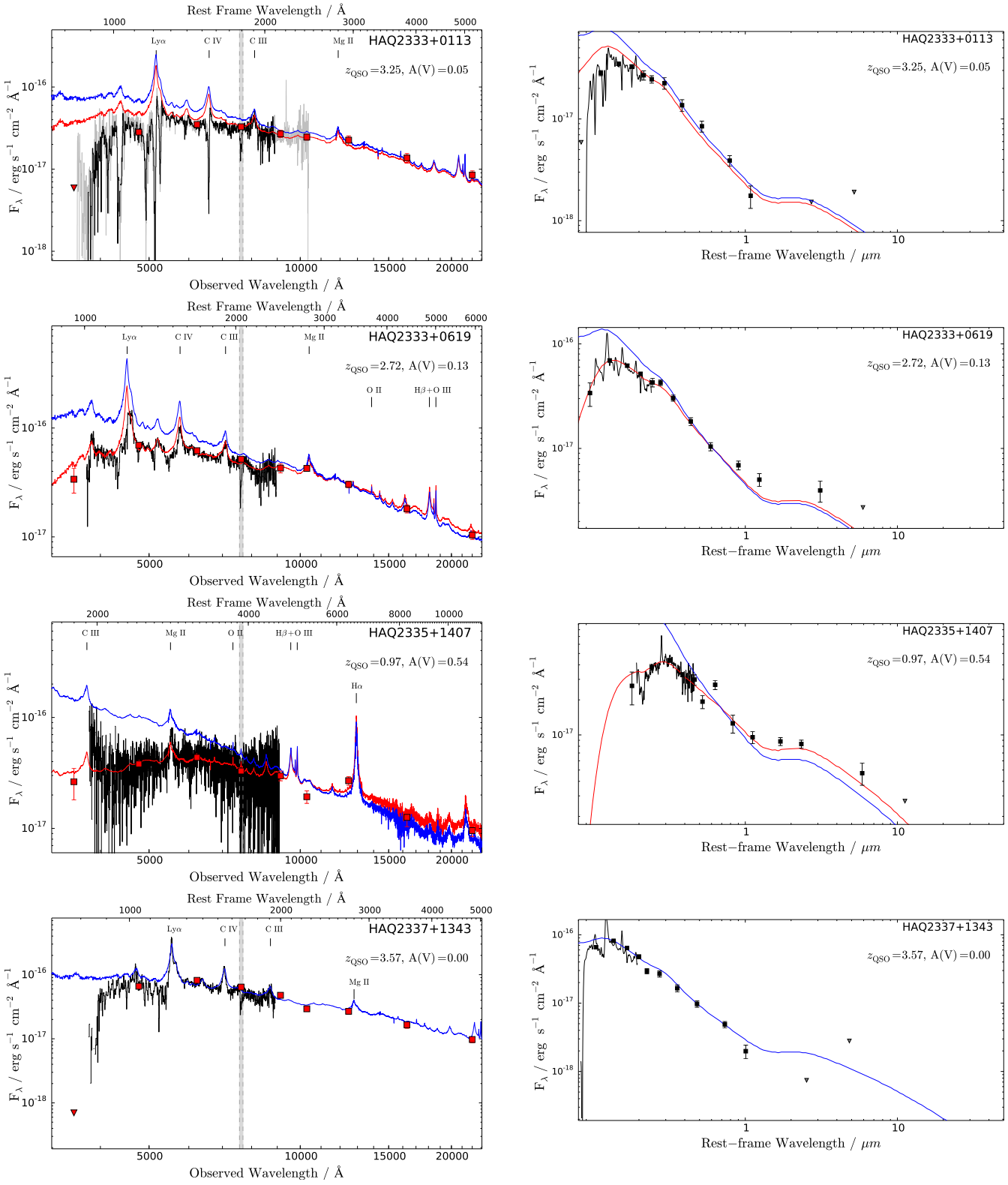

Figure 2.1 (Cont.): The observed spectrum (*left*) and the spectral energy distribution from photometry from SDSS, UKIDSS and WISE (*right*).

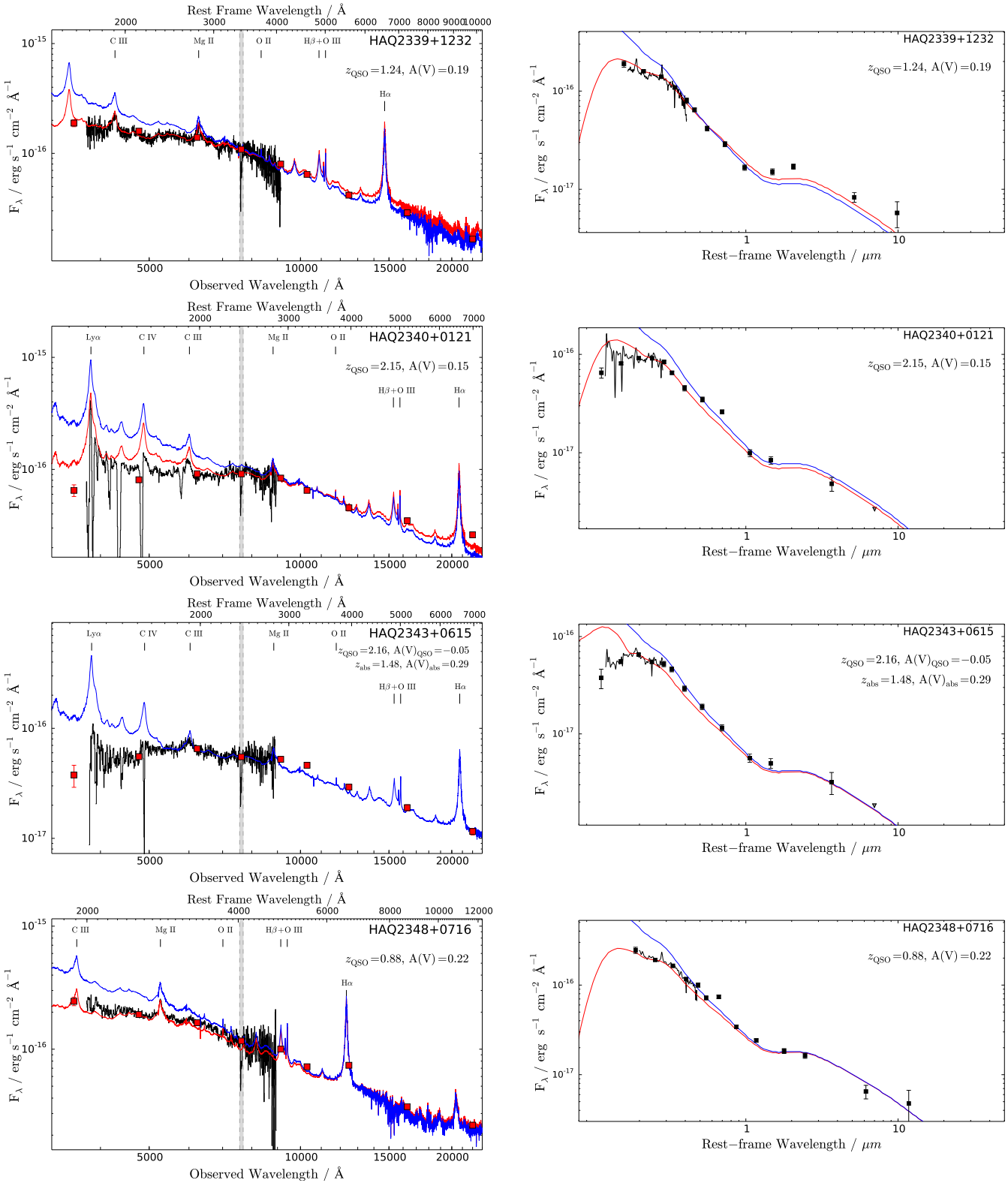

Figure 2.1 (Cont.): The observed spectrum (*left*) and the spectral energy distribution from photometry from SDSS, UKIDSS and WISE (*right*).

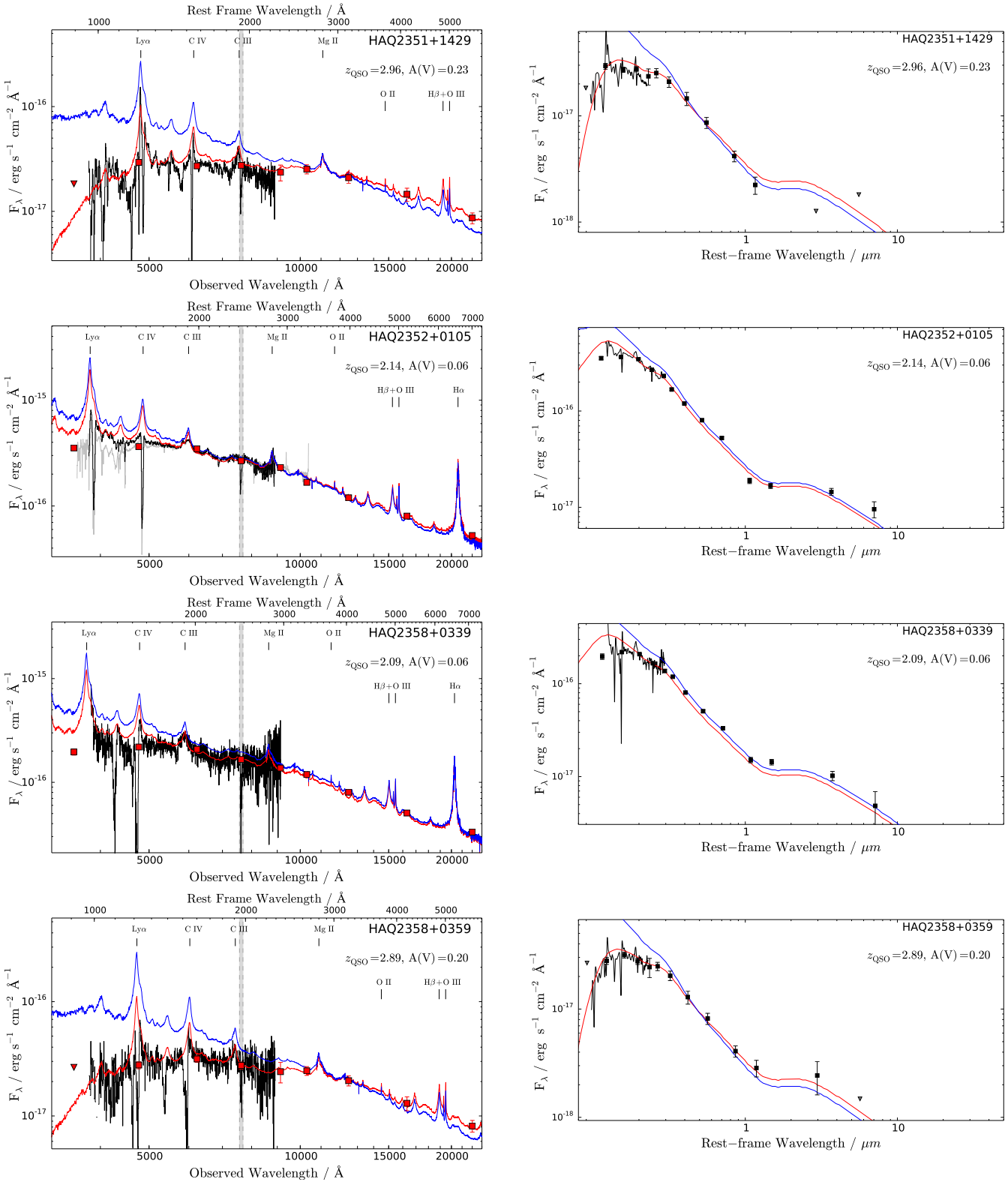

Figure 2.1 (Cont.): The observed spectrum (*left*) and the spectral energy distribution from photometry from SDSS, UKIDSS and WISE (*right*).

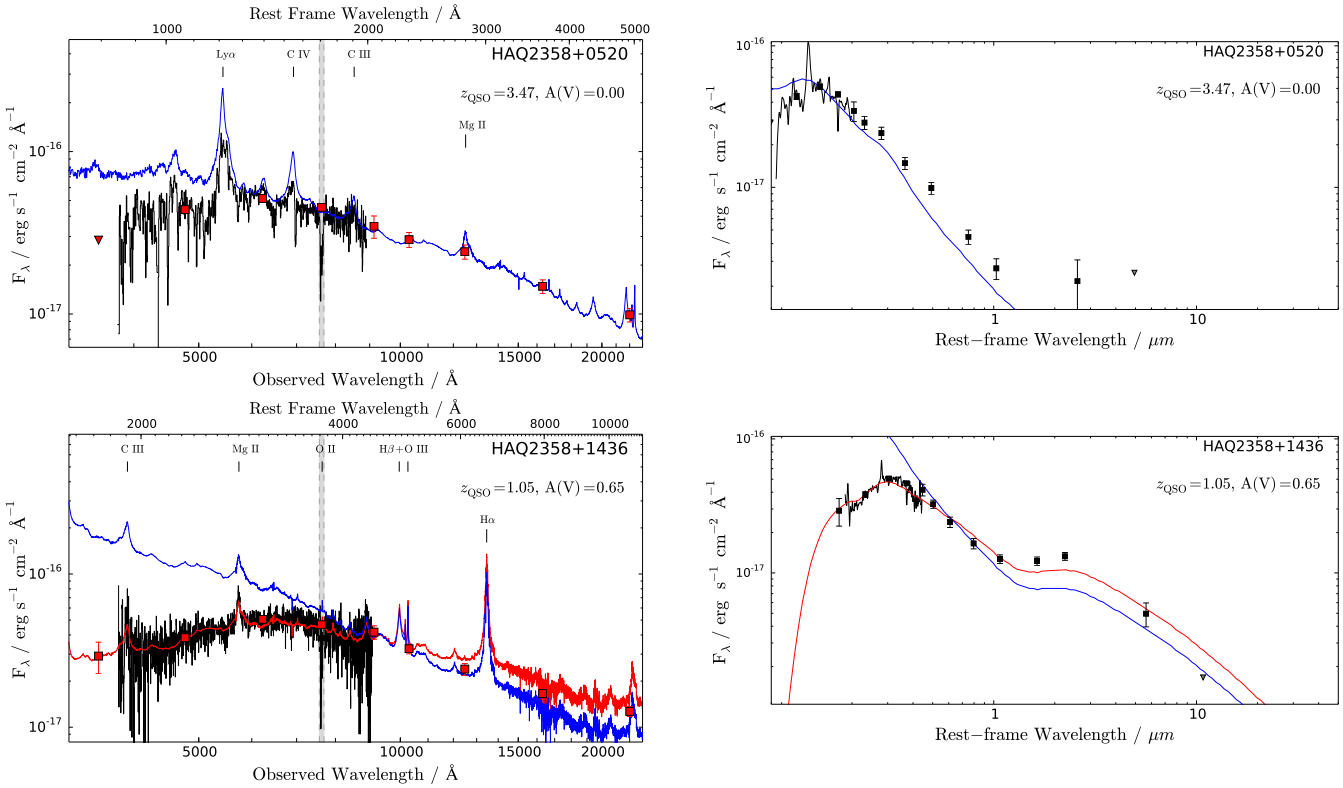

Figure 2.1 (Cont.): The observed spectrum (*left*) and the spectral energy distribution from photometry from SDSS, UKIDSS and WISE (*right*).

C

List of Publications

Number of refereed first-author articles: 4 — Citations: 75.
Number of refereed articles: 12 — Citations: 403.

Refereed Publications

1. Hartoog, O. E.; Malesani, D.; Fynbo, J. P. U.; Goto, T.; Krühler, T.; Vreeswijk, P. M.; De Cia, A.; Xu, D.; Møller, P.; Covino, S.; D'Elia, V.; Flores, H.; Goldoni, P.; Hjorth, J.; Jakobsson, P.; **Krogager, J.-K.**; Kaper, L.; Ledoux, C.; Levan, A. J.; Milvang-Jensen, B.; Sollerman, J.; Sparre, M.; Tagliaferri, G.; Tanvir, N. R.; de Ugarte Postigo, A.; Vergani, S. D.; Wiersema, K.; Datson, J.; Salinas, R.; Mikkelsen, K.; & Aghanim, N.,
"VLT/X-shooter spectroscopy of the afterglow of the Swift GRB 130606A: Chemical abundances and reionisation at $z \sim 6$," *Astronomy & Astrophysics, 2015, vol. 580, id. 139, 15 pp.*

2. **Krogager, J.-K.**; Geier, S.; Fynbo, J. P. U.; Venemans, B. P.; Ledoux, C.; Møller, P.; Noterdaeme, P.; Vestergaard, M.; Kangas, T.; Pursimo, T.; Saturni, F. G.; & Smirnova, O.,
"The High A_V Quasar Survey: Reddened quasi-stellar objects selected from optical/near-infrared photometry – II," *The Astrophysical Journal Supplement Series, 2015, vol. 217, id. 5, 26 pp.*

3. **Krogager, J.-K.**; Zirm, A. W.; Toft, S.; Man, A.; & Brammer, G.,
"A spectroscopic sample of massive, quiescent $z \sim 2$ galaxies: implications for the evolution of the mass–size relation," *The Astrophysical Journal, 2014, vol. 797, id. 17, 14pp.*

4. Toft, S.; Smolčić, V.; Magnelli, B.; Karim, A.; Zirm, A.; Michalowski, M.; Capak, P.; Sheth, K.; Schawinski, K.; **Krogager, J.-K.**; Wuyts, S.; Sanders, D.; Man, A. W. S.; Lutz, D.; Staguhn, J.; Berta, S.; Mccracken, H.; Krpan, J.; & Riechers, D.,
"Submillimeter galaxies as progenitors of compact quiescent galaxies," *The Astrophysical Journal, 2014, vol. 782, id. 68, 12pp.*

5. Fynbo, J. P. U.; Geier, S. J.; Christensen, L.; Gallazzi, A.; **Krogager, J.-K.**; Krühler, T.; Ledoux, C.; Maund, J. R.; Møller, P.; Noterdaeme, P.; Rivera-Thorsen, T.; & Vestergaard, M.,
"On the two high-metallicity DLAs at z = 2.412 and 2.583 towards Q 0918+1636," *Monthly Notices of the Royal Astronomical Society, 2013, vol. 436, pp. 361–370.*

6. **Krogager, J.-K.**; Fynbo, J. P. U.; Ledoux, C.; Christensen, L.; Gallazzi, A.; Laursen, P.; Møller, P.; Noterdaeme, P.; Péroux, C.; Pettini, M.; & Vestergaard, M.,
"Comprehensive study of a z = 2.35 DLA galaxy: mass, metallicity, age, morphology and SFR from HST and VLT", *Monthly Notices of the Royal Astronomical Society, 2013, vol. 433, pp. 3091–3102.*

7. Dahle, H.; Gladders, M. D.; Sharon, K.; Bayliss, M. B.; Wuyts, E.; Abramson, L. E.; Koester, B. P.; Groeneboom, N.; Brinckmann, T. E.; Kristensen, M. T.; Lindholmer, M. O.; Nielsen, A.; **Krogager, J.-K.**; & Fynbo, J. P. U.,
"SDSS J2222+2745: A Gravitationally lensed sextuple quasar with a maximum image separation of 15.″1 discovered in the Sloan Giant Arcs Survey",
The Astrophysical Journal, 2013, vol. 773, id. 146, 10pp.

8. Ilbert, O.; McCracken, H. J.; Le F'evre, O.; Capak, P.; Dunlop, J.; Karim, A.; Renzini, M. A.; Caputi, K.; Boissier, S.; Arnouts, S.; Aussel, H.; Comparat, J.; Guo, Q.; Hudelot, P.; Kartaltepe, J.; Kneib, J. P.; **Krogager, J. K.**; Le Floc'h, E.; Lilly, S.; Mellier, Y.; Milvang-Jensen, B.; Moutard, T.; Onodera, M.; Richard, J.; Salvato, M.; Sanders, D. B.; Scoville, N.; Silverman, J. D.; Taniguchi, Y.; Tasca, L.; Thomas, R.; Toft, S.; Tresse, L.; Vergani, D.; Wolk, M.; & Zirm, A.,
"Mass assembly in quiescent and star-forming galaxies since $z \sim 4$ from UltraVISTA,"
Astronomy & Astrophysics, 2013, vol. 556, id. 55, 19 pp.

9. Fynbo, J. P. U.; **Krogager, J.-K.**; Venemans, B.; Noterdaeme, P.; Vestergaard, M.; Møller, P.; Ledoux, C.; & Geier, S.,
"Optical/near-infrared selection of red quasi-stellar objects: Evidence for steep extinction curves toward galactic centers?,"
The Astrophysical Journal Supplement Series, 2013, vol. 204, id. 6, 14 pp.

10. **Krogager, J.-K.**; Fynbo, J. P. U.; Møller, P.; Ledoux, C.; Noterdaeme, P.; Christensen, L.; Milvang-Jensen, B.; & Sparre, M.,
"On the sizes of $z \gtrsim 2$ damped Lyα absorbing galaxies," *Monthly Notices of the Royal Astronomical Society: Letters, 2012, vol. 424, pp. L1–L5.*

11. Fynbo, J. P. U.; Ledoux, C.; Noterdaeme, P.; Christensen, L.; Møller, P.; Durgapal, A. K.; Goldoni, P.; Kaper, L.; **Krogager, J.-K.**; Laursen, P.; Maund, J. R.; Milvang-Jensen, B.; Okoshi, K.; Rasmussen, P. K.; Thorsen, T. J.; Toft, S.; & Zafar, T.,
"Galaxy counterparts of metal-rich damped Lyα absorbers – II. A solar-metallicity and dusty DLA at $z_{\rm abs} = 2.58$," *Monthly Notices of the Royal Astronomical Society, 2011, vol. 413, pp. 2481–2488.*

12. Cupani, G.; Cristiani, S.; D'Odorico, V.; Milvang-Jensen, B.; & **Krogager, J.-K.**,
"When two become one: an apparent QSO pair turns out to be a single quasar,"
Astronomy & Astrophysics, 2011, vol. 529, id. 99, 3 pp.

Forthcoming Publications

1. **Krogager, J.-K.**; Fynbo, J. P. U.; Noterdaeme, P.; Møller, P.; Zafar, T.; Ledoux, C.; Stockton, A.; & Krühler, T.,
   "A Quasar reddened by a sub-parsec sized, metal-rich and dusty damped Lyα absorbing cloud at $z = 2.13$," submitted to *Monthly Notices of the Royal Astronomical Society, Aug, 2015.*

2. Selsing, J.; Fynbo, J. P. U.; Christensen, L.; & **Krogager, J.-K.**,
   "X-shooter composite of bright $1 < z < 2$ quasars from UV to infrared,"
   submitted to *Astronomy & Astrophysics, Aug, 2015.*

3. Zafar, T.; Møller, P.; Watson, D.; Fynbo, J. P. U.; **Krogager, J.-K.**; Zafar, N.; Saturni, F. G.; Geier, S.; & Venemans, B. P.,
   "Steep extinction curves in intrinsically reddened quasars,"
   submitted to *Astronomy & Astrophysics, Jun, 2015.*

4. Saturni, F. G.; Møller, P.; Freudling, W.; Fynbo, J. P. U.; Geier, S.; **Krogager, J.-K.**; Ledoux, C.; Noterdaeme, P.; Venemans, B. P.; Vestergaard, M.; & Zafar, T.,
   "The era of BALs at $z \sim 2.5$: observational evidence for QSO feedback as a regulator of star formation and quasar activity," *Monthly Notices of the Royal Astronomical Society, 2015, in review.*

5. Finlator, K.; Christensen, L.; Fynbo, J. P. U.; & **Krogager, J.-K.**,
   "Dust Bias in DLA-galaxy Unification Models," *in preparation for The Astrophysical Journal.*

Bibliography

Arabsalmani, M., Møller, P., Fynbo, J. P. U., et al. 2015, MNRAS, 446, 990

Arnouts, S., Cristiani, S., Moscardini, L., et al. 1999, MNRAS, 310, 540

Asplund, M., Grevesse, N., Sauval, A. J., & Scott, P. 2009, ARA&A, 47, 481

Balashev, S. A., Noterdaeme, P., Klimenko, V. V., et al. 2015, A&A, 575, L8

Balashev, S. A., Petitjean, P., Ivanchik, A. V., et al. 2011, MNRAS, 418, 357

Baloković, M., Smolčić, V., Ivezić, Ž., et al. 2012, ApJ, 759, 30

Banerji, M., McMahon, R. G., Hewett, P. C., et al. 2012, MNRAS, 427, 2275

Barnes, L. A., & Haehnelt, M. G. 2014, MNRAS, 440, 2313

Barthel, P. D., Miley, G. K., Schilizzi, R. T., & Lonsdale, C. J. 1988, A&AS, 73, 515

Barthel, P. D., Tytler, D. R., & Thomson, B. 1990, A&AS, 82, 339

Becker, R. H., White, R. L., & Helfand, D. J. 1995a, ApJ, 450, 559

—. 1995b, ApJ, 450, 559

Bedregal, A. G., Scarlata, C., Henry, A. L., et al. 2013, ApJ, 778, 126

Belli, S., Newman, A. B., & Ellis, R. S. 2014, ApJ, 783, 117

Belli, S., Newman, A. B., Ellis, R. S., & Konidaris, N. P. 2014, ApJ, 788, L29

Benn, C. R., Vigotti, M., Carballo, R., Gonzalez-Serrano, J. I., & Sánchez, S. F. 1998, MNRAS, 295, 451

Berg, T. A. M., Ellison, S. L., Prochaska, J. X., Venn, K. A., & Dessauges-Zavadsky, M. 2015, MNRAS, 452, 4326

Bezanson, R., van Dokkum, P. G., Tal, T., et al. 2009, ApJ, 697, 1290

Bird, S., Haehnelt, M., Neeleman, M., et al. 2015, MNRAS, 447, 1834

Bird, S., Vogelsberger, M., Haehnelt, M., et al. 2014, MNRAS, 445, 2313

Boissé, P., Le Brun, V., Bergeron, J., & Deharveng, J.-M. 1998, A&A, 333, 841

Bongiorno, A., Zamorani, G., Gavignaud, I., et al. 2007, A&A, 472, 443

Bouché, N., Murphy, M. T., Péroux, C., et al. 2012, MNRAS, 419, 2

Bowen, D. V., Jenkins, E. B., Pettini, M., & Tripp, T. M. 2005, ApJ, 635, 880

Brammer, G. B., van Dokkum, P. G., & Coppi, P. 2008, ApJ, 686, 1503

Brammer, G. B., Whitaker, K. E., van Dokkum, P. G., et al. 2011, ApJ, 739, 24

Brammer, G. B., van Dokkum, P. G., Franx, M., et al. 2012, ApJS, 200, 13

Bregman, J. N., Miller, E. D., Seitzer, P., Cowley, C. R., & Miller, M. J. 2013, ApJ, 766, 57

Briggs, F. H., Wolfe, A. M., Liszt, H. S., Davis, M. M., & Turner, K. L. 1989, ApJ, 341, 650

Bruce, V. A., Dunlop, J. S., Cirasuolo, M., et al. 2012, MNRAS, 427, 1666

Bruzual, G., & Charlot, S. 2003, MNRAS, 344, 1000

Bruzual A., G. 1983, ApJ, 273, 105

Buitrago, F., Trujillo, I., Conselice, C. J., et al. 2008, ApJ, 687, L61

Caffau, E., Bonifacio, P., François, P., et al. 2011, A&A, 534, A4

Calzetti, D., Armus, L., Bohlin, R. C., et al. 2000, ApJ, 533, 682

Cappellari, M., Emsellem, E., Krajnović, D., et al. 2011, MNRAS, 413, 813

Cappellari, M., Scott, N., Alatalo, K., et al. 2013, MNRAS, 432, 1709

Carollo, C. M., Bschorr, T. J., Renzini, A., et al. 2013, ApJ, 773, 112

Cassata, P., Giavalisco, M., Guo, Y., et al. 2011, ApJ, 743, 96

Cen, R. 2012, ApJ, 748, 121

Chabrier, G. 2003, Publications of the Astronomical Society of the Pacific, 115, 763

Charlot, S., & Fall, S. M. 2000, ApJ, 539, 718

Chevance, M., Weijmans, A.-M., Damjanov, I., et al. 2012, ApJ, 754, L24

Christensen, L., Møller, P., Fynbo, J. P. U., & Zafar, T. 2014, MNRAS, 445, 225

Christensen, L., Wisotzki, L., Roth, M. M., et al. 2007, A&A, 468, 587

Ciotti, L., Lanzoni, B., & Volonteri, M. 2007, ApJ, 658, 65

Cooke, R., Pettini, M., Steidel, C. C., et al. 2010, MNRAS, 409, 679

Cresci, G., Hicks, E. K. S., Genzel, R., et al. 2009, ApJ, 697, 115

Croom, S. M., Smith, R. J., Boyle, B. J., et al. 2004, MNRAS, 349, 1397

Daddi, E., Cimatti, A., Renzini, A., et al. 2004, ApJ, 617, 746

Daddi, E., Renzini, A., Pirzkal, N., et al. 2005, ApJ, 626, 680

Damjanov, I., McCarthy, P. J., Abraham, R. G., et al. 2009, ApJ, 695, 101

Damjanov, I., Abraham, R. G., Glazebrook, K., et al. 2011, ApJ, 739, L44

Davis, S. W., Woo, J.-H., & Blaes, O. M. 2007, ApJ, 668, 682

Dawson, K. S., Schlegel, D. J., Ahn, C. P., et al. 2013, AJ, 145, 10

de Bruijne, J. H. J. 2012, Ap&SS, 341, 31

De Cia, A., Ledoux, C., Savaglio, S., Schady, P., & Vreeswijk, P. M. 2013, A&A, 560, A88

Dijkstra, M., Haiman, Z., & Scharf, C. 2005, ApJ, 624, 85

Draine, B. T. 2003, ARA&A, 41, 241

Eggen, O. J., Lynden-Bell, D., & Sandage, A. R. 1962, ApJ, 136, 748

Elíasdóttir, Á., Fynbo, J. P. U., Hjorth, J., et al. 2009, ApJ, 697, 1725

Ellison, S. L., Churchill, C. W., Rix, S. A., & Pettini, M. 2004, ApJ, 615, 118

Ellison, S. L., Hennawi, J. F., Martin, C. L., & Sommer-Larsen, J. 2007, MNRAS, 378, 801

Ellison, S. L., Pettini, M., Steidel, C. C., & Shapley, A. E. 2001, ApJ, 549, 770

Ellison, S. L., Vreeswijk, P., Ledoux, C., et al. 2006, MNRAS, 372, L38

Elvis, M., Marengo, M., & Karovska, M. 2002, ApJ, 567, L107

Erb, D. K., Shapley, A. E., Pettini, M., et al. 2006, ApJ, 644, 813

Erkal, D., Gnedin, N. Y., & Kravtsov, A. V. 2012, ApJ, 761, 54

Fall, S. M., Pei, Y. C., & McMahon, R. G. 1989, ApJ, 341, L5

Fan, L., Lapi, A., De Zotti, G., & Danese, L. 2008, ApJ, 689, L101

Ferguson, H. C., Dickinson, M., Giavalisco, M., et al. 2004, ApJ, 600, L107

Fitzpatrick, E. L., & Massa, D. 1990, ApJS, 72, 163

—. 2005, AJ, 130, 1127

—. 2007, ApJ, 663, 320

Foltz, C. B., Chaffee, Jr., F. H., & Black, J. H. 1988, ApJ, 324, 267

Foltz, C. B., Chaffee, Jr., F. H., & Weymann, R. J. 1986, AJ, 92, 247

Font-Ribera, A., Miralda-Escudé, J., Arnau, E., et al. 2012, JCAP, 11, 59

Fontana, A., & Ballester, P. 1995, The Messenger, 80, 37

Foreman-Mackey, D., Hogg, D. W., Lang, D., & Goodman, J. 2013, PASP, 125, 306

Frank, S., & Péroux, C. 2010a, MNRAS, 406, 2235

—. 2010b, MNRAS, 406, 2235

Franx, M., van Dokkum, P. G., Schreiber, N. M. F., et al. 2008, ApJ, 688, 770

Franx, M., Labbé, I., Rudnick, G., et al. 2003, ApJ, 587, L79

Frebel, A., Johnson, J. L., & Bromm, V. 2007, MNRAS, 380, L40

Frebel, A., Simon, J. D., Geha, M., & Willman, B. 2010, ApJ, 708, 560

Fumagalli, M., O'Meara, J. M., Prochaska, J. X., Kanekar, N., & Wolfe, A. M. 2014, MNRAS, 444, 1282

Fumagalli, M., O'Meara, J. M., Prochaska, J. X., Rafelski, M., & Kanekar, N. 2015, MNRAS, 446, 3178

Fynbo, J. P. U., Krogager, J.-K., Venemans, B., et al. 2013a, ApJS, 204, 6

Fynbo, J. P. U., Ledoux, C., Møller, P., Thomsen, B., & Burud, I. 2003, A&A, 407, 147

Fynbo, J. P. U., Prochaska, J. X., Sommer-Larsen, J., Dessauges-Zavadsky, M., & Møller, P. 2008, ApJ, 683, 321

Fynbo, J. P. U., Starling, R. L. C., Ledoux, C., et al. 2006, A&A, 451, L47

Fynbo, J. P. U., Laursen, P., Ledoux, C., et al. 2010, MNRAS, 408, 2128

Fynbo, J. P. U., Ledoux, C., Noterdaeme, P., et al. 2011, MNRAS, 413, 2481

Fynbo, J. P. U., Geier, S. J., Christensen, L., et al. 2013b, MNRAS, 436, 361

Fynbo, J. P. U., Krühler, T., Leighly, K., et al. 2014, A&A, 572, A12

Fynbo, J. U., Møller, P., & Warren, S. J. 1999, MNRAS, 305, 849

Gardner, J. P., Katz, N., Hernquist, L., & Weinberg, D. H. 1997, ApJ, 484, 31

—. 2001, ApJ, 559, 131

Gavignaud, I., Bongiorno, A., Paltani, S., et al. 2006, A&A, 457, 79

Glikman, E., Gregg, M. D., Lacy, M., et al. 2004, ApJ, 607, 60

Glikman, E., Helfand, D. J., & White, R. L. 2006, ApJ, 640, 579

Glikman, E., Helfand, D. J., White, R. L., et al. 2007, ApJ, 667, 673

Glikman, E., Urrutia, T., Lacy, M., et al. 2012, ApJ, 757, 51

—. 2013, ApJ, 778, 127

Gnerucci, A., Marconi, A., Cresci, G., et al. 2011, A&A, 528, A88

Gobat, R., Strazzullo, V., Daddi, E., et al. 2013, ApJ, 776, 9

Gordon, K. D., Clayton, G. C., Misselt, K. A., Landolt, A. U., & Wolff, M. J. 2003a, ApJ, 594, 279

—. 2003b, ApJ, 594, 279

Gosling, A. J., Bandyopadhyay, R. M., & Blundell, K. M. 2009, MNRAS, 394, 2247

Gower, J. F. R., Scott, P. F., & Wills, D. 1967, MmRAS, 71, 49

Graham, M. J., Djorgovski, S. G., Drake, A. J., et al. 2014, MNRAS, 439, 703

Gregg, M. D., Lacy, M., White, R. L., et al. 2002, ApJ, 564, 133

Grogin, N. A., Kocevski, D. D., Faber, S. M., et al. 2011, ApJS, 197, 35

Guo, Y., McIntosh, D. H., Mo, H. J., et al. 2009, MNRAS, 398, 1129

Haehnelt, M. G., Steinmetz, M., & Rauch, M. 1998, ApJ, 495, 647

Hall, P. B., Anderson, S. F., Strauss, M. A., et al. 2002, ApJS, 141, 267

Hathi, N. P., Cohen, S. H., Ryan, Jr., R. E., et al. 2013, ApJ, 765, 88

Haynes, M. P., & Giovanelli, R. 1984, AJ, 89, 758

Hazard, C. 1964, Nature, 202, 227

Heckman, T. M., Miley, G. K., Lehnert, M. D., & van Breugel, W. 1991, ApJ, 370, 78

Heintz, K. E., Fynbo, J. P. U., & Høg, E. 2015, A&A, 578, A91

Hewett, P. C., Warren, S. J., Leggett, S. K., & Hodgkin, S. T. 2006, MNRAS, 367, 454

Hollenbach, D., & Salpeter, E. E. 1971, ApJ, 163, 155

Holmberg, J., Nordström, B., & Andersen, J. 2007, A&A, 475, 519

Hopkins, P. F., Somerville, R. S., Hernquist, L., et al. 2006, ApJ, 652, 864

Hopkins, P. F., Strauss, M. A., Hall, P. B., et al. 2004, AJ, 128, 1112

Horne, K. 1986, PASP, 98, 609

Hunstead, R. W., Pettini, M., & Fletcher, A. B. 1990, ApJ, 356, 23

Hunt, L. K., Mannucci, F., Testi, L., et al. 1998, AJ, 115, 2594

Ilbert, O., Arnouts, S., McCracken, H. J., et al. 2006, A&A, 457, 841

Ivezić, Ž., Menou, K., Knapp, G. R., et al. 2002, AJ, 124, 2364

Jiang, P., Ge, J., Prochaska, J. X., et al. 2010, ApJ, 724, 1325

Jiang, P., Zhou, H., Ji, T., et al. 2013, AJ, 145, 157

Jorgenson, R. A., Murphy, M. T., Thompson, R., & Carswell, R. F. 2014, MNRAS, 443, 2783

Jorgenson, R. A., Wolfe, A. M., Prochaska, J. X., et al. 2006, ApJ, 646, 730

Junkkarinen, V., Hewitt, A., & Burbidge, G. 1991, ApJS, 77, 203

Junkkarinen, V. T., Cohen, R. D., Beaver, E. A., et al. 2004, ApJ, 614, 658

Kaplan, K. F., Prochaska, J. X., Herbert-Fort, S., Ellison, S. L., & Dessauges-Zavadsky, M. 2010, PASP, 122, 619

Kaspi, S., Brandt, W. N., Maoz, D., et al. 2007, ApJ, 659, 997

Kassin, S. A., Weiner, B. J., Faber, S. M., et al. 2007, ApJ, 660, L35

Kelvin, L. S., Driver, S. P., Robotham, A. S. G., et al. 2012, MNRAS, 421, 1007

Kennicutt, Jr., R. C. 1998, ARA&A, 36, 189

Kewley, L. J., & Ellison, S. L. 2008, ApJ, 681, 1183

Khare, P., Kulkarni, V. P., Lauroesch, J. T., et al. 2004, ApJ, 616, 86

Khare, P., vanden Berk, D., York, D. G., Lundgren, B., & Kulkarni, V. P. 2011, MNRAS, 1668

—. 2012, MNRAS, 419, 1028

Khochfar, S., & Silk, J. 2006, ApJ, 648, L21

Kim, T.-S., Partl, A. M., Carswell, R. F., & Müller, V. 2013, A&A, 552, A77

Kobulnicky, H. A., & Kewley, L. J. 2004, ApJ, 617, 240

Koekemoer, A. M., Faber, S. M., Ferguson, H. C., et al. 2011, ApJS, 197, 36

Krawczyk, C. M., Richards, G. T., Gallagher, S. C., et al. 2015, AJ, 149, 203

Kriek, M., van Dokkum, P. G., Franx, M., Illingworth, G. D., & Magee, D. K. 2009a, ApJ, 705, L71

Kriek, M., van Dokkum, P. G., Labbé, I., et al. 2009b, ApJ, 700, 221

Kriek, M., van Dokkum, P. G., Franx, M., et al. 2008, ApJ, 677, 219

Krogager, J.-K., Fynbo, J. P. U., Møller, P., et al. 2012, MNRAS, 424, L1

Krogager, J.-K., Fynbo, J. P. U., Ledoux, C., et al. 2013, MNRAS, 433, 3091

Krogager, J.-K., Geier, S., Fynbo, J. P. U., et al. 2015, ApJS, 217, 5

Kudritzki, R.-P., Urbaneja, M. A., Gazak, Z., et al. 2012, ApJ, 747, 15

Kulkarni, V. P., & Fall, S. M. 2002, ApJ, 580, 732

Labbé, I., Huang, J., Franx, M., et al. 2005, ApJ, 624, L81

Lacy, M., Petric, A. O., Sajina, A., et al. 2007, AJ, 133, 186

Lanzetta, K. M., Wolfe, A. M., & Turnshek, D. A. 1995, ApJ, 440, 435

Lanzetta, K. M., Wolfe, A. M., Turnshek, D. A., et al. 1991, ApJS, 77, 1

Larson, K. A., Whittet, D. C. B., & Hough, J. H. 1996, ApJ, 472, 755

Laursen, P., Duval, F., & Östlin, G. 2013, ApJ, 766, 124

Laursen, P., Razoumov, A. O., & Sommer-Larsen, J. 2009, ApJ, 696, 853

Laursen, P., Sommer-Larsen, J., & Andersen, A. C. 2009, ApJ, 704, 1640

Ledoux, C., Noterdaeme, P., Petitjean, P., & Srianand, R. 2015, A&A, 580, A8

Ledoux, C., Petitjean, P., Bergeron, J., Wampler, E. J., & Srianand, R. 1998, A&A, 337, 51

Ledoux, C., Petitjean, P., Fynbo, J. P. U., Møller, P., & Srianand, R. 2006, A&A, 457, 71

Ledoux, C., Petitjean, P., & Srianand, R. 2003, MNRAS, 346, 209

Leighly, K. M., Terndrup, D. M., Baron, E., et al. 2014, ApJ, 788, 123

Levshakov, S. A., & Varshalovich, D. A. 1985, MNRAS, 212, 517

Lissauer, J. J. 1993, ARA&A, 31, 129

Liszt, H. 2014, ApJ, 783, 17

Maddox, N., Hewett, P. C., Péroux, C., Nestor, D. B., & Wisotzki, L. 2012, MNRAS, 424, 2876

Maddox, N., Hewett, P. C., Warren, S. J., & Croom, S. M. 2008, MNRAS, 386, 1605

Maiolino, R., Marconi, A., Salvati, M., et al. 2001, A&A, 365, 28

Malhotra, S. 1997, ApJ, 488, L101

Man, A. W. S., Toft, S., Zirm, A. W., Wuyts, S., & van der Wel, A. 2012, ApJ, 744, 85

Mannucci, F., Cresci, G., Maiolino, R., Marconi, A., & Gnerucci, A. 2010, MNRAS, 408, 2115

Marshall, H. L., Huchra, J. P., Tananbaum, H., et al. 1984, ApJ, 283, 50

Matthews, T. A., & Sandage, A. R. 1963, ApJ, 138, 30

McLure, R. J., Pearce, H. J., Dunlop, J. S., et al. 2013, MNRAS, 428, 1088

Melioli, C., de Gouveia Dal Pino, E. M., & Geraissate, F. G. 2013, MNRAS, 430, 3235

Meusinger, H., Schalldach, P., Scholz, R.-D., et al. 2012, A&A, 541, A77

Meyer, D. M., & Roth, K. C. 1990, ApJ, 363, 57

Misma, A., & Li, A. 2015, arXiv:1507.06599, accepted for publication in ApJ

Møller, P., & Warren, S. J. 1998, MNRAS, 299, 661

Modigliani, A., Goldoni, P., Royer, F., et al. 2010, in Society of Photo-Optical Instrumentation Engineers (SPIE) Conference Series, Vol. 7737, Society of Photo-Optical Instrumentation Engineers (SPIE) Conference Series

Møller, P., Fynbo, J. P. U., & Fall, S. M. 2004, A&A, 422, L33

Møller, P., Fynbo, J. P. U., Ledoux, C., & Nilsson, K. K. 2013, MNRAS, 430, 2680

Møller, P., & Warren, S. J. 1993, A&A, 270, 43

Monier, E. M., Turnshek, D. A., & Rao, S. 2009, MNRAS, 397, 943

Murphy, M. T., & Liske, J. 2004, MNRAS, 354, L31

Muzzin, A., Marchesini, D., Stefanon, M., et al. 2013, ApJS, 206, 8

Naab, T., Johansson, P. H., & Ostriker, J. P. 2009, ApJ, 699, L178

Naab, T., & Trujillo, I. 2006, MNRAS, 369, 625

Nagamine, K., Wolfe, A. M., Hernquist, L., & Springel, V. 2007, ApJ, 660, 945

Neeleman, M., Wolfe, A. M., Prochaska, J. X., & Rafelski, M. 2013, ApJ, 769, 54

Newman, A. B., Ellis, R. S., Bundy, K., & Treu, T. 2012, ApJ, 746, 162

Nilsson, K. K., & Møller, P. 2009, A&A, 508, L21

Nilsson, K. K., Tapken, C., Møller, P., et al. 2009, A&A, 498, 13

Nipoti, C., Treu, T., Auger, M. W., & Bolton, A. S. 2009, ApJ, 706, L86

Nipoti, C., Treu, T., Leauthaud, A., et al. 2012, MNRAS, 422, 1714

Nishiyama, S., Nagata, T., Tamura, M., et al. 2008, ApJ, 680, 1174

Nishiyama, S., Tamura, M., Hatano, H., et al. 2009, ApJ, 696, 1407

Noterdaeme, P., Ledoux, C., Petitjean, P., & Srianand, R. 2008, A&A, 481, 327

Noterdaeme, P., Ledoux, C., Srianand, R., Petitjean, P., & Lopez, S. 2009a, A&A, 503, 765

Noterdaeme, P., Petitjean, P., Ledoux, C., et al. 2010, A&A, 523, A80+

Noterdaeme, P., Petitjean, P., Ledoux, C., & Srianand, R. 2009b, A&A, 505, 1087

Noterdaeme, P., Petitjean, P., & Srianand, R. 2015, A&A, 578, L5

Noterdaeme, P., Petitjean, P., Carithers, W. C., et al. 2012a, A&A, 547, L1

Noterdaeme, P., Laursen, P., Petitjean, P., et al. 2012b, A&A, 540, A63

O'Meara, J. M., Prochaska, J. X., Burles, S., et al. 2007, ApJ, 656, 666

Onodera, M., Daddi, E., Gobat, R., et al. 2010, ApJ, 715, L6

Onodera, M., Renzini, A., Carollo, M., et al. 2012, ApJ, 755, 26

O'Rourke, D. J. P., Shabala, S. S., & Alexander, P. 2011, MNRAS, 418, 2145

Oser, L., Naab, T., Ostriker, J. P., & Johansson, P. H. 2012, ApJ, 744, 63

Pagel, B. E. J., Edmunds, M. G., Blackwell, D. E., Chun, M. S., & Smith, G. 1979, MNRAS, 189, 95

Patel, S. G., van Dokkum, P. G., Franx, M., et al. 2013, ApJ, 766, 15

Pei, Y. C. 1992, ApJ, 395, 130

Pei, Y. C., & Fall, S. M. 1995, ApJ, 454, 69

Pei, Y. C., Fall, S. M., & Bechtold, J. 1991, ApJ, 378, 6

Pei, Y. C., Fall, S. M., & Hauser, M. G. 1999, ApJ, 522, 604

Peng, C. Y., Ho, L. C., Impey, C. D., & Rix, H.-W. 2002, AJ, 124, 266

Péroux, C., Bouché, N., Kulkarni, V. P., York, D. G., & Vladilo, G. 2011, MNRAS, 410, 2237

—. 2012, MNRAS, 419, 3060

Péroux, C., McMahon, R. G., Storrie-Lombardi, L. J., & Irwin, M. J. 2003, MNRAS, 346, 1103

Peth, M. A., Ross, N. P., & Schneider, D. P. 2011, AJ, 141, 105

Pettini, M. 1999, in Chemical Evolution from Zero to High Redshift, ed. J. R. Walsh & M. R. Rosa, 233

Pettini, M. 2006, in The Fabulous Destiny of Galaxies: Bridging Past and Present, ed. V. Le Brun, A. Mazure, S. Arnouts, & D. Burgarella, 319

Pettini, M., King, D. L., Smith, L. J., & Hunstead, R. W. 1997, ApJ, 478, 536

Pettini, M., & Pagel, B. E. J. 2004, MNRAS, 348, L59

Pitman, K. M., Clayton, G. C., & Gordon, K. D. 2000, PASP, 112, 537

Planck Collaboration, Ade, P. A. R., Aghanim, N., et al. 2014, A&A, 571, A16

Poggianti, B. M., Calvi, R., Bindoni, D., et al. 2013, ApJ, 762, 77

Polletta, M. d. C., Wilkes, B. J., Siana, B., et al. 2006, ApJ, 642, 673

Pontzen, A., & Pettini, M. 2009, MNRAS, 393, 557

Pontzen, A., Governato, F., Pettini, M., et al. 2008, MNRAS, 390, 1349

Prochaska, J. X., Chen, H.-W., Dessauges-Zavadsky, M., & Bloom, J. S. 2007, ApJ, 666, 267

Prochaska, J. X., Gawiser, E., Wolfe, A. M., Castro, S., & Djorgovski, S. G. 2003a, ApJ, 595, L9

Prochaska, J. X., Gawiser, E., Wolfe, A. M., Cooke, J., & Gelino, D. 2003b, ApJS, 147, 227

Prochaska, J. X., Madau, P., O'Meara, J. M., & Fumagalli, M. 2014, MNRAS, 438, 476

Prochaska, J. X., & Wolfe, A. M. 1997, ApJ, 487, 73

—. 1998, ApJ, 507, 113

Rafelski, M., Neeleman, M., Fumagalli, M., Wolfe, A. M., & Prochaska, J. X. 2014, ApJ, 782, L29

Rafelski, M., Wolfe, A. M., Prochaska, J. X., Neeleman, M., & Mendez, A. J. 2012, ApJ, 755, 89

Rao, S. M., Prochaska, J. X., Howk, J. C., & Wolfe, A. M. 2005, AJ, 129, 9

Rauch, M. 1998, ARA&A, 36, 267

Rauch, M., Haehnelt, M., Bunker, A., et al. 2008, ApJ, 681, 856

Razoumov, A. O., Norman, M. L., Prochaska, J. X., & Wolfe, A. M. 2006, ApJ, 645, 55

Rees, M. J., & Ostriker, J. P. 1977, MNRAS, 179, 541

Rhoads, J. E., Malhotra, S., Richardson, M. L. A., et al. 2014, ApJ, 780, 20

Richards, G. T., Fan, X., Schneider, D. P., et al. 2001, AJ, 121, 2308

Richards, G. T., Fan, X., Newberg, H. J., et al. 2002, AJ, 123, 2945

Richards, G. T., Hall, P. B., Vanden Berk, D. E., et al. 2003, AJ, 126, 1131

Richards, G. T., Lacy, M., Storrie-Lombardi, L. J., et al. 2006, ApJS, 166, 470

Rodríguez-Ardila, A., & Mazzalay, X. 2006, MNRAS, 367, L57

Ross, N. P., Myers, A. D., Sheldon, E. S., et al. 2012, ApJS, 199, 3

Rudie, G. C., Steidel, C. C., Shapley, A. E., & Pettini, M. 2013, ApJ, 769, 146

Ryabinkov, A. I., Kaminker, A. D., & Varshalovich, D. A. 2003, A&A, 412, 707

Salim, S., Charlot, S., Rich, R. M., et al. 2005, ApJ, 619, L39

Sandage, A. 1965, ApJ, 141, 1560

Sanders, D. B., Phinney, E. S., Neugebauer, G., Soifer, B. T., & Matthews, K. 1989, ApJ, 347, 29

Savage, B. D., & Sembach, K. R. 1991, ApJ, 379, 245

Savaglio, S. 2006, New Journal of Physics, 8, 195

Schlafly, E. F., & Finkbeiner, D. P. 2011, ApJ, 737, 103

Schlegel, D. J., Finkbeiner, D. P., & Davis, M. 1998, ApJ, 500, 525

Schmidt, K. B., Marshall, P. J., Rix, H.-W., et al. 2010, ApJ, 714, 1194

Schmidt, M. 1963, Nature, 197, 1040

Schmidt, M., & Green, R. F. 1983, ApJ, 269, 352

Selsing, J., Fynbo, J. P. U., Christensen, L., & Krogager, J.-K. 2015, A&A, submitted

Shankar, F., Marulli, F., Bernardi, M., et al. 2013, MNRAS, 428, 109

Shapley, A. E. 2011, ARA&A, 49, 525

Shen, S., Mo, H. J., White, S. D. M., et al. 2003, MNRAS, 343, 978

Smette, A., Robertson, J. G., Shaver, P. A., et al. 1995, A&AS, 113, 199

Smith, H. E., Cohen, R. D., & Bradley, S. E. 1986, ApJ, 310, 583

Srianand, R., Gupta, N., Petitjean, P., & Saikia, D. J. 2008a, MNRAS, 391, L69

Srianand, R., Noterdaeme, P., Ledoux, C., & Petitjean, P. 2008b, A&A, 482, L39

Stein, W. A., Odell, S. L., & Strittmatter, P. A. 1976, ARA&A, 14, 173

Stockton, A., Canalizo, G., & Maihara, T. 2004, ApJ, 605, 37

Stockton, A., McGrath, E., Canalizo, G., Iye, M., & Maihara, T. 2008, ApJ, 672, 146

Stockton, A., Shih, H.-Y., Larson, K., & Mann, A. W. 2014, ApJ, 780, 134

Storrie-Lombardi, L. J., & Wolfe, A. M. 2000, ApJ, 543, 552

Sumi, T. 2004, MNRAS, 349, 193

Szomoru, D., Franx, M., & van Dokkum, P. G. 2012, ApJ, 749, 121

Szomoru, D., Franx, M., van Dokkum, P. G., et al. 2010, ApJ, 714, L244

Tanaka, M., Toft, S., Marchesini, D., et al. 2013, ApJ, 772, 113

Taylor, E. N., Franx, M., Glazebrook, K., et al. 2010, ApJ, 720, 723

Taylor, E. N., Franx, M., van Dokkum, P. G., et al. 2009, ApJS, 183, 295

Telfer, R. C., Zheng, W., Kriss, G. A., & Davidsen, A. F. 2002, ApJ, 565, 773

Tepper-García, T. 2006, MNRAS, 369, 2025

—. 2007, MNRAS, 382, 1375

Toft, S., Franx, M., van Dokkum, P., et al. 2009, ApJ, 705, 255

Toft, S., Gallazzi, A., Zirm, A., et al. 2012, ApJ, 754, 3

Toft, S., van Dokkum, P., Franx, M., et al. 2007, ApJ, 671, 285

Truemper, J. 1982, Advances in Space Research, 2, 241

Trujillo, I., Carrasco, E. R., & Ferré-Mateu, A. 2012, ApJ, 751, 45

Trujillo, I., Cenarro, A. J., de Lorenzo-Cáceres, A., et al. 2009, ApJ, 692, L118

Trujillo, I., Ferré-Mateu, A., Balcells, M., Vazdekis, A., & Sánchez-Blázquez, P. 2014, ApJ, 780, L20

Trujillo, I., Förster Schreiber, N. M., Rudnick, G., et al. 2006, ApJ, 650, 18

Tully, R. B., & Fisher, J. R. 1977, A&A, 54, 661

Tyson, N. D. 1988, ApJ, 329, L57

Urrutia, T., Becker, R. H., White, R. L., et al. 2009, ApJ, 698, 1095

van de Sande, J., Kriek, M., Franx, M., et al. 2011, ApJ, 736, L9

—. 2013, ApJ, 771, 85

van der Wel, A., Rix, H.-W., Wuyts, S., et al. 2011, ApJ, 730, 38

van der Wel, A., Bell, E. F., Häussler, B., et al. 2012, ApJS, 203, 24

van der Wel, A., Franx, M., van Dokkum, P. G., et al. 2014, ApJ, 788, 28

van Dokkum, P. G. 2001a, PASP, 113, 1420

—. 2001b, PASP, 113, 1420

van Dokkum, P. G., Kriek, M., & Franx, M. 2009, Nature, 460, 717

van Dokkum, P. G., Franx, M., Kriek, M., et al. 2008a, ApJ, 677, L5

—. 2008b, ApJ, 677, L5

van Dokkum, P. G., Whitaker, K. E., Brammer, G., et al. 2010, ApJ, 709, 1018

Vanden Berk, D. E., Richards, G. T., Bauer, A., et al. 2001, AJ, 122, 549

Veilleux, S., Rupke, D. S. N., & Swaters, R. 2009, ApJ, 700, L149

Vernet, J., Dekker, H., D'Odorico, S., et al. 2011, A&A, 536, A105

Vestergaard, M., & Wilkes, B. J. 2001, ApJS, 134, 1

Vladilo, G., Centurión, M., Levshakov, S. A., et al. 2006, A&A, 454, 151

Vladilo, G., & Péroux, C. 2005, A&A, 444, 461

Vladilo, G., Prochaska, J. X., & Wolfe, A. M. 2008, A&A, 478, 701

Wang, J., Hall, P. B., Ge, J., Li, A., & Schneider, D. P. 2004, ApJ, 609, 589

Wang, J.-G., Zhou, H.-Y., Ge, J., et al. 2012, ApJ, 760, 42

Warren, S. J., Hambly, N. C., Dye, S., et al. 2007, MNRAS, 375, 213

Warren, S. J., Hewett, P. C., & Foltz, C. B. 2000, MNRAS, 312, 827

Weatherley, S. J., Warren, S. J., Møller, P., et al. 2005, MNRAS, 358, 985

Webster, R. L., Francis, P. J., Petersont, B. A., Drinkwater, M. J., & Masci, F. J. 1995, Nature, 375, 469

Weinzirl, T., Jogee, S., Conselice, C. J., et al. 2011, ApJ, 743, 87

Welty, D. E., & Fowler, J. R. 1992, ApJ, 393, 193

Whitaker, K. E., Kriek, M., van Dokkum, P. G., et al. 2012, ApJ, 745, 179

White, R. L., Helfand, D. J., Becker, R. H., Glikman, E., & de Vries, W. 2007, ApJ, 654, 99

Williams, R. J., Quadri, R. F., Franx, M., van Dokkum, P., & Labbé, I. 2009, ApJ, 691, 1879

Williams, R. J., Quadri, R. F., Franx, M., et al. 2010, ApJ, 713, 738

Wolfe, A. M., Gawiser, E., & Prochaska, J. X. 2005, ARA&A, 43, 861

Wolfe, A. M., Lanzetta, K. M., Foltz, C. B., & Chaffee, F. H. 1995, ApJ, 454, 698

Wolfe, A. M., Prochaska, J. X., & Gawiser, E. 2003, ApJ, 593, 215

Wolfe, A. M., Prochaska, J. X., Jorgenson, R. A., & Rafelski, M. 2008, ApJ, 681, 881

Wolfe, A. M., Turnshek, D. A., Smith, H. E., & Cohen, R. D. 1986, ApJS, 61, 249

Wright, E. L. 1981, ApJ, 250, 1

Wu, X.-B., Zuo, W., Yang, J., Yang, Q., & Wang, F. 2013, AJ, 146, 100

Wuyts, S., Cox, T. J., Hayward, C. C., et al. 2010, ApJ, 722, 1666

Wuyts, S., Labbé, I., Franx, M., et al. 2007, ApJ, 655, 51

York, D. G., Adelman, J., Anderson, Jr., J. E., et al. 2000, AJ, 120, 1579

York, D. G., Khare, P., Vanden Berk, D., et al. 2006, MNRAS, 367, 945

Zafar, T., & Watson, D. 2013, A&A, 560, A26

Zafar, T., Watson, D., Elíasdóttir, Á., et al. 2012, ApJ, 753, 82

Zafar, T., Møller, P., Watson, D., et al. 2015, A&A, submitted

Zhou, H., Ge, J., Lu, H., et al. 2010, ApJ, 708, 742

Zirm, A. W., van der Wel, A., Franx, M., et al. 2007, ApJ, 656, 66